Experimental Analysis of Geometric, Pressure Gradient and Surface Temperature Effects on Boundary-Layer Transition in Compressible High Reynolds Number Flows

(*Experimentelle Analyse von Geometrie-, Druckgradienten- und Oberflächentemperatureffekten auf die Grenzschichttransition in kompressiblen Strömungen bei hoher Reynolds-Zahl*)

Von der Fakultät für Maschinenwesen der Rheinisch-Westfälischen Technischen Hochschule Aachen zur Erlangung des akademischen Grades eines Doktors der Ingenieurwissenschaften genehmigte Dissertation

vorgelegt von

Marco Costantini

Berichter: Univ.-Prof. Dr.-Ing. W. Schröder
Univ.-Prof. Dr. rer. nat. Dr.-Ing. habil A. Dillmann

Tag der mündlichen Prüfung: 22. November 2016

boundary layer, transition, step, pressure gradient, non-adiabatic surface, temperature-sensitive paint

Marco COSTANTINI

Experimental Analysis of Geometric, Pressure Gradient and Surface Temperature Effects on Boundary-Layer Transition in Compressible High Reynolds Number Flows

Dissertation Rheinisch Westfälisch Technische Hochschule Aachen, 2016

The effect of sharp forward-facing steps on boundary-layer transition was systematically investigated in this experimental work in combination with the influence of changes in the following parameters: streamwise pressure gradient, Reynolds number, Mach number, and a non-adiabatic surface. The investigations were carried out in a quasi-two-dimensional flow at high Reynolds numbers and at both low and high subsonic Mach numbers in the Cryogenic Ludwieg-Tube Göttingen. The adopted experimental setup allowed an independent variation of the aforementioned parameters and enabled a decoupling of their respective effects on the boundary-layer transition. Transition, measured non-intrusively by means of temperature-sensitive paint, was found to move gradually upstream towards the step location with increasing step Reynolds number and relative step height. Stronger flow acceleration and lower wall temperature ratios led to an increase in the transition Reynolds number even in the presence of forward-facing steps; this favorable influence became, however, less pronounced at larger values of the non-dimensional step parameters. The representation of the results using the relative change in transition location with respect to the step location, plotted against the non-dimensional step parameters, gave good correlation and allowed the effect of the steps on boundary-layer transition to be isolated from the influence of variations in the other parameters. The present results were demonstrated to be applicable and transferable to the practical case of a natural laminar flow airfoil. Criteria for acceptable heights of forward-facing steps on unswept and moderately swept natural laminar flow surfaces can now be derived from the functional relations determined in this work.

Grenzschicht, Transition, Stufe, Druckgradient, nicht-adiabate Wand, temperaturempfindliche Farbe

Marco COSTANTINI

Experimentelle Analyse von Geometrie-, Druckgradienten- und Oberflächentemperatureffekten auf die Grenzschichttransition in kompressiblen Strömungen bei hoher Reynolds-Zahl

Dissertation Rheinisch Westfälisch Technische Hochschule Aachen, 2016

Im Rahmen dieser experimentellen Arbeit wurde die Auswirkung von scharfkantigen vorwärtsgerichteten Stufen auf die Grenzschichttransition in einer quasi-zweidimensionalen kompressiblen Strömung systematisch untersucht. Folgende Parameter wurden hierbei variiert: Stufenhöhe, Oberflächendruckgradient, Oberflächentemperatur, Mach-Zahl und Reynolds-Zahl. Die Untersuchungen wurden bei hohen Reynolds-Zahlen und subsonischen Mach-Zahlen im Kryo-Rohrwindkanal Göttingen durchgeführt. Der gewählte experimentelle Aufbau ermöglichte, die oben genannten Parameter unabhängig voneinander zu variieren und somit deren Auswirkung auf die Grenzschichttransition zu entkoppeln. Mittels temperaturempfindlicher Farbe konnte gezeigt werden, dass sich die Transition mit zunehmender Stufen-Reynolds-Zahl und relativer Stufenhöhe allmählich stromauf verschiebt. Trotz Stufen wurden zunehmende Transitions-Reynolds-Zahlen bei stärkerer Strömungsbeschleunigung und niedrigerem Wandtemperaturverhältnis erzielt. Dieser vorteilhafte Einfluss wurde jedoch mit zunehmender Stufenhöhe schwächer. Die Ergebnisse zeigen eine gute Korrelation, wenn die relative Variation der Transitionslage in Bezug zur Stufenposition als Funktion der dimensionslosen Stufenparameter dargestellt wird. Somit konnte die Auswirkung der Stufen auf die Transition vom Einfluss anderer Faktoren isoliert werden. Es wurde ebenso gezeigt, dass die vorliegenden Ergebnisse auf Laminarprofile übertragbar sind. Somit kann die Bestimmung einer zulässigen Stufenhöhe für Laminaroberflächen ohne bzw. mit moderater Pfeilung auf Grundlage dieser Arbeit erfolgen.

To my grandfather Massimo,
who instilled in me the value of accurate work,
and to my aunt Donatella,
who showed me the passion to discover other cultures.

Acknowledgements

This work is the outcome of about five and a half years of research at the Institute of Aerodynamics and Flow Technology of the Deutsches Zentrum für Luft- und Raumfahrt e. V. (DLR) in Göttingen. The completion of this work would not have been possible without the contribution of a number of people.

First of all, I would like to acknowledge my academic supervisor Prof. Dr. Wolfgang Schröder, Head of the Institute of Aerodynamics, Rheinisch-Westfälische Technische Hochschule Aachen, and my academic co-supervisor Prof. Dr. Andreas Dillmann, Head of the Institute of Aerodynamics and Flow Technology of DLR, for their guidance and advice during this doctoral project and for refereeing this dissertation. I am thankful to Prof. Dr. Schröder also for giving me the chance to present the results of my research at the seminars of the Institute of Aerodynamics, where I benefited from the interesting discussions. I am grateful to Prof. Dr. Dillmann for supporting the measurement campaigns in the Cryogenic Ludwieg-Tube Göttingen (KRG) of the German-Dutch Wind Tunnels organization (DNW).

I would like to express my gratitude to all the members of the Pressure- and Temperature-Sensitive Paint group in the Experimental Methods department, in which I was very glad to work in. In particular, I am deeply indebted to my research coordinator, Dr. Christian Klein, who kindly motivated me, continuously guided and supported my work throughout these years, and also applied the temperature-sensitive paint to the wind-tunnel model. He always found the time for constructive comments that helped me to further improve the quality of my work. I am very grateful to Dr. Walter H. Beck, who generously assisted me during the drafting of this work. The preparation of the experiments, the analysis of the data, and the presentation of the results benefited from the numerous conversations with Dr. Beck. Moreover, I would like to thank: Dr. Ulrich Henne and Dr. Werner E. Sachs, who continuously supported me in the data acquisition and analysis; Dr. Uwe Fey (now in the Fluid Systems department), who assisted me in the first months learning the temperature-sensitive paint measurement technique and in my first test campaign; Steffen Risius, who supported me during my latest test campaigns; and Jonathan Ost and Waldemar Lang, who helped me ordering my thoughts through several conversations in our office.

I am very grateful to Dr. Lars Koop, Head of the Experimental Methods department, for his constant support to this doctoral project. He employed me as a researcher at DLR, supported the design and manufacturing of the wind-tunnel model used in the experiments, and allowed me to present the results of my studies at international conferences. Dr. Koop and Dr. Robert Konrath are also acknowledged for their assistance during the drafting of this work.

This work could be completed also thanks to the fruitful cooperation with the High Speed Configurations department. I am very grateful to: Dr. Stefan Hein, who was an inexhaustible source of knowledge on boundary-layer transition, assisted me during the definition of the tests and the analysis of the results, and helped me with the boundary-layer stability computations; Dr. Stefan Koch, who guided me during the preparation and conduction of the experimental campaigns and assisted me in the data evaluation; Dr. Henning Rosemann, who advised me during the definition and conduction of this doctoral project; Lukas Schojda, who supported the design of the wind-tunnel model with numerical investigations; and Uwe G. Becker, who carried out the constructional drawing of the wind-tunnel model.

Airbus S.A.S. is gratefully acknowledged for having financially supported my activities via an industrial partnership. I am thankful that my research was enriched by an interest for practical applications through the interaction with employees of Airbus S.A.S. In particular, I would like to thank: my industrial supervisor, Dr. Winfried Kühn, for his advice in this doctoral project and for encouraging me to further investigate several aspects related to boundary-layer transition; Dr. Sven Schaber for his support to my research activities and his guidance during the preparation of the wind-tunnel model; and Dr. Géza Schrauf for his constructive comments to the results of boundary-layer stability analysis.

The temperature-sensitive paint used in this work was developed in cooperation with the Institute of Bioorganic Chemistry of the University of Hohenheim. Dr. Vladimír Ondruš is acknowledged for its chemical development.

I am grateful to the DLR technicians Carsten Fuchs and Tobias Kleindienst for their support during the preparation and instrumentation of the wind-tunnel model as well as during the modifications of the model configuration. Mr. Fuchs' efforts for achieving a smooth and fair model surface are particularly acknowledged. I would also like to thank the secretaries of the Experimental Methods department, Ilka Micknaus and Catrin Rosenstock, for their administrative support to my research activities during these years.

The experiments were conducted in the DNW-KRG wind tunnel. I am thankful to Rainer Kahle, Martin Aschoff, and Stefan Hucke for their support during the test campaigns and for meeting my wishes regarding the test procedure and the experimental setup.

The wind-tunnel model was manufactured by Deharde Maschinenbau Helmut Hoffmann GmbH. Silke von Deetzen, Matthias Müller, Peter Hayen, Georg Löschen, Holger Tholen, and Ralf Twele are acknowledged for their support.

I would like to thank also my friends and my family, in particular my father Vincenzo, my mother Linda, and my brother Lorenzo, for the affection they have given to me in all these years.

Dulcis in fundo, I deeply thank my wife, Marie, for all the love and the support she has given to me, in the good times and in bad. She brings out the best in me.

Table of contents

1 Introduction

More than three billion passengers made use of air transport in 2014 to help them meet their business and tourism needs [1]. As shown in Fig. 1.1a, world annual air traffic has been continuously growing since 1970, except for short periods coincident with crises. The average world annual traffic growth in terms of revenue passenger kilometers (RPKs) is approximately 5 %, corresponding to a doubling of air traffic every 15 years. Global air traffic is expected to continue to grow at this rate also in the near distant future. Planning for this air travel forecast, the European Commission published in 2001 the Vision 2020 document [2,3], setting for the new aircraft of 2020 the goal of a 50 % cut in CO_2 emissions and an 80 % cut in NO_x emissions. Based on this vision, the European Commission issued ten years later the Flightpath 2050 document [4], in which the aforementioned targets had been updated to a 75 % reduction in CO_2 emissions and a 90 % reduction in NO_x emissions, relative to the capabilities of typical new aircraft in 2000.

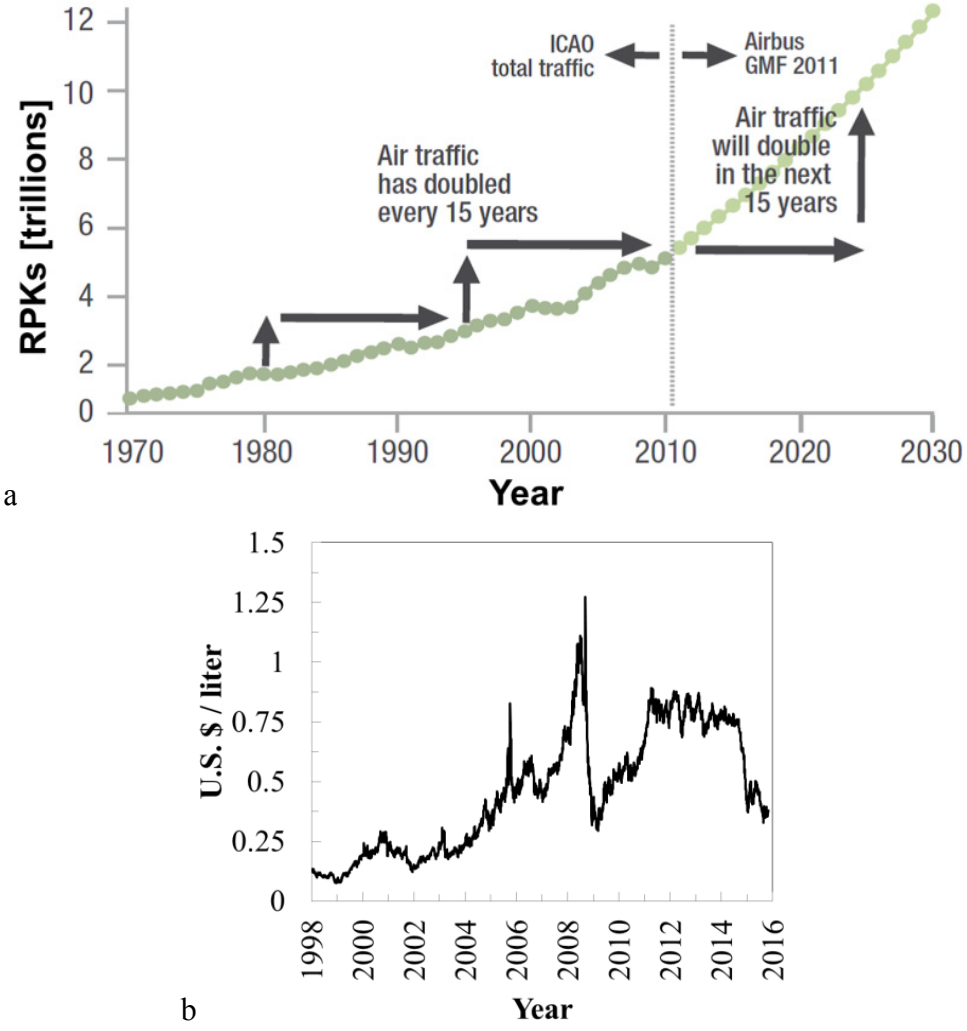

Fig. 1.1. a: development of world annual air traffic [5]. b: development of U.S. Gulf Coast spot price for kerosene-type jet fuel [6].

The environmental impact of aviation has to be mitigated to the extent where it more than offsets the effects of increasing traffic levels. This is to be achieved by a combination of technological development, operational procedures, and market-based incentives. Part of the goal of emission reductions can be attained by improvement in materials, engines, manufacturing processes, systems optimization and integration, infrastructure, fuel, and operational procedures [4]. However, the benefits gained by advances in these disciplines will not be sufficient to reach the Flightpath 2050 targets: improvements in the aircraft aerodynamics, in particular in the reduction of drag, are needed. Implementation of drag reduction technologies is clearly motivated also by the related improvements in aircraft fuel consumption, range, and endurance. Reduction of fuel usage will not only help to reduce aircraft emissions, but also to extend the availability of the limited supplies of petroleum [7]. Airlines are strongly interested in lower fuel consumption of transport aircraft. The fuel price had decreased in the period May 2011 to October 2015, but it nevertheless still remains high. In October 2015, the fuel price was about three times higher than that at the end of 2001 [6], as can be seen in Fig. 1.1b. Fuel costs account for a large proportion of airline operating expenses (e.g., 21.5 % in 2014 for Lufthansa, a globally operating aviation group [8]). Clearly, a decrease in fuel consumption obtained by means of drag reduction technologies would have a significant effect on the airline operating costs. Note that the benefits of reduced drag would be maximized by the reduction of aircraft size that would be made possible by the use of drag reduction technologies [9,10]. Moreover, reduced drag would allow the design of long-range or long-endurance aircraft, such as high-altitude long-endurance vehicles [11,12].

The various components of drag for typical business jet and commercial transport aircraft in cruising flight is shown in Fig. 1.2a [13]. Skin-friction drag is the major source of drag, contributing about half of the total aircraft drag. The boundary layer on current transport aircraft is mostly turbulent [7]. The reduction of turbulent viscous drag can be achieved by means of passive devices such as riblets [14,15], active devices such as spanwise traveling transversal surface waves [16,17], and their combination [18]. Substantial friction drag reduction requires, however, maintaining laminar flow over large portions of the aircraft surfaces: in fact, at the high Reynolds numbers typical for transport aircraft, the skin-friction coefficient of laminar flow is about one order of magnitude lower than that for turbulent flow [10,19-20]. A comparison of the viscous drag breakdown for transport aircraft with and without laminar flow over lifting surfaces [13] is shown in Fig. 1.2b. The process leading a laminar boundary layer to turbulence is discussed later in Chapter 2.

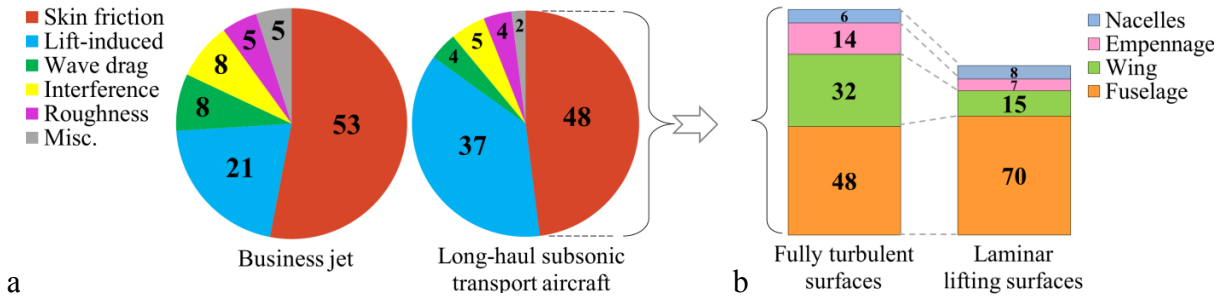

Fig. 1.2. a: various components of total airframe drag for business jet and subsonic transport aircraft. b: viscous drag breakdown for subsonic transport aircraft with and without laminar flow over lifting surfaces. Values in percentage [13].

Several estimates of potential fuel savings and related reductions of airline operating costs by means of laminar flow (LF) technology can be found in the literature [7,9-10,13,15,21]. The substantial performance improvement promised by the attainment of laminar flow has made it the "pot of the gold at the end of the rainbow for aeronautical researchers" [7]. A realistic estimate is probably that of approximately 15-16 % total drag reduction with respect to the turbulent flow baseline [15,21-22], accomplished by achievement of laminar flow over 40 % of the surfaces of wings, horizontal and vertical tail planes, and engine nacelles [22]. This would lead to a cut in airline direct operating costs of more than 3 % for a large transport aircraft [15]. Similarly, attainment of laminar flow on 50 % of the wing upper surface and both surfaces of horizontal and vertical tail planes, with an additional 40 % on the nacelle surface, would lead to reductions of approximately 6 %, 10 %, and 18 % in operating empty weight, take-off gross weight, and block fuel, respectively. It would also lead to an increase of approximately 15 % in lift-to-drag ratio [10]. Achievement of laminar flow on the fuselage is difficult because of the very large Reynolds numbers [22], but even this surface can be designed to help promote laminar flow [13,23]. Transition Reynolds numbers up to $20 \cdot 10^6$ may be possible, corresponding to a preservation of laminar flow over half the length of a typical business aircraft fuselage and over the forward portion of fuselages of large transport aircraft [13]. The main concerns for achievement of laminar flow are more related to several imperfections which may be present on the fuselage surface, as it will be outlined below.

Clearly, LF technology can be combined with other technologies in order to reduce drag; these include the aforementioned devices for turbulent viscous drag reduction [14-18], wing-tip devices for lift-induced drag, shock control devices and trailing-edge devices for wave drag [15]. Nevertheless, LF technology has the largest potential for drag reduction of any of these technologies [7] and can offer breakthrough improvements in aircraft efficiency [10]. Past research [7,10] has demonstrated the effectiveness of LF technology for a wide range of aircraft classes, including commercial large transport aircraft [24]. Nowadays, this technology is a practical reality for sailplanes, general aviation, turboprops, and

business jets [23,25-27], but has not yet been applied to any large transport aircraft. According to press releases in 2013, however, the Boeing Company offers customers the implementation of LF technology on the winglets of the Boeing 737 MAX aircraft and on the surfaces of horizontal and vertical tail planes of the Boeing 787-9 and 787-10 aeroplanes [28,29].

The major concern about LF technology is not whether laminar flow can be obtained, but whether the technology can be applied under typical production standards [27], and whether the increased extent of laminar flow regions can be maintained under normal operating conditions [9,10]. Surface imperfections can induce the amplification of existing (or potentially existing) disturbances within the laminar boundary layer and/or the generation of additional instabilities, thus leading to premature transition to turbulence [30-32]. Knowledge available on the effects of surface imperfections on boundary-layer stability and transition is summarized in Section 2.5. In fact, the main reason for the hesitation of aircraft manufacturers to introduce LF technology to aeroplanes flying at high Reynolds numbers is the stringent requirements for surface quality which have to be fulfilled to achieve laminar flow [7,9-10,27]. From the survey of earlier research (1930's to 1960's) presented in Appendix A.1, it can be seen that the difficulty in manufacturing sufficiently smooth (roughness-free) and fair (wave-free) surfaces was the principal reason for the failure in attaining extensive LF regions on the considered aircraft surfaces [7,9-10,27]. Modern manufacturing techniques for metallic and composite materials can now provide surface smoothness and fairness suitable for laminar flow [10,26]. This was demonstrated in flight experiments on aerodynamic surfaces that did not receive any special contour or surface waviness modification [25,26]. The examined surfaces had modern production-quality smoothness and fairness, achieved on either metallic or composite materials. Currently, the key development necessary for large-scale application of LF technology is that of a structural design capable of fulfilling the stringent aerodynamic requirements for the surface, while at the same time maintaining aircraft weight low, manufacturing costs acceptable, and production rates high [7,27]. The optimal design from an aerodynamic point of view – a continuous surface without any seams – would not be conducive for systems integration and practical needs. A seam between leading-edge part and wing box would facilitate inspection and repair, but steps and/or gaps would exist at the junction [27]. Such surface discontinuities would also arise from the installation of:

- leading-edge panels on wings, nacelles, and tail surfaces;
- high-lift devices such as slats and Krueger flaps;
- inspection and access panels on all surfaces eligible for laminar flow;
- doors and windows on the forward part of the fuselage [30,31].

Further imperfections that can affect aircraft surfaces are waviness (at or between ribs and stringers and in the region of flush rivets) and three-dimensional roughness elements, such as flush screw head slots and incorrectly installed flush rivets. Note that surface imperfections can arise or become more pronounced under aerodynamic loading [9]. Accumulation of dirt, insects, and ice, as well as material erosion, are also major operational concerns for achievement of laminar flow [7,26-27]. Active and passive systems have been shown to be effective in avoiding accumulation of ice and insects [7,10,27]. Icing is not considered as a technical obstacle, but rather as a system-design problem [10]. Erosion-resistant coatings are currently being developed [27].

1.1 Scope of work

The majority of the aforementioned surface imperfections can be avoided on modern aircraft surfaces or, if present, are likely to be of allowable size for maintenance of laminar flow. Discontinuities in the form of steps and gaps at structural joints, however, are probably unavoidable [30-31,33]. Gaps can be smoothed by means of aerodynamic fillers [33]. Backward-facing steps are more critical than forward-facing steps [30,33-34]. Accordingly, the joint on the aircraft surface of interest for laminar flow should be designed to avoid backward-facing steps. Forward-facing steps can still be present at such structural joints, but their size has to be commensurate with laminar boundary-layer maintenance. Therefore, the essential question is whether laminar flow can be achieved over forward-facing steps, thus maintaining the related advantages in terms of drag reduction. Manufacturing tolerances must be specified for the shape and dimension of the imperfections so that laminar flow can still be achieved, without, however, being overly stringent. Fulfilling unnecessarily strict tolerances would have a profound effect on tooling design and overall production approach, which have direct implications on manufacturing costs and time, field support, and aircraft mission turnaround [12,27]. A guide is therefore needed for size and shape of forward-facing steps in order to specify manufacturing tolerances as precisely as possible [10,12,27,30-31,35-36]. Allowable tolerances can be provided only after the effects of the surface imperfections on boundary-layer transition have been understood and quantified. Past experimental and numerical research examined the effect on transition of forward-facing steps only for specific surface geometries and flow conditions [12,30,35-49]. Criteria covering a wide range of boundary-layer stability situations are not available.

This work focuses on sharp forward-facing steps which are perpendicular to the surface of interest. As discussed below and later in Section 2.5, this geometry is the most critical for this type of imperfection and can be regarded as a worst-case scenario. Thus, criteria for allowable tolerances should be developed for this geometry; the tolerances can then be relaxed for less crucial shapes. Gaps and backward-facing steps will not be examined in the present work, since they should be avoided on aircraft surfaces designed to achieve extended regions of

laminar flow (see above). Numerical investigations have improved the understanding of the influence of surface imperfections on boundary-layer stability and transition. However, computation of a flowfield over sharp forward-facing steps is still resource-intensive [31,35-36,45-46], so that a parametric study can be performed only for a selected configuration and a limited variation of flow conditions [35-36,45-46]. Less resource-intensive methods, based on linear stability theory and, more specifically, on the e^N method (see Section 2.2.1 and 2.4, respectively) have been developed to predict transition in the presence of forward-facing steps [38,40-41,50]. However, these methods don't work well when applied at conditions different from those used for their calibration [46]. Numerical studies have been carried out only for flat-plate configurations at zero pressure gradient [35-36,38,45-46]. The influence of a non-adiabatic surface on boundary-layer stability has been examined in only one single case [45]. Experiments can be conducted in flight [30,47], thus allowing also investigation of the effects of Reynolds number and Mach number, but this choice clearly implies higher costs and increasing complexity. Moreover, various other factors influencing boundary-layer stability and transition (especially those related to atmospheric conditions) cannot be controlled in the flight environment. Experiments in low-disturbance wind tunnels remain the most effective research approach to investigate the influence of sharp steps on boundary-layer transition, especially when the effect of other factors is also to be examined. To further illustrate the scope of the present work, it would be beneficial to look at earlier investigations on surface steps, which will be discussed in more detail in Section 2.5. A summary of the flow conditions considered in past work [12,30,35-49] is shown in graphical form in Fig. 1.1.1, where the Reynolds number based on the step location $\mathrm{Re}_{xh} = U_\infty x_h / \nu_\infty$ and the freestream Mach number are chosen as the characteristic flow parameters. (x_h is the step location; U_∞ and ν_∞ are the freestream velocity and the freestream kinematic viscosity, respectively.) The flight conditions characteristic of different wing sections for hypothetical transport aircraft employing natural laminar flow (NLF) wings with the size of an Airbus A320 aeroplane [51] are also shown in Fig. 1.1.1, for comparison. NLF surfaces are designed to achieve extended regions of favorable pressure gradient, thus allowing large areas of laminar flow to be attained without the need for active flow control systems [22,25,33,53]. The flight envelope shown in Fig. 1.1.1 encompasses the flight phases from take-off to cruise conditions. It has been derived from a typical mission of an Airbus A320 aeroplane [52], with forward-facing steps having been placed at x_h/c = 15 % of the NLF wings. The derivation of this flight envelope is discussed in Appendix A.2.

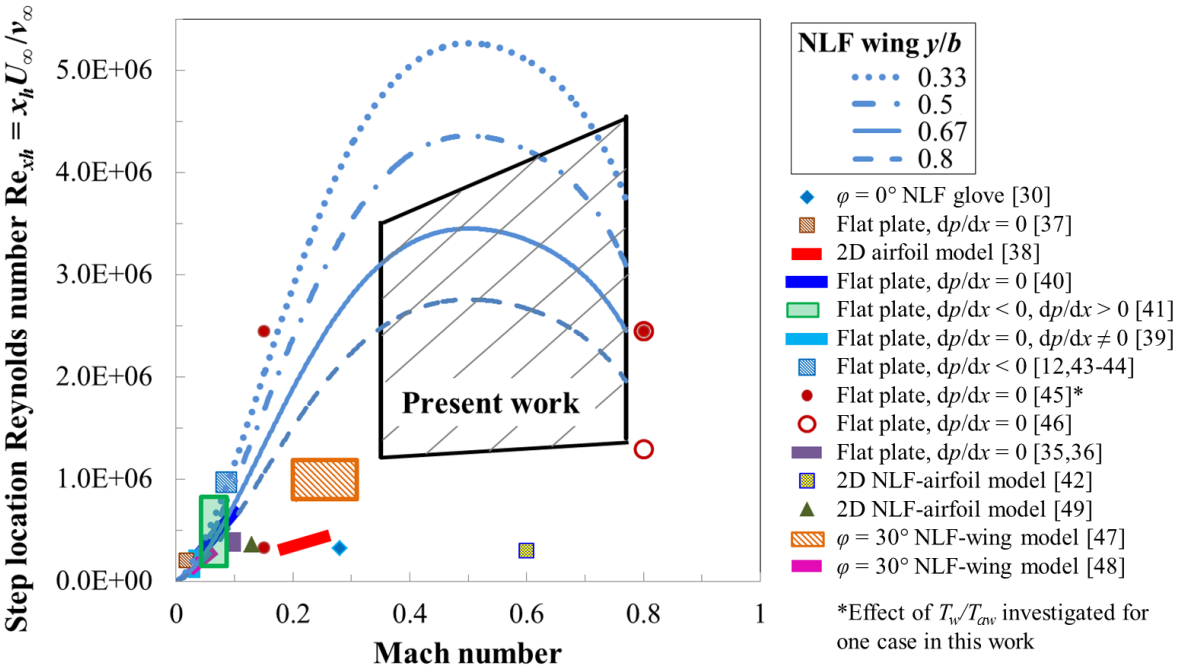

Fig. 1.1.1. Comparison of the flow conditions examined in the present work with those considered in past work. The influence of a non-adiabatic surface on boundary-layer transition has not been investigated in past work (except for one single case in [45] – see legend). Flight conditions characteristic of different wing sections for hypothetical transport aircraft employing NLF wings are also shown. (*y* is the spanwise coordinate, positive starting from the wing root to the wing tip; *b* is the wing span.) The flight envelope for the NLF wing has been derived from a typical mission of an Airbus A320 aeroplane [51,52] (see Appendix A.2).

As can be seen in Fig. 1.1.1, most of the previous work focused on Mach and Reynolds numbers lower than those characteristic of commercial transport aircraft. A brief discussion of earlier experimental investigations on forward-facing steps is given below.

- Experiments in wind tunnels have been performed almost exclusively at low speed [12,37-41,43-44,48]. The Mach number was below $M = 0.3$, except for one single case examined in [42] ($M = 0.6$). The examined unit Reynolds numbers Re/c were also relatively low ($Re/c < 3 \cdot 10^6$ m^{-1} in [12,37,39-44,48-49], $Re/c < 6 \cdot 10^6$ m^{-1} in [38]). Experiments were also conducted in flight [30,47], but still at $M < 0.35$ and $Re/c < 6 \cdot 10^6$ m^{-1}.
- The test configuration of choice in most of the previous wind-tunnel experiments was that of a flat plate [12,37,39-41,43-44]. The streamwise pressure gradient was zero in [37,40]. Some studies considered the influence of the streamwise pressure gradient [12,38-39,41,43-44], but in these cases the pressure distribution in the streamwise direction was generally not uniform. In particular, the pressure gradients at the step location and at the transition location were different. Moreover, the effect of the streamwise pressure gradient on boundary-layer transition had not

been systematically investigated, with only a limited number of pressure distributions being examined.

- The effect on transition of the surface heat flux has never been investigated at subsonic speeds.
- The shape of the imperfection has been shown to have a marked influence on the laminar flow. The allowable step size for maintenance of laminar flow in the case of steps with a sharp edge is considerably smaller than that for steps with a rounded corner [30]. Nominally sharp steps were considered in the majority of past investigations. However, quantitative data about the actual step shape have not been published.
- The spanwise distribution of height and shape of the steps considered in past work is unknown for the majority of the aforementioned investigations [12,30,34,37-40,42-44]. Moreover, the measurements were generally conducted in the streamwise direction but at only one spanwise section, so that the spanwise distribution of the transition location is not known [12,37,39-41,43-44]. Spanwise differences in the transition location according to the local step height and shape are possible.
- In many cases [12,34,37-40,42-44], no data are available about the surface quality of the examined wind-tunnel models. If surface roughness, waviness, and additional imperfections were sufficiently large, they may have affected the results.
- In some cases, steps were generated on the surface of interest by means of inserts [39] or foils attached to the surface [30,38,42]. Inserts have to be tapered to end seamlessly at the original model contour, e.g., by means of a ramp. Thus, the effect of the combination of two imperfections is being investigated. Concerns related to surface quality arise from the application of foils onto the model surface: the results may be affected by foil waviness, step bluntness, and non-uniformity of the step in the spanwise direction. Moreover, when the foils are applied onto the model surface up to the trailing edge, the shape of the trailing edge is modified; this can cause differences in the surface pressure distribution, as compared to that of the smooth configuration.
- Transition in the presence of two-dimensional roughness (including steps) was generally observed to move gradually upstream towards the roughness location as the roughness height was increased. Therefore, the criterion used to define the “critical step height” for transition plays an essential role in the examination and comparison of the results. The definition of critical step height in some earlier work [34] is unknown.

The scope of the present work was the systematic study of the effect of sharp forward-facing steps on boundary-layer transition. Experiments were conducted in a compressible, high Reynolds number flow with various streamwise pressure

gradients and also with different thermal conditions at the surface of interest. The present work focused on the effect of forward-facing steps on two-dimensional flow, which is relevant for aerodynamic surfaces at zero to moderate sweep angles ($\varphi < 15\text{-}20°$ [7,10,22,26,30,32]). At these conditions, transition is generally induced by amplification of streamwise instabilities and the surface is compatible with natural laminar flow [22,25,33]. Various favorable pressure gradients, relevant for NLF surfaces, were examined in this work. Furthermore, zero and adverse pressure gradients were also considered. The range of flow conditions studied in the present work is presented in Fig. 1.1.1 (black pattern-filled trapezoid). Freestream Mach numbers up to $M = 0.77$ and chord Reynolds numbers up to $Re = 13 \cdot 10^6$ were investigated. The examined test conditions are relevant for different flight phases of transport aircraft with NLF surfaces [22,25,32-33], from the initial climb phase to the final descent phase, including cruise conditions (see also Fig. 1.1.1). The considered chord Reynolds numbers are typical for the control surfaces and for the wing region at a location of approximately 50 % to 80 % of the wing span. The examined test conditions also cover typical flight conditions for aircraft with piston and turboprop engines, and also for business jets [25,26]. Moreover, various temperature differences between flow and surface of interest were implemented. The influence of surface heat flux on boundary-layer transition is significant when fuel is stored inside wings employing laminar flow technology. When the aircraft is operated after extensive exposure to sunlight, the wing surfaces would be warmer than the surrounding air during take-off and climb, and this temperature difference may also persist well into the early cruise phase [54].

The experiments were carried out in a wind tunnel with good flow quality [55,56], where suitable conditions for the investigation of boundary-layer transition at high Reynolds numbers are available. For this study, a (nominally) two-dimensional wind-tunnel model was designed to achieve a (quasi-) uniform streamwise pressure gradient over a large portion of the model chord length. This enabled a decoupling, and thus a systematic study, of the effect on boundary-layer transition of various contributing factors such as the height of forward-facing steps, the surface heat flux, and the pressure gradient itself. The wind-tunnel model was designed to provide steps of variable height on the surface of interest. Two-dimensional (nominally) steps were placed perpendicular to the freestream direction and normal to the surface. The model construction ensured sharpness of the step, as required in this study. The quality of the model surface in the absence of the step was suited for the investigation of “natural” boundary-layer transition, as induced by amplification of streamwise instabilities. Quality of the model surface, size and shape of the steps were documented. A temperature-sensitive paint [57] enabled non-intrusive global transition detection and thus examination of boundary-layer transition also in the spanwise direction.

From the survey of previous work, the main unsolved questions can be summarized as follows:

- What is the effect of forward-facing steps on boundary-layer transition at flight Reynolds numbers?
- Can laminar flow be achieved over forward-facing steps?
- What is the role of the pressure gradient in transition induced by forward-facing steps?
- Does variation in Mach number up to high subsonic conditions influence boundary-layer transition in the presence of forward-facing steps?
- Is step-induced transition influenced by a non-adiabatic surface?
- Can the results obtained on a generic configuration (flat plate) be transferred to practical applications?

The objective of the present research was to address the above questions.

1.2 Outline

The present work is structured in the following manner.

- Theoretical considerations and knowledge on boundary-layer transition available from previous work are summarized in Chapter 2. Emphasis is on the instability and transition process in two-dimensional boundary layers in a low-disturbance environment. Past work on forward-facing steps is also reviewed.
- The experimental setup is presented in Chapter 3. This chapter includes the discussion of the design, construction, and instrumentation of the wind-tunnel model examined in the present study.
- The evaluation of the experimental data is discussed in Chapter 4. Data post-processing for transition detection, definition and evaluation of the test parameters are also presented here.
- The results are presented in Chapter 5. This chapter is subdivided into two main sections. Results obtained with the smooth configuration (no steps installed) are shown and discussed in Section 5.1. Results obtained in the presence of the steps are presented in Section 5.2.
- The results obtained with the step configurations are then discussed in Chapter 6. The discussion encompasses the combination of the effects of forward-facing steps with changes in Reynolds number, Mach number, streamwise pressure gradient, and thermal condition at the model surface.
- This work concludes with a summary of the results and an outlook for future investigations in Chapter 7.

2 Theoretical considerations and available knowledge from previous work

The basic concepts of laminar and turbulent flow, as well as boundary-layer theory, are starting points for the present work. Standard references are [58-61]. In nature and in engineering applications, turbulent flows are the most common [61]. The interest in laminar flow, its instability, and transition to turbulence can be understood by examining the reduction in shear stress and heat transfer acting on a surface with a laminar boundary layer, as compared to the values which exist in a turbulent boundary layer. At Reynolds number $\mathrm{Re}_x = U_\infty x/\nu_\infty > 1 \cdot 10^6$, typical for a transport aircraft flying at high subsonic speed, the laminar skin-friction coefficient $c_f = 2\tau_w/(\rho_\infty U_\infty^2)$ is about an order of magnitude lower than the turbulent value [19,20]. (U_∞, ν_∞, and ρ_∞ are the freestream streamwise velocity component, the freestream kinematic viscosity, and the freestream density, respectively; x is the streamwise coordinate, with origin at the wing leading edge; τ_w is the wall shear stress.) As discussed in Chapter 1, large reductions in skin friction, and thus in drag, can be achieved by maintaining a laminar boundary layer over as large an area as possible on the aerodynamic surfaces of a transport aircraft. Understanding of the transition process and the capability to predict transition are of fundamental importance also in many other fluid dynamics problems, such as for the design of the thermal protection of a re-entry spacecraft and for the design of the cooling system of blades and vanes in gas turbine engines [62,63]. Boundary-layer transition and the different stages of the instability and transition process are discussed in the following sections.

2.1 An introduction to boundary-layer transition

Laminar flow is an "inherently unstable condition" [7], and transition to turbulent flow "occurs because of an incipient instability of the basic flowfield" [63,64]. Transition can be seen as a "consequence of the non-linear response of that very complicated oscillator" – the laminar flow – to forcing disturbances present in the environment in which the flow develops [53]; these include acoustic disturbances, freestream turbulence, surface inhomogeneities, and surface vibrations [53,62,64-65]. Various physical mechanisms of the transition phenomenon are known [63], which "depend essentially on the specific type of flow and the character of environmental disturbances" [66]. This work focuses on transition of subsonic boundary layers in open systems [63]. Several reviews are available for this problem [32,53,62,64-74], thus only a brief summary is given in this and the following sections. Although many years have passed since the pipe flow experiments by Reynolds [58], which were the first where laminar flow, turbulent flow, and transition were systematically investigated, transition can still not be predicted, even for the simple case with an incompressible, steady, zero

pressure gradient flow over a smooth flat plate with an adiabatic wall [63] (Blasius boundary layer [19,75-76]). This is due to:

- the lack in understanding of the fundamental mechanisms leading "initially small disturbances to transition" [77], i.e., of the free response of the laminar boundary layer as a non-linear oscillator [78];
- the incomplete understanding of the influence of environmental disturbances on boundary-layer transition, i.e., of the forced response of the aforementioned non-linear oscillator [77].

Nevertheless, much progress has been made in transition research. The transition process can be qualitatively described following the "transition flowchart" presented in Fig. 2.1.1 [63,79-80]. The first stage of the process is the mechanism, called receptivity, by which external disturbances enter the boundary layer as steady and/or unsteady fluctuations of the basic state [65]. The receptivity process provides the "initial conditions of amplitude, frequency, and phase for the breakdown of laminar flow" [77,81]. In Fig. 2.1.1, the initial amplitude of the environmental disturbances increases schematically from left to right. Five different paths to turbulence are shown; it has to be kept in mind, however, that this is an oversimplified categorization. If the disturbances are weak, path A is followed (shown in blue in Fig. 2.1.1). This transition scenario is generally considered to apply in low-disturbance environments, such as the flight environment and low-disturbance wind tunnels. It will be discussed in more detail in the next section because of its importance in the problem considered in the present work. The remaining paths to turbulence are discussed in [63,80] and in the bibliographies provided therein.

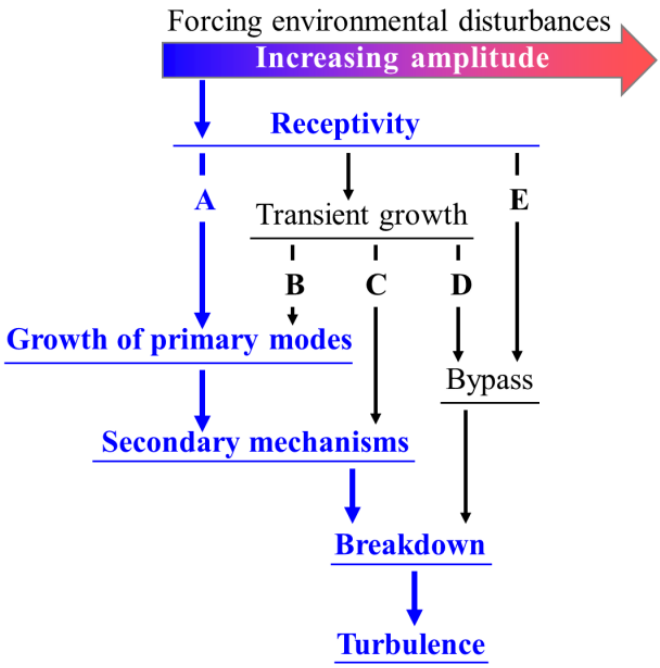

Fig. 2.1.1. Paths to turbulence in boundary layers (after [63,79-80]). Path A for weak disturbances is shown in blue – see text.

In path A, the external disturbances enter the boundary layer and excite its primary modes (i.e., the free oscillations or normal modes of the aforementioned oscillator [53]) through the receptivity process. The main primary instabilities of boundary layer at subsonic and transonic speeds are [80,82]: Tollmien-Schlichting (TS) instability, Rayleigh instability, centrifugal instabilities, crossflow instabilities (CFI), and attachment-line instabilities (ALI). Two-dimensional instabilities are those significant in the experiments discussed in the present work and will be illustrated in more detail in the next section. A qualitative sketch of the main phases of the process leading a two-dimensional, laminar boundary layer on a convex surface to turbulence is shown in Fig. 2.1.2. The initial growth of the primary disturbances is described by linear stability theory (see Section 2.2.1). This growth "is weak and occurs over a viscous length scale" [77]. Moreover, the initial growth of the primary modes can be modulated by the so-called stability modifiers, such as the pressure gradient, the surface mass transfer, and the surface heat flux (see Section 2.3). As the amplitude of the primary disturbances reaches some critical (finite) value, non-linear processes follow. Main features of non-linear growth are: three-dimensionality, mean-flow distortion (leading to changes in frequency and orientation spectra of the disturbances), interaction of modes, generation of harmonics, and secondary instabilities [65]. The growth of the additional, small-scale disturbances is now very rapid, occurs over a convective length scale, and eventually results in breakdown to turbulence [53,77,81,83].

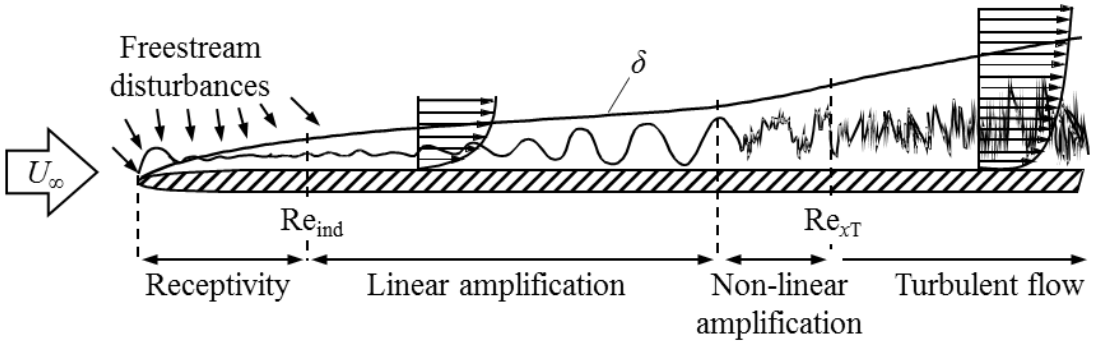

Fig. 2.1.2. Sketch of the main phases of the process leading a two-dimensional, laminar boundary layer on a convex surface to turbulence (after [66,84]).

2.2 The road to turbulence in two-dimensional boundary layers

The stages of the process leading to turbulence will be discussed in this section for two-dimensional boundary layers, since the experiments presented in this work have been conducted in a (quasi) two-dimensional flow over a (nominally) two-dimensional model. u and w are the velocity components in the streamwise (x) and wall-normal (z) directions, respectively. The description is restricted to path A of the transition flowchart shown in Fig. 2.1.1. The phase of linear

amplification of the disturbances within the boundary layer is discussed in Section 2.2.1. Some concepts from this section are helpful for the discussion of boundary-layer receptivity to external disturbances. This is presented in Section 2.2.2, although it is the first main stage of the process leading a laminar boundary layer to turbulence. The non-linear disturbance amplification phase and breakdown to turbulence are briefly discussed in Section 2.2.3. Some aspects of the transition region and the measurement of boundary-layer transition are presented in Section 2.2.4.

2.2.1 Linear amplification of the disturbances (linear stability theory)

The following discussion is taken from [85,86]. For simplicity, the flow is assumed as incompressible. The essential aspects of boundary-layer stability up to high subsonic speeds can be elucidated even with this assumption [86]. Compressible stability theory is discussed in [69,85]. The stability of laminar boundary layers is analyzed using the method of small (infinitesimal) disturbances. An infinitesimal disturbance has been defined as "one whose amplitude is insufficient to alter the basic flow whose stability is being studied" [65]. The motion is decomposed into a basic flow and a perturbation superimposed onto it. Both the basic flow and the perturbation are assumed to satisfy the hydrodynamic equations of motion, and the disturbances are also assumed as two-dimensional. Since the basic flow can be regarded as steady, each flow quantity $q(x,z,t)$ can be expressed as the sum of a basic-state term $Q(x,z)$ and a fluctuating term $q'(x,z,t)$ (i.e., the disturbance). The disturbances originate from the interaction of the basic flow with the environment (receptivity process, see Section 2.2.2). An additional assumption is that the only non-zero velocity component of the basic flow is that in the streamwise direction U, and that this quantity depends only on the coordinate normal to the wall z: $U = U(z)$. This parallel flow assumption is a first approximation of two-dimensional boundary layers at very large Reynolds numbers for which the dependency of the basic flow on the normal coordinate z is much larger than that on the streamwise coordinate x (quasi-parallel flow). Non-parallel flow effects [69,87-91] on the linear amplification of streamwise instabilities were shown to be small [83,85-87,89,92-94]. The flow resulting from the above assumptions has also to satisfy the Navier-Stokes equations. Since the disturbance is infinitesimal, quadratic terms of the disturbance can be neglected. The equations of motion become a set of linear disturbance equations. The question of stability is whether the solution set of the linear disturbance equations "contains disturbances that grow or decay in time (or space)" [86]. A stream function $\psi(x,z,t)$ can be introduced for the perturbation: $u' = \partial\psi/\partial z$ and $w' = -\partial\psi/\partial x$. The perturbation is now assumed to be composed of single modes. The fact that the disturbance equations are linear, with coefficients being only functions of z, suggests a solution in terms of separation of the variables using normal modes: each mode is a wave

propagating in the streamwise direction. The following ansatz is used for the stream function of the single wave: $\psi(x,z,t) = \varphi(z)e^{\mathrm{i}(\alpha x-\omega t)}$. The amplitude function $\varphi(z)$ is the eigenfunction that gives the mode structure through the boundary layer and is a function only of z, since the basic flow depends only on z. In general, α and ω are complex. Temporal amplification theory assumes the wavenumber α as real and the frequency ω as complex: $\omega = \omega_\mathrm{r} + \mathrm{i}\omega_\mathrm{i}$, where ω_r is the physical mode frequency and ω_i is the temporal amplification rate that determines whether the mode grows ($\omega_\mathrm{i} > 0$) or decay ($\omega_\mathrm{i} < 0$) in time. Spatial amplification theory assumes the frequency ω as real and the wavenumber α as complex: $\alpha = \alpha_\mathrm{r} + \mathrm{i}\alpha_\mathrm{i}$, where α_r is the physical mode wavenumber and α_i is the spatial amplification rate that determines whether the mode grows ($\alpha_\mathrm{i} < 0$) or decay ($\alpha_\mathrm{i} > 0$) in the streamwise direction. In the following, the temporal stability problem is considered. The complex phase velocity $c = \omega/\alpha = c_\mathrm{r} + \mathrm{i}c_\mathrm{i}$ can be now introduced, so that the disturbance can be written as $\psi(x,z,t) = \varphi(z)e^{\mathrm{i}\alpha(x-ct)}$. Again, c_r is the physical phase velocity, whereas c_i determines whether the mode grows ($\alpha c_\mathrm{i} > 0$) or decay ($\alpha c_\mathrm{i} < 0$) in time. The lengths and the basic flow velocity in the linear disturbance equations can be made non-dimensional, for example using the boundary-layer reference length $\delta_\mathrm{ref} = (\nu x/U_e)^{1/2}$ and the velocity at the outer edge of the boundary layer U_e. The characteristic Reynolds number for the considered boundary layer flow is $\mathrm{Re}_{\delta\mathrm{ref}} = U_\mathrm{e}\delta_\mathrm{ref}/\nu$. Inserting the above disturbance expression into the linear disturbance equations for non-dimensional quantities (shown with ^), the Orr-Sommerfeld equation (OSE) is obtained:

$$\left(\hat{U}-c\right)\left(\frac{d^2\varphi}{d\hat{z}^2}-\alpha^2\varphi\right)-\frac{d^2\hat{U}}{d\hat{z}^2}\varphi=-\frac{\mathrm{i}}{\alpha\,\mathrm{Re}_{\delta\mathrm{ref}}}\left(\frac{d^4\varphi}{d\hat{z}^4}-2\alpha^2\frac{d^2\varphi}{d\hat{z}^2}+\alpha^4\varphi\right) \qquad (2.2.1.1)$$

This is an homogenous, linear, 4th order ordinary differential equation for the eigenfunction $\varphi(z)$ with boundary conditions $\varphi = \mathrm{d}\varphi/\mathrm{d}z = 0$ at the wall and at large distances from the wall. The stability analysis of a laminar boundary layer results in an eigenvalue problem of the OSE. For a given basic flow $U(z)$, the OSE contains the four parameters α, c_r, c_i, and $\mathrm{Re}_{\delta\mathrm{ref}}$. To perform the stability analysis of the basic flow, the Reynolds number $\mathrm{Re}_{\delta\mathrm{ref}}$ and the wavenumber α (or the wavelength $\lambda = 2\pi/\alpha$) can be prescribed. Besides the trivial solution corresponding to the unperturbed flow, the OSE provides an eigenfunction $\varphi(z)$ and a complex eigenvalue c for each pair α and $\mathrm{Re}_{\delta\mathrm{ref}}$. The results of the stability analysis of the considered boundary layer can thus be presented as in Fig. 2.2.1.1, where a pair of values c_r, c_i is assigned for each point in the $\alpha\delta$-Re_δ plane. (The plots shown in Fig. 2.2.1.1 are for illustrative purposes; δ is an arbitrary boundary-layer thickness, such as δ_ref and the displacement thickness δ_1.) The curve $c_\mathrm{i} = 0$ separates stable from unstable solutions and is called “neutral- (or indifferent-) stability curve”. Waves are neutral at those values of $\alpha\delta$ and Re_δ that lie on the curve $c_\mathrm{i} = 0$, amplified in the region inside the curve, and damped everywhere else. The point on the neutral-stability curve at the lowest Reynolds

number gives the indifferent-stability Reynolds number Re_{ind}, below which all modal disturbances within the boundary layer are asymptotically stable.

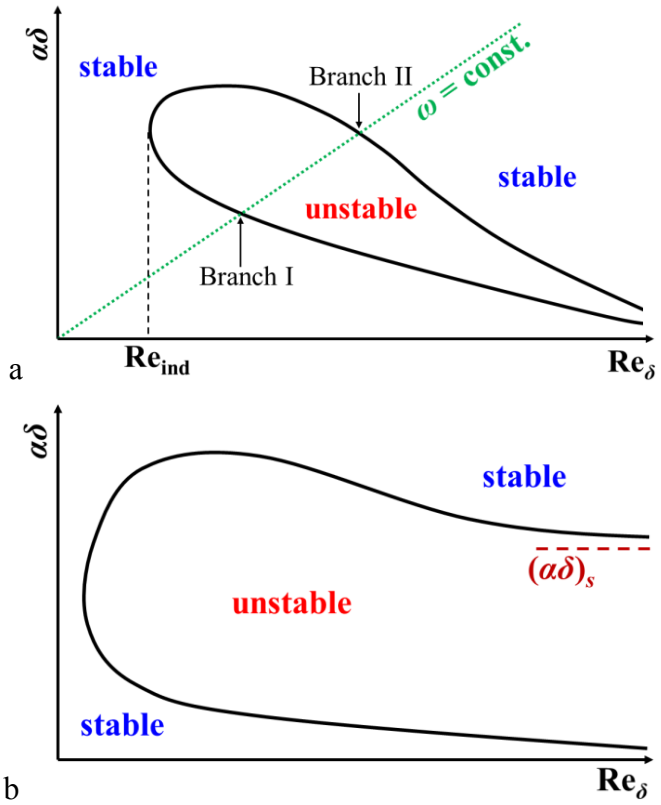

Fig. 2.2.1.1. Typical curves of neutral stability (after [69]). a: mean-velocity profile without inflection points. b: mean-velocity profile with inflection point.

A wave with frequency ω, excited through the receptivity process (see Section 2.2.2), will maintain this frequency as it propagates downstream, whereby its wavenumber will change [69]. As shown in Fig. 2.2.1.1a, for increasing Re_δ the wave will be damped until a point on the neutral-stability curve is reached. This point is called the Branch I (or Lower Branch) neutral-stability point. At larger Re_δ, the amplitude of the wave grows exponentially until it reaches a second point on the neutral-stability curve, which is called the Branch II (or Upper Branch) neutral-stability point. As the Reynolds number is further increased, the wave will be damped again, unless its amplitude has already become large enough before reaching the Branch II location to lead to transition via non-linear processes (see Section 2.2.3). Note that at sufficiently large Reynolds numbers, all waves are stable: the instability of a mean-velocity profile with this kind of neutral-stability curve is called "viscous instability", since only a reduction of the Reynolds number, viz., an increase in viscosity, can induce instabilities. The viscous instability is also often called "Tollmien-Schlichting instability". As shown in Fig. 2.2.1.1a, only Tollmien-Schlichting instability waves with wavenumber and frequency in a certain range become unstable and amplify between the Branch I and Branch II locations. The experiments presented in [95], which were conducted in a low-turbulence

environment, were the first to confirm the predictions of the stability theory discussed in this section.

If the Reynolds number is taken as infinite, the terms on the right hand side of the OSE, which are multiplied by $1/\mathrm{Re}_{\delta\mathrm{ref}}$, disappear. The OSE becomes the inviscid perturbation differential equation, also called "Rayleigh equation". It can be regarded as a simplification for the study of boundary-layer stability at high Reynolds numbers, where the role of the viscosity is restricted to the establishment of the basic flow, and where its influence on the disturbances can be neglected. From the Rayleigh equation it can be demonstrated that a necessary condition for the existence of instabilities in incompressible, inviscid shear flows is that the mean-velocity profile has an inflection point (Rayleigh's criterion)

$$\frac{d^2\hat{U}}{d\hat{z}^2} = 0 \text{ at } z = z_s \qquad (2.2.1.2)$$

where z_s is the location of the inflection point. It has been also shown that the presence of an inflection point is a sufficient condition for the mean-velocity profile of a bounded shear flow to be unstable. Even if viscous effects are considered, an inflectional mean-velocity profile generally remains unstable, since viscosity has only a small influence on the solution of the OSE. Provided that a correction for the viscosity effects is included, Rayleigh's criterion allows a first estimation of boundary-layer stability. In fact, the appearance of an inflection point in the mean-velocity profile usually implies a rapid breakdown to turbulence, since the related instability is strong. The instability of a mean-velocity profile with an inflection point is called "inviscid instability", because the basic flow is unstable even if the Reynolds number is infinite, i.e., even if viscous effects are neglected. It is also often called "Rayleigh instability". The stability diagram related to an inflectional mean-velocity profile is shown in Fig. 2.2.1.1b. It can be seen that a non-zero neutral wavenumber $(\alpha\delta)_s$ exists at large Reynolds numbers, so that waves with wavenumbers $\alpha\delta < (\alpha\delta)_s$ are amplified independently of the value of the Reynolds number. It has been also shown that both the growth rates and the range of unstable frequencies increases rapidly as the inflection point z_s is further away from the wall [21,96].

2.2.2 Boundary-layer receptivity to external disturbances

Unstable modes leading to transition to turbulence have to be excited somewhere in the laminar boundary layer. This occurs through the interaction of the boundary layer with the disturbance environment, a mechanism called receptivity. Note that receptivity is different from stability not only physically, but also mathematically, since it is not an eigenvalue problem, but rather an initial-value problem [53,77]. Reviews of several aspects of the receptivity

problem are given in [81,97-100]. The influence of the freestream disturbance level on boundary-layer transition is discussed in [32,101-104].

The important influence of freestream disturbances on transition had been recognized since the early experiments on pipe flow transition [58,85]. Also the flat-plate boundary-layer studies [95], which provided the first verification of linear stability theory, were "in fact a kind of a receptivity experiment that generated spatially amplifying waves" [97]. In order to be transferred to the fluctuations within the boundary layer, the energy of the external disturbances is required to have an appropriate combination of frequency and wavelength [98]. External disturbances can be grouped into two main categories: forced and natural disturbances [81]. Forced disturbances are produced by artificial means such as a vibrating ribbon or time-harmonic disturbances at the wall (e.g., suction and blowing). These disturbances generally have a broad band of wavelengths. Thus, the input disturbances "contain energy at the appropriate frequency-wavelength combination to directly excite an instability wave" [81]. Natural external disturbances are acoustic and vortical disturbances. Acoustic waves travel at the speed of sound relative to the fluid, whereas vortical disturbances are convected at the freestream speed. Both vortical and acoustic disturbances generally propagate at (much) larger speeds than the instability waves, which have phase speeds that are a fraction of the freestream speed. Thus, for a given frequency, the energy of (natural) external disturbances is typically concentrated in a narrow-band spectrum of wavelengths, which are substantially different from those of the instability waves [81,98]: for example, the wavelength of freestream sound is one or two orders of magnitude larger than the wavelengths of unstable modes in a low-speed boundary layer [77]. This is an essential aspect of "natural" receptivity. Because of this mismatch in wavelengths, unstable modes with a certain frequency f_{TS} can be excited only after a wavelength conversion process [99]. In practice, this means that an incoming freestream disturbance at wavelength λ_∞ and frequency $f_\infty = f_{TS}$ has to interact with an inhomogeneity in the mean flow or at the examined surface "in such a way so as to broaden its spectrum to include" the response wavelength λ_{TS} [77]. The necessary spatial "tuning" process, in which the long-wavelength freestream disturbances are scattered into the shorter-wavelength unstable modes, occurs in regions where the mean flow is required to adjust rapidly in the streamwise direction [32,97-99,105]. On a flat-plate model, these regions are: the leading-edge region, the junction between leading edge and flat plate, regions of adverse pressure gradient, and any inhomogeneity in surface geometry, suction velocity, and surface temperature [77,99]. The receptivity mechanisms are subdivided into three main categories: leading-edge receptivity, localized receptivity, and non-localized receptivity [100]. These receptivity mechanisms are discussed in [81,97-100,106-107] and in the bibliographies provided therein.

2.2.3 Non-linear amplification of the disturbances and breakdown to turbulence

Once linear amplification of the disturbances has led to a certain threshold amplitude (typically 0.5-1 % U_∞ [91,108]), the boundary layer enters a phase of non-linear development, which terminates with an "abrupt change in the character of wave motion" (breakdown) [109] and final transition into a turbulent state [66,68]. At this last stage, "the flow is transformed from a deterministic, regular, often two-dimensional laminar flow into a stochastic and at the same time ordered, three-dimensional" turbulent flow [66]. The initial phase of the non-linear amplification stage is considered as "weakly" non-linear: in this phase, the primary modes are still present, but they also start to interact with each other. These interactions can be very strong, thus leading to marked enhancement of disturbance amplification. The late phase of the non-linear amplification stage is regarded as "essentially" non-linear: in this phase, the primary modes are transformed into intense, concentrated vortices, whose development is substantially different from that of the primary modes at the earlier stages [82]. The boundary-layer development after the linear amplification phase has been shown to be non-unique even for the case of an incompressible flow on a flat plate at zero pressure gradient: two main "regimes of transition" have been identified [66].

2.2.4 Transition region and measurement of boundary-layer transition

Non-linear amplification of disturbances and breakdown generally occur over a short streamwise distance. The development of three-dimensionality up to the start of the breakdown phase was shown to occur over a streamwise extent corresponding to five wavelengths of the fundamental instability wave; the subsequent breakdown phase was shown to occur within one wavelength [71]. In several cases with two-dimensional and axisymmetric boundary layers, the streamwise extent of linear amplification covers the largest part of the distance between the leading edge and the location of transition onset [83,110-111]; the ratio of the extent of these two regions has been estimated to be approximately 75-85 % for a flat plate at zero pressure gradient [68,112] and is even larger for decelerated flows [110]. These observations explain the success of boundary-layer control techniques aiming to reduce disturbance amplification in its linear stage (see Section 2.3). For the same reason, transition prediction methods based on the linear amplification of the disturbances, such as the e^N method discussed in Section 2.4, provide in many cases a good estimation of the transition "location" on aircraft surfaces. Since transition is a process which occurs over a certain – although generally short – distance, the terms "transition location" and "transition point" are not very appropriate and should be avoided. For simplicity, however, they are still widely used. Their use is reasonable when,

with “transition location”, it is meant a certain point in the transition region, which has to be unequivocally and consistently defined and corresponds to a position in the flow with physical significance related to the transition. In this sense, these terms will be used also in the present work.

The transition region is usually defined as the region where localized domains of turbulent behavior (called “turbulent spots” or “Emmons spots” [113]) are initiated, grow, overlap, and finally form a turbulent boundary layer [68,114]. The boundary layer has an “intermittent” character in the transition region [85]. This means that, at a fixed location within the transition region, the flow state changes in time from laminar to turbulent, and vice versa. In the transition region, the signal of a hot-wire placed in the boundary layer or a hot-film placed on the model surface will present an irregular succession of time intervals with fluctuations typical of laminar and turbulent flow [85,115-116]. The intermittency factor γ is defined as the fraction of time for which the flow is turbulent at a certain position [85]. It is zero in a fully laminar flow, whereas it is unity in a fully turbulent flow. In the transition region, the intermittency factor increases continuously from $\gamma = 0$ to 1 [114,117].

When hot-wires are used to detect transition, transition onset is usually determined at the location where the first intense, high-frequency flashes of disturbances appear in the time series of the hot-wire signal [40,118]. These flashes of disturbances are often called “spikes” or “bursts” and can have a magnitude of 30-40 % U_∞. In the case of hot-films used for transition measurements, the location of transition onset is usually taken as the location where the root mean square (rms) value of the hot-film signal becomes larger than the laminar level [115,119]. In other cases, Pitot tubes [38,102,120-121] or Preston tubes [41,43-44] are used for transition detection. These probes are placed at the wall (Preston tube) or close to it (Pitot tube, usually flattened), and traversed in the streamwise direction [38,41,102,120-121]; another possibility is to fix several probes at different streamwise locations [43,44]. In the laminar region, both total pressure measured by a Pitot tube and dynamic pressure measured by a Preston tube (after subtraction of the corresponding wall static pressure from the total pressure measured by the probe) typically decrease along the streamwise coordinate. At a certain location, these pressures start to rise from the laminar values because of the non-linear processes associated with transition; they reach a maximum and then gradually decrease to the values corresponding to a fully turbulent boundary layer. Taking the tangent point to the streamwise pressure distributions at the minimal and maximal values of these pressures gives the locations defined as transition start ($x_{T,start}$) and end ($x_{T,end}$), respectively [41,120]. The wall shear stress and the wall heat flux present an evolution in the streamwise direction similar to that described for the pressures measured by Pitot and Preston tubes [116,122]. The rms value of the fluctuations of streamwise velocity, total pressure, dynamic pressure, static temperature, wall shear stress, wall heat flux, etc., start to increase at a short distance upstream of $x_{T,start}$, reach a

maximum approximately in the middle of the transition region, and decrease further downstream to turbulent levels [115-116,119-120,123-124]. The intermittency factor corresponding to this peak is around 0.5 [115,119,124]. More precisely, the maximum of the rms value of the fluctuations of a certain quantity is reached at a location corresponding to the maximal slope of the mean value of that quantity. This has been discussed in [115] for the wall shear stress measured by hot-films, in [120] for the total pressure measured by a Pitot tube, and in [122] for the surface temperature measured by means of infrared (IR) thermography. This location can be measured more accurately than $x_{T,start}$ and $x_{T,end}$, and is therefore often used to define the "transition location" [116]. It appears clear that the different definitions for the "transition location" measured in experimental work should be taken into account when results from different experiments are compared or used for calibration/validation of transition prediction methods.

It should be also remarked that momentum transfer and heat transfer processes occur at a different rate in a strongly accelerated boundary layer undergoing transition [123,125-126]. In fact, the "development of momentum transport in accelerating transitional flows leads to the development of thermal transport" [123]. Measurements were conducted at low speed and with moderate to high levels of turbulence ($Tu \sim 0.4$ % to 2.5 %) on a heated flat plate, on which a strong, favorable streamwise pressure gradient had been imposed. The length of the transition region indicated by the variation of the convective heat transfer coefficient was found to be larger than that indicated by the change in boundary-layer shape factor, although transition start was found at approximately the same location [123,125]. On a similar test arrangement, spreading angles of turbulent wedges indicated by shear-sensitive liquid crystals were shown to be larger than those indicated by temperature-sensitive liquid crystals [126]. These results were obtained in the presence of strongly favorable pressure gradients characteristic of gas turbine blades. In the presence of pressure gradients in the range of those examined in the current work, both the location of transition onset and the location of maximal slope of the mean wall heat flux distribution, determined by means of a thermographic method, are in agreement with the corresponding transition locations determined using a method based on the measurement of momentum transport [123,125-126].

2.3 Boundary-layer stability modifiers

It has been already discussed in the Section 2.2.1 that basic flow velocity profiles with an inflection point are generally more unstable than those without inflection points. The curvature of the mean-velocity profile $\partial^2 U/\partial z^2$ plays an essential role in the Orr-Sommerfeld equation (Eq. (2.2.1.1)): factors influencing the curvature of the mean-velocity profile have a strong effect on the solutions of the OSE and therefore on boundary-layer stability. These factors are often called "stability modifiers", since they modify the amplification characteristics of the laminar boundary layer [53,127]. The streamwise pressure gradient, the surface mass

transfer, and the surface heat flux are the most important stability modifiers for laminar boundary layers where streamwise instabilities are the predominant mechanism leading to transition. The factors that modify the linear amplification of the disturbances have the strongest influence on the value of the transition Reynolds number, "simply because the linear amplification step is the slowest of the successive multiple steps in the transition process" [128]. Acting on the stability modifiers, it is possible to minimize disturbance growth and thus achieve long runs of laminar flow. "Industrial" laminar flow technologies for two-dimensional flow are mainly based on these stability modifiers. In practice, they aim to modify the shape of the basic flow velocity profile in order to avoid inflection points [21]. This can be shown by a consideration of the two-dimensional, steady, boundary-layer momentum equation in the near-vicinity of a wall (subscript w) for a flat plate [128]:

$$\mu_w \left(\frac{\partial^2 U}{\partial z^2} \right)_w = \frac{\mathrm{d}p}{\mathrm{d}x} + \rho V_w \left(\frac{\partial U}{\partial z} \right)_w - \frac{\mathrm{d}\mu}{\mathrm{d}T} \left(\frac{\partial T}{\partial z} \right)_w \left(\frac{\partial U}{\partial z} \right)_w \qquad (2.3.1)$$

It appears clear that a favorable pressure gradient ($\mathrm{d}p/\mathrm{d}x < 0$), wall-normal suction ($\rho V_w < 0$), and wall cooling in air ($\mathrm{d}\mu/\mathrm{d}T > 0$ and $(\partial T/\partial z)_w > 0$) tend to make the curvature of the mean-velocity profile at the wall $(\partial^2 U/\partial z^2)_w$ more negative and thus the mean-velocity profile more convex than for the Blasius case. Even small variations of the stability modifiers leading to a more negative $(\partial^2 U/\partial z^2)_w$ are very effective in delaying transition in scenarios with predominant streamwise instability mechanism [32]. In contrast, an adverse pressure gradient ($\mathrm{d}p/\mathrm{d}x > 0$), wall-normal blowing ($\rho V_w > 0$), and wall heating in air ($\mathrm{d}\mu/\mathrm{d}T > 0$ and $(\partial T/\partial z)_w < 0$) tend to make the curvature of the mean-velocity profile at the wall less negative, or even positive. If $(\partial^2 U/\partial z^2)_w > 0$, the mean-velocity profile has an inflection point within the boundary layer, and the corresponding stability diagram is of the type shown in Fig. 2.2.1.1b. The related inviscid instability is strong and generally leads to earlier transition than for the Blasius boundary layer. At this point, it should be emphasized that these considerations on the stability modifiers apply to the linear stage of disturbance amplification. As soon as non-linearities come into play, the stability modifiers lose their significant effect on boundary-layer stability [53]. Moreover, this analysis holds strictly only for two-dimensional flow. In the case of three-dimensional flow over a swept wing, the effect of the stability modifiers on crossflow instabilities must be considered [7,9-10,21,74]. In any case, it should be emphasized that "when the crossflow is small enough to be stable, the stability characteristics are essentially those of the streamwise flow" [129]. In the practical application of transport aircraft, streamwise instabilities have been shown to be the predominant mechanism leading to transition on aerodynamic surfaces with sweep angles $\varphi < 15\text{-}20°$ [22,25-26,30,32-33].

2.3.1 Streamwise pressure gradient

The incompressible boundary-layer flow over an adiabatic, solid wall has a mean-velocity profile with an inflection point if subjected to an adverse streamwise pressure gradient. This kind of velocity profile has a much lower limit of stability than mean-velocity profiles without inflection points, such as those of accelerated boundary layers ($dp/dx < 0$). The effect of the streamwise pressure gradient on boundary-layer stability has been examined for single-parameter families of laminar boundary-layer velocity profiles [69,92,112]. The self-similar solution of the boundary-layer equations (Falkner-Skan equation) given by the power law $U(x) = k \cdot x^m$ is an example of these families of velocity profiles, where k is a constant and the shape parameter m determines whether the velocity profile has an inflection point ($m < 0$) or not ($m > 0$) [130]. Such a flow is also called "wedge flow", since it occurs over wedge-shaped bodies with wedge angle $\beta_H = 2m/(m + 1)$, which is often referred as the "Hartree parameter" [131]. The influence of the streamwise pressure gradient on boundary-layer stability has been investigated as a function of m (β_H), clearly showing that a favorable pressure gradient increases the indifferent-stability Reynolds number, reduces the range of wavenumbers for streamwise instabilities, and reduces the amplification of the unstable disturbances [69,92,112]. For example, the indifferent-stability Reynolds number $Re_{x,ind}$ of an accelerated boundary layer with a Hartree parameter $\beta_H = 0.1$ is nine times larger than that for a Blasius boundary layer [32].

The stabilizing effect of a favorable pressure gradient has been exploited since the 1930's for the development of low-drag airfoils [7,9,128], such as the NACA 6- and 7-series. The basic design principle to achieve long runs of laminar flow is to have an extensive region of favorable pressure gradient (natural laminar flow, NLF). Large transition Reynolds numbers $Re_{xT} = x_T U_\infty / \nu_\infty$, where x_T is the chordwise location corresponding to transition, had already been measured on such NLF airfoils in flight experiments in the late 1930's. Once low-turbulence wind tunnels became available, large transition Reynolds numbers were measured on NLF airfoils also in ground test facilities [9]. The effect of the streamwise pressure gradient on boundary-layer stability was already verified in the aforementioned experiments from [95]. In the presence of a pronounced adverse pressure gradient, disturbance amplification was observed almost regardless of frequency and Reynolds number (in the examined range); in this case, transition was initiated shortly downstream of the begin of the adverse pressure gradient region. In contrast, the fluctuations were completely damped by a marked favorable pressure gradient [95]. Analysis of experimental data [132] showed that the difference in the momentum thickness Reynolds number Re_θ between the location of completed transition and the indifferent-stability point ($Re_{\theta T,end} - Re_{\theta,ind}$) increases with increasing flow acceleration. With the assumption that transition occurs when the amplitude of the disturbances has

reached a certain threshold (see Section 2.2.3), this result is clearly due to the reduced disturbance growth in an accelerated boundary layer.

2.3.2 Surface mass transfer

The effect of surface mass transfer on boundary-layer stability will not be discussed in detail, since it has not been part of the investigations presented in the current work. Suction has a markedly favorable effect on boundary-layer stability, similarly to that of flow acceleration discussed above. Homogenous suction has been shown to strongly increase the indifferent-stability Reynolds number $\mathrm{Re}_{\delta 1,\mathrm{ind}}$ for an adiabatic wall flat plate at zero pressure gradient, up to values that can be even one hundred times larger than that of a Blasius profile [133]. Moreover, the range of wavenumbers of Tollmien-Schlichting waves that can become unstable is considerably reduced. Several experiments since the 1940's have demonstrated that large regions of laminar flow can be achieved by sucking away the boundary layer [7,9-10]. Suction thus represents one of the active laminar flow control (LFC) techniques that can be employed to maintain the boundary layer laminar even at flow conditions at which it would be transitional or turbulent in the natural case (without control), such as on aircraft surfaces at sweep angles $\varphi > 20°$ [7,10].

2.3.3 Surface heat transfer

In wind-tunnel experiments in the early 1940's, with air as test fluid, friction drag on a flat plate [134] and an NLF-airfoil model [135] was observed to increase when the model surface was heated. This result was due to premature transition. The transition Reynolds number on a flat plate at zero pressure gradient was found to decrease as the plate surface temperature was increased [136]. (The flow temperature was kept unchanged.) A heated surface was shown to produce a wall-normal temperature distribution within the boundary layer that promotes an inflection point in the mean-velocity profile [135,136]. This effect was confirmed by linear stability computations for air flow [137-141]. In general, the parameter used to characterize the surface heat transfer is the wall temperature ratio T_w/T_{aw}, where T_w and T_{aw} are the wall and adiabatic wall temperatures, respectively. T_w/T_∞ and T_w/T_e have been also used, where T_∞ is the freestream temperature and T_e the temperature at the outer edge of the boundary layer. Wall cooling ($T_w/T_{aw} < 1$) has an influence on boundary-layer stability similar to that of flow acceleration and wall-normal suction: a reduction in T_w/T_{aw} leads to a larger indifferent-stability Reynolds number and to a shrinking of the region of unstable Tollmien-Schlichting waves. An opposite behavior is observed when the surface is heated ($T_w/T_{aw} > 1$) [85,137]. Note that the effect of surface heat transfer on boundary-layer stability in water is opposite to that in air, since in water $\mathrm{d}\mu/\mathrm{d}T < 0$ holds [142]. The effect of surface heat transfer on boundary-layer stability and transition was confirmed in experiments

on a flat plate [143,144], a cone [102,121], and an NLF-airfoil model [145]. A considerable amount of data regarding the effect of wall temperature ratio T_w/T_{aw} on transition is available from experiments conducted in several wind tunnels and in flight using a 10° sharp cone at zero incidence [102,121]. T_w/T_{aw} was evaluated in a region where turbulence was fully developed: the thermocouple measuring the wall temperature was placed at 80 % of the cone length and the adiabatic wall temperature T_{aw} was evaluated at the same location using

$$T_{aw} = T_e\left(1 + \frac{\gamma - 1}{2} r \mathrm{M}_e^2\right) \qquad (2.3.3.1)$$

with a recovery factor $r = 0.88$. (M_e is the Mach number at the outer edge of the boundary layer, γ is the heat capacity ratio of the considered fluid.) The transition location was taken as the location corresponding to completed transition, i.e., $x_T = x_{T,end}$. The influence of T_w/T_{aw} on the transition Reynolds number was found to be well approximated by $\mathrm{Re}_{xT}/\mathrm{Re}_{xT,aw} = (T_w/T_{aw})^{-7}$ over a large range of Mach numbers from $\mathrm{M}_e = 0.5$ to 2, where $\mathrm{Re}_{xT,aw}$ is the transition Reynolds number at adiabatic wall conditions [102,121]. This marked effect of T_w/T_{aw} on transition can be also critical for an aircraft designed with NLF wings. Surface heat transfer is generally regarded as uncritical under typical cruise conditions of transport aircraft because of the high heat conductivity of the wing skin, which leads to a uniform temperature distribution on the wing surface and to only minor differences between the surface temperature and the adiabatic wall temperature [146]. This, however, may not hold true for all flight conditions if fuel is stored inside the wings. When an aircraft is operated after extensive exposure to sunlight, the NLF wing surface would remain warmer than the surrounding air during take-off and climb, and the temperature difference may also persist during the first cruise phase. Under these conditions, the extent of the laminar region can be markedly reduced as compared to design, so that aircraft performance can be dramatically compromised [54]. Since the favorable influence of surface cooling on transition is quite pronounced, one has considered using it for laminar flow control on an aircraft using a cryogenic fuel [129]. By cooling the aircraft surfaces to approximately 170 K, this preliminary study forecast possible drag reductions of about 20 % for a long-range transport aircraft. Finally, it should be remarked that, in supersonic flows, the higher boundary-layer modes are destabilized by wall cooling [69]. With sufficient wall cooling, they can arise even at Mach numbers close to one [65].

2.3.4 Combination of streamwise pressure gradient and surface heat transfer

The effects on boundary-layer stability and transition of streamwise pressure gradient, surface mass transfer, and surface heat transfer are expected to be additive [128]. Their combined effect has so far received little experimental

study, especially with regard to the effect of surface heat flux in combination with the other two stability modifiers [147]. The effect of the combination of streamwise pressure gradient and a non-adiabatic surface on boundary-layer transition was examined by the author in previous experiments on an NLF-airfoil model [145], which was investigated at high Reynolds numbers and at both low and high subsonic Mach numbers. The impact of a non-adiabatic wall on transition was identified to be dependent on the considered boundary-layer stability situation. Stability situations, at which the boundary layer underwent transition on a region with zero or favorable pressure gradient, were shown to be the most sensitive to the influence of the surface heat transfer. In these cases, the (pronounced) variation of the transition Reynolds number as a function of the wall temperature ratio T_w/T_{aw} was found to be in agreement with the approximation function $\mathrm{Re}_{xT}/\mathrm{Re}_{xT,aw} = (T_w/T_{aw})^{-7}$ from [102,121]. In contrast, when transition was induced by an adverse pressure gradient, the sensitivity to the wall temperature ratio was reduced. The less sensitive situation was that of transition occurring over a laminar separation bubble: in this case, the wall temperature ratio had no effect on the transition location. The experimental results were in agreement with trends predicted by linear stability theory [145]. No studies have been found in the literature where the effect on boundary-layer transition of the combination of streamwise pressure gradient and surface heat transfer has been systematically investigated at Mach numbers relevant for cruise conditions of transport aircraft. This study has been carried out for the first time in the present work: the results will be presented in Section 5.1. A set of results – those obtained at a Mach number M = 0.77 – has been presented in [148].

2.4 Transition prediction based on linear, local stability theory (e^N method)

Using the assumptions discussed in Section 2.2.1, linear stability theory enables computation of the disturbance growth rates for given mean-velocity profiles. Spatial stability theory is considered in this case. Temporal growth rates can be converted into spatial growth rates using the so-called "Gaster transformation" [149]. Even though this relation is strictly valid only for small values of the growth rates, numerical computations have shown that it can also be applied with confidence even for larger growth rates [110]. For a boundary layer developing on the surface of the body under investigation, mean-velocity profiles should be available at different streamwise positions. The boundary layer is locally approximated by a parallel flow with constant mean-velocity profile in the downstream direction, the mean-velocity profile being that evaluated at the considered streamwise location [150]. According to this procedure, linear stability computations are performed at each location x_j. The growth rates $-\alpha_i$ are then available at x_j for unstable waves with frequency $f_{TS,k}$. A measure $A(x)$ of the wave amplitude can now be introduced. In practice, e.g., $u'_{rms,max}$ can be taken for this measure. $A(x)$ of an unstable wave with frequency

$f_{TS,k}$ at two neighboring streamwise locations x and $(x+\mathrm{d}x)$ can be expressed as [150]:

$$\frac{A+\mathrm{d}A}{A} = \frac{e^{-\alpha_i (x+\mathrm{d}x)}}{e^{-\alpha_i x}} = e^{-\alpha_i \mathrm{d}x} \tag{2.4.1}$$

The amplitude ratio in Eq. (2.4.1) can be also expressed in logarithmic form and integrated from the Branch I location x_I (where the wave with frequency $f_{TS,k}$ first becomes unstable) to a certain location x. This yields

$$\ln\left(\frac{A(x)}{A_0}\right) = \int_{x_I}^{x} -\alpha_i \mathrm{d}x = N(x), \tag{2.4.2}$$

where A_0 is the amplitude of the considered wave at the Branch I location. The amplification ratio $A(x)/A_0$ of that wave at the streamwise location x is therefore $e^{N(x)}$. $N(x)$ is the corresponding amplification factor and is often simply called the "N-factor". A sketch of the amplification factors of waves with frequencies $f_{TS,1}$, $f_{TS,2}$, and $f_{TS,3}$ computed for a given mean-velocity profile is shown in Fig. 2.4.1a. The curve connecting the maxima of N for all amplified waves at each streamwise location (envelope curve) is also shown.

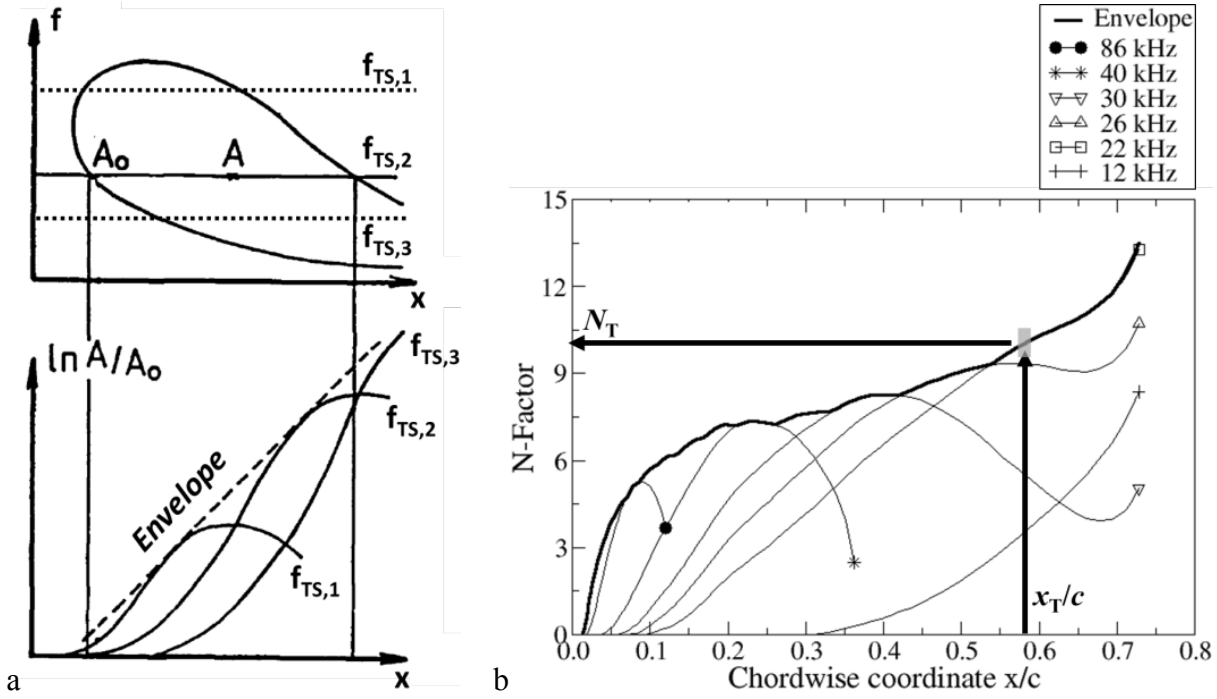

Fig. 2.4.1. a: sketch of the integration of growth rates of Tollmien-Schlichting waves with different frequencies to obtain the *N*-factor envelope curve (after [32]). b: determination of the transition *N*-factor N_T for a certain test condition at which the transition location x_T has been measured (after [145]).

The "e^N method" assumes that transition occurs at the location where a critical amplification ratio e^{N_T} is reached [151,152]. This transition prediction method therefore considers only the linear amplification of primary modes. All other physics, receptivity and non-linear breakdown included, are incorporated into the value of N_T, which is calibrated by means of wind-tunnel or flight tests. As shown in Fig. 2.4.1b, the N-factors are computed for a given test condition, for which the transition location x_T has been measured. The maximal N-factor at the transition location is the transition N-factor $N_T = N_{max}(x_T)$. Typically, the transition N-factor is evaluated with the same model in the same wind tunnel or in flight for various test conditions. These results are then used to calibrate N_T for transition prediction by means of the e^N method [153-155]. It is important to emphasize at this point that there is no a-priori reason to expect that the value of the transition N-factor, calibrated for a particular disturbance environment, is applicable to measurements in a different disturbance environment. This holds also for investigations conducted in the same wind tunnel, at the same test conditions, and with the same test model, which, however, has a different surface quality [100]. Receptivity to external disturbances determines the value of the initial disturbance amplitude A_0 and plays an essential role in the overall transition process [110]. This part of the process is, however, almost completely neglected in the e^N method, since it is taken into account only in the value of N_T [116]. Thus, the e^N method can be expected to work only for experiments with identical disturbance environment and boundary-layer receptivity. The following factors also influence the values of the calibrated N_T: method for the computation of boundary layer and amplification rates [53,150], measurement technique used to detect transition, and definition of "transition location" [32,116].

Since several aspects of the process leading a laminar boundary layer to turbulence are not accounted for, the e^N method "will always be suspect to large errors and should be used with extreme care" [110]. A method for transition prediction on a more physical basis is enabled by non-linear, non-local stability theory, which is capable to reproduce the generation and rapid growth of harmonics (i.e., small-scale structures) in the non-linear disturbance amplification phase of the transition process [83,111]. Moreover, non-linear non-local stability theory is also capable to reproduce the rise in skin friction characteristic of transition onset, which can therefore be used as criterion for transition prediction [62,83,88,91,111]. Thus, transition prediction based on non-linear, non-local stability theory does not involve any empirical correlation of the computed disturbance growth with measured transition locations. It requires, however, the identification of possible transition scenarios and the knowledge of the initial disturbance spectrum (i.e., information about the disturbance environment and modeling of the receptivity process) [83,91,111]. For these reasons, the e^N method is still the only practical method currently available to predict transition in industrial applications [116]. The e^N method is also useful in parametric studies for examining the sensitivity of the transition location to various factors [62]. Transition is assumed to take place when disturbance

amplification reaches the critical amplification ratio e^{N_T}, with N_T being assumed to remain unchanged when the parameters are varied. If transition occurs over a region where the *N*-factor envelope curve is flat, the effect of the change of a parameter that increases (decreases) the amplification ratios is to considerably shift transition into a location more upstream (downstream). In contrast, the transition location is less sensitive to similar parameter changes if transition occurs over a region where the *N*-factor envelope curve presents a steep increase. The trends predicted according to these considerations were shown to be in agreement with results of wind-tunnel experiments that examined the effect of the wall temperature ratio T_w/T_{aw} on boundary-layer transition [145].

2.5 Past work on the effect of surface imperfections on boundary-layer stability and transition with emphasis on forward-facing steps

Modern manufacturing techniques for metallic and composite materials are capable of producing the surface quality required for laminar flow. This had already been demonstrated in a series of NLF flight experiments on production-line versions of various general aviation aeroplanes, including propeller and turbojet-powered configurations [25,26]. Most of the examined aeroplanes had quite long runs of favorable pressure gradient, so that extended regions of laminar flow could be attained without the need for modifications. An NLF glove was mounted on just one of the aeroplanes (a Beechcraft T-34C aeroplane). In this series of experiments [25,26] and in later NLF experiments [7,10,21-22,33], the aforementioned NLF surfaces did not receive special treatment prior to testing, except in a few cases [25,156]. This is a major difference from earlier experiments, for which the aircraft surfaces had had to be carefully finished (see Appendix A.1). Note also that modern business jets and transport aeroplanes cruise at higher altitudes than earlier test aeroplanes, leading to lower flight unit Reynolds numbers and therefore to a less demanding aircraft surface quality [30,33,157]. The positive results of the NLF tests led researchers to conjecture that even moderately large transport aircraft, such as the Airbus A320, or even the Boeing 757 "might be able to use NLF with some modest reduction in leading edge sweep, say 5 to 7 degrees" [33]. At sweep angles up to $\varphi \sim 30°$, large areas of laminar flow can be attained by means of an active control system of reduced complexity via hybrid laminar flow control (HLFC) [7,10]. In this case, wall suction (LFC) is applied in the leading-edge region to control crossflow (and attachment-line) instabilities; further downstream, the wing is shaped for a favorable streamwise pressure gradient (NLF) to reduce growth of Tollmien-Schlichting instabilities. Modern manufacturing technology allowed production of surfaces compatible with laminar flow requirements even in the presence of a HLFC system in the leading-edge region. Experiments demonstrated that HLFC can be operated in an airline-type environment without special maintenance considerations [158]. HLFC gloves, including an anti-ice

system (serving also for prevention against insect contamination) were mounted on both wings of a Dassault Falcon 900 business jet [159]. The aircraft has been in operation at Dassault Falcon Service for two years, thus providing validation of LF technology at operational level [21].

Despite these encouraging results, concerns remain "about the achievement of high quality structural joints at the spar joints or at skin splices" [33] compatible with the attainment of large regions of laminar flow. Significant waviness may be found only in the form of (widely) spaced bumps at structural joints and at surface locations corresponding to spars and ribs. The effect of bumps and waviness on boundary-layer stability and transition has been investigated in earlier work [50,118,160-168]. Bumps originating at the aforementioned locations on the aircraft surfaces appear to be considerably smaller than required to maintain laminar flow, especially for typical cruise conditions of transport aircraft [30,33]. Therefore, they should not be a major concern for maintaining laminar flow. In contrast, steps and gaps at structural joints, which seem to be unavoidable in a practical wing, are more critical [27,33]. The effect of gaps on boundary-layer stability and transition has also been studied in previous work [32,34,38,169-174]. Criteria for allowable gap size are available, based on the gap Reynolds number $\mathrm{Re}_b = U_\infty b/\nu_\infty$ (where b is the gap width) and on the relative gap depth $d/\delta_{1,b}$ [32,34,169,173]. (d is the gap depth and $\delta_{1,b}$ is the displacement thickness at the gap location in the absence of the gap.) It should be emphasized that, if gaps of allowable size cannot be attained during the manufacturing process, they can be smoothed over by means of aerodynamic fillers, which are routinely used today [33].

Sharp steps always induce localized flow separation, leading to marked amplification of instability waves [96,172,175]. Boundary-layer receptivity, instability, and transition in the presence of laminar separation bubbles is discussed in [96,176-179] and in the bibliographies provided therein. In this section, emphasis is placed on spanwise-invariant two-dimensional steps placed on the test surface perpendicular to a (quasi) two-dimensional flow. Forward-facing steps are the main subject of this section. The most important effect of steps of not excessive size is the amplification of existing (or potentially existing) streamwise instabilities in the regions of separated flow [32]. In many cases, boundary-layer stability can still be analyzed by means of linear stability theory to a certain degree of approximation [32,45-46,172]. In this context, two-dimensional steps can be regarded as factors that modify the amplification characteristics of the boundary layer, i.e., as stability modifiers [65,127,172]. As opposed to the case of three-dimensional roughness elements [180,181], the "road to transition" in the presence of such two-dimensional imperfections follows the same path as that on a smooth surface [182].

The first known systematic research on the effect of steps and gaps on laminar flow was that conducted by the Northrop Corporation for the design of the X-21A demonstration aeroplane [34,169]. Criteria for allowable steps were

determined using low-speed wind-tunnel tests on a flat plate [169]. The critical step Reynolds numbers, based on the step height h, provided in [34] are $\mathrm{Re}_{h,\mathrm{cr}} = U_\infty h/\nu_\infty = 1800$ and 900 for forward- and backward-facing steps, respectively. Backward-facing steps are thus more critical for laminar flow than forward-facing steps. Backward-facing steps are considered to be even more effective than cylindrical wires for boundary-layer tripping [12] and should be avoided on a surface designed for laminar flow. Some results from investigations on backward-facing steps are discussed below together with those related to forward-facing steps. Among studies focused on backward-facing steps, the experiments presented in [183] should be mentioned. In that work, sharp backward-facing steps were installed on a flat-plate model and examined in a low-speed, low-turbulence wind tunnel. The unit Reynolds number Re/c was between 0.4 and $1.1 \cdot 10^6$ m^{-1} and the boundary layer was slightly accelerated. The measurements were conducted by means of hot-wire anemometry, a Pitot probe, and a smoke visualization technique. Wall suction was proven to prevent boundary-layer transition in the presence of backward-facing steps, but its influence on boundary-layer stability was shown to depend on the location of the suction region. This effect was also shown in numerical work considering smooth backward-facing steps in a flat-plate boundary layer at zero pressure gradient and Mach numbers up to M = 0.8 [184].

Flight experiments on surface imperfections were conducted on an unswept NLF-airfoil glove mounted on the left wing of a Beechcraft T-34C aeroplane [30]. Transition was measured by sublimating chemicals. Simultaneous transition detection by means of hot-films operated with and without sublimating chemicals showed that chemical coating roughness had no influence on the transition location [26]. Forward-facing steps were generated using cellulose acetate sheets attached to the lower surface of the glove with double-sided adhesive tape [30]. The steps were installed at $x_h/c = 5$ % on the lower surface of the glove, in a region of favorable pressure gradient. Spanwise-invariant steps with different cross-sectional shapes were examined. The shape of the imperfection was shown to play a fundamental role in its effect on boundary-layer transition. For a rounded forward-facing step with a radius of approximately three-quarters of the step height, the critical step height, at which transition occurred at the imperfection location, was found to be at least 50 % larger than that for a sharp forward-facing step. Forward-facing steps and forward- and backward-facing ramps, installed at a certain angle between the imperfection ridge and the freestream, were also examined in these tests [30].

Forward- and backward-facing steps were studied in low-speed experiments on a flat plate [37]. Sketches of the imperfections presented in that work suggest that the steps were sharp. The growth rates evaluated from hot-wire measurements have been compared to those predicted by linear stability analysis of a boundary layer at the same test conditions [165]. The main difference between experimental and numerical cases was the shape of the steps, since smooth steps

were considered in the numerical study. Good agreement of experimental and numerical growth rates was found for large steps ($h/x_h = 0.0044$), whereas for small steps ($h/x_h = 0.0018$), the numerical results underpredicted the experimental findings. This difference is likely to be due to the difference in the shape of the step: in fact, no separation was seen in the numerical study with small steps. This finding confirms the essential role of the shape of the imperfections for boundary-layer stability and transition discussed above.

Numerical and experimental investigations of the influence of surface steps on boundary-layer transition were carried out at ONERA [38,50,172]. The two-dimensional, incompressible flow over a flat plate at zero pressure gradient was examined in the presence of forward- and backward-facing steps by solving the Reynolds averaged Navier-Stokes (RANS) equations [38]. Convective instabilities were assumed to be the only ones that have to be taken into account. This assumption was verified by a comparison of numerical and experimental results [50]. The stability of the computed boundary layer was then studied by means of both local and non-local linear stability theory. The amplification factors calculated with the two approaches were found to be comparable, thus confirming that non-parallel flow effects are small for these two-dimensional configurations (except for the region in proximity of the steps) [38]. For practical purposes, it can be assumed that localized receptivity due to surface imperfections is negligible as compared to the marked amplification of incoming disturbances [172]. Thus, the transition N-factor was assumed to remain the same also in the presence of the surface steps [38]. By means of the e^N method with $N_T \sim 7$, transition in the presence of forward-facing steps was predicted to move rapidly towards the step location when $\mathrm{Re}_{h,\mathrm{cr}} \sim 2000$ had been exceeded. Experiments were performed in a low-speed wind tunnel with a turbulence level $Tu \sim 0.07$ % [38] using a wind-tunnel model whose cross-section was that of the ONERA AFV82 airfoil. Nominally spanwise-invariant steps were created at $x_h/c = 25$ % using plastic foils glued onto the model surface. An IR-camera was used to obtain global information about the natural-transition front, whereas measurements of the transition location were performed by means of a flattened Pitot tube. The experimental results were plotted as $(x_T\text{-}x_h)/(x_{T,0}\text{-}x_h)$ vs. Re_h, where x_T and $x_{T,0}$ are the transition locations in the presence and absence of surface steps, respectively. In the case of forward-facing steps, transition was observed to move markedly towards the step location as $\mathrm{Re}_{h,\mathrm{cr}} \sim 1600\text{-}1800$ had been reached. A semi-empirical method, based on the e^N method, was developed to predict transition in the presence of surface steps. This method will be discussed in Section 6.2.1.

In [40,118], the effect of forward- and backward-facing steps on boundary-layer stability and transition was also experimentally investigated at low speed in a wind tunnel with a very low turbulence level ($Tu < 0.01$ %). The wind-tunnel model was a flat plate. The model angle-of-attack and a trailing-edge flap were adjusted to obtain a nearly-zero streamwise pressure gradient over the flat plate.

Forward- and backward-facing steps of different height were generated by adjusting the bolts and screws holding together the two parts comprising the model [118]. The steps were reported as being sharp [40]. Boundary-layer measurements were conducted by means of hot-wire anemometry. Transition was observed to move progressively towards the step location as the relative step height $h/\delta_{1,h}$ was increased, where $\delta_{1,h}$ had been calculated at the step location for a Blasius flow over the smooth plate. In the case of forward-facing steps, the experimental data, plotted as $\mathrm{Re}_{x\mathrm{T}}$ vs. $h/\delta_{1,h}$, could be approximated by a single curve. The movement of transition towards a more upstream location was observed to be small up to $h/\delta_{1,h} \sim 0.8$. Transition was found immediately downstream of the step location at approximately $h/\delta_{1,h} > 2.3$. Another important finding of this work was obtained by spectral analysis of the hot-wire signals. In the streamwise region between the step location and the transition location, large amplitudes of streamwise velocity fluctuations were found in a frequency range consistent with the unstable region of Tollmien–Schlichting waves, as predicted by linear stability theory for the Blasius flow on the smooth surface. The frequency bands were in agreement also for large steps, even at $h/\delta_{1,h} > 2$ [40]. An experiment similar to that presented in [40,118] was conducted in another low-turbulence wind tunnel ($Tu < 0.05$ %), also using a flat-plate model [41]. The front part of the model was movable in the wall-normal direction and allowed forward- and backward-facing steps of different height to be generated. The height of the steps along the model span was accurately adjusted and controlled, so that the spanwise variation in step height did not exceed $\Delta h = \pm 10$ μm ($\Delta(h/\delta_{1,h}) < \pm 0.02$); moreover, the steps were sharp: defects at the edge of the steps were avoided [185]. The steps were installed at two different streamwise locations, in regions of favorable and adverse streamwise pressure gradients, which were attained using changing wall contours. Transition measurements were performed by means of a Preston tube. Moreover, the mean-velocity profiles and the streamwise velocity fluctuations were measured by means of hot-wire anemometry. Spectral analysis of the hot-wire signals showed that Tollmien-Schlichting waves in the same range of frequencies were responsible for transition on both configurations, with and without steps. The measured amplitudes of the most amplified waves were found to be larger in the presence of the steps [41]. In both studies [40,41], the measured transition locations were correlated with results of linear stability analysis for the smooth configuration. This provided differences in transition N-factors due to the effect of the steps, which can be used for transition prediction based on the e^N method, as will be discussed in Section 6.2.1.

Experimental investigations of the effect of surface steps on boundary-layer transition have been re-initiated at Northrop Grumman Corporation in recent years [12,39,43-44,186]. The experiments focused on the effect of surface steps in the presence of streamwise pressure gradient at low speed. In a first experimental campaign [39], a flat-plate model was tested at unit Reynolds numbers below $0.7 \cdot 10^6$ m^{-1}. The flow quality of the test facility is reported as “very good” (no

data are given) [186]. Forward- and backward-facing steps were directly manufactured on inserts, which were then installed into indents in the model surface. The shape of the imperfection was that of a sharp edge followed by a ramp in the case of forward-facing steps. The ramp was elongated in the streamwise direction (maximal ramp angle of less than 2°). Streamwise pressure gradients were imposed by means of the adjustable upper wall of the test section. The surface pressure gradients were approximately uniform after a certain distance downstream of the leading edge. Note here that the steps were mounted also upstream of this region of nearly-uniform pressure gradient. Mean-velocity profiles were measured in the boundary layer by means of a total pressure tube, whereas transition measurements were conducted using Preston tubes. The data were plotted as $\mathrm{Re}_{x\mathrm{T}}$ vs. Re_k, where $\mathrm{Re}_k = hU_h/\nu_h$ is the roughness Reynolds number evaluated from the boundary-layer velocity profiles of the smooth configuration with $U_h = U(x_h,h)$ and $\nu_h = \nu(x_h,h)$. A pronounced movement of transition towards the step location with increasing Re_k was observed once a critical value of the roughness Reynolds number $\mathrm{Re}_{k,\mathrm{cr}}$ had been exceeded. This critical value was larger for more favorable pressure gradients. However, once $\mathrm{Re}_{k,\mathrm{cr}}$ had been reached, the reduction in $\mathrm{Re}_{x\mathrm{T}}$ due to an increase in Re_k was more marked for more accelerated flows. The most important conclusion of this work was that the streamwise pressure gradient has a pronounced effect on boundary-layer transition induced by surface steps [39]. The range of unit Reynolds numbers was extended to values up to approximately $2 \cdot 10^6$ m^{-1} in a subsequent measurement campaign conducted in a towing wind tunnel [12,43-44,186]. The test models were placed on a carrier vehicle. A low-disturbance environment with $Tu < 0.05$–0.1 % was recorded for all runs. Two different test models were examined in this experimental campaign, both of which had been designed for a certain streamwise pressure gradient corresponding to either moderate or strong acceleration. Forward- and backward-facing steps were created by moving a leading-edge piece with respect to the rest of the model. The imperfections were thus sharp steps, perpendicular to the surface. It was reported that tolerance, perpendicularity, and rigidity of the surface steps was ensured, since the material used for the surface surrounding the step location had been manufactured using stainless steel [43]. The used measurement techniques were the same as those from the previous experiment [39], with the addition of hot-wire anemometry, which was used to obtain spectra of the velocity fluctuations and validate the results of the transition location measurements. An important result of the investigations at the moderately favorable pressure gradient was the agreement between the frequencies corresponding to peaks in the disturbance power spectra for the smooth configuration with those of the peaks measured in the presence of the surface imperfections. However, the amplitude of the velocity fluctuations was observed to increase in the presence of larger steps [44]. The main conclusion from these experiments was that a favorable pressure gradient has a strong stabilizing effect on the laminar boundary layer even in the presence of surface steps [12,43-44].

The flow around sharp forward-facing steps on a flat plate at zero pressure gradient was computed at the University of Stuttgart by means of direct numerical simulations (DNS) [45,46]. Three inflow Mach numbers were examined: M = 0.15, 0.8, and 1.06. The effect of step location x_h and relative step height h/θ_h was also investigated, where θ_h is the boundary-layer momentum thickness at the step location evaluated for the smooth configuration. The majority of the computations were performed with an isothermal wall at a temperature $T_w = T_\infty$. Wall cooling was thus considerable at large Mach numbers: for example, the wall temperature ratio was $T_w/T_{aw} \sim 0.9$ at M = 0.8. At subsonic conditions, the main features of the basic flow were shown to be nearly the same for all cases. Two separation bubbles were found: a first one upstream of the step and a second one immediately downstream of the step corner. This latter bubble was smaller than that upstream of the step, especially in the wall-normal direction, and disappeared at sufficiently small steps. A major change in the flow topology was observed when the inflow Mach number was increased from subsonic to (slightly) supersonic [46]. At M = 1.06, no separation bubble was present downstream of the step corner at all examined test conditions, whereas the region of separated flow upstream of the step was much longer than at subsonic Mach numbers. It is interesting to note that a thin "sub-boundary layer", starting at the step corner, was observed downstream of the step. This sub-boundary layer vanished at a certain distance downstream of the step, where the undisturbed velocity profile was recovered. The sub-boundary layer was observed at both Mach numbers, M = 0.8 and 1.06, being slightly shallower in the supersonic case as compared to the subsonic case. Boundary-layer stability was examined by means of DNS and linear stability theory. For the direct simulation of the disturbances, "a wave packet was introduced into the steady baseflow by suction and blowing at the wall over a short time at the beginning of the simulation" [45]. At subsonic Mach numbers, the influence of the separated flow region led to a marked increase of the amplification ratios as compared to the envelope curve obtained for the smooth configuration. Moreover, a peak in the *N*-factor was observed at the step location. Downstream of the step, after the transient region in its proximity, the evolution of the *N*-factor envelope curve depended on the specific test conditions. In the majority of the examined cases the *N*-factor envelope curve returned to that of the smooth surface only at a large distance downstream of the step [45,46].

Numerical computations were also carried out at the U.S. Air Force Research Laboratory [35-36] to investigate the effect of forward- and backward-facing steps on the flow over a flat-plate configuration at M = 0.1. The flowfield up to transition was fully resolved; the computations thus corresponded to DNS. The turbulent flow further downstream was computed by large eddy simulations (LES). The numerical studies complemented the experiments carried out at Northrop Grumman Corp. discussed above [12,43-44, 186]. In a first numerical study, a roughness Reynolds number $\mathrm{Re}_k \sim 1000$ was considered [36]. Only one separation bubble, upstream of the step, was found in the case of

forward-facing steps. Examination of the instantaneous flowfield showed the presence of "very small coherent two-dimensional structures, which are amplified by the geometric disturbances and convect downstream of the step. Eventually, these structures lose their coherence, break down into more complex forms, and evolve to a chaotic state." [36]. The two-dimensional structures were evident in computations without numerical forcing and had a frequency in the range of unstable waves predicted by linear stability theory. The generation of these structures, however, was not uniform, since the frequency range for unstable waves was relatively large. The evolution of the structures was regularized by forcing at a frequency corresponding to that of the most unstable wave downstream of the step. The obtained transition location was in agreement with the experimental results [36]. A second numerical study considered alternative techniques for transition prediction, which were less resource-intensive [35]. Two-dimensional numerical simulations were performed for the same problem examined above [36], this time with forward- and backward-facing steps at roughness Reynolds numbers $\mathrm{Re}_k \sim 600$, 800, and 1000. DNS/LES with numerical forcing were performed, similar to those in the previous work [36], to determine the transition locations for the three roughness Reynolds numbers. The transition locations were used for correlations with the growth factors, calculated by means of linear stability theory using unforced solutions as the basic flowfield, and with growth factors of the integrated turbulent kinetic energy, computed for both unforced and forced two-dimensional simulations. The results were correlated for one of the three Re_k; the correlated growth factors were then used to predict transition in the other two cases. For forward-facing steps, the accuracy of transition prediction based on the growth factors of the integrated turbulent kinetic energy was reasonable in the case of forced simulations, whereas the accuracy was poor in the case of unforced simulations. Transition prediction based on linear stability analysis was reasonably accurate [35].

Other recent experimental investigations are briefly discussed here. Skin-friction measurements using oil-film interferometry were performed on an NLF-airfoil model at $\mathrm{M} = 0.6$ [42]. Transition was measured almost immediately downstream of a cylindrical wire, whereas it occurred at $\Delta(x_\mathrm{T}/c) \sim 10$ % upstream of the smooth-configuration transition location in the case of a forward-facing step of approximately the same height ($\mathrm{Re}_h \sim 1000$). The effect of distributed roughness and surface steps on the performance of a NACA 63_3-418 airfoil was investigated in a low-speed wind tunnel [49]. Forward-facing steps were used to simulate real imperfections originating from the manufacturing process and from erosion or chipping of the paint in the leading-edge region of wind turbine blades. Transition was measured by means of IR-thermography and a hot-film array. Forward-facing steps at a roughness Reynolds number $\mathrm{Re}_k = 186$ were found to have no influence on boundary-layer transition [49]. Experiments on the effect of surface steps on CFI-dominated transition were carried out in [38,47-48].

3 Experimental setup

3.1 Cryogenic Ludwieg-Tube Göttingen (DNW-KRG)

The tests were conducted in the Cryogenic Ludwieg-Tube Göttingen (DNW-KRG) [55]. It is a Ludwieg-tube facility [187] that uses gaseous nitrogen as test gas. A sketch of DNW-KRG is shown in Fig. 3.1.1a: the dark and light blue areas pertain to the facility components where the gas can be charged to the desired pressure p_c and temperature T_c, and to where they are (generally) kept at atmospheric conditions, respectively. After charging all components upstream of the fast-acting valve to the desired test conditions, this valve is opened in less than one-tenth of a second, whereby the gas accelerates into the test section and, simultaneously, an expansion fan moves with the speed of sound in the opposite direction into the storage tube. After the passage of the expansion fan, the flow in the storage tube has a Mach number that is determined only by the ratio of the cross-sectional areas of the storage tube and of the sonic throat in the facility [187], whereas the Mach number of the flow in the test section depends on the ratio of the cross-sectional areas of the test section and of the sonic throat [55].

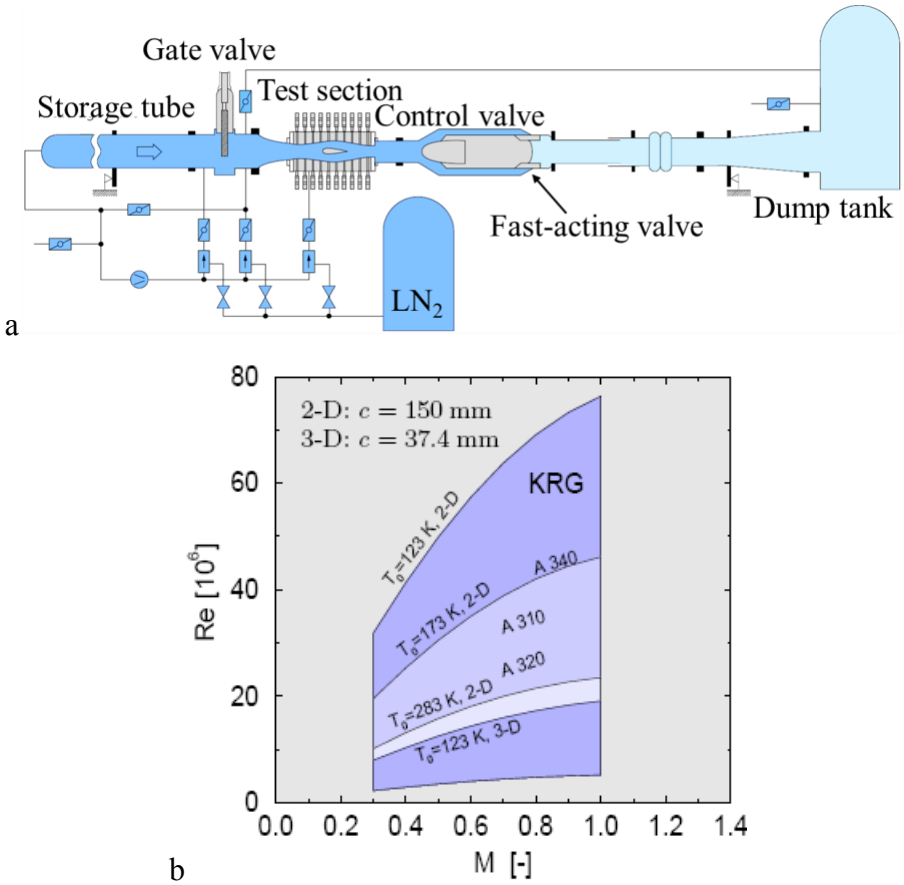

Fig. 3.1.1. a: principle sketch of the DNW-KRG wind tunnel [56]. b: Re-M envelope of DNW-KRG [55].

By increasing the pressure and decreasing the temperature of gaseous nitrogen, the facility is capable of achieving Reynolds and Mach numbers characteristic of transport aircraft flying at high subsonic and transonic speeds. The minimal charge temperature and maximal charge pressure are 105 K and 1.25 MPa, respectively. The envelope of Mach numbers and Reynolds numbers that can be tested at DNW-KRG is shown in Fig. 3.1.1b. Mainly two-dimensional models are investigated in the DNW-KRG wind tunnel. For this type of wind-tunnel model, the reference length used for the Reynolds numbers shown in Fig. 3.1.1b is a model chord length of $c = 150$ mm. The cruise Mach and Reynolds numbers (based on the mean aerodynamic chord of the wing) of aeroplanes produced by Airbus SAS [51,188-189] are also shown for comparison. The minimal test Reynolds number that can be run at DNW-KRG is limited by the minimal pressure difference necessary to operate the wind tunnel when the facility components downstream of the fast-acting valve are kept at atmospheric conditions. The Reynolds number range can be extended to even lower values by reducing the pressure of these latter facility components to less than atmospheric pressure by using a vacuum pump.

A total run time of about one second is attainable in DNW-KRG by the use of a 130 m long storage tube. Steady flow conditions are obtained in the test section for some tenths of a second, as long as viscosity effects can be neglected [55]. The test section is 0.4 m wide, 0.35 m high, and 2 m long and has adaptive upper and lower walls that allow interference-free contours to be set. Two-dimensional wall adaptation in the *x*-*z* plane is accomplished between test runs by means of a non-iterative procedure based on the Cauchy's integral formula, on the pressure distribution measured on the walls, and on the walls deflection [55,190]. After adaptation, the remaining interferences of the upper and lower walls for angle-of-attack and Mach number are less than ±0.01° and ±0.001, respectively. It should be remarked here that the side walls of the test section are straight surfaces that cannot be adapted. Their interference causes a deviation of the experimental pressure distribution from the ideal two-dimensional case, as discussed in [55,145,191] for NLF airfoils. Two-dimensional models with chord length $c \leq 200$ mm are clamped into turntables mounted at the lateral test-section walls. The installation position is approximately at half the height and half the length of the test section. Details on the wind-tunnel instrumentation and on its accuracy are given in [55-56,145,148].

By virtue of the working principle of the DNW-KRG facility, the gaseous nitrogen charged at high pressure in the storage tube quickly expands after the fast-acting valve is opened, whereby this expansion provides a fast temperature drop in the flow; subsequently, this lower temperature remains approximately constant during the actual run (see above), while the model temperature drifts just slightly from its pre-run values. When the pre-run model temperature and the charge temperature of the gas are approximately the same, this leads to a temperature difference between flow and model surface during a run [55,145,192].

In this standard case, the ratio between model surface temperature and adiabatic wall temperature T_w/T_{aw} is significantly larger than one. The standard wall temperature ratio at DNW-KRG depends mainly on the magnitude of the total temperature drop in the incoming gas (i.e., on the freestream Mach number and on the charge termperature) and on the thermal properties of the model. For a model made from austenitic stainless steel and coated with a 0.12 mm thick layer of temperature-sensitive paint (TSP), such as that investigated in the present work (see Section 3.4.1), the wall temperature ratio at $T_c \sim 288$ K is in the range $T_w/T_{aw} = 1.040\text{-}1.065$ at $M = 0.77$. It decreases to $T_w/T_{aw} = 1.020\text{-}1.040$ at $M = 0.35$. An example of the typical development of flow and model temperatures as a function of the run time is shown in Fig. 3.1.2. The surface temperature decreases as a consequence of the freestream temperature drop, although the magnitude of the reduction is markedly smaller. Clearly, the surface temperature reduction depends on the flow conditions and on the boundary-layer state. It can be also seen that the temperature decrease measured below the model surface is less pronounced than that measured within the TSP layer. The gray bar in Fig. 3.1.2 shows the time window during which the wind-tunnel data are evaluated.

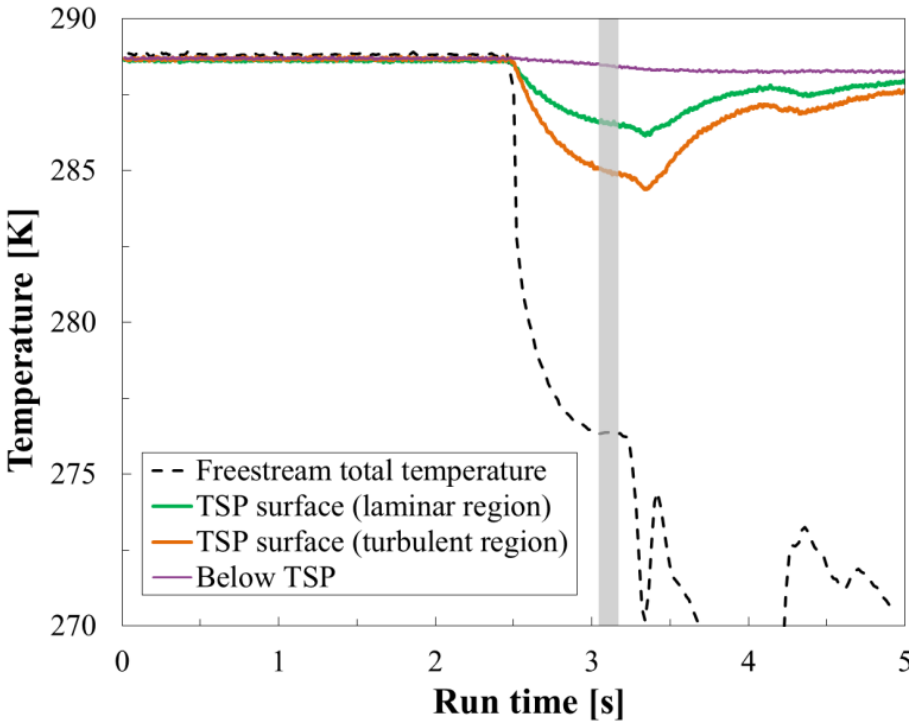

Fig. 3.1.2. Typical evolution of model and flow temperatures during a run in DNW-KRG at M = 0.77 and Re = 7 · 10^6. The gray bar indicates the test window used for evaluation.

The influence of the wall temperature ratio on the experimental data can be examined by means of an unconventional test procedure [55,145], which uses an additional component of the DNW-KRG facility: its gate valve (see Fig. 3.1.1a). Test section and storage tube are separated when the gate valve is closed, so that

the gas in the test section, where the model is installed, can be conditioned independently of the gas in the storage tube. At the same time, the temperature of the gas within the storage tube is kept at the appropriate value that allows the desired test conditions during the run to be attained. This "pre-conditioning procedure" provides an opportunity of implementing a different wall temperature ratio during the actual testing time, generally lower than the standard wall temperature ratio, which occurs when the model and the gas in the storage tube are at the same temperature before the run. Further details on the pre-conditioning procedure are given in [145].

Because of the absence of any mechanical driving, regulating, and throttling devices, Ludwieg tubes have good flow quality [56,193]. In principle, the only variations of flow quantities in space and time are due to the unsteady, turbulent boundary layer developing on the wind-tunnel walls during a test run. Acoustical disturbances traveling from the storage tube into the test section are considered to have a magnitude much lower than that of the noise radiated from the wall boundary layer [193]. The results of extensive measurements of the time and spatial development of various fluctuating quantities at DNW-KRG are discussed in [56].

In conclusion, DNW-KRG provides adequate conditions for NLF testing at high Reynolds numbers. The tests are usually restricted to two-dimensional flows. DNW-KRG allows investigation of boundary-layer transition induced by amplification of streamwise instabilities, and can be carried out at test conditions similar to flight conditions of transport aeroplanes, since large Reynolds numbers and both subsonic and transonic Mach numbers can be achieved. The adaptive upper and lower walls of the DNW-KRG test section can be shaped so that they do not interfere with the airfoil flow. The facility has good flow quality and the model surface can be generally kept free of contaminating particles. The use of the DNW-KRG gate valve allows the effect of the thermal condition at the airfoil surface to be studied. The marked reduction of the flow temperature occurring during a run at DNW-KRG ensures very accurate transition detection by means of temperature-sensitive paints, to be discussed in Section 3.4.1. For these reasons, DNW-KRG was the selected wind tunnel for the investigations planned in the present work.

3.2 Design of the model cross-section

A flat-plate configuration was specifically designed for the transition experiments conducted in the present work. The model was designed for the systematic study of the effect of two-dimensional surface imperfections, changes in Reynolds number, Mach number, and streamwise pressure gradient, and the effect of a non-adiabatic surface on boundary-layer transition in the DNW-KRG facility. The model is called *PaLASTra* model (*flat plate for the analysis of the effect on laminar-turbulent transition of surface imperfections, wall temperature*

ratio and pressure gradient). This name for the test model will be used from now on. The design focused on the upper side of the model, which was the one designated for the transition experiments in the present work. The numerical tools used for the design are presented in Section 3.2.1. The design of the *PaLASTra* model cross-section has been already presented in [148] and is summarized in Section 3.2.2. Additional details are given in Appendix B.1.

3.2.1 Numerical tools

The code MSES [194,195] calculates two-dimensional flows around airfoils with good accuracy for a wide range of Reynolds and Mach numbers, transonic flows included. The irrotational part of the flowfield is described by the Euler equations in conservative integral form; shocks are therefore handled correctly [194]. The boundary-layer formulation employs the momentum integral equation and the energy shape parameter integral equation, obtained from a combination of the momentum integral and energy integral equations. Closure for the integral boundary-layer equations are based on different assumptions for laminar and turbulent flows. A transition prediction formulation, based on the e^N method (see Section 2.4), is incorporated into the boundary-layer formulation. The Euler equations and the integral boundary-layer equations are strongly coupled through the boundary-layer displacement thickness: in fact, the surface streamline is displaced in the wall-normal direction by a distance corresponding to the local displacement thickness. After discretization, the entire set of equations (boundary-layer and transition formulations included) is solved as a fully-coupled system by a global Newton-Raphson method [195].

COCO is a program to compute the wall-normal velocity and temperature profiles of steady, compressible, laminar boundary layers along swept, conical wings [196,197]. The boundary-layer equations are expressed in terms of four variables: an acceleration parameter of the irrotational outer flow (similar to the Hartree parameter, see Section 2.3.1), a wing conicity coefficient (equal to zero for an infinite swept wing), a fluid viscosity coefficient (equal to one for incompressible flows), and a wall suction parameter. In practice, the equations for two-dimensional flow appear as the limiting case of the equations for an infinite swept wing, which are a specific case of the equations for a conical wing. The system of equations resulting after discretization is solved by a Newton-Raphson method [196,197]. The standard version of COCO allows only calculations with an adiabatic wall. The boundary-layer code has been modified to enable calculations with an isothermal wall, so that the thermal boundary condition at the model surface could be accounted for [198]. COCO provides also the first and second derivatives, with respect to the wall-normal coordinate, of the streamwise and spanwise velocity components and of the temperature. These are essential quantities for boundary-layer stability computations based on linear stability theory.

The stability analysis tool LILO [199] calculates the amplification rates and the corresponding amplification factors (*N*-factors) of primary boundary-layer modes. The computations are based on linear stability theory (see Section 2.2.1) and can be carried out assuming that the mean flow is locally parallel (local stability theory) or that the mean-flow quantities change slowly in the streamwise direction (parabolized stability equations, PSE). In this work, the computations were performed using local stability theory, since non-parallel flow effects are negligible for the considered two-dimensional configuration in a two-dimensional flow [38,83,85-87,89,92-94]. Local stability theory formulations for incompressible and compressible flows are available in LILO. In the case of compressible flows, boundary-layer stability is described in terms of the following variables: velocity, pressure, and temperature. The temporal stability problem is considered in LILO, the spatial growth rates being computed from the temporal growth rates using Gaster's transformation [149]. The generalized eigenvalue problem obtained under the assumptions of linear, local stability theory is discretized and the eigenvalues of the resulting matrix are computed using a generalized inverse Rayleigh iteration [199].

3.2.2 Wind-tunnel model requirements and model cross-section shape

The main requirements for the wind-tunnel model were:

1) avoidance of crossflow, attachment-line, and centrifugal instabilities;
2) achievement of a large region of uniform streamwise pressure gradient on the model upper side;
3) attainment of different, but still uniform, streamwise pressure gradients on the same portion of the model chord;
4) limitation to a small chordwise extent of the region of flow acceleration in the leading-edge area;
5) avoidance of local pressure minima in the leading-edge region for the cases with zero and favorable streamwise pressure gradients;
6) continuity of wall contour, slope, and curvature over the whole model upper side.

This study focused on the effect of two-dimensional surface imperfections on transition of boundary layers where streamwise instabilities are predominant. Therefore, other instability mechanisms (see Section 2.1) had to be prevented. Crossflow and attachment-line instabilities were easily avoided by designing a two-dimensional model, i.e., an unswept model with a spanwise-invariant cross-section. This model was mounted perpendicular to the (quasi-) two-dimensional flow of DNW-KRG. Centrifugal instabilities were prevented by designing the

cross-section with convex regions only [11,200]. Requirement 1) was thus fulfilled.

Requirement 2) was essential for the present investigation. Only with a (quasi-) uniform streamwise pressure gradient it is possible to decouple, and thus systematically study, the effect on boundary-layer transition of the various parameters to be examined in this work. In fact, on the curved surface of an airfoil, the local pressure gradient changes continuously along the streamwise coordinate. A variation of the transition location, e.g., due to a change in the wall temperature ratio, leads also to a change in the stability situation, since the new transition location is, in general, on a region where the pressure gradient is different from the previous one [145]. A quasi-uniform pressure gradient can be achieved on a flat test surface, which was chosen as the basic shape for the cross-section of the two-dimensional model. The final shape of the cross-section of the *PaLASTra* model is shown in Fig. 3.2.2.1 at this stage already to serve as a reference for the following discussion.

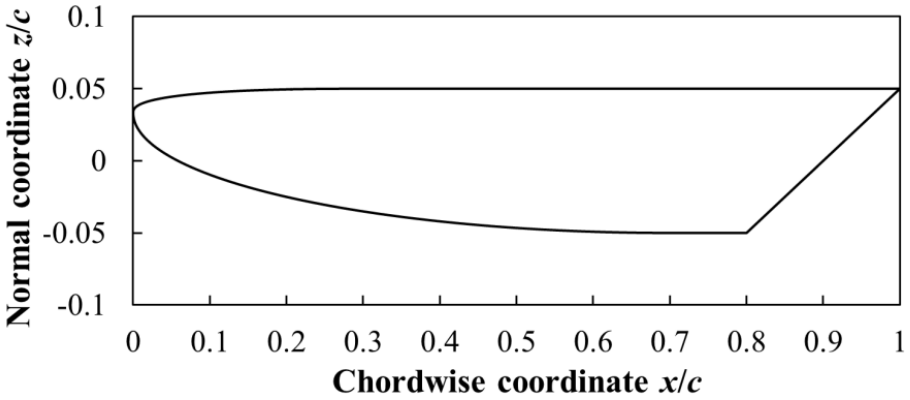

Fig. 3.2.2.1. Cross-section of the *PaLASTra* model. Axes are not equally scaled.

Long flat plates have been typically used for fundamental boundary-layer transition experiments at low speed (see Chapter 2). Challenges for the application at DNW-KRG of typical solutions for flat-plate experiments at low speed are discussed in Appendix B.2. In the present study, the model chord length was limited to $c \leq 0.2$ m, so that the model fitted in the DNW-KRG test section using the available support turntables. This allowed the model angle-of-attack to be easily varied, by which means the surface pressure distribution could be changed and requirement 3) could be fulfilled. The upper and lower test-section walls were adjusted to attain interference-free contours using the adaptation procedure mentioned in Section 3.1, which is standard procedure for airfoil testing in DNW-KRG. As long as boundary-layer transition occurs on the region of uniform pressure gradient, the transition Reynolds number is independent of the unit Reynolds number, provided that the other parameters are kept fixed. When, for example, the streamwise pressure gradient is changed to be more favorable, the boundary layer can remain laminar over the complete surface

under investigation. Nevertheless, the unit Reynolds number can be increased to obtain transition on the model surface. This significant advantage is offered only by model configurations that feature a large chordwise region of uniform pressure gradient, which remains on the same portion of the model chord for different test conditions and, also, different values of the pressure gradient itself. Since transition can be achieved on the model surface by increasing the unit Reynolds number, a model chord length of $c \leq 0.2$ m is sufficient for transition experiments in DNW-KRG using a flat plate. (In fact, the limitation with DNW-KRG is for testing at the lowest unit Reynolds number that can be obtained with the facility, as discussed in Section 3.1.)

When a flat plate is used for transition experiments, the model leading edge has to be to be designed and manufactured with great care, since it has a marked influence on the resulting flowfield [201]. The related requirements are listed under points 4) to 6) at the beginning of this section. Provided that the model surface is smooth, there are two regions where long-wavelength external disturbances can couple to the short-wavelength boundary-layer instability waves: the leading edge and the junction between leading edge and flat plate, as discussed in Section 2.2.2. Requirements 5) and 6) were fulfilled by the choice of a modified super-ellipse (MSE) [202] as the chosen shape for the leading edge on the model upper side. The geometry of a MSE is given by the formula

$$\left(1-\frac{x}{a}\right)^{m(x)}+\left(\frac{z}{b}\right)^{2}=1 \text{ for } 0 \leq x/a \leq 1, \qquad (3.2.2.1)$$

where a and b are the semi-axes of the MSE in the streamwise and normal directions, respectively, and $m(x) = 2 + (x/a)^2$. This shape fairs the junction but at the same time has nose radius and geometry close to those of an ordinary ellipse. The lower side of the leading-edge surface is an ordinary ellipse. The drawback of both elliptic or MSE shapes, as opposed to a sharp leading edge, is that the curved leading-edge region is rather large. At the same time, ordinary ellipses and modified super-ellipses with large aspect ratio lead to a reduction of overall leading-edge receptivity to freestream disturbances [202-205]. (Leading-edge receptivity to acoustic disturbances is actually larger for a smaller nose radius, but overall receptivity is reduced because of the mitigation of the adverse pressure gradient in the leading-edge region.) A compromise was found by reducing the extent of the upper part of the leading edge in the normal direction. The ratio between the minor semi-axis of the MSE (model upper surface) to that of the ordinary ellipse (model lower surface) is 1/5. The small minor semi-axis of the modified super-ellipse allows a large aspect ratio to be maintained, while at the same time it leads to a reduction of the streamwise extent of the flow acceleration region over the model leading edge, thus fulfilling requirement 4). The MSE extends up to $x/c = 30$ %, which corresponds to an aspect ratio of 18:1. This aspect ratio is adequate for keeping overall leading-edge receptivity low, as

shown in previous work [107,203,206]. The cross-section trailing edge is a sharp edge. The streamwise extent of the ordinary ellipse is $\Delta(x/c) = 70$ %. Since flow separation was expected on the model lower side, an abrupt contour change (a corner) was placed at $x/c = 80$ %, so that the separation point was forced to occur at this sharp corner. This choice allowed results obtained at different flow conditions to be easily compared, as will be shown in Chapter 5. The remaining part of the cross-section lower side is a flat surface. The cross-section of the lower side aft of the sharp corner (between $x/c = 80$ % and the trailing edge) is also flat.

Favorable streamwise pressure gradients are obtained on the model upper side by setting the angle-of-attack to AoA < -1.8°. Such pressure gradients well represent those characteristics of boundary-layer development on the upper side of NLF airfoils at small angles-of-attack [22,33,157,207-208]. At these conditions, the boundary layer on the upper side of an NLF airfoil is moderately accelerated, and therewith kept laminar, over a large portion of the chord length. This is also the region where structural joints, such as that between leading edge and wing box, would be present. Continuity of the contour can be interrupted also by leading-edge panels and inspection/access panels. Surface imperfections are probably unavoidable at these locations and they could hence disrupt laminar flow. At design conditions, the boundary layer is accelerated also on the lower side of NLF airfoils; boundary-layer stability on this airfoil side is even enhanced at larger angles-of-attack. In practical applications, the capability of attaining laminar flow on these surfaces also depends on their smoothness. In addition to the sources of imperfections mentioned above for the upper side of NLF surfaces, the corresponding lower side is affected also by imperfections originating from the installation of high-lift devices, such as Krueger flaps. From these considerations, it appears clear that the installation location of forward-facing steps in the current study had to be in the region of moderate flow acceleration, which is at approximately 20 % < x/c < 70 % on the upper surface of the designed cross-section. Moreover, an investigation of the effect of surface imperfections on boundary-layer transition in the presence of various pressure gradients would be systematic only when both imperfection location and transition location are in the same region of quasi-uniform pressure gradient. Therefore, the steps had to be placed in a region where the quasi-uniform pressure gradient has already been developed, i.e., sufficiently downstream of $x/c \sim 20$ %. At the same time, downstream of the step location, a large region with quasi-uniform pressure gradient had to be kept available for examination of the transition location movement due to the effect of the surface imperfection. In order to fulfill both requirements, the step location on the model upper side was chosen to be $x_h/c = 35$ %. Furthermore, in the experiments conducted with the smooth configuration (no steps installed), care was taken to adjust the Reynolds number for a given test case (fixed Mach number, pressure gradient, and wall temperature ratio) to such a value that transition was achieved at $x_T/c \sim 60$-70 %. This distance (x_T - x_h) was large enough to capture the progressive movement of

the transition location all the way upstream towards the step location as the step height was increased.

3.3 Wind-tunnel model

Both wind-tunnel model shape and surface imperfections were designed to be (nominally) invariant in the spanwise direction; this was to ensure that the flow remained (quasi-) two-dimensional, as required in this study. The span width of the model is $b = 500$ mm, so that it can be mounted at the lateral walls of the 400 mm wide test section. The model chord length was chosen as $c = 200$ mm, which is the maximal chord length possible for two-dimensional model testing with the given support turntables at DNW-KRG [55]. The choice of the large model chord length is advantageous because it allows not only larger chord Reynolds numbers to be reached, but also the unit Reynolds number Re/c for given chord Reynolds number to be decreased. This leads to a reduction of the allowable size (with respect to the boundary-layer thickness) of undesired surface imperfections or surface contamination which could potentially trigger premature transition [145,192,209]. The maximal model thickness d was selected as $d = c/10$, viz., 20 mm. This model thickness is comparable to the relative thickness of conventional and NLF airfoils and is sufficient for installation of the instrumentation discussed in Section 3.4. A simplified drawing of the model construction is shown in Fig. 3.3.1. As can be seen from this figure, the model was composed of two major parts, named the front and main parts. The model leading edge was machined directly on the front part, thus ensuring that the wall contour and its first and second derivatives are continuous at the junction between leading edge and flat plate, as required for this study (see Section 3.2.2).

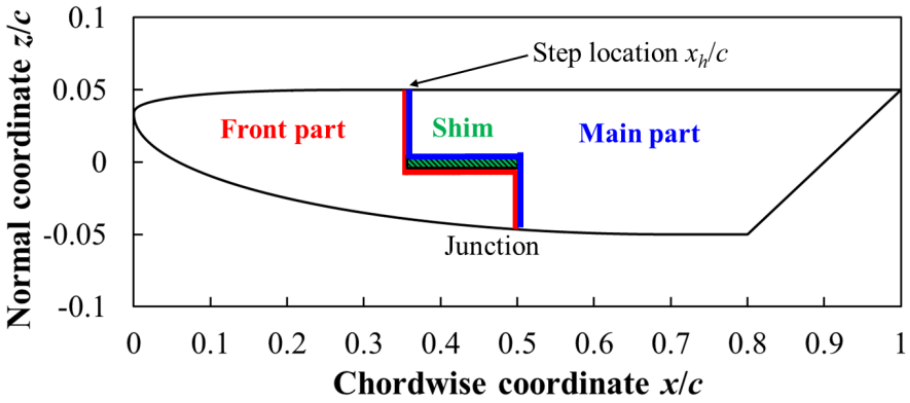

Fig. 3.3.1. Simplified drawing of the *PaLASTra* model construction (side view).

Two-dimensional steps of a desired height can be mounted at the selected chordwise location $x_h/c = 35$ %. This is accomplished by installing shims of appropriate thickness at the horizontal interface between the two major parts comprising the model. The model was designed to achieve a (nominally) smooth surface when a shim of thickness $\tau = 1$ mm is used. Forward-facing steps can be

generated by installing shims with thickness $\tau > 1$ mm. With this design, the shape of the imperfection (abrupt step, perpendicular to the surface, with sharp corners) was assured to be the same for each tested configuration. This was essential for the systematic study to be carried out in this work. It should be also emphasized that, with this setup, the investigated surfaces remain the same for all tested configurations. Besides the shim for the nominally smooth (step-less) contour, three shims with thicknesses $\tau = 1.03$, 1.06, and 1.09 mm were manufactured, so that forward-facing steps of nominal height $h = 30$, 60, and 90 μm could be implemented. These values of step height were selected on the basis of the boundary-layer displacement thickness at the step location $\delta_{1,h} \sim 90$ μm, computed in the design phase for the smooth configuration at M = 0.7–0.8 and Re = $6 \cdot 10^6$. Thus, values of relative step height $h/\delta_{1,h} \sim 1/3$, 2/3, and 1, and step Reynolds numbers $\mathrm{Re}_h = U_\infty h/\nu_\infty \sim 900$, 1800, and 2700 could be investigated at these test conditions. These values of the non-dimensional parameters were relevant for a comparison with data available from previous work [12,34,38,40-41,43-46,169] (see Section 2.5).

The three model components: front part, main part, and shim, were held together by ten screws, which were distributed evenly along the model span and inserted from the model lower side. After assembly, the remaining screw holes were filled with wax before installation of the model in the test section, guaranteeing a smooth surface at these locations. Two dowel pins were used to align the model front and main parts. The contact surface between model front and main parts was provided with two grooves in the spanwise direction, in which sealing cords were installed. Moreover, acrylic sealant was applied onto the port and starboard sides of the wind-tunnel model. In this way, even if small gaps were still present between the front and main parts of the model, one could at least ensure there was no flow through the model. The solution adopted for the implementation of the steps is similar to that in the experiments discussed in [39-40,43,118], in which the leading edge was moved with respect to the rest of the test object. The present setup should provide a more uniform spanwise distribution of the step height than that obtained in earlier work, since the step is generated along the whole model span by a single device (the shim), in contrast to the bolts and jacks [40,118] and the translating slides [43] used to generate the step in those other experiments. Moreover, the current setup should also be more rigid than that used in past work, since the three model components are tightly clamped together by clamping jaws on the sides where they are fixed to the turntables mounted at the side walls of the DNW-KRG test section.

The wind-tunnel model was made from austenitic stainless steel. This material is appropriate to withstand the large aerodynamic loads acting on the model in DNW-KRG when tests are performed at high Mach numbers and at high charge pressures. Finite element analysis of the model structure under the maximal aerodynamic loading encountered in the measurement campaign showed that the largest Von Mises stress in the model was less than 1/6 of the maximally

allowable stress of the material (taken as the tensile limit). Finite element analysis also showed that model deformation was negligible under these conditions.

The model was designed for the application and installation of temperature-sensitive paint, pressure taps, and thermocouples. The instrumentation is discussed in Section 3.4. For the application of temperature-sensitive paint, two pockets were machined into the model surface: one on the model front part and one on the model main part. The pockets were designed to be (nominally) 120 µm deep, so that the applied TSP layer, with a thickness equal to the depth of the pockets, completely filled the pockets. The designed contour was thus preserved. The pockets for TSP application are sketched in Fig. 3.3.2, where the model contour is shown before and after TSP application. The pocket on the model front part extends from $x/c = 33.5$ % on the model upper side all the way around the nose up to $x/c = 5$ % on the model lower side, which assured that the stagnation point was on the TSP coated surface at all angles-of-attack of interest in this study. The pocket on the upper side of the model main part was situated in the region $36.5\ \% \leq x/c \leq 97.5\ \%$. The remaining model surface was left uncoated. Since the model lower surface was not the surface of major interest in this work, transition fixing was applied on this model side for all examined configurations. This led to an improvement in repeatability and reproducibility of the surface pressure distributions, and hence of the results in general [201]. Glass beads (nominal diameters 33–40 µm) for triggering boundary-layer transition were embedded in a spanwise strip made from acrylic material, which was placed at $7\ \% \leq x/c \leq 8\ \%$ on the lower surface.

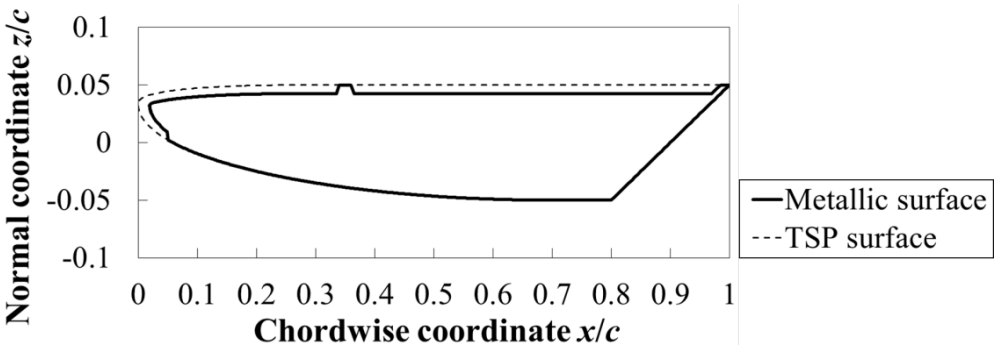

Fig. 3.3.2. Sketch of the *PaLASTra* model contour before and after TSP application (side view).

The use of stainless steel for the regions $33.5\ \% \leq x/c \leq 36.5\ \%$ and $x/c \geq 97.5\ \%$ on the model upper side ensured sharp edges for the step at $x_h/c = 35$ % and for the trailing edge, which would not have been achievable if these regions had been coated with TSP. In fact, sanding down and polishing of the TSP layer, carried out to obtain the desired paint thickness and the appropriate surface smoothness, would round these edges. Furthermore, the use of stainless steel ensured perpendicularity, rigidity, and spanwise-uniformity of the steps, as

already emphasized in [43]. The quality of the model upper surface at the junction between front and main parts was carefully measured before and after each series of tests with a certain model configuration. These measurements were carried out in the chordwise direction at various spanwise locations, using a contact profilometer [210] with a vertical resolution of ±8 nm. In the case of the smooth (step-less) configuration, only a step of less than 1 μm was measured at all spanwise locations. However, a small gap was found between the front and main parts of the model, whose average width was approximately 25 μm. This configuration will be named "smooth" throughout this work, although it is clearly not ideally smooth. In the case of the step configurations, the measurements of the surface quality at the junction showed that the steps were sharp (the radius of the step upper corner was less than 0.5 μm) and perpendicular to the model surface. Furthermore, no gap was found. The spanwise distribution of the step heights is shown in Fig. 3.3.3 for the four tested configurations: the smooth and three step configurations. The step configurations have steps of nominal height $h = 30$, 60, and 90 μm; throughout the rest of this work they will be named "step-1", "step-2", and "step-3" configuration, respectively. A glance at Fig. 3.3.3 shows that the spanwise distribution of the step height is essentially uniform, especially in the region $0.3 \leq y/b \leq 0.7$, which was that of major interest for the study of transition in the present work. In this region, the variation of the step height was less than $\Delta h = \pm 1$ μm. Thus, it could be guaranteed that the (quasi-) two-dimensional boundary layer encountered a (quasi-) two-dimensional step, placed perpendicular to the flow, and nearly invariant in height in the spanwise direction. The variation of step height between the measurements conducted before and after each test series was negligible for the smooth configuration, for the step-1 configuration, and for the majority of the spanwise locations of the step-3 configuration. In the case of the step-2 configuration and some of the spanwise locations of the step-3 configuration, the step height had slightly increased (by 1.5 μm in average) after the tests had been completed. This may be due to the effect of aerodynamic loading in the presence of small differences in model rigging. It is possible that, in the first test runs with these configurations, aerodynamic loading caused the screws to settle and thus led to a slight displacement between model front and main parts. After this had occurred, the model structure (viz., the step heights) remained the same for all subsequent test runs. (An effect of thermal contraction is unlikely, since the charge temperature $T_c \sim 288$ K was close to ambient temperature, and the change in model temperature during a test run was small.) In any case, the variation in step height for these cases was small: less than 3 μm at all spanwise locations. More details on the shape of the junction between model front and main parts (including the measurements) are presented in Appendix B.3.1.

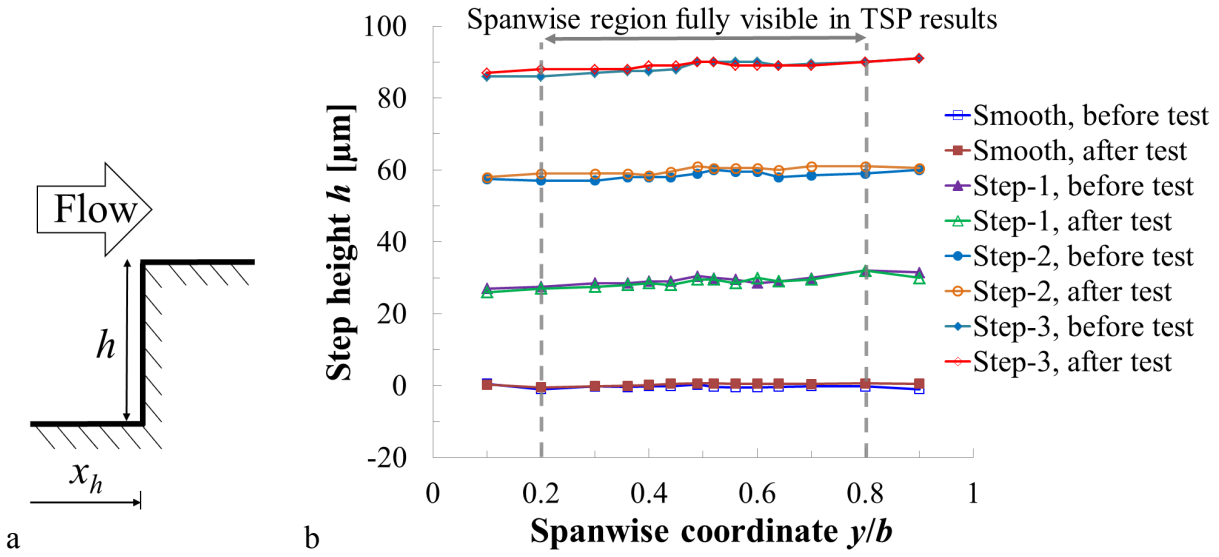

Fig. 3.3.3. a: sketch of step contour (side view). b: spanwise distribution of step height. Measurements conducted over the step location x_h/c = 35 % in the streamwise direction by means of a contact profilometer [210]. The measurements were carried out before installation of each model configuration in the wind tunnel ("before test") and after the tests on that configuration had been completed ("after test").

3.4 Instrumentation of the wind-tunnel model

The *PaLASTra* model was coated with TSP for transition detection, and equipped with pressure taps and thermocouples for measuring, respectively, the surface pressure distribution and the model temperature evolution during a test run. An overview of the model instrumentation is shown in Fig. 3.4.1. The challenges for the application of other measurement techniques for transition experiments at DNW-KRG are discussed in Appendix B.4.

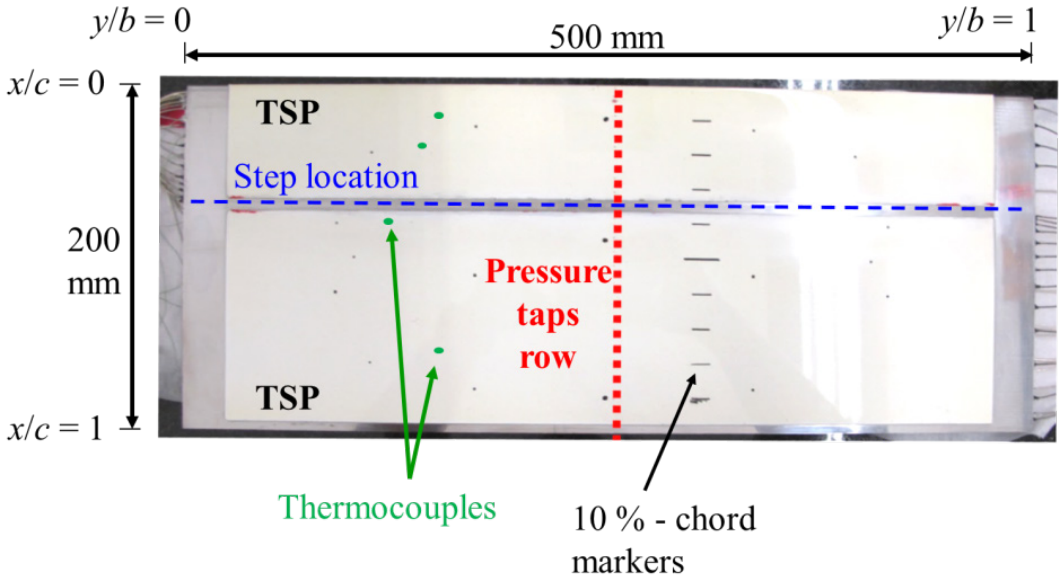

Fig. 3.4.1. Overview of the model instrumentation. Top view of the model with the leading edge at the top of the image.

3.4.1 Temperature-sensitive paint (TSP) measurement technique

The temperature-sensitive paint (TSP) measurement technique [57,211-212] was used for non-intrusive boundary-layer transition detection. The pockets in the wind-tunnel model (see Section 3.3) were coated with a paint which consists of three different layers: a primer layer to ensure adhesion of the paint to the metallic surface, a white screen layer for thermal insulation (which also functions as a diffusive light-scattering background), and an active layer, composed of the temperature-sensitive molecules (luminophores) incorporated in a commercial polyurethane clear-coat binder. The components of the TSP layers were dissolved in a solvent before their application, so that the resulting paint could be applied onto the model surface by means of an air gun. Black circular markers for TSP image mapping (see Appendix C.1) and black tick markers for identifying chordwise positions in 10 % steps of the chord length were applied onto the model surface, as shown in Fig. 3.4.1. These markers were applied on the white screen layer by means of a felt-tip pen before the model was coated with the transparent active layer, so that they had no influence on the final model surface quality. After application of the first two layers, the coating was sanded down to a homogenous paint thickness of approximately 70-80 µm. The paint thickness was measured by means of a coating thickness gauge with a vertical resolution of ±1 µm. The coating was further sanded down after the active layer had been applied. The final thickness of the TSP coating was approximately 80-110 µm. Aspects concerning layer thickness and the final model surface quality are discussed in Appendix B.3.2. On the model upper side, the difference between the actual and design contours was less than $\Delta z = \pm 15$ µm at $x/c < 40$ %; on the remaining model surface, $\Delta z \leq \pm 25$ µm. Care was taken to ensure that the interfaces between TSP and uncoated strip at $x/c = 33.5$ % and 36.5 % were as smooth and fair as possible. The remaining surface waviness h/a was less than 0.0025, thus fulfilling the criterion for allowable waviness compatible with laminar flow [161-162,169]. (h is the half amplitude of the wave, a corresponds to its quarter wavelength in the streamwise direction.) After the final paint thickness had been attained, the model surface was polished to an average roughness of $R_a = 0.038 \pm 0.01$ µm (mean roughness depth of $R_z = 0.32 \pm 0.11$ µm). These values are the average and standard deviation of the roughness measurements conducted in the chordwise direction at 25 different locations on the TSP surface. These measurements were conducted by means of the aforementioned contact profilometer, in this case with a vertical resolution of ±0.8 nm. Care was taken to reduce roughness in the leading-edge region: the values of average roughness and mean roughness depth obtained at $x/c \sim 3$ % were $R_a = 0.027 \pm 0.006$ µm and $R_z = 0.2 \pm 0.06$ µm.

The used luminophore was a Europium complex [213,214], characterized by a peak of excitation at $\lambda_{ex} = 410$ nm and a peak of emission at $\lambda_{em} = 614$ nm. The emitted luminescent intensity decreases with higher temperature: this property is used to detect boundary-layer transition by evaluating the temperature difference

between laminar and turbulent regimes [57,211]. As discussed in Section 3.1, a temperature difference between flow and model surface occurs during a run at DNW-KRG [55,145,192]. This temperature difference equilibrates faster within the turbulent than laminar region because of the different forced convection heat transfer coefficients of the laminar and turbulent boundary layers. Thus, the laminar-turbulent temperature difference at the surface lies above the recovery value: approximately 2-3 K at DNW-KRG [145]. This enables very accurate transition detection using TSP, since the temperature difference resolvable by means of this measurement technique with the used setup is approximately 0.2 K [145,192,209].

The TSP technique entails two characteristic timescales: the luminescent lifetime and the thermal diffusion timescale [215]. The luminescent lifetime of the used luminophore is about 0.1 ms [214], which is much lower than the camera exposure time for TSP image acquisition in the wind-tunnel tests described here. (The latter is of the order of 0.1 s.) The thermal diffusion timescale is generally much larger than the luminescent lifetime, and limits the response time of a TSP. The thermal diffusion time of a TSP layer depends strongly on the thickness and thermal diffusivity of the TSP layer, and on the surface heat transfer [57,209,215-216]. The thermal diffusivity of the used polyurethane-based TSP layer is rather low: about 10^{-7} m^2/s [209]. Nevertheless, the response time of this TSP layer was shown to be short enough for successful measurement in the majority of subsonic and transonic wind tunnels, including DNW-KRG [57,145,192,209,213,217]. The temperature rise from the unsteady heat transfer process on the surface of a ramp model in short-duration tests in the High Enthalpy Shock Tunnel Göttingen, where the measurement time was only a few milliseconds, could be well resolved using a TSP layer with the same composition and approximately the same coating thickness as that used in the present work [218].

Details on the temperature-sensitive paint used in the present work are given in Appendix B.5. The optical setup for transition detection at DNW-KRG by means of the TSP technique has been already presented in [148] and is not discussed in detail here. The luminophores were excited by light at a proper wavelength provided by light-emitting diodes (LEDs). The light emitted by the luminophores was detected by charge-coupled device (CCD) cameras. Two LEDs and one camera were installed on both test-section side walls. They were mounted directly inside the turntables, where the model was also fixed [148].

3.4.2 Pressure taps and thermocouples

The *PaLASTra* model was equipped with 52 pressure taps for measuring the surface pressure distribution and 6 thermocouples for monitoring the model temperature evolution during a test run. The coordinates of the locations of the installed pressure taps and thermocouples are given in Appendix B.6.

The model was provided with a main row of 50 pressure taps distributed in the chordwise direction at its mid-span section ($y/b = 0.5$), and with two additional pressure taps at $y/b = 0.48$. Several pressure taps were installed in the leading-edge region. A good resolution of the surface pressure distribution in this area was essential for the computation of boundary-layer development and stability by means of the numerical tools presented in Section 3.2.1 (COCO and LILO codes), for which the surface pressure distribution served as an input. The two additional pressure taps improved the resolution of the surface pressure distribution in the leading-edge region, but had to be installed at $y/b = 0.48$ because of the lack of space available at $y/b = 0.5$. The pressure taps placed around the junction location enabled the effect of forward-facing steps on the pressure distribution to be examined. Although already quite small, the chordwise distance of these pressure taps from the step location was still too large to measure accurately the strong, local surface pressure gradients occurring immediately upstream and downstream of the step location [35-36,46]. The closest pressure taps had to be placed at a distance $\Delta(x/c) \sim 1$ % from the step location, due to manufacturing constraints. The main row of pressure taps was positioned at the test-section centerline. All pressure taps had an orifice diameter of 0.25 mm. This orifice size was sufficiently small to ensure that its influence on the surface pressure measurement error [219,220] would be negligible; at the same time, the orifice diameter was still sufficiently large to prevent the tap from being easily blocked by dust or other contaminating particles present in the flow, and to keep the response time of the surface pressure measurement system low. The circular shape of the orifices, the tap diameter, and the sharpness of the orifice edges were ensured for all pressure taps, including those embedded in the TSP coating. This was accomplished via additional treatment of the orifices after TSP application [221]. The properties of the pressure taps were checked using a digital three-dimensional scanning microscope with a vertical resolution of ±1 μm [222]. Pressure measurements at all tap positions could be recorded during the whole test campaign. The internal pressure tap passages were shown to be at steady state in less than 0.4 s after opening the fast-acting valve, certainly fast enough when compared with the run time of 0.75 s. An analysis of the measurements of the strong, local pressure gradients occurring in the vicinity of the steps indicated that the tap at $x/c = 37$ % gave spurious results; the reason for this is not known. Hence, the pressure coefficient measured at this location will not be shown in the plots presented in Chapters 5 and 6. The pressure sensors attached to the taps were scanned at 100 Hz for each channel using a 16-bit data acquisition system, which was equipped with electronic pressure-scanning modules with a nominal accuracy of ±170 Pa.

Six fast-acting thermocouples (type K, wire diameter 0.08 mm, accuracy ±0.3 K) were installed in the model in the spanwise region $0.23 \leq y/b \leq 0.3$. The sampling rate for the acquisition of the surface temperature measurements was 1 kHz for each channel. Four of the thermocouples were mounted in such a way that the sensor junction end was situated within the active layer of the TSP coating,

thereby being close to the surface and enabling an accurate monitoring of the temperature evolution at the paint surface during a run with high time resolution. In fact, it would not have been possible to measure surface temperatures with thermocouples mounted in the metallic model part below the surface because of the insulating effect of the screening layer. Nevertheless, the remaining two thermocouples were mounted in the metallic part of the model, 1 mm below the model surface, in order to compare the temperature evolution here with that at the surface. Of the four thermocouples mounted within the TSP active layer, the first two were installed at chordwise locations where laminar flow was generally expected, the fourth one was mounted at a chordwise location where turbulent flow was generally expected, and the remaining one was installed at a small distance downstream of the junction between model front and main parts. This latter thermocouple was also the closest to the side wall of the test section. The procedure adopted for the installation of the thermocouples led to a high quality model surface. The largest variation of the model contour in the wall-normal direction was less than 2 μm. As shown in the TSP results in Chapters 5 and 6, the small surface imperfections at the thermocouples locations did not lead to the development of turbulent wedges in any of the test runs of the whole measurement campaign.

4 Data analysis

4.1 TSP data acquisition

The acquisition rate of TSP images depends on paint, hardware, distance from coated surface to illumination source, and the characteristics of the photosensitive device. In these tests, the TSP images were acquired at a rate of 5 Hz. The acquisition time was mainly limited by the CCD readout time and by the intensity of the light emitted by the TSP. The data acquisition sequence during a run at DNW-KRG can be summarized as follows: charge pressure, charge temperature, and cone position in the control valve were set to the appropriate values to achieve the desired freestream Mach number and Reynolds number. Care was taken to obtain uniform gas temperature inside of the storage tube, which would otherwise affect the flow quality [56]. The data acquisition sequence was the same also in the tests where the pre-conditioning procedure, discussed in Section 3.1 and – in more detail – in [145], had been applied to reduce the model temperature prior to a test run. Once the wind tunnel was ready, the data acquisition was started at 2.25 s ahead of opening the fast-acting valve, i.e., of the actual run start (wind-on). The acquisition of the TSP images was directly initiated by the same trigger that regulated the recording of the wind-tunnel data and the opening of the fast-acting valve, thus ensuring synchronization of the systems. The total data acquisition time was 5 s. A typical data acquisition sequence during a run is displayed in Fig. 4.1.1, where the recorded freestream total pressure and the trigger for TSP-image acquisition are shown. Pre-run TSP images were recorded at reference conditions (*wind-off* images); these images were used in the evaluation procedure of TSP images, which is discussed in Appendix C.1. Three TSP images were acquired during the run window (*wind-on* images). However, only the last one was used for the analysis of the results, thus ensuring that only the image taken under most stable and established flow conditions was used; this is shown as the circled image number (15) in Fig. 4.1.1. The data recorded by pressure sensors and thermocouples from both the wind-tunnel and the model were averaged over 0.1 s in the same time window. The surface temperature evolution during a run is discussed in Appendix C.3.

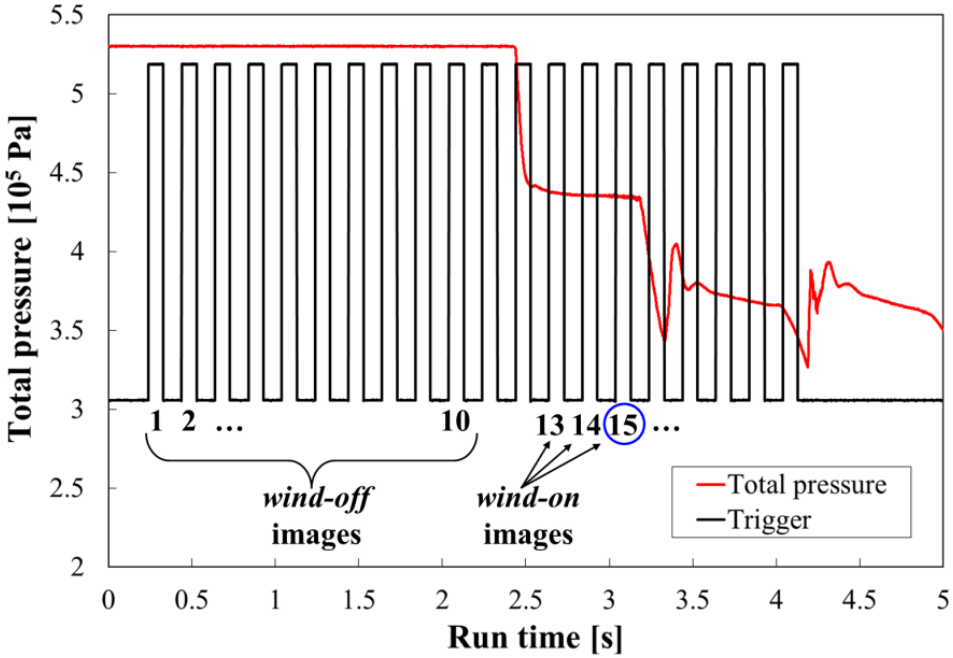

Fig. 4.1.1. Typical TSP image acquisition sequence during a run at DNW-KRG. M = 0.77, Re = 13 · 10^6.

4.2 Detection of boundary-layer transition

Post-processing of TSP images was performed by means of the in-house software package *ToPas* [223-225] and is discussed in Appendix C.1. The TSP images were mapped onto a three-dimensional grid representing the model upper surface extending from $y/b = 0.2$ to 0.8; in fact, the first and last tenth of the span were outside of the test section and the regions $0.1 \leq y/b \leq 0.2$ and $0.8 \leq y/b \leq 0.9$ were not completely visible in the TSP images. This portion of the model surface was discretized using a structured grid, with a grid resolution of one point per millimeter in both chordwise and spanwise direction. An example of final TSP result obtained after post-processing is shown in Fig. 4.2.1a. In all TSP results presented from now on in this work, bright and dark areas will correspond to the laminar and turbulent boundary layers, respectively, and the flow will be from the left. Using *ToPas*, white masking strips were superimposed over the TSP results in the regions $32.5\ \% \leq x/c \leq 38\ \%$ and $x/c \geq 96.5\ \%$ to mask the uncoated model surface areas. Note that these strips also mask the areas close to the uncoated strip $32.5\ \% \leq x/c \leq 33.5\ \%$ and $36.5\ \% \leq x/c \leq 38\ \%$, which were actually coated with TSP: in these regions, the TSP active layer was almost absent for the reasons discussed in Appendix B.3.2. A white strip was applied also at $x/c \leq 2.5\ \%$, since the image distortion in this region was too large to achieve mapping with sufficient accuracy. In any case, this leading-edge region was not of great interest in the present work, since transition occurred considerably downstream of $x/c = 2.5\ \%$. It should be also remarked that the intensity values at the corners of the final TSP results are artefacts: they are produced by mapping of the TSP image (in which the side of the model closest to the CCD camera appears as an arc) onto the three-dimensional grid (whose

plan view is a rectangle). These surface regions were not considered for evaluating the natural-transition location anyway, since the development of the model boundary layer on these areas was affected by the turbulent boundary layer on the test-section side walls. This topic is discussed in Appendix C.3.

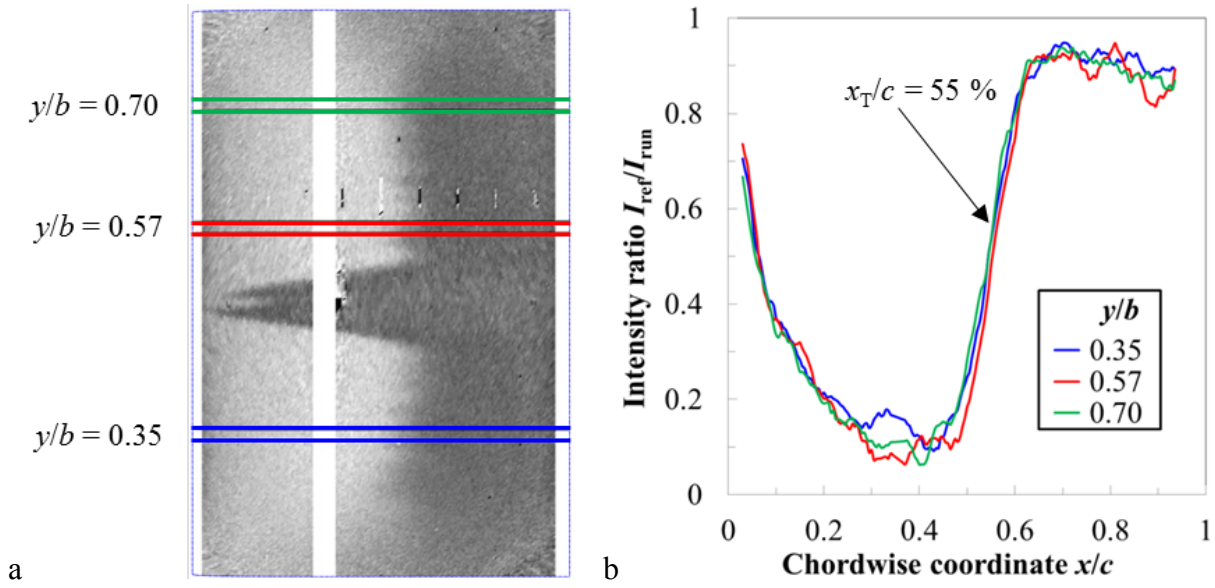

Fig. 4.2.1. Analysis of TSP result at Re = 6 · 10^6, M = 0.77, and AoA = -2.6°. Only three of the spanwise sections used for data analysis are shown. a: TSP result with colored lines indicating the bounds for each spanwise section. b: chordwise distributions of the intensity ratios.

The three-dimensional TSP results enable the accurate study of boundary-layer transition, since the luminescent intensity measured at a certain location on the TSP surface is directly mapped to a node point of the three-dimensional grid. The first step to obtain the transition location x_T/c was the evaluation of the average chordwise intensity distribution in the chosen spanwise sections, as shown in Fig. 4.2.1 (the two lines show the bounds of the sections). The luminescent intensity distributions, which depend on the temperature distributions and therefore on the wall heat flux, were then normalized to values between zero and one. In order to increase the signal-to-noise ratio, the intensity values were averaged over a spanwise range of $\Delta(y/b) = 0.012$ across the chosen spanwise section. In the masked region $33\ \% \leq x/c \leq 38\ \%$, the intensity ratio is linearly interpolated from its neighboring values, whereas at $x/c \geq 96\ \%$ the intensity ratio is taken as uniform and equal to the value at the chordwise location immediately upstream of this masked region. The bounds of the aforementioned spanwise sections are indicated in the TSP result in Fig. 4.2.1a by means of two colored lines. The corresponding intensity ratio distributions for three of the sections are shown in Fig. 4.2.1b. The chordwise intensity distributions were finally analyzed by means of an algorithm capable of detecting the maximal value of the gradient of the intensity ratio in the transitional region. The algorithm is described in Appendix C.1.3. The

transitional region is defined as the region between the point at which the intensity ratio starts to increase from laminar values $x_{T,start}$ and that at which it reaches turbulent values $x_{T,end}$. The location in the transitional region corresponding to the maximal slope of of the intensity ratio is used to define the transition location x_T in the present work. This choice is motivated by the coincidence found between the point corresponding to the maximal slope of the streamwise temperature distribution in the transitional region and that corresponding to the maximum value of the rms signal from hot-film measurements [115,120,122] (see Section 2.2.4). The use of a single, well-defined, accurately measurable "transition location" is advantageous for the systematic analysis of the effect of several factors on boundary-layer transition, which is a main goal of this work.

The transition detection algorithm has been shown to be very robust and to be capable of accurately determining the transition location under the most various conditions [145]. In particular, the transition location could be determined even when the streamwise increase of the intensity ratio in the transition region is not very sharp, as in the case of transition occurring in the presence of a favorable pressure gradient; this is most important for the analysis of all the present experimental results. The value of the transition location x_T/c given in this work is the average of the transition locations evaluated at ten spanwise sections. The evaluation sections were in regions sufficiently distant from the side walls and from the turbulent wedges which arise from the pressure taps in the nose region (see Fig. 4.2.1a). Of the ten spanwise sections, five were at $0.33 \leq y/b \leq 0.44$, and the remaining five at $0.56 \leq y/b \leq 0.7$. The spanwise locations were kept unchanged for all configurations, except for part of the tests with the step-2 configuration; for these latter cases, some of the spanwise locations were varied (within the aforementioned ranges) because of the presence of additional turbulent wedges, which did not allow examination of natural transition at the spanwise locations considered for all other tests. The additional turbulent wedges arose from surface blemishes and contamination on the model surface; this aspect is discussed in Appendix C.2.1. Spanwise averaging of transition locations to obtain a single value x_T/c was possible because the flow was quasi-two-dimensional in the considered spanwise region, the height of the installed steps was essentially uniform in spanwise direction (see Section 3.3), and the transition location did not show marked variations in spanwise direction. This does not necessarily mean that the transition front in spanwise direction was a straight line perpendicular to the flow, as discussed in Appendix C.2.2. The uncertainty in x_T/c was evaluated for each data point as the standard deviation of the transition locations obtained from the sections at the various spanwise locations. Note that this definition of $\Delta(x_T/c)$ can strictly be used only for quasi-two-dimensional flows with quasi-two-dimensional imperfections placed perpendicular to the flow, as in the present work. The variation of the transition location at a certain spanwise section for repeated test runs – same configuration,

same test conditions – was smaller than the variation of the transition location in the spanwise direction in the one run (see Appendix D.1). Thus, the use of the previously defined $\Delta(x_T/c)$ as uncertainty for the transition location is conservative. For the example in Fig. 4.2.1, the transition location was detected at $x_T/c = 55$ % with an uncertainty $\Delta(x_T/c) = \pm 0.5$ %, these values being obtained from an analysis of ten spanwise sections. It should be noted that the transition location was determined using the transition detection algorithm also in the cases with transition occurring over the masked region $33\ \% \leq x/c \leq 38\ \%$; here the related uncertainty was considerably larger ($\Delta(x_T/c)$ of about ±2 %). Finally, it should be emphasized that transition having occurred in the region at approximately $x/c > 80$ % was most unlikely. Rather, the streamwise increase of the intensity ratio observed in this region in some TSP results was most likely related to the local increase of the laminar wall shear stress, combined with the decreased heat capacity of the model in this aft region. This aspect is discussed in Appendix C.2.3.

4.3 Definition and evaluation of the test parameters

The parameters used to describe the flow conditions were the freestream Mach number and the freestream Reynolds number, which were determined from freestream pressure and temperature measurements. It is a matter of choice whether one adopts either the unit or chord Reynolds number, since they only differ by the factor model chord length (here $c = 0.2$ m). In this work, the chord Reynolds number is mainly used.

The Hartree parameter β_H [226,227]

$$\beta_H = \left(\frac{1}{2} - \frac{1 - c_p(x)}{x(\partial c_p / \partial x)} \right)^{-1} \tag{4.3.1}$$

was chosen as the characteristic parameter for the pressure distribution. $c_p(x)$ is the surface pressure distribution measured at the position of the pressure taps. The value of the Hartree parameter was evaluated for each test run as the average value over that chordwise region where the pressure gradient had been essentially uniform. This region was approximately $20\ \% \leq x/c \leq 70\ \%$ for the cases of zero and favorable pressure gradient, which were of major interest in this work, whereas it was approximately $5\ \% \leq x/c \leq 40\ \%$ for the cases with adverse pressure gradient. The Hartree parameter was evaluated for each test run as the average value in this region. The values of the Hartree parameter and of its uncertainty given in this work are the average and the standard deviation of the Hartree parameters evaluated for each test run at the same angle-of-attack.

The wall temperature ratio T_w/T_{aw} was chosen as the characteristic parameter for the thermal boundary condition at the model surface. T_w is the model surface

temperature corresponding to the laminar boundary layer, evaluated as the average of the measurements of the two thermocouples located at the two more upstream positions $x/c = 10$ % and 20 %. The temperatures measured by the forward thermocouples were shown to be in agreement with those obtained from the TSP results at the same locations. This result is shown in Appendix C.1.4. T_w was evaluated as the average measured value in the time window corresponding to the exposure time of the camera for the wind-on image to be evaluated (see Fig. 4.1.1). T_{aw} is the adiabatic wall temperature computed at $x/c = 15$ % using the laminar boundary-layer solver COCO, in which an adiabatic wall boundary condition for the model surface is implemented [196]. The settings for the boundary-layer computations are discussed later in this section. The uncertainty in T_{aw} was taken to be ±0.3 K, as has been used for the other temperature measurements. Note that both temperatures in the wall temperature ratio T_w/T_{aw} were obtained at the same time as that of the TSP image used to determine the transition location. The uncertainty in the wall temperature ratio was evaluated according to the formula for the propagation of uncertainties with independent variables. The use of a single value of T_w/T_{aw} to characterize the thermal boundary condition at the model surface simplified the analysis of the results; it should be kept in mind, however, that the wall temperature ratio is non-uniform in the streamwise direction. This aspect is discussed in Appendix C.4.

Wall-normal velocity and temperature profiles were obtained from boundary-layer computations assuming an isothermal wall. A uniform temperature equal to T_w was imposed at the model surface. The other inputs for the boundary-layer analysis were: the freestream Mach and Reynolds number, the freestream temperature, and the processed surface pressure distribution on the model upper side. The input surface pressure distribution was obtained from interpolation [228] of the measured surface pressure distribution at approximately 120 chordwise locations. The chordwise spacing of the processed pressure distribution increased progressively in the streamwise direction: it was less than $\Delta(x/c) = 1$ % up to $x/c \sim 15$ % and remained below 3 % over the rest of the profile. The geometric sweep angles of leading edge and trailing edge were obviously set to zero. The fluid was assumed to be air, with heat capacity ratio, specific gas constant, and Prandtl number having been taken as $\gamma = 1.4$, $R^* = 287$ J/(kg·K), and $\mathrm{Pr} = 0.72$, respectively [196]. At the test conditions considered in the present work (freestream total pressure up to approximately 700 kPa and freestream total temperature in the range 250 K < T_0 < 290 K), this assumption has a negligible influence on the results of boundary-layer computations [229,230]. At each chordwise station, the wall-normal velocity and temperature profiles were discretized using 100 points whose spacing was progressively stretched by a factor of 1.05 for every successive node point away from the wall.

The boundary-layer computations provided velocity and temperature profiles, which served as input for the boundary-layer stability analysis (see below).

Furthermore, the boundary-layer displacement thickness $\delta_1(x)$ and the roughness Reynolds numbers $\mathrm{Re}_k(x,z)$ were evaluated from the numerical results. For a given roughness of height k, placed at a certain chordwise location x_k, the velocity U_k and the temperature T_k at the top of the roughness were extracted from the corresponding velocity and temperature profiles obtained in the absence of the roughness (smooth configuration). The density at the top of the roughness ρ_k was computed using the ideal gas law, the dynamic viscosity μ_k at the same location was obtained using Sutherland's law:

$$\mu(T) = \mu_{\mathrm{ref}} \left(\frac{T}{T_{\mathrm{ref}}} \right)^{1.5} \left(\frac{T_{\mathrm{ref}} + S}{T + S} \right) \tag{4.3.2}$$

with $T = T_k$. The constants for gaseous nitrogen are: $\mu_{\mathrm{ref}} = 1.665 \cdot 10^{-5}$ Pa·s, $T_{\mathrm{ref}} = 273.15$ K, and $S = 103$ K [231]. The roughness Reynolds number can then be derived as: $\mathrm{Re}_k = \rho_k U_k k / \mu_k$.

The step height h was defined as the average value of the step height measurements conducted in the region $0.3 \leq y/b \leq 0.7$, where transition was to be evaluated. Since small variations of the step height were observed for two configurations between the measurements conducted before and after the test series (see Section 3.3), only the measurements carried out after completion of the test series were considered for the evaluation of h. The values of the step height obtained for the step-1, step-2, and step-3 configurations were $h = 29$, 60, and 89 µm, respectively. The uncertainty in the step height was taken equal to its maximal deviation from the average value $\Delta h = \pm 1$ µm.

An essential parameter to be used in the analysis of the results in Chapters 5 and 6 is the transition Reynolds number $\mathrm{Re}_{x\mathrm{T}}$. This is defined as $\mathrm{Re}_{x\mathrm{T}} = U_\infty x_\mathrm{T}/\nu_\infty = \mathrm{Re} \cdot x_\mathrm{T}/c$, where Re is the chord Reynolds number and x_T/c the transition location obtained from the TSP results (see Section 4.2). The uncertainty in the transition Reynolds number was evaluated according to the formula for the propagation of uncertainties. Note that freestream velocity and freestream kinematic viscosity were used to define $\mathrm{Re}_{x\mathrm{T}}$, rather than the corresponding values at the boundary-layer edge $U_e(x_\mathrm{T}/c)$ and $\nu_e(x_\mathrm{T}/c)$. For the particular type of flow studied in the present work, the differences between U_∞/ν_∞ and U_e/ν_e were found to be small in the region $35\ \% \leq x/c \leq 80\ \%$, which was that of major interest for the examination of boundary-layer transition. The corresponding differences in transition Reynolds numbers were within the measurement uncertainty $\Delta(\mathrm{Re}_{x\mathrm{T}})$. The freestream quantities were thus preferred to the quantities at the boundary-layer edge, since they were directly available from the wind-tunnel data. An additional evaluation step would have been needed to obtain U_e and ν_e from the surface pressure distribution and the freestream quantities, thereby introducing additional uncertainties. For similar reasons, the Hartree parameter was preferred over the Pohlhausen parameter

$\Lambda = (\delta_{99}^2/\nu)(\mathrm{d}U_e/\mathrm{d}x)$ [85] (where δ_{99} is the distance from the wall at which $U(x,\delta) = 99\ \%\ U_e(x)$ [19]) or the acceleration parameter $K = (\nu/U_e^2)(\mathrm{d}U_e/\mathrm{d}x)$ [123,125] because it could be evaluated directly from the measured surface pressure distribution.

The stability of the computed boundary layer was studied using compressible, linear, local stability theory, under the assumption of quasi-parallel flow. The stability computations were performed by means of LILO. The calculations were performed according to compressible stability theory, with a Prandtl number Pr = 0.72. (Note that the results of boundary-layer stability analysis have been shown to remain unchanged if a variable Prandtl number is used in the stability formulation instead of a constant Prandtl number [232].) The most important result of the boundary-layer stability analysis (for this work) was the determination of the evolution of amplification factors (*N*-factors) of streamwise instabilities with different frequencies. The *N*-factors were computed for two-dimensional instability waves, since they showed the largest amplification ratios even at the highest investigated Mach number M = 0.77. This result is in agreement with previous work [32], where it has been reported that the largest growth rate corresponds to two-dimensional waves up to a Mach number of approximately 0.9.

5 Results

The measurement campaign is subdivided into two main phases. In the first one, the (nominally) smooth model configuration was examined. The objectives of this part of the measurement campaign were:

- Verify that the wind-tunnel model met the design requirements discussed in Section 3.2.2, so that the effects on boundary-layer transition of various parameters (streamwise pressure gradient, wall temperature ratio, Reynolds number, Mach number) could be decoupled.
- Check repeatability and reproducibility of the experimental results.
- Investigate the effect of the aforementioned parameters on boundary-layer transition.
- Create a database of boundary-layer stability situations without steps, from which the effect of forward-facing steps on boundary-layer transition could be further investigated.

The results of the first phase of the measurement campaign are summarized in Section 5.1. The effect of forward-facing steps on boundary-layer transition was studied in the second phase of measurement campaign. The results are presented in Section 5.2 and discussed in Chapter 6.

The experiments were conducted at four Mach numbers: M = 0.35, 0.5, 0.65, and 0.77. These covered a large range of flow conditions, which are relevant for different flight phases of transport aircraft employing NLF surfaces with low to moderate sweep angle [22,25,32-33], from the initial climb phase to the final descent phase, including cruise conditions. Chord Reynolds numbers up to $13 \cdot 10^6$ were investigated. Such Reynolds numbers are relevant for the control surfaces and for the wing region at approximately 50 % to 80 % wing span of the aforementioned NLF transport aircraft. The examined test conditions also covered typical flight conditions for aircraft with piston and turboprop engines, and also for business jets [25,26]. The flow on the model upper surface remained subsonic for all the considered test conditions, since the critical pressure coefficient was not reached in any of the test runs. Of main interest were measurements at all Mach numbers with favorable streamwise pressure gradients, which are the most relevant for an NLF surface.

Most of the tests were conducted at standard DNW-KRG thermal conditions on the model surface, which correspond to wall temperature ratios T_w/T_{aw} larger than one. These thermal conditions will be referred as "standard T_w/T_{aw}" throughout this work. For certain test cases, the wall temperature ratio was also reduced to values close to or below one. This was accomplished using the pre-conditioning procedure discussed in Section 3.1 and in [145]. From now on, these thermal conditions on the model surface will be referred to as "reduced T_w/T_{aw}". Since this pre-conditioning procedure is time-consuming, however, it was used

in only a relatively small number of chosen test cases. The charge temperature of the gas in the DNW-KRG storage tube was set to approximately $T_c = 288$ K for all test conditions. This improved the repeatability and reproducibility of the results, since the freestream total temperature is then approximately the same for fixed Mach numbers and charge temperatures. There were two reasons to select this temperature for the tests. First, the time necessary to establish conditions suitable for accessing the model in the test section was much shorter than that needed at lower charge temperatures. This reduced the turnaround time for model inspection and cleaning, which had to be carried out after a certain number of test runs to remove any contaminating particles which could have caused turbulent wedges on the model surface (see Appendix C.2.1). Secondly, the gate valve had not been designed for the implementation of the aforementioned pre-conditioning procedure at charge temperatures lower than $T_c = 223$ K [233]. This choice led to no disadvantages with respect to the testing range, since the desired flow conditions could generally be achieved by adjusting the only charge pressure, and the model itself had been designed to withstand the higher aerodynamic loads acting at the higher charge pressures and Mach numbers (see Section 3.3).

Chronologically speaking, the tests were not performed in one uninterrupted series of runs. Wind-tunnel entries were interrupted in the mid and long term by tests of other customers and by repairs of the wind tunnel, and in the short term for model modification to another configuration. Therefore, the first phase of each new wind-tunnel entry was dedicated to reproducibility tests.

5.1 Smooth configuration

The results obtained with the smooth configuration are summarized in this section. The range of examined test parameters is presented in Table 5.1.1.

Table 5.1.1 Variation of parameters examined for the smooth configuration. Note that also "intermediate" wall temperature ratios in the range T_w/T_{aw} = 1.026-1.033 and T_w/T_{aw} = 1.023-1.026 were examined at M = 0.77 and 0.65, respectively.

M	Re [10^6]	β_H	AoA [°]	T_w/T_{aw} (standard)	T_w/T_{aw} (reduced)
0.77	4 to 13	-0.016 to 0.112	-4.0 to -1.8	1.043 to 1.061	0.994 to 1.016
0.65	4 to 12	0.011 to 0.101	-3.8 to -2.0	1.037 to 1.051	0.998 to 1.011
0.50	4.5 to 11	-0.007 to 0.106	-4.0 to -1.6	1.032 to 1.047	0.968 to 1.018
0.35	3.5 to 10	-0.017 to 0.071	-3.2 to -1.4	1.022 to 1.036	0.981 to 1.007

The first part of the measurement campaign was dedicated to the comparison between the surface pressure distributions computed in the model design phase [148] and the measurements from the pressure taps. The measured and computed pressure distributions on the model upper side were in good agreement for all boundary-layer stability situations considered in this work. This agreement is discussed in [148] for a Mach number M = 0.77. Since this work focused on the influence of forward-facing steps on boundary-layer transition, details about the experiments conducted with the smooth configuration are not given here, but in Appendix D. The experimental results were repeatable and reproducible; this is discussed in Appendix D.1. The change of the streamwise pressure gradient at different angles-of-attack, Reynolds numbers, Mach numbers, and wall temperature ratios is discussed in Appendix D.2. The variation of parameters achievable in the present study is discussed in Appendix D.3. The influence on boundary-layer transition of Reynolds number, pressure gradient, and wall temperature ratio at M = 0.77 has been discussed in [148]. Larger transition Reynolds numbers were obtained with more pronounced flow acceleration and smaller wall temperature ratio, in agreement with results of earlier experimental work and with expectations from linear stability theory (see Sections 2.3.1 and 2.3.3). The transition Reynolds number obtained with a given combination of pressure gradient and thermal condition on the model surface was generally independent of the chord Reynolds number. This result was due to the model shape designed for the present experiments, which ensured an approximately uniform streamwise pressure gradient over a large region of the model upper surface. Further details on the independency of the transition Reynolds number from the chord Reynolds number are given in Appendix D.4. The effect of the Mach number on boundary-layer transition is discussed in Section 5.1.1 and Appendix D.5. The transition *N*-factors of streamwise instabilities are presented in Appendix D.6. The effect on transition of pressure gradient and wall temperature ratio at all considered Mach numbers is discussed in Section 5.1.2, where the experimental results are also compared with those from other workers. This first phase of the measurement campaign is then summarized in Section 5.1.3.

5.1.1 Effect of the Mach number

The following trends were seen at all four Mach numbers M = 0.35, 0.5, 0.65, and 0.77: transition Reynolds number $\mathrm{Re}_{x\mathrm{T},0}$ not dependent on the chord Reynolds number, increase of $\mathrm{Re}_{x\mathrm{T},0}$ at larger Hartree parameters β_H, and increase of $\mathrm{Re}_{x\mathrm{T},0}$ at lower wall temperature ratios T_w/T_{aw}. The results are summarized in Section 5.1.2. Another result will be discussed beforehand in this section. The effect of the freestream Mach number on boundary-layer transition is presented for a case at AoA = -2.3°, Re = $6 \cdot 10^6$, and standard wall temperature ratio. The surface pressure distributions for the four Mach numbers are shown in Fig. 5.1.1.1. The pressure coefficients are in quite good agreement; the largest

deviation is seen for the case at M = 0.5. Accordingly, the corresponding Hartree parameters are also in agreement: the maximal difference is $\Delta\beta_H = 0.004$, which is the difference between β_H at M = 0.77 and 0.5.

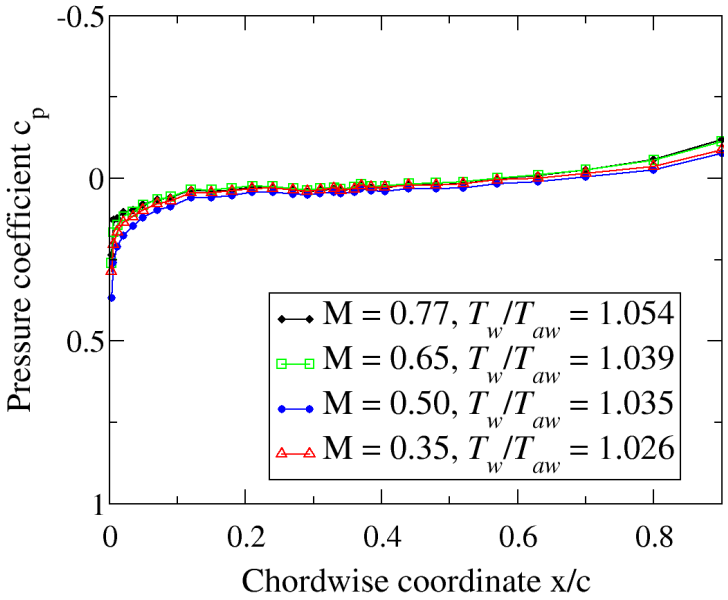

Fig. 5.1.1.1. Surface pressure distributions measured at different Mach numbers (AoA = -2.3°, Re = 6 · 10^6).

The TSP results are shown in Fig. 5.1.1.2. The detected natural-transition location is shown in this figure (and in all following figures) by a dashed white line. The varied parameter (in this case the Mach number) will be underlined in the captions.

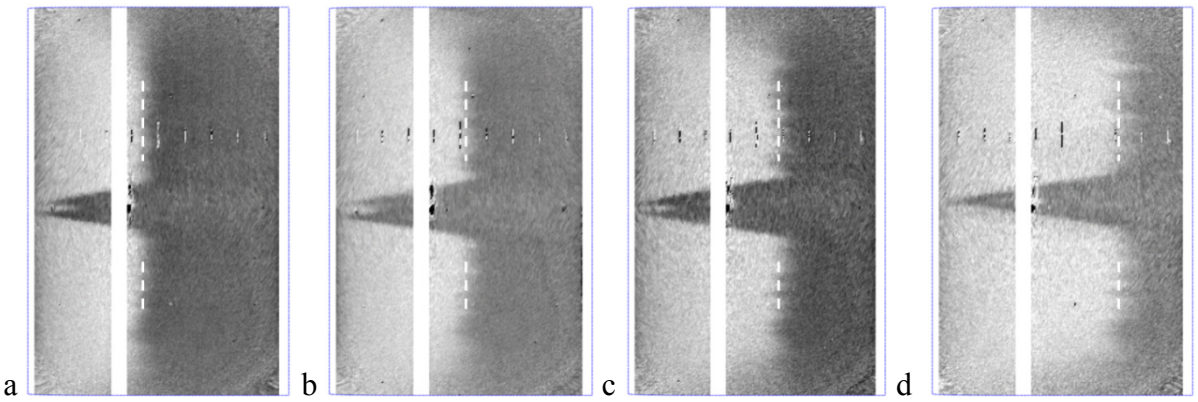

Fig. 5.1.1.2. TSP results for different Mach numbers at Re = 6 · 10^6 and AoA = -2.3° (0.032 ≤ β_H ≤ 0.036). Smooth configuration. a: <u>M = 0.77</u>, β_H = 0.036, T_w/T_{aw} = 1.054, $x_{T,0}/c$ = 44 ±0.3 %; b: <u>M = 0.65</u>, β_H = 0.034, T_w/T_{aw} = 1.039, $x_{T,0}/c$ = 52 ±0.4 %; c: <u>M = 0.5</u>, β_H = 0.032, T_w/T_{aw} = 1.035, $x_{T,0}/c$ = 60 ±0.5 %; d: <u>M = 0.35</u>, β_H = 0.033, T_w/T_{aw} = 1.025, $x_{T,0}/c$ = 71 ±0.8 %.

Transition moves continuously downstream with decreasing Mach number: from $x_{T,0}/c$ = 44 % at M = 0.77 to $x_{T,0}/c$ = 71 % at M = 0.35, corresponding to a

marked increase of the transition Reynolds number from $Re_{xT,0} = 2.7$ to $4.3 \cdot 10^6$. Nevertheless, the streamwise extent of the transition region, when expressed in relative terms (ratio $x_{T0,start}/x_{T0,end}$), is nearly independent of the Mach number. This is shown in Fig. 5.1.1.3, where the chordwise intensity distributions obtained at $y/b = 0.57$ in the TSP results of Fig. 5.1.1.2 are displayed. $x_{T0,start}$ ($x_{T0,end}$) is taken as the location corresponding to the minimal (maximal) value of the intensity ratio immediately upstream (downstream) of its marked rise due to the transition process. A nearly constant value of the ratio $x_{T0,start}/x_{T0,end}$ is in agreement with the behavior reported in [121], although their value of $x_{T0,start}/x_{T0,end} \sim 0.82$-$0.9$. is slightly larger than the value of 0.77-0.81 obtained here.

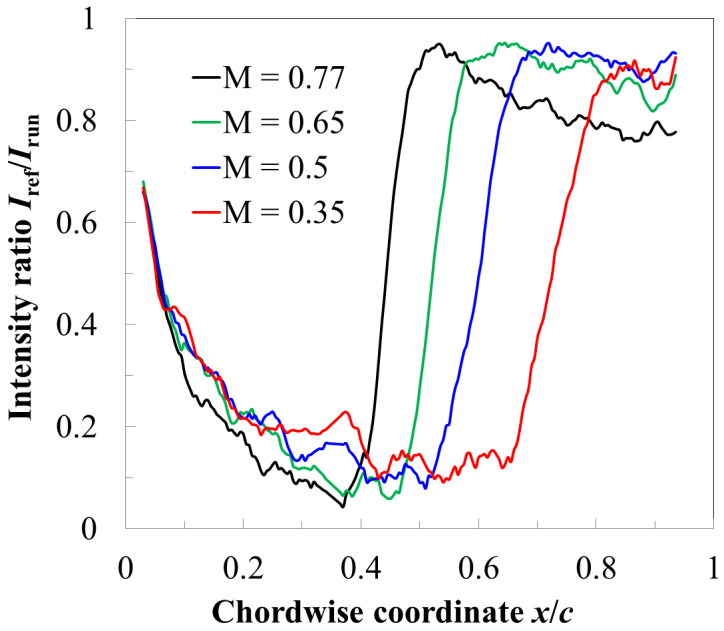

Fig. 5.1.1.3. Chordwise intensity distributions obtained at $y/b = 0.57$ for the cases of Fig. 5.1.1.2. M: a) 0.77, b) 0.65, c) 0.5, d) 0.35.

This influence of the Mach number on boundary-layer transition is in contrast to the expectation from linear stability theory of a stabilizing effect of larger Mach numbers up to $M_e \sim 2$ [116]. Even at high subsonic and transonic speeds, the amplification factors of plane Tollmien-Schlichting waves are reduced when the Mach number increases [13,32,116,234]. Note however that the stabilizing effect of compressibility on both two- and three-dimensional disturbances was found to be negligible in other numerical work, also based on linear stability theory, for the Mach number range $0.6 \leq M_\infty < 0.9$ [139]. The results of the stability computations obtained for the considered test conditions are shown in Fig. 5.1.1.4, where N-factors of Tollmien-Schlichting waves are shown for some selected frequencies only. The amplification factors increase as the Mach number is decreased. The maximal N-factor is observed to increase and to be shifted downstream at lower Mach numbers. (The latter effect, however, is mainly due the less pronounced acceleration at approximately $x/c > 70$ %.).

Moreover, the frequency of the most amplified instability wave at the transition location was found to continuously decrease at smaller Mach numbers: from approximately $f_{TS} = 26$ kHz at M = 0.77 to $f_{TS} = 11$ kHz at M = 0.35. All these results are consistent with past theoretical work [32,69,234]. The envelope curves of the *N*-factors shown separately for the four Mach numbers in Fig. 5.1.1.4 are presented in one plot in Fig. 5.1.1.5.

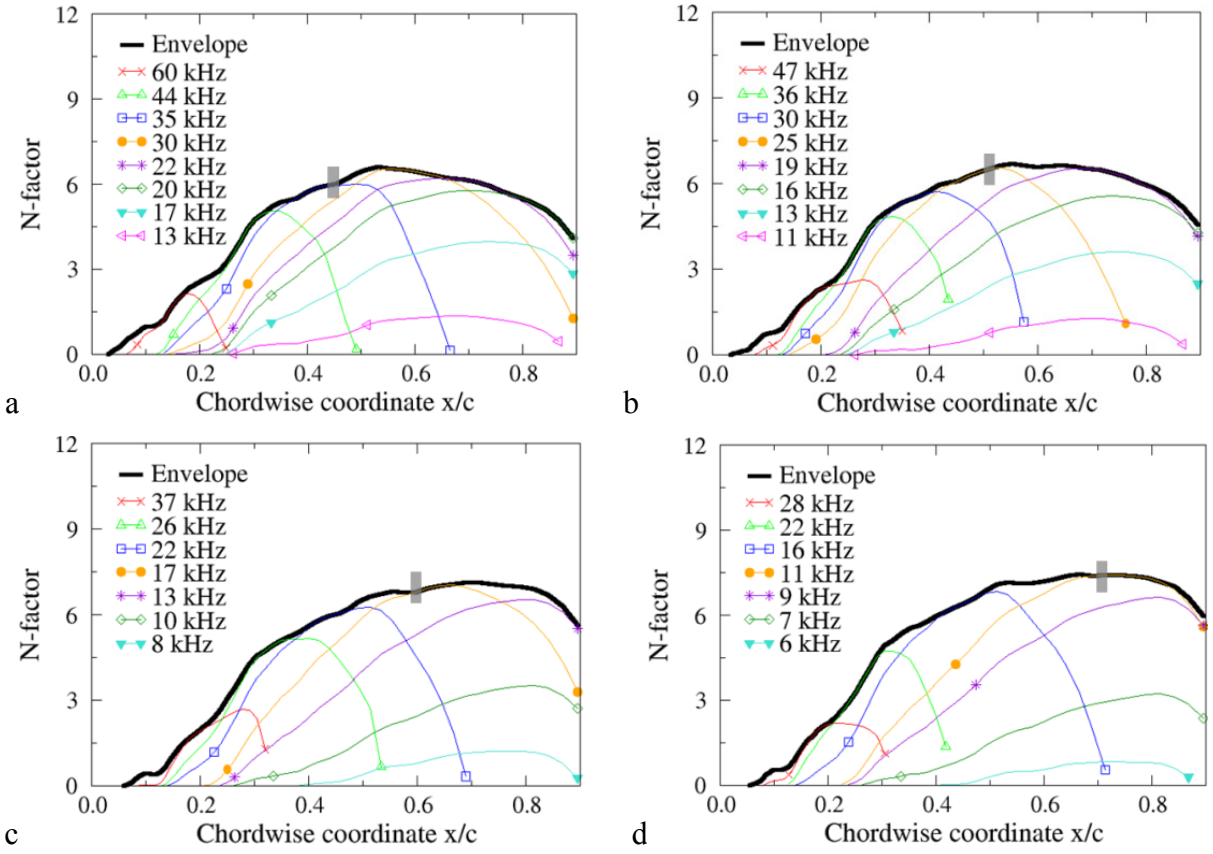

Fig. 5.1.1.4. Stability analysis results for the cases of Fig. 5.1.1.2. M: a) 0.77, b) 0.65, c) 0.5, d) 0.35.

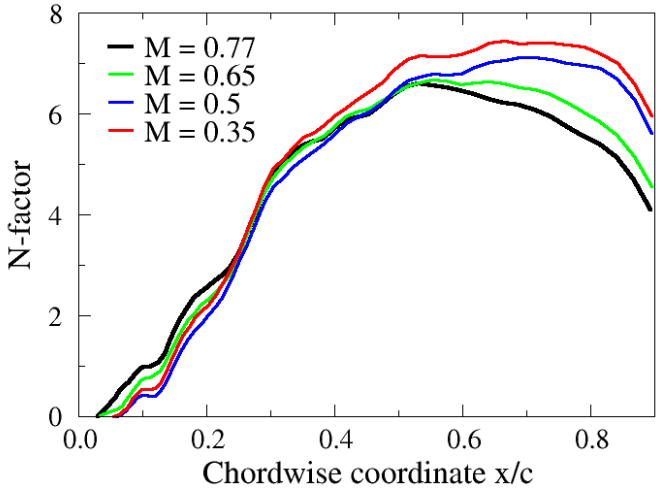

Fig. 5.1.1.5. *N*-factor envelope curves from the stability analysis results in Fig. 5.1.1.4. M: a) 0.77, b) 0.65, c) 0.5, d) 0.35.

Assuming that transition occurs at a constant *N*-factor independent of the Mach number, this is reached earlier at lower Mach numbers, so that transition is expected to be shifted upstream as the Mach number is decreased. This result is opposed to the present experimental observations.

There is a lack of experimental data demonstrating the stabilizing effect of compressibility in the examined range $0.35 \leq M \leq 0.77$. The results from the in-flight experiments on a 10° sharp cone [102,121] showed a marked increase in the transition Reynolds number as the Mach number was increased from $M_e = 0.5$ to 1.6. At the same time, this increase correlated well with the strong reduction in external disturbance level at larger Mach numbers. The general conclusion from both wind-tunnel and flight experiments was that the pressure fluctuation level had the predominant effect on boundary-layer transition. The transition Reynolds number was found to scale with a function of the pressure fluctuation level [102].

The pressure distributions measured on the upper side of the *PaLASTra* model showed only small differences (see Fig. 5.1.1.1). This verifies that the streamwise pressure gradient was not the cause of the observed change in transition location. The thermal condition at the model surface is more favorable at lower Mach numbers (see Section 3.1). Transition Reynolds numbers at wall temperature ratios different from those actually measured can be obtained by linear interpolation or extrapolation of the available data. At $T_w/T_{aw} = 1.054$, the transition Reynolds number at $M = 0.35$ would be $Re_{xT,0} \sim 3.8 \cdot 10^6$, closer to the value obtained at $M = 0.77$ for the considered wall temperature ratio. However, the difference between the adiabatic wall transition Reynolds numbers is larger: $Re_{xT0,aw} \sim 3.1$ and $5.2 \cdot 10^6$ at $M = 0.77$ and 0.35, respectively. This difference in the variation of $Re_{xT,0}$ as a function of T_w/T_{aw} will be discussed in Section 5.1.2. In any case, the reduction of the transition Reynolds number at larger Mach numbers is not only due to a change in the thermal condition at the model surface.

The most probable reason for the reduction of the transition Reynolds number at larger Mach numbers appears to be the increased initial amplitude of the disturbances within the boundary layer. This can originate from increased amplitude of the external disturbances (in the frequency range of amplified instability waves), from enhanced receptivity to the external disturbances, or from a combination of both effects. Additional acoustic disturbances originating from flow separation at the model aft side and then traveling upstream were likely to be the cause for the increased initial amplitude of the boundary-layer disturbances. This aspect has been already discussed in [148] for a Mach number $M = 0.77$ and is discussed in more detail in Appendix D.5. The value of transition *N*-factor for streamwise instabilities was found to decrease at larger Mach numbers. This is obviously in line with the smaller value of transition Reynolds number. Also this result has been already discussed in [148] for a Mach number $M = 0.77$. The transition *N*-factors for all four Mach numbers are presented in Appendix D.6.

5.1.2 Effect of pressure gradient and wall temperature ratio and comparison with published work

The results for all tested conditions are summarized in various plots in this section. This will provide an overview of the trends in the effect of streamwise pressure gradient and wall temperature ratio on boundary-layer transition at different Mach numbers.

First of all, the transition Reynolds number $Re_{xT,0}$ is plotted as a function of the Hartree parameter in Fig. 5.1.2.1 to Fig. 5.1.2.4 for Mach numbers M = 0.77 to 0.35. The results obtained at standard and reduced T_w/T_{aw} are shown by blue and red symbols, respectively. The data points enclosed by black circles indicate lower limits for $Re_{xT,0}$ achievable at these conditions, since the boundary layer remained laminar over the whole model upper surface. Only a few representative error bars for the results are actually plotted in the figures.

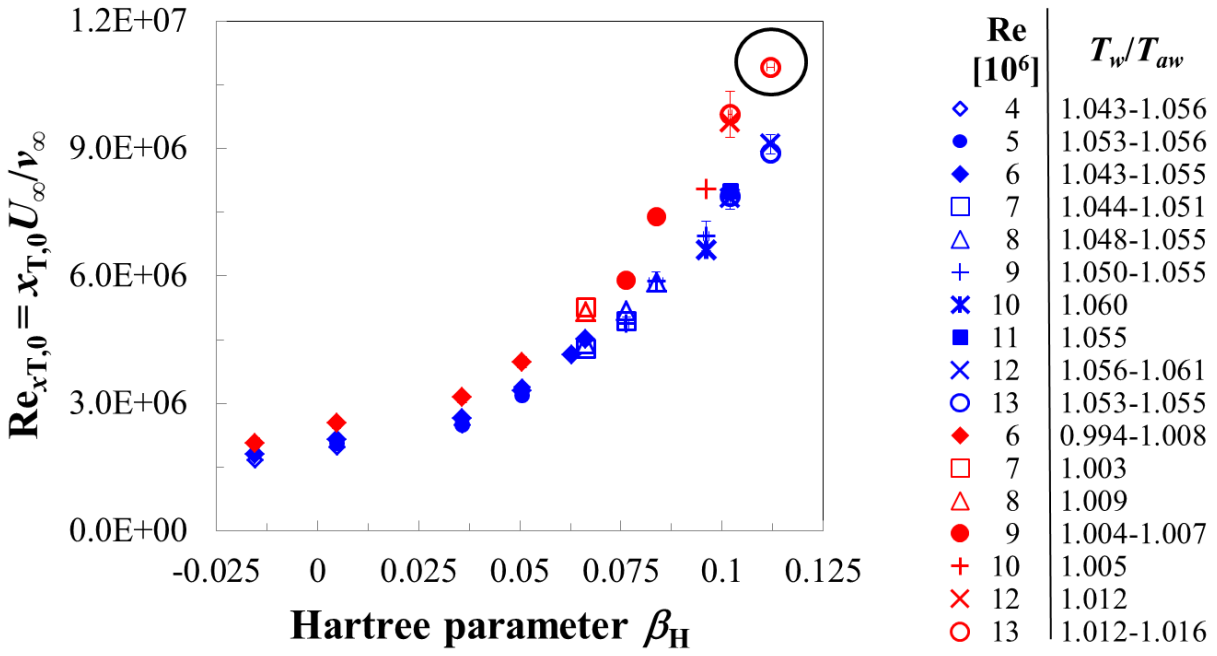

Fig. 5.1.2.1. Transition Reynolds number as a function of the Hartree parameter with the smooth configuration: M = 0.77.

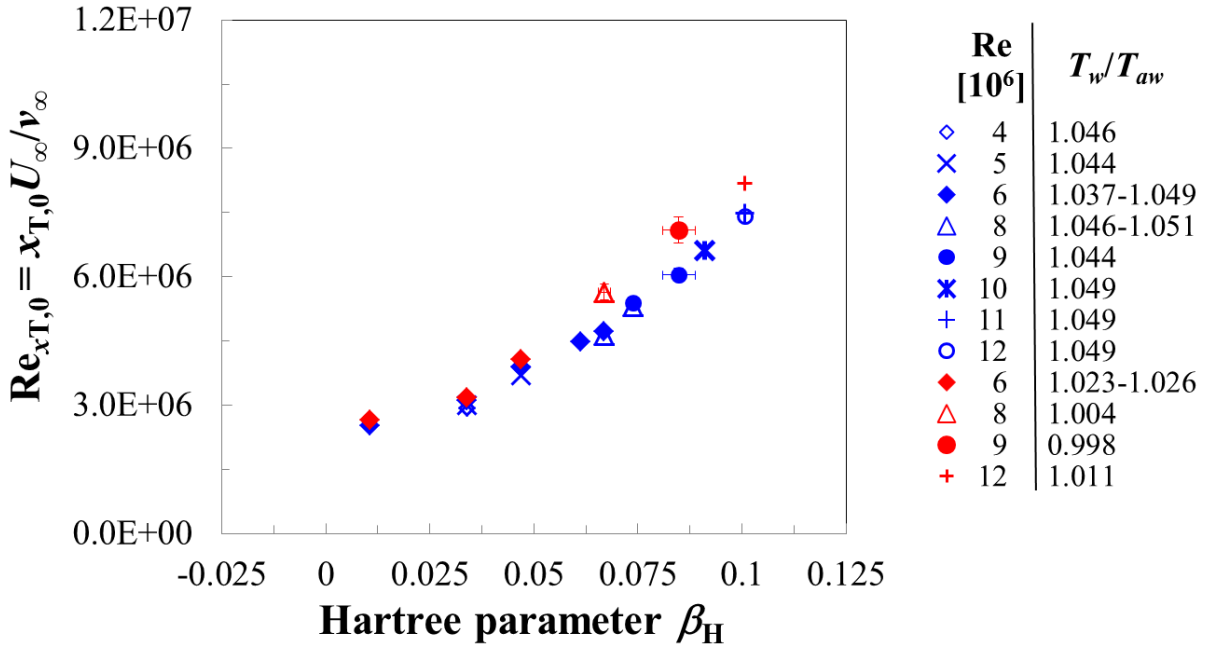

Fig. 5.1.2.2. Transition Reynolds number as a function of the Hartree parameter with the smooth configuration: M = 0.65.

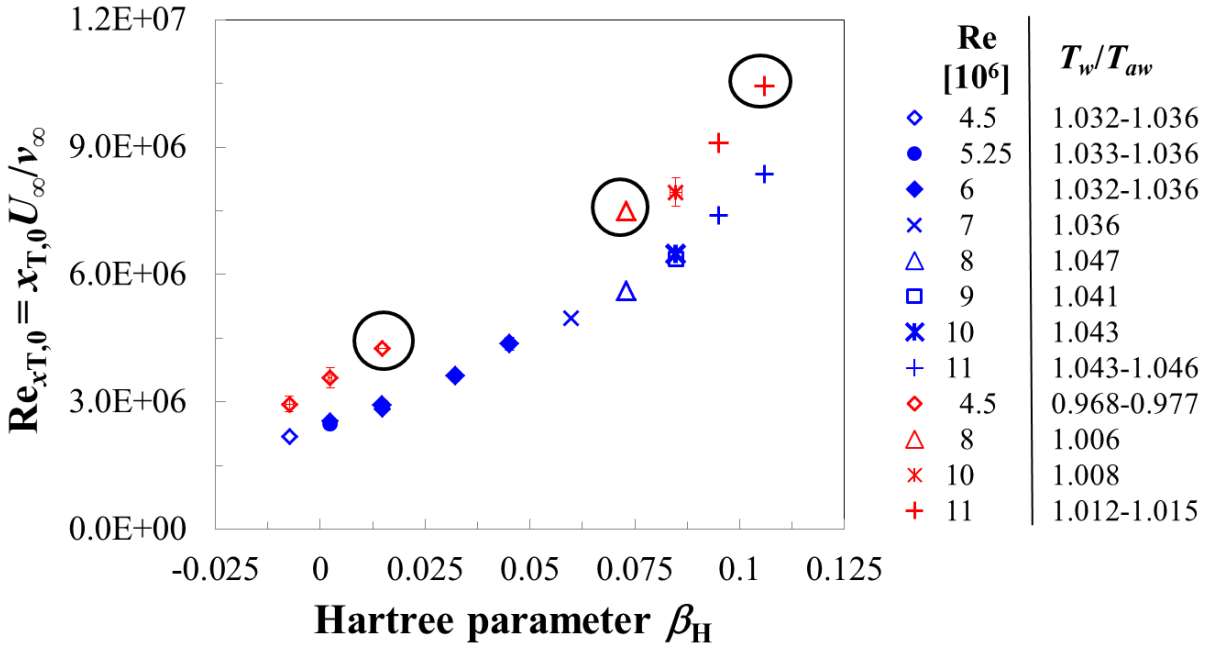

Fig. 5.1.2.3. Transition Reynolds number as a function of the Hartree parameter with the smooth configuration: M = 0.5.

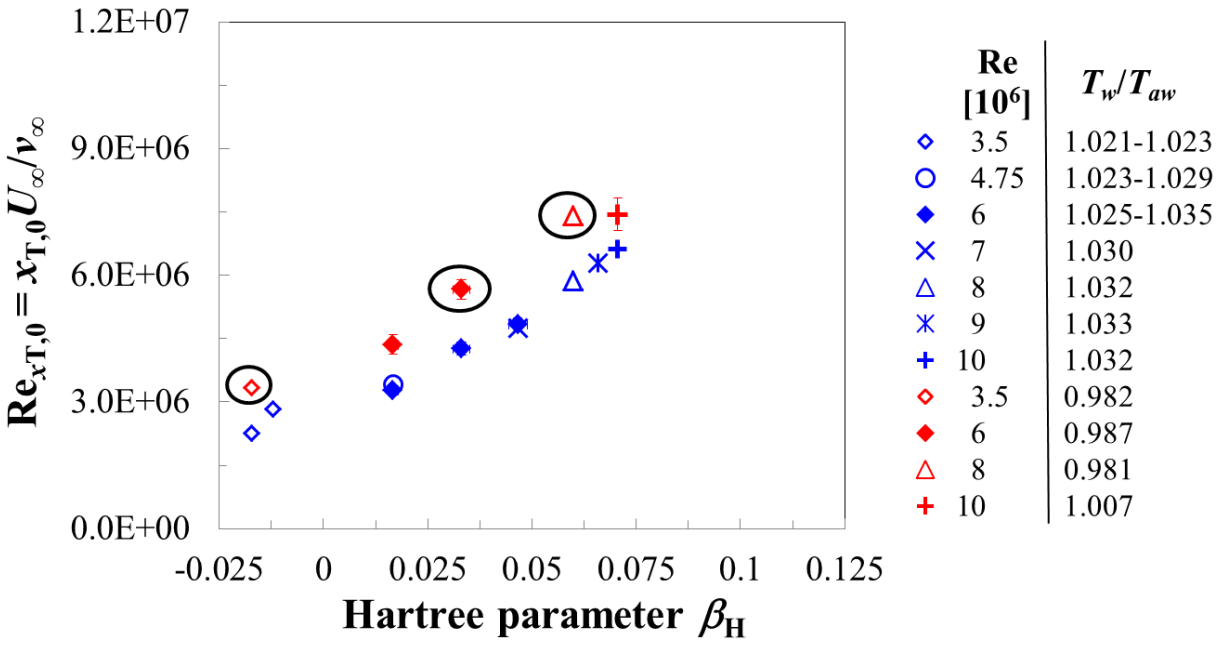

Fig. 5.1.2.4. Transition Reynolds number as a function of the Hartree parameter with the smooth configuration: M = 0.35.

The favorable influence of flow acceleration ($\beta_H > 0$) on boundary-layer transition can clearly be seen by a look at the results obtained for a certain range of wall temperature ratios: a larger value of the Hartree parameter leads to a larger value of $Re_{xT,0}$. Moreover, at fixed streamwise pressure gradient, a lower value of wall temperature ratio also leads to an increase in transition Reynolds number. Although these observations are in line with expectations, the present set of experimental results is the first systematic verification of the effects of streamwise pressure gradient and wall temperature ratio on boundary-layer transition at $0.35 \leq M \leq 0.77$, whereby these effects have been decoupled from each other. The influence of the two parameters on the transition Reynolds number was shown to be additive, confirming earlier considerations [128]. It should be noted here that the more favorable thermal condition at the model surface had, in general, only a small influence on boundary-layer transition at adverse or zero streamwise pressure gradients; the increase in $Re_{xT,0}$ was shown to be more pronounced at larger Hartree parameters. At M = 0.77, for example, the variation in transition Reynolds number with a change in wall temperature ratio was $\Delta Re_{xT,0}/\Delta(T_w/T_{aw}) \sim 33 \cdot 10^6$ at $\beta_H = 0.096$, as compared to $\Delta Re_{xT,0}/\Delta(T_w/T_{aw}) \sim 7 \cdot 10^6$ at $\beta_H = 0.005$ (see Fig. 5.1.2.1). The actual value of the wall temperature ratio at reduced T_w/T_{aw} conditions obviously influences the value of $Re_{xT,0}$. This can be seen, for example, in Fig. 5.1.2.4. The reduced wall temperature ratio was $T_w/T_{aw} = 0.981$ and 1.007 at $\beta_H = 0.060$ and 0.071, respectively: the corresponding increase in transition Reynolds number obtained at $\beta_H = 0.071$ was $\Delta Re_{xT,0} \sim 0.8 \cdot 10^6$, whereas at least $\Delta Re_{xT,0} \sim 1.5 \cdot 10^6$ was obtained at $\beta_H = 0.060$. The effect on $Re_{xT,0}$ of the variation in the wall temperature ratio will be presented later in this section. As a final remark regarding the above figures, it should be emphasized that the transition Reynolds

number was confirmed to be nearly independent of the chord Reynolds number: this was verified for all four Mach numbers and both ranges of wall temperature ratios.

The results obtained at the four different Mach numbers are summarized in Fig. 5.1.2.5 and Fig. 5.1.2.6, where the transition Reynolds number is also plotted as a function of the Hartree parameter. Symbols with different colors correspond to different Mach numbers. The data points and the error bars show the average value and the standard deviation, respectively, of the transition Reynolds numbers obtained at a certain Hartree parameter. A 2nd order polynomial fit to each set of data is also shown. The results obtained at standard wall temperature ratio are plotted in Fig. 5.1.2.5, whereas the adiabatic wall transition Reynolds numbers are shown in Fig. 5.1.2.6. The results at reduced T_w/T_{aw} are presented in Appendix D.7. The values of the adiabatic wall transition Reynolds number were obtained via linear interpolation or extrapolation of available data to adiabatic wall conditions (see also [145]). The uncertainty in $\mathrm{Re}_{x\mathrm{T0},aw}$ was evaluated as for the uncertainty in $\mathrm{Re}_{x\mathrm{T},0}$, with an uncertainty in the transition location at adiabatic wall conditions assumed equal to the maximal uncertainty determined in the test campaign. At standard wall temperature ratio (Fig. 5.1.2.5) and for a given pressure gradient, lower values of $\mathrm{Re}_{x\mathrm{T},0}$ were obtained at larger Mach numbers (see Section 5.1.1).

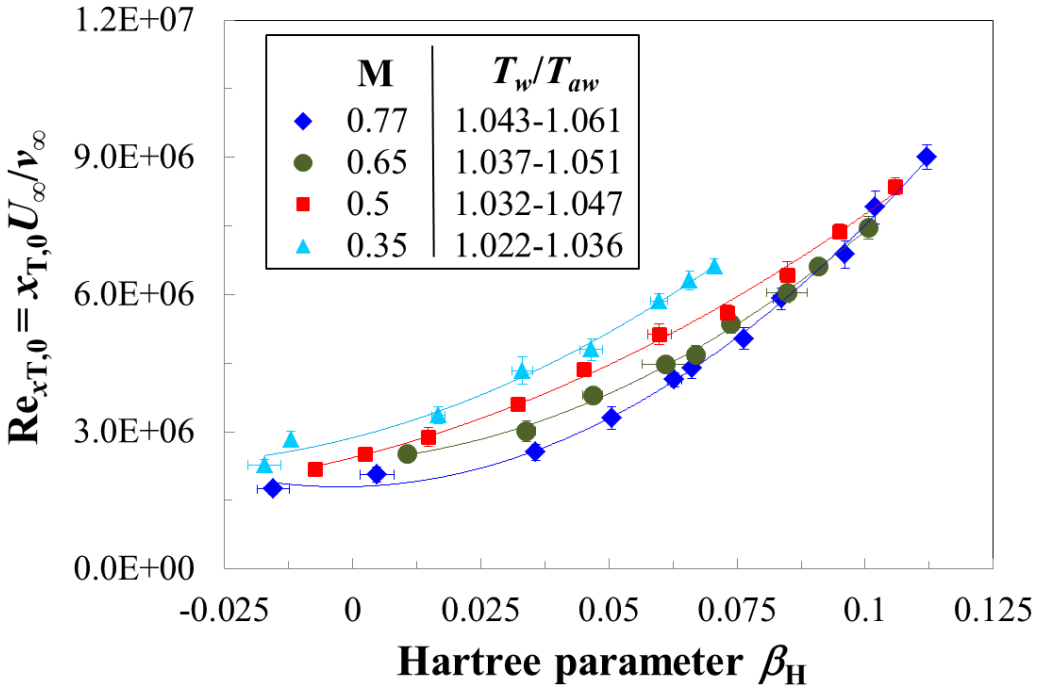

Fig. 5.1.2.5. Transition Reynolds number as a function of the Hartree parameter for the four examined Mach numbers at standard T_w/T_{aw}. Smooth configuration.

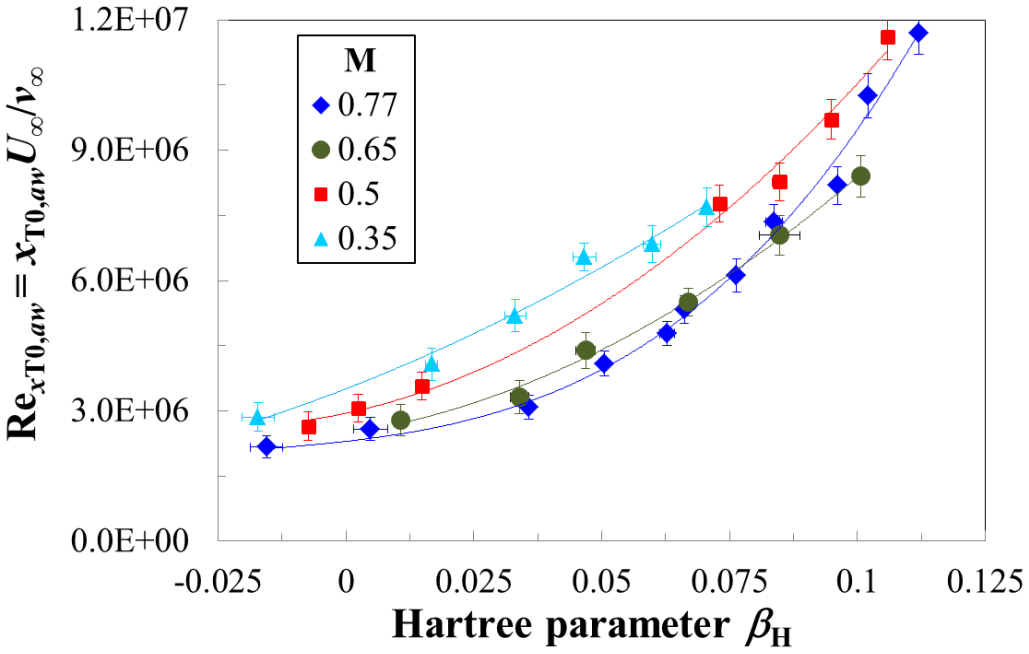

Fig. 5.1.2.6. Adiabatic wall transition Reynolds number as a function of the Hartree parameter for the four examined Mach numbers. Smooth configuration.

T_w/T_{aw} was lower at lower Mach numbers, and this had an additional effect on boundary-layer transition. However, the difference in transition Reynolds numbers obtained at different Mach numbers decreases progressively as the Hartree parameter is increased. This can be seen especially at $\beta_H > 0.08$: the trends of the data obtained at M = 0.65 and 0.77 are in agreement. Also the results obtained at M = 0.5 come closer to those at M = 0.77 (and M = 0.65) as the pressure gradient is increased. At M = 0.35, no experiments were conducted at $\beta_H > 0.071$ (see Appendix D.3), thus a comparison in this range of pressure gradients is not possible. The trends observed at adiabatic wall conditions are similar to those at standard T_w/T_{aw}. A glance at Fig. 5.1.2.6 shows that the effect on boundary-layer transition of increasing Mach number is generally adverse: at fixed Hartree parameter, $Re_{xT0,aw}$ decreases with larger Mach numbers. However, as $\beta_H \sim 0.07$ is reached, the adiabatic wall transition Reynolds number at M = 0.77 and 0.65 essentially coincide; also the difference between the results obtained at M = 0.35 and 0.5 has almost vanished. At larger Hartree parameters, the adiabatic wall transition Reynolds numbers at M = 0.77 are even larger than those obtained at M = 0.65, and the difference with those achieved at M = 0.5 also decreases.

The trends observed above can be elucidated when the influence of the pressure gradient on the transition Reynolds number has been "isolated" from the effects of differences in other parameters. This is attained by considering the relative variation of transition Reynolds number $Re_{xT,0}/Re_{xT,0}(\beta_H = 0)$, a ratio analogous to that used in [144]. $Re_{xT,0}(\beta_H = 0)$ is the linearly interpolated value of the transition Reynolds number at $\beta_H = 0$ for the corresponding Mach number (linearly extrapolated for M = 0.65). The uncertainty in $Re_{xT,0}(\beta_H = 0)$ is the sum

of the uncertainties in the values of $Re_{xT,0}$ used for the interpolation/extrapolation. The uncertainty in the ratio $Re_{xT,0}/Re_{xT,0}(\beta_H = 0)$ is then calculated using the formula for the propagation of uncertainties with independent variables. The ratio $Re_{xT,0}/Re_{xT,0}(\beta_H = 0)$ at standard T_w/T_{aw} is shown in Fig. 5.1.2.7 as a function of the Hartree parameter. The values $Re_{xT,0}/Re_{xT,0}(\beta_H = 0)$ obtained for the different Mach numbers overlap quite closely up to $\beta_H \sim 0.07$, after which the trends at M = 0.65 and 0.5 are almost coincident, whereas the values at M = 0.77 are higher (but still within error bars, except for $\beta_H > 0.1$). These results are still influenced by the wall temperature ratio, which was generally lower for the data points at smaller Hartree parameters.

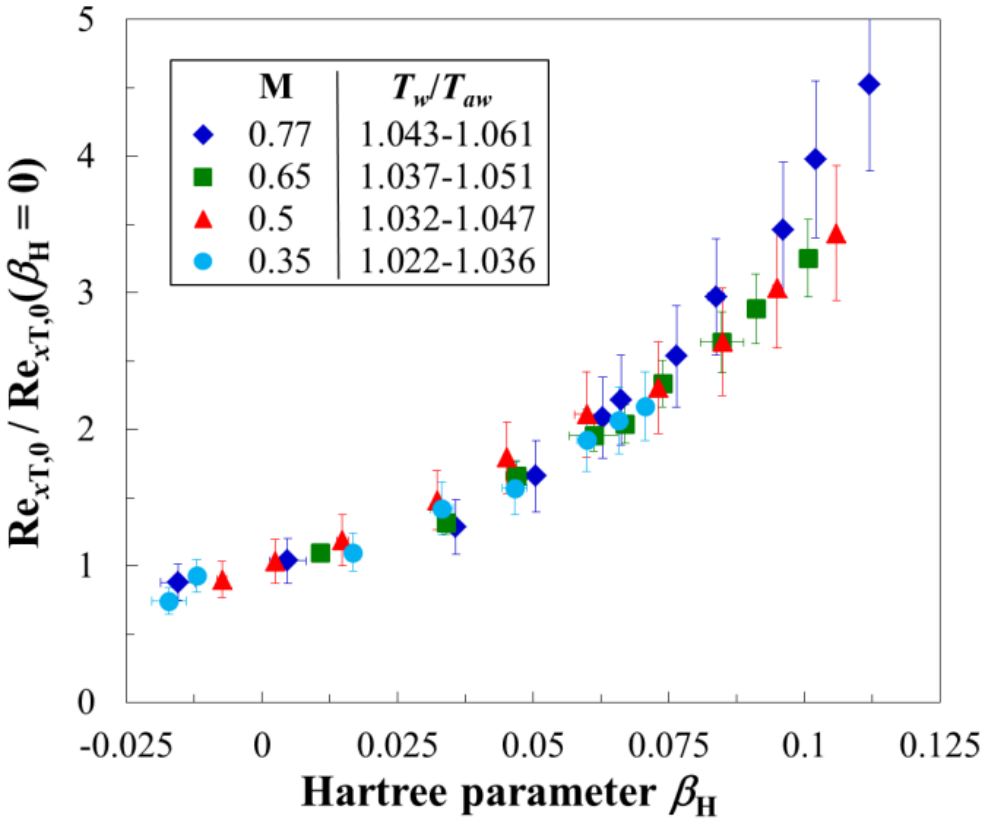

Fig. 5.1.2.7. Relative variation of the transition Reynolds number as a function of the Hartree parameter for the four examined Mach numbers at standard T_w/T_{aw}. Smooth configuration.

The transition Reynolds number interpolated at $\beta_H = 0$ for a certain wall temperature ratio is not appropriate to form the ratio $Re_{xT,0}/Re_{xT,0}(\beta_H = 0)$ for results obtained at another wall temperature ratio. This effect can be "corrected" (or at least mitigated) when the aforementioned adiabatic wall transition Reynolds number $Re_{xT0,aw}$ is considered for the analysis. For each Mach number, $Re_{xT0,aw}(\beta_H = 0)$ is linearly interpolated (or extrapolated) at $\beta_H = 0$ from the adiabatic wall transition Reynolds numbers. The ratio $Re_{xT0,aw}/Re_{xT0,aw}(\beta_H = 0)$ can then be plotted as a function of the Hartree parameter β_H in Fig. 5.1.2.8. The

uncertainties in $Re_{xT0,aw}(\beta_H = 0)$ and in the ratio $Re_{xT0,aw}/Re_{xT0,aw}(\beta_H = 0)$ are evaluated in the same manner as for the uncertainties in $Re_{xT,0}(\beta_H = 0)$ and $Re_{xT,0}/Re_{xT,0}(\beta_H = 0)$. A glance at Fig. 5.1.2.8 shows that the influence of the pressure gradient on the relative change in transition Reynolds number is nearly independent of the Mach number, once it has been "isolated" from the effects of differences in other parameters. This is significant especially at Hartree parameters larger than $\beta_H \sim 0.065$, where the value of $Re_{xT0,aw}$ is more than double that at zero pressure gradient. The data points can be fitted quite well to a 3rd order polynomial function, shown in Fig. 5.1.2.8 by the dashed line. This function is quasi-independent of the Mach number; this implies also a quasi-independency from changes in disturbance environment and boundary-layer receptivity. (Of course, they still influence the absolute values of the transition Reynolds number). As a final remark to this analysis, note that the values of $Re_{xT0,aw}/Re_{xT0,aw}(\beta_H = 0)$ are obtained after three steps of data processing (evaluation of $Re_{xT,0}$, interpolation/extrapolation of $Re_{xT0,aw}$, interpolation/extrapolation of $Re_{xT0,aw}(\beta_H = 0)$) and therefore have large uncertainties.

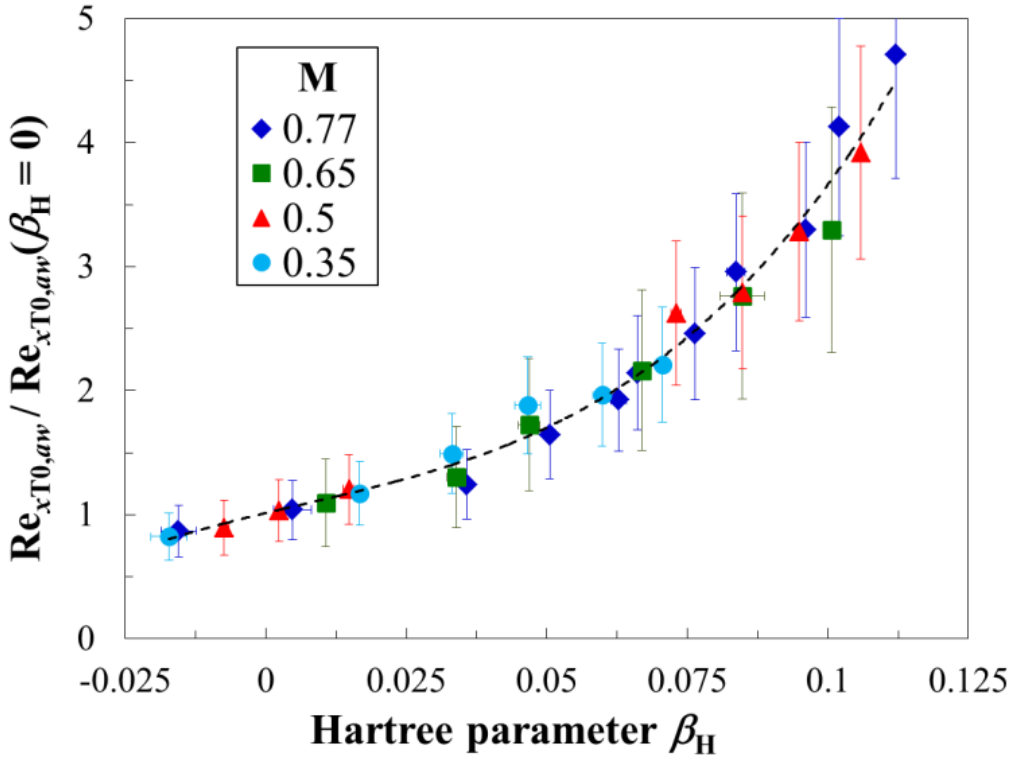

Fig. 5.1.2.8. Relative variation of the adiabatic wall transition Reynolds number as a function of the Hartree parameter for the four examined Mach numbers. Smooth configuration.

The effect of the wall temperature ratio on boundary-layer transition is now examined. The results are presented in the form $Re_{xT,0}/Re_{xT0,aw}$ vs. T_w/T_{aw}, which had already been used in [102,121] to represent the experimental results obtained on a 10° cone. The results are presented in different figures, one for each Mach

number: Fig. 5.1.2.9 and Fig. 5.1.2.10 correspond to Mach numbers M = 0.77 and 0.35, whereas the figures for M = 0.65 and 0.5 are shown in Appendix D.8. In each figure, the results obtained at different pressure gradients are shown by filled symbols with different colors. The approximation function $Re_{xT,0}/Re_{xT0,aw} = (T_w/T_{aw})^{-7}$ from [102,121] is shown by a dashed line. At some test conditions, the boundary layer remained laminar over the model upper surface when the wall temperature ratio was reduced; the corresponding data points are shown by open symbols. In these cases, even larger values of $Re_{xT,0}$ may be possible at the reduced values of T_w/T_{aw}. The uncertainty in the ratio $Re_{xT,0}/Re_{xT0,aw}$ is calculated as before. Only a few representative error bars for the results are actually plotted in the following figures. The representation of the results as $Re_{xT,0}/Re_{xT0,aw}$ vs. T_w/T_{aw} allows the influence of T_w/T_{aw} on boundary-layer transition to be "isolated" from other effects. Since the streamwise pressure gradient remains essentially unchanged when tests at the same test conditions but at different wall temperature ratio are carried out (see Appendix D.2), a "correction" of the data, such as that performed to obtain $Re_{xT0,aw}/Re_{xT0,aw}(\beta_H = 0)$ in Fig. 5.1.2.8, is not needed in this case.

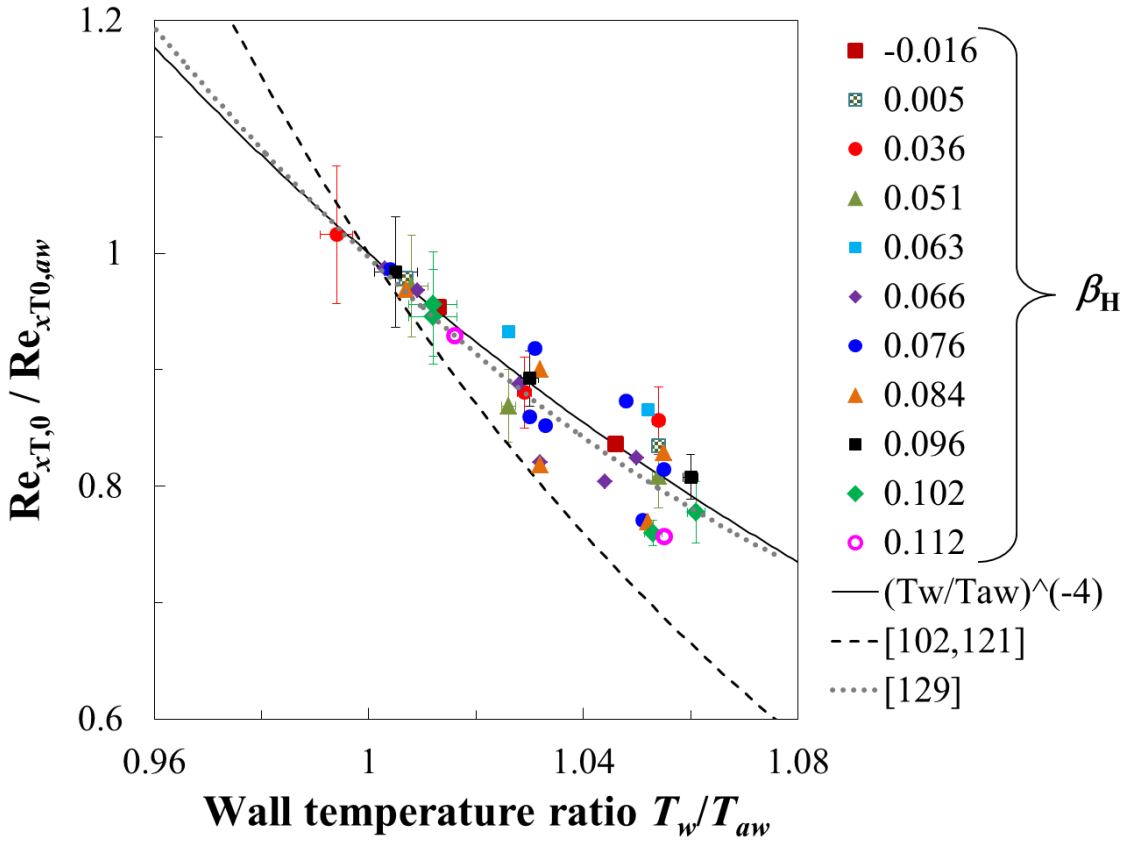

Fig. 5.1.2.9. Relative variation of transition Reynolds number as a function of the wall temperature ratio for different pressure gradients (β_H) with the smooth configuration: M = 0.77.

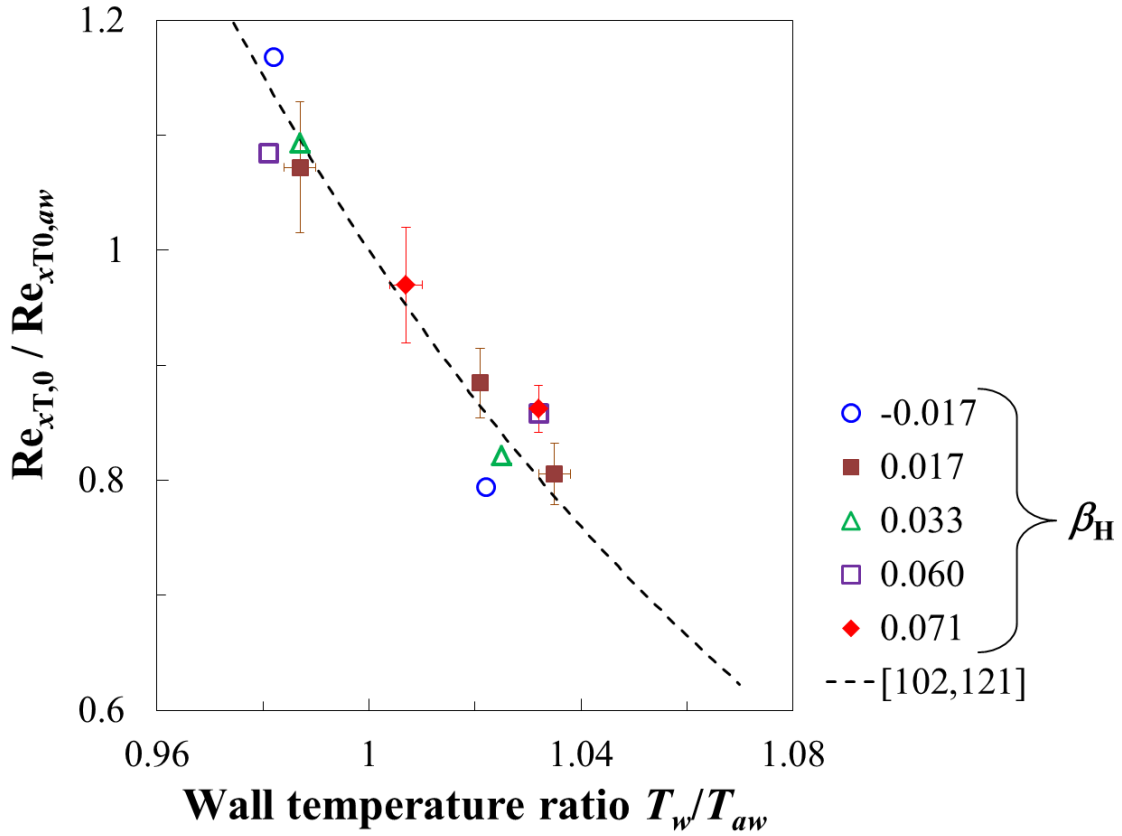

Fig. 5.1.2.10. Relative variation of transition Reynolds number as a function of the wall temperature ratio for different pressure gradients (β_H) with the smooth configuration: M = 0.35.

Different streamwise pressure gradients do not have a marked influence on the above plots of $Re_{xT,0}/Re_{xT0,aw}$ vs. T_w/T_{aw}. The first result to be discussed here is that obtained at M = 0.77 (see Fig. 5.1.2.9). The scatter of the data points from the present study is comparable to that of the results from [102,121]. Although some of the current results can be fitted reasonably well by the approximation function $Re_{xT,0}/Re_{xT0,aw} = (T_w/T_{aw})^{-7}$, the majority of them can be better fitted by the function $Re_{xT,0}/Re_{xT0,aw} = (T_w/T_{aw})^{-4}$, shown in Fig. 5.1.2.9 by a solid line. This difference from [102,121] can be explained – at least partially – by the fact that T_w/T_{aw} was taken in the present work in the laminar region, whereas T_w/T_{aw} in [102,121] corresponds to temperatures in a turbulent boundary layer. If the wall temperature ratio would have been calculated in the present work as in [102,121], the values of T_w/T_{aw} would have been closer to one, so that the data points in Fig. 5.1.2.9 would have been also closer to the approximation function $Re_{xT,0}/Re_{xT0,aw} = (T_w/T_{aw})^{-7}$. It should be emphasized here that the current experimental results agree quite well with the prediction for a flat plate at zero pressure gradient from [129], which is shown in Fig. 5.1.2.9 by a dotted line. This curve was obtained at M = 0.85 using the e^N method: the indifferent-stability Reynolds numbers were interpolated from the numerical results of [139] and transition was assumed to occur when the amplification ratio of streamwise instabilities reaches e^9 [142]. Obviously, wall temperature ratios for a laminar

boundary layer were considered in [129]. The curve from [129] and the function $Re_{xT,0}/Re_{xT0,aw} = (T_w/T_{aw})^{-4}$ are indeed in agreement. Hence it is justifiable to use this function to fit the present experimental results. The results at the lowest Mach number, M = 0.35, are well approximated by the function $Re_{xT,0}/Re_{xT0,aw} = (T_w/T_{aw})^{-7}$, see Fig. 5.1.2.10. It should be also noted that, at lower Mach numbers, the difference between the wall temperature ratio obtained in the laminar region and that obtained in the turbulent region is reduced, so that the data can be more realistically compared to those of [102,121].

Larger variations of the ratio $Re_{xT,0}/Re_{xT0,aw}$ are observed at lower Mach numbers. This can be seen from the exponent k of the power functions $Re_{xT,0}/Re_{xT0,aw} = (T_w/T_{aw})^{-k}$ used to approximate the results: it corresponds to k = 4 at M = 0.77 and increases to 7 at M = 0.35. This behavior may seem in contrast with that observed in earlier flight tests [102,121], where the function $Re_{xT,0}/Re_{xT0,aw} = (T_w/T_{aw})^{-7}$ provided a good approximation of the results, independent of the Mach number in the range $0.5 < M_e \leq 2$. However, it has been already discussed above that wall temperature ratios for a turbulent boundary layer were used in that work. If the same would have been done in the present work, the data points obtained at different Mach numbers, when represented as $Re_{xT,0}/Re_{xT0,aw}$ vs. T_w/T_{aw}, would have shown a similar trend. At M = 0.77, a typical wall temperature ratio for a laminar boundary layer was $T_w/T_{aw} \sim 1.055$, whereas that for a turbulent one was lower by more than $\Delta(T_w/T_{aw}) = 0.01$. In contrast, the variation for the wall temperature ratio typical for a laminar boundary layer $T_w/T_{aw} \sim 1.028$ at M = 0.35 is less than $\Delta(T_w/T_{aw}) = 0.005$. Nevertheless, it cannot be excluded that a larger level of external disturbances also leads to a weaker sensitivity of boundary-layer transition to the influence of the wall temperature ratio: the data obtained on the aforementioned 10° test cone [102,121] in the AEDC 4T wind tunnel showed a negligible change in transition Reynolds number in the range of wall temperature ratios $0.97 < T_w/T_{aw} < 1.02$ [102]. (The data points then tend to follow the general trend from the flight tests at $T_w/T_{aw} < 0.97$ and $T_w/T_{aw} > 1.02$.) The AEDC 4T wind tunnel was one of the noisy facilities where the experiments were conducted [120]: the achieved transition Reynolds numbers were generally smaller than those obtained in the same Mach number range $0.4 \leq M_\infty \leq 1.3$ in quiet wind tunnels and in flight [102]. Such a marked reduction of transition sensitivity to changes in the wall temperature ratio was not observed in the present work, but larger initial amplitude of the boundary-layer disturbances may have contributed to the variation of the relation between $Re_{xT,0}/Re_{xT0,aw}$ and T_w/T_{aw} at different Mach numbers. In any case, the present experimental results at M = 0.77 are in reasonable agreement with the prediction from [129] (see Fig. 5.1.2.9), and the relation between $Re_{xT0,aw}/Re_{xT0,aw}(\beta_H = 0)$ and β_H in Fig. 5.1.2.8 does not change appreciably with different Mach numbers.

5.1.3 Summary of investigations with the smooth configuration

- The pressure distributions on the model upper surface matched the objectives of the model design: a quasi-uniform streamwise pressure gradient was achieved over a large region of this surface. This allowed the effect of the test parameters on boundary-layer transition to be decoupled.
- The effect on boundary-layer transition of chord Reynolds number, streamwise pressure gradient, and a non-adiabatic surface was systematically investigated at four different Mach numbers. The results were in overall agreement with expectations based on linear stability theory and with the results of past experimental work.
- Larger chord Reynolds numbers, larger wall temperature ratios, and lower Hartree parameters led to earlier transition. This is in line with the increase in the amplification factors of streamwise instabilities predicted by means of linear stability theory.
- The transition Reynolds number was essentially independent of the chord Reynolds number. This result is consistent with the quasi-uniform pressure gradient that was achieved on a large region of the model upper surface.
- The effect of Mach number on boundary-layer transition was opposite to that expected from linear stability theory. The amplification factors of streamwise instabilities decrease at larger Mach numbers, but transition was shifted upstream, leading to smaller values of the transition Reynolds number. This effect was very likely caused by an increase in the initial disturbance amplitude, due to a larger level of external disturbances and/or to enhanced boundary-layer receptivity.
- A change in the Mach number did not appreciably affect the relation between $\mathrm{Re}_{x\mathrm{T0},aw}/\mathrm{Re}_{x\mathrm{T0},aw}(\beta_\mathrm{H} = 0)$ and the Hartree parameter. A larger variation of $\mathrm{Re}_{x\mathrm{T},0}/\mathrm{Re}_{x\mathrm{T0},aw}$ as a function of the wall temperature ratio was observed at lower Mach numbers; nevertheless, the present results were in overall agreement with those from previous work.
- The results obtained with the smooth configuration were repeatable and reproducible.

5.2 Step configurations

The range of parameters examined with the step-1, step-2, and step-3 configurations is presented in Table 5.2.1, Table 5.2.2, and Table 5.2.3, respectively. It is basically the same as that for the previous phase of measurements, except for the lowest Hartree parameter examined at M = 0.77 and 0.65. This was limited by the transition location on the smooth configuration: at smaller Hartree parameters, transition was measured close to or upstream of the step location. The effect of the steps on boundary-layer transition was clearly not quantifiable at these conditions. Moreover, the number of test runs with the step-3 configuration at reduced T_w/T_{aw} was strongly limited. This was due to the large number of particle impacts onto the model leading edge after operation of the gate valve, which was necessary for the pre-conditioning procedure (see Section 3.1 and [145]). This topic is discussed in Appendix C.2.1.

Table 5.2.1 Variation of parameters examined with the step-1 configuration.

M	Re [10^6]	β_H	AoA [°]	T_w/T_{aw} (standard)	T_w/T_{aw} (reduced)
0.77	4 to 13	0.005 to 0.112	-4.0 to -2.0	1.047 to 1.064	1.004 to 1.014
0.65	6 to 12	0.034 to 0.101	-3.8 to -2.3	1.042 to 1.056	0.995 to 1.007
0.50	4.5 to 11	-0.007 to 0.106	-4.0 to -1.6	1.032 to 1.051	0.985 to 1.011
0.35	3.5 to 10	-0.017 to 0.071	-3.2 to -1.4	1.024 to 1.036	0.971 to 1.000

Table 5.2.2 Variation of parameters examined with the step-2 configuration.

M	Re [10^6]	β_H	AoA [°]	T_w/T_{aw} (standard)	T_w/T_{aw} (reduced)
0.77	4 to 13	0.005 to 0.112	-4.0 to -2.0	1.047 to 1.063	1.000 to 1.026
0.65	4 to 12	0.034 to 0.101	-3.8 to -2.3	1.045 to 1.057	0.998 to 1.020
0.50	4.5 to 11	-0.007 to 0.106	-4.0 to -1.6	1.035 to 1.046	0.986 to 1.009
0.35	3.5 to 10	-0.017 to 0.071	-3.2 to -1.4	1.026 to 1.035	0.973 to 0.988

Table 5.2.3 Variation of parameters examined with the step-3 configuration.

M	Re [10^6]	β_H	AoA [°]	T_w/T_{aw} (standard)	T_w/T_{aw} (reduced)
0.77	4 to 10	0.005 to 0.096	-3.6 to -2.0	1.044 to 1.062	1.010, 1.013
0.65	4 to 10	0.034 to 0.091	-3.6 to -2.3	1.040 to 1.052	-
0.50	4.5 to 11	-0.007 to 0.106	-4.0 to -1.6	1.037 to 1.049	0.984
0.35	3.5 to 9	-0.017 to 0.066	-3.05 to -1.4	1.026 to 1.037	0.966, 0.971

The values of the Hartree parameters given for the tests with the step configurations are not those evaluated from the actual surface pressure distributions, since the presence of the step caused local changes in the surface pressure in the region around the step location. This effect will be discussed in Section 5.2.1. Provided that the surface pressure distributions on the remaining areas of the model upper surface were the same as with the smooth configuration, then the value of the Hartree parameter was assumed to be also the same. The number of test runs progressively decreased as larger steps were investigated. Some test runs with the step-2 and step-3 configurations, where the transition location had already reached the region close to the step location in the presence of a lower step, were not carried out. This was especially the case for the step-3 configuration at the largest Reynolds numbers.

The structure of this section is as follows. The effect of the steps on boundary-layer transition is presented in Section 5.2.1. The influence of Reynolds number, pressure gradient, wall temperature ratio, and Mach number in the presence of the steps is shown in Sections 5.2.2 to 5.2.5. The results are then discussed in Chapter 6. Repeatability and reproducibility of the results are discussed in Appendix E.1.

5.2.1 Effect of the step height

The effect of forward-facing steps on the surface pressure distribution is shown in Fig. 5.2.1.1 for a case at $M = 0.77$, $Re = 6 \cdot 10^6$, $\beta_H = 0.066$, and standard T_w/T_{aw}. The surface pressure distributions with different configurations (with and without steps) are essentially coincident for most of the chord length, except for the region around the step location. A zoomed-in plot of this region is shown in Fig. 5.2.1.1b. These differences in the pressure coefficient, small in absolute terms but characterized by large local gradients, are due to the presence of the steps. The larger the step, the larger was the difference to the undisturbed flow (no step present).

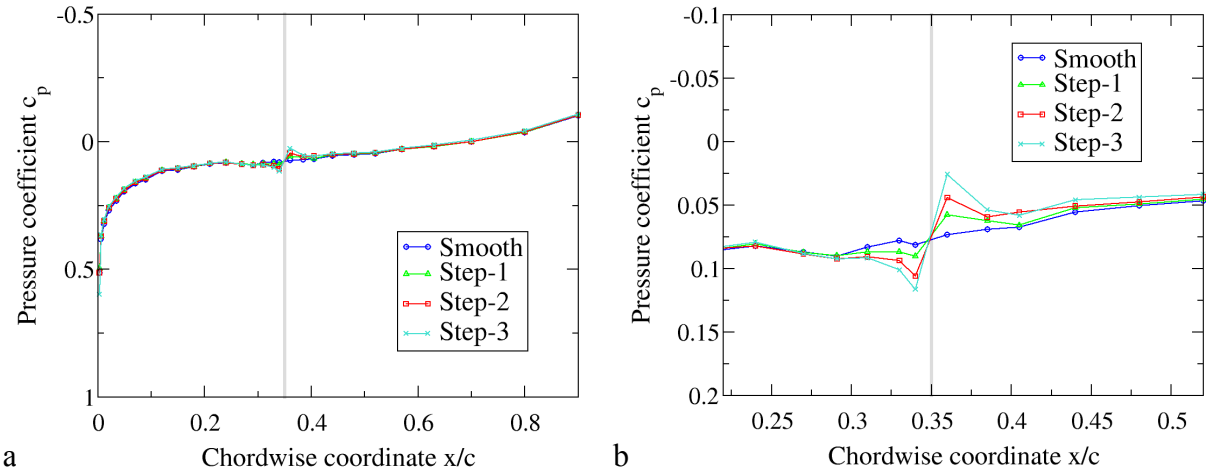

Fig. 5.2.1.1. Surface pressure distributions with different step configurations. $Re = 6 \cdot 10^6$, $M = 0.77$, $\beta_H = 0.066$, and standard T_w/T_{aw}. Step-1: $h/\delta_{1,h} = 0.32$; step-2: $h/\delta_{1,h} = 0.65$; step-3: $h/\delta_{1,h} = 0.97$. a: over the whole chord length; b: zoomed-in around the step location. The gray bar indicates the step location.

As can be seen in Fig. 5.2.1.1b, the flow evolution begins to be influenced by the presence of the step from $x/c \sim 29$ %. The boundary layer is no longer accelerated as on the smooth configuration; depending on the height of the step, the pressure gradient at approximately $29\ \% \leq x/c \leq 33\ \%$ is either almost zero or adverse. The acceleration of the base flow competes here with the step-induced deceleration. Proceeding in the streamwise direction, the flow undergoes a strong local deceleration immediately upstream and immediately downstream of the step edge: these very pronounced, adverse pressure gradients can be seen in results from DNS [35-36,46], but the spatial resolution of the surface pressure measurements here was not sufficient to be able to measure them very close to the step. This aspect has to be kept in mind when the region in proximity of the step $34\ \% < x/c < 36\ \%$ is considered; otherwise, the connecting line between the pressure coefficients measured by the pressure taps at $x/c = 34$ % and 36 % might be misinterpreted. Note also that the pressure measured at a certain location is that averaged over the orifice cross-section, which has a diameter of 0.25 mm. With all step configurations, the flow is decelerated in the region downstream of the step edge up to the pressure tap at $x/c = 40.5$ %. The exact location of the recovery of the smooth-configuration pressure distribution appears to be more downstream with increasing step height.

The surface pressure distribution in the regions close to the step shows the same trends as those shown by results from DNS [35-36,46], at least in the regions resolvable with the used spacing of pressure taps. The region(s) of separated flow immediately upstream (and downstream) of the step edge [30,35-36,45-46,50] could not be resolved. In earlier numerical work, a separation bubble had always been found upstream of the step edge [35-36,45-46,50]. Depending on the flow conditions [50], a second laminar separation bubble may or may not occur downstream of the step edge [36,45-46]. In any case, when present, this separation bubble is smaller than that upstream of the step, especially in the wall-

normal direction [45,46]. The size of the separated flow region(s) and the presence of the separation bubble downstream of the step edge depend mainly on step height, Mach number, Reynolds number, and step location. For the subsonic cases considered in [45,46], the largest regions of separated flow were obtained at $M = 0.8$ and $h/\theta_h \sim 4.1$ ($Re_h \sim 4400$) for a step placed at $Re_{xh} = U_\infty x_h/\nu_\infty \sim 2.5 \cdot 10^6$: the streamwise extent of the separation bubbles upstream and downstream of the step edge was $\Delta x \sim 13\,h$ and $\Delta x \sim 8\,h$, respectively [45]. By way of comparison, the largest values of Re_h and $h/\delta_{1,h}$ examined in the present work were $Re_h \sim 5300$ and $h/\delta_{1,h} \sim 1.5$. (Transition occurred immediately downstream of the step at these conditions.) Even if the streamwise extent of the separation bubbles had been $\Delta x \sim 15$-$18\,h$, this would have been unresolvable with the used pressure tap spacings.

The effect of forward-facing steps on boundary-layer transition for the same test conditions as in Fig. 5.2.1.1 is shown with the TSP results in Fig. 5.2.1.2. Even with the smallest forward-facing step of relative height $h/\delta_{1,h} = 0.32$, the laminar boundary layer became more unstable; this led to a displacement of the transition location towards the step location. Steps of approximately double and triple this height caused a further displacement of the transition location. Note that transition does not occur immediately downstream of the step location, not even for the case with the largest step installed, whose height is close to the boundary-layer displacement thickness ($h/\delta_{1,h} = 0.97$). These effects of the forward-facing steps were generally observed for all other combinations of parameters examined in this work; only in a few cases with the step-1 configuration was the observed movement of the transition location small and then comparable with the measurement uncertainty.

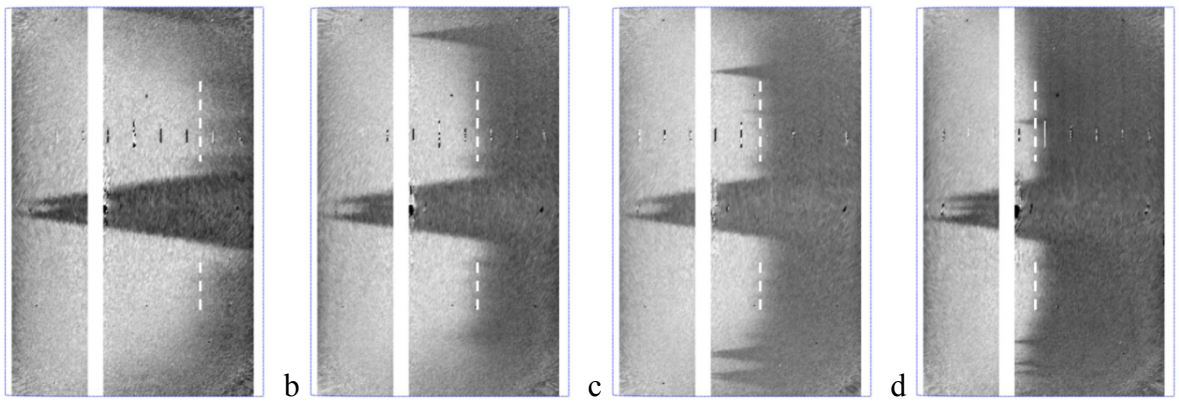

Fig. 5.2.1.2. TSP results obtained with different step configurations. $Re = 6 \cdot 10^6$, $M = 0.77$, $\beta_H = 0.066$, and standard T_w/T_{aw}. a: smooth, $T_w/T_{aw} = 1.043$, $x_{T,0}/c = 75 \pm 1.1$ %; b: step-1, $h/\delta_{1,h} = 0.32$, $T_w/T_{aw} = 1.054$, $x_T/c = 65 \pm 0.9$ %; c: step-2, $h/\delta_{1,h} = 0.65$, $T_w/T_{aw} = 1.050$, $x_T/c = 58 \pm 0.6$ %; d: step-3, $h/\delta_{1,h} = 0.97$, $T_w/T_{aw} = 1.055$, $x_T/c = 47 \pm 0.3$ %.

The steps influenced the transition process in general and not only the transition location. As can be seen in Fig. 5.2.1.2, the natural-transition front becomes a straighter line in the spanwise direction as the step height increases. The

uncertainty in the measured transition location $\Delta(x_T/c)$ accordingly decreases for larger step heights. Moreover, the streamwise extent of the transition region shortens as $h/\delta_{1,h}$ is increased: this can better be seen in Fig. 5.2.1.3, where the streamwise distributions of the intensity ratio obtained at $y/b = 0.63$ for the four cases presented in Fig. 5.2.1.2 are displayed in the one plot.

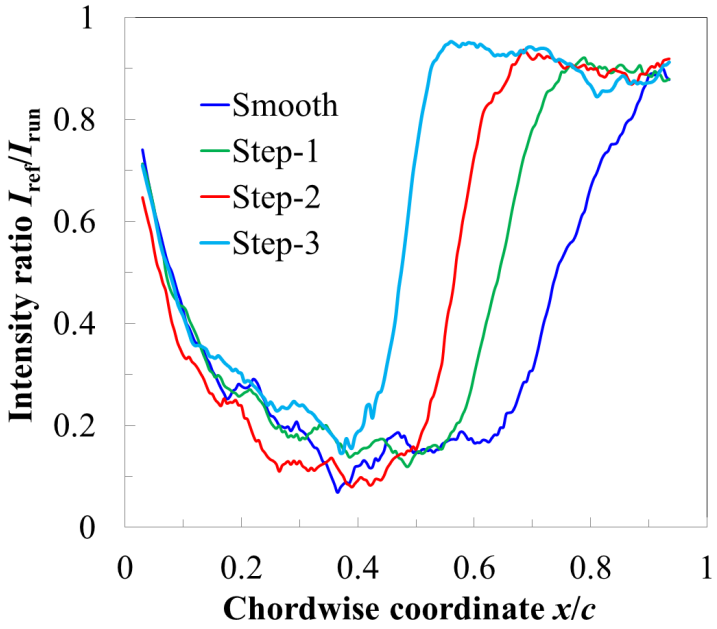

Fig. 5.2.1.3. Normalized intensity distributions at $y/b = 0.63$ for the cases of Fig. 5.2.1.2. Configuration: a) smooth, b) step-1, c) step-2, d) step-3.

These results appear to be due to the larger "relative weight" of the step-induced amplification in the overall amplification process. This aspect will be discussed in more detail in Chapter 6. In practice, it seems here that increasing $h/\delta_{1,h}$ enhances boundary-layer transition and also counteracts the influence of flow acceleration on the extent of the transition region. This effect of the steps is in some manner similar to that of a reduction of the global pressure gradient, which leads to a reduction in the length of the transition region [67,117,123,125,235-237] and to a straightening of the natural-transition front [145]. Note also that, when transition starts at a location close to that of the step, the global pressure gradient has not been recovered and the local pressure gradient is less favorable or even adverse. This is the case of the step-3 configuration in Fig. 5.2.1.2d, as shown in Fig. 5.2.1.3: the extent of the transition region and the straightness of the natural-transition front are consistent with the local pressure gradient.

5.2.2 Effect of the chord Reynolds number

The chord Reynolds number had no appreciable influence on the surface pressure distribution. This can be seen in Fig. 5.2.2.1, where the surface pressure distributions measured on the model upper surface with the step-2 configuration at different Reynolds numbers are presented. The test conditions are: $\beta_H = 0.066$,

M = 0.77, and standard T_w/T_{aw}. The surface pressure distribution is essentially unaffected by the variation in chord Reynolds number, although this leads to a change in the relative step height $h/\delta_{1,h}$. The variation in Re considered for the case in Fig. 5.2.2.1 was $\Delta\text{Re} = 2 \cdot 10^6$: the corresponding change in relative step height was $\Delta(h/\delta_{1,h}) = 0.1$. However, the "step location" in terms of Re_{xh} also increases at larger Reynolds numbers: in this case by $\Delta(\text{Re}_{xh}) = 0.7 \cdot 10^6$. This appears to be the reason for the negligible variation in $c_p(x)$ when forward-facing steps with fixed height h are examined at different chord Reynolds numbers.

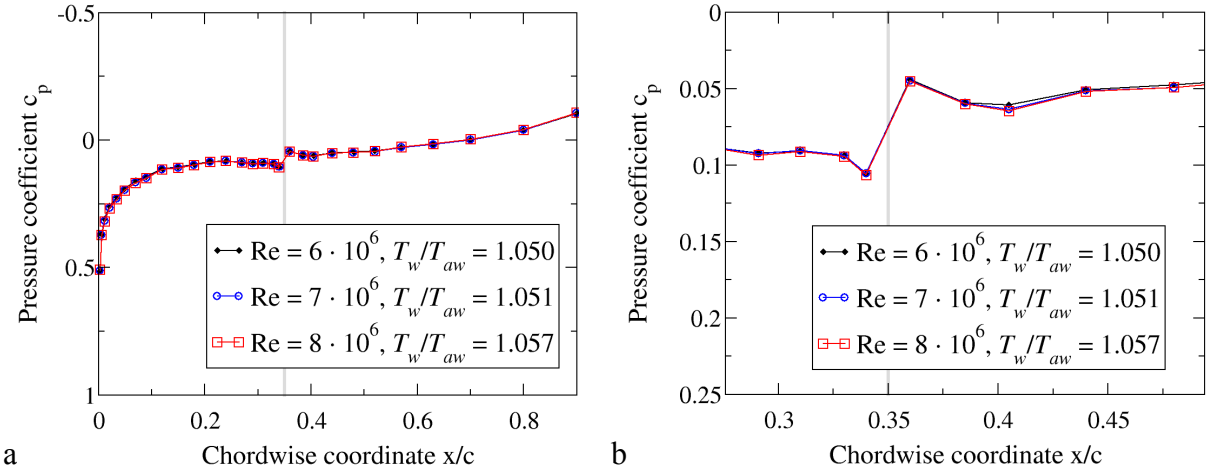

Fig. 5.2.2.1. Surface pressure distributions for different chord Reynolds numbers. M = 0.77, $\beta_H = 0.066$, and standard T_w/T_{aw}. Step-2 configuration. $h/\delta_{1,h}$ increases from 0.65 at Re = $6 \cdot 10^6$ to 0.75 at Re = $8 \cdot 10^6$. a: over the whole chord length; b: zoomed-in around the step location. The gray bar indicates the step location.

The effect of the chord Reynolds number on the transition location is shown in Fig. 5.2.2.2, where the TSP results for the cases shown in Fig. 5.2.2.1 are presented.

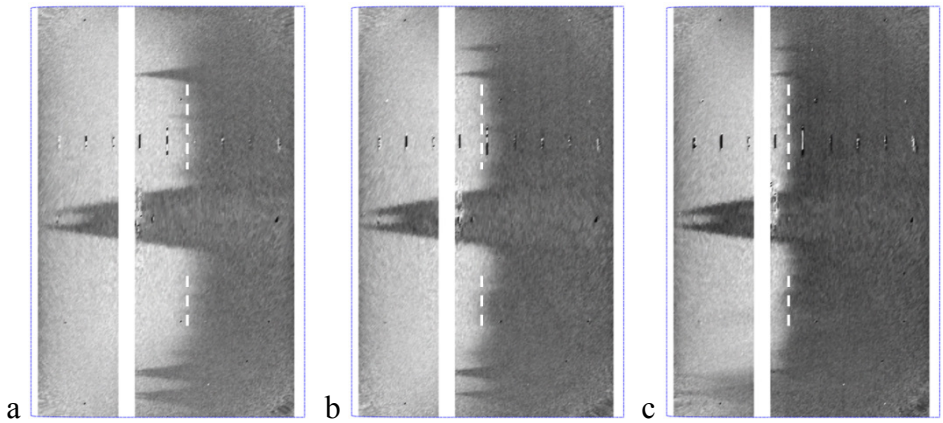

Fig. 5.2.2.2. TSP results for different chord Reynolds numbers. Step-2 configuration. M = 0.77, $\beta_H = 0.066$, and standard T_w/T_{aw}. a: Re = $6 \cdot 10^6$, $T_w/T_{aw} = 1.050$, $h/\delta_{1,h} = 0.65$, $x_T/c = 58 \pm 0.6$ %, $\text{Re}_{xT} = 3.5 \cdot 10^6$; b: Re = $7 \cdot 10^6$, $T_w/T_{aw} = 1.051$, $h/\delta_{1,h} = 0.71$, $x_T/c = 49 \pm 0.3$ %, $\text{Re}_{xT} = 3.4 \cdot 10^6$; c: Re = $8 \cdot 10^6$, $T_w/T_{aw} = 1.057$, $h/\delta_{1,h} = 0.75$, $x_T/c = 44 \pm 0.2$ %, $\text{Re}_{xT} = 3.5 \cdot 10^6$.

The effect of a larger chord Reynolds number is to make the boundary layer more unstable and thus induce earlier transition. Nevertheless, the transition Reynolds number changed by less than $\pm 0.1 \cdot 10^6$ about an average value of $Re_{xT} = 3.5 \cdot 10^6$. The chordwise intensity distributions at $y/b = 0.63$ for the cases of Fig. 5.2.2.2 are shown in Fig. 5.2.2.3. Here also the streamwise extent of the transition region ($Re_{xT,end} - Re_{xT,start}$) appears to be approximately independent of the chord Reynolds number. The streamwise extent of the transition region for the three examined Reynolds numbers was $(Re_{xT,end} - Re_{xT,start}) = 0.9 \pm 0.2 \cdot 10^6$.

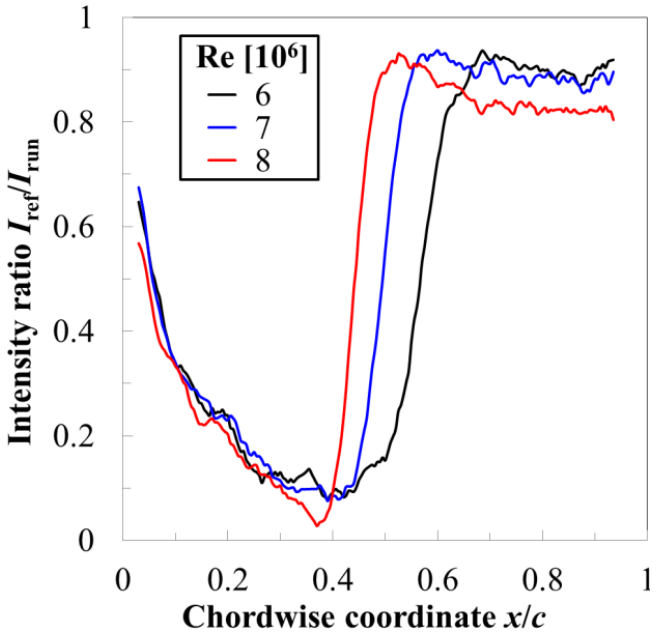

Fig. 5.2.2.3. Normalized intensity distributions at $y/b = 0.63$ for the cases of Fig. 5.2.2.2. Re: a) $6 \cdot 10^6$, b) $7 \cdot 10^6$, c) $8 \cdot 10^6$.

It is noteworthy that the transition Reynolds number is nearly independent of the chord Reynolds number, although the turbulence Tu_{p0} in the DNW-KRG test section increases with larger Re/c. This aspect is discussed with regard to the smooth configuration in Appendix D.4. Given this independence it is also possible to "predict" the change in transition location due to a variation of the chord Reynolds number, once Re_{xT} has become known at a certain Re; thus, test runs with transition occurring in proximity of the step location could be avoided. (As a check on the applicability of this "prediction", some of these tests were conducted anyway.) Further results are presented in Sections 5.2.3 and 5.2.4. Finally, it should be remarked that the transition Reynolds number does not remain unvariant when transition has reached the proximity of the step location, since a further increase in chord Reynolds number does not lead to a shift of the transition location. (Unless the increase in Re is so large that transition would occur upstream of the step location also with the smooth configuration.)

5.2.3 Effect of the streamwise pressure gradient

The surface pressure distributions and the TSP results obtained with the step-2 configuration for a case at M = 0.77, Re = 6 · 10^6, and standard T_w/T_{aw} are shown in Fig. 5.2.3.1 and Fig. 5.2.3.2, respectively.

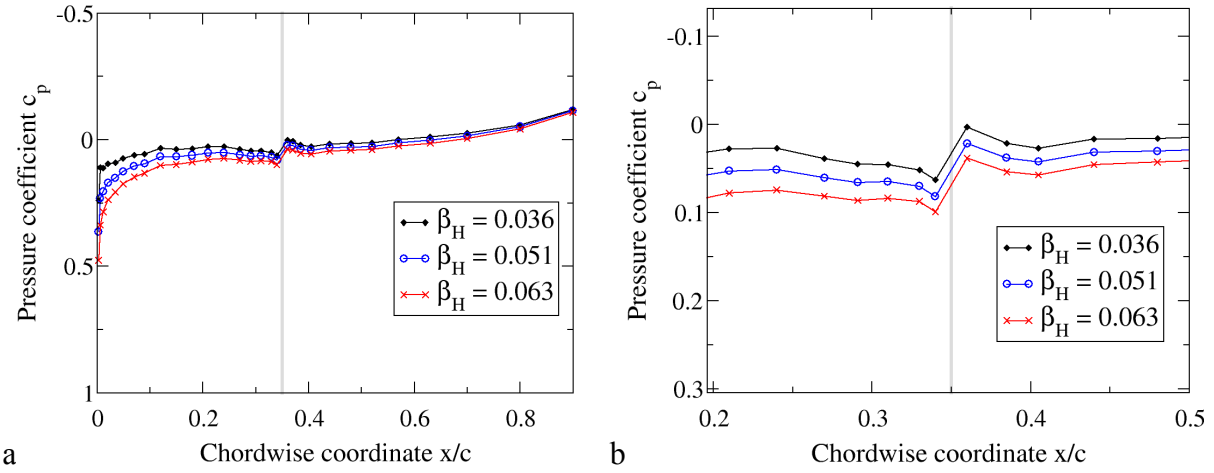

Fig. 5.2.3.1. Surface pressure distributions for different streamwise pressure gradients. M = 0.77, Re = 6 · 10^6, and standard T_w/T_{aw}. Step-2 configuration ($0.62 \leq h/\delta_{1,h} \leq 0.65$). a: over the whole chord length; b: zoomed-in around the step location. The gray bar indicates the step location.

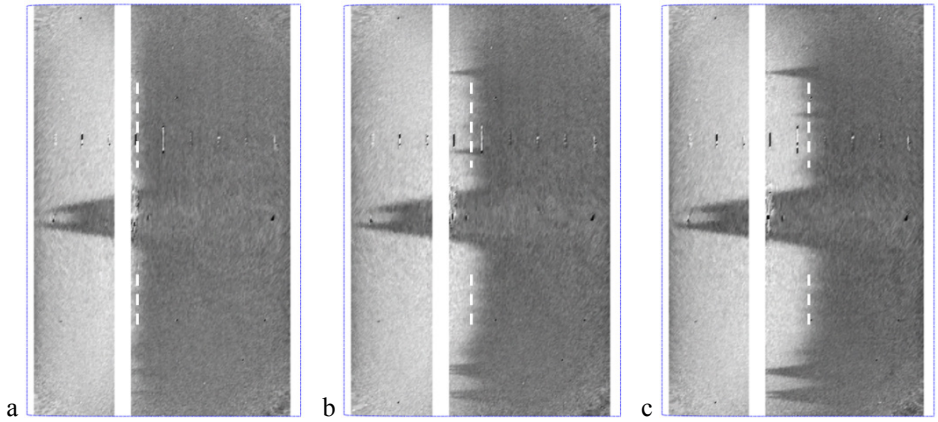

Fig. 5.2.3.2. TSP results for different different streamwise pressure gradients. M = 0.77, Re = 6 · 10^6, and standard T_w/T_{aw}. Step-2 configuration. a: $\underline{\beta_H = 0.036}$, T_w/T_{aw} = 1.049, $h/\delta_{1,h}$ = 0.62, x_T/c = 40 ±0.5 %; b: $\underline{\beta_H = 0.051}$, T_w/T_{aw} = 1.051, $h/\delta_{1,h}$ = 0.63, x_T/c = 47 ±0.2 %; c: $\underline{\beta_H = 0.063}$, T_w/T_{aw} = 1.054, $h/\delta_{1,h}$ = 0.65, x_T/c = 54 ±0.4 %.

As can be seen in Fig. 5.2.3.1b, larger flow acceleration does not lead to appreciable differences in the local surface pressure variation induced by the step. Similarly to the results obtained with the smooth configuration, a larger Hartree parameter has a favorable effect on boundary-layer transition: the laminar run length was increased, as shown in Fig. 5.2.3.2. The shift in transition location, however, is not as pronounced as for the smooth configuration at the same test conditions: $\Delta(x_T/c) = 14$ %, compared with $\Delta(x_{T,0}/c) = 25$ %. The

streamwise extent of the transition region ($x_{T,end} - x_{T,start}$) also increases at larger Hartree parameter: this is shown in Fig. 5.2.3.3, where the streamwise intensity distributions at $y/b = 0.63$ are presented.

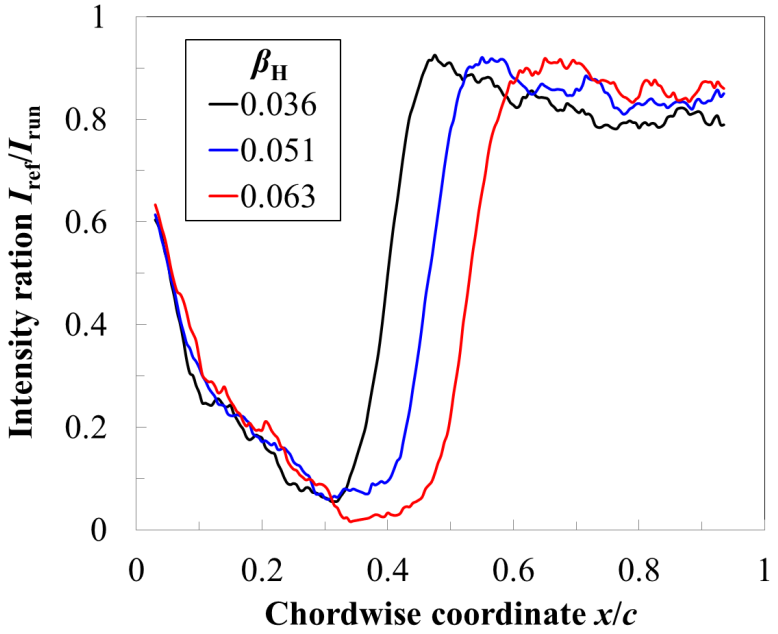

Fig. 5.2.3.3. Normalized intensity distributions at $y/b = 0.63$ for the cases of Fig. 5.2.3.2. β_H: a) 0.036, b) 0.051, c) 0.063.

The results with the step-2 configuration at M = 0.77 and standard T_w/T_{aw} are presented in Fig. 5.2.3.4, where Re_{xT} is plotted as a function of β_H. For comparison, the results obtained with the smooth configuration at the same test conditions (see data points at M = 0.77 in Fig. 5.1.2.5) are also shown (black circles). As discussed in Section 5.2.2, the transition Reynolds number obtained at a given pressure gradient is essentially independent of the chord Reynolds number. The beneficial effect of flow acceleration on boundary-layer transition is apparent, even for the step-2 configuration. The increase in transition Reynolds number for a given increase in Hartree parameter is, however, smaller in the presence of the steps. For example, Re_{xT} at the largest Hartree parameter is about 3.1 times the value at $\beta_H \sim 0$, whereas the increase with the smooth configuration is about 4.5 times. Note also that the reduction in Re_{xT} due to the effect of the steps is larger at larger Hartree parameters.

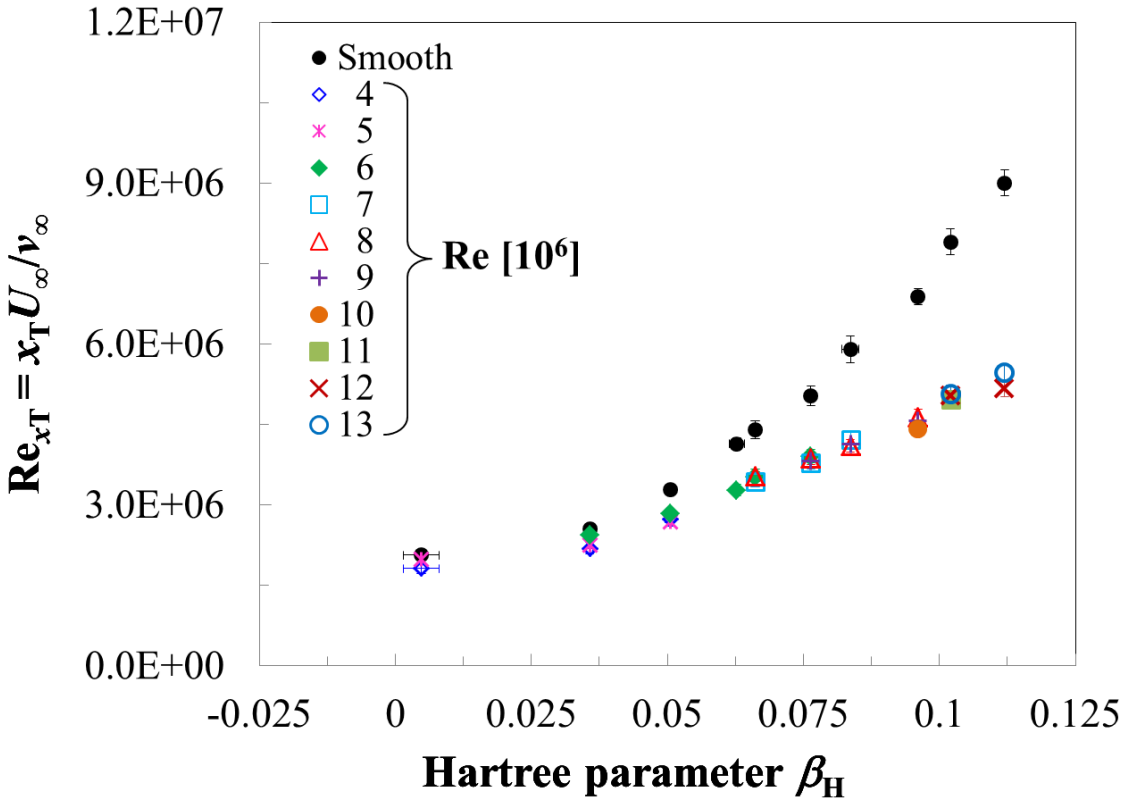

Fig. 5.2.3.4. Transition Reynolds number as a function of the Hartree parameter at M = 0.77 and standard wall temperature ratio. Smooth configuration (black circles) and step-2 configuration (colored symbols).

5.2.4 Effect of the wall temperature ratio

The influence of the wall temperature ratio on boundary-layer transition is presented in this section for two cases examined at M = 0.77 with the step-2 configuration. The first case is with $\beta_H = 0.076$ and $\mathrm{Re} = 6 \cdot 10^6$. The wall temperature ratio was reduced from $T_w/T_{aw} = 1.047$ to 1.008. The surface pressure distributions and the TSP results are presented in Fig. 5.2.4.1 and Fig. 5.2.4.2, respectively. The surface pressure distributions obtained at different wall temperature ratios are in agreement (see Fig. 5.2.4.1). As can be seen in Fig. 5.2.4.2, the effect of the reduction of T_w/T_{aw} is to delay transition. Since the surface pressure distributions are almost unchanged, the movement of the transition location is only due to the stabilizing effect of the wall temperature ratio. Note that the reduction of T_w/T_{aw} has a favorable effect on boundary-layer transition, even though the relative step height $h/\delta_{1,h}$ has slightly increased. (The variation in $h/\delta_{1,h}$ is however small: $\Delta(h/\delta_{1,h}) = 0.02$.) The increase in transition Reynolds number is less marked than that obtained with the smooth configuration (at the same conditions and for approximately the same reduction in T_w/T_{aw}): approximately $\Delta\mathrm{Re}_{xT} \sim 0.5 \cdot 10^6$ for the former as compared to approximately $\Delta\mathrm{Re}_{xT} \sim 0.9 \cdot 10^6$ for the latter. In Fig. 5.2.4.2 it can be seen that the number of turbulent wedges is larger with the lower wall temperature ratio: this aspect is discussed in Appendix C.2.1. In spite of this, natural transition can

still be measured in some regions, where enough space is available in the spanwise direction between turbulent wedges.

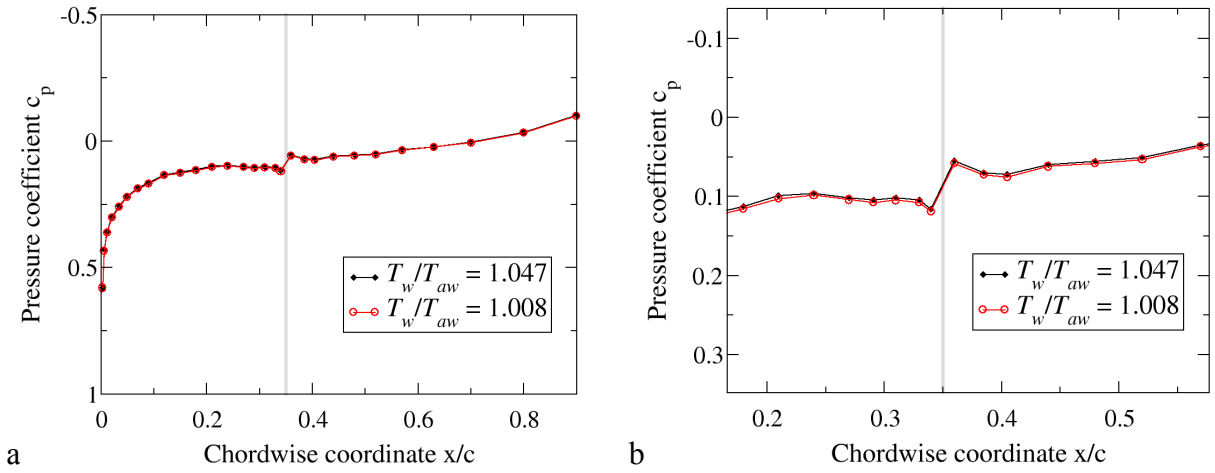

Fig. 5.2.4.1. Surface pressure distributions for different wall temperature ratios. M = 0.77, Re = 6 · 10^6, and β_H = 0.076. Step-2 configuration ($0.66 \leq h/\delta_{1,h} \leq 0.68$). a: over the whole chord length; b: zoomed-in around the step location. The gray bar indicates the step location.

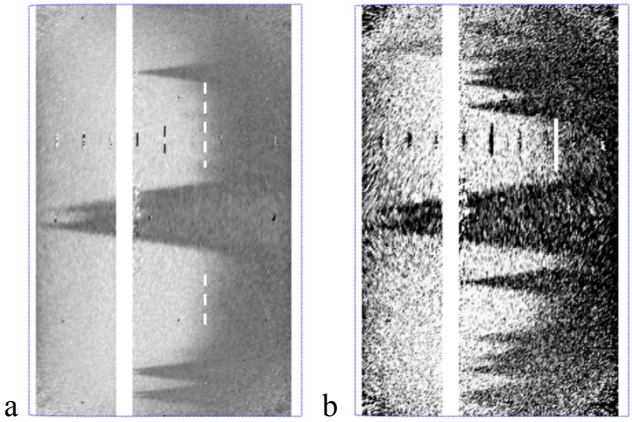

Fig. 5.2.4.2. TSP results for different wall temperature ratios. M = 0.77, Re = 6 · 10^6, and β_H = 0.076. Step-2 configuration. a: T_w/T_{aw} = 1.047, $h/\delta_{1,h}$ = 0.66, x_T/c = 65 ±1.2 %; b: T_w/T_{aw} = 1.008, $h/\delta_{1,h}$ = 0.68, x_T/c = 72 ±2.7 %.

The effect of a non-adiabatic surface for the step-2 configuration is now examined for a case at M = 0.77, Re = 10 · 10^6, and β_H = 0.096. As can be seen in Fig. 5.2.4.3, the surface pressure distributions are in agreement also in this case. The TSP results are shown in Fig. 5.2.4.4. Transition was measured at approximately the same location with both wall temperature ratios. In this case, a change in the wall temperature ratio has no appreciable effect on boundary-layer transition in the presence of forward-facing steps (at least for the examined change of T_w/T_{aw}).

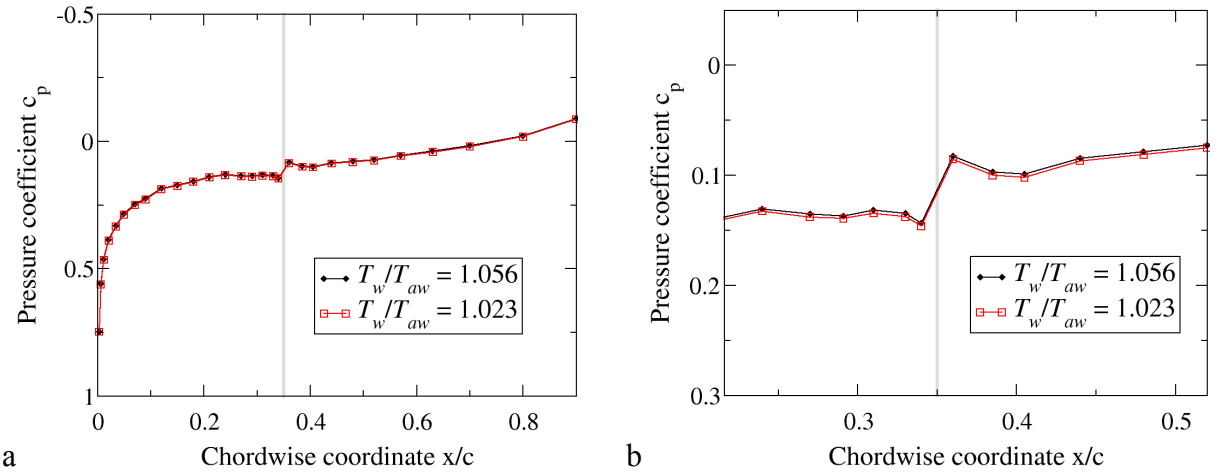

Fig. 5.2.4.3. Surface pressure distributions for different wall temperature ratios. M = 0.77, Re = 10 · 10^6, and β_H = 0.096. Step-2 configuration ($0.88 \leq h/\delta_{1,h} \leq 0.92$). a: over the whole chord length; b: zoomed-in around the step location. The gray bar indicates the step location.

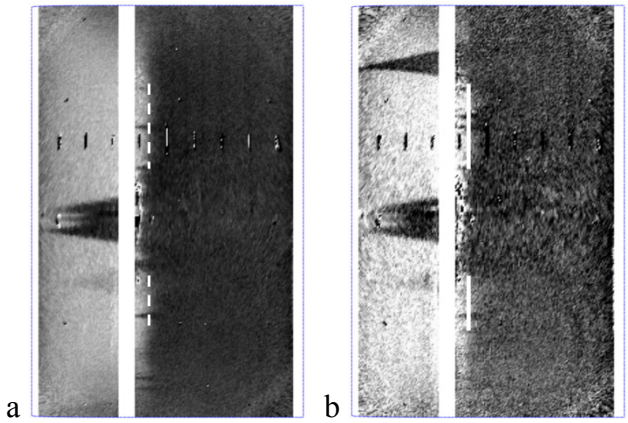

Fig. 5.2.4.4. TSP results for different wall temperature ratios. M = 0.77, Re = 10 · 10^6, and β_H = 0.096. Step-2 configuration. a: T_w/T_{aw} = 1.056, $h/\delta_{1,h}$ = 0.88, x_T/c = 44 ±0.5 %; b: T_w/T_{aw} = 1.023, $h/\delta_{1,h}$ = 0.92, x_T/c = 44 ±0.9 %.

The results obtained with the step-2 configuration at M = 0.77 and both standard and reduced T_w/T_{aw} are presented in Fig. 5.2.4.5, where the transition Reynolds number Re_{xT} is plotted as a function of the pressure gradient β_H. The results obtained at larger wall temperature ratio (standard T_w/T_{aw}) are shown by black open squares: these values correspond to the average of Re_{xT} obtained at each Hartree parameter (colored symbols in Fig. 5.2.3.4). The red symbols correspond to the results at reduced T_w/T_{aw}.

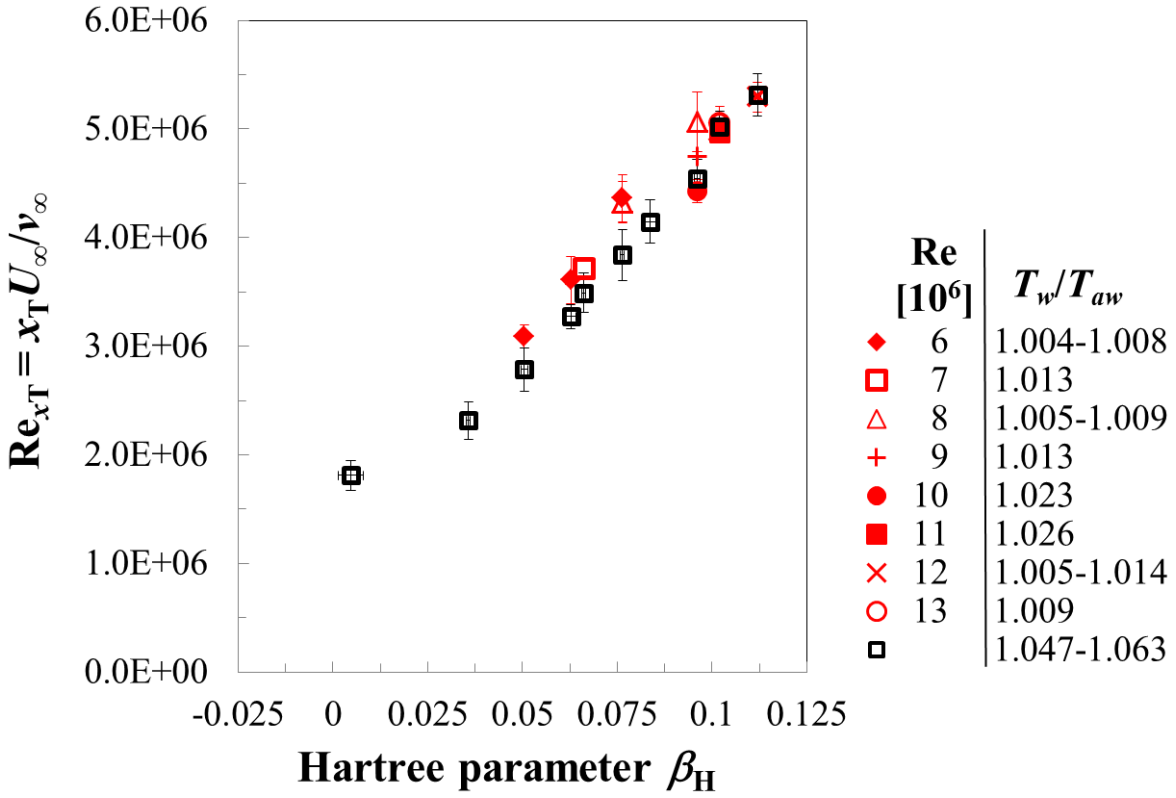

Fig. 5.2.4.5. Transition Reynolds number as a function of the Hartree parameter at standard T_w/T_{aw} (black open squares) and reduced T_w/T_{aw} (red symbols). Step-2 configuration.

The favorable influence of stronger flow acceleration on boundary-layer transition is confirmed also for the results obtained at reduced T_w/T_{aw}. For $0.051 \leq \beta_H \leq 0.076$, a reduction in the wall temperature ratio leads to larger transition Reynolds numbers; this increase is more pronounced at larger Hartree parameters. In contrast, at the largest Hartree parameters $\beta_H = 0.102$ and 0.112, no change in the transition Reynolds number was found for different thermal conditions on the model surface. At $\beta_H = 0.096$, at least one result at reduced T_w/T_{aw} showed a clear increase of the transition Reynolds number, whereas the other data are close to the data point for standard T_w/T_{aw}. The results obtained at this pressure gradient show a different behavior of boundary-layer transition under the influence of the wall temperature ratio. This topic will be discussed in Section 6.5.

5.2.5 Effect of the Mach number

The effect of the freestream Mach number on boundary-layer transition is shown for the test conditions of the case considered in Section 5.1.1 (i.e., at $\mathrm{Re} = 6 \cdot 10^6$, Hartree parameters in the range $0.032 \leq \beta_H \leq 0.036$, and standard T_w/T_{aw}), but this time with the step-2 configuration. The TSP results are presented in Fig. 5.2.5.1.

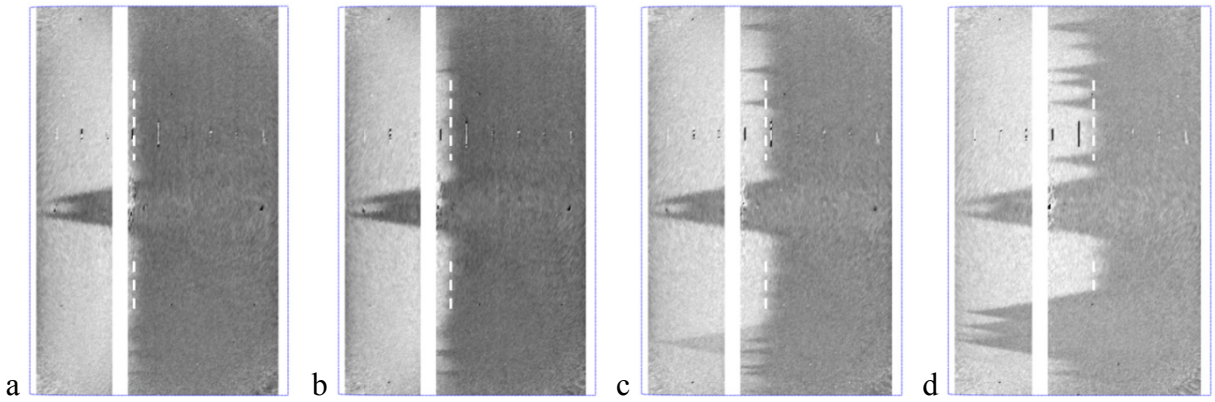

Fig. 5.2.5.1. TSP results for different Mach numbers at $\mathrm{Re} = 6 \cdot 10^6$ and $0.032 \leq \beta_H \leq 0.036$. Step-2 configuration. a: M = 0.77, $\beta_H = 0.036$, $T_w/T_{aw} = 1.049$, $h/\delta_{1,h} = 0.62$, $x_T/c = 40 \pm 0.5$ %; b: M = 0.65, $\beta_H = 0.034$, $T_w/T_{aw} = 1.051$, $h/\delta_{1,h} = 0.65$, $x_T/c = 44 \pm 0.4$ %; c: M = 0.5, $\beta_H = 0.032$, $T_w/T_{aw} = 1.036$, $h/\delta_{1,h} = 0.68$, $x_T/c = 49 \pm 0.4$ %; d: M = 0.35, $\beta_H = 0.033$, $T_w/T_{aw} = 1.028$, $h/\delta_{1,h} = 0.70$, $x_T/c = 56 \pm 1.2$ %.

Transition moved into a more downstream location as the Mach number was decreased from M = 0.77 to 0.35: the corresponding increase in transition Reynolds number is $\Delta \mathrm{Re}_{xT} \sim 1 \cdot 10^6$. Note also that the number of turbulent wedges in the TSP results is larger at lower Mach numbers, especially at M = 0.35. This is probably due to the thinner boundary layer at lower Mach numbers. The relative size (with respect to the boundary-layer thickness) and therefore the influence of three-dimensional roughness elements, such as particles adhering onto the surface, accordingly increases, so that they are more likely to trigger premature transition [238,239].

The chordwise intensity distributions at the spanwise section $y/b = 0.63$ for the cases of Fig. 5.2.5.1 are shown in Fig. 5.2.5.2. Similar to the cases with the smooth configuration (Fig. 5.1.1.3), the ratio $x_{T,start}/x_{T,end}$ in the presence of a forward-facing step is nearly independent of the Mach number, in agreement with the observations of [121]. The ratio $x_{T,start}/x_{T,end}$ is slightly smaller than that for the smooth configuration: $x_{T,start}/x_{T,end} \sim 0.76\text{-}0.78$ as compared to $x_{T,start}/x_{T,end} \sim 0.78\text{-}0.81$.

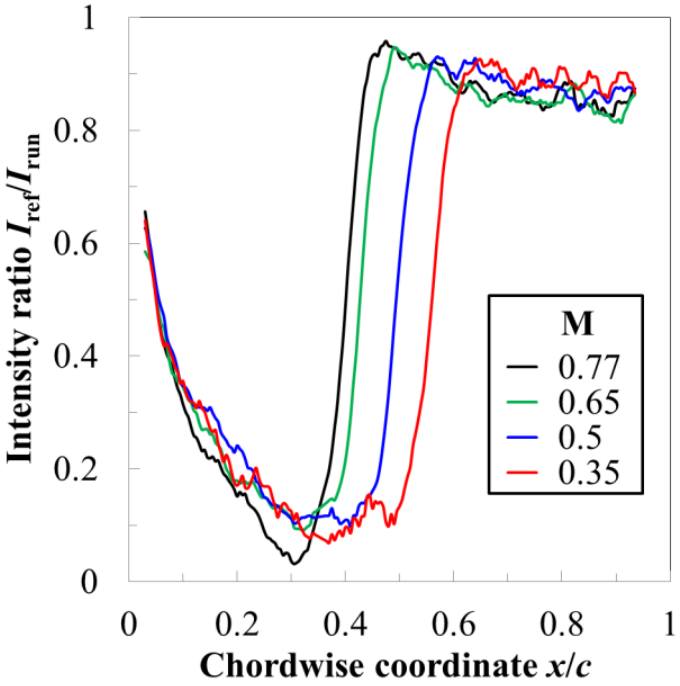

Fig. 5.2.5.2. Normalized intensity distributions at y/b = 0.63 for the cases of Fig. 5.2.5.1. M: a) 0.77, b) 0.65, c) 0.5, d) 0.35.

The surface pressure distributions for the cases of Fig. 5.2.5.1 are presented in Fig. 5.2.5.3. The change in the pressure distribution (Fig. 5.2.5.3a) over the whole chord length at different Mach numbers was small and comparable to that observed with the smooth configuration (see Fig. 5.1.1.1). However, there are some differences in the pressure gradients in the vicinity of the steps. These can be seen in Fig. 5.2.5.3b, where the surface pressure distributions for the Mach numbers M = 0.77 and 0.35 (black and red lines, respectively) are shown for the smooth and step-2 configurations (solid and dashed lines, respectively). Upstream of the step, the step-induced deviation from the undisturbed flow at M = 0.77 occurs approximately $\Delta(x/c) = 5$ % more upstream than that at M = 0.35; also downstream of the step, the smooth-configuration pressure distribution appears to be recovered more downstream at the larger Mach number. Moreover, the local adverse pressure gradients are strengthened by the larger Mach number: this effect is shown in Fig. 5.2.5.3b by the larger deviation in pressure coefficient in the regions immediately upstream and downstream of the step location. It should be emphasized here that larger deviations in the local $c_p(x)$ are observed at larger Mach numbers, although the relative step height decreases: for the case of Fig. 5.2.5.3, $h/\delta_{1,h}$ is approximately 0.70 at M = 0.35, as compared to $h/\delta_{1,h} \sim 0.62$ at M = 0.77. The larger step-induced changes in surface pressure distributions at larger Mach numbers are in agreement with the results of previous numerical work on smooth bumps [31,165-166,240] and smooth backward-facing steps [241]. Those imperfections induced flow separation. An increase of the Mach number up to M = 0.8 was clearly shown to enhance flow separation and shift the reattachment location considerably downstream, thus leading to an increase in wall-normal and streamwise extent of

the separation bubble. For the case of sharp forward-facing steps in a flow at zero pressure gradient, results from DNS are available for a step with given Re_{xh}, Re_h, and h/θ_h, examined at two subsonic Mach numbers: M = 0.15 and 0.8 [45]. The change in the pressure distribution around the step location between M = 0.15 and 0.8 is not shown in [45]; nevertheless, in the presence of a step with $h/\theta_h \sim 2.4$ and approximately the same step Reynolds number $\mathrm{Re}_h \sim 2600$, the streamwise extent of the separation bubbles upstream and downstream of the step edge was found to remain almost constant as the Mach number was increased.

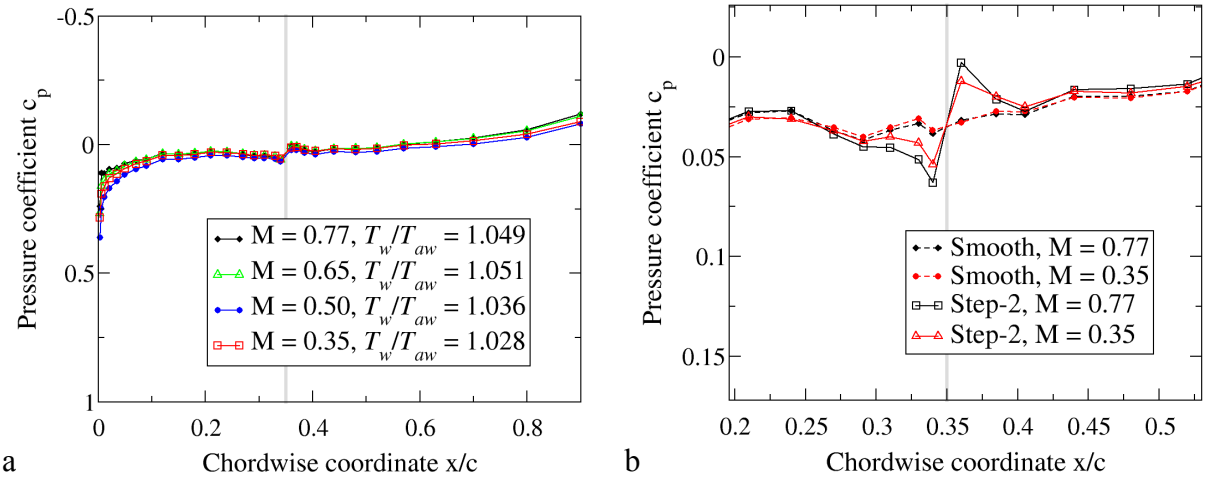

Fig. 5.2.5.3. a: surface pressure distributions for different Mach numbers. Re = 6 · 10^6, $0.032 \le \beta_H \le 0.036$, and standard T_w/T_{aw}. Step-2 configuration ($0.62 \le h/\delta_{1,h} \le 0.70$). b: comparison of the surface pressure distributions with those on the smooth configuration (M = 0.77 and M = 0.35 only), zoomed-in around the step location. The gray bar indicates the step location.

The considerations on the decrease of Re_{xT} at larger Mach number, discussed in Section 5.1.1, hold also for the step configurations and will therefore not be repeated here. It should be noted, however, that the reduction in Re_{xT} at larger Mach numbers is less pronounced than that observed with the smooth configuration: the difference in transition Reynolds number obtained at M = 0.77 and 0.35 is $\Delta\mathrm{Re}_{xT} \sim 0.9 \cdot 10^6$, as compared to $\Delta\mathrm{Re}_{xT} \sim 1.6 \cdot 10^6$ with the smooth configuration. The results obtained with the step-2 configuration at the four different Mach numbers are collected in Fig. 5.2.5.4, where the transition Reynolds number is shown as a function of the Hartree parameter. Different colors are used for the results obtained at different Mach numbers. Each data point corresponds to the average transition Reynolds number at a certain Mach number and Hartree parameter. The four sets of data are approximated by 2nd order polynomial functions, shown by dotted lines. A glance at Fig. 5.2.5.4 shows that larger transition Reynolds numbers are obtained at lower Mach numbers, but these differences are smaller than those found with the smooth configuration (see Fig. 5.1.2.5). It should be also remarked here that the wall temperature ratio was larger at larger Mach numbers; this contributed to the

difference in transition Reynolds number obtained at different Mach numbers, at least for the cases where boundary-layer transition was sensitive to changes in T_w/T_{aw} (see Section 5.2.4). Note that the difference between the values of $\mathrm{Re}_{x\mathrm{T}}$ obtained at M = 0.77, 0.65, and 0.5 progressively decreases as the Hartree parameter is increased, until it essentially vanishes at $\beta_\mathrm{H} \geq 0.1$.

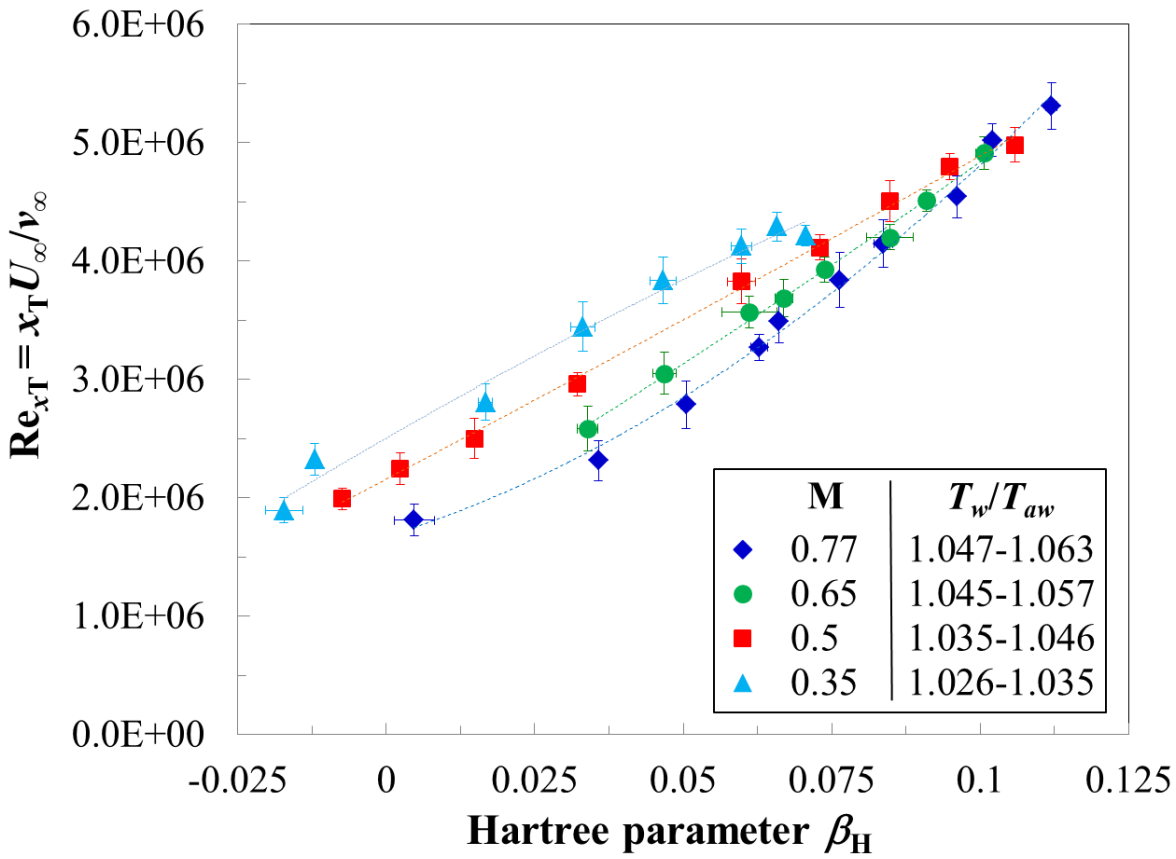

Fig. 5.2.5.4. Transition Reynolds number as a function of the Hartree parameter at standard T_w/T_{aw} for different Mach numbers. Step-2 configuration.

6 Discussion of the results

The experimental results will be analyzed in this chapter. Sections 6.1 to 6.4 consider the results obtained at standard wall temperature ratio. The discussion will initially focus on the largest Mach number M = 0.77. The effect of chord Reynolds number and streamwise pressure gradient in the presence of forward-facing steps is examined in Sections 6.1 and 6.2, respectively. The influence of the Mach number is analyzed in Section 6.3. The results achieved at standard wall temperature ratio are summarized and compared to available data from earlier work in Section 6.4. The influence on boundary-layer transition of the thermal condition at the model surface is discussed in Section 6.5.

Dimensional analysis will be used to examine the experimental data, following earlier approaches to determine the effect of roughness on boundary-layer transition in subsonic flows [242]. For a flat plate experiment, where are given: fluid stream, disturbance environment, pressure gradient, thermal condition at the model surface, and shape of the roughness, the transition location x_T is a function only of the roughness height h, the location of the roughness element x_h, the flow velocity u, and the fluid viscosity ν. These five variables involve only the units of length and time: dimensional analysis "tells us that the general functional relation between the five dimensional quantities can be reduced to a relation between three independent non-dimensional parameters" [242]. A possible choice of these parameters of physical meaning is: the transition Reynolds number Re_{xT}, the roughness Reynolds number $\mathrm{Re}_k = U_h h/\nu_h$, and the ratio x_T/x_h. U_h and ν_h are, respectively, the streamwise mean-velocity component and the kinematic viscosity, which would be found at $x = x_h$ and $z = h$ in the undisturbed laminar boundary layer (no roughness present). Instead of the roughness Reynolds number, the relative roughness height $h/\delta_{1,h} = h/\delta_1(x_h)$ can be also used as roughness parameter. Note that $h/\delta_{1,h}$ is a linear function of the roughness height h, whereas the dependence of Re_k is quadratic [242,243]. For simplicity, the step Reynolds number $\mathrm{Re}_h = h/c \cdot \mathrm{Re}$ has been also used as a characteristic roughness parameter, especially in the case of steps [34,38,50,172]. Although this parameter does not contain any information about the roughness location and the local boundary-layer state, Re_h is not necessarily worse than the other two parameters to characterize the effect of the roughness, since U_∞ and ν_∞ can be seen as mean values of the velocity and kinematic viscosity that are "felt" by the roughness [244]. Criteria based on Re_h are still used in industrial applications [172].

6.1 Combined effect of forward-facing steps and chord Reynolds number

The following analysis is carried out for fixed Mach number, streamwise pressure gradient, and thermal condition at the model surface. The simplest

manner to present the effect on boundary-layer transition of forward-facing steps and chord Reynolds number is to show the transition Reynolds number as a function of the step height. This is done in Fig. 6.1.1a for an accelerated flow with $\beta_H = 0.066$, $T_w/T_{aw} = 1.043\text{-}1.062$, and $M = 0.77$. Three chord Reynolds numbers were investigated: $Re = 6$, 7, and $8 \cdot 10^6$. The smooth configuration and the three step configurations were examined at the three Reynolds numbers, except for the step-3 configuration at $Re = 8 \cdot 10^6$. (The transition location was expected to be near the step at such test conditions.) The transition Reynolds number clearly decreases as the step height is increased: higher steps enhance amplification of disturbances within the laminar boundary layer and lead to earlier transition. The variation of Re_{xT} can be approximated by a linear function of the step height, shown in Fig. 6.1.1a by the dashed line. The transition Reynolds number is nearly independent of the chord Reynolds number. This result is confirmed here as a general finding of the present experiments, even with the step-3 configuration. It appears to be related to the increase in Re_{xh} with increasing chord Reynolds number. In order to study the effect of the chord Reynolds number on boundary-layer transition at fixed Re_{xh}, it would be necessary to design a wind-tunnel model with several locations for the installation of the steps; this would, however, increase model complexity and the risk of undesired imperfections at the step locations. Alternatively, various wind-tunnel models with the same cross-section but different step locations could be built, but this would obviously lead to increased experimental costs. For these reasons, this effect could not be investigated in the present work.

The ratio $Re_{xT}/Re_{xT,0}$ remains unchanged when the chord Reynolds number is varied. A representation of the results as $Re_{xT}/Re_{xT,0}$ vs. $h/\delta_{1,h}$ (or another non-dimensional step parameter) would therefore be misleading: it would seem that larger chord Reynolds numbers lead to stabilization of the boundary layer, since the same reduction in transition Reynolds number $Re_{xT}/Re_{xT,0}$ is obtained at a larger value of $h/\delta_{1,h}$. In order to "isolate" the effect of the increased Reynolds number, and hence of the related increase in $h/\delta_{1,h}$, the relative change in transition location with respect to the step location has to be analyzed. In fact, only the region downstream of the step is of interest, since a shift of the transition location due to the effect of the step is limited to this area. The relative change in transition location is defined as $s = (x_T\text{-}x_h)/(x_{T,0}\text{-}x_h)$. This ratio has been preferred to a ratio derived from the Reynolds numbers Re_{xT}, $Re_{xT,0}$, and Re_{xh}, because the difference is negligible and the transition locations (and the step location) are quantities that are known or have been measured directly. The same parameter was used in [38,48,50]. The relative change in transition location is plotted as a function of the relative step height in Fig. 6.1.1b for the same data points as in Fig. 6.1.1a. Besides the data points at $0.3 < h/\delta_{1,h} < 0.4$, this representation of the results shows that s decreases as $h/\delta_{1,h}$ increases, in line with the expectation of larger disturbance amplification due to the larger relative step height. The variation of s can be approximated by a linear function of the relative step height, shown in Fig. 6.1.1b by the dashed line. In the range

$0.3 < h/\delta_{1,h} < 0.4$, the data point for $\mathrm{Re} = 7 \cdot 10^6$ is above the approximation function because of the influence of the wall temperature ratio: x_T was measured at a value of the wall temperature ratio lower than that in the corresponding measurements at Re = 6 and $8 \cdot 10^6$. This effect will be discussed in Section 6.5.

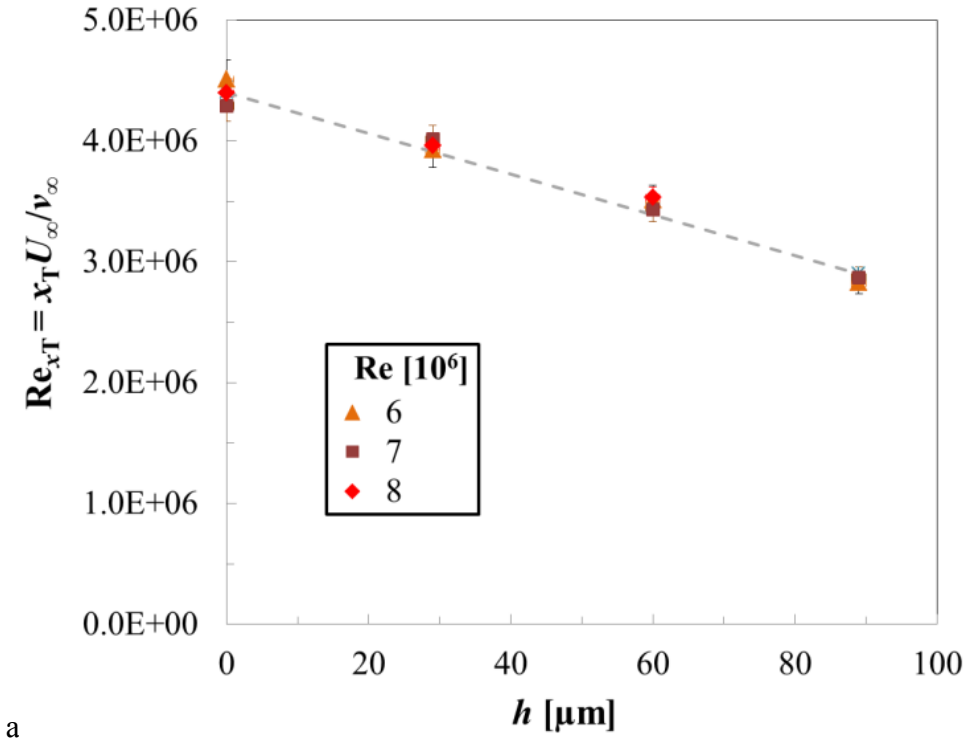

a

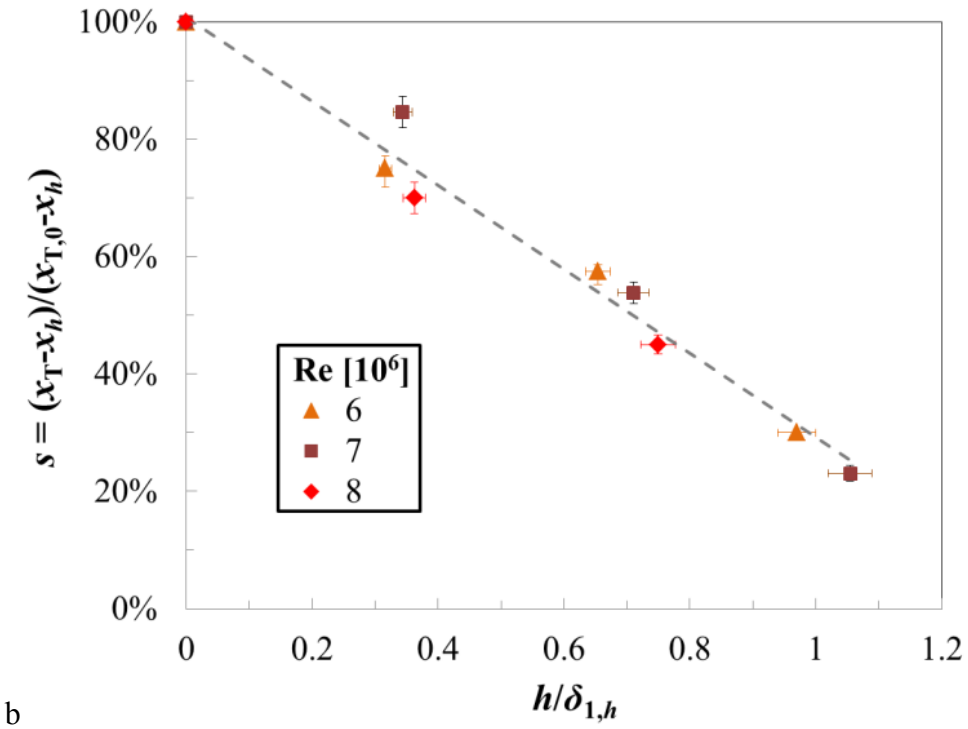

b

Fig. 6.1.1. a: transition Reynolds number as a function of the step height. b: relative change in transition location as a function of the relative step height. M = 0.77, β_H = 0.066, and T_w/T_{aw} = 1.043-1.062.

6.2 Combined effect of forward-facing steps and streamwise pressure gradient

The effect of the streamwise pressure gradient in the presence of forward-facing steps at $M = 0.77$ has been already discussed in [245]. The results are summarized in this section. Details are given in Appendix E.2.

6.2.1 Sensitivity of boundary-layer transition to the effect of forward-facing steps at different pressure gradients

The results obtained with the various configurations at $M = 0.77$ and $Re = 6 \cdot 10^6$ are summarized in Fig. 6.2.1.1a, where the transition Reynolds number is plotted as a function of the step Reynolds number Re_h. Symbols with different colors are used for different streamwise pressure gradients. Linear functions, approximating the results obtained at the same β_H, are shown by dotted lines. At fixed streamwise pressure gradient, the effect of a larger Re_h is clearly to decrease the transition Reynolds number. Two further trends can be seen in Fig. 6.2.1.1a. First, the transition Reynolds number increases at larger Hartree parameters: at fixed step Reynolds number, Re_{xT} increases as the Hartree parameter increases. Secondly, the slope of the linear fits increases as β_H increases. Boundary-layer transition becomes more sensitive to the destabilizing effect of the forward-facing step as the streamwise pressure gradient is increased: this leads to larger variations in Re_{xT} at larger β_H for the same change in step Reynolds number. The change in sensitivity is illustrated at $Re = 6 \cdot 10^6$ and standard wall temperature ratio for two streamwise pressure gradients: $\beta_H = 0.036$ and 0.063. The ratio of transition Reynolds numbers $Re_{xT}/Re_{xT,0}$ is plotted in Fig. 6.2.1.1b as a function of $h/\delta_{1,h}$. (The corresponding TSP results are shown in Appendix E.2.1.) Second order polynomial functions, approximating the data sets for the different pressure gradients, are shown by dashed lines. As can be seen from this figure, not only the absolute variation of transition Reynolds number (ΔRe_{xT}) due to the effect of the step is larger at a more pronounced pressure gradient (see Fig. 6.2.1.1a), but also the variation in $Re_{xT}/Re_{xT,0}$.

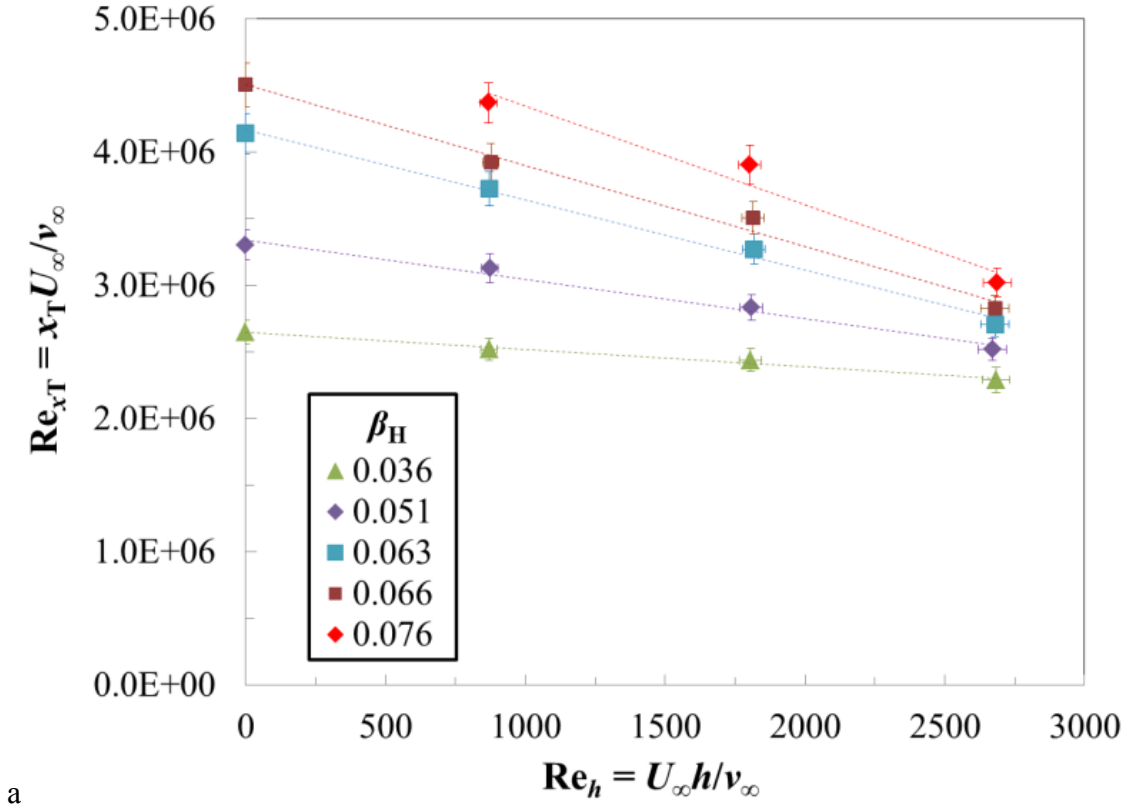

a

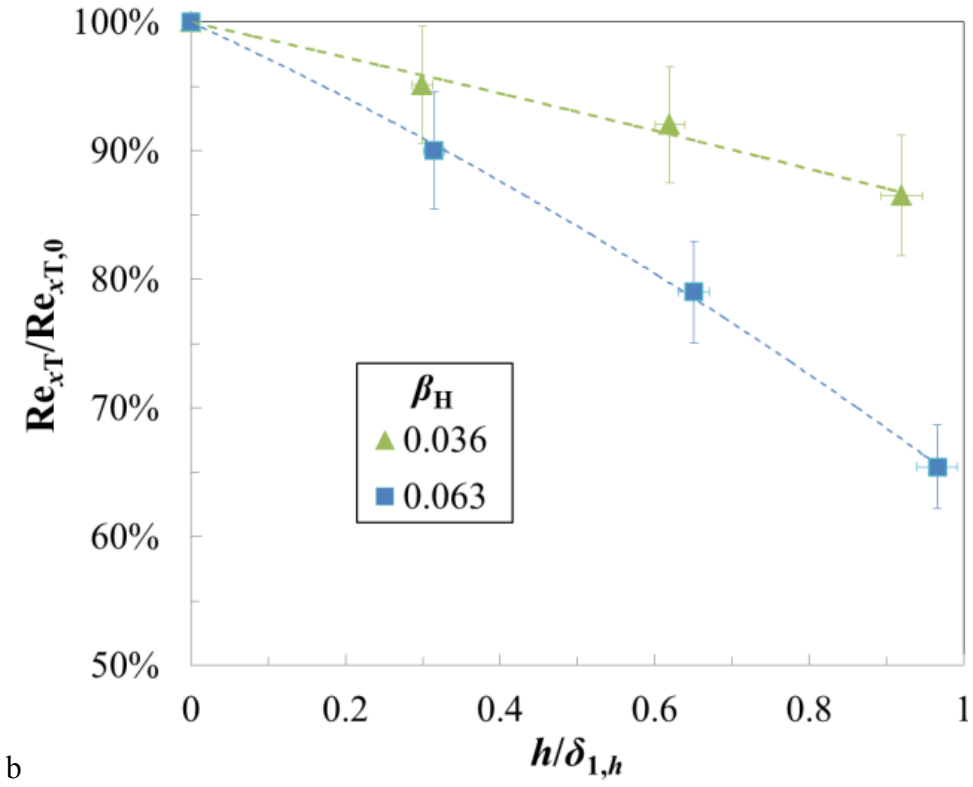

b

Fig. 6.2.1.1. a: transition Reynolds number as a function of the step Reynolds number Re_h at M = 0.77, Re = 6 · 10^6, and T_w/T_{aw} = 1.043-1.060. b: variation of the ratio $Re_{xT}/Re_{xT,0}$ as a function of the relative step height $h/\delta_{1,h}$ for the two cases at β_H = 0.036 and β_H = 0.063.

This difference in the sensitivity of boundary-layer transition can be explained (at least semi-quantitatively) using linear stability theory. The *N*-factors computed for the smooth configuration of the two cases considered in Fig. 6.2.1.1b are presented in Fig. 6.2.1.2; the envelope curve is shown by the thicker dark line, the transition location by a gray bar. The red dashed curves in Fig. 6.2.1.2 represent the *N*-factor envelope curves in the presence of forward-facing steps, which were modeled according to the following considerations. In previous numerical investigations on surface imperfections in a subsonic flow at zero pressure gradient [38,45-46], it had been shown that the most significant effect of a forward-facing step on boundary-layer stability is to cause a marked rise in the amplification factors of streamwise instabilities in the region around the step location. Downstream of the step, the *N*-factor envelope curve for a step configuration was seen to return to that corresponding to the smooth configuration [38,45-46]. The recovery of the smooth-configuration curve can occur, however, at a considerable distance from the step location. In the case of forward-facing steps placed at a short distance downstream of the Branch I location, the *N*-factor envelope curve for the step configuration was found to evolve almost parallel to the x-axis [38,45]. In contrast, when steps with the same h/θ_h were placed at a considerable distance from the Branch I location, the *N*-factor envelope curves for the step and smooth configurations were observed to be nearly parallel for a significant streamwise extent downstream of the step location [45,46]. In this region, the difference between the two curves (increment function) can be reasonably modeled as a uniform offset ΔN. This was the principle of the strategy pursued in [40-41,118], where the transition locations x_T and $x_{T,0}$ were measured with and without steps, respectively, and the uniform offset was evaluated as $\Delta N = N(x_{T,0}) - N(x_T) = N_{T,0} - N_T$; $N(x)$ is the *N*-factor envelope curve obtained for the smooth configuration. The value of ΔN was then determined as a function of the relative step height. The increment function is not well modeled by a uniform value in the regions immediately downstream and far away downstream of the step; nevertheless, the correlation from [41] was shown to provide a value of ΔN comparable to that predicted by DNS, this being observed for a notable distance downstream of the step location [45,46]. A semi-empirical method was developed to predict transition in the presence of steps [38,40-41,50,172], based on the e^N method and on the following assumptions: only convective instabilities have to be taken into account; only instabilities already excited upstream of the steps (viscous instabilities) undergo marked amplification due to the effect of the steps; and the value of transition *N*-factor remains the same also in the presence of the steps. In this numerical approach, linear stability computations are first performed for the smooth surface. The increment function $\Delta N(x)$, accounting for the amplification in the step region, is then added to the *N*-factor envelope curve obtained for the smooth configuration. The modified *N*-factor envelope curve is used for transition prediction, assuming that transition occurs when the threshold *N*-factor N_T is reached. The *N*-factor envelope curves for the step-2 configuration in Fig. 6.2.1.2

were determined using this procedure. The increment was assumed as a uniform offset ΔN, similarly to [40,41].

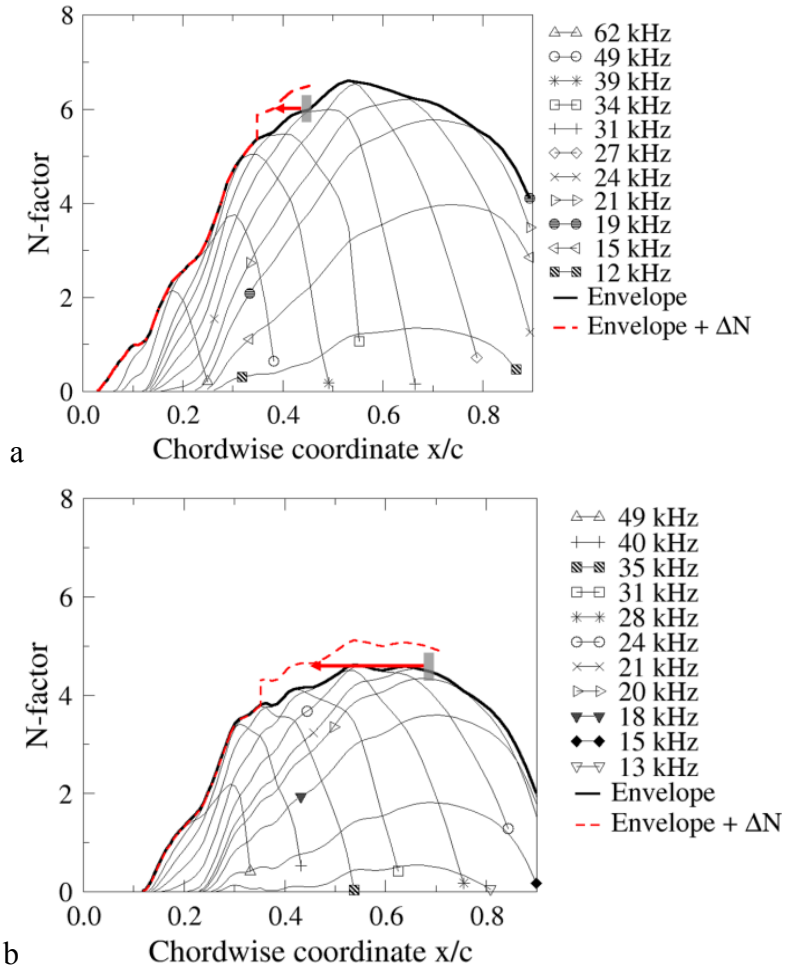

Fig. 6.2.1.2. Stability analysis results for the cases of Fig. 6.2.1.1b (smooth configurations). a: $\beta_H = 0.036$; b: $\beta_H = 0.063$. Dashed red curves: *N*-factor envelope curves accounting for the step-induced disturbance, which is modeled as a uniform increment ΔN. The (semi-quantitatively) predicted transition movement, due to the step disturbance, is shown by a red arrow.

The actual value of ΔN used for obtaining the dashed red curves in Fig. 6.2.1.2 is not of great importance, since all this serves here only for illustrative purposes. The same value of ΔN is, however, assumed for both examined pressure gradients. Values of ΔN determined from the present experimental data will be presented in Section 6.4.2. In the case with $\beta_H = 0.036$, shown in Fig. 6.2.1.2a, transition occurs on a region where the *N*-factor envelope curve has a positive gradient, whereas with the larger Hartree parameter $\beta_H = 0.063$ (Fig. 6.2.1.2b) the slope of the curve at the transition location is almost zero. In the latter boundary-layer stability situation, transition is more sensitive to the effect of a forward-facing step, as compared to the former case with less pronounced flow acceleration. As shown in Fig. 6.2.1.2, the movement of the transition location – predicted using the modified *N*-factor envelope curve according to the aforementioned procedure – is more pronounced for the case where

$\partial N_{T,0}/\partial(x/c) \sim 0$ ($\beta_H = 0.063$) than that for $\partial N_{T,0}/\partial(x/c) > 0$ ($\beta_H = 0.036$). This is in agreement with the behavior observed in the present experiment. It should be remarked here that, even if the N-factor envelope curve for the step configuration was not to evolve parallel to that of the smooth configuration downstream of the step location [38,45], it would still be expected to be influenced by the global pressure gradient. Thus, the conclusion regarding the different transition sensitivities in the presence of forward-facing steps at different pressure gradients would be the same.

In Fig. 6.2.1.1b, the ratio of transition Reynolds numbers $Re_{xT}/Re_{xT,0}$ has been shown to depend on relative step height and streamwise pressure gradient. As discussed in Section 6.1, the effect of the forward-facing steps on boundary-layer transition can be "isolated" by examining the relative change in transition location with respect to the step location. This is done in Fig. 6.2.1.3, where $s = (x_T\text{-}x_h)/(x_{T,0}\text{-}x_h)$ is plotted as a function of $h/\delta_{1,h}$ for the cases of Fig. 6.2.1.1b. A glance at Fig. 6.2.1.3 shows that this representation of the results gives a good correlation. The values of s obtained at different pressure gradients, but at nearly the same value of relative step height, are in agreement, so that the curves approximating the single data sets are essentially coincident. Note that $h/\delta_{1,h}$ is slightly larger when flow acceleration is more pronounced, and the corresponding value of s is slightly smaller.

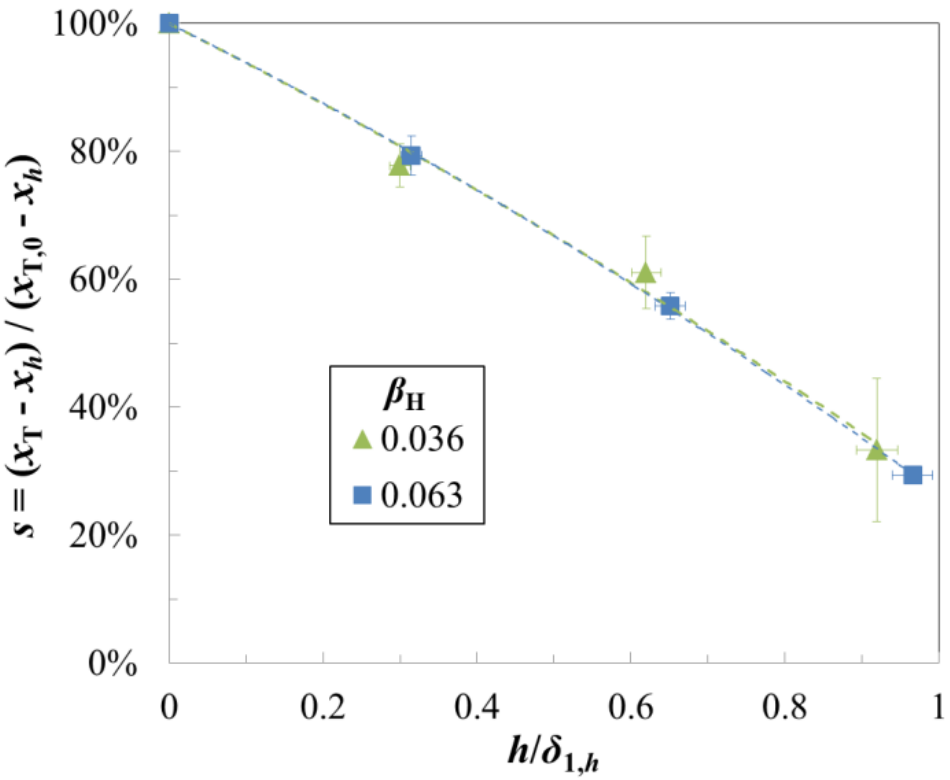

Fig. 6.2.1.3. Relative change in transition location as a function of the relative step height for the cases of Fig. 6.2.1.1b.

6.2.2 Summary and discussion of the results obtained at M = 0.77 and standard wall temperature ratio

In this section, the results obtained at M = 0.77 and standard wall temperature ratio (T_w/T_{aw} = 1.043-1.064) are grouped into single plots. The transition Reynolds number is plotted as a function of the Hartree parameter in Fig. 6.2.2.1. Different colors are used for different configurations, and different symbols are used for the results obtained at different chord Reynolds numbers. The fitted curves are 2nd order polynomial functions that approximate the data sets for the different configurations. As discussed in Sections 5.2.2 and 6.1, the transition Reynolds number is essentially independent of the chord Reynolds number. At a fixed streamwise pressure gradient, higher steps lead to a reduction of the transition Reynolds number. The transition Reynolds numbers Re_{xT} obtained with different configurations are quite similar at low Hartree parameters (e.g., at $\beta_H = 0.036$), whereas their values diverge more and more at the larger Hartree parameters (e.g., at $\beta_H = 0.096$). This behavior is related to the increased sensitivity of boundary-layer transition to forward-facing steps when the streamwise pressure gradient is more pronounced, as discussed in Section 6.2.1. Larger Hartree parameters are confirmed to have a favorable influence on boundary-layer stability and transition, even with the step-3 configuration; this favorable influence becomes, however, less marked as the step height increases, leading to smaller increases in Re_{xT} at larger step heights for the same change in β_H.

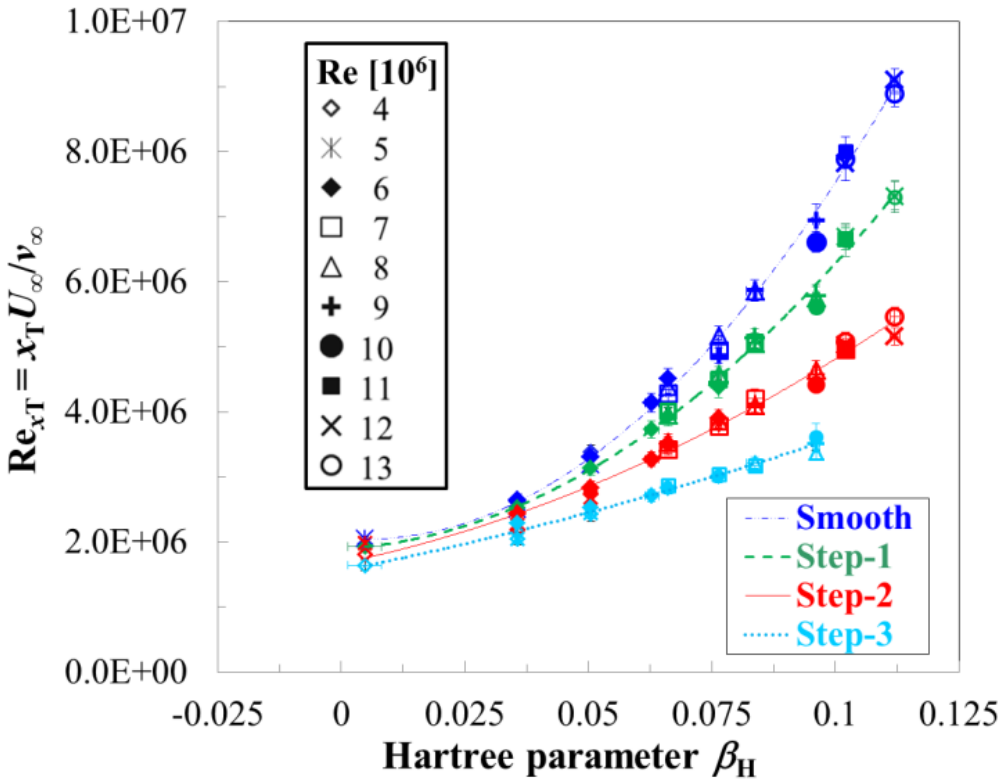

Fig. 6.2.2.1. Transition Reynolds number as a function of the Hartree parameter at M = 0.77. T_w/T_{aw} = 1.043-1.064.

The lessening of the favorable influence of the streamwise pressure gradient on boundary-layer transition is due to the amplification of streamwise instabilities around the step location. As discussed in earlier work for cylindrical wires [244,246], the effect of the roughness is of a local nature: the local pressure gradients generated by the step are much larger than the global pressure gradient [244], so that the step-induced amplification is independent of the global pressure gradient (at least to a first approximation). The reduction in growth rates due to a larger Hartree parameter is distributed over the whole amplification region. In contrast, the step-induced amplification is localized in the region around the step location. The overall amplification of the disturbances can be described (semi-quantitatively) as the sum of step-induced and step-independent amplifications. The relative contribution of the step-induced amplification increases as Re_h, $h/\delta_{1,h}$, and Re_k increase; the relative contribution of the step-independent amplification accordingly decreases. Since it is this step-independent amplification that is modulated by the pressure gradient, a decrease of the growth rates due to a certain increase in β_H leads to smaller displacements of the location where the threshold disturbance amplitude is reached, as compared to the displacement at lower values of Re_h, $h/\delta_{1,h}$, and Re_k. (The critical disturbance amplitude is assumed to remain the same). Therefore, also the displacements of the transition location are smaller.

These considerations are expected to hold also for surface heat flux and surface mass transfer, since they act on the mean-velocity profile in a manner similar to that of the pressure gradient (see Section 2.3). In [183], wall suction was demonstrated to be a means of preventing boundary-layer transition in the presence of backward-facing steps. However, the minimal suction rates required to maintain laminar flow at the measurement station (located at $\Delta x = 133\,h$ downstream of the step location) were shown to markedly increase at larger step Reynolds numbers. This result is in line with the current observations on the effect of the pressure gradient on boundary-layer transition in the presence of forward-facing steps: a larger pressure gradient is required to achieve a certain transition Reynolds number when the step height is increased. For example, it can be seen in Fig. 6.2.2.1 that $\mathrm{Re}_{x\mathrm{T}} \sim 5 \cdot 10^6$ is at $\beta_\mathrm{H} = 0.076$ with the smooth configuration, whereas the same $\mathrm{Re}_{x\mathrm{T}}$ ($5 \cdot 10^6$) is at $\beta_\mathrm{H} = 0.102$ for the step-2 configuration.

The relative change in transition location $s = (x_\mathrm{T}\text{-}x_h)/(x_{\mathrm{T},0}\text{-}x_h)$ is used to examine the influence of forward-facing steps on boundary-layer transition. A change in a test parameter such as the pressure gradient influences the values of both x_T and $x_{\mathrm{T},0}$, and is thus accounted for in s. This, however, is not sufficient to isolate the effect of the step on boundary-layer transition: only the region over which the boundary layer develops, after it has undergone amplification in the step area, should be considered. This is done by examining the change of transition location with respect to the step location x_h. Note that $\mathrm{Re}_{x\mathrm{T}}$ or $\mathrm{Re}_{x\mathrm{T}}/\mathrm{Re}_{x\mathrm{T},0}$ were

used as characteristic parameters for transition in [242-243,246], where they were plotted against the relative roughness height $h/\delta_{1,h}$. The non-dimensional roughness location x_h/h was used to form limiting curves for the correlation [242,246]: the experimental data approached these curves as transition moved closer to the roughness location. With the present choice of s, the characteristic parameter for transition goes to zero as the transition location approaches the step location, without the need for any limiting curves for the correlation. The relative change in transition location s at M = 0.77 has been already presented as a function of the non-dimensional step parameters Re_h and $h/\delta_{1,h}$ in [245]. The former plot is shown in Fig. 6.2.2.2. The latter plot will not be shown here; instead, s is plotted as a function of the roughness Reynolds number Re_k in Fig. 6.2.2.3. Note that the x-axis in Fig. 6.2.2.3 has a logarithmic scale to highlight the results obtained at low values of roughness Reynolds number. Symbols with different colors are used for the data obtained with different Hartree parameters. Only a few representative error bars for the results are actually plotted in these figures. Functions fitted to the experimental data are shown by solid lines. A Gaussian function has the best fit to the data in Fig. 6.2.2.2, whereas a 4th order polynomial function is used in Fig. 6.2.2.3.

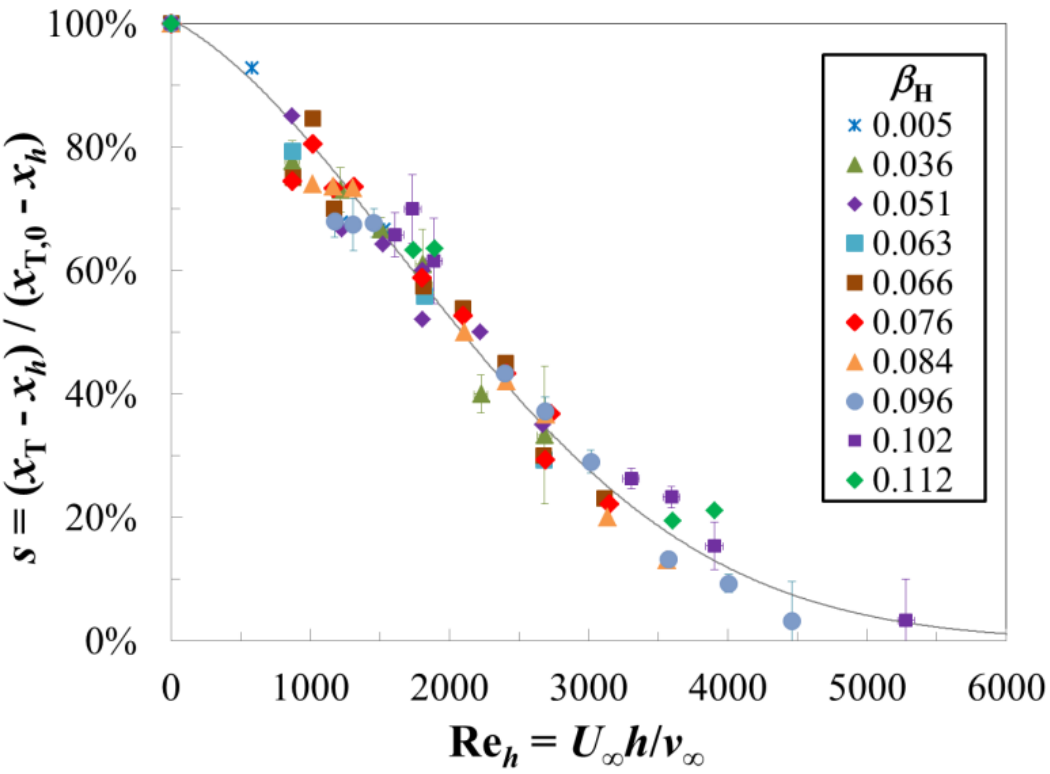

Fig. 6.2.2.2. Relative change in transition location s as a function of the step Reynolds number at M = 0.77 and T_w/T_{aw} = 1.043-1.064.

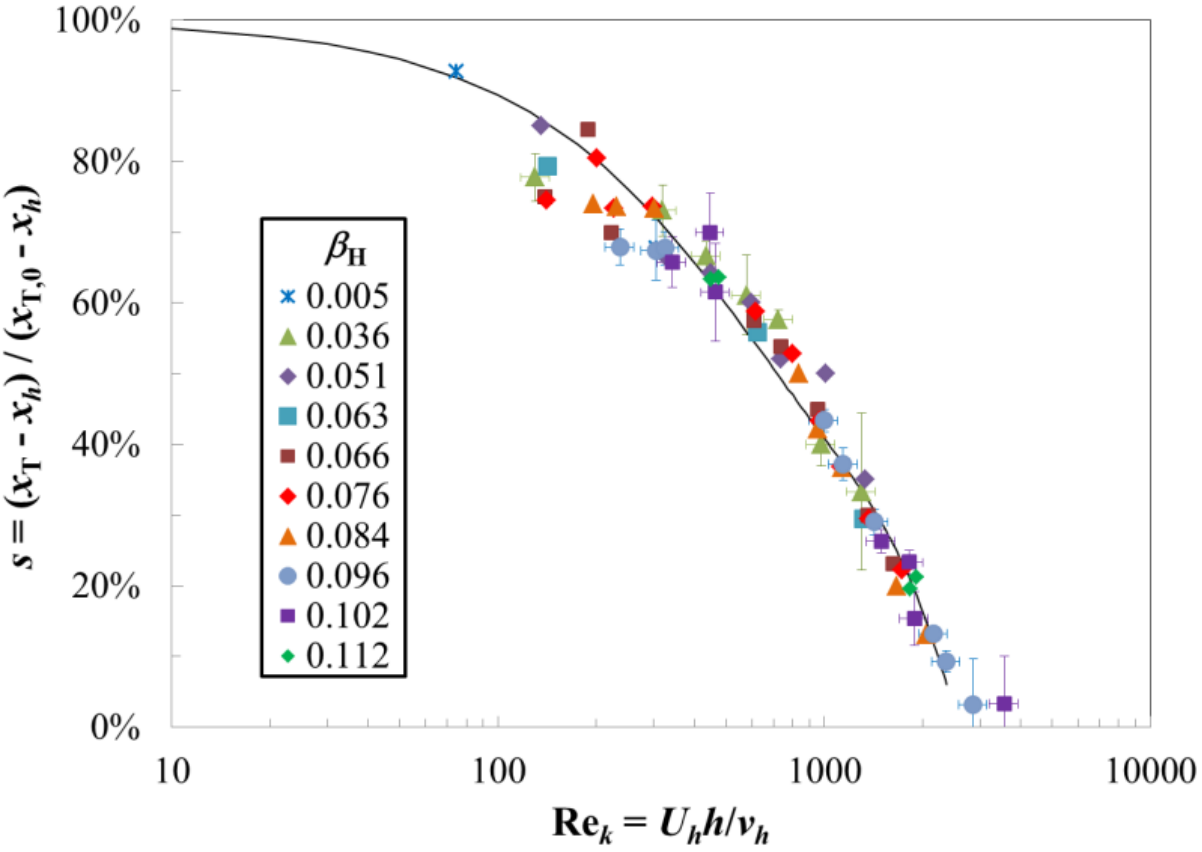

Fig. 6.2.2.3. Relative change in transition location *s* as a function of the roughness Reynolds number at M = 0.77 and T_w/T_{aw} = 1.043-1.064.

The three functional plots give a good correlation of the results. The value of $s = (x_T\text{-}x_h)/(x_{T,0}\text{-}x_h)$ decreases at larger values of Re_h, $h/\delta_{1,h}$ [245], and Re_k. The correlations shown in Fig. 6.2.2.2 and Fig. 6.2.2.3 are essentially independent of chord Reynolds number and streamwise pressure gradient. The values of x_T for the data below the approximation functions in the range $850 < Re_h < 1350$ (Fig. 6.2.2.2) and $100 < Re_k < 350$ (Fig. 6.2.2.3) were obtained at a wall temperature ratio $T_w/T_{aw} \sim 1.06$: this was a little larger than the wall temperature ratio at which the smooth configuration was investigated ($T_w/T_{aw} \sim 1.05$). The deviation of these data from the overall trend is due to this difference in T_w/T_{aw} (see Section 6.5).

The chord Reynolds number has no appreciable effect on the relations between *s* and the non-dimensional step parameters in Fig. 6.2.2.2, Fig. 6.2.2.3, and in [245]. This is in line with previous observations on the effect of cylindrical wires on boundary-layer transition [242,246]. The results of previous experiments conducted at different unit Reynolds numbers [247,248] were collected in [242] in a single plot and presented as $Re_{xT}/Re_{xT,0}$ vs. $h/\delta_{1,h}$. The ratio of transition Reynolds numbers was shown to be a unique function of $h/\delta_{1,h}$ for changes in unit Reynolds numbers, provided that transition occurred at a location sufficiently downstream of the roughness location. The independency from the streamwise pressure gradient of the above relations is also in line with

observations from previous work, where the effect on boundary-layer transition of forward-facing steps [38,41] and cylindrical wires [242,246,248-249] had been examined. The experimental results of [38], plotted as $s = (x_T\text{-}x_h)/(x_{T,0}\text{-}x_h)$ vs. Re_h, showed a strong reduction in s as the step Reynolds number changed from $Re_h \sim 1600$ to 2150. This behavior had been observed at both angles-of-attack examined in that work. Forward-facing steps were installed at two different streamwise locations on the flat-plate model investigated in [41]: these locations corresponded to regions of favorable and adverse pressure gradients, which were created using different wall contours. The transition Reynolds number was then plotted as a function of the relative step height $h/\delta_{1,h}$. Although the data show considerable scatter at $h/\delta_{1,h} < 1$, the streamwise pressure gradient does not have a large influence on the relation between Re_{xT} and $h/\delta_{1,h}$. It should be emphasized that only the step location was changed in that work [41], whereas the (non-uniform) pressure distribution was maintained the same for all test conditions. Thus, the effects on boundary-layer transition of streamwise pressure gradient and step location were not decoupled, since both parameters had been changed at the same time. The influence on boundary-layer transition of cylindrical wires placed in nearly-uniform favorable and adverse pressure gradients has been also studied [242,246,248-249]. Concerning the relation between transition Reynolds number and relative roughness height, the effect of pressure gradient (if any) was found to be very small. After the results of various investigations had been analyzed [243], it was concluded that "pressure distribution effects are of minor importance in determining critical roughness". ("Critical roughness" was defined as the value of the roughness parameter for which $Re_{xT}/Re_{xT,0}$ had decreased to 95 %.) This was verified for a wide range of Hartree parameters from $\beta_H = -0.2$ to 0.64, covering all practical applications for the design of NLF airfoils [243]. The reason for this insensitivity was identified as the local nature of the roughness effect [244,246]. These observations from past work have been discarded in latest publications [12,43-44], since the earlier reported data were considered ambiguous with regard to the effect of the pressure gradient [12]. In [12,43-44,186], steps were generated on two generic test models with nearly-uniform streamwise pressure gradients, which were mounted on a carrier vehicle and investigated in a towing wind tunnel. The boundary layer over the first test model was moderately accelerated ($K = (\nu/U_e^2)(dU_e/dx) = 2 \cdot 10^{-8}$); however, the steps were placed at a location immediately downstream of a region of adverse pressure gradient, which followed a (moderate) pressure minimum in the leading-edge region. Thus, the steps were not immersed in a region of uniform pressure gradient, as they had been in the case of the second model; in this latter case, the boundary-layer acceleration had been more pronounced than that on the first model ($K = 5 \cdot 10^{-8}$). The most important conclusion from those experiments was that manufacturing tolerances for NLF surfaces can "be loosened in areas where even mild favorable pressure gradients exist" [44] because of the favorable influence of flow acceleration on boundary-layer transition. The experimental data from [12,43-44], however, do not seem to unequivocally support this

conclusion. The results were plotted as ($Re_{xT} - Re_{xh}$) vs. Re_k, Re_{xT} vs. Re_k, and Re_{xT} vs. $h/\delta_{1,h}$. Especially for forward-facing steps in the presence of more pronounced flow acceleration ($K = 5 \cdot 10^{-8}$), the data points are rather sparse and do not allow one to identify a clear trend. Some critical aspects should be remarked at this point. The boundary layer remained laminar over the whole measurement region for several test conditions; in particular, data of the transition Reynolds number for the smooth configuration $Re_{xT,0}$ are missing [44]. Because of the lack of these data, it is not possible to compare the results obtained at the two streamwise pressure gradients by examining relative changes in transition Reynolds number, e.g., by using $Re_{xT}/Re_{xT,0}$. The representation of the results used in [12,43-44] does not appear as appropriate for the analysis of the effect of the pressure gradient, since not only Re_{xT}, but also $Re_{xT,0}$ change when the pressure gradient is varied. Moreover, the larger flow acceleration on the second test model made the laminar boundary layer very stable, so that the indifferent-stability Reynolds number Re_{ind} was not reached on the smooth configuration [44]. This situation is different from that considered in this and in previous work for the investigation of surface imperfections (see Section 2.5). Finally, it was reported in [43] that tolerance, perpendicularity, and rigidity of the steps were ensured, but no data of the imperfection profile in both streamwise and spanwise direction were presented. Based on these remarks, the results of those experiments [12,43-44] should be interpreted with caution.

The results of the present experiments confirm that, even in the presence of forward-facing steps, favorable pressure gradients permit larger laminar areas to be obtained, as compared to zero or adverse pressure gradients. This finding is in agreement with observations from the aforementioned work [12,43- 44], but it does not necessarily imply that manufacturing tolerances can be relaxed in the presence of favorable pressure gradients. This depends on the criterion used to define the manufacturing tolerances. Suppose that a criterion based on the relative change of Re_{xT} as a function of a non-dimensional step parameter is used, such as $Re_{xT}/Re_{xT,0}$ vs. $h/\delta_{1,h}$ shown Fig. 6.2.1.1b. If the criterion has been calibrated at zero pressure gradient, it would underpredict the effect of the steps at favorable pressure gradients; in contrast, it would overpredict the effect of the steps at zero pressure gradient if the criterion had been calibrated for a favorable pressure gradient. These considerations are of crucial importance for the design of an NLF surface. A criterion based on the correlation between the relative change in transition location (s) and a non-dimensional step parameter (Re_h, $h/\delta_{1,h}$, or Re_k) appears as appropriate for establishing manufacturing tolerances for forward-facing steps on NLF surfaces, at least for the examined range of test parameters.

As a final remark for this section, it should be emphasized that the present correlations of the results have been obtained for a certain step location, and are not expected to necessarily hold for all possible step locations. It has been discussed in the beginning of this chapter that a third non-dimensional parameter,

accounting for the location of the roughness, has to be considered for a general relation between the variables involved in the problem. The non-dimensional roughness location x_h/h, used to form limiting curves for the correlation of the data in [242,246], does not seem to be a suitable parameter: $(h/\delta_{1,h})_{cr}$ and $Re_{k,cr}$ for cylindrical wires were found to increase as the wire was moved upstream on the test surface [243], independent of the presence of the limiting curves in the correlations. The effect on boundary-layer stability of forward-facing steps located at different streamwise locations was examined in [45,46]. At each Mach number considered in the numerical studies, two steps with different height were investigated, so that the relative step height h/θ_h could be maintained constant. (The step Reynolds number Re_h, however, was larger for the steps at a more downstream location.) The streamwise extent of the separated flow region(s) near the step location was found to increase as the step location was moved further downstream (with constant h/θ_h). Larger values of Re_{xh} also led to larger values of the increment function $\Delta N(x)$ downstream of the step. Nevertheless, the curves $Re_{xT}/Re_{xT,0}$ vs. h/θ_h obtained in [243] were observed to move closer as the cylindrical wires were placed farther downstream from the leading edge of the examined test surface. The correlation of the data in [242] was obtained for cylindrical wires placed at various streamwise locations, but all of them were at distances from the leading edge larger than those examined in [243]. Thus, plotting the data as $Re_{xT}/Re_{xT,0}$ vs. $h/\delta_{1,h}$ gave a universal curve, almost independent of the roughness location, when the roughness element was placed at a sufficiently large value of Re_{xh} [242,243]. It is therefore expected that the present correlations of the results hold also for forward-facing steps placed at locations different from that examined in the present work, at least after a certain distance from the leading edge. This has been verified in a study on another two-dimensional test model, having the cross-section of an NLF airfoil [250].

6.3 Combined effect of forward-facing steps, pressure gradient, and Mach number

The influence of chord Reynolds number and pressure gradient on boundary-layer transition in the presence of forward-facimg steps discussed in the previous sections for M = 0.77 was observed also at M = 0.65, 0.5, and 0.35. Therefore, the discussion will not be repeated here; the related plots are shown in Appendix E.3. In the case of the smallest Mach number, M = 0.35, these effects have been presented and discussed in [250].

It has been already shown in Section 5.2.5 that, at approximately the same Hartree parameter, the transition Reynolds number with the step-2 configuration is larger at smaller Mach numbers. This was observed also for the smooth configuration (see Section 5.1) and for the step-1 and step-3 configurations as well. The latter comparisons are shown in Appendix E.3. In all these cases, an increase in the initial disturbance amplitude, due to a change in the disturbance environment and/or in the boundary-layer receptivity to external disturbances, is

likely to be the cause of the decrease in transition Reynolds number at larger Mach numbers. The difference in Re_{xT} for a certain Hartree parameter, however, becomes smaller as the step height is increased. This is probably due to the larger amplification of streamwise instabilities occurring in the step region: the influence of the step-induced amplification on the transition Reynolds number increases at larger values of the non-dimensional step parameters, so that the relative contribution of the initial disturbance amplitude decreases, in a manner similar to that of the streamwise pressure gradient discussed in Section 6.2.2. Note also that, at larger Hartree parameters, the difference in transition Reynolds numbers obtained at different Mach numbers decreases (see Fig. 5.2.5.4). This behavior is observed for all step configurations. In order to analyze this behavior in more detail, the relative variation in transition Reynolds number $Re_{xT}/Re_{xT}(\beta_H = 0)$ for the step-2 configuration is plotted in Fig. 6.3.1 as a function of the Hartree parameter. This figure is the analogous to Fig. 5.1.2.7. The corresponding plots for the step-1 and step-3 configurations are shown in Appendix E.3. As can be seen in Fig. 6.3.1, the values of $Re_{xT}/Re_{xT}(\beta_H = 0)$ are almost coincident up to $\beta_H \sim 0.05$, but with increasing β_H the values drift apart. As compared to the smooth configuration, the influence of the wall temperature ratio on boundary-layer transition in the presence of forward-facing steps is generally weaker, and is essentially negligible for several cases with the step-2 and step-3 configurations. This aspect will be discussed in detail in Section 6.5. The important message for the current analysis is that a "correction" for temperature effects, such as that carried out for the smooth configuration in Section 5.1.2 (see Fig. 5.1.2.8), would not lead to significant differences in the trends for the plots shown in Fig. 6.3.1. The reduction of the difference in Re_{xT} at larger Hartree parameters observed in Fig. 5.2.5.4, and the corresponding larger values of $Re_{xT}/Re_{xT}(\beta_H = 0)$ at larger Mach numbers, are likely to be due to a favorable influence of compressibility. As discussed in Sections 1.1 and 2.5, there are no experimental data available on the influence of Mach number (in the range considered in this work) on boundary-layer transition in the presence of forward-facing steps. A larger Mach number has a favorable effect on the growth rates of boundary-layer disturbances in the attached flow regions, but also a destabilizing effect due to the larger separated flow regions [31,165-166,240-241]. The stabilizing effect can be partially [166] or completely offset [241], depending on the relative strengths of these competing mechanisms [31,165]. In past numerical investigations of forward-facing steps at subsonic speeds [45], compressibility was shown to have a damping influence on the increment function $\Delta N(x)$.

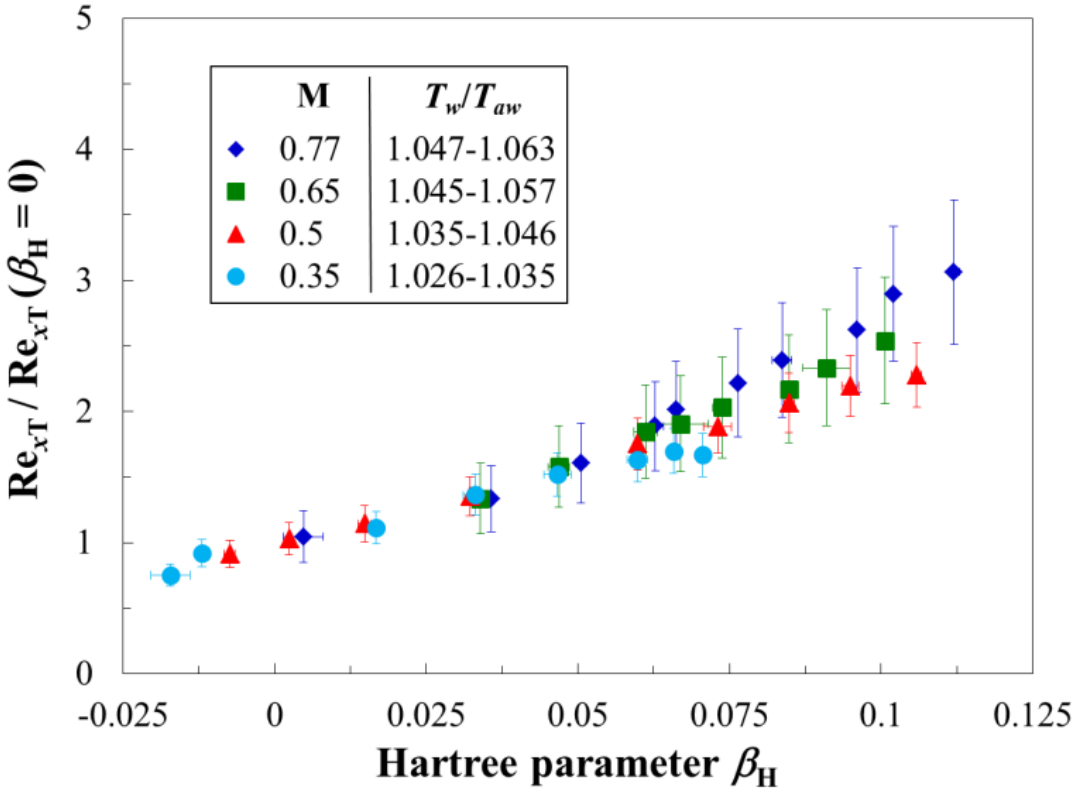

Fig. 6.3.1. Relative variation of the transition Reynolds number as a function of the Hartree parameter for the four examined Mach numbers. Step-2 configuration.

Boundary-layer transition was also observed to be more sensitive to the influence of forward-facing steps at smaller Mach numbers: under the same test conditions, larger reductions in $Re_{xT}/Re_{xT,0}$ were found at smaller values of the Mach number. The discussion is similar to that presented in Section 6.2.1 for the change in sensitivity due to the streamwise pressure gradient. Therefore, this discussion is not given here but in Appendix E.3.1.

The results obtained at each one of the Mach numbers M = 0.65, 0.5, and 0.35 are grouped into single plots, where $s = (x_T-x_h)/(x_{T,0}-x_h)$ is shown as a function of one non-dimensional step parameter. These plots are analogous to those for the largest Mach number M = 0.77 presented in Fig. 6.2.2.2, Fig. 6.2.2.3, and in [245]. The relative change in transition location at M = 0.65 is presented as a function of the step Reynolds number Re_h in Fig. 6.3.2; s is plotted against $h/\delta_{1,h}$ for M = 0.5 in Fig. 6.3.3; s vs. Re_k for M = 0.35 is shown in Fig. 6.3.4. (Note that the scale of the x-axis in Fig. 6.3.4 is logarithmic.) Data obtained at different pressure gradients are shown by symbols with different colors. Gaussian functions are fitted to the data in Fig. 6.3.2 and Fig. 6.3.3, whereas a 4th order polynomial function is used in Fig. 6.3.4. These curves, shown by solid lines, were the better matched by the experimental data. The relative change in transition location at M = 0.35 has been also shown as a function of Re_h and $h/\delta_{1,h}$ in [250]. The plots of s as a function of the other two non-dimensional step parameters at M = 0.65 and 0.5 are shown in Appendix E.3.

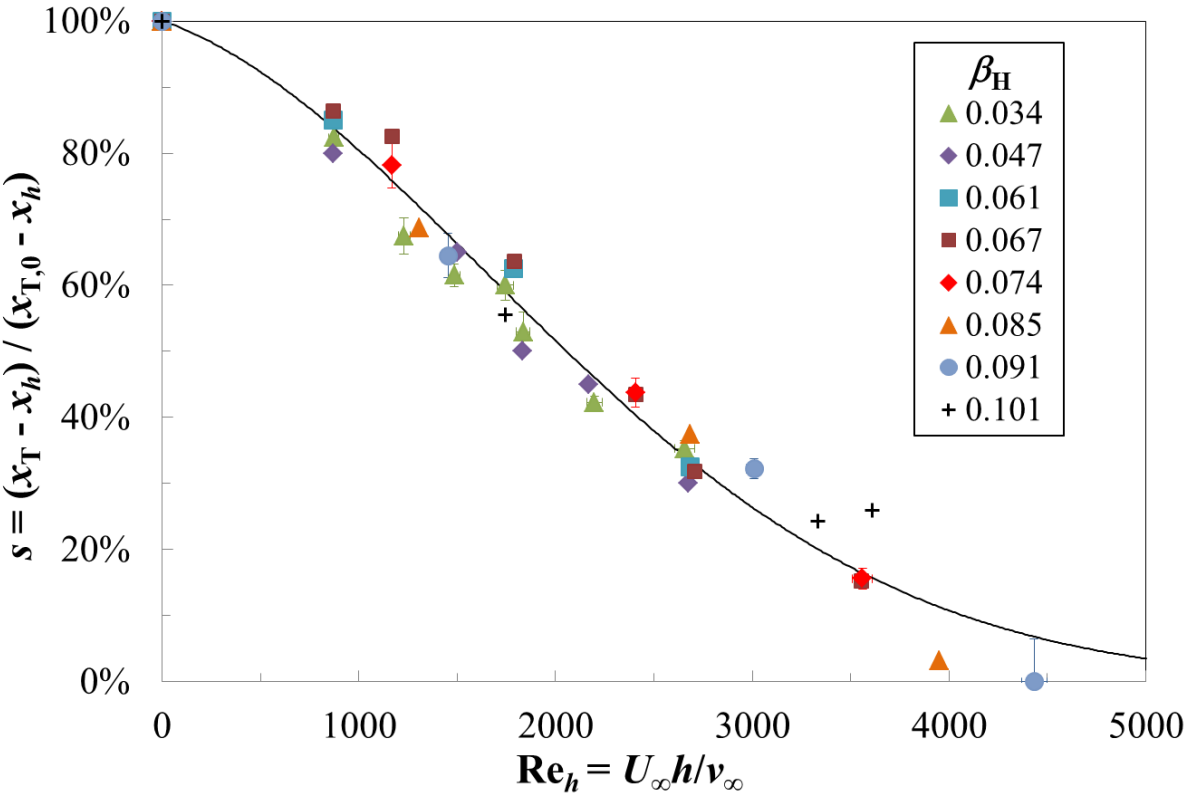

Fig. 6.3.2. Relative change in transition location as a function of the step Reynolds number at M = 0.65 and T_w/T_{aw} = 1.037-1.057.

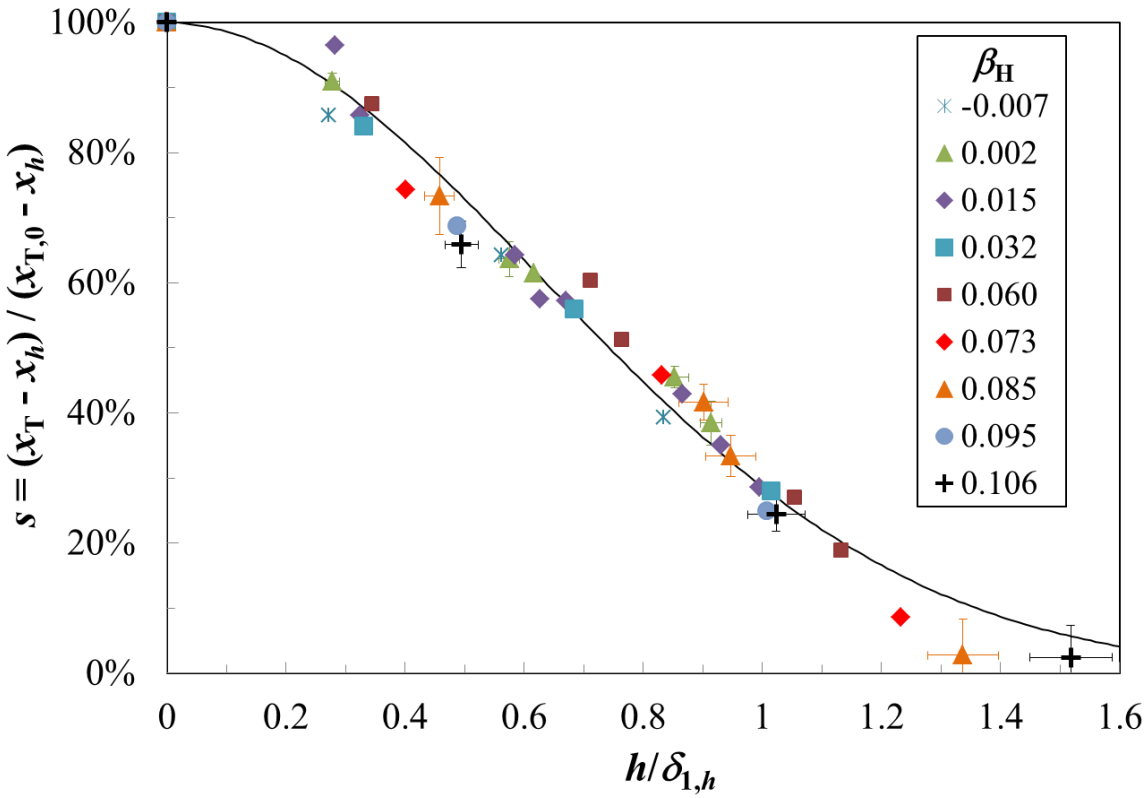

Fig. 6.3.3. Relative change in transition location as a function of the relative step height at M = 0.5 and T_w/T_{aw} = 1.032-1.051.

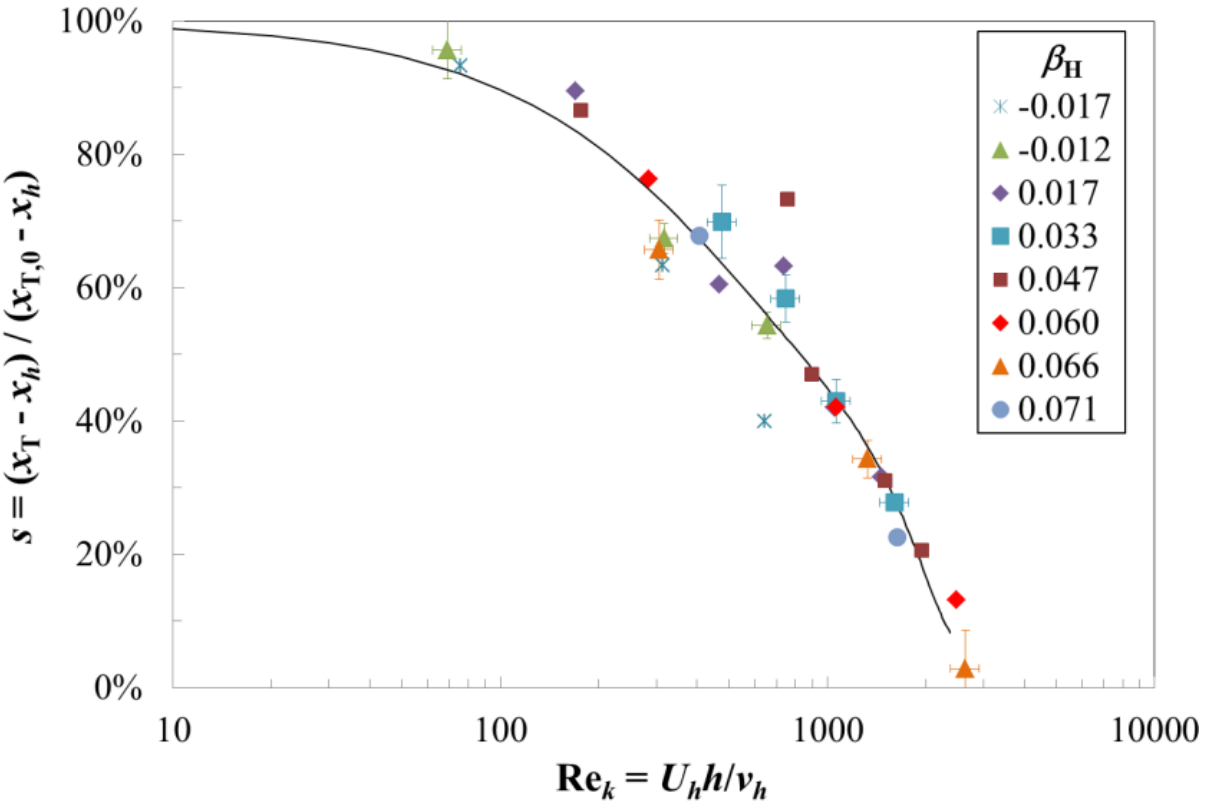

Fig. 6.3.4. Relative change in transition location as a function of the roughness Reynolds number at M = 0.35 and T_w/T_{aw} = 1.022-1.037.

The above plots of the results show good correlation. The relations between s and the non-dimensional step parameters are essentially independent of chord Reynolds number and streamwise pressure gradient, in agreement with the observations at the largest Mach number. Moreover, the aforementioned relations do not appear to be a function of the Mach number. This result will be shown even more clearly in Section 6.4. The larger deviations of some data points from the overall trends in Fig. 6.3.2 to Fig. 6.3.4 are generally due to the different values of T_w/T_{aw} at which x_T and $x_{T,0}$ were measured. For example, the transition location x_T for the data point at M = 0.35, β_H = 0.047, and $Re_k \sim 750$ in Fig. 6.3.4 was measured at T_w/T_{aw} = 1.026 with the step-2 configuration, whereas the transition location $x_{T,0}$ was measured at T_w/T_{aw} = 1.036 in the test with the smooth configuration.

6.4 Summary and discussion of the results at standard T_w/T_{aw} and comparison with data from previous work

All experimental data obtained at the four examined Mach numbers are now collected in single plots: s is presented as a function of Re_h, $h/\delta_{1,h}$, and Re_k in Fig. 6.4.1, Fig. 6.4.2, and Fig. 6.4.3, respectively. The data obtained at different Mach numbers are shown by symbols with different colors. A curve approximating the whole set of data is also shown in each plot by a solid line.

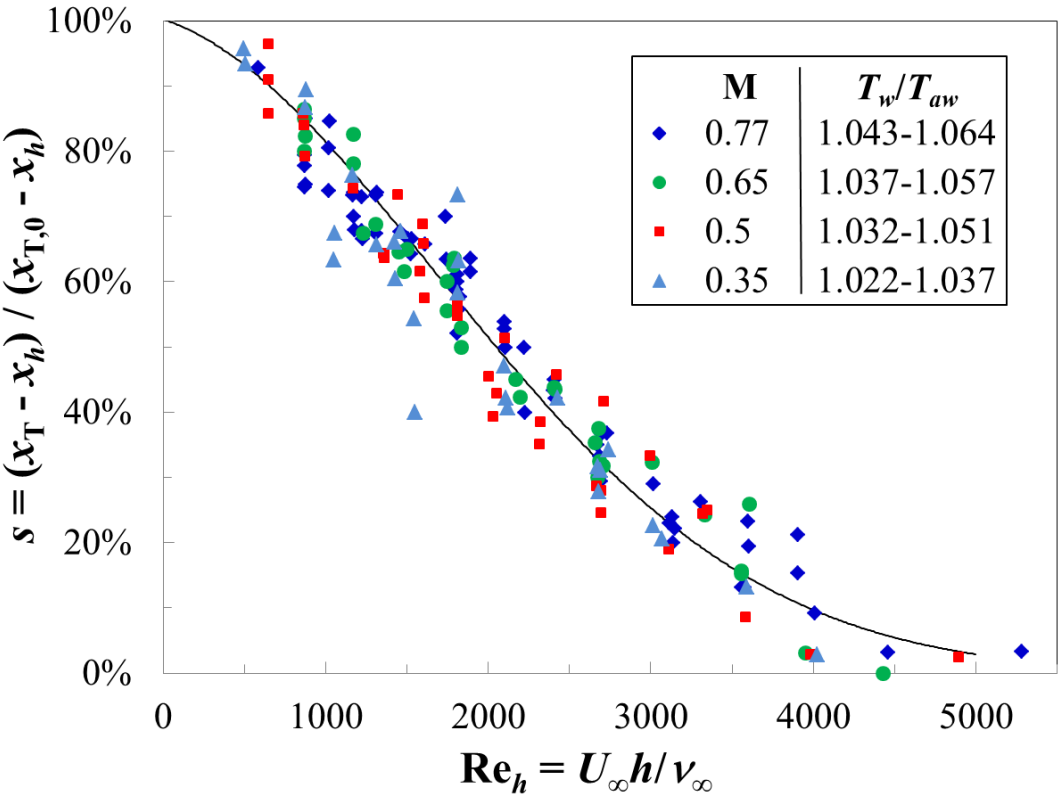

Fig. 6.4.1. Relative change in transition location as a function of the step Reynolds number for all Mach numbers.

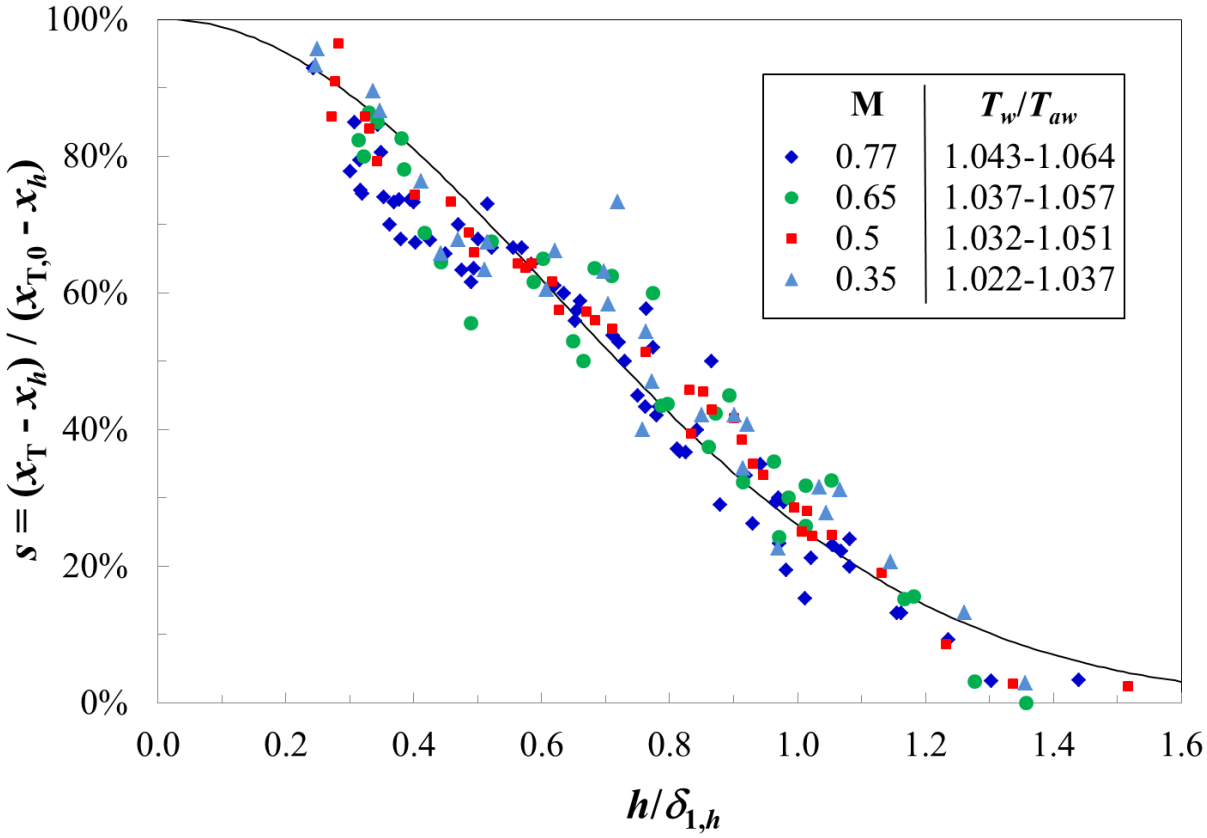

Fig. 6.4.2. Relative change in transition location as a function of the relative step height for all Mach numbers.

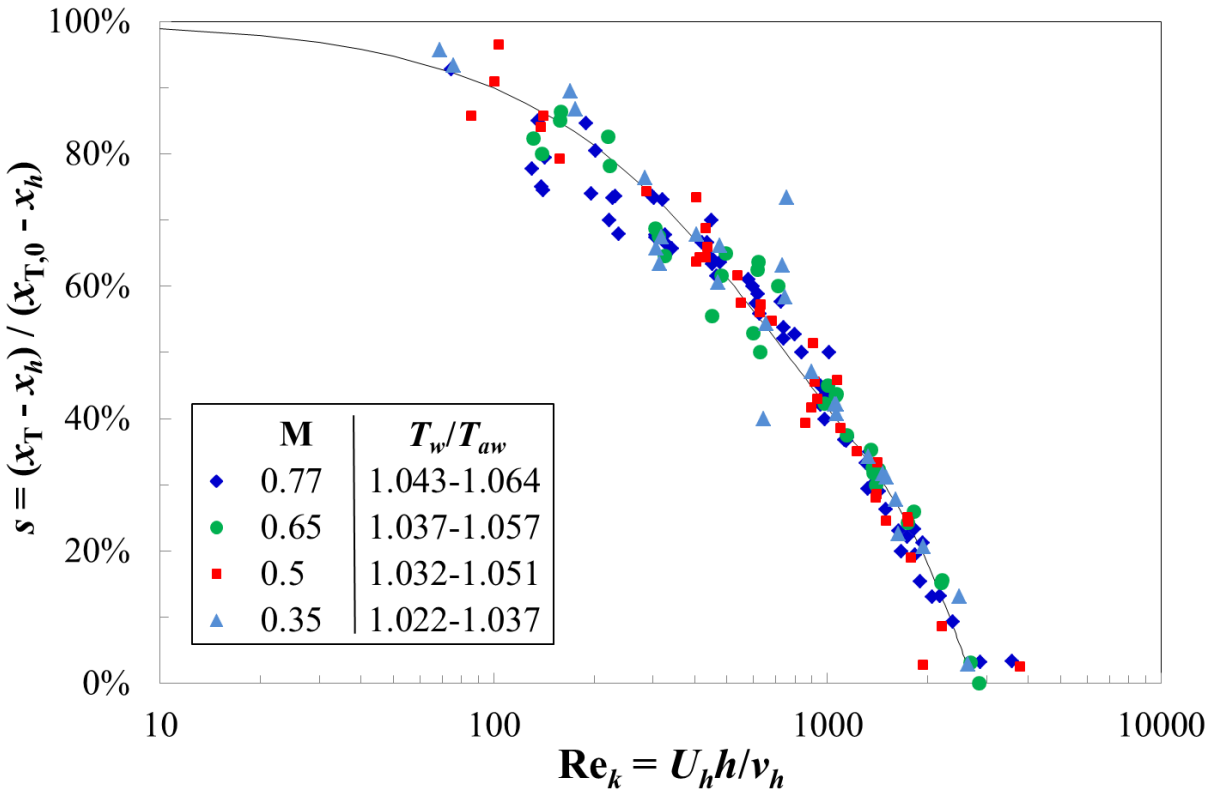

Fig. 6.4.3. Relative change in transition location as a function of the roughness Reynolds number for all Mach numbers.

The results obtained at different Mach numbers follow the same trend when represented as in Fig. 6.4.1 to Fig. 6.4.3. Besides the Mach number itself, the results obtained at the four different Mach numbers differ also in their disturbance environment, boundary-layer receptivity, and thermal condition at the model surface (see Sections 5.1.1 and 5.2.5). Nevertheless, at fixed Mach number, Reynolds number, and model angle-of-attack, the wall temperature ratio was approximately the same, and the level and spectrum of the external disturbances (as well as boundary-layer receptivity to such disturbances) are expected to remain unchanged. Thus, the transition locations x_T and $x_{T,0}$ were measured under almost the same conditions. The use of $s = (x_T\text{-}x_h)/(x_{T,0}\text{-}x_h)$ as the parameter to describe the change in transition location allows the effect of steps on boundary-layer transition to be "isolated", since the influence of the other factors is minimized. The insensitivity of the relations between s and the non-dimensional step parameters to variations in the disturbance environment is consistent with previous observations on the effect of cylindrical wires on boundary-layer transition [242,246]. A unique relation between $\mathrm{Re}_{xT}/\mathrm{Re}_{xT,0}$ vs. $h/\delta_{1,h}$ was obtained in [242] for experimental data obtained in facilities with a different disturbance environment [247,248], provided that transition occurred sufficiently downstream of the roughness location. The results of earlier work on cylindrical wires in a zero pressure gradient flow, obtained in facilities with a different disturbance environment [246,249], were grouped in [246] into a single plot of Re_{xT} vs. $h/\delta_{1,h}$. In this case, the effect of freestream disturbances was

found to be confined to small values of relative roughness height in the range $0.2 < h/\delta_{1,h} < 0.4$, and was to slightly increase the critical roughness height [246]. However, only a few data are presented in this range of relative roughness height to support this conclusion. A similar result was reported in [243], but in this case the increase in disturbance level was large: a tenfold increase in turbulence level (from $Tu \sim 0.03$ % to 0.3 %) led to a 50 % increase in critical roughness Reynolds number for cylindrical wires, from $\mathrm{Re}_{k,\mathrm{cr}} \sim 130$ to 195. ($\mathrm{Re}_{k,\mathrm{cr}}$ was defined as the value of roughness Reynolds number for which $\mathrm{Re}_{x\mathrm{T}}/\mathrm{Re}_{x\mathrm{T},0}$ had decreased to 95 % – see Section 6.2.2.) In the present work, the relations between s and the non-dimensional step parameters were not appreciably altered either by the different disturbance environment, boundary-layer receptivity, and wall temperature ratios, or by the Mach number itself, as shown in Fig. 6.4.1 to Fig. 6.4.3. Aspects to be considered concerning the effect of the wall temperature ratio will be discussed in Section 6.5. Other combinations of freestream disturbance level, boundary-layer receptivity, and Mach number may affect the relations between s and the non-dimensional step parameters, especially when they might induce a change of the mechanism leading to transition (e.g., bypass of the growth of primary modes – see Section 2.1). Experiments have to be designed to specifically decouple, and thus systematically study, these three effects on boundary-layer transition in the presence of surface imperfections. This is a very complex and ambitious task, and it is not surprising that such experiments have not been conducted up to now (not even for smooth surfaces) in the examined range of Mach numbers. In any case, it appears improbable that the effects of compressibility, disturbance environment, and receptivity on the aforementioned relations compensated each other over the whole range of step parameters examined in this work. Rather, these effects on boundary-layer transition are included in x_T and $x_{\mathrm{T},0}$, and thereby accounted for when $s = (x_\mathrm{T}\text{-}x_h)/(x_{\mathrm{T},0}\text{-}x_h)$ is used to describe the shift in transition location due to the steps, in a manner similar to that discussed in Sections 6.2.2 and 6.3 for the streamwise pressure gradient.

The following Gaussian functions were the better matched by the data presented as s vs. Re_h and s vs. $h/\delta_{1,h}$ in Fig. 6.4.1 and Fig. 6.4.2, respectively:

$$s = \frac{x_\mathrm{T} - x_h}{x_{\mathrm{T},0} - x_h} = \mathrm{a} \cdot e^{\left(\frac{-(\mathrm{b}-\mathrm{Re}_h)^2}{2\cdot \mathrm{c}^2}\right)} \tag{6.4.1}$$

with a = 1.016, b = -326, and c = 1995, and

$$s = \frac{x_\mathrm{T} - x_h}{x_{\mathrm{T},0} - x_h} = \mathrm{p} \cdot e^{\left(\frac{-(\mathrm{q}-h/\delta_{1,h})^2}{2\cdot \mathrm{r}^2}\right)} \tag{6.4.2}$$

with p = 1.0005, q = 0.007, and r = 0.6.

The data in Fig. 6.4.3, plotted as s vs. Re_k, have been fitted to a 4th order polynomial function

$$s = 3.4 \cdot 10^{-14}\, \mathrm{Re}_k^4 - 2.6 \cdot 10^{-10}\, \mathrm{Re}_k^3 + 7.1 \cdot 10^{-7}\, \mathrm{Re}_k^2 - 1.1 \cdot 10^{-3}\, \mathrm{Re}_k + 1 \quad (6.4.3)$$

The deviations of the experimental data from the overall trends are mainly due to different wall temperature ratios between the tests with the smooth configuration and those with the step configurations. It should be also remarked that the above approximation functions do not represent well the behavior of boundary-layer transition at very large values of the non-dimensional step parameters, viz.: at approximately $\mathrm{Re}_h > 4000$, $h/\delta_{1,h} > 1.3$, and $\mathrm{Re}_k > 2500$. At these conditions, however, transition occurs at a location very close to that of the step, so that the transition location can be approximated by the step location for all practical purposes. A more accurate representation of the results at such large values of the non-dimensional step parameters would be of interest for boundary-layer tripping, but other means than forward-facing steps would most likely be preferred; for example, backward-facing steps, which are known to be more effective than forward-facing steps in inducing premature transition (see Section 2.5), or a combination of both steps in the form of a square bump.

6.4.1 Comparison with results from previous work

Boundary-layer transition was observed to move gradually towards the step location as the non-dimensional step parameters were increased, in agreement with previous work on forward-facing steps in the presence of a nearly-zero pressure gradient [40,118]. A gradual shift of the transition location can be also observed within the data scatter of the results presented in [41], which were obtained in the presence of favorable and adverse pressure gradients. The data shown in [12,44] do not present unequivocal trends, especially in the presence of a markedly favorable pressure gradient ($K = 5 \cdot 10^{-8}$, see Section 6.2.2); in the case of a moderately favorable pressure gradient ($K = 2 \cdot 10^{-8}$), the movement of the transition location with increasing Re_k and $h/\delta_{1,h}$ appears to be more pronounced [12,44] than that observed in the present work and in [40,118]. In experiments conducted on a two-dimensional airfoil model [38], transition was observed to remain at, or close to, the corresponding location for a smooth configuration until a critical value of step Reynolds number $\mathrm{Re}_{h,\mathrm{cr}}$ was reached, and then to move rapidly towards the step location as Re_h was further increased. This behavior can be due to the particular boundary-layer stability situation examined in that work [38]. Boundary-layer transition was investigated at two angles-of-attack: AoA = -1° and -6°. The boundary layer was accelerated up to $x/c \sim 50$ % (except for a pressure minimum in the leading-edge region at AoA = -1°) and decelerated further downstream; in the absence of surface steps, transition was measured at both angles-of-attack on this latter region of adverse pressure gradient. The N-factor envelope curve had a markedly positive slope in

this region. It seems that at the critical condition, corresponding to the critical step Reynolds number $\mathrm{Re}_{h,\mathrm{cr}}$, transition came close to a region where $\partial N/\partial(x/c) \sim 0$, so that a further increase in step Reynolds number led to the observed large change in transition location [38]. It is interesting to note that, in the presence of backward-facing steps, a gradual change of the transition location with varying non-dimensional step parameters was observed in most of the aforementioned experiments [38,40-41,118]. This behavior is characteristic also of transition induced by cylindrical wires [242,246-249].

Criteria for allowable tolerances for forward-facing steps on NLF surfaces can now be derived from Eqs. (6.4.1) to (6.4.3). At this point, it should be emphasized that the criterion used to define the "critical" step height is crucial. In fact, a critical value of a non-dimensional roughness parameter, such as $\mathrm{Re}_{k,\mathrm{cr}}$ for three-dimensional roughness elements [67,238-239,244,246], cannot be defined. This definition expects that the transition location moves forward very rapidly as a critical roughness height has been exceeded, but that below this critical value the roughness has little or no effect on transition. As discussed above, this generally does not correspond to the behavior of boundary-layer transition in the presence of two-dimensional roughness. (In this sense, two-dimensional roughness is said to be "less critical" than three-dimensional roughness [251].) Rather, a definition of "critical roughness", such as that used in [243], should be used: the critical value of a certain non-dimensional step parameter is that for which transition has moved by a certain extent from its smooth-configuration location towards the step location, or the transition Reynolds number has decreased by a certain amount (e.g., $\mathrm{Re}_{x\mathrm{T}}/\mathrm{Re}_{x\mathrm{T},0} = 95$ % in [243]). The critical values of Re_h, $h/\delta_{1,h}$, and Re_k, corresponding to a certain loss of laminarity Δs, are evaluated from Eqs. (6.4.1) to (6.4.3), and are given in Table 6.4.1.1. These values can be used as a guide for manufacturing tolerances of NLF surfaces (with zero to moderate sweep angles) at different flow conditions and streamwise pressure gradients, at least for the examined range of test parameters.

Table 6.4.1.1 Critical values of non-dimensional roughness parameters for forward-facing steps based on the approximation functions shown in Fig. 6.4.1 to Fig. 6.4.3.

Loss of laminarity	$\mathrm{Re}_{h,\mathrm{cr}}$	$(h/\delta_{1,h})_{\mathrm{cr}}$	$\mathrm{Re}_{k,\mathrm{cr}}$
$\Delta s \sim 10$ %	660	0.29	100
$\Delta s \sim 20$ %	1050	0.41	215
$\Delta s \sim 50$ %	2050	0.72	750
$\Delta s \sim 80$ %	3270	1.10	1920

The value of step Reynolds number that corresponds to a laminarity loss of $\Delta s \sim 10$ % is considerably lower than critical values reported in previous work [34,38]. The value provided in [34] is $\mathrm{Re}_{h,\mathrm{cr}} = 1800$, but no further

information is available about these experiments, except for a private communication reported in [30]. According to this communication, the experiments were carried out in a manner consistent with that for the determination of the criteria for allowable waviness [162], i.e., using moderate wall suction to achieve full-chord laminar flow over a smooth surface. $Re_{h,cr}$ was then "established based on the conditions where the first turbulent bursts occurred far downstream from the surface imperfection" [30]. This implies, however, that steps at $Re_h < 1800$ may have induced a reduction of the transition Reynolds number, but this was still too large for transition to be measured on the test model. The value of critical step Reynolds number provided in [38] is $Re_{h,cr} = 2000$, defined as the value of Re_h above which transition moved rapidly towards the step location. The experimental data were also plotted as s vs. Re_h, but the number of points was rather small; the range of Re_h corresponding to the pronounced movement of the transition location is not well resolved. The steps were created using plastic foils glued onto the model surface. It is unclear whether this method led to an appreciable change of the surface pressure distribution between smooth and step configurations. (Also the trailing-edge shape was modified.) Moreover, surface quality concerns arising from the application of foils onto the model surface must be addressed: the results may be affected by step bluntness, foil waviness, and non-uniformity of the step in the spanwise direction. The shape of the imperfection has been shown to have a marked influence on boundary-layer transition [30]. Forward-facing steps with different cross-sectional shape were installed in a region of favorable pressure gradient on the lower surface of an NLF glove, which was mounted on a Beechcraft T-34C aircraft. For a rounded forward-facing step with a radius of approximately three-quarters of the step height, the critical step height was at least 50 % larger than that for a (nominally) sharp forward-facing step [30]. In fact, at a step Reynolds number $Re_h = 2720$, transition occurred right at the step in the case of the sharp forward-facing step, but far downstream for the rounded step. This result does not preclude that, in the case of a sharp forward-facing step, transition could occur at the imperfection location even for lower values of Re_h, but no information from these tests is available under these conditions. The effect of a forward-facing step on boundary-layer transition was also investigated in [42]. The imperfection was generated by means of a plastic strip attached onto the surface of an NLF-airfoil model. The step was followed in the streamwise direction by an elongated backward-facing ramp, tapered to almost zero at the downstream end of the strip. A laminarity loss of $\Delta s = 20$ % was measured at $Re_h = 1010$ [42], in agreement (within error tolerances) with that found in the present work at the same step Reynolds number. Quantitative geometrical data about the actual shape of the steps examined in the aforementioned experiments [30,34,38,42] were not provided, neither in the streamwise nor in the spanwise directions. It should be remarked that, at $Re_h \sim 2150$, the relative change in transition location in [38] was as low as $s \sim 25$ %, as compared to $s = 47$ % measured in the present work. This is clearly related to the different

shapes of the functional relations between s and Re_h obtained in this work and those in [38]. Note also that the relative change in transition location at $\mathrm{Re}_h = 2720$ was measured to be at $s \sim 32$ % in the present work, whereas in [30] transition was found right at the step location.

The critical value of relative step height $(h/\delta_{1,h})_{\mathrm{cr}} \sim 0.29$, corresponding to a laminarity loss of $\Delta s \sim 10$ %, is considerably lower than $(h/\delta_{1,h})_{\mathrm{cr}} \sim 1.3\text{-}1.4$ obtained in [40] for approximately the same amount of laminarity loss. The wind-tunnel model was in that case a flat plate, consisting of two major parts: a front part, fixed to the test-section walls by screws, and a rear part, held by clamping bolts and jacking screws to the front part. The model angle-of-attack and the trailing-edge flap and tab were adjusted to obtain a nearly-zero streamwise pressure gradient over the flat plate. Forward- and backward-facing steps of different height were obtained at $x/c \sim 23$ % (where c is the distance between the leading edge and the trailing-edge flap and tab) by adjusting the bolts and screws holding together the two model parts. A small gap existed between the two model parts; it was sealed with fine plaster filler [118]. The final shape of the imperfection (filled gap included) is not documented, and also the spanwise distribution of the step height is not known. In the case of forward-facing steps, the experimental data, plotted as $\mathrm{Re}_{x\mathrm{T}}$ vs. $h/\delta_{1,h}$, were approximated by a single curve. A closer look at the data, however, reveals four sets of results, corresponding to the four step heights that were investigated. The absolute value of the step height may have had some residual influence in those experiments, but the small amount of data points available in the range $0 \leq h/\delta_{1,h} \leq 1.7$ does not help to clarify this point. Nevertheless, once $(h/\delta_{1,h})_{\mathrm{cr}} \sim 1.3\text{-}1.4$ has been exceeded, the behavior of boundary-layer transition with increasing $h/\delta_{1,h}$ is similar to that observed in the present work (see Fig. 6.4.2): s changes from approximately 90 % to 10 % with an increase in relative step height of $\Delta(h/\delta_{1,h}) \sim 1$ [40,118]. The experimental results from [38] were also plotted as x_{T}/c vs. $h/\delta_{1,h}$, clearly showing a behavior similar to that observed from the representation of the data as s vs. Re_h. The pronounced shift in transition location due to the influence of forward-facing steps was found at $h/\delta_{1,h} \sim 1.8\text{-}2$ [38]. In [41], the large data scatter and the semi-logarithmic axes used for the plot $\mathrm{Re}_{x\mathrm{T}}$ vs. $h/\delta_{1,h}$ makes the identification of a critical $h/\delta_{1,h}$ difficult; nevertheless, it seems that a reduction by 10 % of $\mathrm{Re}_{x\mathrm{T}}$ was obtained at $h/\delta_{1,h} < 1$.

Some data on the critical value of roughness Reynolds number are available from [12,44]; the critical aspects of those investigations, which were outlined in Section 6.2.2, should be kept in mind when those results are considered. A limiting curve was drawn in the plots presenting the experimental data as $(\mathrm{Re}_{x\mathrm{T}} - \mathrm{Re}_{xh})$ vs. Re_k [12]. This curve showed a very pronounced variation of the transition Reynolds number once a certain value of roughness Reynolds number had been exceeded: this value corresponded to $\mathrm{Re}_{k,\mathrm{cr}} \sim 800$ at a moderately favorable pressure gradient ($K = 2 \cdot 10^{-8}$) and increased to $\mathrm{Re}_{k,\mathrm{cr}} \sim 2100$ with larger flow acceleration ($K = 5 \cdot 10^{-8}$) [12]. Both these values are markedly larger

than those found in the current work for $\Delta s \sim 10$ % and even 20 % (see Table 6.4.1.1). However, it should be emphasized that, for $\mathrm{Re}_k < 900$, transition had not occurred on the measurement region in any of the cases examined in [12,44], smooth configuration included. Thus, it is not possible to determine the value of $\mathrm{Re}_{k,\mathrm{cr}}$ for which transition moved from its original (smooth-surface) location $x_{\mathrm{T},0}$. Only the value of Re_k at which transition was measured for the first time on the test model can be obtained, but a significant reduction of transition Reynolds number may have occurred already at lower values of Re_k. This is a reasonable explanation for the larger values of $\mathrm{Re}_{k,\mathrm{cr}}$ given in [12], as compared to those obtained in the current work: a large value of Re_k was needed to bring about transition over the test model, especially in the presence of markedly favorable pressure gradients, for which $\mathrm{Re}_{x\mathrm{T},0}$ is large. At fixed Re, M, T_w/T_{aw} and step height, a larger laminar run length x_T was measured in the current work with stronger flow acceleration (see Section 6.2). Since the roughness Reynolds number changes only slightly in the considered range of Hartree parameters, a larger value of $\mathrm{Re}_{x\mathrm{T}}$ was obtained at approximately the same value of Re_k. In other words, at fixed M and T_w/T_{aw}, a larger value of Re_k is needed to reduce $\mathrm{Re}_{x\mathrm{T}}$ to a certain value with more pronounced flow acceleration. This is in line with the results of [12]. A straight forward-facing step was also investigated in [49]. It was generated on a two-dimensional model (which had the cross-section of a NACA 63_3-418 airfoil) by means of contact paper. At $\mathrm{Re}_k = 186$, the step had no influence on boundary-layer transition. No quantitative information about the shape of the step was given.

A "conventional laminar-flow tolerance" for the size of forward-facing steps reported in [12] is $\mathrm{Re}_{k,\mathrm{cr}} = 150$. This value is in agreement (within error tolerances) with the present values of $\mathrm{Re}_{k,\mathrm{cr}}$ corresponding to $\Delta s \sim 10$ % and 20 % (see Table 6.4.1.1), but the criterion used to define this tolerance in [12] is unclear. Interestingly, the critical values of the non-dimensional step parameters, obtained in the present work for $\Delta s \sim 10$ % and 20 %, are in agreement (within confidence bands) with the critical values for backward-facing steps and two-dimensional roughness elements given in the literature:

- In the case of backward-facing steps, the value of critical step Reynolds number given in [34] is $\mathrm{Re}_{h,\mathrm{cr}} = 900$. A relative change in transition location $s \sim 90$ % was obtained in [38] at $\mathrm{Re}_{h,\mathrm{cr}} \sim 500$ and 900, depending on the model angle-of-attack; these values of critical step Reynolds number correspond to $(h/\delta_{1,h})_{\mathrm{cr}} \sim 0.4$-0.5. A critical value of relative step height $(h/\delta_{1,h})_{\mathrm{cr}} \sim 0.5$ for $s \sim 90$ % was found in [40]. Note also that transition was found at the step location at $h/\delta_{1,h} \sim 1.5$ [40], a value in agreement (within error tolerances) with that of $h/\delta_{1,h} \sim 1.3$-1.4 measured in the present work for transition immediately downstream of the step location.
- The value of relative roughness height corresponding to $\mathrm{Re}_{x\mathrm{T}}/\mathrm{Re}_{x\mathrm{T},0} \sim 90$ % for cylindrical wires is $h/\delta_{1,h} \sim 0.25$ [242]. The average

value of critical roughness Reynolds number found in [243] for two-dimensional roughness elements is $Re_{k,cr} = 125$, where the "critical condition" was defined as that corresponding to $Re_{xT}/Re_{xT,0} \sim 95$ %. Critical roughness Reynolds numbers as low as $Re_{k,cr} \sim 40$-50 were also found for two-dimensional roughness elements [243,252]. Note that the tripping condition, at which transition has moved to the roughness location, corresponds in the present work to $Re_{k,cr} \sim 2600$-3000; these values are much larger than those found in earlier work for two-dimensional roughness: $Re_{k,cr} \sim 150$-400 [243,246-247,253-254].

In conclusion, the trends shown by the relations between the relative change in transition location $s = (x_T - x_h)/(x_{T,0} - x_h)$ and the non-dimensional step parameters Re_h, $h/\delta_{1,h}$, and Re_k were found to be in overall agreement with those observed in earlier work on two-dimensional roughness, and in particular with some studies on forward-facing steps [40-41,118]. The value of s obtained in the present work at $Re_h = 1010$ is in agreement with that obtained in [42] at the same step Reynolds number. However, the critical values $Re_{h,cr}$ and $(h/\delta_{1,h})_{cr}$, corresponding to laminarity losses of $\Delta s \sim 10$ % and 20 %, are lower than the values provided in earlier work for forward-facing steps [30,34,38,40]. The most probable sources for these differences in critical values of non-dimensional step parameters are the following three:

- Shape of the step. Imperfections with the shape of a rounded step or a ramp are less critical than a sharp step for the stability and transition of the laminar boundary layer, because the streamwise extent of the separated flow region is reduced [30]. Concerns arise in particular about the shapes of the steps generated by foils, sheets, etc., attached onto the model surface [30,38]. Besides differences in step geometry and surface quality, this method can also cause differences in the surface pressure distribution. The steps in [40] were reported as sharp, but it is also known that a small gap, sealed with fine plaster filler, was present upstream of the step [118]. It has been recently shown [174] that gaps placed immediately upstream of a forward-facing step can even have a stabilizing effect. In general, only inadequate documentation is available about the shapes of the steps in streamwise and spanwise directions.
- Boundary-layer stability situation. The sensitivity of boundary-layer transition to surface imperfections depends (among other factors) on the surface pressure distribution and on the location at which transition occurs in the absence of imperfections. If transition is induced, for example, by a strong pressure increase on the rear of an NLF airfoil [38], the sensitivity of boundary-layer transition to the influence of steps is expected to be lower than that in the case of a flat plate at zero or favorable pressure gradient.

- Step position. For cylindrical wires, $(h/\delta_{1,h})_{cr}$ was found to increase as the wire was moved upstream on the test surface [243]. Results from DNS showed that the increase in amplification factors of streamwise instabilities, due to the effect of forward-facing steps of given relative height $h/\delta_{1,h}$, is larger for larger Reynolds numbers based on the step location Re_{xh} [45,46]. In the present work, the step location was further downstream than that examined in previous work [38,40].

It should be also remarked that transition measurements in [38,40] were performed at only one spanwise section, so that the spanwise distribution of the transition location is not known. Spanwise variations of the transition location, according to the local step height and shape, have been possible. Moreover, turbulent wedges may have been superimposed onto the natural-transition front, especially in the presence of larger steps, as has been observed in present work. These issues show the advantage of the use of a surface measurement technique, such as the TSP measurement technique, for global transition detection. This enabled the identification of the natural-transition front and thus the systematic study of the influence on natural transition of the various parameters considered in the present work. Different measurement techniques have been used to detect transition in this study and in previous investigations [30,34,38,40]. The criteria applied for determining the transition location were also different. As discussed in Section 2.2.4, this can lead to significant differences in the absolute values of the transition Reynolds number. However, the discrepancies are expected to be small when only the relative variation of the transition Reynolds number is of interest, such as in this case.

Finally, it should be emphasized that the results obtained for the *PaLASTra* model have been already shown to be in agreement with those obtained for another two-dimensional model, having the cross-section of an NLF airfoil [250]. The agreement of the results is significant: it demonstrates the applicability and transferability of the present results with a generic configuration (flat plate) to the practical case of an NLF airfoil. This agreement was observed for two models with similar surface quality, which were tested with a comparable boundary-layer stability situation in the same wind tunnel. However, the steps on the NLF-airfoil model had been generated at a chordwise location more upstream than that on the *PaLASTra* model, and the development of the boundary layer up to the region of quasi-uniform pressure gradient was also different. Moreover, the disturbance environment was different, since the acoustic disturbances, originating from downstream of the *PaLASTra* model, were not present in the case of the NLF-airfoil model. This confirms the value of the correlations obtained using the parameter $s = (x_T-x_h)/(x_{T,0}-x_h)$ to represent the effect of surface imperfections on boundary-layer transition: the influence on transition of the disturbance environment is eliminated by expressing the variation of the transition location with respect to its value measured on the smooth configuration.

6.4.2 Increase in amplification factors (ΔN) due to forward-facing steps

A method to account for the effect of steps in the e^N method for transition prediction has been discussed in Section 6.2.1. The amplification of incoming disturbances due to the presence of the steps is incorporated in the increment function $\Delta N(x)$, which is to be added to the N-factor envelope curve computed for the smooth configuration [38,172]. The increment function varies, in general, with the streamwise coordinate [38,45-46]. In some cases, however, the effect of the imperfection on the N-factor envelope curve vanishes at a location so far downstream of the step location that the increment function can be approximated by a uniform offset ΔN for a considerable streamwise distance [45-46]. This was the strategy pursued in [40-41,118], where ΔN was determined from the transition locations x_T and $x_{T,0}$ (measured with and without steps, respectively) and the N-factor envelope curve $N(x)$ obtained for the smooth configuration. In practice, the value of the uniform offset was evaluated as $\Delta N = N_{T,0} - N_T$, where $N_{T,0} = N(x_{T,0})$ and $N_T = N(x_T)$. This procedure assumes that receptivity at the step can be neglected, and that the N-factors of the instability waves are increased by the same ΔN. Note that there exists experimental verification that amplified Tollmien-Schlichting waves, predicted by linear stability theory for the smooth surface, are responsible for transition also in the presence of surface steps of considerable relative height [40-41,118]. Moreover, when transition occurred at a location sufficiently downstream of the step location, the frequency band of the most amplified disturbances was found to be unchanged for both configurations, with and without steps [41,44].

The procedure described in [40-41,118] to determine the (uniform) increment ΔN was applied also to the data obtained in the present work. The results are plotted as ΔN vs. $h/\delta_{1,h}$ in Fig. 6.4.2.1. The approximation functions from [40] and [41] are shown in these figures by solid and dashed lines, respectively. The present data show some scatter, which is, however, still less than that observed in the data obtained in a similar experiment with a favorable streamwise pressure gradient [41]. Nevertheless, a general trend can be seen from Fig. 6.4.2.1: the increment ΔN increases with larger relative step heights $h/\delta_{1,h}$. The experimental data can be fitted using 2nd order polynomial functions, shown by the dash-dotted lines. These functions have a shape similar to the curve used to fit the data in [40,118] in the considered range $0 \le h/\delta_{1,h} \le 1.6$; they fit the experimental data better than the linear functions used in [41]. The correlation function from [38] has not been considered for this comparison, since it was calibrated for a certain set of flow parameters and was seen to fail when applied to another range of parameters [46]. The fitted function from [41] seems to represent an upper bound for the present data, a result similar to that obtained in [41] for a favorable pressure gradient. There are only a few data points in Fig. 6.4.2.1c/d (those at $h/\delta_{1,h} > 0.9$) that are above this curve. On the other hand, the approximation function from [40] seems to represent a lower bound for the present data.

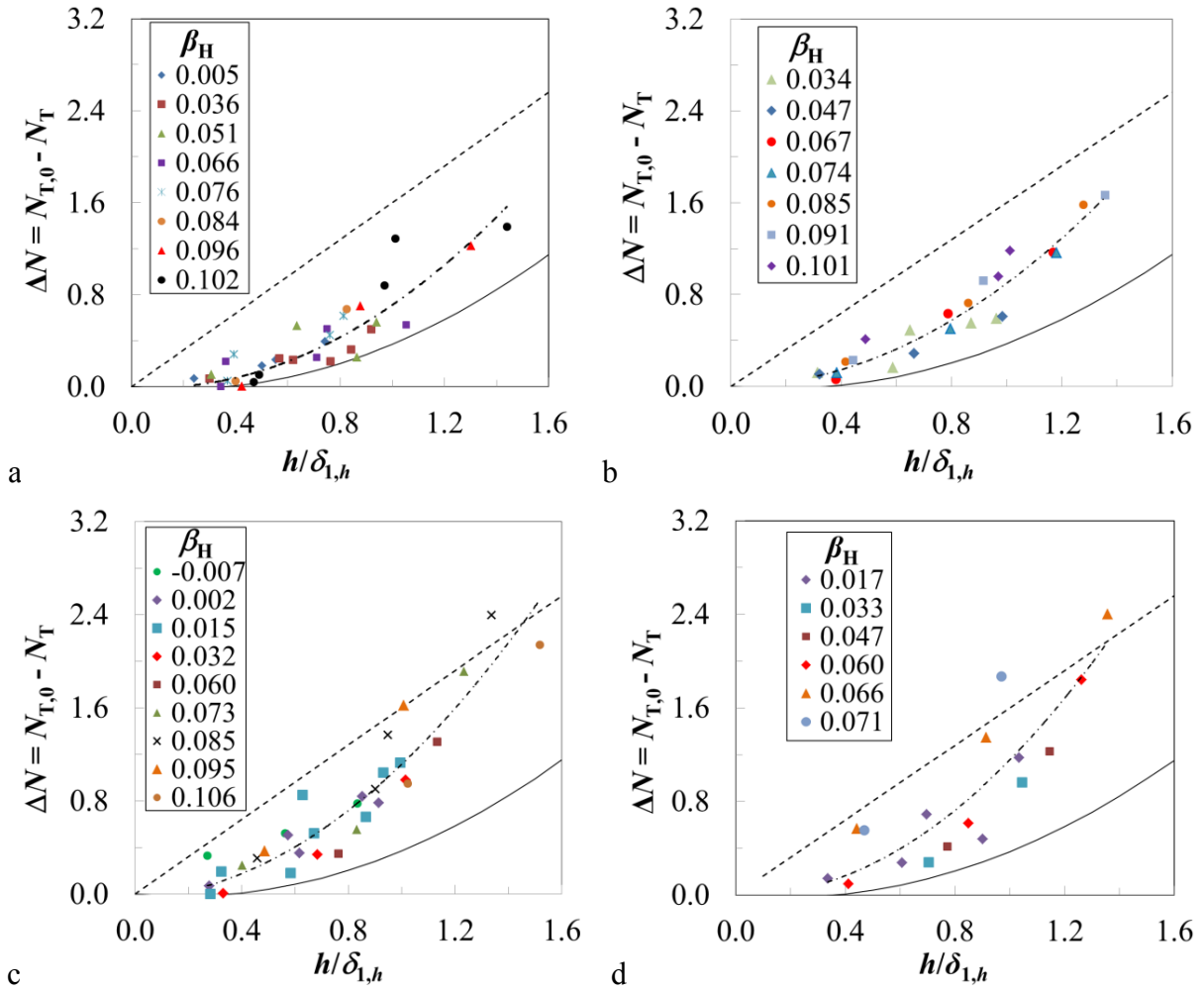

Fig. 6.4.2.1. Uniform step-induced increment of amplification factors ΔN as a function of the relative step height for different Mach numbers. a: M = 0.77, T_w/T_{aw} = 1.043-1.064; b: M = 0.65, T_w/T_{aw} = 1.037-1.057; c: M = 0.5, T_w/T_{aw} = 1.032-1.051; d: M = 0.35, T_w/T_{aw} = 1.022-1.037. Dashed-dotted lines: fitted functions of present data. Solid and dashed lines: fitted functions from [40] and [41], respectively.

With decreasing Mach number, the slope of the current fitted functions (dash-dotted lines) and, in general, the value of the increment ΔN at fixed relative step height increases. This result appears to be due to the damping influence of compressibility on ΔN, in agreement with the results obtained in [45] for Mach numbers M = 0.15 and 0.8. The streamwise pressure gradient has no clear effect on the relation between the step-induced increment ΔN and the relative step height $h/\delta_{1,h}$. In summary, the function $\Delta N = 1.6\ h/\delta_{1,h}$ [41] models conservatively the effect of forward-facing steps on the N-factor envelope curve; the present data, however, show a trend different from that given by the aforementioned function [41]. The trend is closer to that of the fitted function from [40], although the present values of ΔN are generally larger.

Another form of correlation of the experimental data with the results from linear stability computations of the smooth configuration is discussed in Appendix E.4.

6.5 Combined effect of forward-facing steps and wall temperature ratio

The effect of the wall temperature ratio T_w/T_{aw} on boundary-layer transition in the presence of forward-facing steps is discussed in this section for the two Mach numbers M = 0.77 and 0.35. The results at the other two Mach numbers, M = 0.65 and 0.5, are not analyzed in detail here, since they are in line with those at M = 0.77 and 0.35. The plots of the results obtained at M = 0.65 and 0.5 are presented in Appendix E.5. The results obtained with the step configurations at reduced T_w/T_{aw} are collected in Fig. 6.5.1 and Fig. 6.5.2, where the transition Reynolds number is plotted as a function of the Hartree parameter for the Mach numbers M = 0.77 and 0.35, respectively. The results obtained at standard T_w/T_{aw} are also shown for comparison (black symbols), but only the average value of Re_{xT} at each Hartree parameter is presented. The data points enclosed by black circles represent lower limits for Re_{xT} at these conditions, since the boundary layer had remained laminar over the whole model upper surface. For the dashed circle in Fig. 6.5.2, the boundary layer remained laminar over the whole model upper surface only with the step configurations at reduced T_w/T_{aw}, whereas transition did occur on the smooth configuration at T_w/T_{aw} = 1.022-1.036.

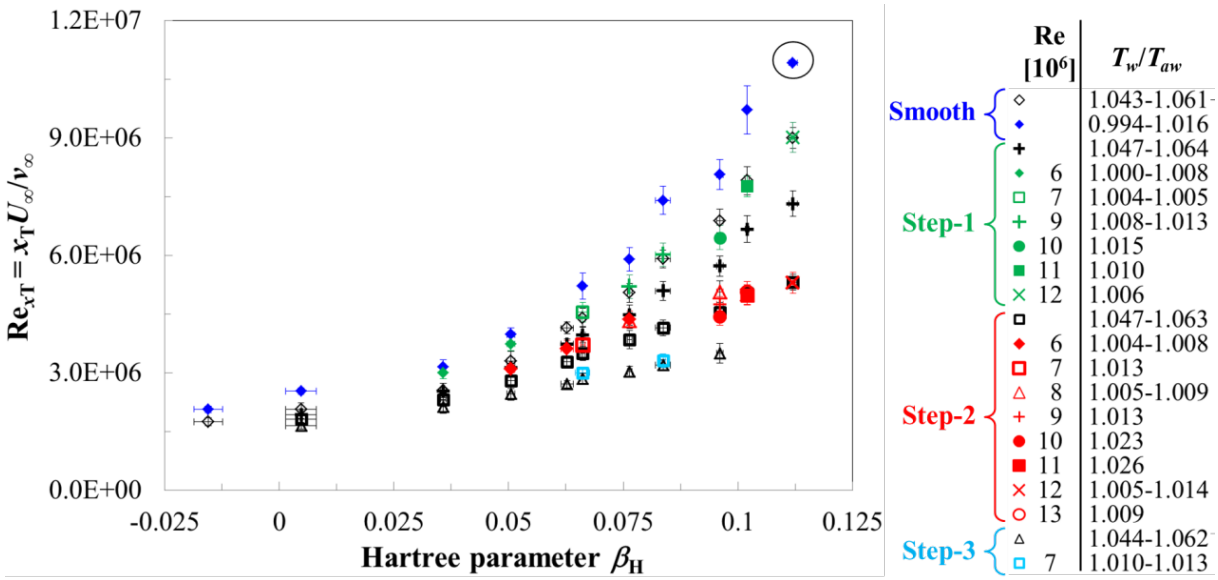

Fig. 6.5.1. Transition Reynolds number as a function of the Hartree parameter at M = 0.77.

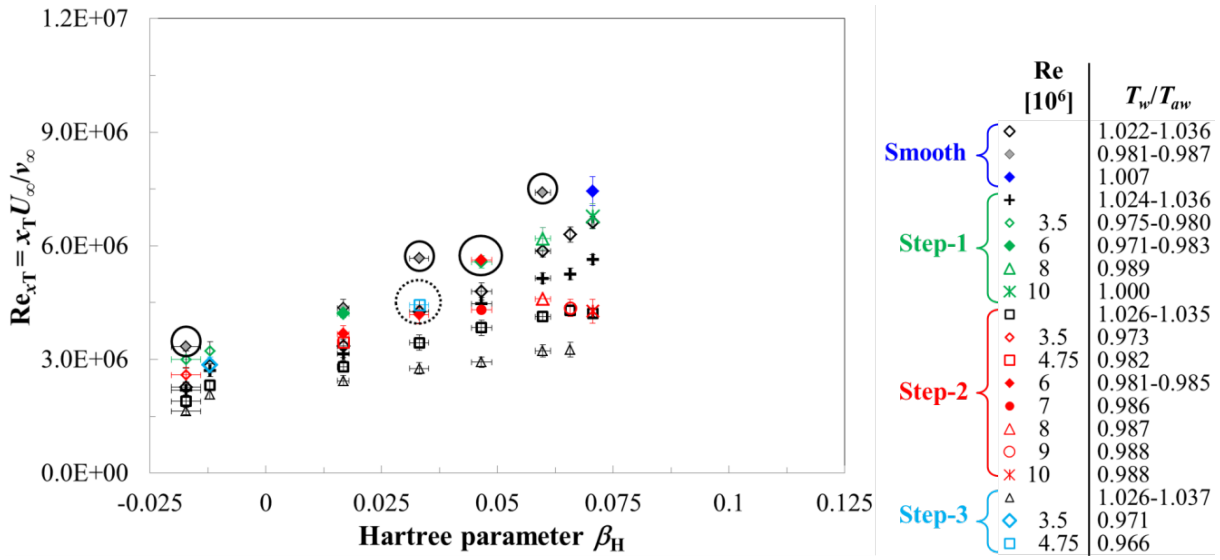

Fig. 6.5.2. Transition Reynolds number as a function of the Hartree parameter at M = 0.35.

6.5.1 Step-1 configuration ($h/\delta_{1,h} < 0.5$)

The favorable effect of a lower wall temperature ratio on boundary-layer transition can clearly be seen in Fig. 6.5.1 and Fig. 6.5.2 for the step-1 configuration. Note that the reduction of T_w/T_{aw} has a favorable effect on boundary-layer transition in the presence of forward-facing steps, even though the height of the step relative to the boundary-layer thickness becomes larger. The change in $h/\delta_{1,h}$ for the step-1 configuration is, however, not very marked: even at the largest Reynolds number considered here, $h/\delta_{1,h}$ was reduced by $\Delta(h/\delta_{1,h}) \sim 0.02$ as the wall temperature ratio was decreased from $T_w/T_{aw} = 1.063$ to 1.006. As the model surface temperature T_w was reduced to values close to or below the adiabatic wall temperature T_{aw}, the transition Reynolds number was increased to values almost coincident with those obtained with the smooth configuration at standard T_w/T_{aw}. An example of these results is shown in Fig. 6.5.1.1, where the TSP results at M = 0.77, Re = $11 \cdot 10^6$, and $\beta_H = 0.102$ are shown. A laminar run length close to that obtained with the smooth configuration is attained with the step-1 configuration by reducing T_w/T_{aw} from 1.061 to 1.010. Note in Fig. 6.5.1 and Fig. 6.5.2 that, at small and moderate pressure gradients (approximately $\beta_H < 0.07$), the values of Re_{xT} for the step-1 configuration at reduced T_w/T_{aw} were even larger than those obtained with the smooth configuration at standard T_w/T_{aw}. In these cases, the sensitivity of the transition location to the influence of the step was weaker than with larger Hartree parameters (see Section 6.2.1), so that the corresponding variation of the transition location was small. The reduction of T_w/T_{aw} led to a marked shift of the transition location.

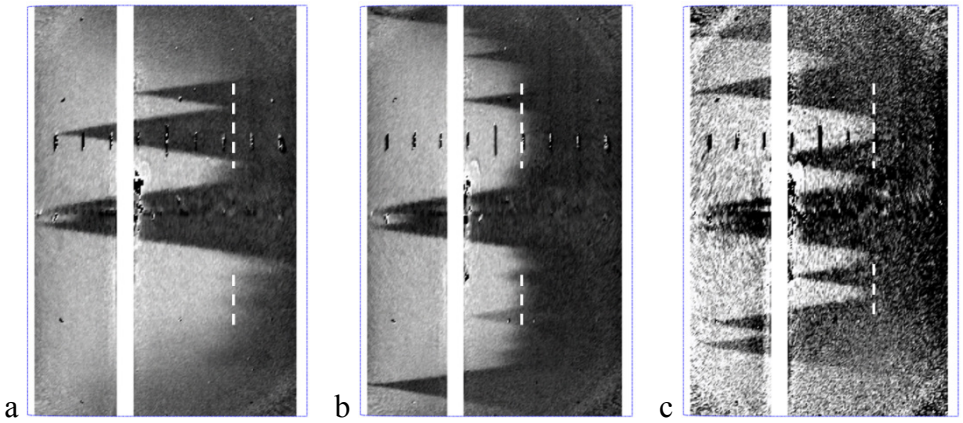

Fig. 6.5.1.1. TSP results at M = 0.77, Re = 11 · 10^6, and β_H = 0.102. a: $h/\delta_{1,h} \sim 0$, T_w/T_{aw} = 1.055, x_T/c = 73 ±1.5 %; b: $h/\delta_{1,h}$ = 0.45, T_w/T_{aw} = 1.061, x_T/c = 60 ±1 %; c: $h/\delta_{1,h}$ = 0.47, T_w/T_{aw} = 1.010, x_T/c = 70 ±2 %.

The variation in transition Reynolds number $Re_{xT}/Re_{xT,aw}$ for the step-1 configuration is plotted as a function of T_w/T_{aw} for M = 0.77 and 0.35 in Fig. 6.5.1.2 and Fig. 6.5.1.3, respectively. Colored symbols correspond to the results obtained with the step-1 configuration, whereas open black squares correspond to the data points from the smooth configuration, which have already been shown in Fig. 5.1.2.9 and Fig. 5.1.2.10. At some test conditions with the step-1 configuration, the boundary layer at reduced T_w/T_{aw} remained laminar over the whole model upper surface; the corresponding data points are indicated by open colored symbols. Power functions, fitted to the experimental data, are shown by solid lines, whereas the approximation function $Re_{xT}/Re_{xT,aw} = (T_w/T_{aw})^{-7}$ from [102,121] is shown by a dashed line. Only a few representative error bars for the results are shown. At M = 0.77, the results obtained with the step-1 configuration are in agreement (within the data scatter) with those from the smooth configuration, showing a comparable sensitivity of the transition Reynolds number to changes in wall temperature ratio. However, the data obtained with the step-1 configuration lie in the upper range of the bounds of data from the smooth configuration: these data presented a less pronounced variation of $Re_{xT}/Re_{xT,aw}$ as a function of T_w/T_{aw}. The function $Re_{xT}/Re_{xT,aw} = (T_w/T_{aw})^{-3.5}$ is used to fit the data from the step-1 configuration at M = 0.77. At M = 0.35, the sensitivity of boundary-layer transition is, in general, reduced, as compared to that observed for the smooth configuration. Nevertheless, some results obtained with the step-1 configuration are still in agreement with those from the smooth configuration. The function $Re_{xT}/Re_{xT,aw} = (T_w/T_{aw})^{-5}$ provides a better overall fit than $Re_{xT}/Re_{xT,aw} = (T_w/T_{aw})^{-7}$ [102,121], which had been used for the smooth configuration at the same Mach number (see Fig. 5.1.2.10).

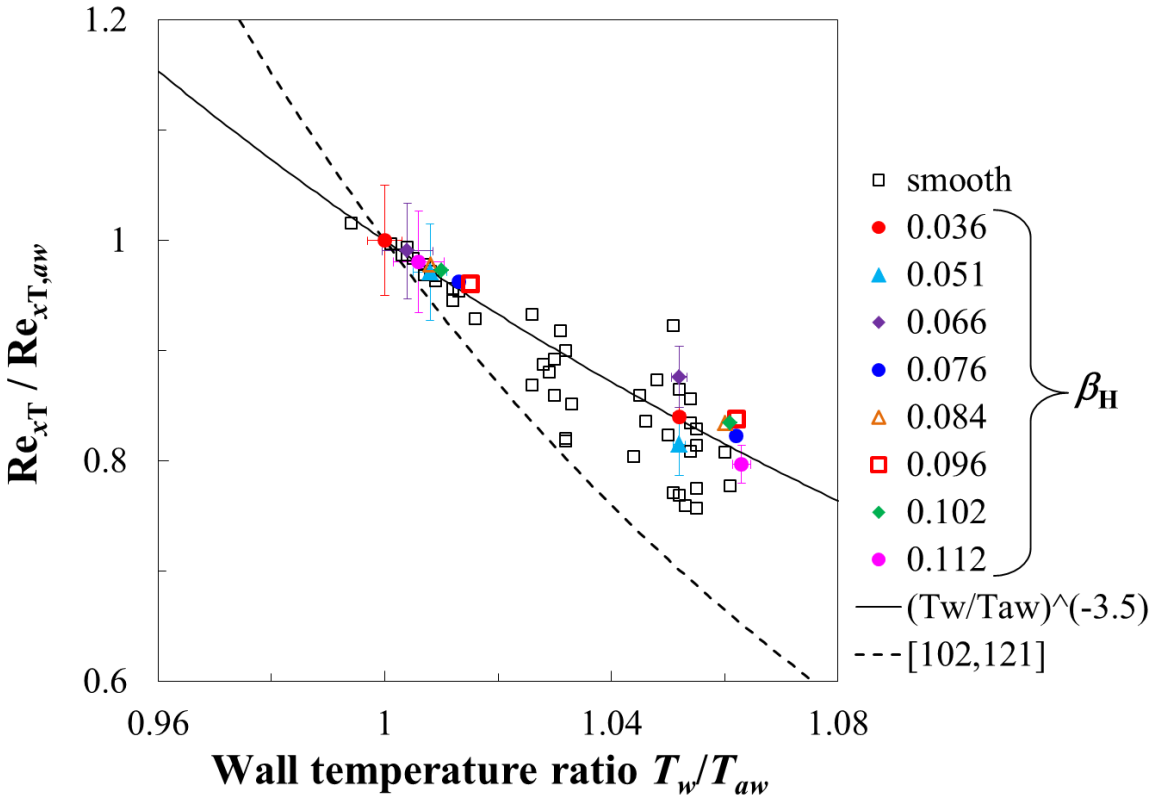

Fig. 6.5.1.2. Relative variation of transition Reynolds number as a function of the wall temperature ratio with the step-1 configuration: M = 0.77.

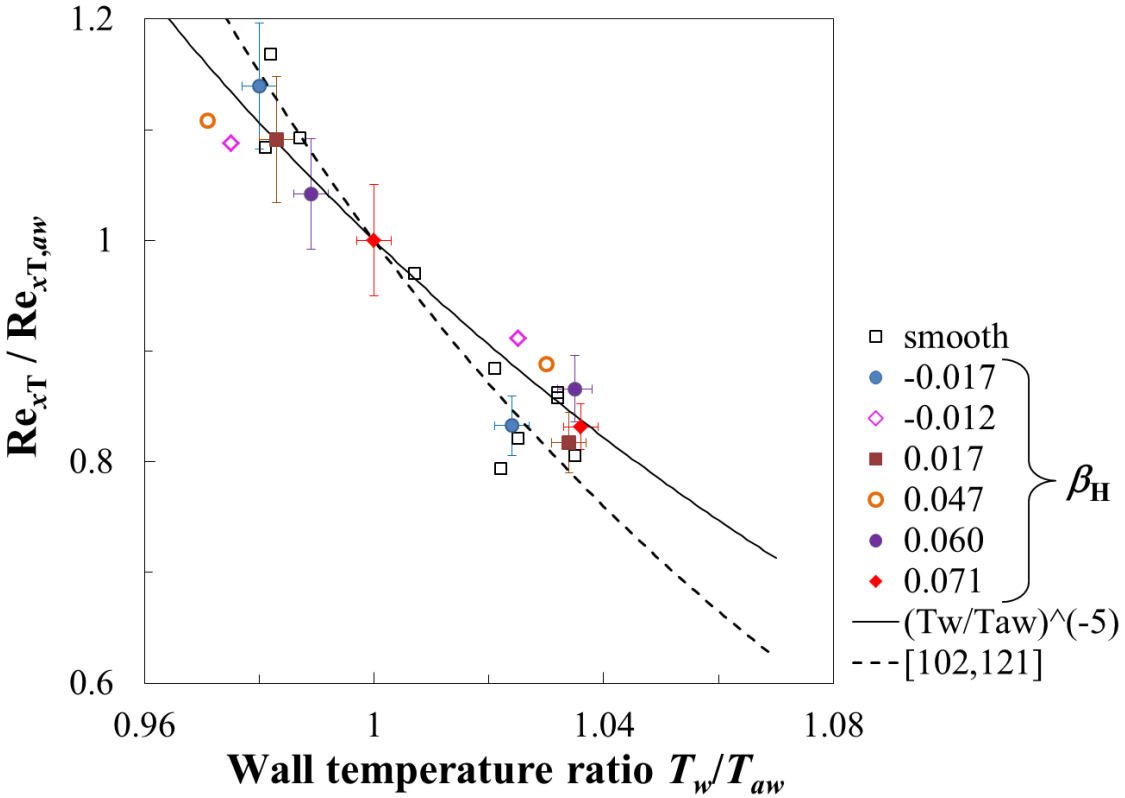

Fig. 6.5.1.3. Relative variation of transition Reynolds number as a function of the wall temperature ratio with the step-1 configuration: M = 0.35.

6.5.2 Step-2 and step-3 configurations ($0.5 \leq h/\delta_{1,h} \leq 1.5$)

Up to a certain Hartree parameter, a reduction in wall temperature ratio generally led to an increase in transition Reynolds number also for the step-2 configuration: this can be seen in Fig. 6.5.1 and Fig. 6.5.2. At these conditions, the wall temperature ratio had a favorable influence on boundary-layer transition, although the relative step height increases as the wall temperature ratio is reduced. (The change in $h/\delta_{1,h}$ was, however, less than $\Delta(h/\delta_{1,h}) \sim 0.05$ even for a variation in wall temperature ratio of $\Delta(T_w/T_{aw}) \sim 0.05$.) At M = 0.77 and $\beta_H < 0.08$, the transition Reynolds number obtained with the step-1 configuration at standard T_w/T_{aw} was almost reproduced on the step-2 configuration by reducing T_w/T_{aw}. At M = 0.35 and $\beta_H < 0.04$, the value of Re_{xT} obtained at reduced T_w/T_{aw} was close to or even larger than that obtained for the smooth configuration at T_w/T_{aw} = 1.022-1.036. At larger Hartree parameters, the increase in transition Reynolds number due to lower T_w/T_{aw} progressively decreases, until it vanishes at the largest Hartree parameters. This behavior is observed at all Mach numbers (see also Appendix E.5). An example for the change in sensitivity of boundary-layer transition to variations in T_w/T_{aw} is provided by the three cases examined at M = 0.77 and at the same Hartree parameter $\beta_H = 0.096$. The TSP results for this example are presented in Section 5.2.4 and Appendix E.6. With the step-3 configuration, only five tests at reduced wall temperature ratio were completed, as already mentioned in Section 5.2. Also with this configuration, the influence of the surface heat flux on boundary-layer transition depended on the test conditions. At M = 0.77 (see Fig. 6.5.1), the increase in transition Reynolds number observed at $\beta_H = 0.066$ and 0.084 was within the measurement uncertainty. Marked changes in the transition location due to a favorable influence of the wall temperature ratio were observed at M = 0.35 (see Fig. 6.5.2), so that the transition Reynolds number of the smooth configuration (but at larger T_w/T_{aw}) was completely recovered with the step-3 configuration at lower wall temperature ratio. Note that with the step-3 configuration at $\beta_H = 0.033$ and $T_w/T_{aw} = 0.966$ the boundary layer remained laminar over the whole upper surface of the *PaLASTra* model; the transition Reynolds number was evaluated by taking a value of x_T/c = 94 %, but this could be even larger.

The results obtained with the step-2 and step-3 configuration are collected in Fig. 6.5.2.1 and Fig. 6.5.2.2 as plots of $Re_{xT}/Re_{xT,aw}$ vs. T_w/T_{aw}. These plots are prepared in a manner analogous to that described in Section 6.5.1 for the step-1 configuration. The functions fitted to the experimental results with the step-1 configurations (see Fig. 6.5.1.2 and Fig. 6.5.1.3) are shown by dashed lines.

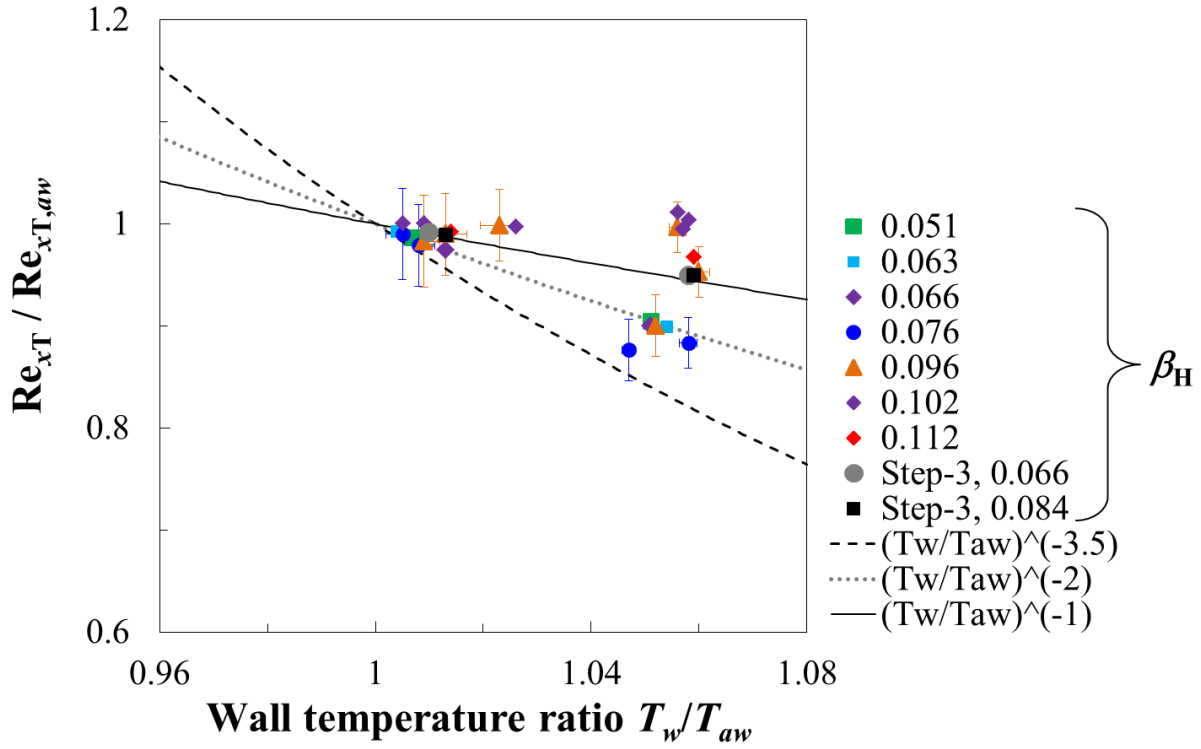

Fig. 6.5.2.1. Relative variation of transition Reynolds number as a function of the wall temperature ratio at M = 0.77. Step-2 and step-3 configurations.

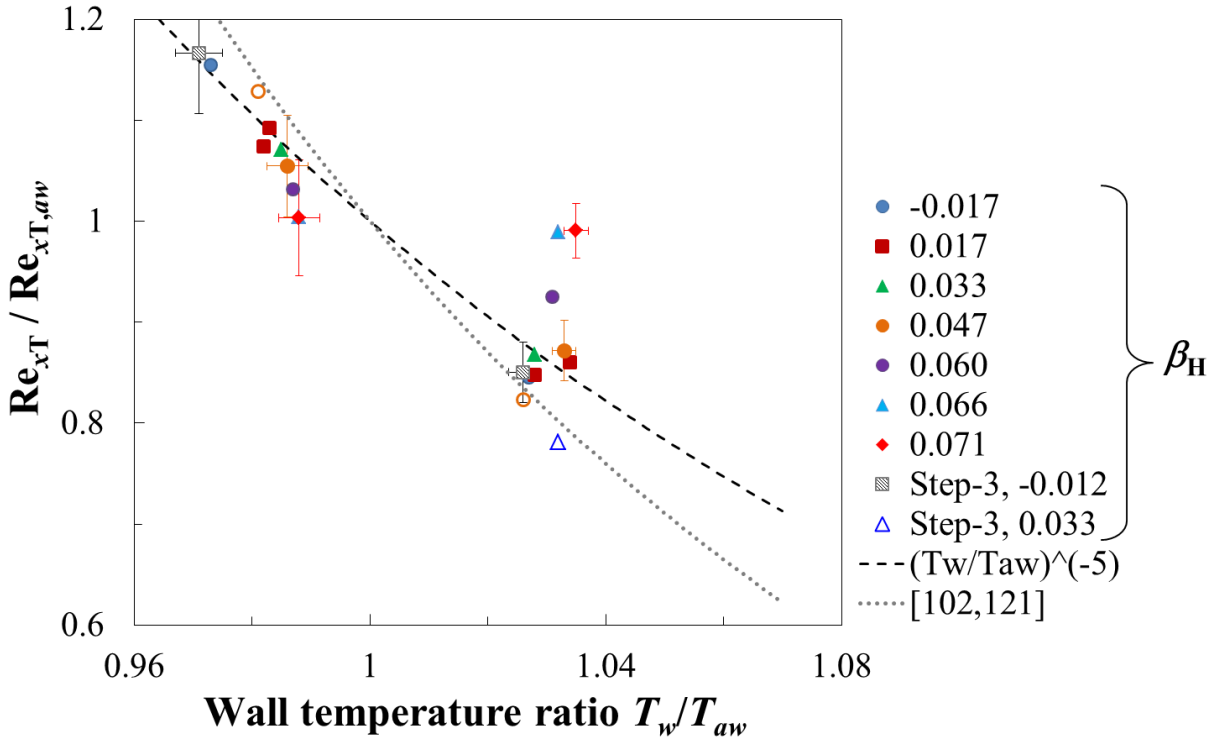

Fig. 6.5.2.2. Relative variation of transition Reynolds number as a function of the wall temperature ratio at M = 0.35. Step-2 and step-3 configurations.

In general, the sensitivity of boundary-layer transition to changes in wall temperature ratio is further reduced with the step-2 and step-3 configurations, as compared to that of the step-1 configuration (and, clearly, also to that of the

smooth configuration). At least two groups of data can be identified in these plots. At M = 0.77, a first group of data shows a variation of $Re_{xT}/Re_{xT,aw}$ with changing wall temperature ratio which can be fitted by the function $Re_{xT}/Re_{xT,aw} = (T_w/T_{aw})^{-2}$ (dotted line in Fig. 6.5.2.1). A second group of data presents a sensitivity to changes in T_w/T_{aw} that is lower than that of the first group; the data are better fitted by the function $Re_{xT}/Re_{xT,aw} = (T_w/T_{aw})^{-1}$ (solid line in Fig. 6.5.2.1). The remaining data at M = 0.77 show that the transition Reynolds number is nearly independent of the wall temperature ratio. The trends found at M = 0.35 are generally different from those at M = 0.77. Although the data points at $\beta_H \geq 0.06$ show a reduced or even negligible variation of $Re_{xT}/Re_{xT,aw}$, all other results present a sensitivity of the transition Reynolds number to changes in T_w/T_{aw} that is comparable to that observed with the step-1 configuration. In some cases, the data points are well fitted by the function $Re_{xT}/Re_{xT,aw} = (T_w/T_{aw})^{-7}$, which was used to fit the results obtained with the smooth configuration (see Fig. 5.1.2.10); this is shown in Fig. 6.5.2.2 by a dotted line.

6.5.3 Analysis and discussion of the results

The different sensitivity of the transition Reynolds number to changes in T_w/T_{aw} may be related to the value of the non-dimensional step parameter at which transition is examined. In order to analyze this effect, the change in transition location $s = (x_T-x_h)/(x_{T,0}-x_h)$ at M = 0.77 is plotted as a function of Re_h and $h/\delta_{1,h}$ in Fig. 6.5.3.1. These plots are analogous to those shown in the previous sections, such as those in Fig. 6.4.1 and Fig. 6.4.2. The results obtained at reduced wall temperature ratio are also plotted against $h/\delta_{1,h}$ obtained at standard T_w/T_{aw} for the same test conditions. This is not strictly correct, because $h/\delta_{1,h}$ increases slightly as T_w/T_{aw} is reduced, but this choice facilitates the comparison of the results obtained with different thermal conditions on the model surface. The results obtained at standard wall temperature ratio are shown by red symbols, with the corresponding fitted function being shown by a red line. The results obtained at reduced wall temperature ratio are shown by blue symbols. Note here that the value of $x_{T,0}$ used to determine s for these data points is also that obtained at standard T_w/T_{aw}. At approximately $Re_h < 1500$ and $h/\delta_{1,h} < 0.5$ (i.e., with the step-1 configuration), a reduction of T_w/T_{aw} led to a displacement of transition location to an even more downstream position than $x_{T,0}$. Thereby, values of s even larger than one were obtained. The very large values of s pertain to cases with $x_{T,0}$ quite close to the step location x_h, i.e., with small values of the denominator in s. As an example, at M = 0.77, $\beta_H = 0.036$, and $Re_h \sim 870$ ($h/\delta_{1,h} \sim 0.3$), the measured transition locations $x_{T,0}/c = 44$ % and $x_T/c = 51$ % led to an increase in s to about 180 %. With increasing step Reynolds number and relative step height, the difference between the values of s obtained at standard and reduced T_w/T_{aw} decreased progressively. The data points at reduced wall temperature ratio are quite well fitted by 3rd and 2nd order

polynomial functions in Fig. 6.5.3.1a and Fig. 6.5.3.1b, respectively; these functions are shown as blue lines.

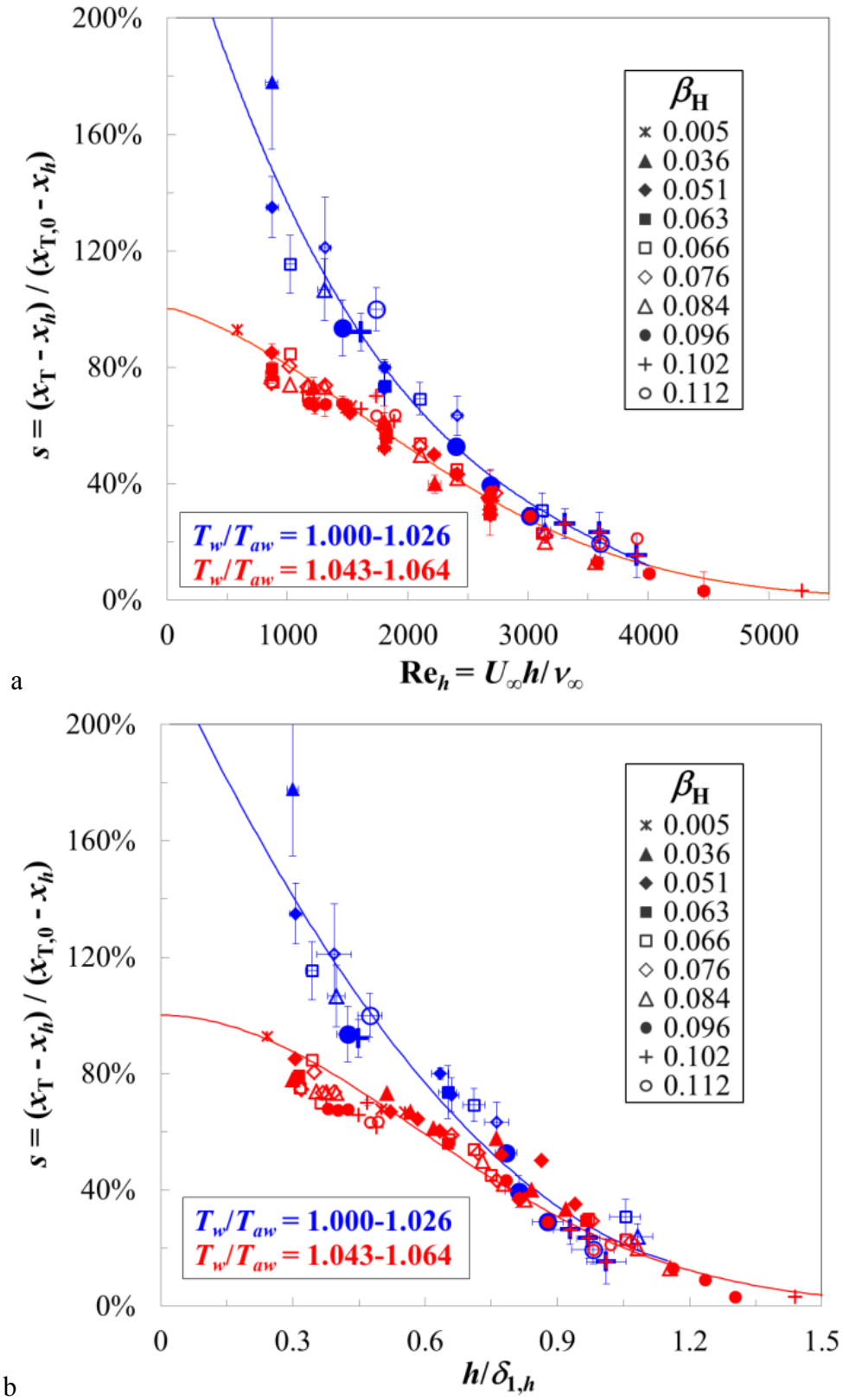

Fig. 6.5.3.1. Relative change in transition location at M = 0.77 as a function of the step Reynolds number (a) and of the relative step height (b).

At $\mathrm{Re}_h \sim 2700$ and $h/\delta_{1,h} \sim 0.8$ there seems to be a change in sensitivity of the transition location to variations in T_w/T_{aw}. At values of Re_h and $h/\delta_{1,h}$ lower than these critical values, boundary-layer transition is influenced by the surface heat flux. This influence becomes weaker with increasing step Reynolds number and relative step height. The values of s obtained at standard and reduced T_w/T_{aw} are essentially coincident for $\mathrm{Re}_h > 2700$ and $h/\delta_{1,h} > 0.8$: at these conditions, a change in the wall temperature ratio (in the examined range) has a negligible effect on boundary-layer transition in the presence of forward-facing steps. It should be emphasized that, although the transition location is insensitive to variations in T_w/T_{aw}, it is not so close to the step location: it has occurred already for approximately $20\ \% < s < 40\ \%$. This different behavior of boundary-layer transition with respect to changes in T_w/T_{aw} can be explained as the result of the following effects, which counteract the favorable influence of the wall temperature ratio:

- A first effect that leads to weakening of the influence of the wall temperature ratio on boundary-layer transition is the step-induced amplification of streamwise instabilities in the vicinity of the step location. This effect is analogous to that discussed in Section 6.2.2 with respect to the effect of the pressure gradient. To a first approximation, the disturbance amplification due to the presence of the step can be taken as independent of the wall temperature ratio: this has been observed in results from DNS at $\mathrm{M} = 0.8$ [45], where an increase in wall temperature ratio from $T_w/T_{aw} \sim 0.9$ to 1 did not lead to major changes in the step-induced increment of the amplification factors $\Delta N(x)$. With increasing non-dimensional step parameters (e.g., Re_h and $h/\delta_{1,h}$), this contribution to the overall amplification of the disturbances increases, and the step-independent contribution accordingly decreases. The growth rates of streamwise instabilities in the regions far away from the step location are still decreased by a reduction in wall temperature ratio, but this effect leads to smaller displacements of the transition location, as compared to those observed with the smooth configuration. This is consistent with the general reduction of the variation of $\mathrm{Re}_{x\mathrm{T}}/\mathrm{Re}_{x\mathrm{T},aw}$ as a function of T_w/T_{aw} in the presence of larger steps, which has been seen in Sections 6.5.1 and 6.5.2.
- Another finding that has to be considered is the different sensitivity of boundary-layer transition to variations in T_w/T_{aw}, which had been observed for the step-2 and step-3 configurations (see Fig. 6.5.2.1 and Fig. 6.5.2.2). This is illustrated for three cases with the step-2 configuration at $\mathrm{M} = 0.77$ and $\beta_\mathrm{H} = 0.096$ but at different chord Reynolds numbers. The corresponding data points in Fig. 6.5.2.1 (orange triangles) have different values of $\mathrm{Re}_{x\mathrm{T}}/\mathrm{Re}_{x\mathrm{T},aw}$ in the range $1.05 \le T_w/T_{aw} \le 1.06$, even though T_w/T_{aw} varies little. The surface pressure distributions in the region around the step location are shown in Fig. 6.5.3.2a.

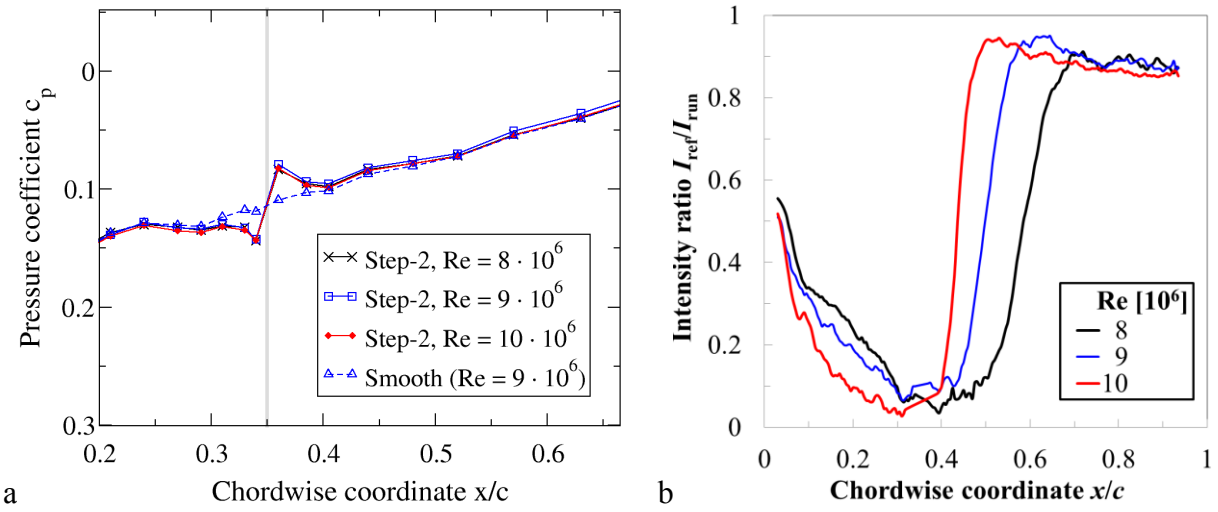

Fig. 6.5.3.2. Results obtained for different chord Reynolds numbers at M = 0.77, β_H = 0.096, and standard T_w/T_{aw}. Step-2 configuration. a: surface pressure distributions near the step location. The gray bar indicates the step location. b: normalized intensity distributions extracted at y/b = 0.36 from the TSP results.

As already discussed in Section 5.2.2, the pressure coefficients at different chord Reynolds numbers are essentially coincident. However, transition occurs in regions where the local pressure gradients are different. The TSP results for these three cases are shown in Section 5.2.4 and Appendix E.6. The chordwise intensity distributions from the TSP results, obtained at the spanwise location $y/b = 0.36$, are shown in Fig. 6.5.3.2b. The location where transition starts is $x_{T,start} \sim 40$ % and 50 % at Re = 10 and $8 \cdot 10^6$, respectively. The local pressure gradient is still adverse in the first case, whereas in the second case the favorable global pressure gradient has been recovered already. As shown in [145], boundary-layer transition is less sensitive to changes in the wall temperature ratio when it occurs in a region of adverse pressure gradient. Note also that the natural-transition front is in this case quite a straight line (see Fig. 5.2.4.4): this is consistent with the local adverse pressure gradient. An adverse pressure gradient results in a large gradient of the *N*-factor envelope curve, as shown semi-quantitatively in Fig. 6.5.3.3a for the aforementioned case at Re = $10 \cdot 10^6$. The envelope curves obtained for the smooth and step-2 configurations are shown by a black dashed line and a red solid line, respectively. It should be emphasized that the *N*-factors computed for the step-2 configuration are not correct, since the amplification of streamwise instabilities near the step location cannot be captured with the used numerical tools [196,197]. The *N*-factor envelope curve for the step-2 configuration is presented in Fig. 6.5.3.3a only for illustrative purposes, since it strictly follows the changes in the streamwise pressure distribution (shown by a thin black line). *N*-factor envelope curves computed by means of linear stability theory and DNS for a flat plate with zero pressure gradient [46] are shown for comparison in Fig. 6.5.3.3b.

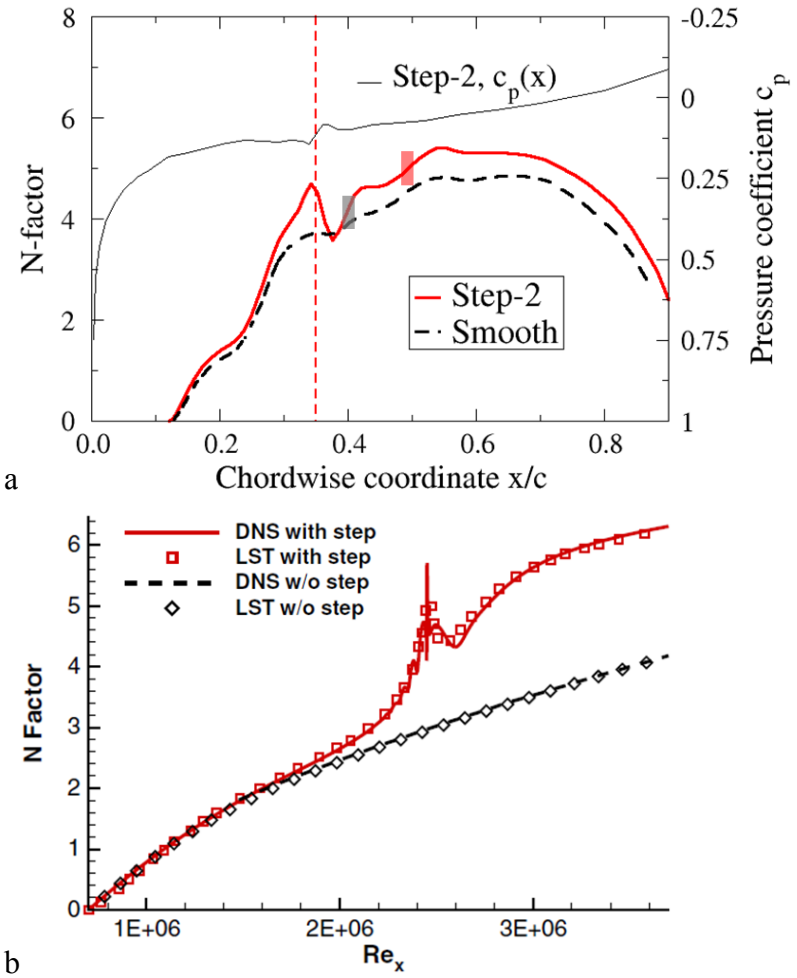

Fig. 6.5.3.3. Distributions of amplification factors of streamwise instabilities (envelopes only). a: present experiment at Re = 10 · 10^6, M = 0.77, β_H = 0.096, and standard T_w/T_{aw}, computed using linear stability theory. (The amplification factors close to the step have not been captured correctly – see text.) The red dashed line indicates the step location. b: M = 0.8, β_H = 0, T_w/T_∞ = 1, Re$_{xh}$ = 2.45 · 10^6, Re$_h$ = 2640, and h/θ_h ~ 2.4, results from linear stability theory (LST) and DNS from [46], with permission.

The slope of the *N*-factor envelope curve in the region at $\Delta Re_x \sim 0.5 \cdot 10^6$ downstream of the step location (which is at $Re_{xh} = 2.45 \cdot 10^6$) is larger than that of the smooth-configuration curve. A similar behavior is observed in the present work in the region 37 % < *x*/*c* < 44 % (see Fig. 6.5.3.3a). At Re = 10 · 10^6, transition starts approximately in the middle of the region where $\partial N/\partial(x/c)$ is large; this location is shown by a gray bar. The sensitivity of boundary-layer transition to changes in T_w/T_{aw} is expected to be low in this case. In contrast, at Re = 8 · 10^6, transition starts in the region of (recovered) favorable pressure gradient downstream of the step location, where $\partial N/\partial(x/c)$ is small. This location is indicated by a red bar in Fig. 6.5.3.3a. (The *N*-factor envelope curve for Re = 8 · 10^6 is not shown here; it has a similar shape to that for Re = 10 · 10^6, but with lower values of the *N*-factors.) Boundary-layer transition is expected to be more sensitive to changes in T_w/T_{aw} at Re = 8 · 10^6 than at Re = 10 · 10^6: this is

confirmed by the experimental observations. The results at $\mathrm{Re} = 9 \cdot 10^6$ are similar to those obtained at $\mathrm{Re} = 10 \cdot 10^6$: very likely, this is due to the influence of the local adverse pressure gradient on boundary-layer transition ($x_{\mathrm{T,start}} \sim 43$ %).

- Although a reduction of T_w/T_{aw} has a favorable influence in the attached flow regions, it also leads to an increase of the amplification factors in the separated flow regions. This effect has been discussed in numerical studies of a smooth backward-facing step placed on a flat plate at zero pressure gradient [164]. For the same test case, a similar influence was observed for wall suction, which was found to have a destabilizing influence in the separation bubble [184]. (The overall effect of continuous suction was, however, found to be stabilizing.) In the experiments on sharp backward-facing steps presented in [183], the effect of localized suction was shown to depend strongly on the location of the suction region. Suction slots located slightly upstream of the reattachment location were the most effective in preventing transition, because they markedly reduced the streamwise extent of the separated flow region. In contrast, the favorable effect of localized suction in the region downstream of reattachment was weak, and became even detrimental when the suction slots were placed in the separated flow region immediately downstream of the step. Both these stabilizing and destabilizing effects of wall cooling and wall suction are basically due to the increase in wall curvature of the mean-velocity profile. This can be seen in Eq. (2.3.1): when the flow is attached, the velocity gradient at the wall is positive, $(\partial U/\partial z)_w > 0$, and the effect of wall cooling (suction) is to make more negative the curvature of the mean-velocity profile at the wall. However, when the flow is separated, the velocity gradient at the wall is negative, $(\partial U/\partial z)_w < 0$, and wall cooling (suction) leads to a more positive curvature of the mean-velocity profile at the wall (although the mean-velocity profiles "are still fuller away from the wall" [164]). The reversed mean-velocity profile is more pronounced at lower wall temperature ratios (see also [255]), leading to larger growth rates in the separated flow region [164]. Thus, a reduction in wall temperature ratio has three effects: first, it reduces the growth rates in the attached flow region; secondly, it reduces the size of the separated flow regions; and thirdly, it enhances amplification in the separated flow regions. For a flat plate at zero pressure gradient, numerical investigations performed up to M = 0.8 showed that there exists a critical value of T_w/T_{aw} below which the overall effect of surface cooling in the presence of smooth backward-facing steps and cubic bumps is destabilizing [164]. This counteracting effect in the separated flow regions, as opposed to a favorable effect in the attached flow regions, is an additional contribution to the reduction of sensitivity of boundary-layer transition to changes in T_w/T_{aw} in the presence of forward-facing steps. The amplification of

streamwise instabilities in the separated flow regions becomes more pronounced at larger values of Re_h and $h/\delta_{1,h}$, and this is further enhanced by a reduced wall temperature ratio; therefore, the aforementioned counteracting effect is also expected to become more pronounced at larger values of Re_h and $h/\delta_{1,h}$.

- Finally, the boundary layer becomes thinner with decreasing wall temperature ratio, which leads to larger values of the relative step height. (The step Reynolds number Re_h remains unchanged.) This variation seems negligible for the range of $h/\delta_{1,h}$ examined with the step-1 configuration ($\Delta(h/\delta_{1,h}) \leq 0.02$), but can have a (small) influence on boundary-layer transition for the step-2 and step-3 configurations, where $\Delta(h/\delta_{1,h}) \leq 0.05$. This variation in $h/\delta_{1,h}$ due to a change in T_w/T_{aw} was, however, smaller than or comparable to the uncertainty in $h/\delta_{1,h}$.

The results obtained at M = 0.35 are now analyzed in the light of the above considerations. The change in transition location $s = (x_T\text{-}x_h)/(x_{T,0}\text{-}x_h)$ is plotted as a function of Re_h and $h/\delta_{1,h}$ in Fig. 6.5.3.4, in the same manner as for Fig. 6.5.3.1 at M = 0.77. The data points at reduced wall temperature ratio are approximately fitted by 2nd order polynomial functions, shown in Fig. 6.5.3.4 as blue lines. A glance at these two figures shows that the experimental data at lower T_w/T_{aw} are more scattered than in the corresponding plots at M = 0.77; this is especially noticeable when plotted as s vs. $h/\delta_{1,h}$ (Fig. 6.5.3.4b). Nevertheless, a clear increase in laminar run length with reduced wall temperature ratio can be seen at step Reynolds numbers up to $\mathrm{Re}_h \sim 2700$ and for most of the examined values of $h/\delta_{1,h}$. In many cases, the transition location in the presence of forward-facing steps but at smaller T_w/T_{aw} was even at a more downstream position than that obtained with the smooth configuration at standard T_w/T_{aw}, leading to $s > 1$. In general, the difference between the values of s obtained at M = 0.35 at standard and reduced wall temperature ratios decreases at larger Re_h and $h/\delta_{1,h}$, but the trends are less obvious than those observed at M = 0.77. In the case of s vs. Re_h (Fig. 6.5.3.4a), no appreciable shift of the transition location due to changes in T_w/T_{aw} was observed at $\mathrm{Re}_h > 2700$, whereas a clear limiting value of this type for the relation s vs. $h/\delta_{1,h}$ could not be found.

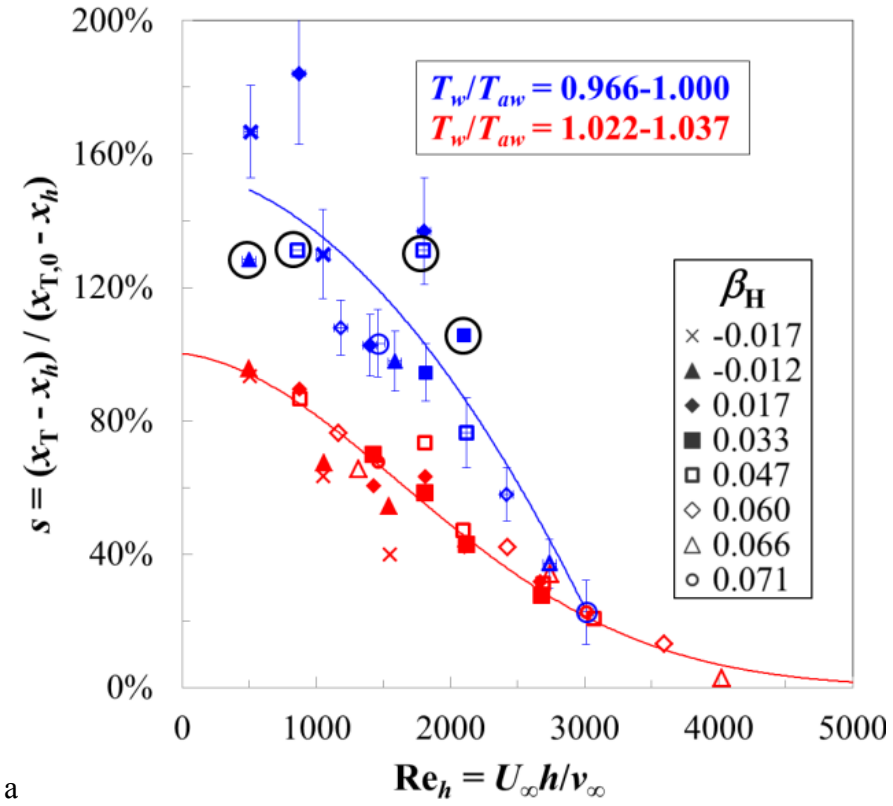

a

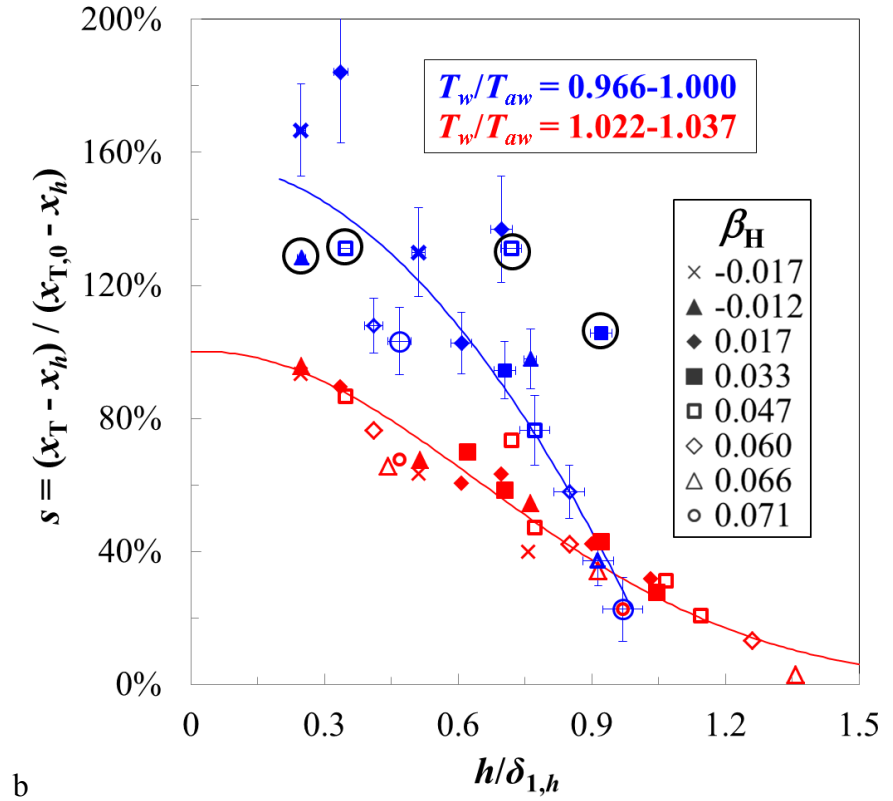

b

Fig. 6.5.3.4. Relative change in transition location at M = 0.35 as a function of the step Reynolds number (a) and of the relative step height (b).

The scatter of the data at reduced T_w/T_{aw} is partially due to the different values of T_w/T_{aw} that were implemented: the scatter in the values of T_w/T_{aw} was generally more pronounced than that at larger Mach numbers. For example, the values of

wall temperature ratio for the cases at $h/\delta_{1,h} = 0.41$ ($\beta_H = 0.060$), 0.47 ($\beta_H = 0.071$), and 0.51 ($\beta_H = -0.017$) are: $T_w/T_{aw} = 0.989$, 1, and 0.973, respectively; the corresponding values of s are: $s = 108$ %, 103 %, and 130 %. Moreover, the boundary layer remained laminar over the whole upper surface of the model in some of the cases at reduced wall temperature ratio. The corresponding data points in Fig. 6.5.3.4 are enclosed by black circles. In these cases, the value assigned to the transition location was $x_T/c = 94$ %, but even larger values may have been possible if the model chord length would have been larger. Nevertheless, the different results obtained at $h/\delta_{1,h} \sim 0.91$-0.92 are due to the different sensitivity of boundary-layer transition to changes in T_w/T_{aw}; this can be seen also in Fig. 6.5.2.2 (step-2 configuration at $\beta_H = 0.066$ and step-3 configuration at $\beta_H = 0.033$). For the case at $\beta_H = 0.066$, which was examined at $Re = 9 \cdot 10^6$, transition was measured at $x_T/c = 47$ % at $T_w/T_{aw} = 1.032$; a reduction of the wall temperature ratio to $T_w/T_{aw} = 0.988$ led only to a negligible change in the transition location. At $\beta_H = 0.033$, $Re = 4.75 \cdot 10^6$, and $T_w/T_{aw} = 1.032$, transition was found at $x_T/c = 59$ %, but the boundary layer remained laminar over the whole upper surface of the model as the wall temperature ratio was reduced to $T_w/T_{aw} = 0.966$. The TSP results demonstrating this large effect of the wall temperature ratio on boundary-layer transition are shown in Fig. 6.5.3.5.

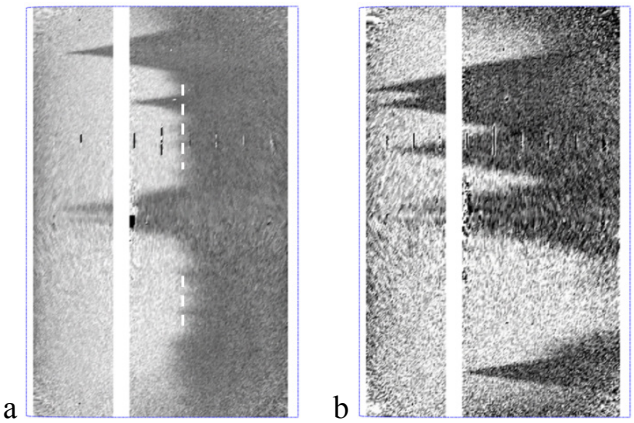

Fig. 6.5.3.5. TSP results at M = 0.35, Re = 4.75 · 10^6, and $\beta_H = 0.033$. a: $h/\delta_{1,h} = 0.92$, $T_w/T_{aw} = 1.032$, $x_T/c = 59 \pm 1.1$ %; b: $h/\delta_{1,h} = 0.96$, $T_w/T_{aw} = 0.966$, no transition. In this latter TSP result, the wind-on images were divided by the wind-off images (I_{run}/I_{ref}).

The surface pressure distributions for the two cases discussed above (step-2 configuration at $\beta_H = 0.066$ and step-3 configuration at $\beta_H = 0.033$) are shown in Fig. 6.5.3.6a. The corresponding chordwise intensity distributions for the step configurations at standard T_w/T_{aw}, obtained from the TSP results at the spanwise location $y/b = 0.64$, are presented in Fig. 6.5.3.6b. In the first of the two aforementioned cases ($\beta_H = 0.066$), transition was initiated at $T_w/T_{aw} = 1.032$ in the recovery region downstream of the step location, where the pressure gradient is adverse (and the slope of the N-factor envelope curve is pronounced); for the reasons discussed above with regard to the cases at M = 0.77, the sensitivity of

boundary-layer transition to changes in T_w/T_{aw} is low under these conditions. In contrast, transition was measured in the second case ($\beta_H = 0.033$) at $x_T/c = 59$ %, in a region where the streamwise pressure gradient of the smooth configuration has been already recovered: the transition sensitivity to variations in the wall temperature ratio is large under these conditions, in line with the previous considerations.

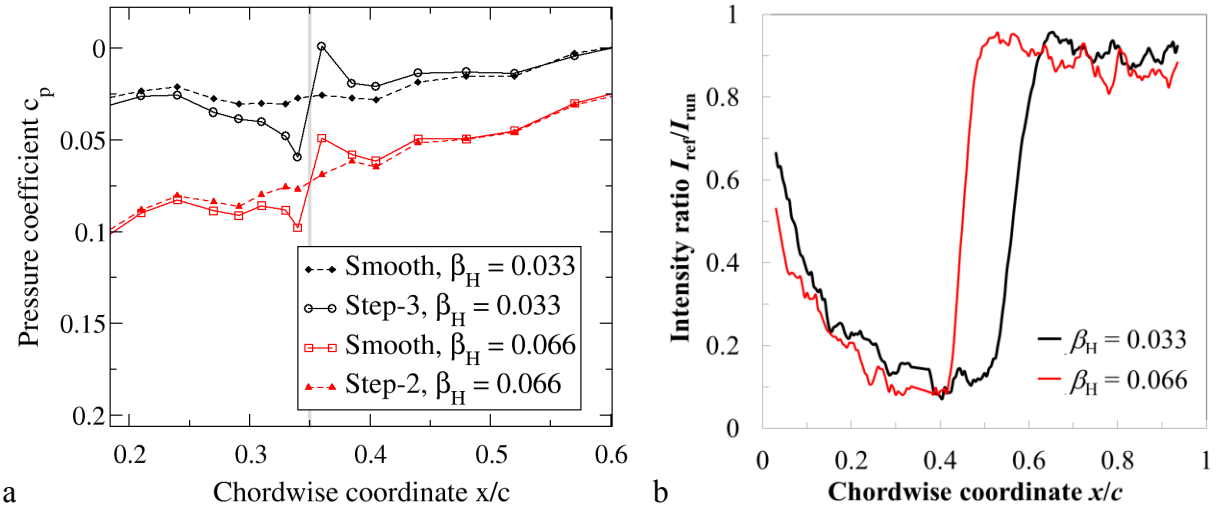

Fig. 6.5.3.6. Results obtained for test conditions at M = 0.35 that showed different sensitivity of boundary-layer transition to changes in T_w/T_{aw}. The shown results were obtained at standard T_w/T_{aw}. a: surface pressure distributions (zoomed-in around the step location). The gray bar indicates the step location. b: normalized intensity distributions obtained at $y/b = 0.64$ from the TSP results in the presence of the steps.

In conclusion, up to $h/\delta_{1,h} \sim 0.8$-0.9, a reduction in the wall temperature ratio allowed larger laminar runs to be achieved for all considered Mach numbers, independent of the value of the transition location at standard T_w/T_{aw}. At $h/\delta_{1,h} > 0.8$-0.9, transition was still influenced by the thermal condition at the model surface when it occurred at approximately $x_T/c > 48$-52 % (measured at standard T_w/T_{aw}), whereas the change in transition location for $x_T/c < 48$-52 % was found to be negligible. Details on the conditions under which boundary-layer transition at M = 0.35 and 0.77 was sensitive to changes in the wall temperature ratio are given in Appendix E.7. In any case, $Re_h \sim 2700$ appears as a limiting value for temperature effects on boundary-layer transition at all examined Mach numbers, at least for the variation of T_w/T_{aw} attainable in these tests. Plotting the results as s vs. Re_k does not provide significant new information, as compared to that obtained from the analysis of the plots s vs. Re_h and s vs. $h/\delta_{1,h}$. Thus, these plots are presented in Appendix E.8. Note here, however, that a limiting value for effects of the wall temperature ratio on boundary-layer transition of approximately $Re_k = 1200$ has been identified for all four Mach numbers examined in this work.

6.5.4 Effect of forward-facing steps on boundary-layer transition at the same, reduced wall temperature ratio

It is now interesting to examine the relative change in transition location due to the effect of forward-facing step with respect to the value measured at the same, reduced wall temperature ratio: this enables one to demonstrate whether the functional relations obtained at standard T_w/T_{aw} (Sections 6.2 to 6.4) hold also for different thermal conditions at the model surface. In this case, the value of $x_{T,0}$ used to evaluate the relative change in transition location $s = (x_T-x_h)/(x_{T,0}-x_h)$ is that measured with the smooth configuration but at reduced T_w/T_{aw}. The results obtained at M = 0.77 are plotted as s vs. Re_h in Fig. 6.5.4.1a. The function fitted to the experimental data at standard T_w/T_{aw} (see Fig. 6.2.2.2) is shown by a solid line in the figure. Note that the number of experimental data present in these plots is markedly reduced as compared to that in Fig. 6.2.2.2, since the number of completed runs at reduced T_w/T_{aw} had been strongly limited by surface contamination (see Appendix C.2.1). The results in Fig. 6.5.4.1a show a trend similar to that observed for the cases at standard T_w/T_{aw}. The larger deviations of the experimental data from the fitted function are mainly due to different values of T_w/T_{aw} for x_T and $x_{T,0}$: for example, in the case of the data point at $\beta_H = 0.076$ and $Re_h = 2400$, x_T and $x_{T,0}$ were measured at $T_w/T_{aw} = 1.005$ and 1.031, respectively. A means to compensate for these differences is, however, available when transition is measured for both configurations (with and without steps) and at both wall temperature ratios (standard and reduced T_w/T_{aw}). If these four measurements are available, the adiabatic wall transition locations $x_{T,aw}$ and $x_{T0,aw}$ for step configuration and smooth configuration, respectively, can be evaluated. The relative change in transition location is defined in this case as $s_{aw} = (x_{T,aw} - x_h) / (x_{T0,aw} - x_h)$. The adiabatic wall transition locations $x_{T0,aw}$ and $x_{T,aw}$ are obtained from the adiabatic wall transition Reynolds number $Re_{xT0,aw}$ and $Re_{xT,aw}$, respectively (see Sections 5.1.2, 6.5.1, and 6.5.2), as $x_{T0,aw} = Re_{xT0,aw}/Re$ and $x_{T,aw} = Re_{xT,aw}/Re$. The relative change in transition location s_{aw} at M = 0.77 is plotted as a function of Re_h in Fig. 6.5.4.1b. The step Reynolds number Re_h is that obtained at reduced T_w/T_{aw}. (This choice has a negligible influence on the representation of the results, since Re_h is independent of T_w/T_{aw}.) After the data had been "corrected" for adiabatic wall conditions, the plot provided an even better correlation of the experimental results, as compared to that presented in Fig. 6.5.4.1a. This confirms the influence of the wall temperature ratio on the data scatter observed in several figures, where the relative change in transition location $s = (x_T-x_h)/(x_{T,0}-x_h)$ was used to represent the results (see, e.g., Fig. 6.2.2.2, Fig. 6.2.2.3, and Fig. 6.3.2 to Fig. 6.3.4). The experimental data in Fig. 6.5.4.1b are well approximated by the function determined at standard T_w/T_{aw}, which is shown by a solid line.

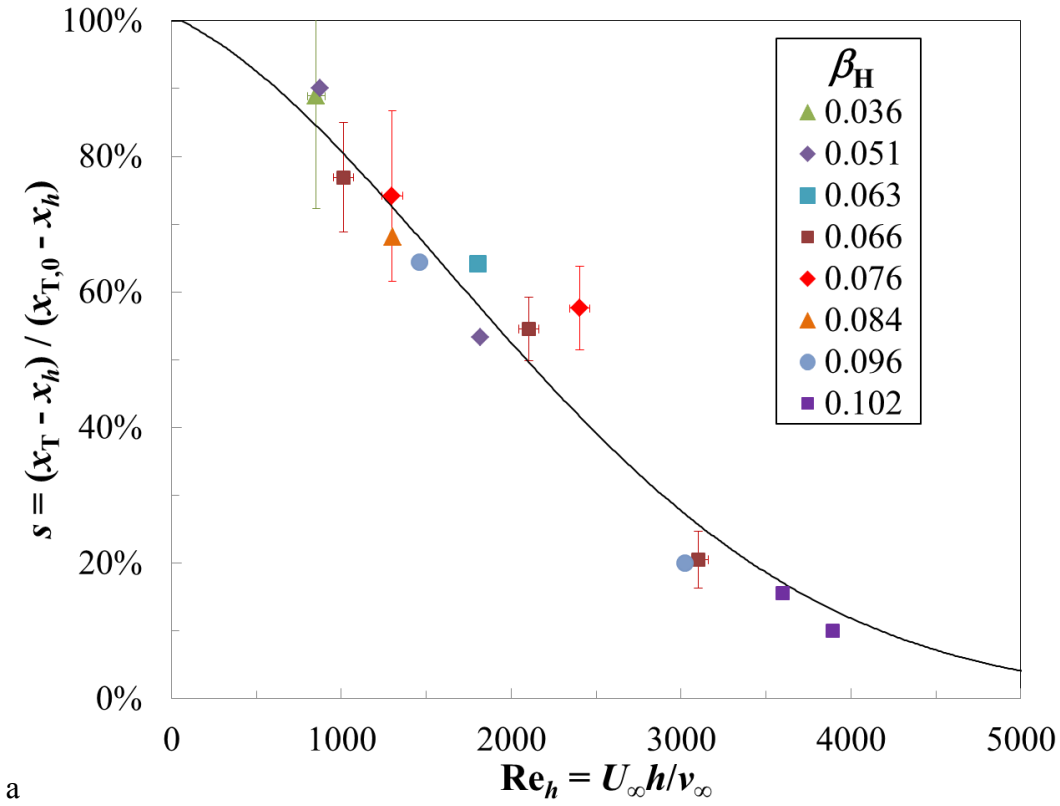

a

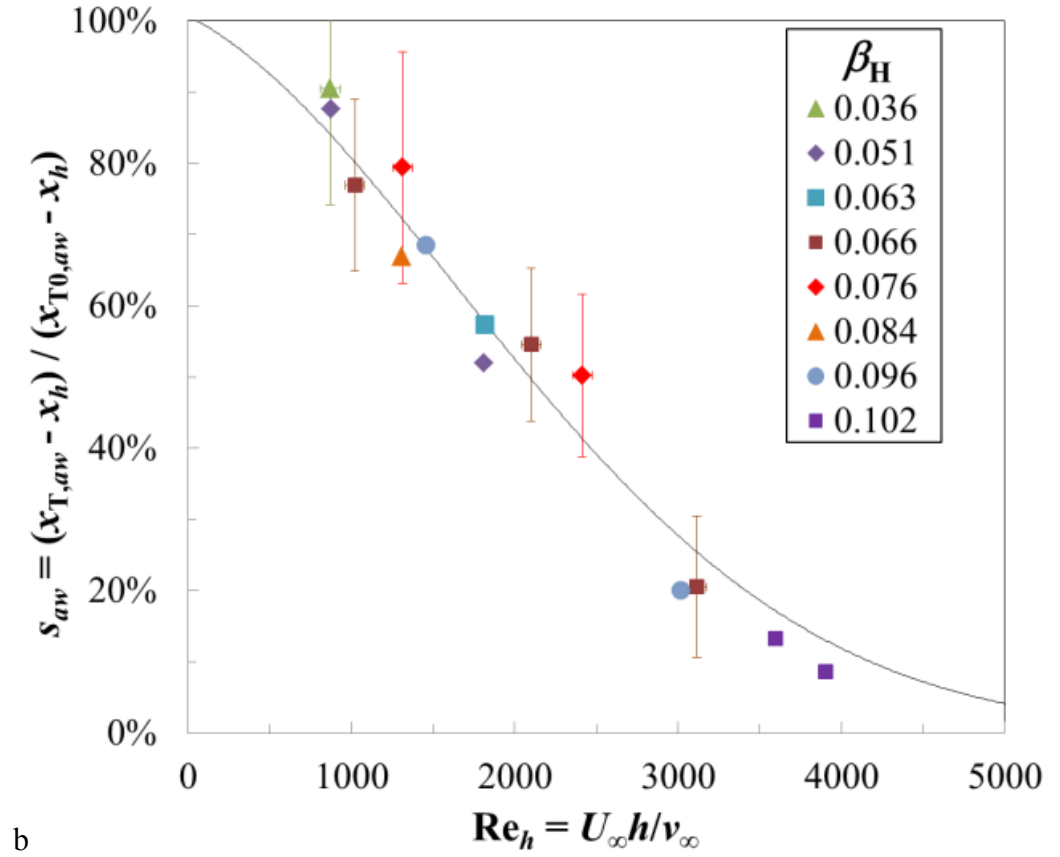

b

Fig. 6.5.4.1. a: relative change in transition location as a function of the step Reynolds number at T_w/T_{aw} = 0.994-1.016. The transition location $x_{T,0}$, obtained on the smooth configuration, was also measured at reduced T_w/T_{aw}. b: relative change of the adiabatic wall transition location as a function of the step Reynolds number. M = 0.77.

The results for the Mach numbers M = 0.35, 0.5, and 0.65 are not discussed here, since only a few data points are available at these conditions and they show trends similar to those discussed above. They are presented in Appendix E.9.

6.5.5 Summary of the results obtained at different wall temperature ratios in the presence of forward-facing steps

The results presented in the previous sections show a notable influence of surface heat flux on boundary-layer transition even in the presence of forward-facing steps up to $\mathrm{Re}_h \sim 2700$, $h/\delta_{1,h} \sim 0.8\text{-}0.9$, and $\mathrm{Re}_k \sim 1200$: a certain reduction in T_w/T_{aw} led to an increase in transition Reynolds number. This influence became, in general, less pronounced as the non-dimensional step parameters increased. Moreover, the sensitivity of $\mathrm{Re}_{x\mathrm{T}}$ to changes in T_w/T_{aw} at M = 0.35 was larger than that at larger Mach numbers. The reasons for this variation of the function $\mathrm{Re}_{x\mathrm{T}}/\mathrm{Re}_{x\mathrm{T},aw}$ vs. T_w/T_{aw} for different Mach numbers, which were presented in Section 5.1.2 for the smooth configuration, are also the same for the step configurations, except that further effects have to be considered in the presence of these steps (see Section 6.5.3). At $\mathrm{Re}_h > 2700$ and $\mathrm{Re}_k > 1200$, transition is insensitive to changes in wall temperature ratio in the examined range. This was observed also at $h/\delta_{1,h} > 0.8\text{-}0.9$, unless the boundary layer lasts over the recovery zone downstream of the step without undergoing transition: in this case, surface heat flux maintains its influence on boundary-layer transition.

The above considerations concern the effect of the wall temperature ratio on the transition Reynolds number in absolute terms. If the change in transition location is analyzed with respect to its value at the same test conditions but with the smooth configuration, and expressed relative to the step location, the effect of forward-facing steps on boundary-layer transition is independent of the thermal condition at the model surface (at least up to $\mathrm{Re}_h \sim 2700$, $h/\delta_{1,h} \sim 0.8\text{-}0.9$, and $\mathrm{Re}_k \sim 1200$). In this range of parameters, $s = (x_\mathrm{T}\text{-}x_h)/(x_{\mathrm{T},0}\text{-}x_h)$ is a universal function of the non-dimensional step parameters. In fact, this representation of the results allows the effect of the step on transition to be "isolated" from that of the surface heat flux, insofar as the sensitivity of boundary-layer transition to changes in the wall temperature ratio remains approximately unchanged. At approximately $\mathrm{Re}_h > 2700$, $h/\delta_{1,h} > 0.8\text{-}0.9$, and $\mathrm{Re}_k > 1200$ the change in transition sensitivity to variations in T_w/T_{aw} has to be accounted for by the relations between $s = (x_\mathrm{T}\text{-}x_h)/(x_{\mathrm{T},0}\text{-}x_h)$ and the aforementioned non-dimensional step parameters. At these conditions, however, transition occurs at a location close to that of the step, so that this change in the functional relations between $s = (x_\mathrm{T}\text{-}x_h)/(x_{\mathrm{T},0}\text{-}x_h)$ and the non-dimensional step parameters is mainly interesting for boundary-layer tripping, but not for the design of an aerodynamic surface with laminar flow technology.

Finally, it should be emphasized that the above considerations hold for the examined variations of wall temperature ratio. It is likely that marked wall

cooling (to values of T_w/T_{aw} significantly lower than those implemented in this work) would lead to a shift in the transition location even at $\mathrm{Re}_h > 2700$ and $\mathrm{Re}_k > 1200$. Nevertheless, if present, this effect would be expected to weaken as the non-dimensional step parameters are increased, in a manner similar to the favorable influence of the pressure gradient discussed in Section 6.2.2. In this context, it should be remarked that the effect on the smooth-configuration transition Reynolds number $\mathrm{Re}_{x\mathrm{T},0}$ due to the examined variation in β_H is much more pronounced than that due to the considered change in T_w/T_{aw} (see Section 5.1.2). A pressure gradient corresponding to $\beta_\mathrm{H} \sim 0.1$ leads to a transition Reynolds number $\mathrm{Re}_{x\mathrm{T},0}$ that is about four times the value obtained at $\beta_\mathrm{H} \sim 0$; in contrast, the largest change in $\mathrm{Re}_{x\mathrm{T},0}$, attained by a variation of the wall temperature ratio in the considered range, is less than 30 % of the adiabatic wall transition Reynolds number. (This is a significant change in any case.) Therefore, it is not surprising that the examined variation in the Hartree parameter has still a (small) influence on $\mathrm{Re}_{x\mathrm{T}}$ in the presence of large steps, whereas the change of the wall temperature ratio has a negligible effect at the same conditions.

7 Conclusion

7.1 Summary

The effect of sharp forward-facing steps on boundary-layer transition was systematically investigated in this experimental work in combination with the influence of streamwise pressure gradient, Mach number, Reynolds number, and a non-adiabatic surface. A new wind-tunnel model was designed to achieve a (quasi-) uniform streamwise pressure gradient over a large portion of the model chord length. This enabled a decoupling of the effects of the aforementioned factors on boundary-layer transition. The surface quality of the nominally two-dimensional wind-tunnel model was compatible with laminar flow. Forward-facing steps of different height were obtained on the surface of interest by installing shims of appropriate thickness at the interface between the two parts comprising the model. The generated imperfection was an abrupt step, perpendicular to both surface and freestream, with sharp corners. The spanwise distribution of the step height was almost uniform, thus ensuring that a (quasi-) two-dimensional laminar boundary layer encountered a (quasi-) two-dimensional step, placed perpendicular to the flow. This situation is relevant for aerodynamic surfaces at zero to moderate sweep angles, designed for the achievement of large regions of (natural) laminar flow. At these conditions, transition is generally due to the amplification of streamwise instabilities. Forward-facing steps, originating at structural joints, leading-edge panels, inspection and access panels, etc., can enhance amplification of these instabilities, thus inducing premature transition. To quantify the effect of forward-facing steps on the extent of laminar flow, the wind-tunnel model was coated with temperature-sensitive paint (TSP), which enabled transition detection over the whole surface. A robust algorithm was used to measure accurately, reliably, and consistently the transition location. Moreover, the wind-tunnel model was equipped with pressure taps for measuring the surface pressure distribution and thermocouples for monitoring the model temperature evolution during the tests. The experiments were carried out in the Cryogenic Ludwieg-Tube Göttingen. This test facility provided suitable conditions for the investigation of boundary-layer transition at high Reynolds numbers and subsonic to transonic Mach numbers, thereby covering the typical flight envelopes of aircraft with piston and turboprop engines, business jets, and transport aeroplanes. The experimental setup allowed the independent variation (in the considered range) of step height, Mach number, Reynolds number, streamwise pressure gradient, and thermal condition at the model surface.

The investigations were conducted at four freestream Mach numbers from $M = 0.35$ to 0.77 and chord Reynolds numbers from 3.5 to $13 \cdot 10^6$. Favorable streamwise pressure gradients, which are most relevant for a surface designed for natural laminar flow (NLF), were mainly considered. Zero and adverse pressure gradients were also examined. Most of the experiments were carried out with a

non-adiabatic model surface, i.e., at a wall temperature ratio T_w/T_{aw} larger than one. The influence of the wall temperature ratio on boundary-layer transition was examined by reducing the model surface temperature before the run, thus attaining wall temperature ratios close to or even lower than one. The experimental results were shown to be repeatable and reproducible. The first part of the investigations was conducted with the smooth configuration, i.e., without steps, to create a database of boundary-layer stability situations for which, later, the effect of the steps on transition could be examined and compared. Amplification factors of streamwise instabilities were calculated for the smooth configuration via linear stability analysis, using the measured pressure distributions and wall temperature ratios as input for the boundary-layer computations. The stability computations were performed by means of compressible, linear, local stability theory under the (quasi-) parallel flow assumption. In general, the experimental results were consistent with predictions based on linear stability theory and with expectations from earlier work. Nevertheless, the present study is the first systematic experimental verification of the effects of pressure gradient and wall temperature ratio, taken separately and in combination, on boundary-layer transition at high subsonic Mach numbers. The observed influence of the Mach number was opposite to that expected from linear stability theory: the transition Reynolds number decreased at larger Mach numbers. This effect was very likely caused by an increase in the initial amplitude of the boundary-layer disturbances, due to a larger level of external disturbances and/or to enhanced boundary-layer receptivity.

The effect of forward-facing steps on boundary-layer transition is outlined by re-addressing the questions presented in Section 1.1:

- What is the effect of forward-facing steps on boundary-layer transition at flight Reynolds numbers?

  Transition was observed to move gradually towards the step location with increasing step Reynolds number $\mathrm{Re}_h = U_\infty h/\nu_\infty$, relative step height $h/\delta_{1,h}$, and roughness Reynolds number $\mathrm{Re}_k = U_h h/\nu_h$. An increase in chord Reynolds number induced a movement of transition towards the step location, but the transition Reynolds number was essentially independent of the chord Reynolds number, provided that the other parameters were kept fixed. Note, however, that the Reynolds number based on the step location $\mathrm{Re}_{xh} = U_\infty x_h/\nu_\infty$ did vary.

- Can laminar flow be achieved over forward-facing steps?

  Extended laminar flow areas, corresponding to a relative change in transition location with respect to the value for a smooth surface $s = (x_T - x_h)/(x_{T,0} - x_h) > 90$ %, can still be achieved for forward-facing steps with $\mathrm{Re}_h < 650$, $h/\delta_{1,h} < 0.3$, and $\mathrm{Re}_k < 100$. The extent of the laminar flow regions progressively decreases at larger values of the non-dimensional step parameters. The flow is turbulent over most of the surface

downstream of the step location for $\mathrm{Re}_h > 3200$, $h/\delta_{1,h} > 1.1$, and $\mathrm{Re}_k > 1900$.

- What is the role of the pressure gradient in transition induced by forward-facing steps?

  Flow acceleration has a favorable influence on boundary-layer transition in the presence of forward-facing steps: longer runs of laminar flow were obtained with larger Hartree parameters β_H. This favorable influence becomes, however, less pronounced at larger values of the non-dimensional step parameters: the slope of the function $\mathrm{Re}_{x\mathrm{T}}/\mathrm{Re}_{x\mathrm{T}}(\beta_\mathrm{H} = 0)$ vs. β_H decreases. Boundary-layer transition was shown to be more sensitive to the effect of forward-facing steps (in terms of reduction of transition Reynolds number, $\mathrm{Re}_{x\mathrm{T}}/\mathrm{Re}_{x\mathrm{T},0}$) in the presence of larger flow acceleration.

- Does variation in Mach number up to high subsonic conditions influence boundary-layer transition in the presence of forward-facing steps?

  Larger values of transition Reynolds numbers were obtained at lower Mach numbers. This result, however, is mainly related to the test facility and to the examined wind-tunnel model. Similar to the results obtained with the smooth configuration, the reduction of transition Reynolds number at larger Mach numbers is likely to be due to increased initial amplitudes of the boundary-layer disturbances. Nevertheless, this effect was less marked at larger values of the non-dimensional step parameters. Moreover, boundary-layer transition was shown to be less sensitive to the effect of forward-facing steps (in terms of $\mathrm{Re}_{x\mathrm{T}}/\mathrm{Re}_{x\mathrm{T},0}$) at larger Mach numbers.

- Is step-induced transition influenced by a non-adiabatic surface?

  Up to moderate values of the non-dimensional step parameters, a reduced wall temperature ratio had a favorable influence on boundary-layer transition: larger transition Reynolds numbers were obtained with smaller values of T_w/T_{aw}. This favorable influence becomes less pronounced as the values of the non-dimensional step parameters increase: the slope of the function $\mathrm{Re}_{x\mathrm{T}}/\mathrm{Re}_{x\mathrm{T},aw}$ vs. T_w/T_{aw} decreases. The effect of a reduced T_w/T_{aw} vanishes at approximately $\mathrm{Re}_h > 2700$ and $\mathrm{Re}_k > 1200$. This was observed also at approximately $h/\delta_{1,h} > 0.8$-0.9, unless the laminar flow lasts over the region of step-induced adverse pressure gradient without undergoing transition: in this case, a reduced wall temperature ratio maintains its favorable influence. It should be emphasized that these considerations hold strictly only for the examined range of wall temperature ratios. It is likely (but was not tested here) that wall cooling to significantly low values of T_w/T_{aw} would lead to a shift in the transition location even at

$Re_h > 2700$ and $Re_k > 1200$, but this effect would be also expected to weaken as the non-dimensional step parameters are increased.

Dimensional analysis of the variables involved in the problem showed that the general functional relation between dimensional quantities could be reduced to a relation between two independent non-dimensional parameters. In the present work, the parameter $s = (x_T\text{-}x_h)/(x_{T,0}\text{-}x_h)$ was used to describe the relative change in transition location with respect to the step location, whereas Re_h, $h/\delta_{1,h}$, and Re_k were used as the non-dimensional step parameters. This choice of non-dimensional parameters allowed the effect of the steps on boundary-layer transition to be "isolated" from the influence of the other factors. The representation of the results using $s = (x_T\text{-}x_h)/(x_{T,0}\text{-}x_h)$, plotted against the non-dimensional step parameters, gave good correlation of the results. In general, the best step parameter for the correlation appears to be the "simple" step Reynolds number Re_h. These relations are almost unaffected by variations in Reynolds number, Mach number (and initial disturbance amplitude), streamwise pressure gradient, and wall temperature ratio, provided that x_T and $x_{T,0}$ for each data point were measured at the same conditions. In the case of the wall temperature ratio, this holds only up to the values of non-dimensional step parameters at which boundary-layer transition becomes insensitive to changes in T_w/T_{aw}; the variations of the aforementioned relations due to this change in sensitivity are, however, small.

- Can the results obtained on a generic configuration (flat plate) be transferred to practical applications?

  The results obtained on the examined flat-plate configuration are in agreement with those obtained on an NLF-airfoil model, whose construction, instrumentation, and surface quality were basically the same as that of the flat-plate configuration. The present results were thus demonstrated to be applicable and transferable to the practical case of an NLF airfoil. Criteria for acceptable heights of forward-facing steps on unswept and moderately swept NLF surfaces, which are designed for transport aeroplanes, business jets, and aircraft with piston and turboprop engines, can now be derived from the functional relations determined in this work.

The present results provide an experimental data set for various boundary-layer stability situations and for documented step geometry. It can serve as a database for the development and calibration of transition prediction tools based on linear stability theory or more sophisticated boundary-layer stability formulations. These tools can then be used for the design and analysis of NLF surfaces at zero to moderate sweep angles, large Reynolds numbers, and low to high subsonic Mach numbers. In the present work, the measured transition locations were correlated with the results of linear local stability computations for the smooth configuration. The step-induced increment in amplification factors

$\Delta N = N_{T,0} - N_T$ increased, in general, at larger relative step height $h/\delta_{1,h}$. Compressibility appears to reduce the value of ΔN. The linear function $\Delta N = 1.6\ h/\delta_{1,h}$ represents a rough upper bound for the step-induced increment in amplification factors. It can be used for a conservative estimation of the transition location in the presence of forward-facing steps using the e^N method.

7.2 Outlook

The functional relations between the relative change in transition location $s = (x_T\text{-}x_h)/(x_{T,0}\text{-}x_h)$ and the non-dimensional step parameters have been obtained in the present work for fixed step location and for a set of test parameters and boundary-layer stability situations, which correspond to a certain range of flight conditions for an NLF surface. The validity of the functional relations should be verified also for other flight conditions and step locations. An important case for practical applications is that of boundary-layer transition induced by strong deceleration, e.g., at $x/c > 50$ % on an NLF airfoil. At these conditions, transition is expected to be less sensitive to the influence of surface imperfections, especially if it is induced by a shock. This can be studied by generating steps on an NLF-airfoil model and then examining their effect at those test conditions at which transition is induced by the adverse pressure gradient on the rear of the airfoil. In the present work, the variation of the thermal condition at the model surface by means of the applied pre-conditioning procedure was limited to a certain range of wall temperature ratios. Moreover, the temperature difference implemented between flow and model surface at the beginning of the test runs was uniform. Different values of T_w/T_{aw} and non-uniform temperature distributions can occur on aircraft surfaces in flight. The range of wall temperature ratios can be broadened to larger ($T_w/T_{aw} > 1$) and smaller ($T_w/T_{aw} < 1$) values by installing below the TSP layer a heating/cooling system, which could take the form of a series of tubes functioning as a heat exchanger. This setup can also be designed to intentionally generate a non-uniform surface temperature distribution in the streamwise direction and selectively cool/heat surface regions to different extents. Larger values of wall temperature ratio can be also achieved by mounting a heating layer below the TSP layer, such as a layer of carbon nanotubes. As discussed above, the location of the imperfection was fixed in the current work. The design of an aircraft surface, however, may require joints and/or panels to be placed at a location further upstream than that considered here. The influence of the step location (i.e., of the Reynolds number based on the step location Re_{xh}) on the functional relations between $s = (x_T\text{-}x_h)/(x_{T,0}\text{-}x_h)$ and the non-dimensional step parameters can be examined by constructing a wind-tunnel model with several locations for the installation of the steps or by building various models with the same cross-section but different step installation locations.

The present work focused on sharp forward-facing steps. This geometry is the most critical for this type of imperfection. Allowable manufacturing tolerances

for steps, obtained from criteria developed for this worst-case scenario, can be relaxed for rounded steps and ramps. The effect of the radius of the step corner can be studied by sanding down or milling the step to the desired geometry, but this would irreversibly modify the wind-tunnel model. Alternatively, inserts with the shape of a rounded step or a ramp can be installed between model front and main parts. Further imperfections that can be present on aircraft surfaces are: bumps, waviness, gaps, and backward-facing steps. Bumps and waviness should not be a major concern for NLF surfaces, since modern manufacturing techniques can provide surface fairness compatible with laminar flow. Criteria available for allowable size and shape of surface bumps and waviness on NLF surfaces can be verified by means of the experimental setup used in the present work: the aforementioned inserts can also have the shape of these imperfections. Gaps and backward-facing steps should be avoided on surfaces designed for natural laminar flow. If this is not possible, manufacturing tolerances have to be specified also for these imperfections. Criteria for allowable size and shape of gaps and backward-facing steps can be developed in a manner analogous to that discussed in this work for forward-facing steps. The wind-tunnel model in its present form can already be used to study the effect of backward-facing steps on boundary-layer transition. Gaps can be also generated with just small modifications to the interface between model front part, main part, and shim. Combinations of steps and gaps can also be examined.

The transition scenario on aircraft surfaces can be dominated by instability mechanisms different from that examined in the present work. The effect of surface imperfections on boundary-layer transition should be investigated also for these transition scenarios. Crossflow instabilities are the predominant mechanism leading to transition on aircraft surfaces with favorable pressure gradients and large sweep angles (approximately $\varphi > 25°$). Investigations of transition induced by crossflow instabilities at the considered Mach numbers can be performed only in large cryogenic wind tunnels or in flight. Such experiments are very expensive, so they should be carried out within the framework of a large-scale national or international project. Flight tests are desirable also for the verification of the applicability and transferability of the results from the present wind-tunnel experiments to real flight conditions. An aircraft wing should be equipped with a glove shaped as to reproduce the surface pressure distributions examined in this work. Alternatively, the considered surface pressure distributions can be obtained on a test model directly attached to the carrier aircraft. Transient growth and bypass transition can occur in the presence of external disturbances with large amplitude. The related instability and transition process may be enhanced by large amplitude fluctuations intentionally generated in DNW-KRG, such as turbulent wakes originating from blunt bodies installed upstream of the nozzle. This would allow transition induced by transient growth and/or bypass mechanisms to be studied at DNW-KRG. If this cannot be achieved, the experiments could be conducted in another test facility, e.g., in one for gas turbine blade testing.

Practical numerical methods available for the prediction of boundary-layer transition in the presence of surface imperfections are based on linear stability theory. These methods have been shown to fail when applied at conditions different from those used for their calibration. Further experimental and numerical investigations are required to improve the understanding of the physics involved in imperfection-induced transition and thus also improve transition prediction methods. Boundary-layer receptivity and stability should be studied up to high subsonic Mach numbers in a series of dedicated experiments. The first essential step for such measurements is the design of a measurement system for the spectral characterization of the disturbance environment in the test facility. The measurements would need to be carried out with the model in place in the test section, but at the same time the interference between the measurement system and the model would have to be avoided or minimized. Moreover, the wind-tunnel model would need to be instrumented to obtain information about the disturbances within the boundary layer. Currently, the only method to perform these measurements appears to be the installation of several sensors at discrete locations at the model surface. Sensors providing the required temporal and amplitude resolution, such as Kulite © pressure sensors, hot-films, or wall hot-wires, would have to be used. Loudspeakers could also be installed in the wind tunnel to excite the disturbances within the boundary layer at given, selectable frequencies. Particle image velocimetry (PIV) and/or particle tracking velocimetry (PTV) should be developed for boundary-layer measurements in the considered wind tunnel. Although micro-PIV and micro-PTV cannot resolve the very low amplitude of the disturbances within the laminar boundary layer, measured mean-velocity profiles would enable validation of boundary-layer computations. The results of this series of experiments should be compared with the predictions of numerical methods, which should include receptivity modeling, linear and non-linear stability theory, and DNS. In particular, the numerical methods can provide essential information about receptivity mechanism, amplification of instabilities in the region around the step location, and transition process. The information made available from these combined experimental and numerical effors can then be used to develop transition prediction methods on a more physical basis.

Finally, general features of the transition front should be examined in more detail, i.e., the spanwise modulation of the natural-transition front and the regions with larger laminar run length close to turbulent wedges. These features have been observed also on the smooth configuration. Their investigation would contribute to the understanding of fundamental fluidmechanical phenomena involved in the transition process. The TSP measurement system can be modified to increase temporal resolution and thus investigate the temporal development of the natural-transition front. This can be accomplished by means of cameras with higher frame rates. More powerful light sources are needed to increase the intensity of the light emitted by the TSP, thus allowing the exposure time of the cameras to be reduced. By this means, a temporal resolution of about

1 kHz can be obtained with the used TSP coating. A very thin TSP layer (about 1 μm thickness) composed of a binder with large thermal diffusivity can be used to reduce the response time of the temperature-sensitive paint, but its capability to withstand the aerodynamic forces for several test runs should be proven. The aforementioned additional instrumentation for the study of boundary-layer receptivity and stability would probably provide also information about the spanwise modulation of the natural-transition front. The investigation of the three-dimensional flow at the sides of a turbulent wedge can be started at low speed, with the related advantages in terms of usable measurement techniques.

Appendix

A Supplements to the introduction

A.1 Historical review of the effects of surface imperfections in past laminar flow research

The advantage in terms of drag reduction related to the achievement of laminar flow on aircraft surfaces has been known since the earliest experiments on LF technology in the 1930's. Contemporary to these positive results, the adverse effect of surface irregularities was also observed. As discussed in Section 2.3.1, natural laminar flow airfoils have been around since the 1930's. Flight tests showed that the drag coefficients of NLF airfoils were significantly lower than those of conventional airfoils, but only after the wing surfaces had been carefully prepared [256-261]: in particular, the surfaces were carefully smoothened and faired to remove imperfections due to rivets, skin joints, and access doors and to reduce surface waviness. Note that the negative effect of surface imperfections on laminar flow was exacerbated by the high unit Reynolds numbers at which the test surfaces were investigated [33]. Already in 1938 it had been concluded that, rather than atmospheric turbulence, it was mainly vehicle-generated disturbances such as surface imperfections (and also vibrations and noise) that were the main factors inducing boundary-layer transition [262]. In 1945, it was stated that "the effects of surface condition on the lift and drag characteristics are at least as large as the effects of the airfoil shape" [263]. Further improvements in aircraft surface finish were possible, but involved increased production and maintenance difficulties. Therefore, researchers had already pointed out at that time that quantification of the necessary improvement in surface quality had to be made available to the designers so that they could assess whether such improvements could be cost-effectively incorporated into the aircraft design [9,264]. Transition Reynolds numbers as high as $16 \cdot 10^6$ were later measured on a NACA $65_{(215)}$-114 NLF-airfoil model in a low-turbulence wind tunnel, but only after the model surface had been polished to "aerodynamic smoothness" [265]. Laminar flow control by wall suction (see Section 2.3.2) encountered similar difficulties in the 1940's because of the lack of surface smoothness and fairness [7,9]. The necessary condition for the success of LFC was that the object surface had to be "sufficiently free from waviness, roughness, and steps" [266]. Full-chord laminar flow was attained in the 1950's at chord Reynolds numbers larger than $15 \cdot 10^6$ via continuous suction through a porous surface [267,268] and via suction through multiple slots [269]. However, these results could be obtained only after a very high degree of surface quality had been attained. In 1954, the essential pre-requisite for an aircraft laminarized via LFC was identified as "a surface finish that is compatible with the maintenance of a laminar boundary layer thinned down by suction" [270]. Later LFC research

focused on perforated metal sheets (strips) [9,271], which represent an approach closer to ideal continuous suction [21]. One of the main drawbacks for the successful application of this LFC technique was the formation, under aerodynamic loading, of two-dimensional discontinuities at the joint between perforated strip and solid surface [271].

The Northrop group made major contributions to the development of LF technology in the 1950's and 1960's. Full-chord laminar flow was obtained at $\mathrm{Re} = 30 \cdot 10^6$ on the upper side of a glove mounted on a Lockheed F-94 aeroplane wing [272]. Nearly complete laminar flow was achieved on the upper side of an X-21 demonstration aeroplane, whereas transition occurred at $x_T/c \sim 75$ % on the lower side [169]. In both cases, these results were obtained using suction through slots. It should be emphasized that the surface of the laminar glove on the F-94 aeroplane was exceptionally fair and maintained in a very smooth condition, whereas problems related to surface smoothness and fairness were of larger significance in the X-21 project [7]. The difficulty in manufacturing and then maintaining fair and smooth surfaces suitable for laminar flow was one the major reasons for the demise of LF technology research. (The most important reasons were the diversion of resources to cater for the needs of the Vietnam War in the United States, and the general downturn of the national economy in Great Britain at that time.) A hiatus in LF research of about ten years followed after the X-21 project, with the exception of continuing basic, primarily theoretical efforts. Research on LF technology was resumed in the 1970's, mainly in response to the 1973-1974 oil embargo that caused fuel shortages and drove up costs [7,9-10]. The emphasis, however, then changed from military to commercial applications, leading to even more demanding challenges related to cost and times for manufacture and operation [7,9-10]. The various experiments conducted in the United States and in Europe are reviewed in [7,10,21,25-26,33]. Among the NLF experiments, those carried out on a Fokker F100 aircraft [22,153-154,156] should receive special attention regarding the effects of surface imperfections. An NLF glove was installed on the wing of this medium-size airliner. The NLF glove was designed to promote growth of crossflow instabilities on the leading-edge region; these, however, were not large enough to induce transition. An appropriate pressure distribution damped CFI further downstream. Transition was caused by the amplification of Tollmien–Schlichting waves and occurred on the mid-chord region. Such large regions of laminar flow were achieved for leading-edge sweep angles below 23°, Mach numbers up to 0.75, and Reynolds numbers up to $25 \cdot 10^6$ [22], but only after surface waviness causing premature transition in the first flight tests had been detected and faired [27,156]. From the HLFC experiments, those conducted on a Lockheed JetStar business jet [7,273] are worthy of mention. Different gloves were installed on the wings: an LFC system with slots on both upper and lower sides was mounted on the left wing, whereas a perforated titanium skin was used for LFC on the upper side of the right wing. Both gloves had a 30° leading-edge sweep and LFC systems extending up to the front spar of the wing ($x/c = 12$ %).

Using the LFC systems and Gaster bumps [274] to avoid attachment-line contamination, laminar flow was obtained over both examined leading-edge regions for all flight conditions. At the design conditions, laminar flow up to $x/c = 83$ % was observed on the right wing. Large regions of laminar flow were achieved also on the left wing, but its performance was generally poorer because of the poor quality of the slotted suction surface [7].

A.2 Flight envelope for hypothetical transport aircraft employing natural laminar flow wings

The flight envelope shown in Fig. 1.1.1 has been derived from a typical mission of an Airbus A320 aeroplane [51]: a flight connection between two European capitals at a distance of more than 1000 km. The variation of aircraft speed as a function of the altitude was taken from [52] and is shown in Fig. A.2.1 The flight envelope encompasses the flight phases from take-off to cruise conditions.

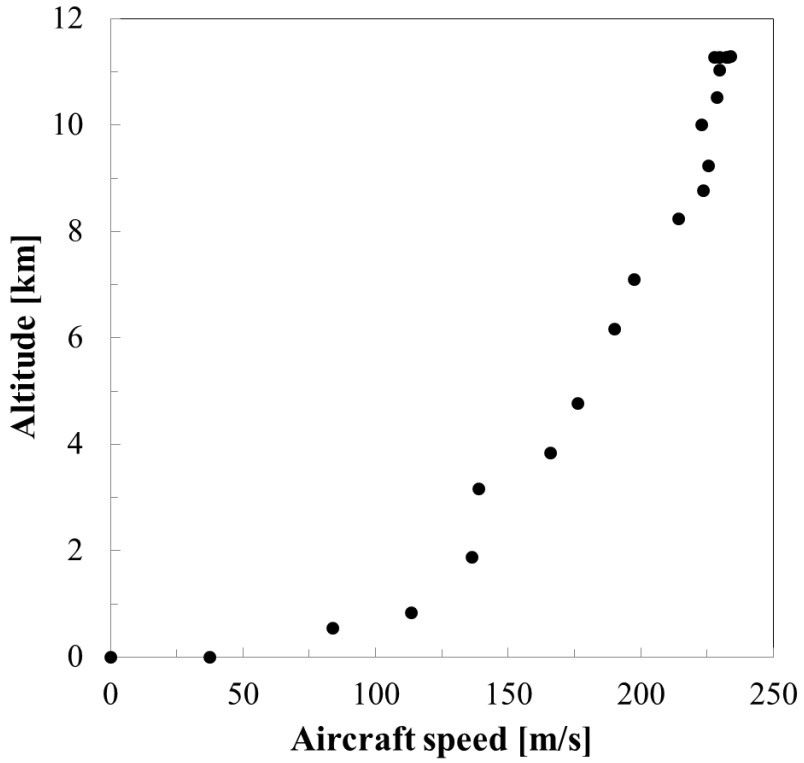

Fig. A.2.1. Variation of aircraft speed as a function of the altitude for a typical mission of an Airbus A320 aeroplane [52]. The flight envelope encompasses the flight phases from take-off to cruise conditions.

The flight Mach number was computed from the data points in Fig. A.2.1 as the ratio of aircraft speed and speed of sound. The latter quantity was evaluated with the heat capacity ratio and specific gas constant for air ($\gamma = 1.4$ and $R^* = 287$ J/(kg·K), respectively) and with the temperature at the corresponding altitude calculated according to the International Standard Atmosphere model. The unit Reynolds number was computed with aircraft speed, air density, and air

dynamic viscosity. The air density was also calculated according to the International Standard Atmosphere model, whereas the air dynamic viscosity was obtained using Sutherland's law (see Eq. (4.3.2)), with $\mu_{ref} = 1.789 \cdot 10^{-5}$ Pa·s, $T_{ref} = 288.15$ K, $S = 110.4$ K, and with the temperature at the corresponding altitude (see above). The wings of the hypothetical transport aircraft with the size of an Airbus A320 aeroplane [51] were assumed to be designed for natural laminar flow and to have forward-facing steps located at $x_h/c = 15$ %. Four wing cross-sections were considered: at a location of 33, 50, 67, and 80 % of the wing span. The chord length was taken as $c = 4.34$, 3.60, 2.84, and 2.27 m, respectively. The step location Reynolds number Re_{xh} was then computed for the four cross-sections as the product of unit Reynolds number and corresponding step location x_h. The curves of Re_{xh} vs. M plotted in Fig. 1.1.1 are 5^{th} order polynomial functions fitted to the data sets.

B Experimental setup

B.1 Results of boundary-layer computations and linear stability analysis of the model cross-section

After the design of the model cross-section had been completed, the pressure distributions obtained on the model upper side by means of MSES [194,195] were used to perform compressible boundary-layer calculations by means of the laminar boundary-layer solver COCO [196,197] (see Section 3.2.1). The model surface was assumed to be adiabatic. The test gas was assumed to be air, with heat capacity ratio, specific gas constant, and Prandtl number having been taken as $\gamma = 1.4$, $R^* = 287$ J/(kg·K), and Pr = 0.72, respectively. The influence of this assumption on the results of boundary-layer computations has been shown to be negligible for the operating range of transonic, cryogenic wind tunnels, where nitrogen is used as a test gas [229,230]. The wall-normal velocity and temperature profiles were discretized at each chordwise station using 50 points; the wall-normal grid spacing was progressively increased by a factor of 1.05 with increasing distance from the wall. An example of the results of the boundary-layer computations is presented in Fig. B.1.1 for the case with a flat pressure distribution.

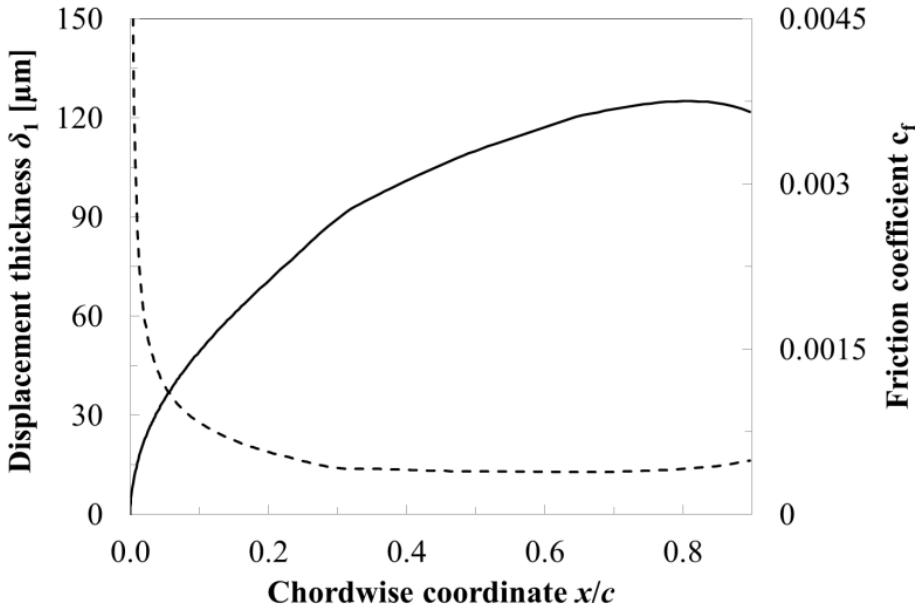

Fig. B.1.1. Results of laminar boundary-layer computations performed using COCO. M = 0.78, Re = 6 · 10^6, T_∞ = 235 K, AoA = -1.8°. Solid line: displacement thickness. Dashed line: laminar skin-friction coefficient.

The first grid point in the boundary layer was at a non-dimensional wall-normal distance $z^+ = u_\tau z/\nu(z) < 1.5$, where $u_\tau = (\tau_w/\rho_w)^{1/2}$ is the friction velocity. The chordwise distributions of the laminar boundary-layer displacement thickness $\delta_1(x)$ and the laminar skin-friction coefficient $c_f(x) = 2\,\tau_w/(\rho_e U_e^2)$ are shown by

solid and dashed lines, respectively. The boundary layer is very thin: the displacement thickness is less than 100 μm up to $x/c \sim 40$ % and remains below 150 μm for the whole chord length. Note also that, because of the local flow acceleration, the boundary-layer thickness decreases at approximately $x/c > 85$ %, and the laminar skin-friction coefficient increases.

The stability of the computed boundary layer was then analyzed by means of LILO [199] (see Section 3.2.1) using linear, local stability theory, under the quasi-parallel flow assumption. The amplification factors (N-factors) of Tollmien-Schlichting waves were computed for waves with fixed propagation direction and different frequencies. The propagation direction was fixed to zero degrees because two-dimensional waves have the largest amplification rates up to a Mach number of approximately 0.9 [32]. The computations were performed according to compressible stability theory, with a Prandtl number $Pr = 0.72$. (Note that the results of boundary-layer-stability analysis have been shown to remain unchanged if a variable Prandtl number is used in the stability formulation instead of a constant Prandtl number [232].) The results of the stability computations for the case considered in Fig. B.1.1 are shown in Fig. B.1.2a. The results obtained according to incompressible stability theory are presented for comparison in Fig. B.1.2b. The incompressible formulation of the boundary-layer stability equations is not appropriate at such Mach numbers ($M = 0.78$), but has nevertheless still been often used [154,277-278]. A glance at Fig. B.1.2 shows that the instability waves start to be amplified in the leading-edge region, once the strong boundary-layer acceleration has decreased. In this case, and in all other boundary-layer stability situations considered in the current work, instability waves were shown to grow already at a location upstream of the step. The N-factor envelope curves present a gradual increase with increasing chordwise coordinate up to $x/c \sim 65$-70 %. This development of the N-factor envelope curve is more suitable for the present study than that of an NLF airfoil (compare with [145]). It should be remarked, however, that the envelope curve obtained for the current model presents three regions with different (average) slope: (1) with positive slope up to $x/c \sim 35$ %; (2) up to $x/c \sim 65$-70 %, also with positive slope, but less marked than that on the upstream region; (3) with negative slope, at approximately $x/c > 65$-70 %. Nevertheless, the slope of the N-factor envelope curve is approximately uniform in the region $35\ \% < x/c < 65\ \%$, which was that of major interest for the examination of the influence of surface steps on boundary-layer transition. The decrease of the amplification factors at approximately $x/c > 65$-70 % is due to the flow acceleration on the last portion of the chord.

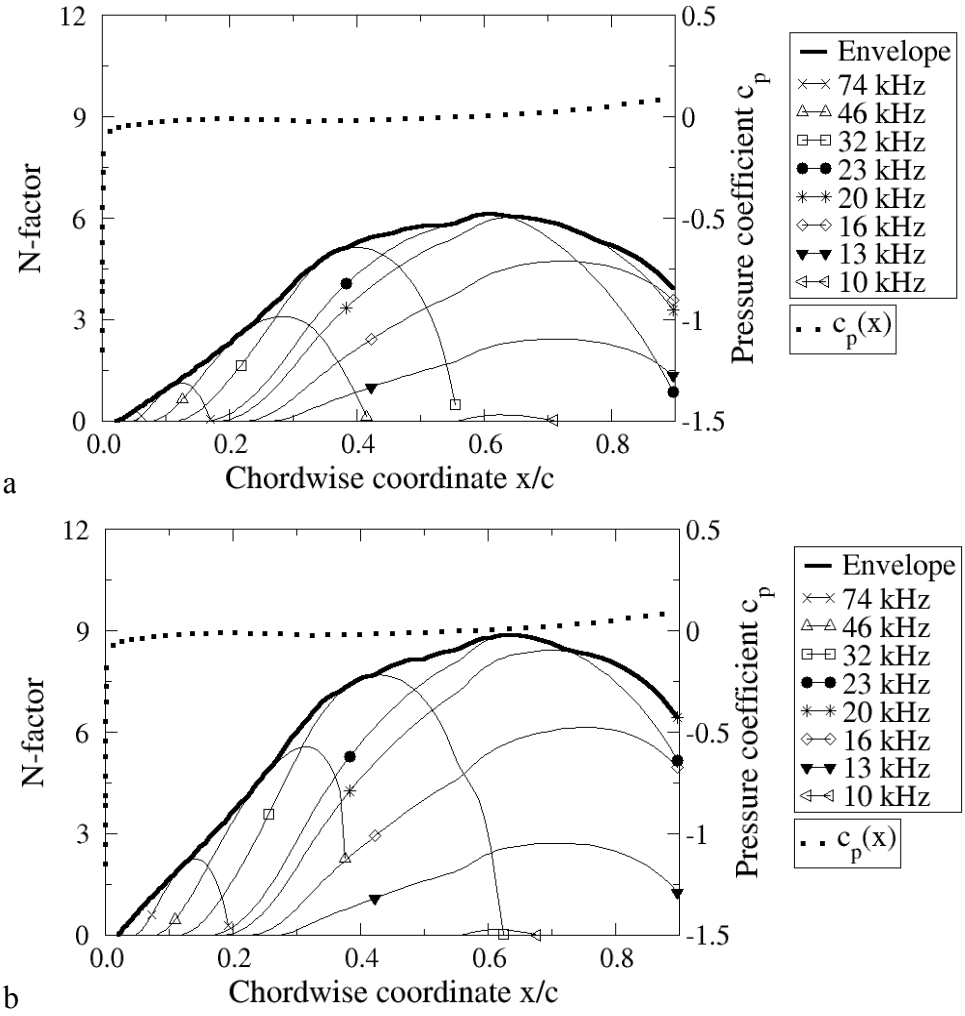

Fig. B.1.2. Results of boundary-layer-stability analysis for the case shown in Fig. B.1.1. Computations performed using LILO according to linear, local stability theory, under the quasi-parallel flow assumption. Amplification factors shown only for some selected frequencies. Dotted lines: computed pressure distribution. a: compressible formulation of the boundary-layer-stability equations. b: incompressible formulation.

B.2 Challenges for the application at DNW-KRG of typical solutions for low-speed transition experiments on flat plates

Long flat plates have been typically used for fundamental boundary-layer transition experiments at low speed (see Chapter 2). In most cases, the streamwise pressure gradient was set to zero. Nevertheless, also favorable and adverse pressure gradients have been examined: the streamwise pressure gradient was imposed by adjusting the flexible test-section walls [39,123,236] or using an appropriate (and in some experiments adjustable) displacement body [41,95,144,237]. In principle, experiments using a fixed flat plate can be performed also at DNW-KRG, since the upper and lower walls of the test section can be used to impose a certain streamwise pressure gradient. The flexible walls are adjusted by means of 19 jacks, equally spaced in the streamwise direction and operated by stepper motors. The maximally allowable vertical displacement

of the DNW-KRG adaptive walls is ±45 mm. This, however, cannot be completely used in the upstream part of the test section, since wall contour and wall slope have to be continuous at the interface between rigid and flexible walls at the beginning of the test section [276]. Thus, the maximal deflection angle achievable with oblique upper and lower walls is approximately ±1.3°. Larger deflection angles can be obtained over a streamwise distance shorter than the test.section length: in this case, the maximal wall displacement can be used both upstream and downstream of the considered test-section region. This would allow a pronounced, uniform pressure gradient to be imposed on the surface of a flat plate with chord length comparable to that of airfoil models typically tested at DNW-KRG ($c \sim 0.15$-0.2 m [55]). The upper and lower walls, however, cannot be deformed to an arbitrary shape because of constraints on the wall curvature, which prevent a permanent deformation of the walls. Note also that the achievement of a certain wall deflection angle in the test-section region corresponding to the model installation position implies the creation of convergent and/or divergent sections upstream and downstream of the region of interest. This additional wall deformation leads to certain freestream Mach number and surface pressure distribution. For each data point, the solution of an inverse aerodynamic problem is required, in order to set the appropriate Mach number at the test-section entrance and the appropriate test-section wall shape, which allow the desired freestream Mach number and the desired surface pressure gradient to be attained. The problem has to account for wall interference effects, model blockage effects, and constraints on wall displacement and wall curvature.

In low-speed wind tunnels, flat plates used for transition experiments generally have large chord length; therefore, the model leading edge can be rather long, although it still remains relatively short as compared to the total length of the model. The model leading edge can be designed to avoid local pressure minima on its surface and discontinuities (up to the second derivative of the surface contour) at the junction between leading edge and flat plate. At the same time, a sufficiently large "working surface", with a uniform streamwise pressure gradient, is ensured on the rest of the model. Moreover, the models feature, in general, a trailing-edge flap to control circulation and thereby the position of the stagnation line. The deflection of this device can be varied in combination with the model angle-of-attack to obtain the optimal streamwise distribution of the surface pressure for the particular study [40,118,201]. Usually, the deflection of the trailing-edge flap can be adjusted manually, since the models can be quickly accessed by the test engineers. A flat plate of chord length $c \leq 0.2$ m, to be used for transition experiments at DNW-KRG, has more limitations. Since the model chord length is rather small, the leading edge has to be designed properly to fulfill requirements related to boundary-layer receptivity, while at the same time ensuring achievement of a uniform pressure gradient with sufficient streamwise extent. Furthermore, a trailing-edge flap cannot be easily accessed at DNW-KRG, so that manual adjustment of its deflection can be performed only after

nitrogen in the test section has been brought to atmospheric conditions, and subsequently the test section has been opened. This clearly leads to long interruptions of the measurement campaign and high wind-tunnel operation costs per data point. A remotely-controlled trailing-edge flap has high design, manufacturing, and integration costs.

A sharp leading edge, asymmetric with respect to the plate longitudinal axis, allows a large flat surface to be obtained on the model upper side. However, separation can occur because of the sharp tip, and for various test conditions the stagnation point can be on the model side opposite to that under investigation [201]. Because of this sensitivity of a sharp leading edge, and because of the related need of a trailing-edge flap to control circulation and flow separation, an elliptic or super-elliptic (MSE) leading edge is generally preferred at subsonic conditions.

B.3 Model surface quality

B.3.1 Analysis of the surface quality at the step location

The quality of the upper model surface at the junction between front part and main part was examined by means of the contact profilometer [210] mentioned in Section 3.3. The measurements were conducted at 14 different spanwise locations, which were not equally spaced along the model span: a larger number of measurements was carried out in the range $0.3 \leq y/b \leq 0.7$, which was that of major interest for the study of transition in the present work (see Section 4.2). The spacing was $\Delta(y/b) = 0.1$ in the regions $0.1 \leq y/b \leq 0.3$ and $0.7 \leq y/b \leq 0.9$; a finer spacing of $\Delta(y/b) = 0.04$ was used in the range $0.36 \leq y/b \leq 0.64$. (The measurement location in the mid-span area, however, was $y/b = 0.49$ instead of $y/b = 0.48$, so that information in proximity of the main row of pressure taps could be obtained.) The first investigated configuration was the smooth configuration. The contact profilometer was operated with a vertical measurement range of ±25 μm, a vertical resolution of ±0.8 nm, and a longitudinal measurement length of 1.75 mm. The longitudinal resolution is 11200 points, independent of the longitudinal measurement length. An example of the surface quality at the junction for the smooth configuration is shown in Fig. B.3.1.1, where the measurement at the spanwise location $y/b = 0.4$ is presented. Note that the leading edge is on the left in this figure, but the measurement was conducted from the right to the left of the figure. The measurements were conducted before installation of the model in the DNW-KRG test section. Note also that the oscillations superimposed onto the measured profile were not due to surface roughness. They were caused by vibrations in the building structure where the measurements were conducted or by vibration of the stylus when placed in contact with the surface. It can be seen in Fig. B.3.1.1 that practically no step was generated at the junction for this configuration. However, a gap is observed between the model front part and model main part.

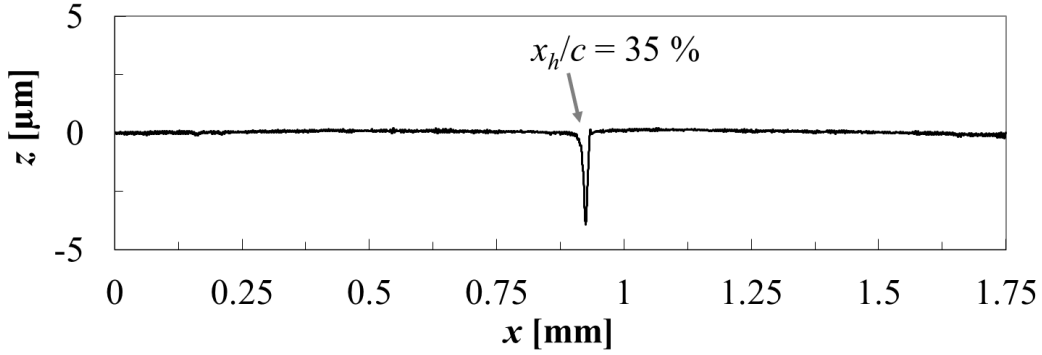

Fig. B.3.1.1. Measurement in the chordwise direction across the model junction at the spanwise location y/b = 0.4. Smooth configuration.

It should be remarked here that the measurement of the model contour at the junction is affected by the shape of the stylus tip of the contact profilometer. The stylus tip has a conical shape with an apex angle of 90° and a tip radius of 2 µm. Just after it has passed the forward corner of the junction (on the right in Fig. B.3.1.1), the stylus tip loses its contact with the surface and only the forward side of the 90° stylus cone remains in contact with it. Further moving in the chordwise direction, the device does not register any reliable signal, since the vertical displacement of the stylus tip is only dictated by the sliding of the forward side of the stylus cone over the forward corner or the forward side of the junction. At a certain longitudinal location, the aft side of the stylus cone encounters the aft edge of the junction (on the left in Fig. B.3.1.1) and begins to slide along it. The measured profile is again reliable when the stylus tip has recovered its contact with the surface, i.e., just ahead of the aft corner of the junction. Note that this issue is not relevant for imperfections with rounded edges, such as the bumps and the waviness discussed in Appendix B.3.2, since their contour can be followed by the stylus tip. In contrast, it is significant for abrupt surface changes that have sharp corners and wall-normal edges. This description corresponds to that of the surface imperfections (steps and, although undesired, gaps) that were to be examined in this work. Only position and shape of the upper corner(s) of such geometries can be accurately measured. Nevertheless, these give the essential information needed in the present study. In the case shown in Fig. B.3.1.1, the vertical distance between the forward and aft corner of the junction and the shape of the corners can be determined with great accuracy. The height difference between the two corners is the step height for the smooth configuration; it is less than 0.5 µm in the considered case. The gap width can be determined by virtually prolonging the contour of the model component at lower height until it reaches the opposite side of the junction. The longitudinal distance between its corner and this virtual intersection point is taken to be the gap width. For the reasons discussed above, this method provides only an approximation of the actual gap width, since the opposite side of the junction is not resolved well by the contact profilometer. Nevertheless, the

approximation is reasonable when the height difference between the corners is not large, as in the case shown in Fig. B.3.1.1. For this spanwise location, the gap width was approximately 25 µm. The step height for the smooth configuration was less than 1 µm at all examined spanwise locations; the average value of the gap width was approximately 25 µm.

The contact profilometer was also used to measure the height of the steps that were intentionally generated at $x_h/c = 35$ % on the model upper side. For these measurements, the device was operated with a vertical measurement range of ±250 µm and a vertical resolution of ±8 nm. The measurements were carried out at the same spanwise locations as those discussed above for the smooth configuration. An example of the surface profile across the junction for the step-1 configuration (nominal height $h = 30$ µm) is shown in Fig. B.3.1.2. The measurement was conducted at $y/b = 0.4$. A forward-facing step, with a height of approximately 29 µm, can clearly be seen at the junction. The upper corner of the step was observed to be sharp, with a very small radius of less than 0.5 µm. The measurement was conducted in the direction opposite to that of the flow. (The leading edge is however on the left in the figure.) Just upstream of the upper step corner, the stylus tip lost its contact with the surface and recovered it only on the model front part, at a certain distance from the step edge. The result of the measurement thus indicates a step perpendicular to the model surface; the step profile appears as a ramp in Fig. B.3.1.2 for the aforementioned behavior of the stylus when its tip is no longer in contact with the surface. This appearance of sharp steps as ramps is known from past work [279], where a contact profilometer has been used to measure the thickness of a thin film.

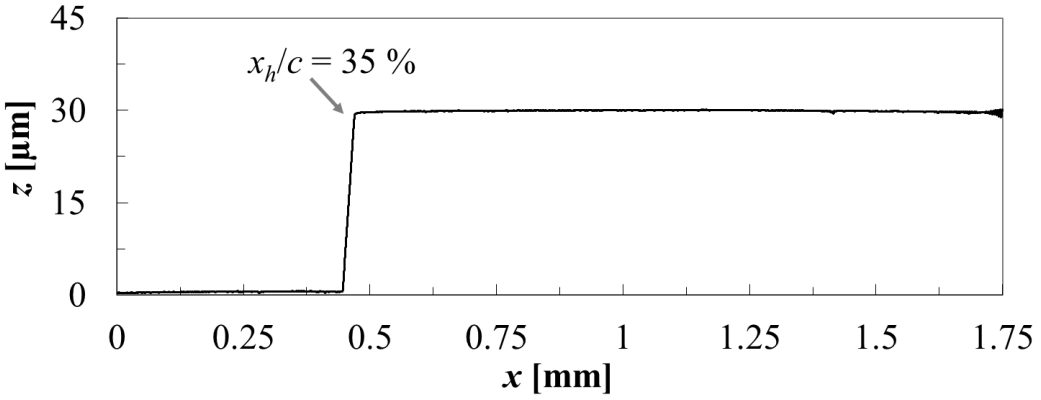

Fig. B.3.1.2. Measurement in the chordwise direction across the model junction at the spanwise location $y/b = 0.4$. Step-1 configuration (nominal step height $h = 30$ µm).

The "deformation" of sharp steps clearly becomes more pronounced with increasing step height. The shape of the step was verified by changing the angle between tracing arm and model surface to a non-zero value. An example of a measurement with a tilted tracing arm is shown in Fig. B.3.1.3 for a step of nominal height $h = 60$ µm (step-2 configuration). The measurement was conducted in the streamwise direction at $y/b = 0.8$.

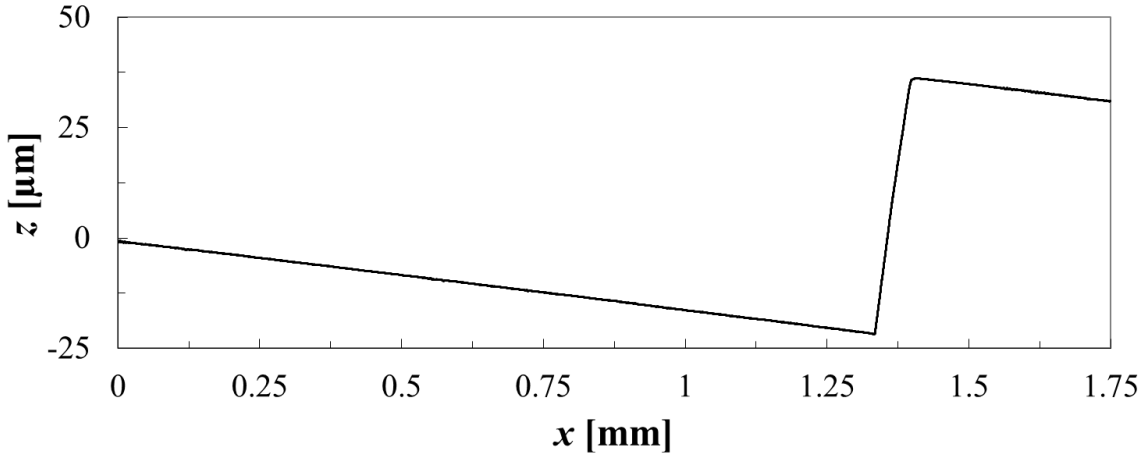

Fig. B.3.1.3. Measurement in the chordwise direction across the model junction at the spanwise location y/b = 0.8. Step-2 configuration (nominal step height h = 60 µm).

The step was confirmed to be perpendicular to the model surface and to have a sharp upper corner with a radius of less than 0.5 µm. The step height was found to be approximately 59 µm. It should be noted that no gap is visible either in Fig. B.3.1.2 or Fig. B.3.1.3. This observation is common to all other measurements of the junction on step configurations, which were conducted with both parallel and tilted tracer arm. The presence of a narrow gap in front of the step, of width 15 µm or less, cannot be excluded a priori, but the used stylus tip, with a 90° apex angle, did not allow a better resolution of the surface close to the bottom corner of the step.

B.3.2 Analysis (and improvement) of model surface quality

The manufacturing tolerances for the *PaLASTra* wind-tunnel model were established on the basis of available criteria for allowable waviness and contour deviation [161-162,169] and results of previous wind-tunnel experiments at high unit Reynolds numbers in DNW-KRG and ETW. The allowable deviations of the model contour from design were:

- $\Delta z = \pm 15$ µm on the model upper side at $x/c < 40$ % and on the model lower side at $x/c < 5$ %;
- $\Delta z = \pm 25$ µm on the remaining model surface.

The allowable surface waviness was:

- $h/a = \pm 0.0025$ on the model upper side at $x/c < 90$ % and on the model lower side at $x/c < 5$ %;
- $h/a = \pm 0.005$ on the remaining model surface.

The required average surface roughness and mean roughness depth were $0.15\ \mu m \leq R_a \leq 0.6\ \mu m$ and $1\ \mu m \leq R_z \leq 4\ \mu m$, respectively. These requirements on surface roughness were not related to surface quality for the wind-tunnel tests,

since this was provided by the final polishing carried out after TSP application. This requirement was rather a compromise between an acceptable start value for final polishing, which allowed the desired smoothness to be achieved, and a minimal roughness that ensured adhesion of TSP to the metallic surface. The surface quality was verified after manufacturing by means of a coordinate measuring machine with an accuracy of ±3 µm. Contour deviations and surface waviness were within the requested tolerances at all measurement locations. The deviations from the design contour are summarized in Table B.3.2.1 for seven spanwise locations and nine chordwise locations on the model upper side. Note that the measurements were conducted in the region $0.18 \leq y/b \leq 0.82$, with emphasis on the mid-span region, since this was the region of major interest in the experiments.

Table B.3.2.1 Deviation of the contour of the *PaLASTra* model from design. Measurements conducted after manufacturing by means of a coordinate measuring machine. Values of Δz in µm. Color coding: green for $|\Delta z| < 10$ µm, yellow for $10\ \mu m \leq |\Delta z| < 15\ \mu m$, orange for $15\ \mu m \leq |\Delta z| < 20\ \mu m$, and red for $|\Delta z| \geq 20$ µm. The approximate position of the junction between model front part and model main part is indicated by a thicker separation line.

	y/b = **0.18**	**0.34**	**0.42**	**0.5**	**0.58**	**0.66**	**0.82**
x/c = **0.1**	-8	-3	-9	0	-5	-5	-6
0.2	-9	-2	-8	-2	-7	-9	-8
0.3	-11	-5	-5	2	-2	-5	-5
0.4	16	20	16	24	19	16	9
0.5	10	20	21	25	19	17	10
0.6	9	17	20	22	19	16	12
0.7	10	17	19	23	21	18	15
0.8	9	14	21	23	22	19	17
0.9	13	17	22	24	23	22	15

The contour accuracy was excellent on the model front part (deviation from the design contour of less than ±10 µm at almost all measurement locations), but larger deviations were seen at $x/c \geq 40$ %, especially in the mid-span region. Although these deviations were within the tolerance, they were very close to the maximally allowable value. In particular, the depth of the pocket for application of TSP on the model main part was up to 25 µm lower than the desired 120 µm. This, however, could be taken into account when the TSP coating was sanded down: the coating thickness was adjusted according to the actual pocket depth on the considered region.

An example of the surface waviness evaluated from the measured contour is shown in Fig. B.3.2.1 for the spanwise section $y/b = 0.42$. Surface waviness was below $h/a = \pm 0.0025$ at all chordwise locations; large values of h/a were however

seen on the model upper surface in the region 33.5 % ≤ x/c ≤ 36.5 % (strip to be left uncoated) and in some regions of the model lower surface.

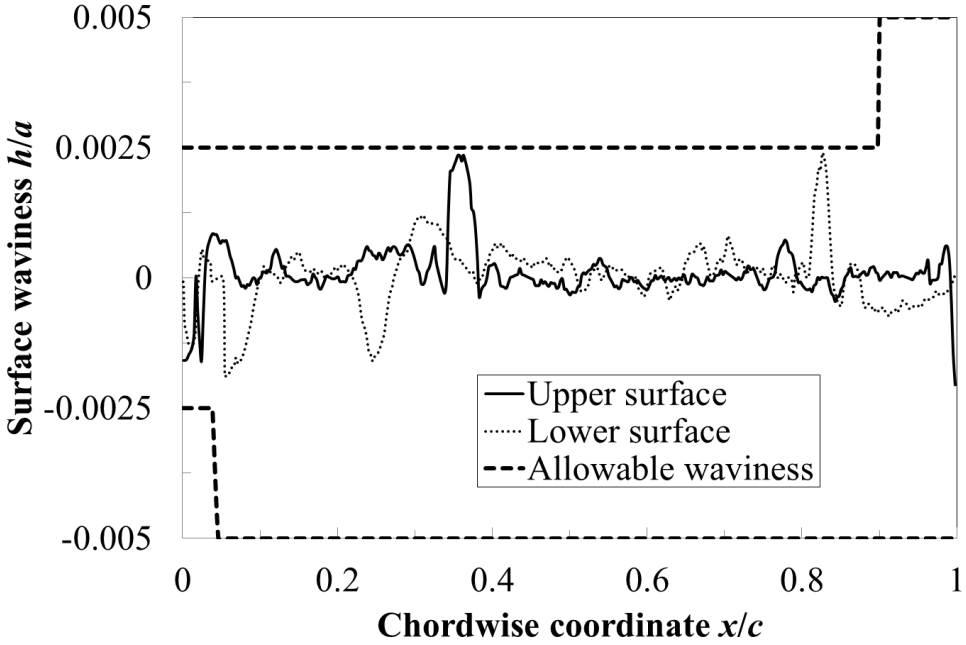

Fig. B.3.2.1. Surface waviness evaluated at the spanwise section y/b = 0.42.

The wind-tunnel model was accepted in this status and delivered to DLR after the surface had been polished to achieve an average roughness of R_a ~ 0.2 µm (R_z ~ 1.5 µm), matching the requirement on surface roughness. The surface roughness was measured at DLR by means of the aforementioned contact profilometer [210] with a vertical measurement range of ±25 µm, a longitudinal measurement length of 1.75 mm, and a vertical resolution of ±0.8 nm. The TSP was then applied and sanded down as described in Section 3.4.1. The thickness of the TSP layer after sanding down was approximately 100-130 µm, depending on the local depth of the pocket, as discussed above. The surface quality was then verified using the contact profilometer, with emphasis on the interfaces between TSP and uncoated strip at x/c = 33.5 and 36.5 %. For this investigation, the vertical measurement range of the measuring device was set to ±250 µm, corresponding to a vertical resolution of ±8 nm. The edges of the uncoated strip were requested as sharp, but the measurements in the chordwise direction showed that they were rounded indeed. An example of the model contour variation in the chordwise direction is presented in Fig. B.3.2.2a, where the measurement of the contact profilometer at y/b = 0.4 is shown. The measurement length in the chordwise direction was Δx = 17.5 mm (corresponding to $\Delta(x/c)$ = 8.75 %). The nominal start and end of the uncoated strip are shown by vertical dashed lines. The spike in the profile between the two dashed lines corresponds to the junction at x_h/c = 35 % between model front and main parts.

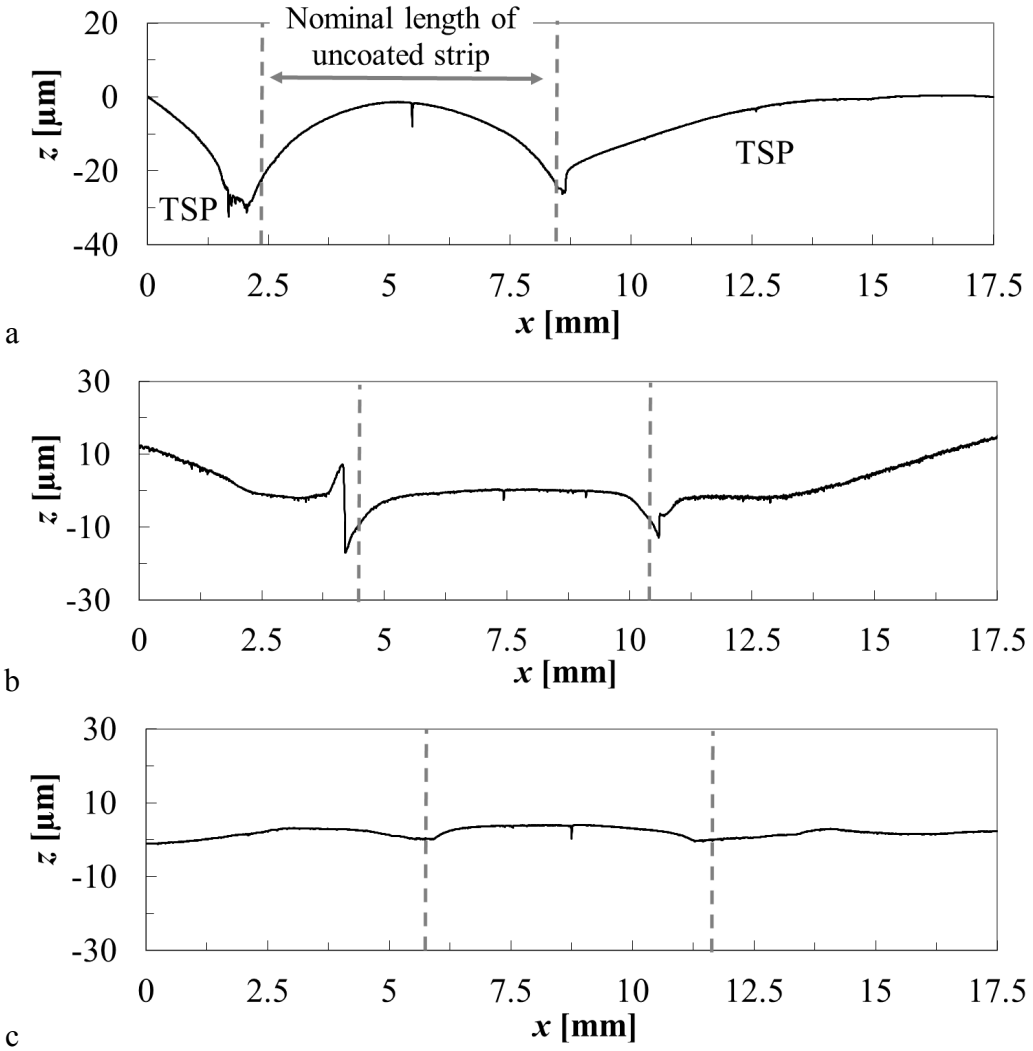

Fig. B.3.2.2. Surface quality across the uncoated strip located at 33.5 % ≤ *x*/*c* ≤ 36.5 %. Measurements conducted in the chordwise direction at *y*/*b* = 0.4 by means of a profilometer [210]. Leading edge is on the right. a: before additional milling of uncoated strip; b: after additional milling; c: after sanding down of TSP.

A glance at Fig. B.3.2.2a shows that the uncoated strip had the shape of a bump in the chordwise direction. The height of the bump was approximately 30 µm, corresponding to a bump height-to-length ratio $h/a \sim 0.0100$, being a half of the uncoated strip length in the chordwise direction. This value of h/a is significantly larger than the maximally allowable waviness for that region of the surface. Moreover, after sanding down of the TSP, an indent formed between the coating and the crest of the uncoated strip. A model surface with such imperfections in the chordwise direction was not adequate for the present study, since such surface waviness would have induced premature transition. In order to improve the quality of the model surface, the height of the uncoated strip was reduced by approximately 20 µm by milling. Clearly, there was at this point a difference in height between the TSP surface and the crest of the uncoated strip, as shown in Fig. B.3.2.2b. The TSP thickness on the upper side of the model front part was also reduced by approximately 20 µm by sanding down. The final thickness of

the coating in this region was thus approximately 100-110 µm. (In some regions on the upper side of the model front part, the thickness of the TSP layer was approximately 130 µm before reduction.) On the model main part, the thickness of the TSP layer was reduced by approximately 20 µm at the interface between TSP and uncoated strip at $x/c = 36.5$ %. The thickness of the TSP layer was then gradually reduced when moving upstream in the chordwise direction. At the interface at $x/c = 97.5$ %, i.e., between TSP and uncoated strip close to the trailing edge, the coating thickness was left unchanged. In this manner, no strong contour deviations were present in proximity of the two interfaces. The thickness of the temperature-sensitive paint was gradually adjusted also on the lower side of the model front part, so that no step formed at the interface between TSP and uncoated surface at $x/c = 5$ %.

The thickness of the top layer of the TSP, where the luminophores were incorporated, was reduced by approximately 20-30 µm on most of the model surface. The total thickness of the TSP layer was generally 100-110 µm. This was still sufficient to obtain adequate luminescent intensity from the TSP. However, as discussed above, the pocket was too shallow in some localized areas on the model main part, and the thickness of the TSP layer was already reduced to adjust it to the local pocket depth. In the mid-span region immediately downstream of the uncoated strip, the further reduction of the coating thickness led to the complete removal of the active layer, so that no TSP signal was available on these areas. The final deviation of the actual contour from design was either within the aforementioned tolerances, or just slightly larger than them. This was accepted, since the scope of this work was not the accurate measurement of aerodynamic loads on a certain airfoil. Analogously, the final contour gradient on the model main part, approximately 20 µm over more than 120 mm, was considered as negligible. In fact, all contour variations over a large distance were accounted for by measuring the actual surface pressure, which was used to determine the pressure gradient parameter and the boundary-layer displacement thickness (see Section 4.3).

Great care was taken to avoid localized imperfections in the region $30\ \% \leq x/c \leq 40\ \%$, since undesired steps, gaps, bumps, or waviness would have caused premature transition on the (nominally) smooth configuration. In particular, the gaps upstream and downstream of the uncoated strip, visible in Fig. B.3.2.2b, had to be filled up. A procedure was found to repair these locations. The uncoated strip was accurately cleaned by means of a silicone remover and via plasma-cleaning. A 3 mm wide tape was then applied onto the uncoated strip on the region around $x_h/c = 35$ % to ensure that the junction remained uncoated. The model surface at approximately $x/c < 31.5$ % and $x/c > 38.5$ % was also masked to prevent that additional coating was applied onto these regions. The masked surface was coated with approximately 40 µm of the same material as that used for the primer layer. The surface was locally sanded down to remove discontinuities and, finally, polished to reduce surface

roughness. An example of the final contour in the chordwise direction is shown in Fig. B.3.2.2c, again for the spanwise location $y/b = 0.4$. The improvement of the model contour is apparent. The gaps upstream and downstream of the uncoated strip were completely filled by the additional coating. Note that the used coating also adhered to the outward surfaces of the (originally) uncoated strip; this smoothed the interfaces at $x/c = 33.5$ and 36.5 % and reduced the height difference over the uncoated strip. The remaining surface waviness was less than $h/a = 0.0025$: the requirement on surface waviness discussed in the beginning of this section was thus fulfilled.

Surface roughness was measured after final polishing using the contact profilometer, in this case with a vertical measurement range of ±25 µm, a longitudinal measurement length of 1.75 mm, and a vertical resolution of ±0.8 nm. The center of the measurement length was placed at $x/c \sim 3$, 15, 31, 34, and 40 % for each one of the five examined spanwise locations: $y/b = 0.3$, 0.4, 0.5, 0.6, and 0.7. Note that the measurement locations included also the repaired area and the uncoated strip. The obtained values of average roughness and mean roughness depthe were discussed in Section 3.4.1.

B.4 Challenges for the application of other measurement techniques for transition experiments at DNW-KRG

Conventional measurement techniques, widely used for the investigation of laminar boundary layers at low speed, are not suitable for the study of the (very) thin boundary layer developing over the surface of models tested at DNW-KRG. The boundary layer over the first tenth of the model chord is extremely thin: the boundary-layer displacement thickness is less than 20-50 µm at $\mathrm{Re} \sim 6\text{-}13 \cdot 10^6$ (see also Fig. B.1.1). Although it grows in the streamwise direction, its maximal displacement thickness is generally less than approximately 80-130 µm at $\mathrm{Re} \sim 6\text{-}13 \cdot 10^6$. Flattened Pitot tubes [38,95,121] and Preston tubes [41,43,280] are impracticable because their wall-normal dimension is comparable to or even larger than the boundary-layer thickness. Moreover, the presence of the probes and, even in a larger measure, of their support produces large disturbances in the boundary layer. The probe support should be sufficiently rigid to withstand the forces generated by the interaction with the flowfield in DNW-KRG. The blockage due to the support can also influence the measurement at the probe location. The measurement can be affected by probe and support vibrations. These problems are also common to hot-wire anemometry [77]. Near-wall measurements by means of hot-wires are contaminated by the heat flux towards the model surface; therefore, hot-wires have to be kept at a distance larger than approximately 100 µm from the model surface [48,201], which is even outside of the boundary layer over the *PaLASTra* model at $x/c < 5$ % for $\mathrm{Re} > 6 \cdot 10^6$. These techniques provide only a punctual measurement. A multi-probe array or a transverse mechanism for a single probe are therefore necessary to obtain spatial

information. The probes in an array have to be distributed in a staggered order, so that the measurement at any one sensor is not affected by the disturbances caused by the upstream sensors; this arrangement, however, allows the boundary-layer to be examined only along the multi-probe array. Furthermore, it reduces the size of the model surface region available for investigation of the undisturbed boundary layer by means of other measurement techniques. A transverse mechanism ensures spatial resolution, but also increases blockage effects and introduces additional disturbances [201]. Note also that access to hot-wires for repair of damaged solder joints is limited in a cryogenic environment. Surface mounted sensors, such as hot-films, microphones, or Kulite © pressure sensors, are an alternative for the investigation of laminar boundary layers. Microphones cannot withstand the large pressure drop occurring at DNW-KRG after the fast-acting valve has been opened, and therefore cannot be used in this facility. The typical thickness of the substrate carrying hot-films is 50-70 μm [201,281], which is clearly too large for boundary-layer experiments at DNW-KRG. The substrate can be installed into pockets, so that only the hot-film and the copper leads are immersed in the boundary layer. Their thickness is 4-8 μm [281,282]. This thickness is still sufficient to affect the development of the laminar boundary layer over a considerable chordwise region: the corresponding roughness Reynolds number Re_k for models tested at DNW-KRG is indeed in the range of critical values for inducing premature transition [243]. Moreover, the sensor generates a thermal wake that influences boundary-layer measurements downstream of the hot-film location. Note that these problems are also common to wall hot-wires [283]. Microphones and Kulite © pressure sensors are generally attached to orifices drilled in the model surface. These orifices have a small diameter (typically 0.2-0.3 mm), which is however sufficient to introduce a strong disturbance into the laminar boundary layer over the surface of a model tested at DNW-KRG, thus causing the development of a turbulent wedge immediately downstream of the orifice. In order to obtain spatial information, hot-films and Kulite pressure sensors have to be arranged (in a staggered order) into arrays, with the related drawbacks discussed above. The spatial resolution is limited by the spacing between the sensors, which is, in general, a few millimeters [282,284]. Sublimating chemicals and oil-film interferometry are not suitable measurement techniques for the investigation of boundary layers in cryogenic wind tunnels. Most of the sublimating chemicals, which are typically used for boundary-layer studies, have arisen human health concerns and their use is therefore no longer recommended [201]. An oil film (and a layer of sublimating chemicals as well) has to be removed and re-applied for each data point: the conduction of this activity leads to long interruptions of the measurement campaign and very high wind-tunnel operation costs per data point, as discussed in Appendix B.2 for the deflection of a trailing-edge flap. In the specific case of DNW-KRG, it should be also verified if the run time of a single test run is sufficient for the applied film to reach steady conditions [285]. The run time is probably the limiting factor for the use of oils with large viscosity,

whereas the gas circulation speed induced by the DNW-KRG blower can be sufficient to smear a film of low-viscosity oil before the actual test run has started. Micro particle image velocimetry (micro-PIV) has been used to investigate boundary layers applying long-distance microscopes [286]. The use of this measurement technique, however, is limited by aspects related to the imaging system and to the particle seeding [286]. Further limitations are related to the specific case of DNW-KRG. The relatively short run time allows only a small number of images to be recorded, so that several test runs have to be repeated to measure accurately the mean-velocity profile [286-288]. Repeatability of particle concentration and uniformity in a blow-down facility has to be ensured. A four-frame setup with two cameras and two lasers with polarization filters can be used to double the image recording rate; in this case, however, vibrations, camera calibration errors, and temperature changes lead to measurement errors. Because of the large flow speed, the lasers must be capable of providing light pulses with a time interval of the order of hundred nanoseconds. Light reflection from the highly polished model surface, necessary to guarantee surface smoothness compatible with natural laminar flow, can also affect the measurement. Additional concerns of practical nature are: the limited optical access available at DNW-KRG; the need of a window, not subjected to strain, in the clamping jaw supporting the model; the difficult system alignment; and the necessity of a rigid measurement system to withstand the forces acting during a test run. Measurements by means of laser Doppler anemometry (LDA) also suffer of many of the limitations discussed above and in [286] for micro-PIV, in particular of those related to particle seeding, light reflection from the model surface, temperature variations, system vibrations, and system misalignment. Furthermore, the smallest measurement volume that can be used has a diameter of 35 μm and a length of 60 μm [289], and the lowest uncertainty in the measurement volume localization is of the order of 60 μm [290]. These limitations lead to large bias errors in the measurement of boundary layers [288]. Note also that LDA systems with high spatial resolution have a low data sampling rate [289]. As a final remark, it should be emphasized that neither micro-PIV nor LDA can resolve the very low amplitude of the disturbances within a laminar boundary layer, which is of the order of 0.1 % U_∞ or less [201].

B.5 Temperature-sensitive paint used in the present work

The images shown in Fig. B.5.1a, Fig. B.5.1b, and Fig. B.5.1c correspond to the following respective TSP application phases: before application of the primer layer, after application of the screen layer, and with the final coating. The layer composition of the various coatings is sketched in Fig. B.5.1d.

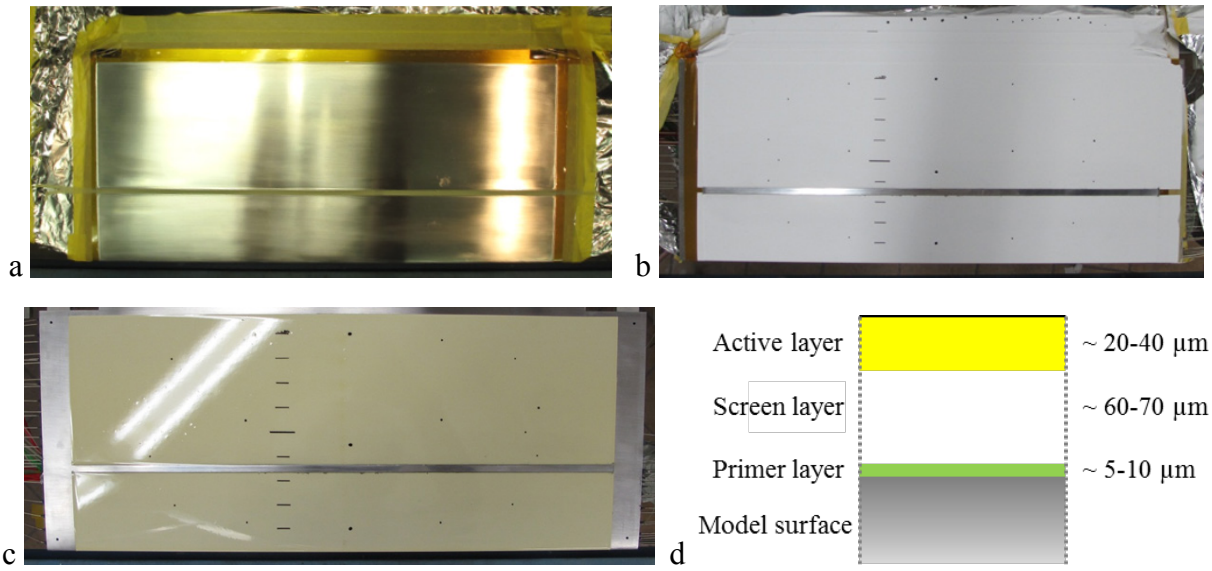

Fig. B.5.1. TSP application on the *PaLASTra* wind-tunnel model. a: before any coating; the regions of the model surface that had to be left uncoated were masked using tape. b: after application of the screen layer. c: final coating. d: layer composition of the various TSP coatings.

The chemical structure of the used luminophore is shown in Fig. B.5.2a [214]. The excitation and emission spectra of the used temperature-sensitive paint are shown in Fig. B.5.2b.

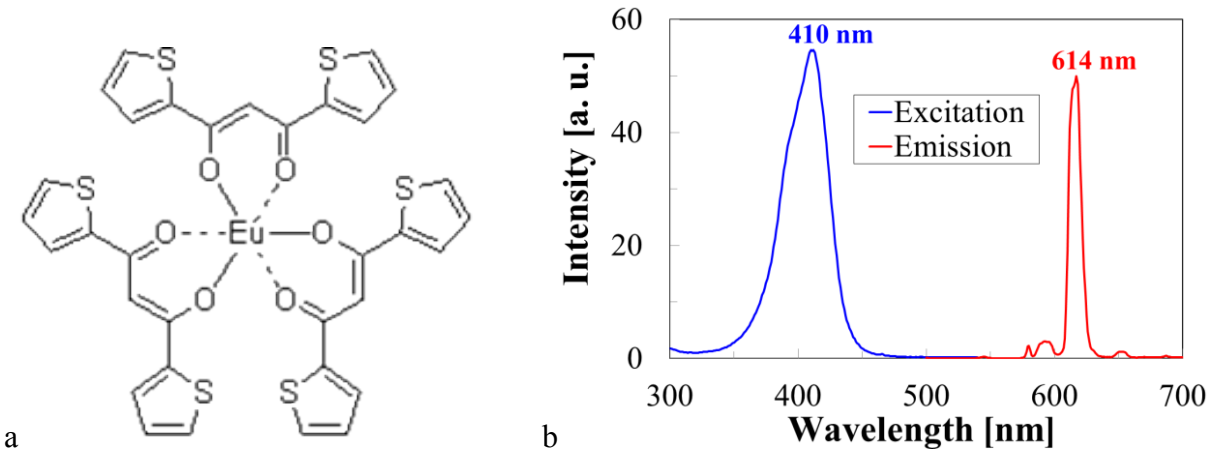

Fig. B.5.2. a: chemical structure of the used luminophore [214]. b: excitation and emission spectra of the used temperature-sensitive paint.

The relation between emitted luminescent intensity I and temperature T was determined experimentally using the calibration system discussed in [291]. The setup for the calibration was basically the same as that used later in the wind-tunnel tests. For the calibration, a square aluminum sample of 15 mm side and 1 mm thickness was coated contemporarily to the wind-tunnel model, so that the applied TSP was as in the wind-tunnel tests. The luminescent intensity was detected by a CCD camera with a 12-bit dynamic range. A bandpass filter for the

wavelength range 590–665 nm was placed in front of the camera. Excitation light in a narrow band about $\lambda_{ex} = 405$ nm was provided by a monochromator. The wavelength of the excitation light was selected to match the wavelength corresponding to the peak intensity of the light provided by the LEDs used in the wind-tunnel experiments. Luminescent images were acquired with fixed settings at various temperatures, with an interval of $\Delta T = 5$ K. The temperature was set with an accuracy of ±0.2 K. The temperature range of the calibration covered that of the wind-tunnel tests. The intensity was evaluated at each temperature on a fixed square region of 20 pixel side over the sample surface. The luminescent intensity on the evaluation surface was assumed to be represented by a Gaussian distribution; the average intensity and the standard deviation were calculated accordingly. The ratio of average intensities I/I_{ref} obtained from the calibration is plotted in Fig. B.5.3a as a function of the temperature, with I_{ref} having been taken at $T_{ref} = 288$ K.

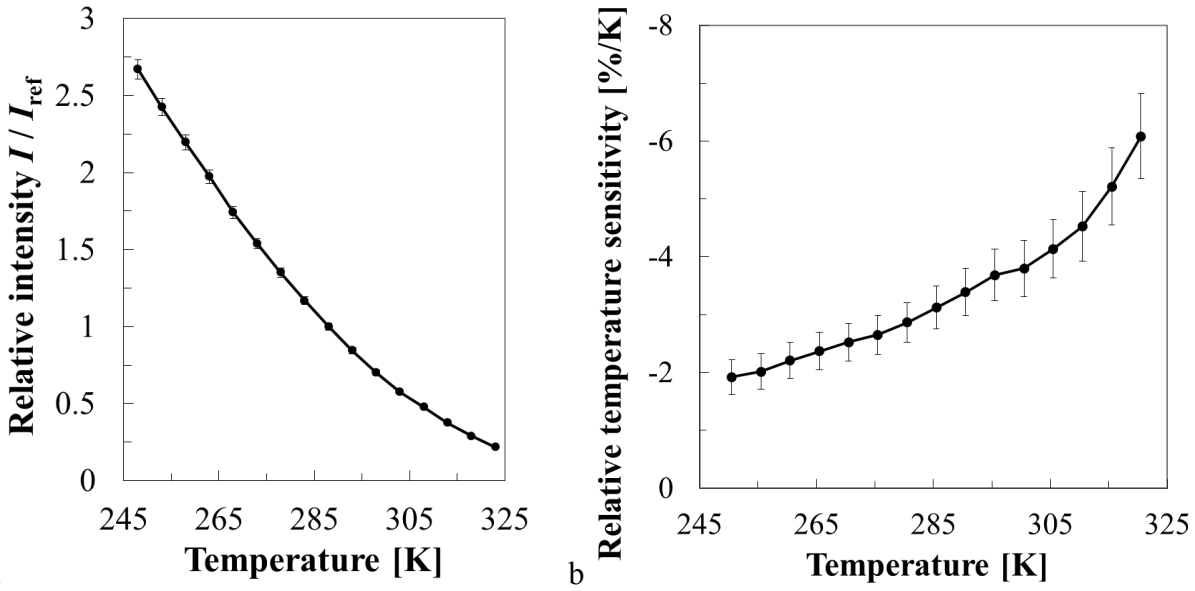

Fig. B.5.3. a: relation between relative intensity and temperature for the used TSP, with $I_{ref} = I(T_{ref} = 288$ K). b: relative temperature sensitivity for the used TSP, plotted as a function of the temperature.

The value of the luminescent intensity emitted by a temperature-sensitive paint and detected by the camera is an important property of the measurement system. In general, it can be increased (within a certain range) by increasing the exposure time of the camera, enlarging the aperture area of the objective lens, and increasing the intensity of the excitation light. Essential requirement of a TSP measurement system to succeed in transition detection is its capability to resolve a certain temperature difference. This is quantified by the relative temperature sensitivity *RS* of the TSP coating, defined as

$$RS = \frac{\partial I}{\partial T}\frac{1}{I} \qquad \text{(B.5.1)}$$

For given luminescent intensity and temperature, a larger value of RS means that the same temperature difference ΔT produces larger differences in luminescent intensity ΔI, which are more easily detected [57]. A relative temperature sensitivity of $|RS| < 2\ \%$ is generally considered as low, whereas $2\ \% \leq |RS| < 4\ \%$ and $|RS| \geq 4\ \%$ are considered good and excellent values, respectively [213,291]. The sensitivity of the TSP used in the experiments discussed in this work is shown in Fig. B.5.3b as a function of the temperature. As can be seen from this plot, the relative temperature sensitivity increases continuously with increasing temperature. The used TSP shows good sensitivity in the temperature range $260\ \mathrm{K} \leq T \leq 290\ \mathrm{K}$, at which the wind-tunnel tests have been conducted.

B.6 Locations of pressure taps and thermocouples installed on the *PaLASTra* model

Table B.6.1 Locations of pressure taps and thermocouples installed on the *PaLASTra* model. Pressure tap on model leading edge listed on model upper side.

Pressure taps, upper side			
#	*x*/*c*	*y*/*b*	*z*/*c*
1	0.000	0.50	0.033
2	0.003	0.48	0.037
3	0.006	0.50	0.038
4	0.012	0.50	0.040
5	0.021	0.50	0.041
6	0.035	0.50	0.043
7	0.050	0.50	0.044
8	0.071	0.50	0.046
9	0.090	0.50	0.047
10	0.120	0.50	0.048
11	0.150	0.50	0.049
12	0.180	0.50	0.049
13	0.210	0.50	0.050
14	0.240	0.50	0.050
15	0.270	0.50	0.050
16	0.291	0.50	0.050
17	0.310	0.50	0.050
18	0.330	0.50	0.050
19	0.340	0.50	0.050
20	0.360	0.50	0.050
21	0.370	0.50	0.050
22	0.385	0.50	0.050
23	0.405	0.50	0.050
24	0.440	0.50	0.050
25	0.480	0.50	0.050
26	0.520	0.50	0.050
27	0.570	0.50	0.050
28	0.630	0.50	0.050
29	0.700	0.50	0.050
30	0.800	0.50	0.050
31	0.900	0.50	0.050
32	0.980	0.50	0.050

Pressure taps, lower side			
#	*x*/*c*	*y*/*b*	*z*/*c*
33	0.001	0.48	0.029
34	0.004	0.50	0.025
35	0.011	0.50	0.019
36	0.023	0.50	0.012
37	0.051	0.50	0.002
38	0.100	0.50	-0.010
39	0.151	0.50	-0.018
40	0.210	0.50	-0.026
41	0.280	0.50	-0.033
42	0.361	0.50	-0.040
43	0.420	0.50	-0.043
44	0.490	0.50	-0.046
45	0.581	0.50	-0.049
46	0.690	0.50	-0.050
47	0.720	0.50	-0.050
48	0.790	0.50	-0.050
49	0.810	0.50	-0.045
50	0.830	0.50	-0.035
51	0.880	0.50	-0.010
52	0.950	0.50	0.025

Thermocouples			
#	*x*/*c*	*y*/*b*	*z*/*c*
1	0.101	0.30	0.047
2	0.201	0.29	0.050
3	0.400	0.27	0.050
4	0.850	0.30	0.050
5	0.650	0.30	0.045
6	0.150	0.30	0.044

C Data analysis

C.1 Post-processing of TSP data

The initial phase of the TSP-image processing was carried out in the image plane of each of the two cameras (model port side and model starboard side). The wind-off images were first averaged to improve the signal-to-noise ratio. Although it had been clamped at the test-section side walls, the *PaLASTra* model had moved slightly under aerodynamic loading during a run. This effect caused deformation and distortion of the luminescent model image in the wind-on images with respect to that in the wind-off images (no aerodynamic loading). The black circular markers applied to the model surface (see Section 3.4.1) were used to align wind-off and wind-on images in the image plane (image registration) [292]. This procedure is discussed in Appendix C.2.2. After alignment had been accomplished, the wind-off images were divided by the aligned wind-on images. In this manner, the intensity differences between the laminar and turbulent areas were enhanced, and the influence of inhomogeneous excitation light and coating thickness distribution could be compensated for. Model deformation during a run also causes a variation of the distribution of excitation light intensity on the TSP surface between wind-off and wind-on images, but this effect was not compensated for. This influence would be relevant only for a quantitative measurement of the surface temperature using TSP, which was not the primary scope of this work. Transition measurements by means of TSP are generally not affected by a variation of the excitation light intensity distribution between wind-off and wind-on images [57]. This effect is negligible also for the quantitative evaluation of the surface temperature conducted in this work (see Appendix C.1.4). This is likely to be due to the only quite small model deformation (estimated to be less than 0.02° in angle-of-attack) and to the rather homogenous excitation light intensity distribution provided by the used setup (less than 50 % light intensity variation over the region $0.2 \leq y/b \leq 0.5$). Examples of divided TSP images are shown in Fig. C.1.1. Bright and dark areas correspond to the laminar and turbulent boundary layers, respectively. It should be noted here that laminar regions are at higher temperatures than turbulent, and are, therefore, darker in the raw TSP images; the representation shown in Fig. C.1.1 is given by the division of the wind-off images by the (aligned) wind-on images. As can be seen in this figure, each camera could observe almost the whole upper side of the model, all the way to the opposite side wall, but the spatial resolution decreased considerably with increasing distance between model surface location and camera. This problem is particularly noticeable at the model leading and trailing edges. On the model leading edge, its small radius of curvature led to a further image distortion. In spite of this, a sufficient image resolution is still provided by each camera for more than half of the model span. The image resolution of the investigated model

surface was approximately 4.1, 3.4, and 2.8 pixels per millimeter at distances from the test-section side walls $\Delta(y/b) \sim 0.2$, 0.3, and 0.4, respectively.

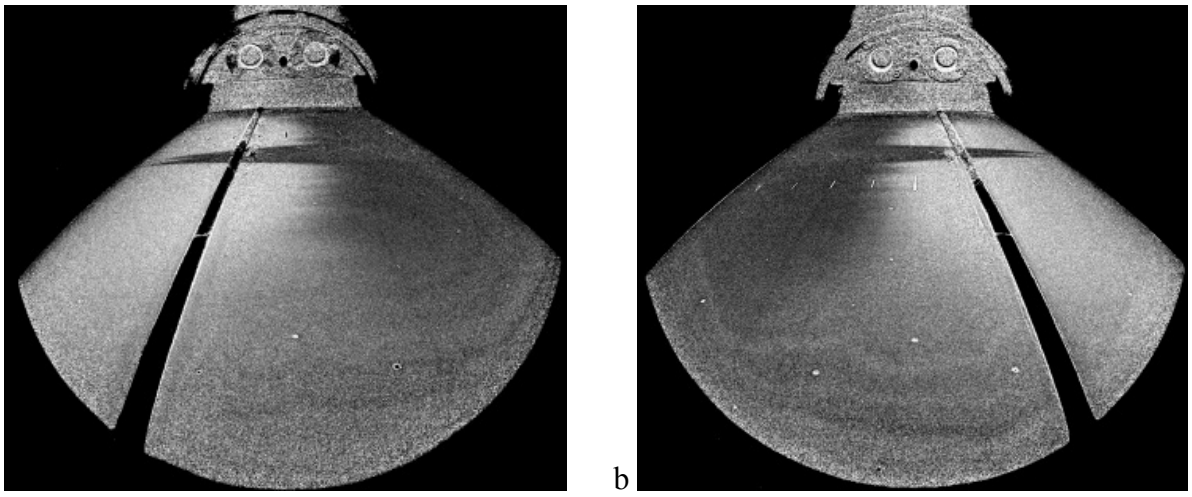

Fig. C.1.1. TSP images after alignment in the image plane and division of wind-off by aligned wind-on images. a: image from model port side (flow is from the left); b: image from model starboard side (flow is from the right). Bright and dark areas correspond to the laminar and turbulent boundary layers, respectively. M = 0.77, Re = $6 \cdot 10^6$, and AoA = -2.6°.

A glance at Fig. C.1.1 clearly shows that TSP results in the image plane are not suitable for accurate transition detection, mainly because of the pronounced perspective distortion of the image. This is caused by the short focal length of the camera lenses, by the oblique camera observation angle, and by the model curvature in the leading-edge region. An approximate transition location can be obtained using as reference points the tick markers that identify chordwise positions in 10 % steps of the chord length (see Section 3.4.1). This method, although still widely used (for example for the evaluation of transition measurements by means of IR-thermography in flight experiments [27,156] and in wind-tunnel tests [49]), can however lead to significant errors in the transition location, especially when this is to be evaluated at a considerable spanwise distance from the tick markers or in the region of lower spatial resolution (central model area in the present case). Note also that the transition location is often determined simply by sight [49]: the results therefore depend on both operator and used scale for image intensity (or temperature). Moreover, evaluation of many data points is time-consuming (no automation possible). Accuracy of transition detection by means of the TSP technique can be improved by projecting the TSP images onto a three-dimensional grid representing the model surface (mapping). Since a two-dimensional model was the test object in the current work, the three-dimensional geometry was simply generated by protruding the model cross-section in the spanwise direction. As discussed in Section 4.2, the geometry of interest is the region of model upper surface extending from $y/b = 0.2$ to 0.8. This portion of the model surface was discretized using a structured grid, as required in the *ToPas* software [223-225].

The grid resolution was one point per millimeter in both chordwise and spanwise direction. This corresponds to a grid node spacing of $\Delta(x/c) = 0.5$ % and $\Delta(y/b) = 0.002$. Mapping was carried out using the circular markers applied to the model surface. The three-dimensional grid was initially divided into two blocks, each of which extends in the spanwise direction from one grid side ($y/b = 0.2$ and $y/b = 0.8$) to $y/b = 0.49$. Each TSP image was mapped onto the corresponding block. This operation is discussed in Appendix C.1.2. The mapped TSP images were merged at the coincident edge of the two grid blocks, leading to one combined TSP result over the whole upper surface, as shown in Fig. C.1.2. Using the software *ToPas*, the final TSP result can be viewed on the monitor from any arbitrary point-of-view. In the present work, the chosen observation position for the analysis was that of the model upper surface, as would be seen from the inaccessible top wall of the test section, with the flow coming from the left; this is shown in Fig. C.1.2b (same test conditions as in Fig. C.1.1).

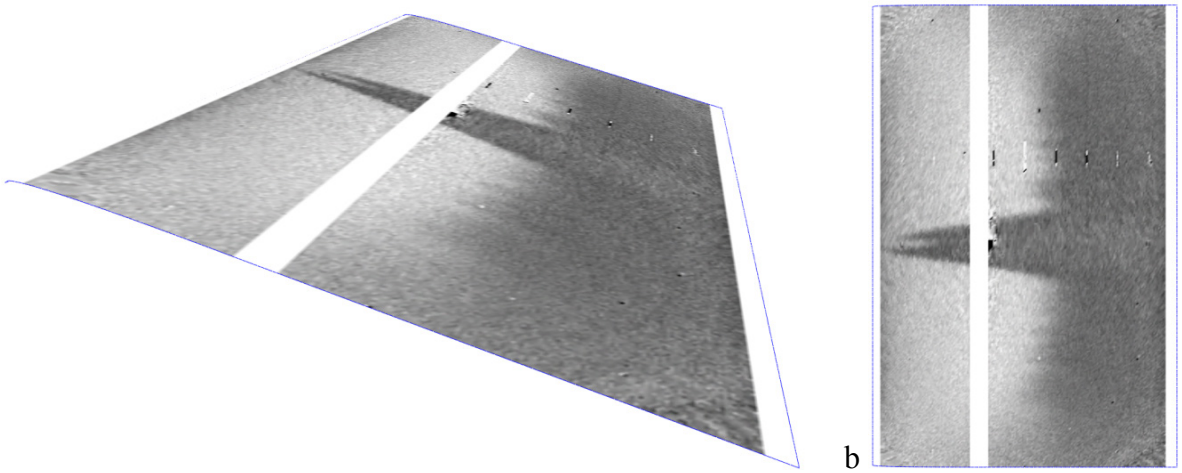

a b

Fig. C.1.2. Final TSP result at M = 0.77, Re = 6 · 10^6, and AoA = -2.6°. a: arbitrary point of view; b: as would be seen from the inaccessible top wall of the DNW-KRG test section, with the flow coming from the left.

As already discussed in Section 4.2, white masking strips were superimposed over the TSP results in the regions 32.5 % $\leq x/c \leq$ 38 % and $x/c \geq$ 96.5 % to mask the uncoated model surface areas. Note the area with absent TSP active layer extended up to $x/c \sim$ 40-42 % in the region $0.48 \leq y/b \leq 0.55$. No luminescent signal was available in this area, as can be seen in Fig. C.1.2b. It has been also mentioned in Section 4.2 that the intensity values at the corners of the final TSP results are artefacts. At $y/b = 0.2$, the maximal size of these (approximately) triangular regions was $\Delta(x/c) \sim 20$ % and 25 % from the model leading and trailing edges, respectively; they extended up to $y/b \sim 0.25$ at the leading and trailing edge. For $y/b = 0.8$, the corresponding values were $\Delta(x/c) \sim 23$ % and 27 %, with an extent up to $y/b \sim 0.72$. The surface regions at $y/b < 0.26$, $0.48 \leq y/b \leq 0.55$, and $y/b > 0.71$ were not considered for evaluating the natural-

transition location anyway, since the development of the model boundary layer on these areas was affected by the turbulent boundary layer on the test-section side walls and by the turbulent wedges in the mid-span region.

The final three-dimensional TSP results enable the accurate study of boundary-layer transition (see Section 4.2). Moreover, three-dimensional TSP results are of great help in examining flow signatures on the model surface: for example, they facilitate the identification of the locations on the model surface from which turbulent wedges originate. After these locations have been analyzed (by sight or by means of a measurement device), a procedure could be applied to prevent formation of turbulent wedges in subsequent tests, such as removal of dust particles adhering to the surface or repair of localized damage (see Appendix C.2.1).

C.1.1 Image registration

The wind-on images were aligned to the wind-off images by quadratic warping [293]. The first step to perform this operation is to find the positions of the circular markers in both wind-off and wind-on images. A "marker pair" is defined in this context as the same marker in the wind-off and wind-on image. Marker finding was accomplished manually in this work. This operation had to be repeated after the first run of any new series of tests with a certain model configuration, since the model could not be installed at exactly the same position in the spanwise direction. The marker locations could then be kept unchanged for all test conditions in the same test series. (This is straightforward for the wind-off images, but also the differences between wind-on images with various aerodynamic loadings were found to be negligible.) A system of equations for the (known) coordinates of the marker pairs is then written by means of the quadratic mapping functions. The system has to be solved for the unknown mapping function coefficients. Since 11 markers were used for each image, this system is overdetermined; its approximate solution is obtained via least-squares method by minimizing the errors at the marker positions.

C.1.2 Mapping

Mapping was carried out for the images acquired by each of the two cameras, which were mapped onto the corresponding grid block. The two blocks composing the three-dimensional grid are shown in Fig. C.1.2.1a. The positions of the marker centers on the model surface were measured using a sheet of millimeter paper, which edge was carefully attached to the model trailing edge. The measurement was sufficiently precise for the surface under investigation, which was flat at $x/c \geq 30\ \%$ and rather flat at $5\ \% \leq x/c \leq 30\ \%$: in fact, all markers were placed at $x/c \geq 10\ \%$. Mapping of the nodes of the (three-

dimensional) grid onto the points in the (two-dimensional) image is formulated as a combination of the following transformations:

- translation,
- rotation,
- perspective,
- projection from the three-dimensional space to the two-dimensional one,
- scaling in the two-dimensional space,
- lens correction.

All transformations are linear, except for the lens correction. The mapping problem is thus described by 11 unknown parameters: three for translation, three for rotation, two for perspective, two for scaling in the two-dimensional space, and one for lens correction. The mapping problem is presented in Fig. C.1.2.1b for a TSP image acquired by the camera on the model port side. The corresponding three-dimensional grid, representing the model upper surface from $y/b = 0.2$ to approximately the model mid-span, is shown in green. The positions of the markers on the three-dimensional grid and the positions of these markers transformed in the image plane are shown by red and orange dots, respectively.

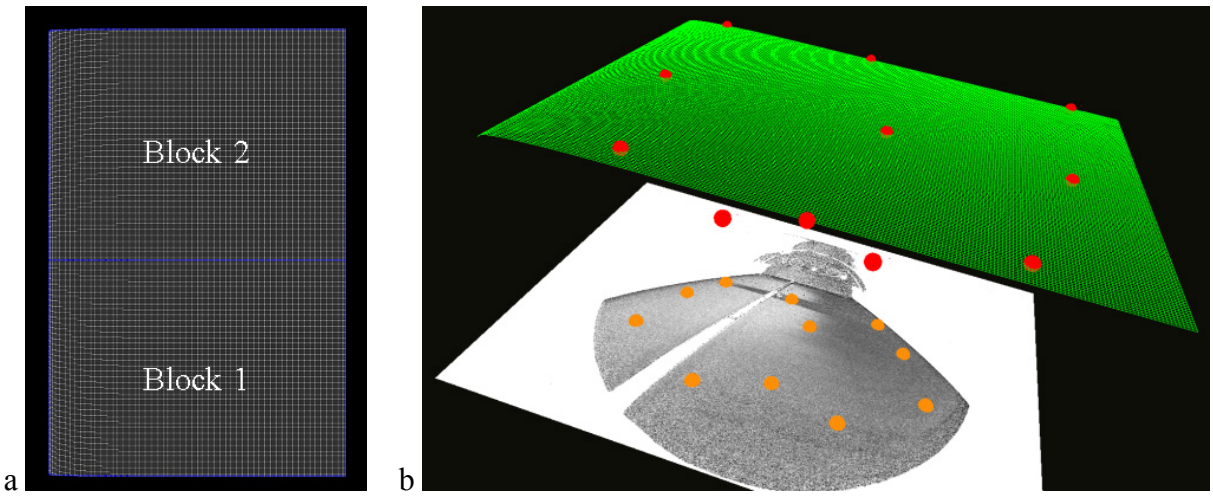

Fig. C.1.2.1. a: three-dimensional grid representing the model upper surface with block 1 (port side) and 2 (starboard side). b: three-dimensional grid for model port side (in green) with position of the markers shown by red dots. The TSP image acquired by the camera on the model port side at M = 0.77, Re = 6 · 10^6, and AoA = -2.6° is also shown. The positions of the markers transformed in the image plane are shown by orange dots.

Analogously to the alignment in the image plane discussed in Appendix C.1.1, the system of equations describing the mapping is written for the 11 markers in each TSP image ("two-dimensional markers") and the corresponding markers on the three-dimensional grid ("three-dimensional markers"). The coordinates of the marker sets in the respective frames are known. The resulting system of equations is non-linear and, in the present case, overdetermined. The approximate solution of this system is provided by the eleven mapping

parameters that minimize the difference between the positions of the two-dimensional markers in the image plane and those of the transformed three-dimensional markers, also in the image plane. The problem to be solved is shown in Fig. C.1.2.2 for the same case presented in Fig. C.1.2.1b. The positions of the two-dimensional markers and those of the three-dimensional markers, transformed in the image plane, are shown by blue and orange dots, respectively. The differences between their positions are shown by red lines. The parameters that minimize the sum of these differences are the sought mapping parameters.

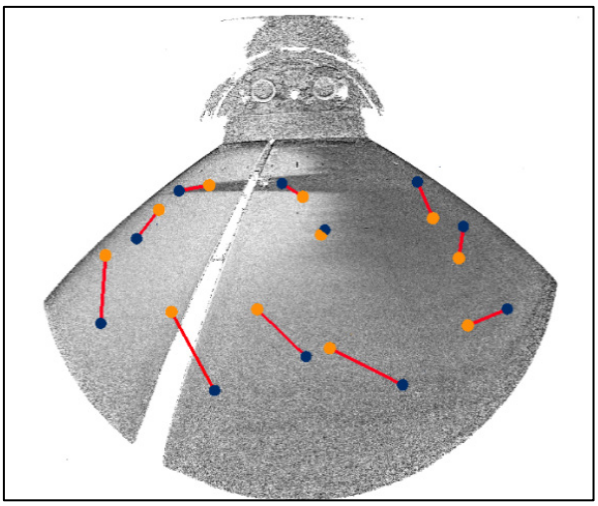

Fig. C.1.2.2. TSP image acquired by the camera on the model port side at M = 0.77, Re = 6 · 10^6, and AoA = -2.6°. The positions of the two-dimensional markers and those of the three-dimensional markers, transformed in the image plane, are shown by blue and orange dots, respectively. Red lines show the differences between these positions.

The solution of the minimal problem presented above is obtained iteratively through the method of steepest descent. Mapping of the TSP image onto the three-dimensional grid is then accomplished using the obtained mapping parameters. In the present work, the median value of squares with three pixel side was mapped from the TSP images onto the grid. This removed noise from the surface intensity distribution while at the same time preserved strong intensity gradients.

C.1.3 Transition detection algorithm [294]

The transition location x_T is defined in the present work as the location in the transitional region corresponding to the maximal slope of the luminescent intensity ratio in the chordwise direction (see Section 4.2). This location has to be determined accurately, reliably, and consistently even in the presence of noise and artefacts in the surface intensity distributions and under the most various test conditions. Therefore, the chordwise distribution of the normalized intensity ratio obtained at a certain spanwise section is first filtered using an 11 × 1 ($x \times y$) mean spatial filter before its derivative is computed. Moreover, plausibility criteria are implemented in the transition detection algorithm to ensure that the

global maximum of the intensity ratio derivative in the transitional range is detected. These criteria and the operations performed by the algorithm are listed and discussed below.

- The maximal slope of the intensity ratio distribution at the considered spanwise section is identified. The corresponding chordwise location has to fulfill the following two requirements:
  - it is in a region where the normalized intensity ratio is between 0.2 and 0.8;
  - no local maxima of the intensity ratio are present within $\Delta(x/c) = \pm 1.5$ % from this chordwise location.
- If the above requirements are not fulfilled, the chordwise location with the second largest intensity ratio derivative is considered. The search is continued until the requirements are fulfilled.
  - If none of the locations fulfills the requirements, the unphysical value of $x_T(y/b)/c = -1$ % is returned.
- A chordwise evaluation domain is identified, where the derivative of the normalized intensity ratio is larger than 75 % of its maximal value.
  - If the first (last) point of this domain is upstream (downstream) of the chordwise location where the intensity ratio is 0.2 (0.8), the limiting point for the evaluation domain is taken as that corresponding to the intensity ratio of 0.2 (0.8).
  - If the evaluation domain is smaller than $\Delta(x/c) = 4.5$ %, the threshold on the intensity ratio derivative is reduced from 75 % to 50 % of its maximal value, and the evaluation domain is determined again.
- Average and root mean square of the normalized intensity ratio are computed in the evaluation domain and in regions immediately upstream and downstream of it. These regions have approximately the same chordwise extent as that of the evaluation domain.
  - If the root mean square of the intensity ratio is smaller than that computed in the upstream and downstream regions, the unphysical value of $x_T(y/b)/c = -1$ % is returned.
- The transition location $x_T(y/b)/c$ is finally evaluated as the center of mass of the chordwise evaluation domain, using the derivative of the intensity ratio as weighting factor.

Obviously, the spanwise sections where the algorithm returned the unphysical value $x_T(y/b)/c = -1$ % were not considered for the computation of the average transition location x_T/c (see Section 4.2).

C.1.4 Quantitative evaluation of surface temperature

The surface temperature distribution was evaluated quantitatively by means of TSP using the measured luminescent intensity distribution and the paint calibration discussed in Appendix B.5. The model temperature was assumed to be uniform in the wind-off TSP images. Scope of this analysis is the determination of the model surface temperature during a run, i.e., in the wind-on images. Since the wind-off images were divided by the wind-on images to obtain the TSP results, the functional relation between luminescent intensity and temperature is written as

$$T = g\left(\frac{I_{ref}}{k \cdot I(T)}\right) \tag{C.1.4.1}$$

where g is the calibration function and I_{ref} and k are a reference intensity and a paint characteristic constant, respectively. The inverse function is

$$\frac{I_{ref}}{I(T)} = k \cdot g^{-1}(T) \tag{C.1.4.2}$$

For each point on the TSP surface, it holds that

$$g^{-1}\left(T_{wind-on}\right) = \frac{I_{wind-off}}{I_{wind-on}} g^{-1}\left(T_{wind-off}\right) \tag{C.1.4.3}$$

Note that I_{ref} and k cancel out in Eq. (C.1.4.3). The surface temperature during a run is finally obtained as

$$T_{wind-on} = g\left(\frac{I_{wind-off}}{I_{wind-on}} g^{-1}\left(T_{wind-off}\right)\right) \tag{C.1.4.4}$$

The luminescent intensity distribution on the model surface in wind-off and wind-on images is measured for each test run. Both the function g and its inverse g^{-1} have to be known to obtain the surface temperature during a run. In the present work, these functions were spline functions [295] approximating the data obtained from the paint calibration (see Appendix B.5). The maximal deviation from the calibration data allowed for the spline function approximating g was 0.1 K. The maximal allowed value for the sum of differences over all calibration points was 0.5 K. The corresponding values for the spline function approximating g^{-1} were 10^{-4} and 10^{-3}. The uniform surface temperature in the wind-off images was taken as the average of the temperatures measured by the model thermocouples before opening of the fast-acting valve; these were evaluated for each sensor as the time-average signal in the window between 0.4

and 2.2 s after data acquisition had been started (see Section 4.1). An example of the surface temperature distribution obtained using this procedure is shown in Fig. C.1.4.1a. In this case, transition occurred over the uncoated strip ($x_T/c = 35$ %), so that the regions upstream and downstream of this strip were fully laminar and fully turbulent, respectively. Surface temperature distributions in the streamwise direction, extracted along spanwise sections of width $\Delta(y/b) = 0.02\text{-}0.03$ in the region $0.26 \leq y/b \leq 0.39$, are presented in Fig. C.1.4.1b, where the temperatures measured by the thermocouples installed within the TSP layer are also shown. No value of the surface temperature is shown for the masked region at $33\ \% \leq x/c \leq 38\ \%$. As can be seen from Fig. C.1.4.1b, the results obtained using the two measurement techniques are in agreement. In particular, the variation of the surface temperature in the laminar areas is well captured by TSP. It should be also noted that the temperature distribution in the spanwise direction is not uniform. This effect can be seen more clearly in the laminar region and will be discussed in Appendix C.2.3.

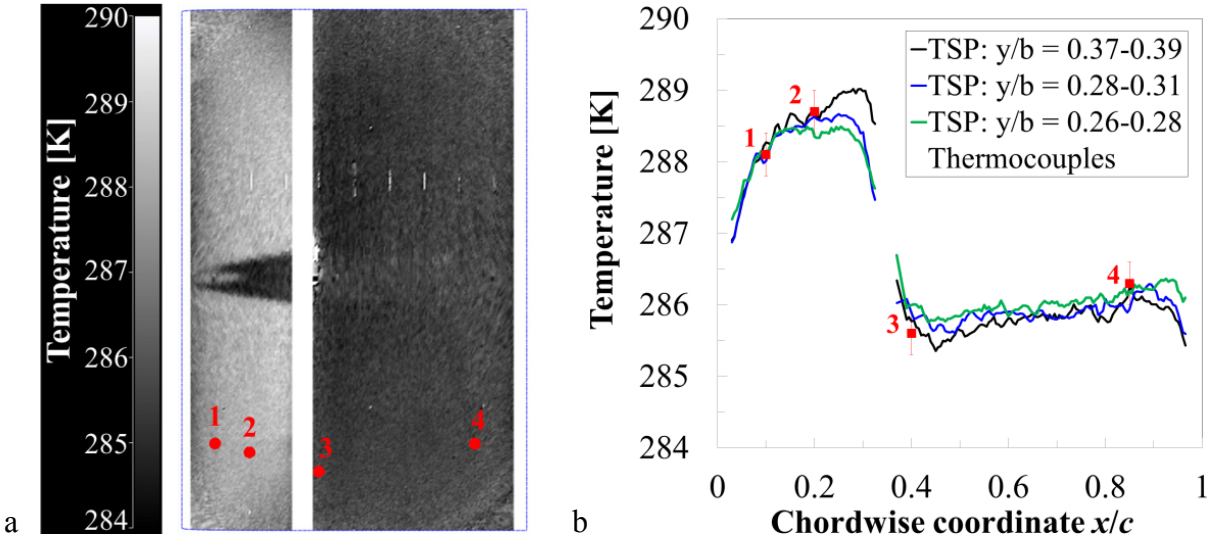

Fig. C.1.4.1. Surface temperature distribution obtained from TSP result at M = 0.77, Re = 6 · 10^6, AoA = -2.0°, and T_w/T_{aw} = 1.054. a: global surface temperature distribution. The locations of the thermocouples mounted within the TSP layer (see Table B.6.1) are shown by red dots. b: surface temperature distributions in the streamwise direction extracted along three strips of width $\Delta(y/b) = 0.02\text{-}0.03$ and comparison with temperatures measured by the thermocouples. Streamwise temperature distribution from TSP results filtered using a 3 × 1 ($x \times y$) median spatial filter.

Streamwise surface temperature distributions were extracted from the TSP results also in the spanwise regions where transition was evaluated ($0.33 \leq y/b \leq 0.44$ and $0.56 \leq y/b \leq 0.7$, see Section 4.2). Examples of the obtained data are shown in Fig. C.1.4.2.

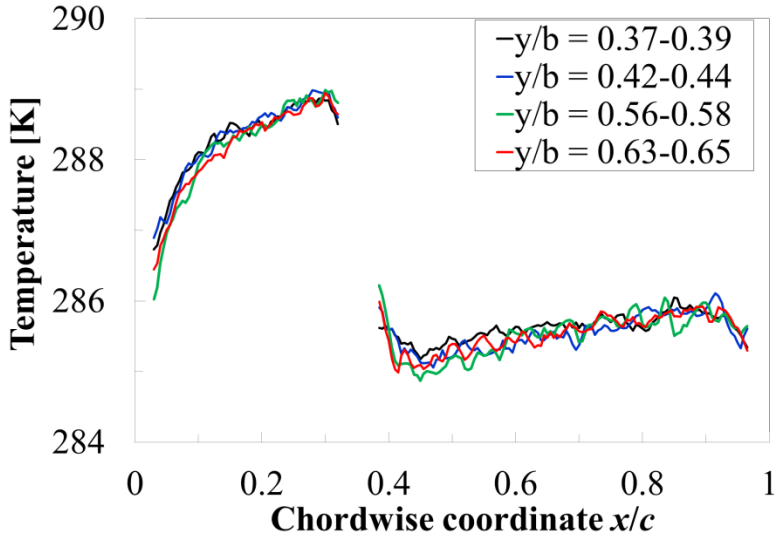

Fig. C.1.4.2. Surface temperature distributions in the streamwise direction obtained from TSP result at M = 0.77, Re = 6 · 10^6, AoA = -2.0°, and T_w/T_{aw} = 1.054. Temperatures extracted along four strips of width Δ(y/b) = 0.02 in the spanwise regions where transition was evaluated. TSP results filtered using a 3 × 1 (x × y) median spatial filter.

A glance at Fig. C.1.4.2 shows that the streamwise surface temperature distributions in the transition evaluation regions are in good agreement. Spanwise uniformity of the surface temperature was thus verified in these regions.

C.2 General features of TSP results

C.2.1 Turbulent wedges observed on the model surface

Some turbulent wedges were observed superimposed on the transition pattern at all test conditions (see, e.g., Fig. C.1.2). Transition to turbulence occurred in these cases via strong, fast (i.e., over a short distance) amplification of disturbances caused by three-dimensional roughness [238-239,243-244,246], such as pressure taps or dust particles adhering to or impinging onto the surface. Turbulent wedges generally arose from the leading-edge region, where the boundary layer is very thin, or from the region around the step installation location. As shown in the results presented in Chapters 5 and 6, the number of the turbulent wedges mainly depended on the flow conditions and on the investigated configuration. One turbulent wedge was observed at all considered test conditions: it arose from the pressure taps in the leading-edge region at y/b = 0.5. In most of the examined cases, a second turbulent wedge was found to originate from the pressure tap at y/b = 0.48. The number of additional turbulent wedges, originating from surface contamination in the leading-edge region, increased at larger Reynolds numbers, since the roughness Reynolds number Re_k, characteristic for a three-dimensional roughness element, also increased. Similarly, a larger number of turbulent wedges was observed at lower Mach numbers, since the thinning of the boundary layer – at fixed unit Reynolds number – led to larger values of Re_k [238-239,243]. Localized surface damage in

the leading-edge region, for example due to the impact onto the surface of dust particles or particles of other nature in the flow, was generally not observed, except when the pre-conditioning procedure had been applied to investigate the effect of the wall temperature ratio on boundary-layer transition. This situation will be discussed later in this section. At the largest Reynolds numbers investigated with the smooth configuration, turbulent wedges were also seen to arise from the region around x_h/c = 35 %. These turbulent wedges were probably generated by dust particles or similar particles transported by the flow, which remained trapped in the small gap between front part and main part of the model (see Appendix B.3.1). In general, the sources of these turbulent wedges could be removed by careful surface cleaning, but this region was cleaned only when strictly necessary, i.e., when the turbulent wedges made the investigation of natural transition impossible. In fact, some of the rub-off from the wiping process used for surface cleaning could remain trapped in the gap, thus causing additional turbulent wedges. The number of turbulent wedges with apex in the region around x_h/c = 35 % was larger for the step configurations and was seen to increase as the step height was increased. This was likely to be due to dust or similar particles adhering to the step surface, which introduced disturbances that triggered boundary-layer transition. Nevertheless, natural transition also occurred further upstream with increasing step height, so that it could still be detected in the spanwise regions between turbulent wedges (see Sections 5.2 and 6.5). The region around the step location was therefore cleaned only when absolutely necessary, for similar reasons to those discussed above for the smooth configuration. The final TSP results also allowed the spanwise spreading angles of the turbulent wedges to be determined. The turbulent wedges were found to develop at a half-included angle of approximately ±8-12°, which compares well with other results available in the literature for quasi-two-dimensional flow [114,145,296-297].

Streamwise pressure gradient and wall temperature ratio did not appear to have a significant influence on the number of turbulent wedges. Earlier work showed that these parameters scarcely affect the critical value of roughness Reynolds number $\mathrm{Re}_{k,\mathrm{cr}}$ for three-dimensional roughness elements [67,238-239,244,246]. There would be an adverse effect of more pronounced flow acceleration and lower wall temperature ratio on transition induced by three-dimensional roughness, since the roughness Reynolds number would be larger [238,239]. The negligible effect of streamwise pressure gradient and wall temperature ratio on the number of turbulent wedges was probably due to the relatively small change in Re_k. An increase of the number of turbulent wedges was observed when the pre-conditioning procedure had been applied. This was not due to the aforementioned effect of T_w/T_{aw} on Re_k, but rather to the impact of particles onto the model leading edge and onto the step surface. An example of localized damage of the model leading edge due to the impact of particles is shown in Fig. C.2.1.1a.

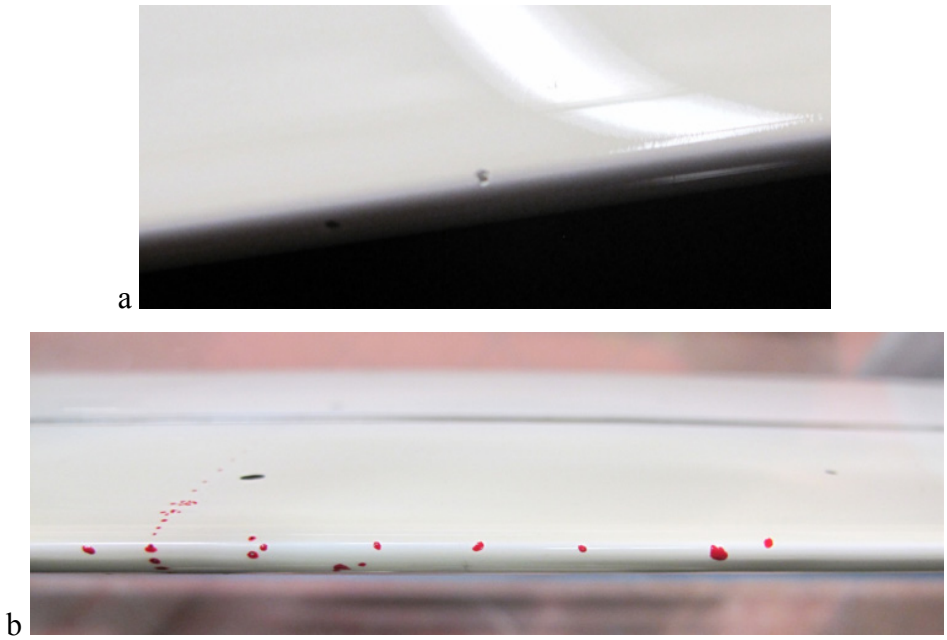

Fig. C.2.1.1. a: localized damage of the model leading edge after pre-conditioning procedure had been applied. b: repaired TSP-surface (before polishing).

No clear increase in the number of turbulent wedges was observed in the TSP results for tests at the standard DNW-KRG thermal conditions (no pre-conditioning applied). This is shown for the step-3 configuration in Fig. C.2.1.2: more than 70 runs had been performed between the TSP results shown in Fig. C.2.1.2a and Fig. C.2.1.2b. The TSP result in Fig. C.2.1.2c was obtained in the fifth run where the pre-conditioning procedure had been applied: three additional turbulent wedges, arising from the leading-edge region, are visible.

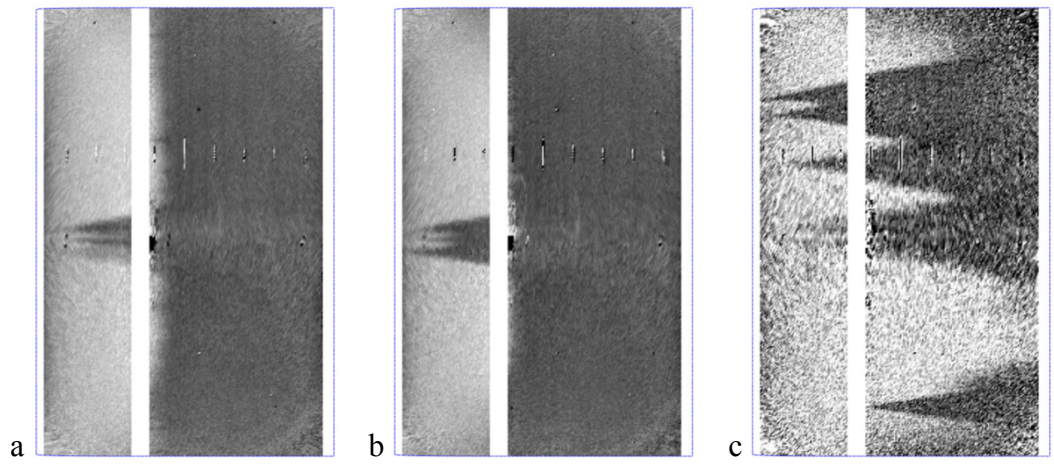

Fig. C.2.1.2. Increase of the number of turbulent wedges with pre-conditioning procedure applied. Step-3 configuration. a: second run after the model had been installed in the wind tunnel (M = 0.77, Re = 6 · 10^6, β_H = 0.051, T_w/T_{aw} = 1.054). b: last run with standard T_w/T_{aw} (M = 0.65, Re = 8 · 10^6, β_H = 0.067, T_w/T_{aw} = 1.051). c: fifth run with pre-conditioning procedure applied (M = 0.35, Re = 4.75 · 10^6, β_H = 0.033, T_w/T_{aw} = 0.966). In this latter TSP result, the wind-on images were divided by the wind-off images (I_{run}/I_{ref}).

Localized surface damage could be repaired, as shown in Fig. C.2.1.1b, but this activity was time-consuming, since the model had to be removed from the wind tunnel to carry out the repair procedure, and then installed again in the test section. Thus, the number of tests at lower T_w/T_{aw} had to be limited, not only because the pre-conditioning procedure itself was time-consuming, but also to protect the model from excessive damage. The number of particle impacts onto the model leading edge increased dramatically at the end of the measurement campaign, when the influence of the wall temperature ratio on boundary-layer transition was being studied with the step-3 configuration. Consequently, the measurement campaign was stopped. In subsequent investigations of the wind tunnel, it was found that particles had been generated via shear friction between the gate and the internal walls of the valve while the gate valve was operated in the presence of a temperature difference of 20 K between the two sides of the gate. A major modification of the gate valve had to be carried out. This modification took several months, so that it was not possible to perform further tests. With the step-3 configuration, only five data points at reduced wall temperature ratio were obtained. Note that an increased number of turbulent wedges with apex at (or just downstream of) $x_h/c = 35$ % was generally observed when step configurations were examined at reduced wall temperature ratios, as compared to that at standard T_w/T_{aw}. This was also very likely to be due to an increased number of particles adhering to the step surface, which were generated during operation of the gate valve. Since the surface material in this region was stainless steel, the impact of these particles did not cause any major damage to the test model.

C.2.2 Natural-transition front

The TSP results show that the natural-transition front between laminar and turbulent regions is not a straight line in spanwise direction. The turbulent boundary layer on the wind-tunnel side walls had an influence on boundary-layer transition on the model upper surface even at distances from the side walls larger than $\Delta(y/b) = 0.1$ (viz., $\Delta y = 50$ mm). In the TSP results, the transition front is three-dimensional in the spanwise regions closer to the side walls. This effect is discussed in Appendix C.3. In general, the natural-transition front here is not a straight line in spanwise direction, as would be expected for transition occurring over a laminar separation bubble [145,192,298-299]. The natural-transition front is seen to be frayed: this is characteristic of transition induced by amplification of streamwise instabilities [145,192,298-299]. Two examples of the frayed natural-transition front are shown in Fig. C.2.2.1 for TSP results obtained under different test conditions. It is interesting to note that a region with larger laminar run length, as compared to the remaining transition front, is present in this figure at $y/b \sim 0.42$ (i.e., on the port side of the turbulent wedges in the mid-span area). A closer look at the TSP results obtained on an NLF-airfoil model at DNW-KRG [145] revealed a similar region with larger laminar run length in the vicinity

of a turbulent wedge, which arose also in that case from the pressure taps line in the mid-span area. This effect may be related to the three-dimensional flow at the sides of the turbulent wedge, which may be advantageous for maintenance of laminar flow in a manner similar to that employed for reducing the growth of Tollmien-Schlichting waves using cylindrical roughness elements [227] and miniature vortex generators [300]. Specific examination of the turbulent wedge would, however, be needed to verify this hypothesis. The spanwise modulation of the remaining natural-transition front is likely to be due to lack of two-dimensionality in the freestream (in terms of both mean and fluctuating quantities), in the model contour, and in surface fairness, which lead to different amplification of boundary-layer disturbances at different spanwise locations.

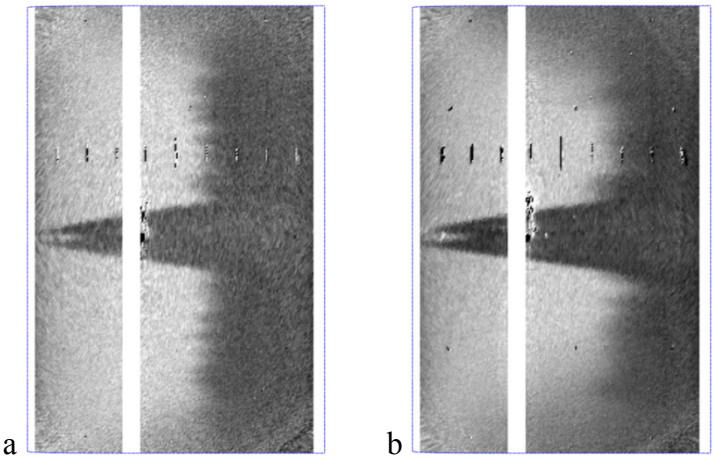

Fig. C.2.2.1. TSP results showing a spanwise-modulated natural-transition front. Smooth configuration. a: M = 0.5, Re = 6 · 10^6, β_H = 0.034. b: M = 0.77, Re = 9 · 10^6, and β_H = 0.084.

Surface roughness does not appear to be a cause for the above effect. As discussed in Section 3.3, the surface had been polished to very low values of average roughness and mean roughness depth. For successful NLF wind-tunnel testing at high unit Reynolds numbers in cryogenic facilities, the typical requirement for surface finishing is $R_a < 0.1$ µm up to $x/c \sim 20$ % [275] and $R_a < 0.15$-0.2 µm on the remaining surface [192,209,275,301]. The average roughness measured on the surface of the *PaLASTra* model met these criteria. Moreover, it was verified that the roughness Reynolds number Re_k did not exceed the critical values available from previous work [238-239,243,302]. The roughness Reynolds number obtained for a roughness height equal to the mean roughness depth ($k = R_z = 0.32$ µm) was $Re_k < 1$ at all considered test conditions; this was verified also for the leading-edge region. Even by taking as roughness height k the largest value of the maximal roughness depth measured on the model surface ($R_{max} = 1.22$ µm), the corresponding roughness Reynolds number was $Re_k < 10$. These values of Re_k are well below the critical values of roughness Reynolds number given in the literature: $Re_{k,cr} \sim 100$-900 for three-dimensional roughness elements (depending on the ratio between vertical and spanwise size

of the roughness element) [238-239,243] and $\mathrm{Re}_{k,\mathrm{cr}} \sim 300\text{-}600$ for distributed roughness [181,243,302]. Below these values, "the roughness has no influence on the natural transition" [239]. The values of roughness Reynolds numbers obtained in the present work were even smaller than the limit for tolerable roughness $\mathrm{Re}_{k,\mathrm{cr}} = 25$ given in [243], below which roughness is said to be in the "safe region".

Two-dimensionality of the mean flow in the test section of DNW-KRG (at a certain distance from the side walls) has not been verified yet, whereas fluctuations of total pressure and static pressure have been measured at only three spanwise locations [56]. Despite all efforts in ensuring a two-dimensional shape, the model contour presented very small, but inevitable changes in the spanwise direction. Besides the small gap observed at $x_h/c = 35$ % on the upper side of the smooth configuration, the model surface was not perfectly fair, but showed small-amplitude waviness in both streamwise and spanwise directions. Amplitude of surface waviness and gap Reynolds number (based on the gap width) did not exceed the critical values for premature transition [161-162,169] at any of the test conditions considered in the present work. Nevertheless, the small spanwise variation of model contour and surface quality can have led to different boundary-layer receptivity and amplification of disturbances; in addition to that, the spanwise distribution of mean and fluctuating flow quantities can also be non-uniform in the test section of DNW-KRG. Finally, it should be remarked that spanwise modulation of the natural-transition front may be also related to the final stages of the instability-amplification process and breakdown, which are of three-dimensional nature [66,82,108-109].

In view of the above considerations, the natural-transition front on the upper side of the *PaLASTra* model could be considered as essentially two-dimensional. The investigation of the effects leading to the spanwise modulation of the transition front requires extensive measurement of the disturbance environment and of the amplification of the disturbances within the boundary layer. For the reasons outlined in Appendix B.4, the implementation in DNW-KRG of the measurement techniques needed for such a study is very difficult.

C.2.3 Transition location in the region close to the model trailing edge

Changes in wall heat flux (and thereby in the surface temperature) are related to variations in wall shear stress. A strong increase in wall heat flux occurs in the transition region, and this is used for transition detection by means of TSP. Besides the transition region, however, there are two other regions on the investigated model surface where the wall heat flux is larger than on the rest of the model, provided that the boundary-layer state is the same. These two regions are the leading-edge and the trailing-edge regions. The boundary layer is strongly accelerated in the leading-edge region, in a manner similar to that of the

boundary layer on an NLF airfoil; because of the adopted cross-section shape, it undergoes significant acceleration also in the trailing-edge region (see [148] and Appendix B.1). Moreover, the heat capacity of the model in these two regions is smaller than that of the rest of the model, since the model thickness diminishes close to leading and trailing edges. Larger wall shear stress, due to stronger flow acceleration, and smaller heat capacity of the model lead to faster variation of the model surface temperature in the leading-edge and trailing-edge regions. These areas are seen as darker regions in the TSP image results. The streamwise extent of the lower temperature region close to the leading edge was limited to a few percent of the model chord length, so that most of this region was masked by the white strip applied at $x/c \leq 2.5$ %. However, the streamwise extent of the corresponding region close to the trailing edge was larger. This had to be accounted for in the measurement of the transition location in the last portion of the model chord length, as will be illustrated through the following two examples. TSP results obtained at $\mathrm{Re} = 6 \cdot 10^6$, $\mathrm{M} = 0.77$, and $T_w/T_{aw} = 1.043$-1.045 are shown in Fig. C.2.3.1a and Fig. C.2.3.2a for the Hartree parameters $\beta_H = 0.066$ and 0.076, respectively. The boundary layer was laminar on most of the model upper side in both cases. (The values of the intensity ratio are significantly lower than those in the mid-span areas covered by turbulent wedges.) In the case with weaker flow acceleration, $\beta_H = 0.066$, the intensity ratio (which is a function of the temperature) increases in the streamwise direction in the region at approximately $x/c > 65$ %. Transition was found at $x_T/c = 75 \pm 1.1$ % in this case. The transition detection algorithm provided transition locations also at some spanwise sections for the case at $\beta_H = 0.076$, with average at $x_T/c = 86$ %. However, the streamwise increase of the intensity ratio was not caused by the transition process in this case. In order to clarify this point, the intensity ratio distributions extracted from the TSP results were compared to the laminar skin-friction coefficient distributions obtained using the boundary-layer solver COCO. The comparisons are presented in Fig. C.2.3.1b and Fig. C.2.3.2b. A glance at Fig. C.2.3.1b shows that the increase in the computed laminar skin-friction coefficient starts downstream of the rise in the intensity ratio, by a chordwise distance of at least $\Delta(x/c) = 10$ %. In contrast, the laminar skin-friction coefficient and intensity ratio distributions have similar forms in the case with larger flow acceleration, as shown in Fig. C.2.3.2b.

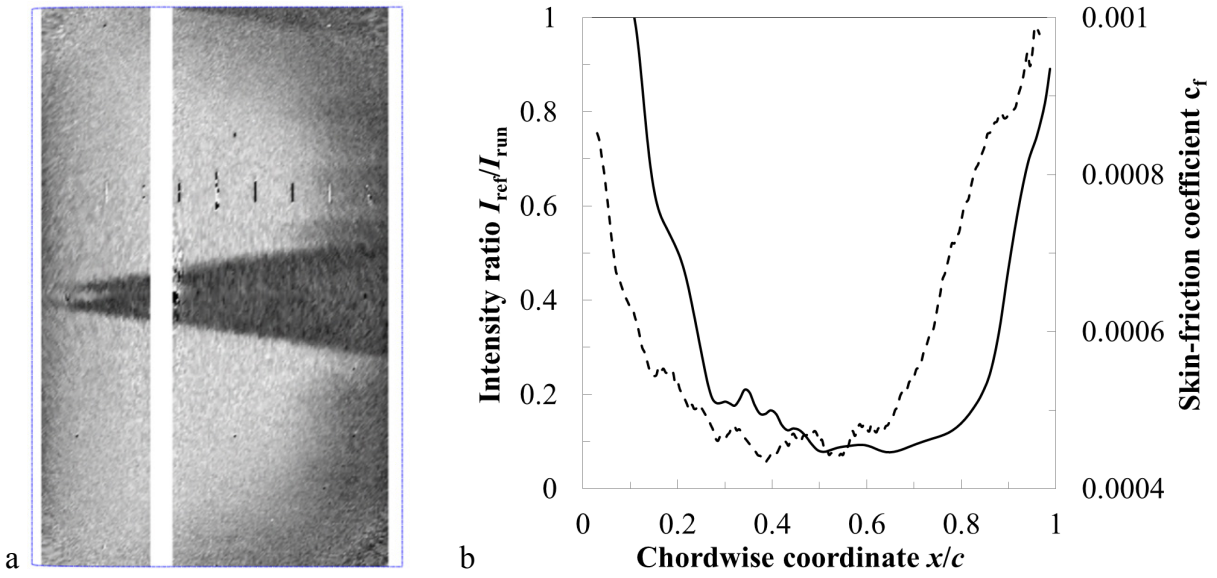

Fig. C.2.3.1. Re = 6 · 10^6, M = 0.77, and T_w/T_{aw} = 1.043, β_H = 0.066. a: TSP result. b: chordwise distribution of the intensity ratio at y/b = 0.36 (dashed line) and of the laminar skin-friction coefficient (solid line).

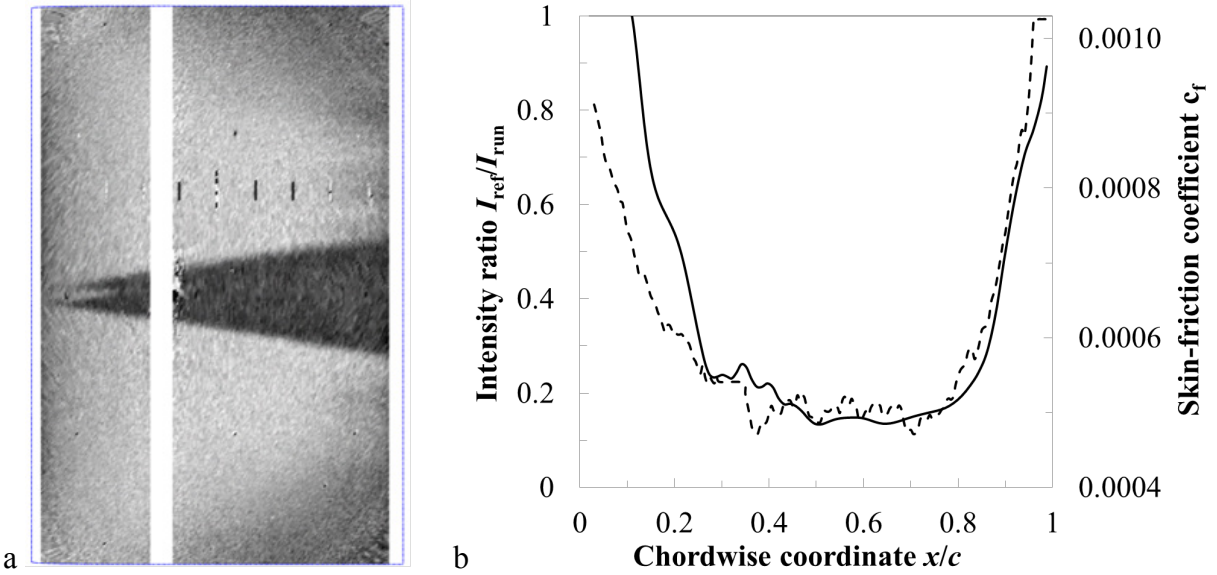

Fig. C.2.3.2. Re = 6 · 10^6, M = 0.77, and T_w/T_{aw} = 1.045, β_H = 0.076. a: TSP result. b: chordwise distribution of the intensity ratio at y/b = 0.43 (dashed line) and of the laminar skin-friction coefficient (solid line).

It appears that the streamwise increase of the intensity ratio had been caused in this case by the rise of the laminar wall shear stress, which was induced by the favorable pressure gradient on the last portion of the model chord. The used algorithm detected the maximal slope of the intensity ratio distribution, which was, however, not related to transition in this case. In order to further elucidate this finding, the results of linear stability analysis of the two considered cases are plotted in Fig. C.2.3.3. Linear stability analysis was performed using LILO, according to the procedure discussed in Section 4.3. The locations corresponding

to the maximal slope of the intensity ratio distribution, as determined by the aforementioned algorithm, are shown by gray bars.

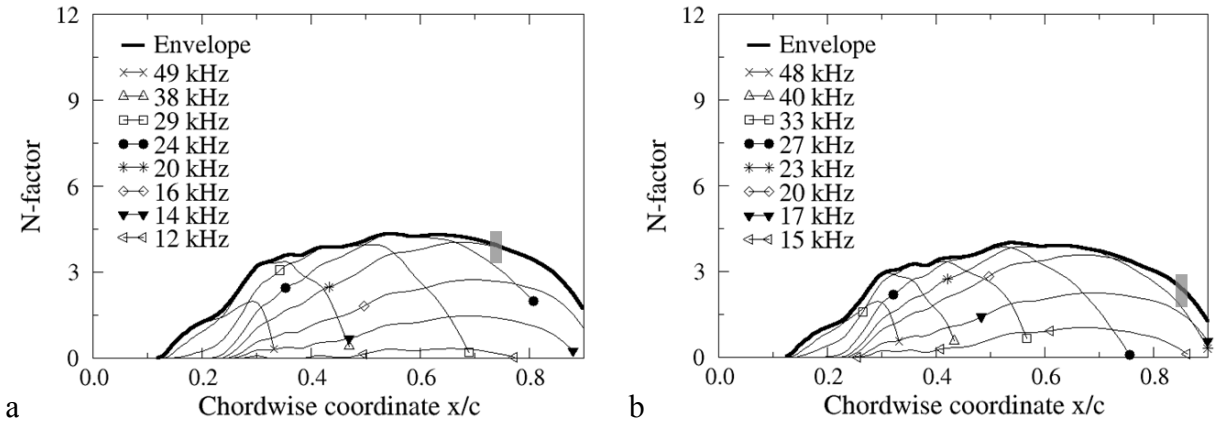

Fig. C.2.3.3. Results of linear stability analysis for the cases of Fig. C.2.3.1 (a) and Fig. C.2.3.2 (b). *N*-factors shown only for some selected frequencies.

As discussed in [148] and in Appendix B.1, the strong flow acceleration in the region close to the trailing edge leads to a negative slope of the *N*-factor envelope curve. Transition can still occur in the region 70 % < x/c < 80 % even if linear stability theory predicts a reduction of the amplification rates: unstable disturbances can reach critical amplitudes upstream of this region, and non-linear processes bring transition to completion over a finite distance (see Sections 2.2.3 and 2.2.4). However, transition at x/c > 80 %, in a region where the *N*-factors are strongly reduced, appears unlikely.

Both comparisons (that between intensity ratio and laminar skin-friction coefficient distributions and that between *N*-factor envelope curves and locations of maximal intensity ratio slope) lead to the conclusion that transition occurrence in the region at approximately x/c > 80 % was most unlikely. Rather, the observed streamwise increase of the intensity ratio was most likely related to the local increase of the laminar wall shear stress, combined with the decreased heat capacity of the model in this aft region. Thus, locations corresponding to the maximal intensity ratio slope at x/c > 80 % were not taken as transition locations, and the boundary layer was considered as laminar over the whole region of the model upper side coated with TSP. Nevertheless, the locations of maximal intensity ratio slope at values of x/c < 80 % were interpreted as transition locations and hence could be used in the data analysis in Chapters 5 and 6.

C.3 Influence of the turbulent boundary layer developing on the wind-tunnel side walls

In Appendix C.2.2, it has been mentioned that the turbulent boundary layer developing on the DNW-KRG side walls had an influence on boundary-layer transition on the model upper side, leading to a curved transition front in the

regions close to the test-section side walls. This effect was examined by analyzing the temperature distribution in the spanwise direction and the temporal development of the surface temperature during a run at DNW-KRG. The temperature distribution on the model upper surface was obtained from the TSP results, using the evaluation procedure discussed in Appendix C.1.4.

Surface temperature distributions in the spanwise direction were extracted from the TSP result of Fig. C.2.2.1b at some chordwise locations, which correspond to those of the thermocouples installed within the TSP coating. To increase the signal-to-noise ratio, the temperatures were averaged over a chordwise range of $\Delta(x/c) = 5$ % across the chosen chordwise section. (In the case of thermocouple no. 3, this chordwise range was reduced to $\Delta(x/c) = 4$ % because of the masked region at 33 % $\leq x/c \leq$ 38 %.) The temperatures evaluated from the TSP results are shown in Fig. C.3.1, where they are also compared to those measured by the four thermocouples installed within the TSP coating. Temperature information is missing in the regions close to the corners of the final TSP results and in the region $0.48 \leq y/b \leq 0.55$ at $x/c \sim 40$ %, for the reasons discussed in Appendix C.1 (absent TSP active layer and artefacts produced by mapping, respectively). Moreover, no luminescent signal was available at the considered chordwise sections in the region $0.59 \leq y/b \leq 0.62$, because of the tick markers for identifying chordwise positions in $\Delta(x/c) = 10$ % steps (see Section 3.3). The temperature was linearly interpolated in this region. Transition was detected in this case at $x_T/c = 65 \pm 1$ %. The results in the regions $0.33 \leq y/b \leq 0.44$ and $0.56 \leq y/b \leq 0.7$ clearly show an increase in the streamwise direction of the surface temperature in the laminar region (related to the decreasing wall shear stress), and a lower surface temperature in the turbulent region. In the aforementioned spanwise regions, the surface temperature was confirmed to be reasonably uniform. The two minima in surface temperature at $y/b = 0.48$ and 0.5 observed for the two forward chordwise sections are due to the turbulent wedges originating from the pressure taps in the leading-edge region. It can also be seen that the width of the region of lower temperature in the mid-span area increases in the streamwise direction, according to the increasing width of the turbulent wedges. Spanwise uniformity of the surface temperature was found at all spanwise locations available for the chordwise section at $x/c \sim 10$ %. In contrast, surface temperature was observed to decrease in the regions closer to the test-section side walls for the chordwise sections at $x/c \sim 20$ % and 40 %. This effect was more pronounced at $x/c \sim 40$ % and was due to the turbulent boundary layer developing on the areas of the model upper side closer to the side walls. In the turbulent region, at $x/c \sim 85$ %, the surface temperature rather increases in the regions closer to the test-section side walls. This appears also to be due to the turbulent boundary layer that has already developed from a chordwise location further upstream of the transition location in the central model area, thus leading to a lower wall shear stress. The temperatures measured by the two forward thermocouples were shown to be in agreement with those obtained from the TSP results. Larger differences can be seen at the locations corresponding to the two

aft thermocouples. These are likely to be due to the thermal conduction in the spanwise direction and to the temporal dependency of the surface temperature observed in these regions (discussed below). In any case, it should be noted here that the temperature measured by thermocouple no. 3 is between those measured by the two forward thermocouples, confirming the difference between the streamwise temperature distribution at $y/b = 0.27\text{-}0.3$ and that at $0.33 \leq y/b \leq 0.44$ and $0.56 \leq y/b \leq 0.7$ (see Fig. C.2.2.1b and Fig. C.3.1).

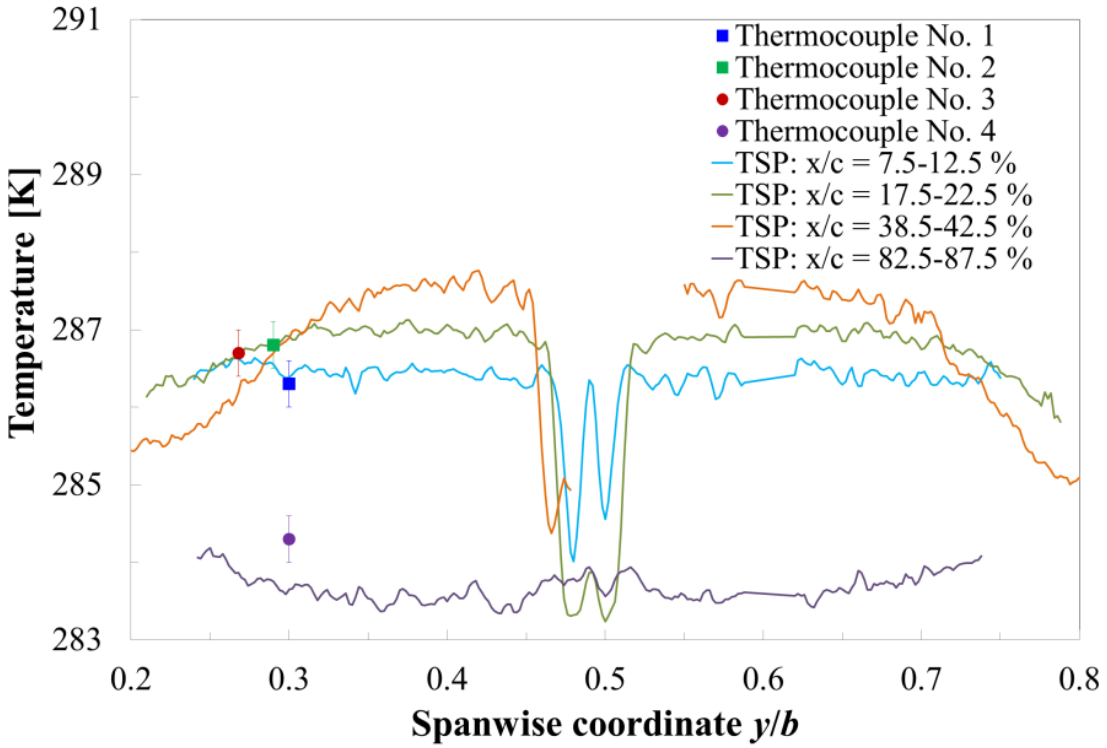

Fig. C.3.1. Surface temperature distributions in the spanwise-direction obtained from the TSP result shown in Fig. C.2.2.1b (M = 0.77, Re = 9 · 10^6, $\beta_H = 0.084$, $T_w/T_{aw} = 1.052$). Temperatures extracted along four strips of width $\Delta(x/c) = 5$ % (4 % in the case of $x/c = 40$ %). TSP result filtered using a 3 × 1 median spatial filter.

The temporal evolution of the temperatures obtained from the TSP results and those measured by the thermocouples is shown in Fig. C.3.2 and Fig. C.3.3 for the same test case of Fig. C.2.2.1b and Fig. C.3.1. The TSP results in Fig. C.3.2 correspond, from left to right, to the wind-on images 13 to 15 (see Section 4.1). The locations of the thermocouples installed within the TSP coating are shown by red dots.

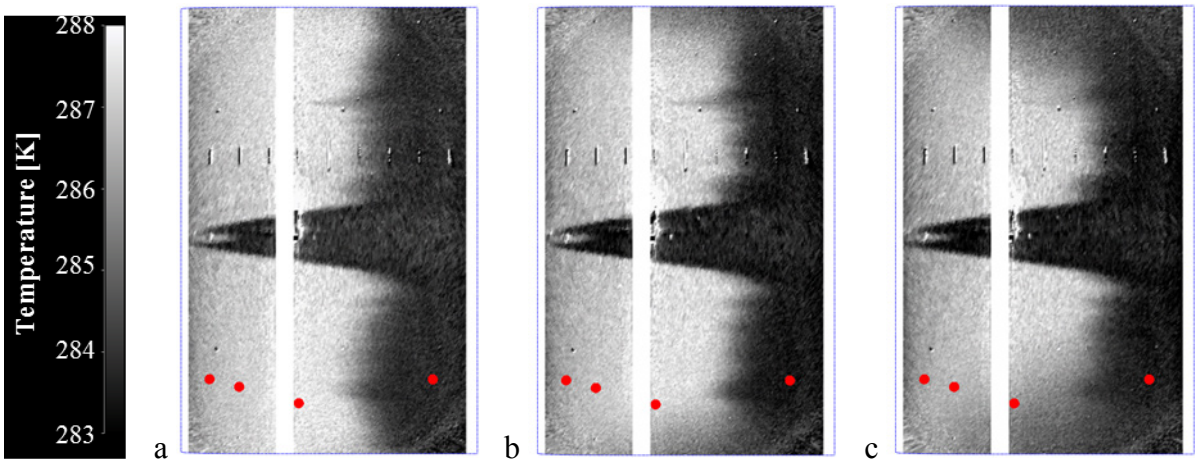

Fig. C.3.2. Evolution of the surface temperature during a run at DNW-KRG. M = 0.77, Re = 9 · 10^6, β_H = 0.084, T_w/T_{aw} = 1.052. From a to c: TSP results for images 13, 14, and 15 (see Fig. 4.1.1). The locations of the thermocouples installed within the TSP layer are shown by red dots.

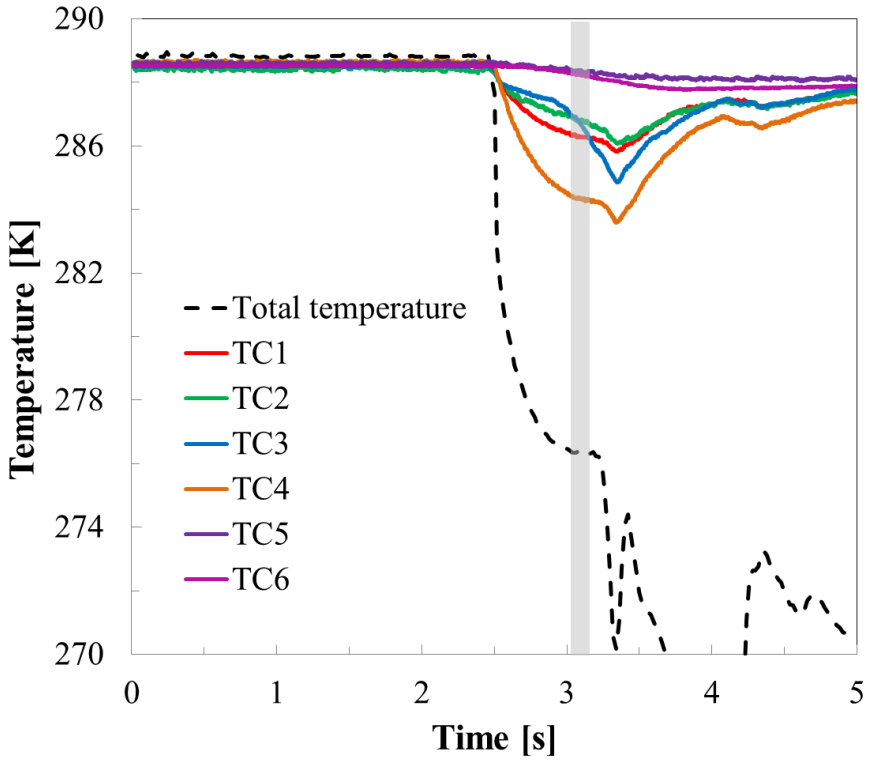

Fig. C.3.3. Evolution of the flow total temperature and of the temperatures measured by the thermocouples installed in the *PaLASTra* model for the case of Fig. C.3.2.

As can be seen in Fig. C.3.2, from image 14 to 15 the natural-transition front does not essentially change in the central area of the model surface, where the transition location is evaluated. In image 13, however, transition occurs at a more upstream location as compared to that of the subsequent TSP results. Thus, the natural-transition front was shown to be steady from approximately 0.4 s after the fast-acting valve had been opened, whereas at 0.2-0.3 s it had not reached stable conditions. In the surface regions closer to the test-section side walls, the

laminar run length in image 13 is at least as large as that in the central surface area. However, the surface temperature in the surface regions closer to the side walls decreases to turbulent levels in image 14, and both the chordwise and spanwise extent of this low-temperature region increases in image 15.

The temporal development of the model temperatures is shown even more clearly in Fig. C.3.3. The gray bar in this figure shows the time window where the wind-tunnel data were evaluated. The temperatures measured below the TSP surface (thermocouples no. 5 and 6) drifted only slightly from the pre-run values, confirming the need of installing thermocouples within the TSP layer to measure its temperature during a run at DNW-KRG. The decrease of the temperature measured in the turbulent region (thermocouple no. 4) was larger than that measured in the laminar region (thermocouples no. 1 and 2). Note that the temperature reduction measured by thermocouple no. 1 was larger than that measured by thermocouple no. 2, in agreement with their chordwise locations in the laminar surface region. The most interesting temporal evolution is that of the temperature measured by thermocouple no. 3. In the first phase of the run window, the boundary layer at this location is still laminar (see Fig. C.3.2a), and the temperature reduction is less pronounced than that measured by the two forward thermocouples. Approximately 0.4 s after the fast-acting valve has been opened, a clear increase in the temperature reduction rate can be seen in Fig. C.3.3, so that the average temperature measured in the data-evaluation window at this location has become lower than that measured by thermocouple no. 2. In practice, the temperature reduction rate has changed for laminar to turbulent levels approximately 0.4 s after the opening of the fast-acting valve: this finding is in agreement with the upstream movement of the transition front observed in the TSP results in the regions close to the test-section side walls, which starts from image 14. The temporal evolution of transition of the model boundary layer appears to be due to the temporal evolution of the turbulent boundary layer on the wind-tunnel side walls [55,56]. With increasing run time, the thickness of the turbulent boundary layer developing on storage tube and test-section walls continuously increases. As already discussed in [56], the fluctuations of freestream static pressure and, in larger measure, flow total pressure are larger at $\Delta(y/b) = 0.12$ from the test-section side walls than in the test-section center. Larger pressure fluctuations are likely to induce premature transition of the model boundary layer, and the spanwise-varying level of pressure fluctuations was probably the cause of the upstream shift of the transition location with increasing spanwise distance from the test-section center. It should be also emphasized that the spanwise and streamwise extent of the turbulent regions close to the test-section side walls were observed to increase at larger unit Reynolds numbers and larger Mach numbers, as can be seen in the TSP results shown in Chapter 5. This finding is consistent with the increase of the total pressure fluctuations measured at larger unit Reynolds numbers and larger Mach numbers: an increase in both flow parameters indeed leads to a thickening of the turbulent boundary layer on the wind-tunnel walls.

C.4 Streamwise variation of the wall temperature ratio

The wall temperature ratio T_w/T_{aw} and the Mach number M_e at the boundary-layer edge are plotted in Fig. C.4.1a as a function of the chordwise coordinate for a run at M = 0.77, Re = $9 \cdot 10^6$, and $\beta_H = 0.084$. The corresponding TSP result is shown in Fig. C.4.1b. The surface temperature distribution was evaluated from the TSP result according to the procedure described in Appendix C.1.4. $T_w(x)$ was then extracted at the spanwise section $y/b = 0.64$, the surface temperature having been averaged over a spanwise range of $\Delta(y/b) = 0.02$ to increase the signal-to-noise ratio. $T_{aw}(x)$ was computed using the laminar boundary-layer solver COCO, assuming an adiabatic wall. Note that the values of T_w/T_{aw} shown in Fig. C.4.1a have physical significance only up to $x/c \sim 58$ %, since downstream of this location the boundary layer was no longer laminar. (Transition was in this case detected at $x_T/c = 65 \pm 1$ %.)

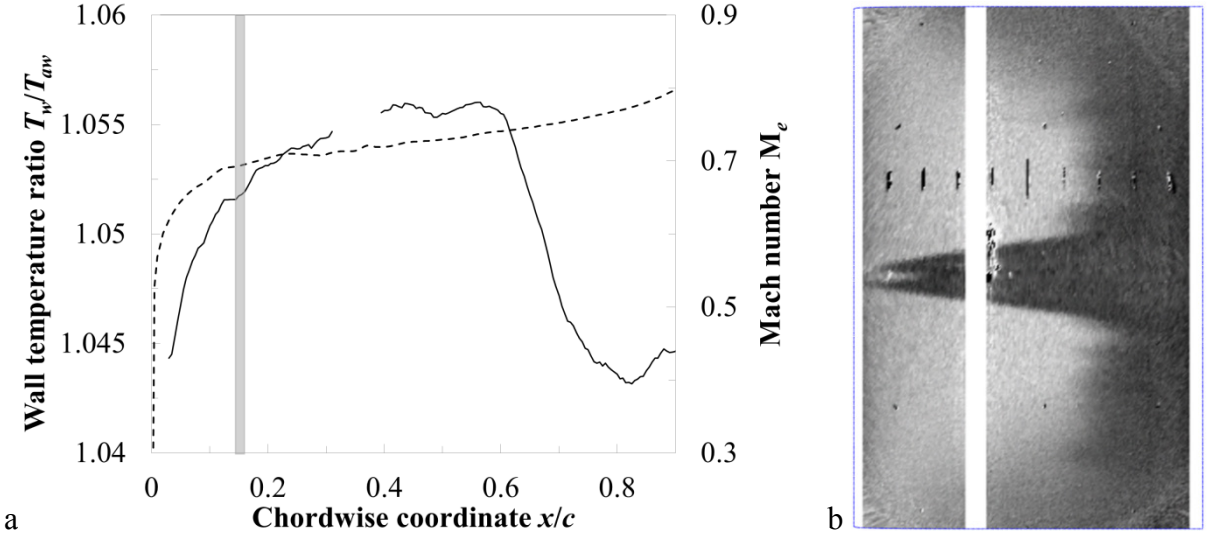

Fig. C.4.1. Smooth configuration at at M = 0.77, Re = $9 \cdot 10^6$, and $\beta_H = 0.084$. a: streamwise distribution of wall temperature ratio T_w/T_{aw} (solid line) and Mach number at boundary-layer edge M_e (dashed line). The value of the wall temperature ratio used for the analysis of the results is shown by a gray bar. b: TSP result.

T_w/T_{aw} changes by more than 0.01 from the leading-edge region to $x/c \sim 58$ %. Because of the particular cross-section geometry of the model used in the present experiments, the contour-induced velocity variation was small, and the value of the Mach number M_e at the boundary-layer edge was close to that in the freestream (M = 0.77). Nevertheless, larger variations are observed in the leading-edge region. The local Mach number M_e at $x/c = 15$ % was used to compute T_{aw}, according to Eq. (2.3.3.1). This was automatically accounted for by taking the adiabatic wall temperature from the boundary-layer computations. It should be remarked that the surface thermal properties of the uncoated strip at $33.5\ \% \le x/c \le 36.5\ \%$ were different from those of the TSP layer. During a test run in DNW-KRG, this difference in thermal properties led to a difference in the

temperature of coated and uncoated surfaces, which is, however, markedly smaller than that between flow and model surface. The flow was generally laminar in this region, so that the maximal temperature difference between coated and uncoated surfaces was less than 2 K even at high subsonic Mach numbers. This difference is comparable to the surface temperature change from the leading-edge region to $x/c \sim 20$ %. Moreover, the streamwise extent of this region is rather small. For these reasons, this surface temperature variation was considered to have a negligible influence on boundary-layer stability. (The value of T_w could not be measured at $33.5\ \% \leq x/c \leq 36.5\ \%$, so that no value of T_w/T_{aw} can be shown for this region in Fig. C.4.1a.)

D Results with the smooth configuration

D.1 Repeatability and reproducibility of the experimental results

Care was taken in achieving the flow parameters and the surface pressure distributions which were required for the testing. Deviations not larger than $\pm 0.15 \cdot 10^6$ in the desired chord Reynolds number and ±0.001 in the desired Mach number could be tolerated; otherwise at least one additional test was performed with adjusted charge pressure and/or area of the sonic throat cross-section. Only fully adapted upper and lower wind-tunnel walls were accepted (see Section 3.1), so that interference-free contours of these walls were assured for all tests. Once the flow conditions had been achieved, the pressure distribution on the model upper surface was checked to make sure that the results were repeatable when compared with other runs carried out at the same conditions. An example is shown in Fig. D.1.1 for $\mathrm{Re} = 12 \cdot 10^6$, M = 0.77, and AoA = -3.8° for two runs which were separated in time by 28 hours.

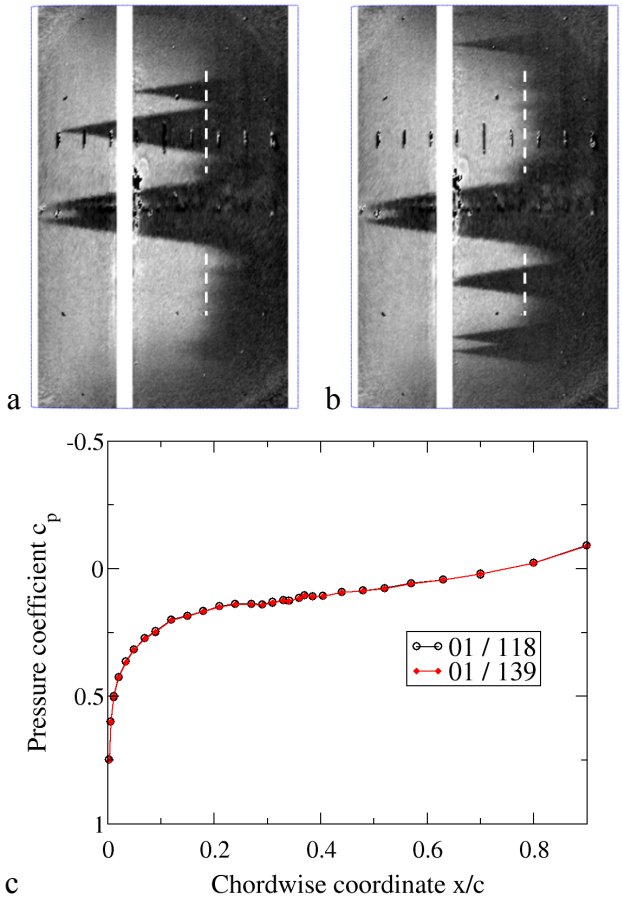

Fig. D.1.1. Repeatability of TSP results and surface pressure distributions within the same wind-tunnel entry (no. 01). $\mathrm{Re} = 12 \cdot 10^6$, M = 0.77, AoA = -3.8°, and standard T_w/T_{aw}. a: TSP result, run no. 118; b: TSP result, run no. 139; c: pressure distributions for a) and b) measured on the model upper surface.

The model surface was cleaned between the two test runs to remove surface contamination that caused turbulent wedges on the model starboard side (region on top of Fig. D.1.1a). These turbulent wedges were no longer present in the second run, but other turbulent wedges caused by surface contamination appeared, this time on the model port side (bottom region in Fig. D.1.1b). The change in transition location measured in the surface regions free from turbulent wedges was less than $\Delta(x_{T,0}/c) = 1$ %. This variation in $x_{T,0}/c$ was probably influenced also by the variation in the other parameters: the differences in chord Reynolds number, Mach number, Hartree parameter, and wall temperature ratio were $\Delta\mathrm{Re} = 0.04 \cdot 10^6$, $\Delta\mathrm{M} = 0.002$, $\Delta\beta_H = 0.001$, and $\Delta(T_w/T_{aw}) = 0.002$. In general, when a run was repeated within the same wind-tunnel entry, the variations of $x_{T,0}/c$, Re, M, and β_H were smaller than the corresponding measurement uncertainties for that data point. The repeatability of T_w/T_{aw} will be discussed later in this section.

Between the different wind-tunnel entries with the same test conditions, small differences in the surface pressure coefficients had been observed. This was caused by an offset in the angle-of-attack. Between the first and the second wind-tunnel entry it was necessary to increase the angle-of-attack by 0.02° to correct for this offset; in the third entry the angle-of-attack had to be reduced by 0.02° with respect to the corresponding values in the first entry. These small deviations were likely to be due to misalignments during the installation of the model. However, repairs of the DNW-KRG facility conducted between wind-tunnel entries led to small changes in test-section geometry, which could have also influenced the flow alignment. The pressure distributions, measured on the model upper surface after correction of the angle-of-attack, were almost coincident, as shown in Fig. D.1.2c at $\mathrm{Re} = 6 \cdot 10^6$, M = 0.77, and AoA = -2.3° (reference value in the first test campaign). The TSP results are shown in Fig. D.1.2a/b. The differences in chord Reynolds number, Mach number, Hartree parameter, and transition location were $\Delta\mathrm{Re} = 0.02 \cdot 10^6$, $\Delta\mathrm{M} = 0.002$, $\Delta\beta_H = 0.002$, and $\Delta(x_{T,0}/c) = 0.8$ % of the model chord length. By correcting the angle-of-attack in the way previously described, the variation in the Hartree parameter was thus less than $\Delta\beta_H = 0.003$ and that in the measured transition location less than $\Delta(x_{T,0}/c) = 1$ % for all tested cases. The differences in the chord Reynolds number and in the Mach number were within the aforementioned allowable deviations.

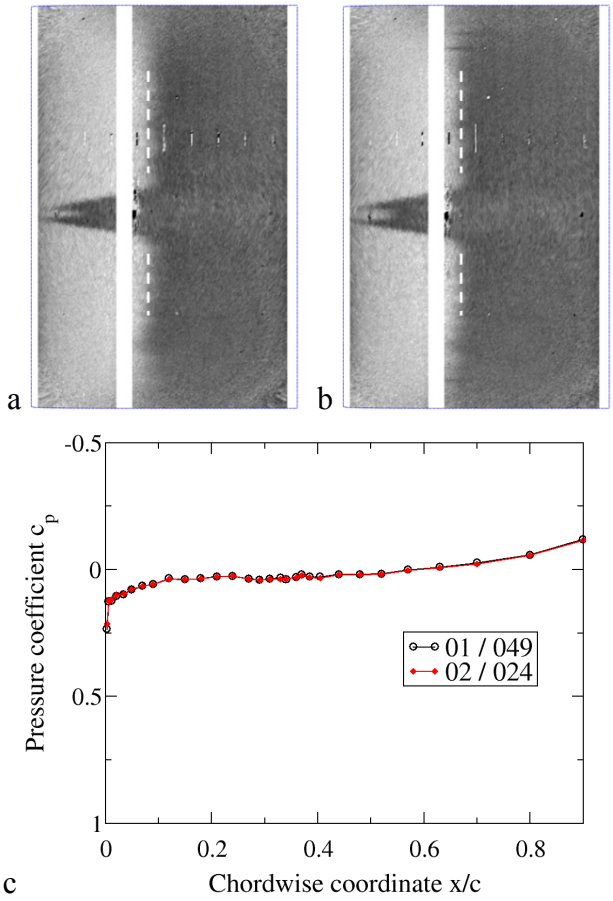

Fig. D.1.2. Reproducibility of TSP results and surface pressure distributions in different wind-tunnel entries. Re = 6 · 10^6, M = 0.77, AoA = -2.3°, and standard T_w/T_{aw}. a: TSP result, first wind-tunnel entry (no. 01); b: TSP result, second wind-tunnel entry (no. 02); c: pressure distributions for a) and b) measured on the model upper surface.

The wall temperature ratio for a certain test case could not be set at a particular value with accuracy comparable to that of the other parameters. Because of the possible increase in the turbulence level discussed in [56], temperature uniformity of the gas in the storage tube had priority over achievement of exactly the same gas and model temperatures as in another run. In some cases, this caused small differences between the temperature of the model surface and that of the gas in the storage tube, leading to variations of the wall temperature ratio between test runs. For example, a difference of 1 K between model and gas temperature at M = 0.77 and T_c = 288 K leads to a variation in the wall temperature ratio of $\Delta(T_w/T_{aw}) \sim 0.004$.

D.2 Variation of the streamwise pressure gradient

The streamwise pressure gradient was systematically varied by adjusting the angle-of-attack of the model. Although chord Reynolds number and wall temperature ratio have a marked influence on boundary-layer transition, they were not expected to appreciably influence the surface pressure distribution (at least for the considered range of parameters). This was verified for all examined

cases and is shown in Fig. D.2.1 for six different runs. The differences in the pressure distributions on the model upper surface are smaller than the error bars. This was essential to ensure that the effects on boundary-layer transition of streamwise pressure gradient, chord Reynolds number, and wall temperature ratio were decoupled. It also allowed the Hartree parameter and its uncertainty to be evaluated as the average and the standard deviation of the values of β_H obtained for all test runs conducted at fixed Mach number and angle-of-attack (see Section 4.3).

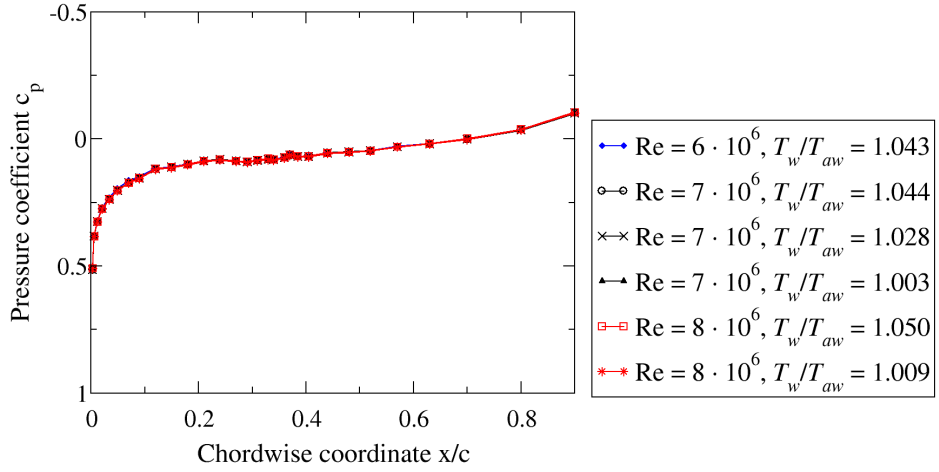

Fig. D.2.1. Surface pressure distributions measured at different chord Reynolds numbers and wall temperature ratios. M = 0.77, AoA = -3.0°, Re = 6-8 · 10^6, T_w/T_{aw} = 1.003-1.050.

The variation of the Hartree parameter as a function of the angle-of-attack is shown in Fig. D.2.2 for the largest Mach number M = 0.77. The Hartree parameter increases almost linearly with decreasing angle-of-attack at AoA ≤ -2.3° ($\beta_H > 0$). The results for fixed angle-of-attack and but with varying chord Reynolds number show, as expected, no influence of the latter parameter (see Fig. D.2.2).

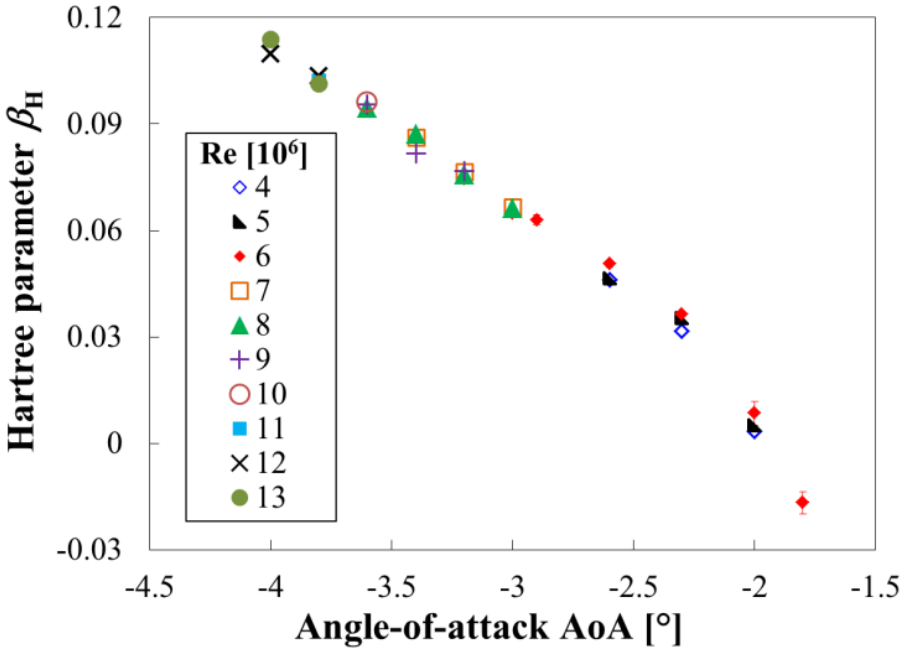

Fig. D.2.2. Hartree parameter as a function of angle-of-attack AoA at M = 0.77.

In general, the surface pressure distribution depends on the Mach number. In the range of angles-of-attack $-3.2° \leq AoA \leq -2.3°$, however, the change in surface pressure distribution was observed to be small. This has been shown in Fig. 5.1.1.1 for an angle-of-attack AoA = -2.3°. The variation of the Hartree parameter as a function of the angle-of-attack is presented in Fig. D.2.3 for the four examined Mach numbers. At fixed angle-of-attack in the range $-3.2° \leq AoA \leq -2.3°$, the difference between Hartree parameters obtained at different Mach numbers was less than 0.006 (i.e., less than 13 %). Larger differences were found at AoA > -2.3°: these were due to the more pronounced pressure minima observed in the leading-edge region at larger Mach numbers. The opposite trend was seen at AoA < -3.2°: this effect was due to stronger flow acceleration at larger Mach numbers, especially at $x/c > 50$ %. It should be emphasized here that the differences observed at AoA > -2.3° and AoA < -3.2° are not significant for the analysis of the results, since it was possible to compare the results obtained at approximately the same Hartree parameter anyway. For example, the results obtained at AoA = -3.8° at a Mach number M = 0.5 could be compared with those obtained at AoA = -3.6° at Mach numbers M = 0.65 and 0.77 (see Fig. D.2.3).

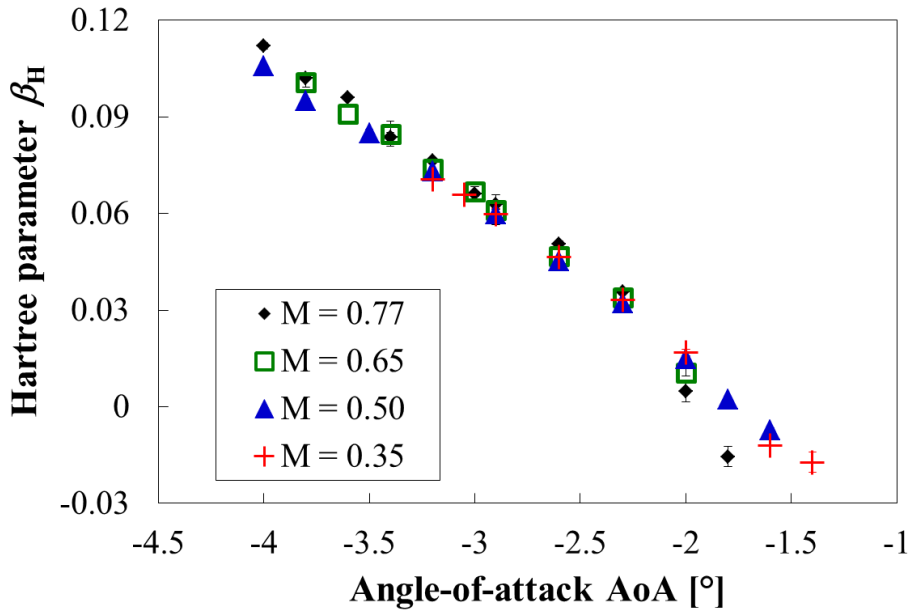

Fig. D.2.3. Hartree parameter as a function of the angle-of-attack at different Mach numbers.

D.3 Achievable variation of parameters

- The lowest possible Hartree parameter was determined by the pressure minimum in the leading-edge region at large angles-of-attack. The adverse pressure gradient downstream of this pressure minimum was so strong as to induce transition upstream of $x_h/c = 35$ %, i.e., the location where the steps were to be installed. When this occurred, the effect of the steps on boundary-layer transition could not be investigated. These test conditions were therefore not used.
- The minimum Reynolds number was limited by the minimum pressure difference necessary to operate the wind tunnel (see Section 3.1). With the dump tank at atmospheric conditions, the minimum chord Reynolds number achievable at M = 0.35 and 0.5 was $3.5 \cdot 10^6$ and $4.5 \cdot 10^6$, respectively. At larger Mach numbers, a minimum Reynolds number of $6 \cdot 10^6$ was attained. In order to increase the test range at M = 0.65 and 0.77 to lower Reynolds numbers, the pressure of the gas in the dump tank was reduced. By this means, a minimum chord Reynolds number of $4 \cdot 10^6$ could be tested at M = 0.65 and 0.77. (In this case, the pressure of the gas in the dump tank was 60 kPa.)
- The constraints on the maximal Reynolds number and Hartree parameters were coupled. At large Reynolds numbers, the boundary layer was more unstable, so that lower (more negative) angles-of-attack had to be implemented to attain a transition location at $x_{T,0}/c \sim$ 60-70 %. Such a transition location on the smooth configuration was desired for the investigation of the effect of forward-facing steps on transition (see

Section 3.2.2), which was conducted in the second phase of the measurement campaign. However, at M = 0.77 and 0.65, the lowest angle-of-attack was restricted by the maximally allowable curvature of the test-section lower wall; here it was not possible to attain an interference-free lower wall by changing the wall contour as required by the adaptation procedure. In principle, larger Reynolds numbers (and hence Hartree parameters) were possible at M = 0.5, but the number of turbulent wedges on the model surface increased at larger Reynolds numbers. The spanwise extent of the region free of turbulent wedges, where natural transition could be measured, was thereby markedly reduced. The constraint on the maximal Reynolds number at M = 0.35 was of another nature: charge pressures larger than 720 kPa were required to increase the test range at larger Reynolds numbers, but the wind tunnel was not certified for such high pressures [303]. This also limited the largest Hartree parameter that could be attained at M = 0.35, since the boundary layer would have remained laminar over the whole upper surface of the model at larger values of β_H.

- The lowest examined Mach number M = 0.35 was close to the minimal Mach number that can be tested at DNW-KRG (M = 0.3) [55,276]. Mach numbers larger than M = 0.77 were not considered because of the limitation on the largest possible Hartree parameter, as discussed above. At fixed, negative angle-of-attack, the deformation of the test-section lower wall required for wall adaptation was more pronounced at larger Mach numbers. Thus, the maximally allowable curvature was reached at larger (less negative) angles-of-attack; this did not permit favorable pressure gradients to be implemented at Mach numbers larger than M = 0.77.
- The standard value of T_w/T_{aw} at DNW-KRG depends on the Mach number, as discussed in Section 3.1. The maximally allowable temperature difference between storage tube and test section prior to a run is $\Delta T = 20$ K [233]. This placed a limit on the lowest value of T_w/T_{aw} that could be implemented. Note that also the minimal value of T_w/T_{aw} depends on the Mach number. At the lower Mach numbers M = 0.35 and 0.5, $T_w/T_{aw} < 1$ could be achieved; at larger Mach numbers, the lowest value of T_w/T_{aw} was generally kept slightly greater than one, since the wall temperature difference between laminar and turbulent regions at adiabatic wall conditions is so small that it cannot be resolved by the TSP measurement technique [57,192,209,211,217]. Moreover, the wall temperature ratio could not be reduced while the vacuum pump was operating [303]. Thus, the low Reynolds number tests (Re = 4 and $5 \cdot 10^6$) at M = 0.65 and 0.77 could be carried out only at standard T_w/T_{aw}.

D.4 Effect of the chord Reynolds number

The chord Reynolds number was shown in Appendix D.2 to have a negligible influence on the surface pressure distribution. The effect of the chord Reynolds number on the transition location is shown in Fig. D.4.1, where the TSP results at $\beta_H = 0.066$, $M = 0.77$, and standard T_w/T_{aw} are presented. The chordwise intensity distributions at $y/b = 0.57$ are shown in Fig. D.4.2.

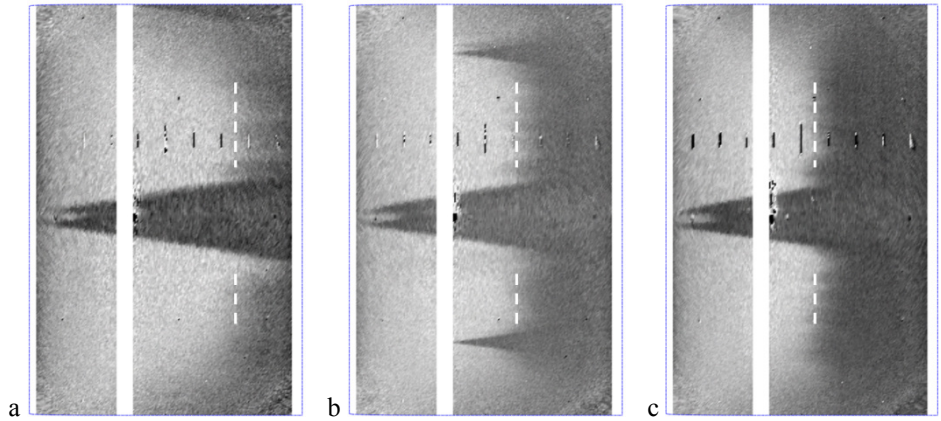

Fig. D.4.1. TSP results for different chord Reynolds numbers at M = 0.77 and $\beta_H = 0.066$. Smooth configuration. a: Re = 6 · 10^6, $T_w/T_{aw} = 1.043$, $x_{T,0}/c = 75 \pm 1.1$ %, Re$x_{T,0} = 4.5 \pm 0.07 \cdot 10^6$; b: Re = 7 · 10^6, $T_w/T_{aw} = 1.044$, $x_{T,0}/c = 61 \pm 0.6$ %., Re$x_{T,0} = 4.3 \pm 0.04 \cdot 10^6$; c: Re = 8 · 10^6, $T_w/T_{aw} = 1.050$, $x_{T,0}/c = 55 \pm 0.6$ %, Re$x_{T,0} = 4.4 \pm 0.05 \cdot 10^6$.

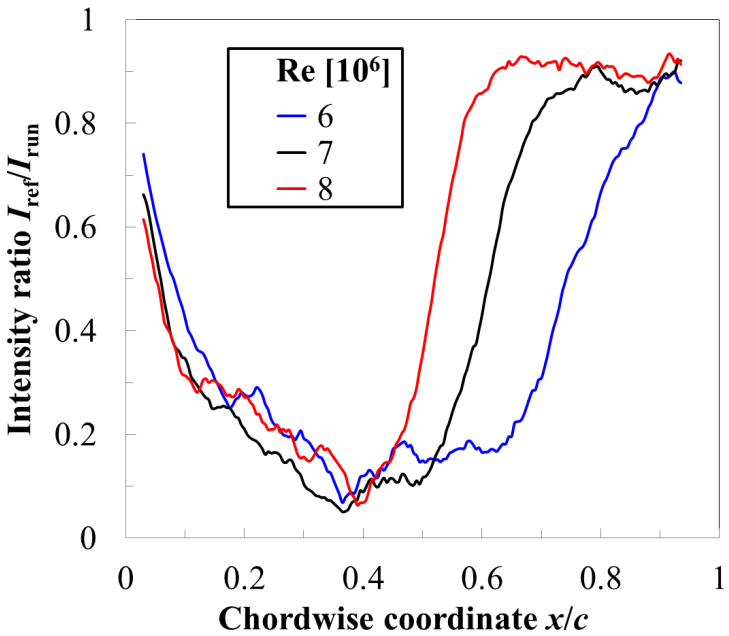

Fig. D.4.2. Normalized intensity distributions at $y/b = 0.57$ for the runs shown in Fig. D.4.1. Re: a) 6 · 10^6, b) 7 · 10^6, c) 8 · 10^6.

An increase in the chord Reynolds number made the boundary layer more unstable, so that the transition location moved further upstream. This is clearly in

agreement with results of earlier experimental work and with expectations from linear stability theory (see, e.g., [85]).

The results of the stability computations for the considered test conditions are presented in Fig. D.4.3, where amplification factors of Tollmien-Schlichting waves are shown for some selected frequencies only. The measured transition locations are shown by gray bars.

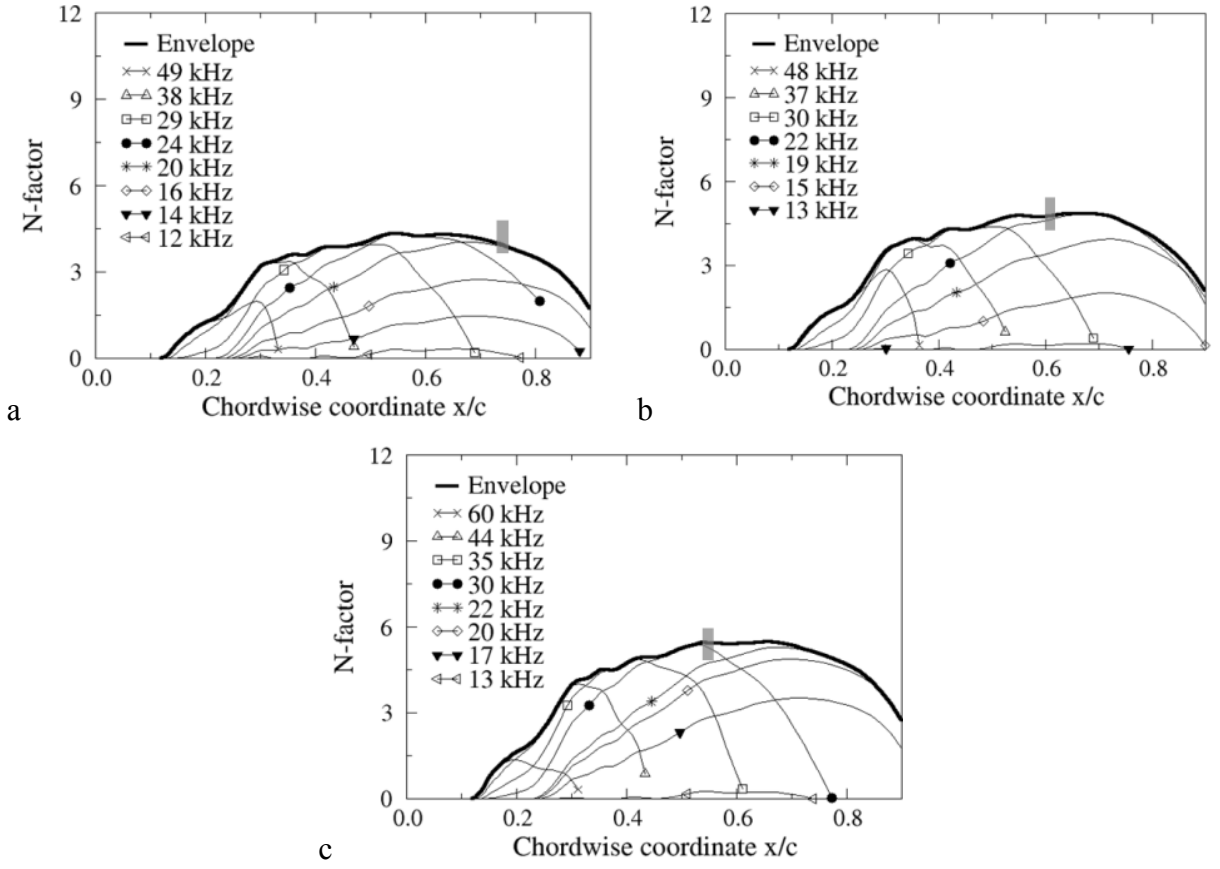

Fig. D.4.3. Stability analysis results for the cases of Fig. D.4.1. Re: a) 6 Mio, b) 7 Mio, c) $8 \cdot 10^6$.

Larger chord Reynolds numbers lead to an increase in the amplification factors. According to the e^N method for transition prediction, transition is assumed to occur when the critical transition N-factor N_T is reached. A certain value of the transition N-factor, assumed to be independent of the Reynolds number, is reached at a more upstream location as the Reynolds number is increased, in line with the experimental observations here.

It should be emphasized that the transition Reynolds number was almost independent of the chord Reynolds number when the other parameters (Mach number, wall temperature ratio, and streamwise pressure gradient) were kept constant. The transition Reynolds number obtained for the runs presented in Fig. D.4.1 was $4.4 \cdot 10^6$ with a variation about this value of $\pm 0.1 \cdot 10^6$. Note that also the streamwise extent of the transition region ($\mathrm{Re}_{x\mathrm{T0,end}} - \mathrm{Re}_{x\mathrm{T0,start}}$) appears to be

approximately independent of the chord Reynolds number: ($\mathrm{Re}_{x\mathrm{T0,end}} - \mathrm{Re}_{x\mathrm{T0,start}}$) = 1.5 ±0.4 · 10^6. (The significant uncertainty in the extent of the transition region is due to the inaccuracy in the detection of $x_{\mathrm{T0,end}}$ and $x_{\mathrm{T0,start}}$, as discussed in Section 2.2.4.) These findings are due to the model shape designed for the present experiments: as the chord Reynolds number was changed, transition occurred at a different chordwise location, but still in a region where the pressure gradient was nearly the same. The value of $\mathrm{Re}_{x\mathrm{T,0}}$ thus remained practically unchanged, so long as transition remained on the region of quasi-uniform pressure gradient.

The independency of the transition Reynolds number of the chord Reynolds number is significant, also with respect to the increase of the level of total pressure fluctuations Tu_{p0} in the DNW-KRG test section at larger unit Reynolds numbers [56]. At a Mach number of M = 0.8, close to that considered here (M = 0.77), the increase in fluctuation level is approximately ΔTu_{p0} = 0.05 % for an increase of chord Reynolds number of ΔRe = 2 · 10^6, such as for that shown in Fig. D.4.1. This insensitivity is likely to be related to the spectral content of the external disturbances. Unfortunately, spectral information is available only up to a frequency of 10 kHz [56]: as can be seen in Fig. D.4.3, waves at frequencies below 10 kHz are not amplified at all at the examined test conditions. Note also that the flow quality measurements presented in [56] were conducted in the presence of a shock on the plate supporting the measurement system, so that possible contributions of upstream traveling acoustic disturbances could not be measured. In any case, it appears reasonable that the external disturbance level in the frequency range of the most amplified instability waves does not increase significantly, at least in the range of chord Reynolds numbers ΔRe = 2-3 · 10^6 with a fixed pressure gradient.

In the region 70 % < x/c < 80 %, the streamwise pressure gradient actually starts to deviate from that on the upstream region 20 % < x/c < 70 %. The last stages of the transition process, however, occur over a finite distance; in the presence of the favorable pressure gradients considered in the present work, this distance can be even larger than $\Delta(x/c)$ = 10 % (see Section 2.2.4). It appears reasonable to link transition locations measured in the region 70 % < x/c < 80 % to the streamwise pressure gradient on the upstream region 20 % < x/c < 70 %, since it is the pressure gradient on this portion of the chord length that influences the linear amplification of the boundary-layer disturbances. This can be seen by a look at the results obtained at Re = 6 · 10^6. Transition was detected at $x_{\mathrm{T,0}}/c$ = 75 %, but the transition process starts already upstream at $x_{\mathrm{T0,start}}/c$ ~ 65 % (see the blue curve in Fig. D.4.2). The N-factor envelope curve (shown in Fig. D.4.3a by a thicker line) has a negative slope at approximately x/c > 70 %, because growth of boundary-layer disturbances is damped by the more pronounced flow acceleration in this region. Linear amplification of instability waves with the largest amplification ratios at approximately x/c ~ 60-70 % occurs in the region 20 % < x/c < 70 %, which corresponds to the region

where the pressure gradient parameter has been evaluated. These instability waves can reach the threshold disturbance amplitude [82,91,108] and lead to transition in the region 70 % < x/c < 80 % via non-linear processes, which are obviously not captured by linear stability theory. It should be emphasized here that the transition Reynolds numbers corresponding to transition locations in the region 70 % < $x_{T,0}/c$ < 80 % were found to be in agreement with those obtained at the same test conditions but larger unit Reynolds numbers (i.e., for $x_{T,0}/c$ < 70 %): this result supports the above considerations. Instability waves with the largest N-factors at x/c < 35 % undergo considerable amplification upstream of the region 20 % < x/c < 70 %. These instability waves are significant for cases with transition occurring at x/c < 35 %; this was, however, not the topic of this work. In the cases where transition was measured in the region 35 % < x/c < 50 %, a small contribution to the total linear amplification of these disturbances was seen at approximately 15 % < x/c < 20 %. This contribution was however small, and the Hartree parameter was evaluated in the region of quasi-uniform pressure gradient 20 % < x/c < 70 % also for these data points. In all other cases, growth of the instability waves which have the largest amplification factors at the measured transition locations occurs completely, or almost completely, in the region 20 % < x/c < 70 %.

Since $\mathrm{Re}_{xT,0}$ was independent of the chord Reynolds number, non-usable test runs could be avoided. In fact, at a considered test condition, the transition Reynolds number could be already evaluated when the transition location at a just one chord Reynolds number was available. On the basis of this transition Reynolds number, it was possible to "predict" the transition location at another chord Reynolds with a certain degree of confidence. In general, the tests were not run when transition was expected to occur in proximity (or even upstream) of the step location, nor when the boundary layer was expected to remain laminar over the whole upper surface of the model. These tests were run only in a few cases, in order to verify these expectations.

D.5 Effect of the Mach number (details)

The effect of the Mach number on $\mathrm{Re}_{xT,0}$ presented in Section 5.1.1 was observed for all considered pressure gradients. In the case of a flat pressure distribution (almost zero streamwise pressure gradient) the adiabatic wall transition Reynolds number was $\mathrm{Re}_{xT0,aw} \sim 2.6 \cdot 10^6$ at M = 0.77, whereas $\mathrm{Re}_{xT0,aw} \sim 3.8 \cdot 10^6$ at M = 0.35. Note that these values confirm the good flow quality of DNW-KRG (and also good quality of the model surface). The value of $\mathrm{Re}_{xT,0}$ at M = 0.35 is in the range of transition Reynolds number typical for low-speed facilities with a very low level of freestream disturbances [85,95,101]. Also the value of $\mathrm{Re}_{xT0,aw}$ measured at M = 0.77 and $\beta_H \sim 0$ is comparable to that characteristic of low-disturbance facilities [40,95], which had, however, been run at lower speeds. In the same Mach number range, a larger value of transition Reynolds number had been measured on a 10° sharp cone: $\mathrm{Re}_{xT,0} \sim 3.5\text{-}4.0 \cdot 10^6$ [102,121]. This range of

values had been achieved in both flight experiments and wind-tunnel tests in quiet facilities. When the present results are compared to those in [102,121], however, at least two aspects should be kept in mind. First, the location corresponding to completed transition was taken as the transition location [102,121]. If the transition location would have been defined in the same manner as in the current work, the values of transition Reynolds number would have been reduced by approximately 5 % to 10 %. Second, the streamwise pressure gradient along the cone surface at subsonic flow conditions was favorable in the wind-tunnel experiments [121]. Note that a transition Reynolds number of approximately $4.0 \cdot 10^6$ was also measured on the *PaLASTra* model at a moderately favorable pressure gradient ($\beta_H = 0.051$) and at $T_w/T_{aw} = 1.008$. In the flight experiments on the 10° cone, the streamwise pressure gradient was nearly zero because of the influence of the forward fuselage [102,121]. Although the streamwise pressure gradient was less favorable than in the wind-tunnel tests, the transition Reynolds numbers were in agreement in the subsonic Mach number range; this was probably due to the lower level of acoustic disturbances in the flight experiments, which counteracted the aforementioned difference in streamwise pressure gradient. The pressure fluctuation level Tu_p in the flight tests was found to decrease at larger Mach numbers, a behavior opposite to that observed in the wind-tunnel experiments up to M ~ 0.9. If the aforementioned differences in the definition of the transition location and in the streamwise pressure gradient are taken into account, the difference between the value of $Re_{xT,0}$ obtained in the present work at $\beta_H \sim 0$ and that reported for the wind-tunnel experiments of [102,121] is less pronounced. In any case, it is apparent that there is some factor that induced the observed variation of the transition Reynolds number as a function of the Mach number. Since the model surface quality was the same for runs at all Mach numbers, this factor could be the disturbance environment and/or the receptivity of the boundary layer.

Previous flow quality measurements in the DNW-KRG test section [56] did not show major changes of $Tu_{\rho u}$ and Tu_{T0} at larger Mach numbers. In contrast, the level of total pressure fluctuations was observed to increase from $Tu_{p0} \sim 0.06$ % to 0.1 % as the Mach number was increased from M = 0.45 to 0.8 (at $Re/c = 30 \cdot 10^6$ m^{-1}). The value of Tu_{p0} at M = 0.35 is expected to be comparable with that at M = 0.45. This variation of the level of acoustic disturbances suggests an explanation for the reduction of $Re_{xT,0}$ at larger Mach numbers, provided that the frequencies of the freestream disturbances matched those of the amplified instability waves. For the case discussed in Section 5.1.1 (Fig. 5.1.1.1 to Fig. 5.1.1.5), the frequencies of the most amplified instability waves in the transition region were approximately f_{TS} = 10–20 kHz at M = 0.35, and increased at larger Mach numbers up to approximately f_{TS} = 20–40 kHz at M = 0.77 (see Fig. 5.1.1.4). As discussed in Appendix D.4, available information about the disturbance environment at DNW-KRG [56] does not permit one to address this

matter. Moreover, acoustic disturbances could originate also from flow separation at the model aft side (see Section 3.2.2).

In order to obtain further information about the disturbance environment, a Kulite © pressure sensor was mounted on the starboard side wall of the wind-tunnel test section, in a flange located approximately 600 mm upstream of the model leading edge. The measurement of the pressure fluctuations at the side wall is not ideal, since it is influenced by the turbulent boundary layer developing on this surface. Nevertheless, it was still expected to provide useful information, as was shown in [120], especially with regard to energy concentrated in specific frequency ranges. The signal from the pressure sensor was sampled at 200 kHz and then analyzed using Welch's overlapped segment averaging estimator [304]. The number of discrete Fourier transform points used in the calculation was 2^{12}, with a number of overlapped samples corresponding to half the window length. The spectra of the signal measured for the cases of Section 5.1.1 are plotted in Fig. D.5.1, where the amplitude of the signal is presented as relative to a reference pressure of $p_{ref} = 20$ µPa.

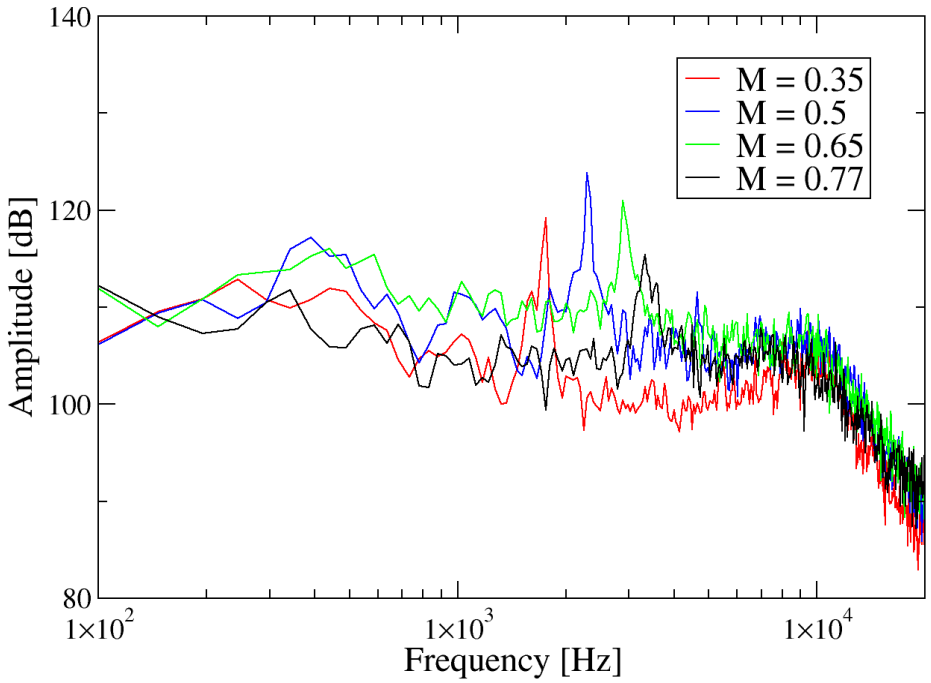

Fig. D.5.1. Power spectral density distribution of the pressure fluctuations measured at the test-section side wall for the cases of Section 5.1.1 (Fig. 5.1.1.1 to Fig. 5.1.1.5). Amplitude of the signal presented as relative to a reference pressure of $p_{ref} = 20$ µPa.

The measured disturbance level is large for all Mach numbers. One peak can be seen for each Mach number in the frequency range 1.5 kHz $< f <$ 3.5 kHz. The frequency of the peak at M = 0.35 is approximately $f_{peak} = 1.8$ kHz and increases to approximately $f_{peak} = 3.3$ kHz at M = 0.77. The magnitude of the measured pressure fluctuations decreases continuously with increasing frequency at approximately $f > 10$ kHz. This was caused by the filtering effect due the

Helmholtz resonance in the cavity between the test-section side wall and the actual sensor. The estimated resonant frequency in this cavity was approximately f_{HR} = 12 kHz [305].

The peaks in the power spectra of the measured signals are very likely the manifestation of pressure fluctuations caused by alternate shedding of vortices from the aft part of the model, which propagated upstream. The alternate shedding of vortices from the upper and lower side of a blunt trailing edge of a flat plate is characterized by a linear dependency of the shedding frequency on the freestream velocity [306-311]. The corresponding Strouhal number, defined as $St = f_{peak} U_\infty / d$, where d is the thickness of the plate, was found to be between approximately St = 0.2 and 0.28 over a wide range of Reynolds numbers [306-309,312]. The Strouhal number was observed to be dependent on the plate thickness-to-chord ratio [307,312]. In contrast, the effect of the boundary-layer thickness on the shedding frequency was shown to be relatively small, and to become negligible at plate thickness-to-chord ratios d/c such that of the *PaLASTra* model, where $d/c = 0.1$ [310,311]. The trailing-edge geometry has a significant effect on both the shedding frequency and the intensity of the produced pressure fluctuations [306-307,310-311]. An asymmetric trailing edge, such as that adopted for the *PaLASTra* model, was found to be "very effective for suppression of all types of vortex excitation including acoustic resonances" [306]. The increase of the peak frequency at larger Mach numbers, observed in Fig. D.5.1, is consistent with the dependency of the vortex shedding frequency on the freestream velocity. The corresponding Strouhal number is larger at M = 0.35 and decreases for larger Mach numbers, but still remains within the range St ~ 0.27–0.30. A Strouhal number St ~ 0.27 was also found in [56] for the vortices shed by the sharp trailing edge of the support plate used in that work. A peak similar to those in Fig. D.5.1 was observed in the power spectra; the corresponding frequency was found to vary almost linearly as a function of the freestream velocity [56]. "Trailing-edge-bluntness vortex-shedding noise" has been shown to be an important contributor to aircraft noise radiation [310,311]. Less is known about the interaction between airfoil self-noise, caused by vortex shedding due to trailing-edge bluntness, and the transition process on an airfoil upper side (suction side) [313]. DNS at low chord Reynolds numbers ($Re \leq 0.1 \cdot 10^6$) showed that acoustic waves, radiating from the trailing edge of a NACA 0012 airfoil, can couple into the laminar boundary layer by means of the receptivity process and trigger boundary-layer transition [314,315]. In this case, however, transition occurred over a laminar separation bubble.

The most probable reason for the reduction of the transition Reynolds number at larger Mach numbers, observed on the *PaLASTra* model, appears to be the increased initial amplitude of the disturbances within the boundary layer. This can originate from increased amplitude of the external disturbances (in the frequency range of amplified instability waves), from enhanced receptivity to the

external disturbances, or from a combination of both effects. As discussed above, the level of total pressure fluctuations in the DNW-KRG test section is larger at larger Mach numbers; this was however measured in a frequency range below that of main interest for the amplification of instability waves in the present work. The results of the linear stability computations in Fig. 5.1.1.4 show that the most amplified instability waves have frequencies larger than 10 kHz. Note also that waves with frequency below 10 kHz are not amplified at all at M = 0.77 (see Fig. 5.1.1.4a). In fact, there is no available information about the disturbance environment in the frequency range of main interest, since also the latest data are reliable only up to $f \sim 10$ kHz (see Fig. D.5.1). Direct forcing of instability waves at the peak frequencies of the external disturbances $f_{peak} \sim 1.8$-3.4 kHz is not possible: waves in this frequency range are damped at all Mach numbers, as shown in Fig. 5.1.1.4. It is possible that the energy of the external disturbances is also concentrated in harmonics of these frequencies, but further peaks have not been detected in the spectra shown in Fig. D.5.1. In any case, receptivity to the external disturbances plays an essential role. The coupling between the long-wavelength acoustic disturbances and the boundary-layer instabilities, which have shorter wavelength, can take place when the flow has to adjust rapidly in the streamwise direction. This can occur on the upper surface of the *PaLASTra* model in two regions. The first one is the leading-edge region, where the mean flow undergoes strong acceleration. The second region is at approximately $30\ \% < x/c < 40\ \%$, where the model surface has small inhomogeneities (see Appendix B.3.2). Furthermore, the uncoated strip at $33.5\ \% \leq x/c \leq 36.5\ \%$ was generally warmer than the surrounding TSP regions during a run at DNW-KRG. Heating strips can also be a source of receptivity [99,317], but the surface temperature change across this region is so small that its influence is expected to be insignificant. Leading-edge receptivity is generally regarded as less effective than that due surface inhomogeneities, because the instability waves are generated upstream of the indifferent-stability point and decay before they reach this location [97,106]. However, at the examined test conditions, the indifferent-stability point for the most amplified instability waves in the transition region is at $x/c \sim 15$-25 %, approximately half way between the leading edge and the region at $x/c \sim 30$-40 %. Thus, these waves grow markedly already upstream of the region with surface inhomogeneities. Moreover, the instability waves, which start to grow at $x/c > 30$ %, are predicted to undergo only weak amplification, as compared to those that are amplified starting from a more upstream location. The initial amplitude of these weakly amplified instability waves would need to be much larger than that of the most amplified ones to be predominant in the transition process. In cases such as that at M = 0.77 in Fig. 5.1.1.4a, the required initial amplitude would then be so large that the disturbance would be already in its non-linear amplification stage (see Section 2.2.3). It is more likely that receptivity to the external disturbances occurred in the leading-edge region. Leading-edge receptivity to acoustic waves has been investigated by means of asymptotic theory [316]; the receptivity coefficient for an infinitely-thin leading

edge was shown to decrease markedly at larger Mach numbers, but this study was restricted to Mach numbers only up to 0.1. Localized and non-localized receptivity to acoustic disturbances was examined using the "finite Reynolds number approach" at Mach numbers up to 0.9 [99,317]: receptivity due to single and multiple suction or heating/cooling strips was found to be enhanced at lower Mach numbers. These predictions are opposite to what has been observed in the present experiment, but the level and spectral content of the freestream disturbances should also be accounted for to enable conclusions about the effect of Mach number to be drawn. Nevertheless, receptivity to acoustic disturbances was shown to be most efficient for acoustic waves traveling upstream [99,316-318], such as those generated from the aft part of the model in the present work. This was observed in theoretical studies of leading-edge receptivity [316,318] and of localized and non-localized receptivity [99,317].

In any case, the influence of the Mach number on the level and spectral content of the freestream disturbances, on the receptivity to these disturbances, and then on the transition process still has to be elucidated. Because of the complicated nature of the phenomena involved, a large number of detailed measurements would be required, which was beyond the scope of the present study and is planned as future work. The accurate measurement of the disturbance environment in which the boundary layer on the *PaLASTra* model surface is developing is already a complex task: the measurement has to be performed in the presence of the model, but at the same time interference between the measurement system and the model has to be avoided. Moreover, the measurement system has to be designed to obtain information about the disturbances at frequencies up to (at least) 40 kHz. Given that such measurements can be accomplished, a further investigation of boundary-layer receptivity to these external disturbances represents an even more ambitious task. Experiments on boundary-layer receptivity have been successful at low-speed [77,106-107,175,203,206], but there are no available data in the Mach number range $0.35 \leq \mathrm{M} \leq 0.77$. Measurement techniques which are typically used in receptivity experiments at low speed (mainly hot-wires and microphones) cannot be used for experiments at DNW-KRG, for the reasons discussed in Appendix B.4.

D.6 Transition *N*-factors for the *PaLASTra* model at DNW-KRG

The computed *N*-factors are now correlated to the transition locations measured on the smooth configuration to obtain the transition *N*-factor $N_{\mathrm{T},0}$, i.e., the maximum *N*-factor at the transition location $x_{\mathrm{T},0}/c$. This correlation provides the value of the critical amplification ratio $e^{N_{\mathrm{T},0}}$ for a given model surface in a certain disturbance environment, which is the basis for the application of the e^N method for transition prediction (see Section 2.4). Transition *N*-factors were determined for all considered test conditions with $\beta_{\mathrm{H}} \geq 0$ and are plotted in Fig. D.6.1 as a function of the Hartree parameter. Obviously, $N_{\mathrm{T},0}$ could be determined only for

those cases at which transition could be seen on the model upper surface. Different colors are used for the transition N-factors obtained at different ranges of wall temperature ratio.

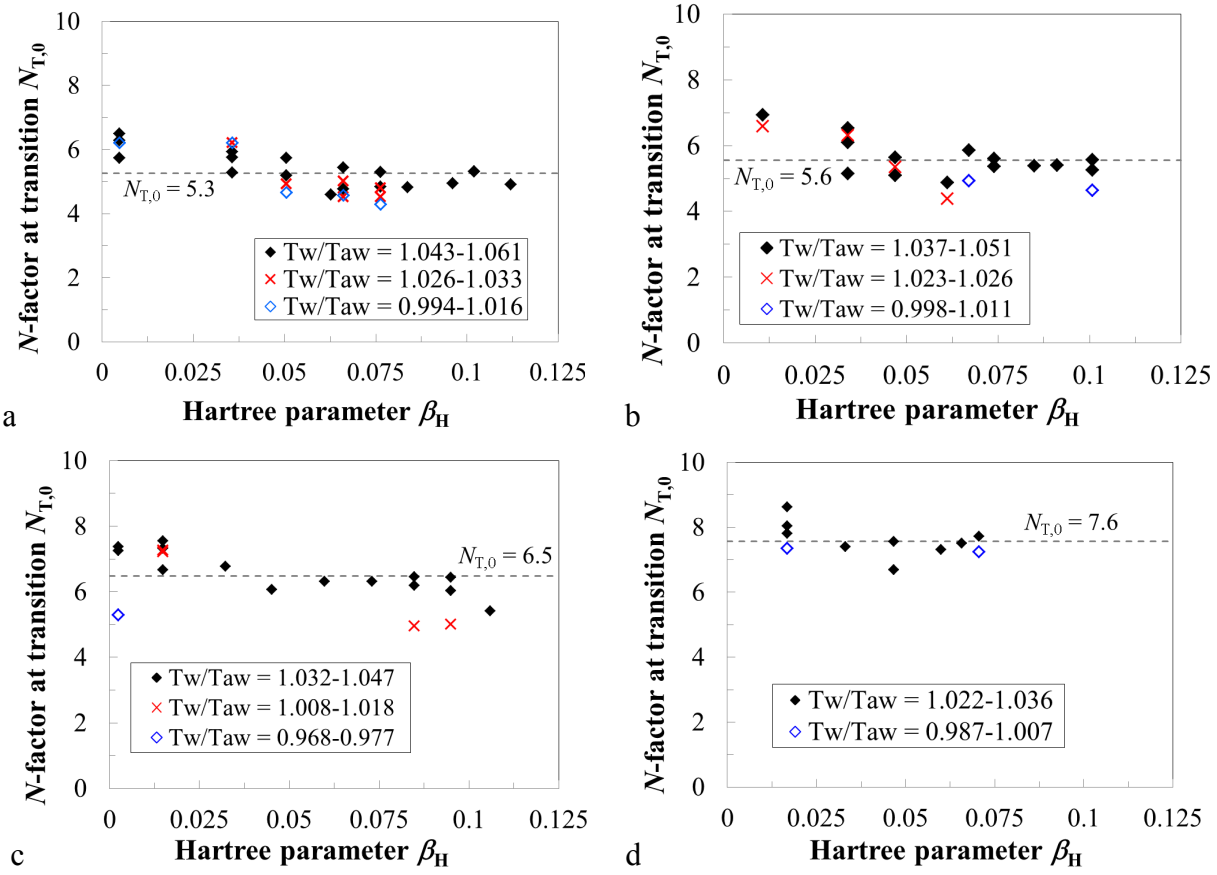

Fig. D.6.1. Transition N-factor for the smooth configuration. a: M = 0.77; b: M = 0.65; c: M = 0.5; d: M = 0.35. Dashed lines: average values of $N_{T,0}$.

Provided that the other parameters are kept unchanged, the transition N-factor decreases with decreasing wall temperature ratio. At Mach numbers M = 0.5 to 0.77, the results obtained for a given range of wall temperature ratio show a general decrease of $N_{T,0}$ up to $\beta_H \sim 0.05$; at larger Hartree parameters, the transition N-factor remains almost constant. This trend is not observed at M = 0.35. The effects of the stability modifiers (pressure gradient and wall temperature ratio) should be automatically included in the e^N method through the variations in the shape of the mean-velocity profile. The value of N_T should be unaffected by the stability modifiers, provided that the environmental disturbances are unchanged [116]. However, in [319] it has been mentioned that the value of the transition N-factor obtained from experiments on a two-dimensional, transonic flow depends on the streamwise pressure gradient. The present results show that the e^N method is not fail-safe. The e^N method generally gives satisfactory results when transition occurs in regions of zero or adverse pressure gradient [110,150]: in these cases, the linear phase of disturbance amplification covers the largest part of the distance between leading edge and the

location of transition onset. However, when the flow is accelerated, the extent of the non-linear region is larger, and a semi-empirical extension of linear theory may be not sufficient to cover the gap between the linear amplification phase and breakdown to turbulence [150]. This is a reasonable explanation for the variations of $N_{T,0}$ observed in the present work.

The average transition *N*-factors, evaluated at each Mach number for all examined values of T_w/T_{aw}, decrease with increasing Mach number: from $N_{T,0} = 7.6$ at M = 0.35 to $N_{T,0} = 5.3$ at M = 0.77. The average values of $N_{T,0}$ for each Mach number are shown in Fig. D.6.1 by dashed lines. At fixed Mach number, the transition *N*-factors are within a band of approximately ±25 % about the corresponding average values. Such a variation is not uncommon for the correlations between *N*-factors and transition locations when one test parameter is changed. For example, a similar variation was found in other work [153] for varying Reynolds number, and the deviations from the average value of $N_{T,0}$ were even larger in [278].

The smaller value of transition *N*-factor is obviously in line with the smaller value of transition Reynolds number discussed in Appendix D.5. An influence of the Mach number on $N_{T,0}$ has been also found in past work [145,154,277-278]. Lower values of $N_{T,0}$ were generally obtained at larger Mach numbers. In wind-tunnel experiments [145,278], this may have been due to an increase in the environmental disturbance level at larger Mach numbers; a change in the external disturbance level does not seem to be a possible explanation for the reduction of $N_{T,0}$ found in flight tests [154,277], since the pressure fluctuation level is more likely to decrease as the Mach number increases [102,121]. As discussed in Appendix D.5, receptivity to freestream disturbances can be influenced by the Mach number, and this may also have affected the dependency of $N_{T,0}$ on the Mach number. Note that agreement of the values of $N_{T,0}$ obtained at different Mach numbers was found in previous work when the amplification factors were computed by means of incompressible, linear stability theory, which is unphysical but is often used [154,277-278]. It is currently unclear whether a single "compressible" transition *N*-factor can exist for a certain test case at fixed test conditions but with varying Mach numbers. It should be also emphasized that not all experimental data are suitable for a rigorous calibration of N_T. The *N*-factor envelope curve should present a regular evolution from the indifferent-stability point, where disturbances are first amplified, to the transition location [116]. *N*-factor envelope curves that are either too steep or too flat are actually inadequate for the calibration of N_T [116,122].

It has become customary to define the quality of a wind tunnel by stating "its" critical *N*-factor [150]. This value depends, however, also on the model surface quality and on boundary-layer receptivity at the considered test conditions [100], provided that the method for the computation of the amplification factors, the measurement technique used to detect transition, and the definition of "transition location" are the same [116,150]. At M = 0.65 and 0.77, the values of transition

N-factors obtained in the present work for the considered model are lower than those usually associated with low-turbulence, quiet, transonic facilities [116]. A relatively low value of transition N-factor ($N_{T,0} \sim 6.7$) has been found also for an NLF-airfoil model tested at DNW-KRG at a comparable Mach number M = 0.7 [145]. The latter value of $N_{T,0}$ was, however, larger than that obtained in the present work. The reduction in transition N-factor is even more pronounced when the transition N-factor $N_{T,0} \sim 10.4$, obtained in [145] at M = 0.35, is compared to the corresponding value $N_{T,0} \sim 7.6$ in the present work. This reduction in $N_{T,0}$ with respect to the values obtained in previous work [145] is likely to be due to the additional acoustic disturbances which originated from flow separation at the aft side of the *PaLASTra* model and then travelled upstream. Nevertheless, the value $N_{T,0} \sim 7.6$ obtained at M = 0.35 lies just below the range $N_{T,0} \sim 8$-10, which is a range of values typical for quiet facilities [116,150]. This result is clearly consistent with the large value of $\mathrm{Re}_{xT0,aw}$ obtained in the present work at M = 0.35, which is in the range of transition Reynolds number typical for such facilities (see Appendix D.5).

D.7 Comparison of transition Reynolds numbers at reduced wall temperature ratio

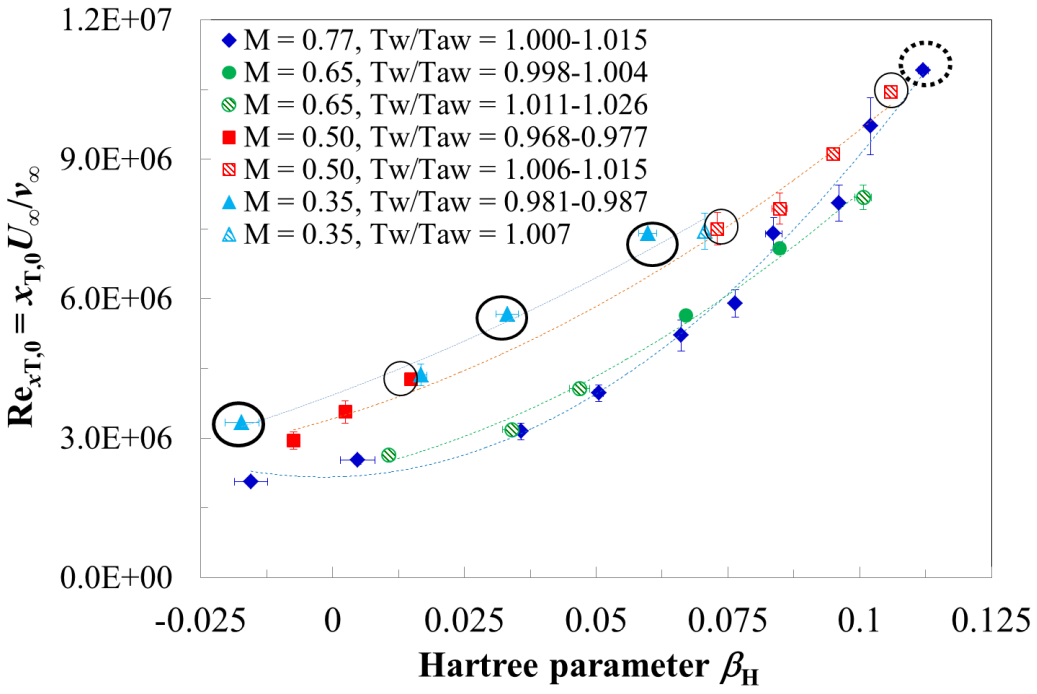

Fig. D.7.1. Transition Reynolds number as a function of the Hartree parameter for the four examined Mach numbers at reduced T_w/T_{aw}. Smooth configuration. The data points enclosed by dashed, thin solid, and thick solid circles indicate lower limits for $\mathrm{Re}_{xT,0}$ achievable at M = 0.77, 0.5, and 0.35, respectively, since the boundary layer remained laminar over the whole model upper surface. Second order polynomial fits to each set of data are shown by dashed lines.

D.8 Relative variation of transition Reynolds number as a function of the wall temperature ratio for M = 0.65 and 0.5

The variation of the ratio of transition Reynolds numbers $Re_{xT,0}/Re_{xT0,aw}$ is plotted as a function of the wall temperature ratio for M = 0.65 and M = 0.5 in Fig. D.8.1 and Fig. D.8.2, respectively. At a Mach number M = 0.65, a wall temperature ratio close to one was examined only for three test conditions (closed symbols in Fig. D.8.1). The experimental data show values of $Re_{xT,0}/Re_{xT0,aw}$ closer to one, as compared to those given by $Re_{xT,0}/Re_{xT0,aw} = (T_w/T_{aw})^{-7}$ [102,121] at the same value of T_w/T_{aw}. The function $Re_{xT,0}/Re_{xT0,aw} = (T_w/T_{aw})^{-3.5}$, shown by a solid line in Fig. D.8.1, provides a fair approximation of these data points. At the other pressure gradients examined at M = 0.65 (pattern-filled symbols in Fig. D.8.1), the values of $Re_{xT0,aw}$ are not reliable, since the reduced wall temperature ratio was not close to one.

At M = 0.5, the data points shown by closed symbols are fitted quite well by the curve from [102,121]; a better fit to these data is provided by the function $Re_{xT,0}/Re_{xT0,aw} = (T_w/T_{aw})^{-6}$, shown by a solid line in Fig. D.8.2.

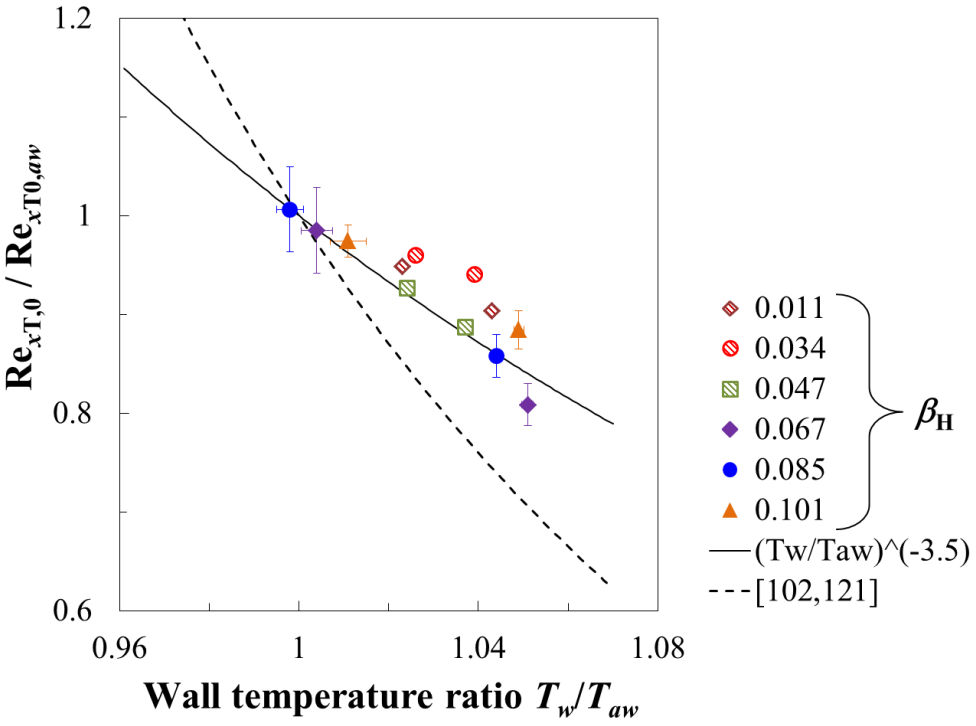

Fig. D.8.1. Relative variation of transition Reynolds number as a function of the wall temperature ratio for different pressure gradients (β_H) at M = 0.65. Smooth configuration.

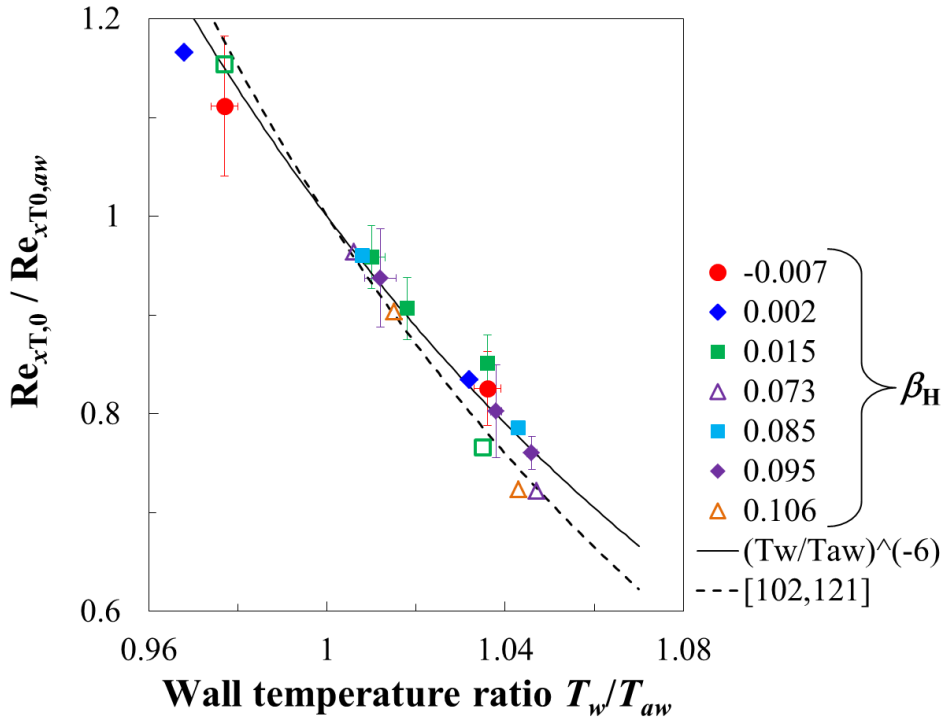

Fig. D.8.2. Relative variation of transition Reynolds number as a function of the wall temperature ratio for different pressure gradients (β_H) with the smooth configuration: M = 0.5. Open symbols show data points for which the boundary layer remained laminar over the model upper surface when the wall temperature ratio was reduced.

E Results with the step configurations

E.1 Repeatability and reproducibility of the experimental results

Repeatability and reproducibility studies were carried out also for the tests conducted with the step configurations. The constraints for acceptance of Mach number and Reynolds number were the same as those reported in Appendix D.1. The results were again shown to be repeatable and reproducible when the same conditions were tested in the same and in a different wind-tunnel entry. Between the different wind-tunnel entries, the angle-of-attack had to be slightly corrected, in the manner described in Appendix D.1. After the angle-of-attack had been corrected, the pressure distributions were practically the same. The reproducibility of the results obtained at the same test conditions, with the same (step-2) configuration, but in different wind-tunnel entries is shown by the example in Fig. E.1.1.

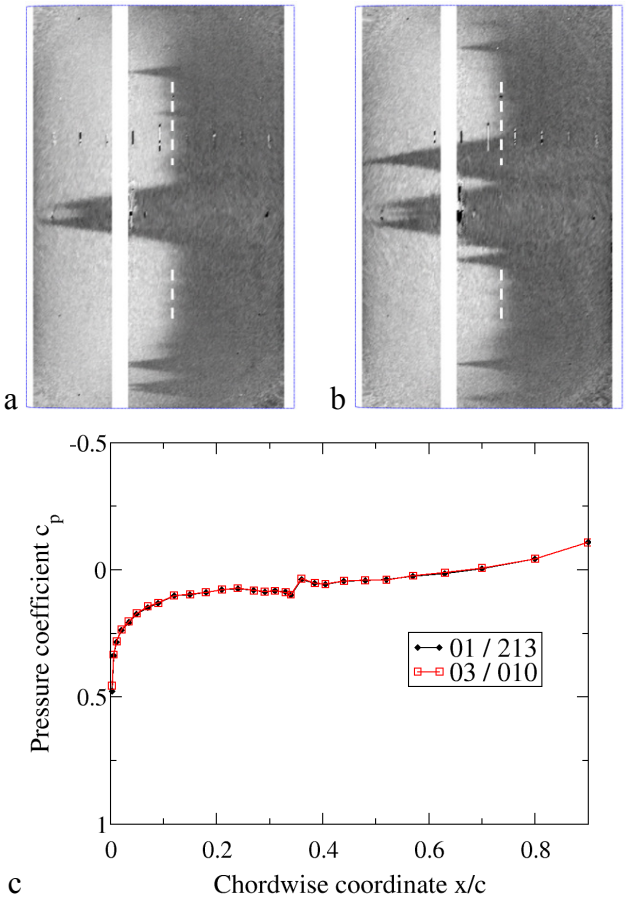

Fig. E.1.1. Reproducibility of TSP results and surface pressure distributions in different wind-tunnel entries. Re = 6 · 10^6, M = 0.77, β_H = 0.063, and standard T_w/T_{aw}. a: TSP result, first wind-tunnel entry (no. 01); b: TSP result, third wind-tunnel entry (no. 03); c: pressure distributions for a) and b) measured on the model upper surface.

The differences in the test parameters were: $\Delta\mathrm{Re} = 0.07 \cdot 10^6$, $\Delta\mathrm{M} = 0.005$, and $\Delta(T_w/T_{aw}) = 0.002$. The difference in the evaluated transition location was less than $\Delta(x_T/c) = 0.5$ %. At fixed Mach number and angle-of-attack, the surface pressure distributions, measured at various step heights, chord Reynolds numbers, and wall temperature ratios, were also in agreement. This has been shown in Sections 5.2.1, 5.2.2, and 5.2.4.

E.2 Combined effect of forward-facing steps and streamwise pressure gradient at M = 0.77

All results obtained at M = 0.77 and standard T_w/T_{aw} are collected in Fig. E.2.1, where the transition Reynolds number is plotted as a function of the step Reynolds number Re_h. Linear functions, approximating the results obtained at the same β_H, are shown by dotted lines. Only a few representative error bars for the results are shown in the figure. Since the transition Reynolds number with the smooth configuration was shown to be nearly independent of Re (see Section 5.1 and Appendix D.4), only the mean value of $\mathrm{Re}_{xT,0}$ at different β_H is plotted for $\mathrm{Re}_h = 0$.

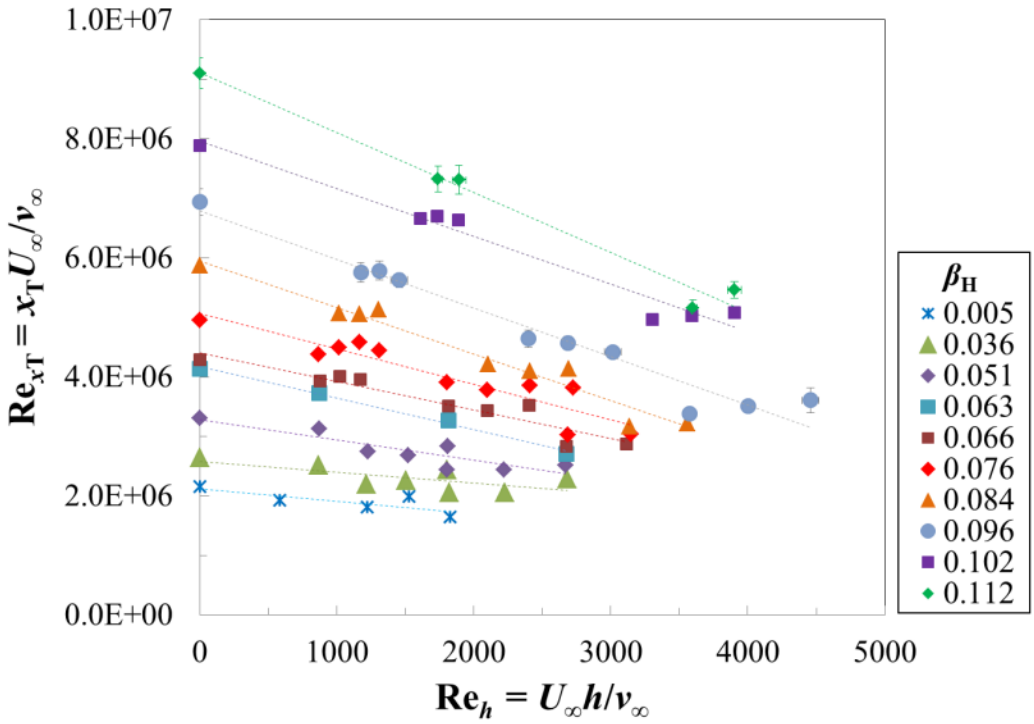

Fig. E.2.1. Transition Reynolds number as a function of the step Reynolds number at M = 0.77 and T_w/T_{aw} = 1.043-1.064.

Note that this representation of the results is not suitable for an analysis of the effects of the steps on boundary-layer transition. This is mainly due to the change of Re_h at different chord Reynolds number, which at the same time has almost no influence on Re_{xT} (see Section 6.1). This leads to groupings of data points with

approximately the same Re_{xT} for a certain step height but at different chord Reynolds numbers (and therefore different Re_h), as shown, e.g., by the results at $\beta_H = 0.084$ lying in the range $1000 < Re_h < 1400$. Note also that, when transition occurs near the step location, a further increase in chord Reynolds number leads to an increase in transition Reynolds number [242]: this is the case, e.g., for the data points at $\beta_H = 0.096$ for an increase of step Reynolds number from $Re_h \sim 4000$ to 4450. In any case, the main trends discussed in Section 6.2.1 with regard to Fig. 6.2.1.1a can also be observed in Fig. E.2.1.

As discussed in Section 6.2.2, the favorable influence of larger Hartree parameters on boundary-layer transition becomes less marked as the step height increases. This effect is shown in more detail in Fig. E.2.2, where the relative change of transition Reynolds number with respect to its value at $\beta_H = 0$ is plotted as a function of the Hartree parameter. Different colors are used for different configurations. The fitted curves are 2nd order polynomial functions that approximate the data sets for the different configurations. The value of $Re_{xT}/Re_{xT}(\beta_H = 0)$ at a certain Hartree parameter was computed from the corresponding mean value of Re_{xT}, whereby the value of Re_{xT} at $\beta_H = 0$ with the step configurations was extrapolated.

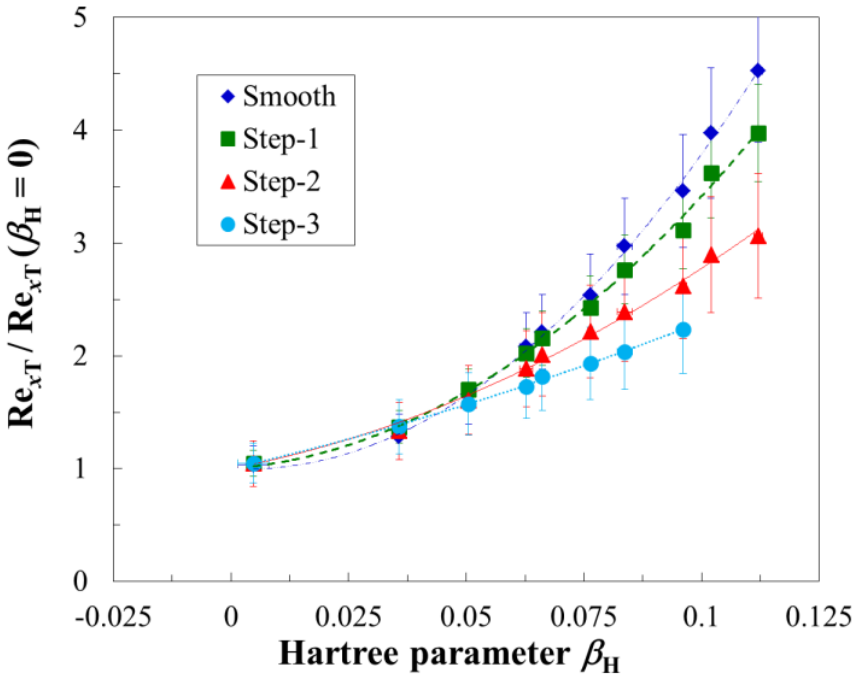

Fig. E.2.2. Relative variation of the transition Reynolds number as a function of the Hartree parameter for the four examined configurations at M = 0.77 and T_w/T_{aw} = 1.043-1.064.

E.2.1 TSP results showing the change in sensitivity of boundary-layer transition to forward-facing steps at different pressure gradients

The change in sensitivity of boundary-layer transition to forward-facing steps has been illustrated in Section 6.2.1 at $\mathrm{Re} = 6 \cdot 10^6$ and standard wall temperature ratio for two streamwise pressure gradients: $\beta_H = 0.036$ and 0.063. The corresponding TSP results are shown in Fig. E.2.1.1 and Fig. E.2.1.2, respectively.

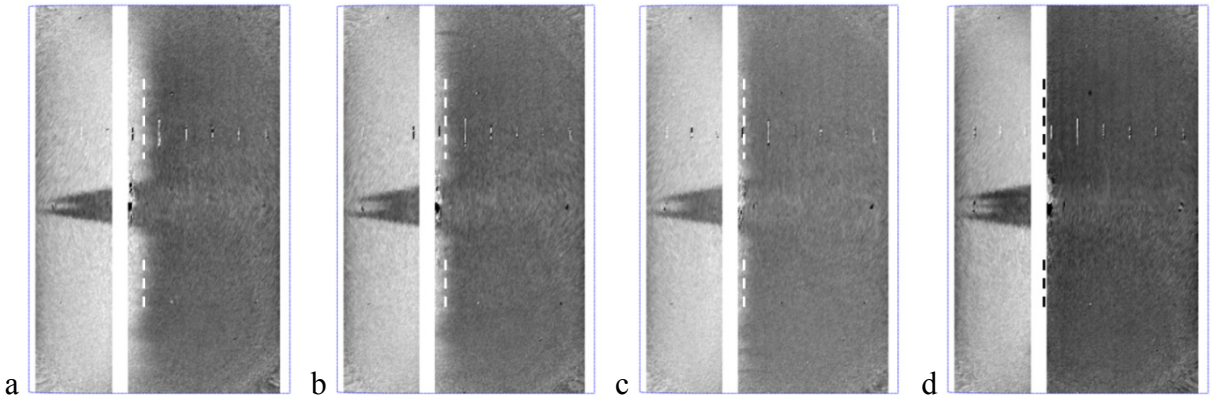

Fig. E.2.1.1. TSP results obtained with different step configurations at $\beta_H = 0.036$, M = 0.77, $\mathrm{Re} = 6 \cdot 10^6$, and standard T_w/T_{aw}. a: smooth, $T_w/T_{aw} = 1.054$, $x_{T,0}/c = 44 \pm 0.3$ %; b: step-1, $h/\delta_{1,h} = 0.3$, $T_w/T_{aw} = 1.052$, $x_T/c = 42 \pm 0.2$ %; c: step-2, $h/\delta_{1,h} = 0.62$, $T_w/T_{aw} = 1.049$, $x_T/c = 40 \pm 0.5$ %; d: step-3, $h/\delta_{1,h} = 0.92$, $T_w/T_{aw} = 1.060$, $x_T/c = 38 \pm 1$ %.

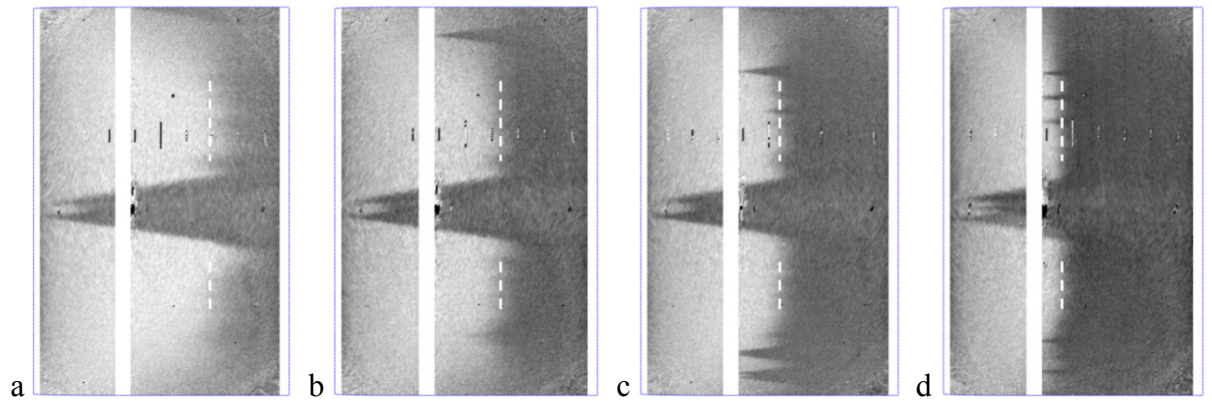

Fig. E.2.1.2. TSP results obtained with different step configurations at $\beta_H = 0.063$, M = 0.77, $\mathrm{Re} = 6 \cdot 10^6$, and standard T_w/T_{aw}. a: smooth, $T_w/T_{aw} = 1.052$, $x_{T,0}/c = 69 \pm 1$ %; b: step-1, $h/\delta_{1,h} = 0.32$, $T_w/T_{aw} = 1.052$, $x_T/c = 62 \pm 0.7$ %; c: step-2, $h/\delta_{1,h} = 0.65$, $T_w/T_{aw} = 1.054$, $x_T/c = 54 \pm 0.4$ %; d: step-3, $h/\delta_{1,h} = 0.97$, $T_w/T_{aw} = 1.057$, $x_T/c = 45 \pm 0.4$ %.

The effect of the increasing step height on boundary-layer transition can clearly be seen in Fig. E.2.1.2 (with $\beta_H = 0.063$). Transition moved continuously upstream with larger relative step height: from $x_T/c = 69$ % with the smooth configuration to $x_T/c = 45$ % at $h/\delta_{1,h} = 0.97$. In contrast, at $\beta_H = 0.036$, the change in transition location due to the effect of the step was much smaller (see

Fig. E.2.1.1). Even at $h/\delta_{1,h} = 0.62$ (Fig. E.2.1.1c), the transition location could still be detected in the TSP image region at $x/c \geq 40$ %; the TSP region downstream of the step location became fully turbulent only with the largest step, at $h/\delta_{1,h} = 0.92$.

E.3 Combined effect of forward-facing steps, pressure gradient, and Mach number

In Fig. E.3.1 to Fig. E.3.3, the transition Reynolds number is plotted as a function of the step Reynolds number for the Mach numbers M = 0.65 to 0.35. These plots are analogous to Fig. E.2.1. Linear functions, approximating the results obtained at the same β_H, are shown by dotted lines. Only a few representative error bars for the results are actually plotted in the figures.

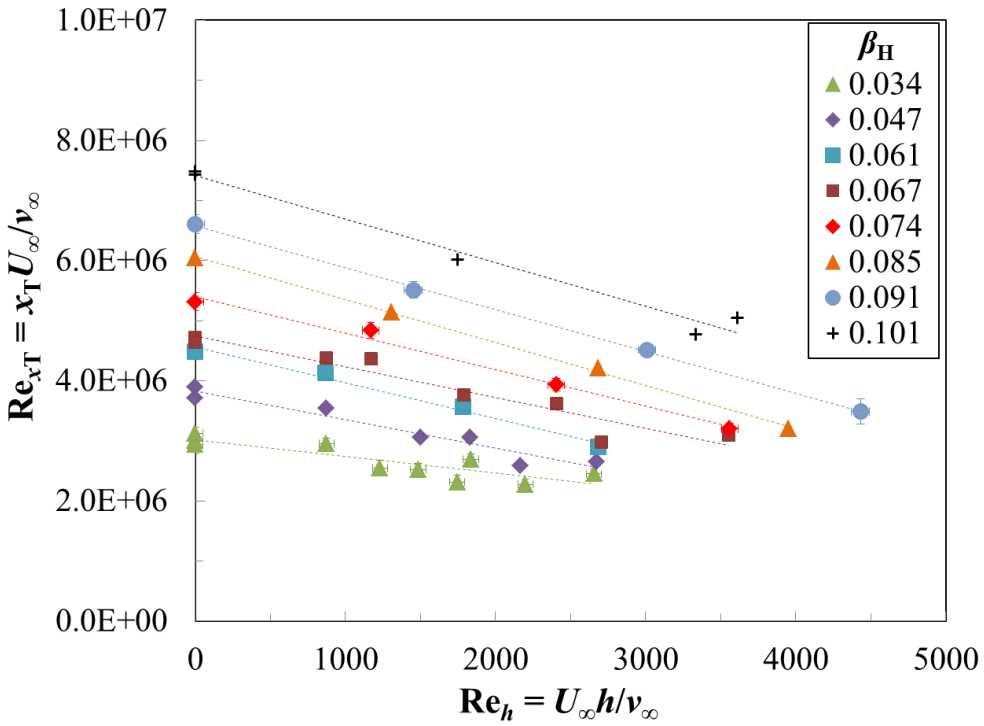

Fig. E.3.1. Transition Reynolds number as a function of the step Reynolds number at M = 0.65 and T_w/T_{aw} = 1.037-1.057.

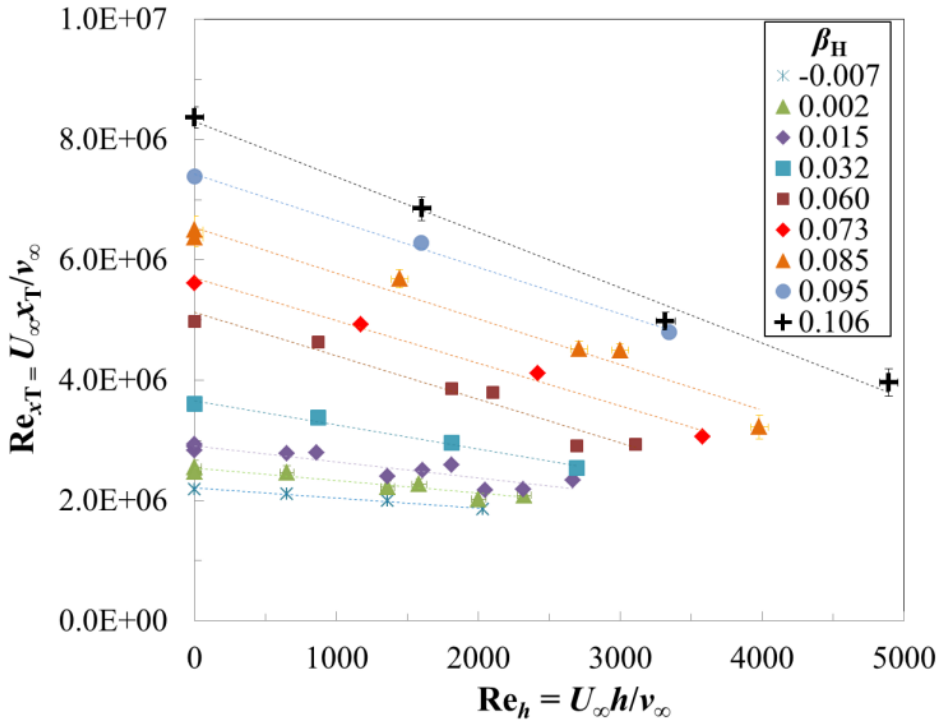

Fig. E.3.2. Transition Reynolds number as a function of the step Reynolds number at M = 0.5 and T_w/T_{aw} = 1.032-1.051.

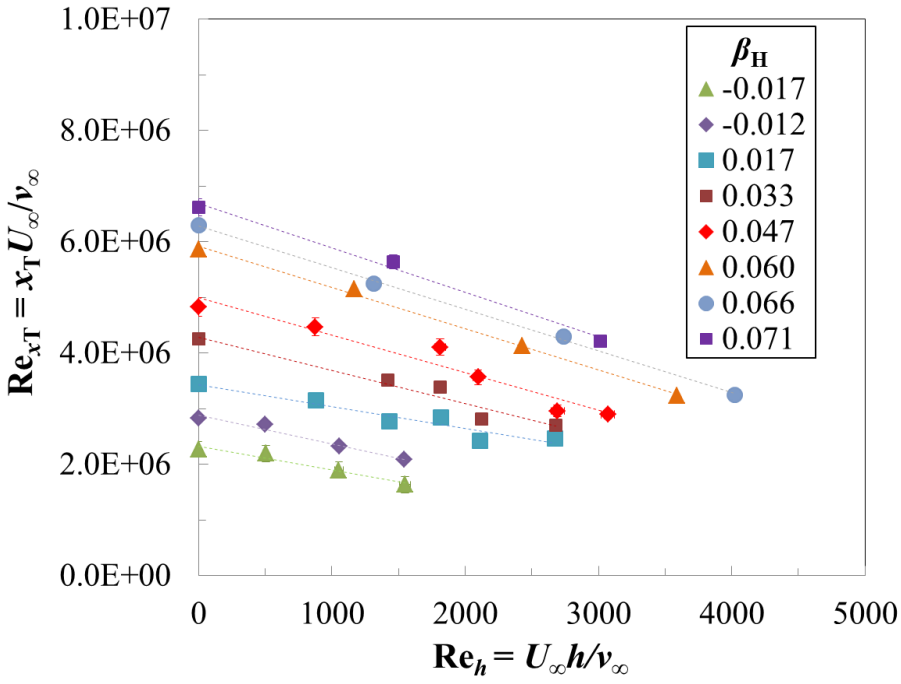

Fig. E.3.3. Transition Reynolds number as a function of the step Reynolds number at M = 0.35 and T_w/T_{aw} = 1.022-1.037.

In Fig. E.3.4 to Fig. E.3.6, the transition Reynolds number is shown as a function of the Hartree parameter for Mach numbers M = 0.65 to 0.35. These plots are analogous to Fig. 6.2.2.1. Second order polynomial functions approximate the results obtained with the smooth and step-1 configurations, whereas linear

functions approximate the results obtained with the step-2 and step-3 configurations.

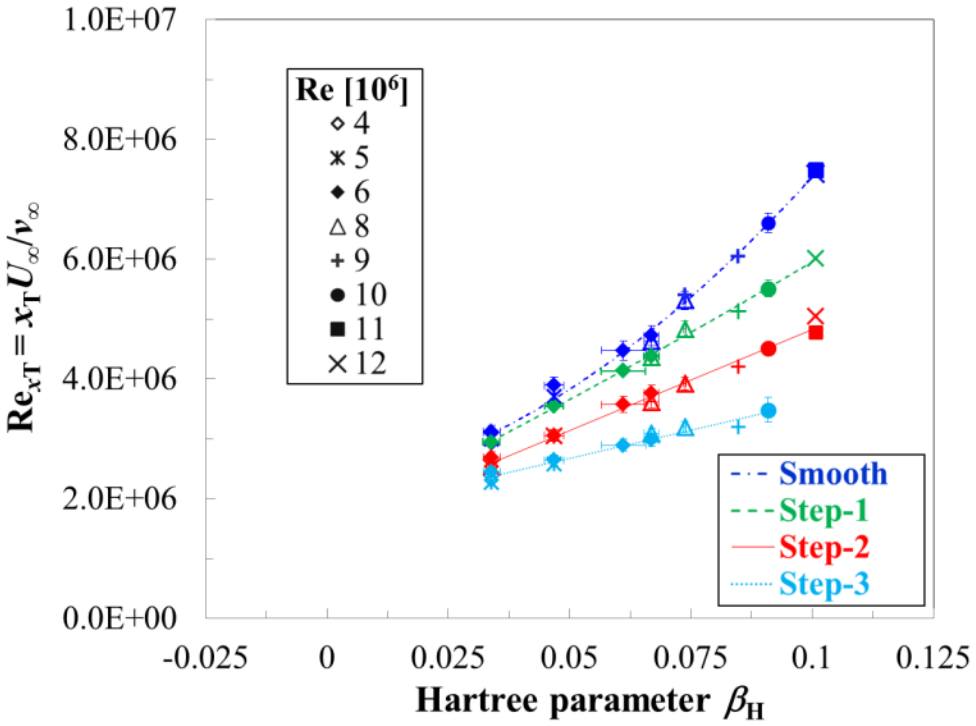

Fig. E.3.4. Transition Reynolds number as a function of the Hartree parameter at M = 0.65 and T_w/T_{aw} = 1.037-1.057. The abscissa starts at β_H = -0.025 for comparison with the following two figures.

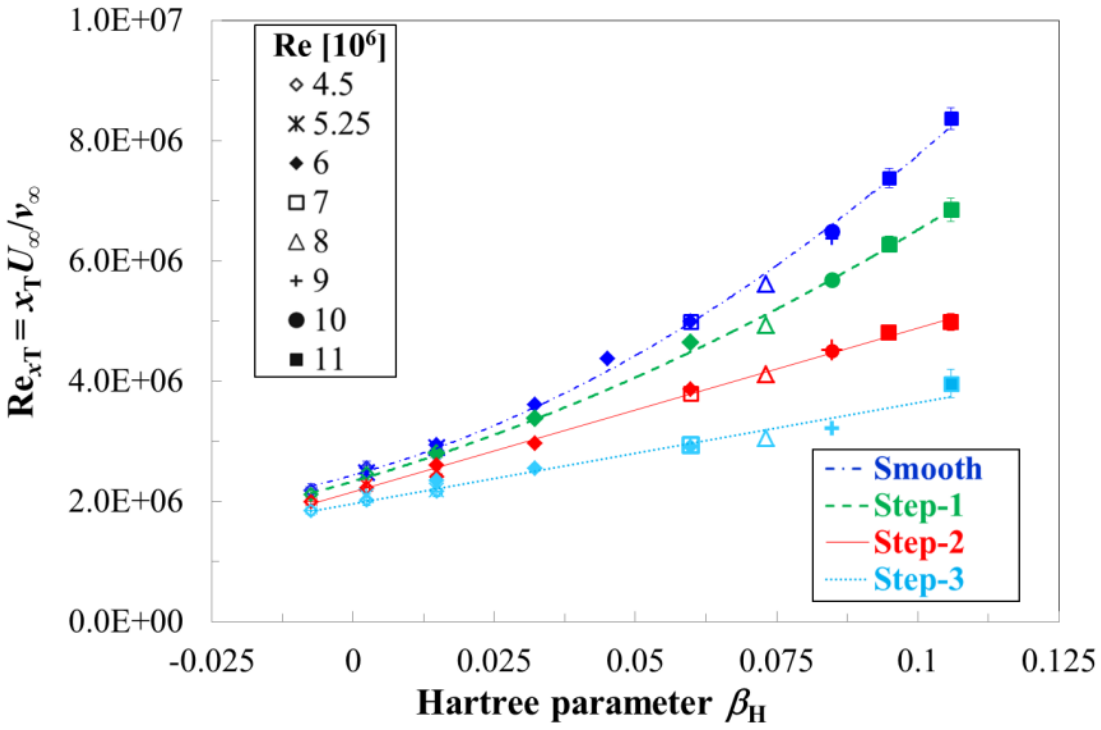

Fig. E.3.5. Transition Reynolds number as a function of the Hartree parameter at M = 0.5 and T_w/T_{aw} = 1.032-1.051. Note that transition was found immediately downstream of the step location for the data point with the step-3 configuration at the largest Hartree parameter.

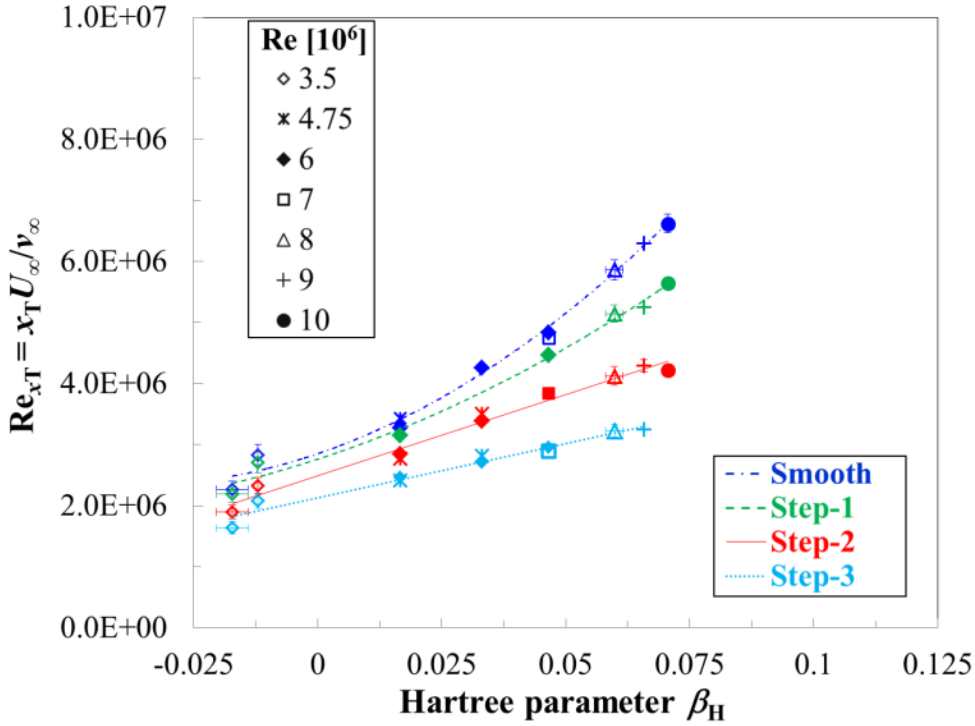

Fig. E.3.6. Transition Reynolds number as a function of the Hartree parameter at M = 0.35 and T_w/T_{aw} = 1.022-1.037. The abscissa ends at β_H = 0.125 for comparison with the above two figures.

The patterns seen at M = 0.77 are found also at lower Mach numbers:

- At fixed streamwise pressure gradient, the transition Reynolds number decreases as the step height is increased. This can be seen by following a certain fitted line in Fig. E.3.1 to Fig. E.3.3 from left to right, and also by examining the data points at fixed β_H from the top to the bottom in Fig. E.3.4 to Fig. E.3.6.
- The transition Reynolds number remains essentially unchanged when the chord Reynolds number is varied. This can be clearly seen in Fig. E.3.4 to Fig. E.3.6 for fixed Hartree parameter and configuration. It can be seen also in Fig. E.3.1 to Fig. E.3.3 that, at fixed step height and Hartree parameter, a change in Re leads to a variation in Re_h, but Re_{xT} remains almost unchanged. This is the case, for example, for the pair of data points at β_H = 0.033 and $Re_h \sim$ 1400 and 1800 in Fig. E.3.3.
- For a certain configuration, larger Hartree parameters lead to larger transition Reynolds numbers. This can be seen in Fig. E.3.1 to Fig. E.3.3 by examining the curves from the bottom to the top at a certain value of Re_h, and by following a certain curve from the left to the right in Fig. E.3.4 to Fig. E.3.6.

- The favorable influence of a larger Hartree parameter on the transition Reynolds number is less marked as the step height increases, leading to smaller increases of Re_{xT} for the same change in β_H. In Fig. E.3.1 to Fig. E.3.3, this results in a reduction of the difference in Re_{xT} between data points at different Hartree parameters when the step Reynolds number is increased. Similarly, the slope $\partial Re_{xT}/\partial\beta_H$ of the curves in Fig. E.3.4 to Fig. E.3.6 decreases for configurations with larger steps.
- Boundary-layer transition is more sensitive to the effect of the step when the streamwise pressure gradient is larger. This can be seen in Fig. E.3.1 to Fig. E.3.3, where the slope $\partial Re_{xT}/\partial Re_h$ of the approximation functions increases at larger pressure gradients, and in Fig. E.3.4 to Fig. E.3.6, where the reduction in Re_{xT} due to the effect of the steps is larger with increasing Hartree parameter.

The results obtained with the step-1 and step-3 configurations at the four different Mach numbers are collected in Fig. E.3.7 and Fig. E.3.8, respectively, where the transition Reynolds number is shown as a function of the Hartree parameter. Different colors are used for the results obtained at different Mach numbers. Each data point corresponds to the average transition Reynolds number at a certain Mach number and Hartree parameter. The four sets of data are approximated by 2nd order polynomial functions, shown by dotted lines. These figures are supplements to Fig. 5.1.2.5 (smooth configuration) and Fig. 5.2.5.4 (step-2 configuration).

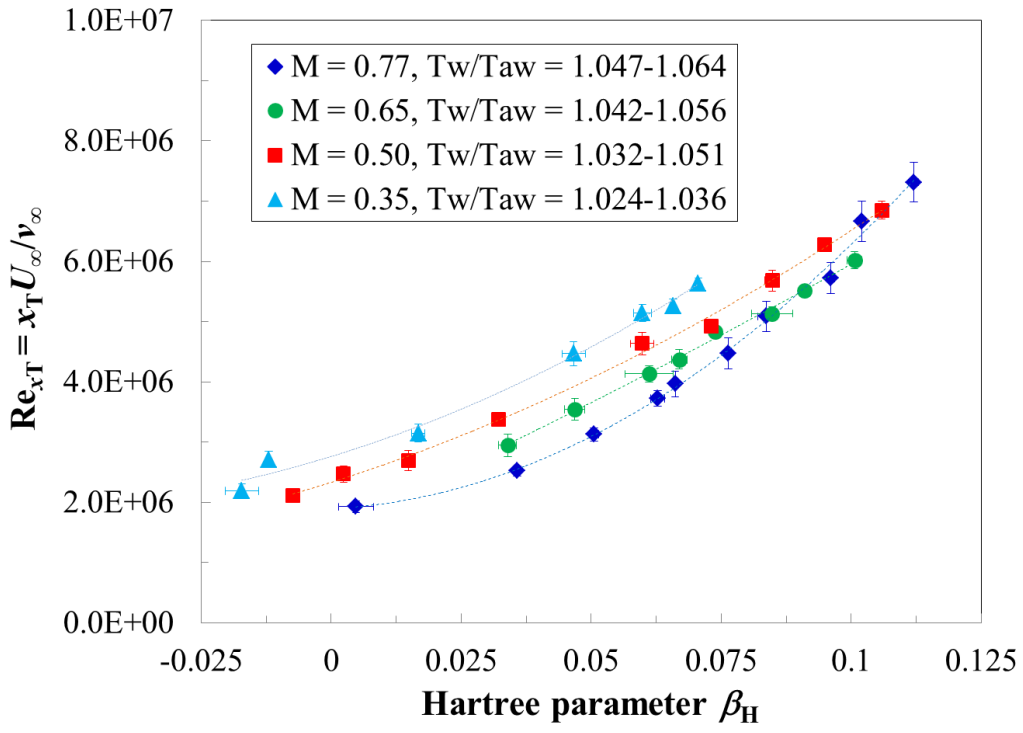

Fig. E.3.7. Transition Reynolds number as a function of the Hartree parameter at standard T_w/T_{aw} for different Mach numbers. Step-1 configuration.

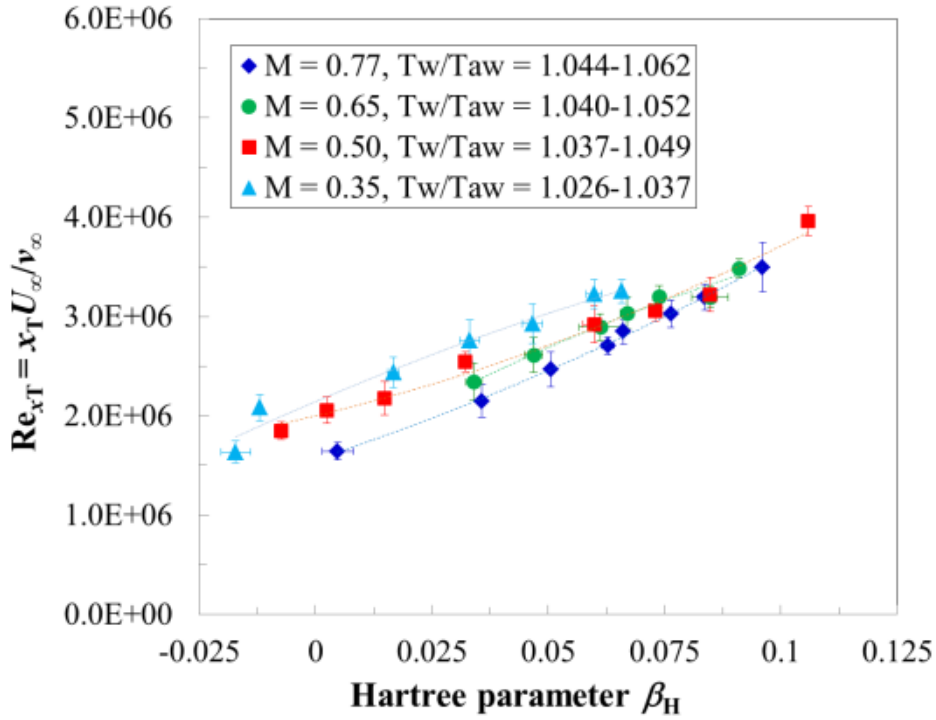

Fig. E.3.8. Transition Reynolds number as a function of the Hartree parameter at standard T_w/T_{aw} for different Mach numbers. Step-3 configuration.

The relative variation in transition Reynolds number $Re_{xT}/Re_{xT}(\beta_H = 0)$ for the step-1 and step-3 configurations is plotted as a function of the Hartree parameter in Fig. E.3.9 and Fig. E.3.10, respectively. These figures are supplements to Fig. 5.1.2.7 (smooth configuration) and Fig. 6.3.1 (step-2 configuration).

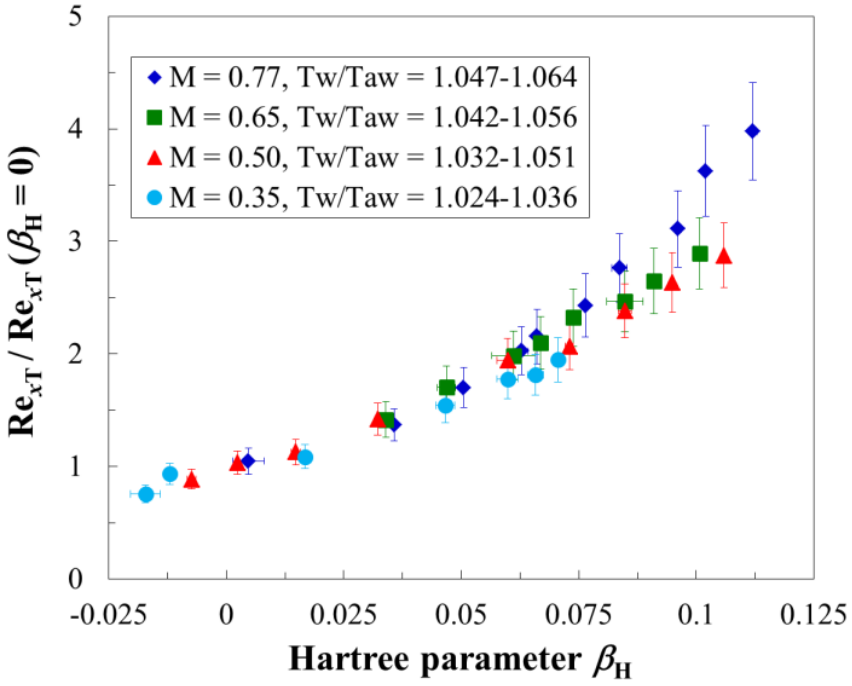

Fig. E.3.9. Relative variation of the transition Reynolds number as a function of the Hartree parameter for different Mach numbers. Step-1 configuration.

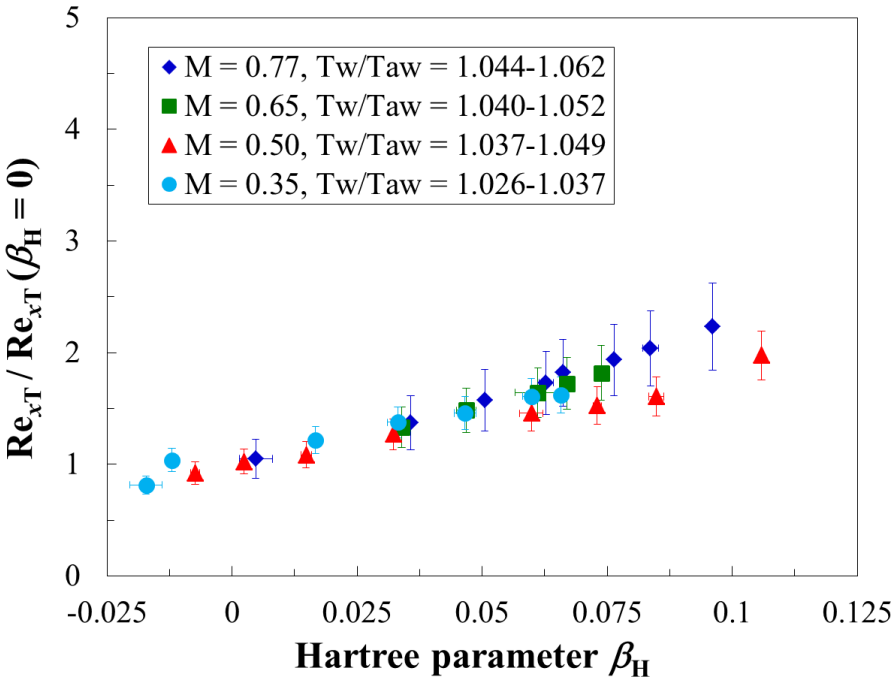

Fig. E.3.10. Relative variation of the transition Reynolds number as a function of the Hartree parameter for different Mach numbers. Step-3 configuration.

The relative change in transition location $s = (x_T\text{-}x_h)/(x_{T,0}\text{-}x_h)$ at M = 0.65 is presented as a function of relative step height $h/\delta_{1,h}$ and roughness Reynolds number Re_k in Fig. E.3.11 and Fig. E.3.12, respectively. For M = 0.5, s is plotted as a function of step Reynolds number Re_h and roughness Reynolds number Re_k in Fig. E.3.13 and Fig. E.3.14, respectively. These figures are supplements to Fig. 6.3.2 and Fig. 6.3.3. The solid lines shown in the figures are functions fitted to the experimental data: Gaussian functions in Fig. E.3.11 and Fig. E.3.13, 4th order polynomial functions in Fig. E.3.12 and Fig. E.3.14.

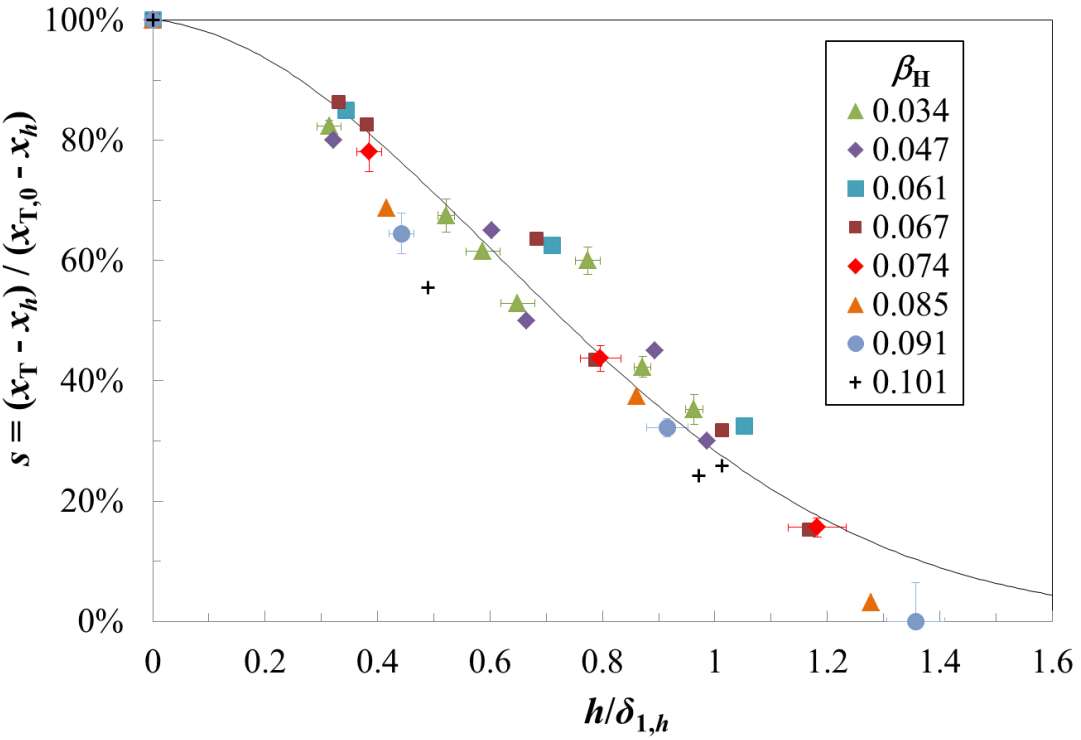

Fig. E.3.11. Relative change in transition location as a function of the relative step height at M = 0.65 and T_w/T_{aw} = 1.037-1.057.

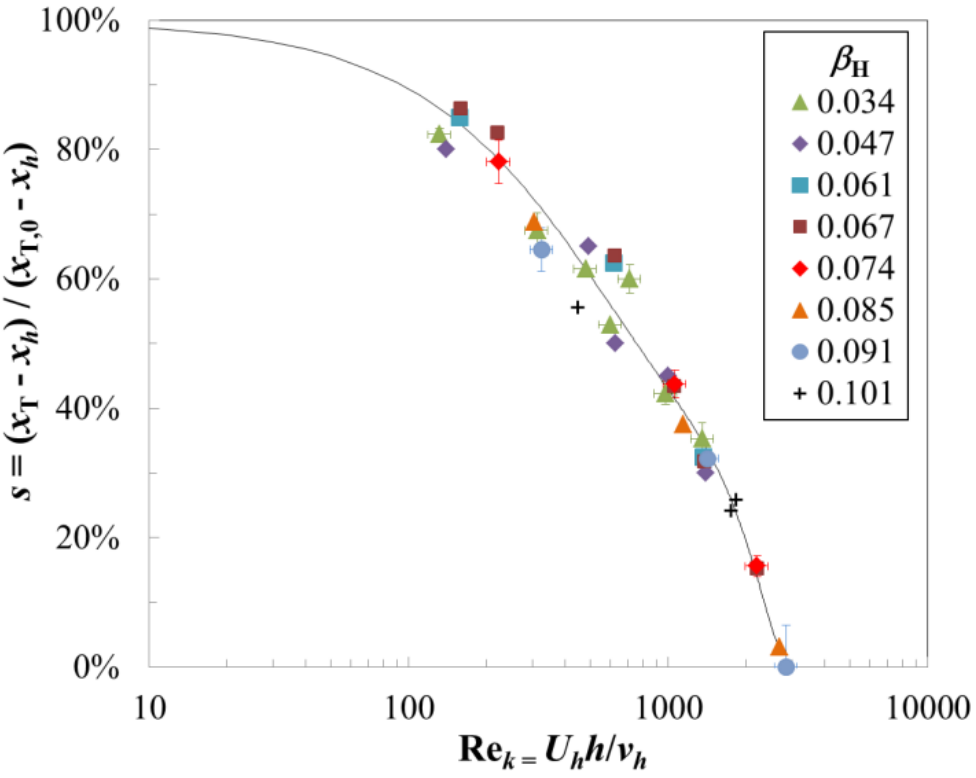

Fig. E.3.12. Relative change in transition location as a function of the roughness Reynolds number at M = 0.65 and T_w/T_{aw} = 1.037-1.057.

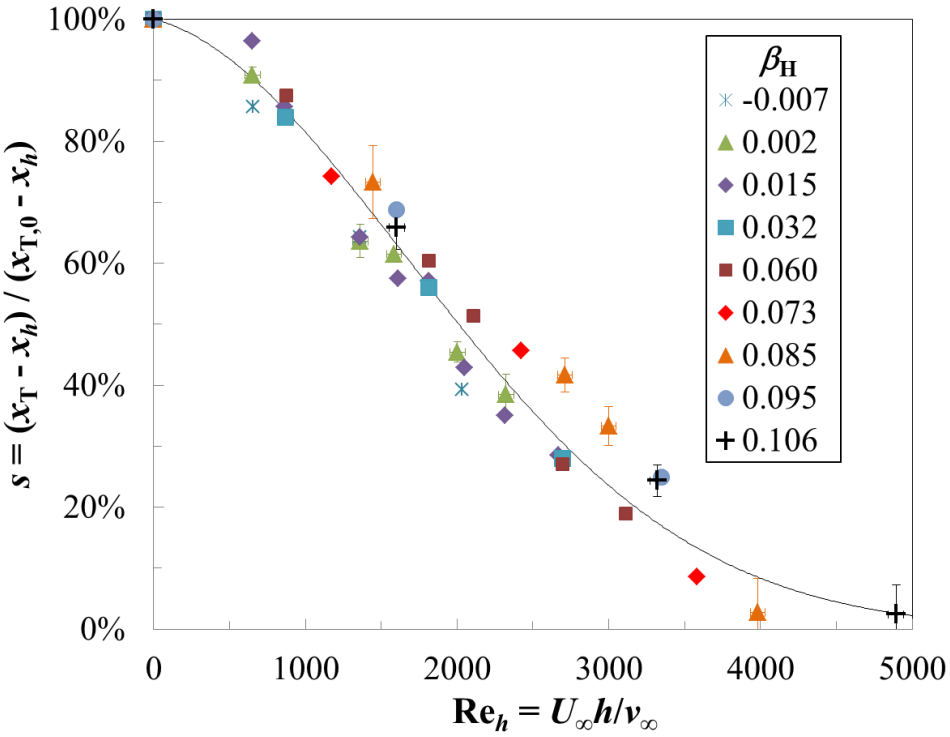

Fig. E.3.13. Relative change in transition location as a function of the step Reynolds number at M = 0.5 and T_w/T_{aw} = 1.032-1.051.

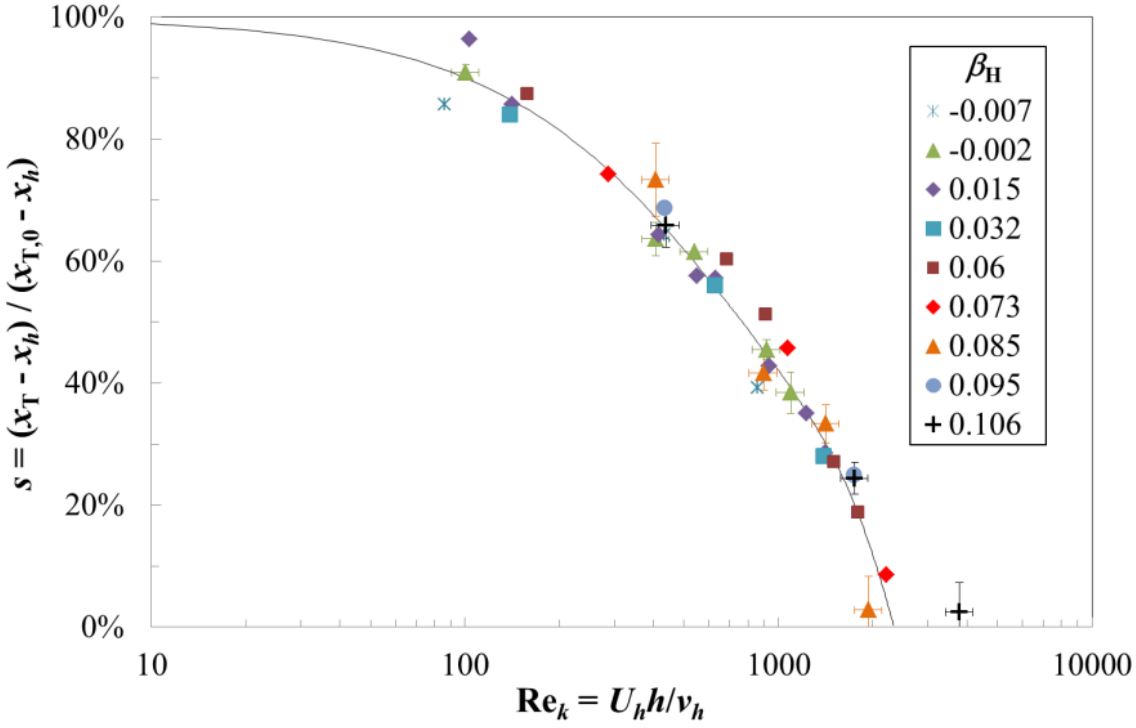

Fig. E.3.14. Relative change in transition location as a function of the roughness Reynolds number at M = 0.5 and T_w/T_{aw} = 1.032-1.051.

E.3.1 Sensitivity of boundary-layer transition to the effect of forward-facing steps at different Mach numbers

Results obtained at the same Reynolds number $\mathrm{Re} = 6 \cdot 10^6$ and approximately the same Hartree parameter (in the range $0.032 \leq \beta_H \leq 0.036$) are considered in this section. The investigations were conducted at standard wall temperature ratio, which however decreases at lower Mach numbers. Note also that the relative step height increases slightly as the Mach number is reduced. The TSP results for the smooth and step-2 configurations have been presented in Fig. 5.1.1.2 and Fig. 5.2.5.1, respectively. The variation of the ratio of transition Reynolds numbers $\mathrm{Re}_{xT}/\mathrm{Re}_{xT,0}$ is shown in Fig. E.3.1.1 as a function of the relative step height. The dashed lines are 2nd order polynomial functions fitted to the data sets at different Mach numbers. Larger reductions in $\mathrm{Re}_{xT}/\mathrm{Re}_{xT,0}$ are found at smaller values of the Mach number, showing a larger sensitivity of boundary-layer transition to the effect of the steps.

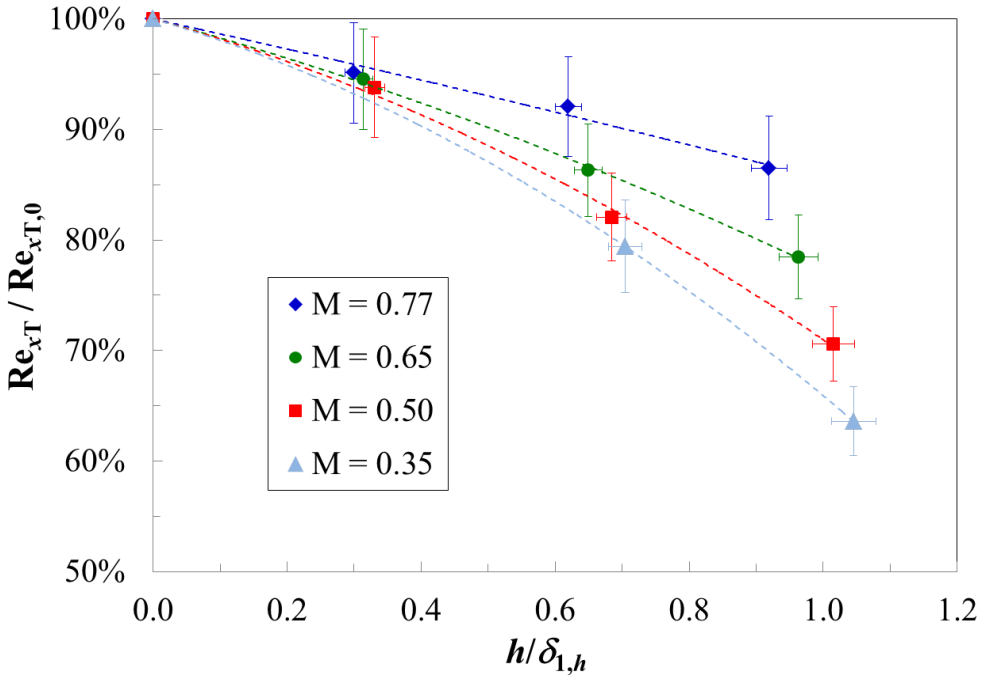

Fig. E.3.1.1. Variation of the ratio $\mathrm{Re}_{xT}/\mathrm{Re}_{xT,0}$ as a function of the relative step height for different Mach numbers at $\mathrm{Re} = 6 \cdot 10^6$, $0.032 \leq \beta_H \leq 0.036$, and standard T_w/T_{aw}.

This change in sensitivity can be illustrated (semi-quantitatively) with the help of linear stability theory, as has been done in Section 6.2.1 for the change in sensitivity due to the streamwise pressure gradient. The amplification factors for the smooth configuration were shown in Fig. 5.1.1.4; those at M = 0.77 and 0.35 are shown again in Fig. E.3.1.2, with the addition of the red dashed curves showing the step-induced modification of the *N*-factor envelope curve (obtained following the procedure described in Section 6.2.1). The value of ΔN is larger for the lower Mach number, according to the results from DNS in [45]. This plays, however, a minor role in the present discussion. Values of ΔN determined from the present experimental data at different Mach numbers have been discussed in

Section 6.4.2. At M = 0.77, transition occurs on a region where $\partial N_{T,0}/\partial(x/c) > 0$, whereas $\partial N_{T,0}/\partial(x/c) \sim 0$ at M = 0.35. For the latter stability situation at the lower Mach number, boundary-layer transition is expected to be more sensitive to the effect of the step than at M = 0.77. This is consistent with the present experimental observations.

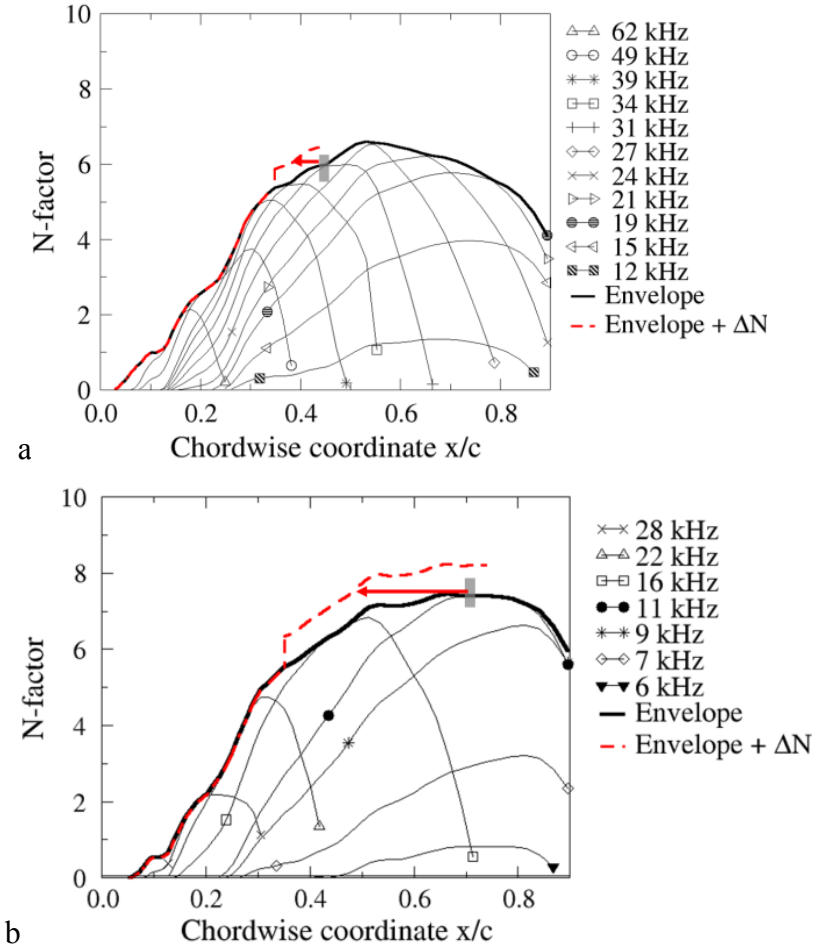

Fig. E.3.1.2. Stability analysis results for the smooth configuration (black lines) and *N*-factor envelope curves accounting for the step-induced disturbance (red dashed curves). The red arrow shows the transition movement due to the step disturbance, predicted semi-quantitatively – see text. a: M = 0.77, Re = 6 · 10^6, β_H = 0.036, T_w/T_{aw} = 1.054; b: M = 0.35, Re = 6 · 10^6, β_H = 0.033, T_w/T_{aw} = 1.025.

The effect of the step on boundary-layer transition can be "isolated" also in this case. The relative change in transition location $s = (x_T\text{-}x_h)/(x_{T,0}\text{-}x_h)$ is plotted in Fig. E.3.1.3 as a function of $h/\delta_{1,h}$ for the cases of Fig. E.3.1.1. This representation of the results provides, again, a good correlation, which is nearly independent of the Mach number (and of the initial amplitude of the boundary-layer disturbances). Note that this result is not inconsistent with the damping effect of compressibility on the step-induced increment $\Delta N(x)$ discussed above, since the amplification factors for the smooth configuration are also reduced at larger Mach numbers (see Section 5.1.1). Thus, at a larger Mach number, a smaller $\Delta N(x)$ is applied to an envelope curve with smaller values of N: this is

expected to induce a relative change in transition location comparable to that at a lower Mach number, in line with the present experimental observations.

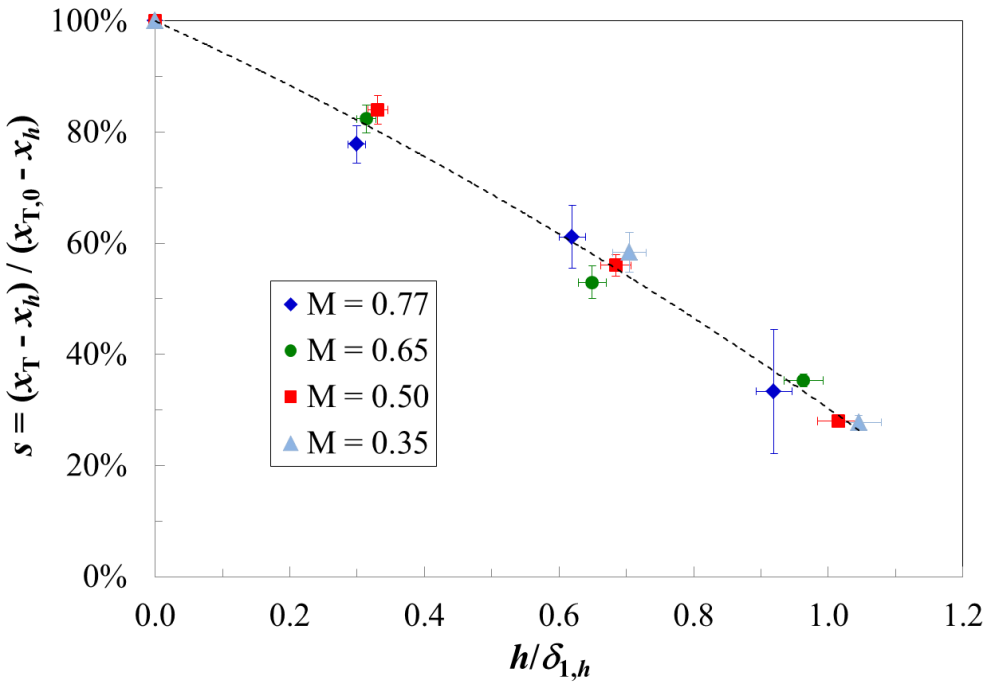

Fig. E.3.1.3. Relative variation of transition location as a function of the relative step height for different Mach numbers at Re = 6 · 10^6, 0.032 ≤ β_H ≤ 0.036, and standard T_w/T_{aw}. Dashed line: 2nd order polynomial fit to all data points.

E.4 Alternative correlation of the experimental data with results from linear stability computations

Under the same assumptions discussed in Section 6.4.2, only the amplification of streamwise instabilities occurring at and downstream of the step has to be accounted for in the correlation, since the growth of disturbances upstream of the step is unaffected by the presence of the step. (This is reasonable only for a certain distance upstream of the step location [38,45-46].) The amplification factor at the step location N_h is thus introduced into the correlation and is used to build a new parameter: $s_N = (N_T\text{-}N_h)/(N_{T,0}\text{-}N_h)$. This parameter is plotted in Fig. E.4.1 as s_N vs. $h/\delta_{1,h}$. The principle is similar to that considered in Chapter 6 and in the previous sections for the relative change in transition location $s = (x_T\text{-}x_h)/(x_{T,0}\text{-}x_h)$. The representation of the results as s_N vs. $h/\delta_{1,h}$ provides a reasonable correlation of most of the data at M = 0.65 and 0.35 (Fig. E.4.1b and Fig. E.4.1d, respectively) and only a fair correlation at the other Mach numbers. Second order polynomial functions, fitted to the data, are shown in the plots as solid lines. The trends are similar for all considered Mach numbers. The approximation functions can be used as an alternative to the ΔN functions presented in Section 6.4.2 for transition prediction in the presence of forward-facing steps within the framework of the e^N method.

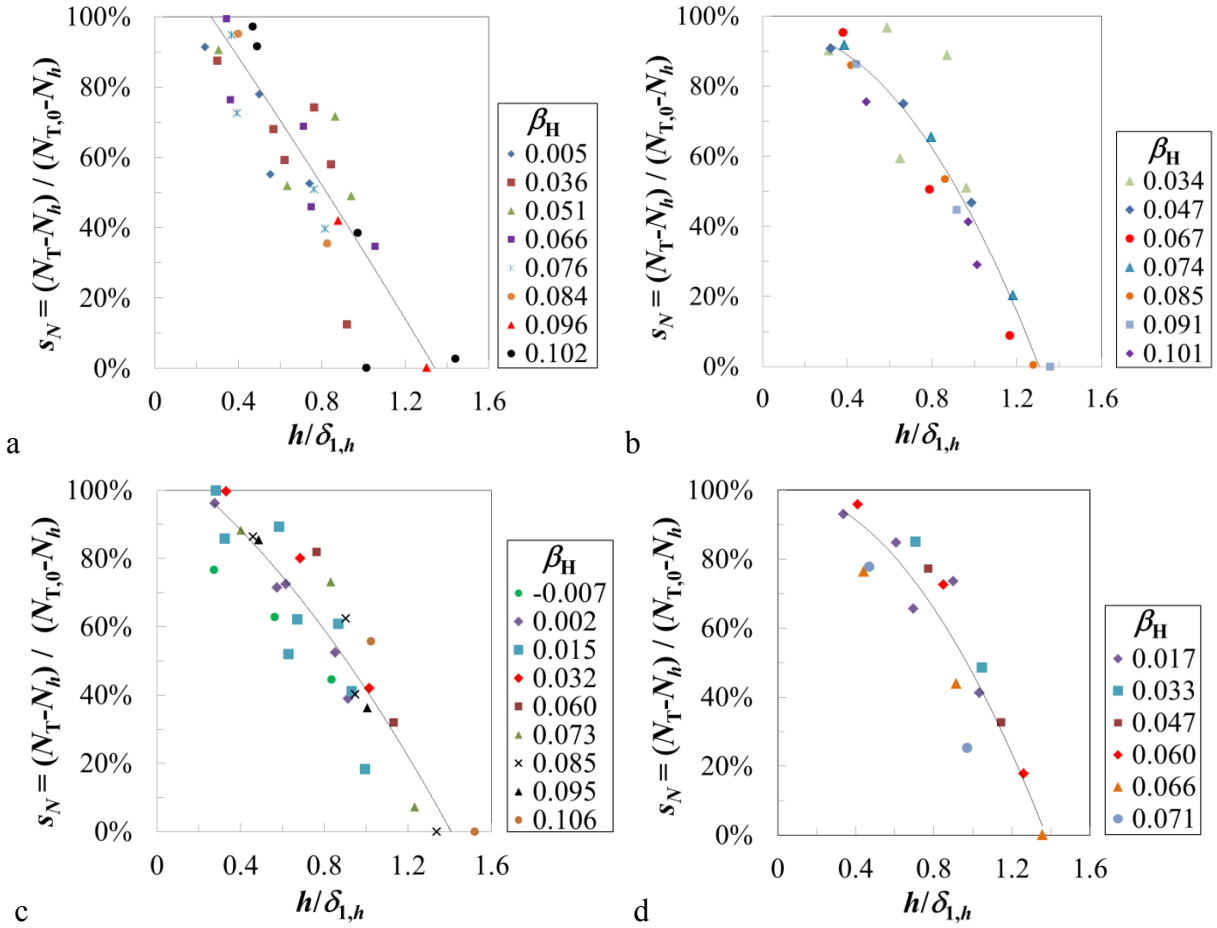

Fig. E.4.1. Relative variation of the transition *N*-factor as a function of the relative step height for different Mach numbers. a: M = 0.77, T_w/T_{aw} = 1.043-1.064; b: M = 0.65, T_w/T_{aw} = 1.037-1.057; c: M = 0.5, T_w/T_{aw} = 1.032-1.051; d: M = 0.35, T_w/T_{aw} = 1.022-1.037. Solid lines: fitted functions.

E.5 Combined effect of forward-facing steps and wall temperature ratio at M = 0.65 and 0.5

In Fig. E.5.1 and Fig. E.5.2, the transition Reynolds number is plotted as a function of the Hartree parameter for the Mach numbers M = 0.65 and 0.5, respectively.

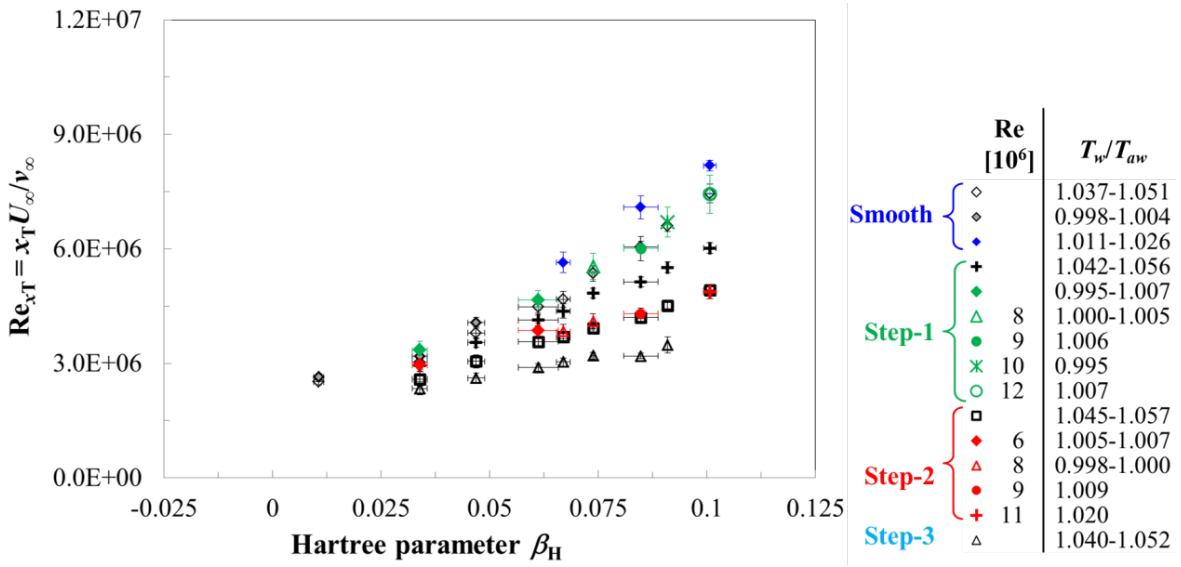

Fig. E.5.1. Transition Reynolds number as a function of the Hartree parameter at M = 0.65.

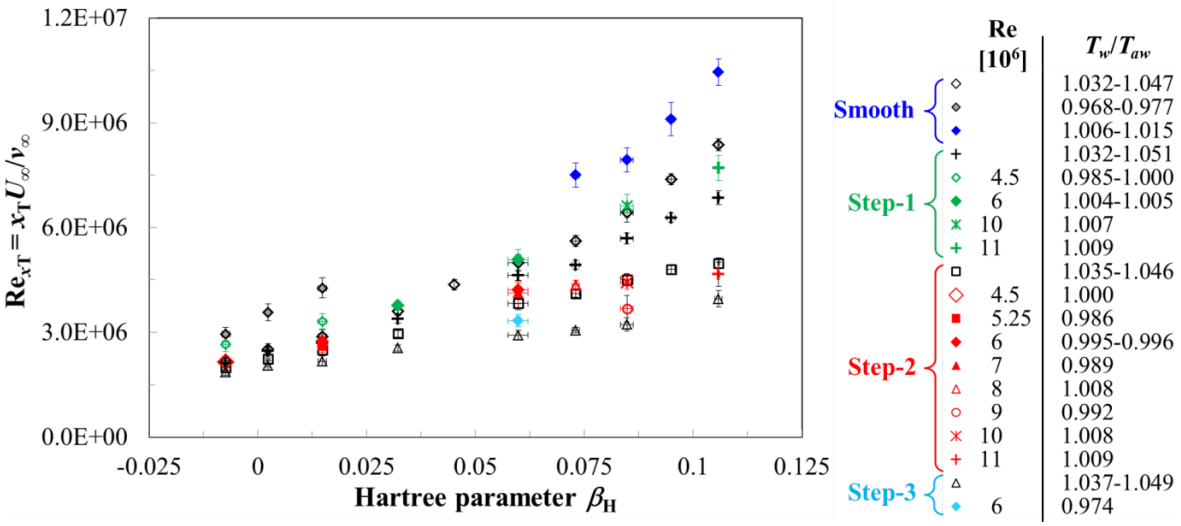

Fig. E.5.2. Transition Reynolds number as a function of the Hartree parameter at M = 0.5.

The variation in transition Reynolds number $Re_{xT}/Re_{xT,aw}$ for the step-1 configuration is plotted as a function of T_w/T_{aw} for M = 0.65 and 0.5 in Fig. E.5.3 and Fig. E.5.4. At M = 0.65, the results obtained with the step-1 configuration show a sensitivity of the transition Reynolds number to changes in wall temperature ratio comparable to that of the smooth configuration (see Fig.

D.8.1). The data points are well fitted by the same approximation function $Re_{xT}/Re_{xT,aw} = (T_w/T_{aw})^{-3.5}$. At M = 0.5, the function $Re_{xT}/Re_{xT,aw} = (T_w/T_{aw})^{-4}$, already used in Fig. D.8.2 to approximate the results for the smooth configuration at M = 0.77, gives a good fit to the experimental data.

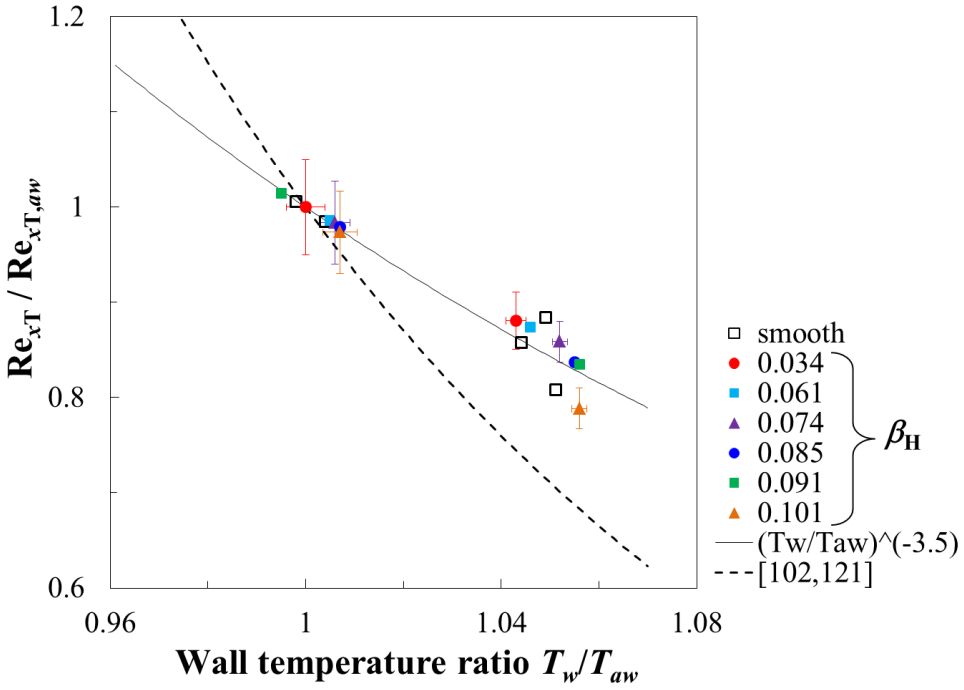

Fig. E.5.3. Relative variation of transition Reynolds number as a function of the wall temperature ratio with the step-1 configuration: M = 0.65.

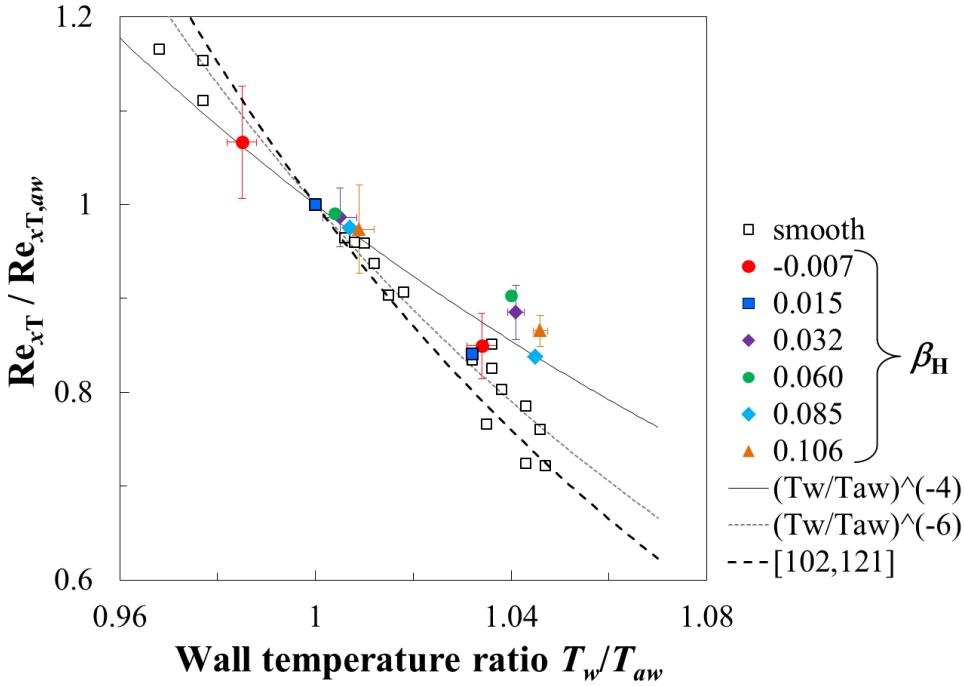

Fig. E.5.4. Relative variation of transition Reynolds number as a function of the wall temperature ratio with the step-1 configuration: M = 0.5.

The variation in transition Reynolds number $Re_{xT}/Re_{xT,aw}$ for the step-2 and step-3 configurations is plotted as a function of T_w/T_{aw} in Fig. E.5.5 (for M = 0.65) and Fig. E.5.6 (for M = 0.5).

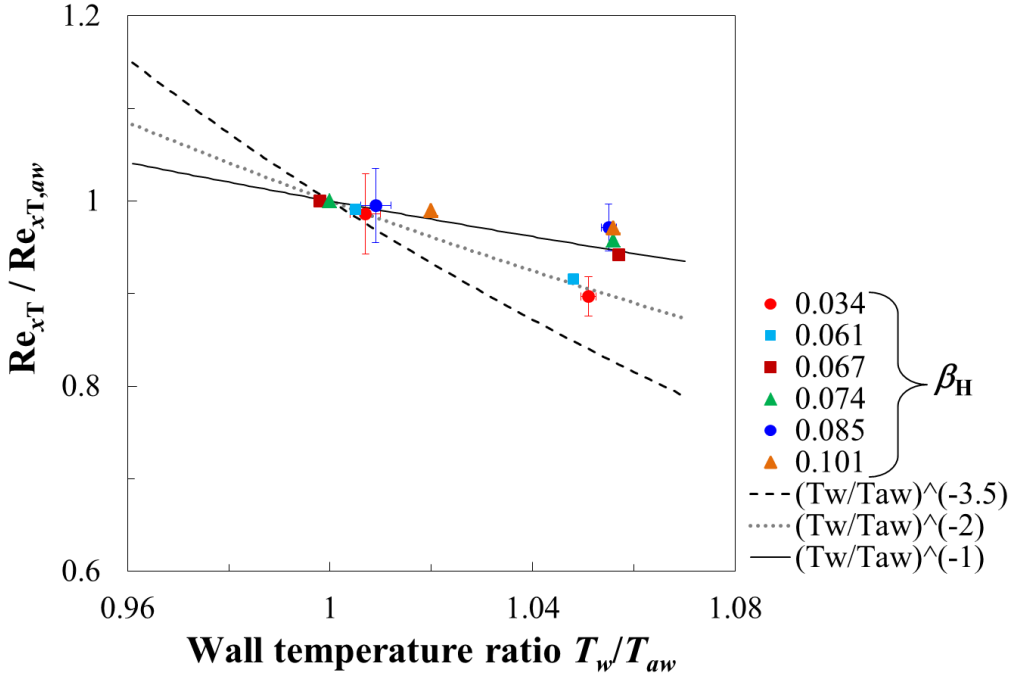

Fig. E.5.5. Relative variation of transition Reynolds number as a function of the wall temperature ratio at M = 0.65. Step-2 configuration.

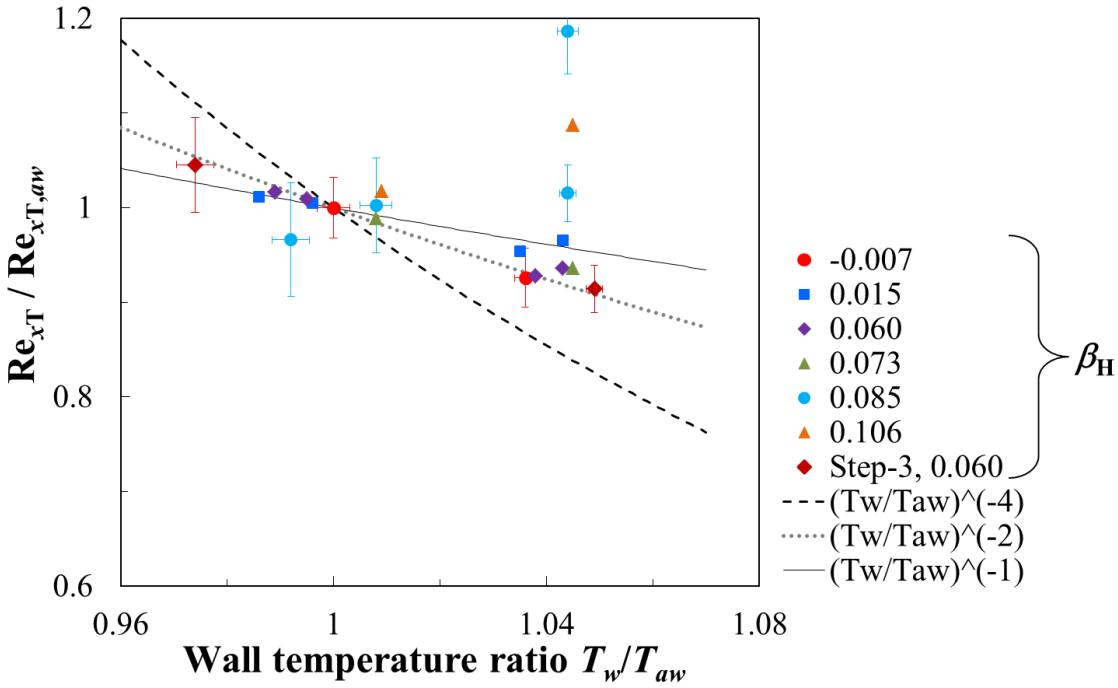

Fig. E.5.6. Relative variation of transition Reynolds number as a function of the wall temperature ratio at M = 0.5. Step-2 and step-3 configurations.

Two groups of data can be identified in these plots: a first group of data shows a variation of $Re_{xT}/Re_{xT,aw}$ with changing wall temperature ratio which can be fitted by the function $Re_{xT}/Re_{xT,aw} = (T_w/T_{aw})^{-2}$ (dotted lines in Fig. E.5.5 and Fig. E.5.6), whereas a second group of data is better fitted by the function $Re_{xT}/Re_{xT,aw} = (T_w/T_{aw})^{-1}$ (solid lines in Fig. E.5.5 and Fig. E.5.6). Furthermore, in a couple of cases at M = 0.5, Re_{xT} became even lower with decreased T_w/T_{aw} (see Fig. E.5.6). This can be seen also in Fig. E.5.2: the two cases are with the step-2 configuration at $\beta_H = 0.085$ ($Re = 9 \cdot 10^6$) and $\beta_H = 0.106$ ($Re = 10 \cdot 10^6$). It seems plausible that this reduction of Re_{xT} was due to the enhanced amplification of streamwise instabilities in the separated flow regions around the step at smaller T_w/T_{aw} (see Section 6.5.3), which led the disturbances to reach the threshold amplitude further upstream than at larger T_w/T_{aw}, and thus induced the observed movement of transition.

The change in transition location $s = (x_T\text{-}x_h)/(x_{T,0}\text{-}x_h)$ is plotted as a function of Re_h and $h/\delta_{1,h}$ in Fig. E.5.7 (for M = 0.65) and Fig. E.5.8 (for M = 0.5). These plots are analogous to those shown in Figs. 6.5.3.1 and 6.5.3.4 for the Mach numbers M = 0.77 and 0.35. The results obtained at standard wall temperature ratio are shown by red symbols, with the corresponding fitted functions being shown by red lines (see Fig. 6.3.2, Fig. E.3.11, Fig. E.3.13, and Fig. 6.3.3). The results obtained at reduced wall temperature ratio are shown by blue symbols; they are fitted by 3rd order polynomial functions, which are shown by blue lines. A change in sensitivity of the transition location to variations in T_w/T_{aw} is observed at $Re_h \sim 2700$ and $h/\delta_{1,h} \sim 0.8\text{-}0.9$, similar to that discussed in Section 6.5.3 for the Mach numbers M = 0.77 and 0.35. In the case of the data points at M = 0.5, $\beta_H = 0.06$, and $h/\delta_{1,h} = 1.05$ (open squares in Fig. E.5.8b), the laminar boundary layer at standard T_w/T_{aw} lasted over the recovery zone without undergoing transition, so that a reduction in wall temperature ratio still induced a movement of transition into a more downstream location (see Section 6.5.3). Two data points at M = 0.5 and reduced T_w/T_{aw} are below the fitted curves cases for standard T_w/T_{aw} in Fig. E.5.8a/b (blue open triangle and blue cross at $2700 \le Re_h < 3400$ and $0.9 \le h/\delta_{1,h} < 1.05$): they correspond to the data points at $\beta_H = 0.085$ ($Re = 9 \cdot 10^6$) and $\beta_H = 0.106$ ($Re = 10 \cdot 10^6$) discussed above with regard to Fig. E.5.6, for which Re_{xT} became even lower with decreased T_w/T_{aw}.

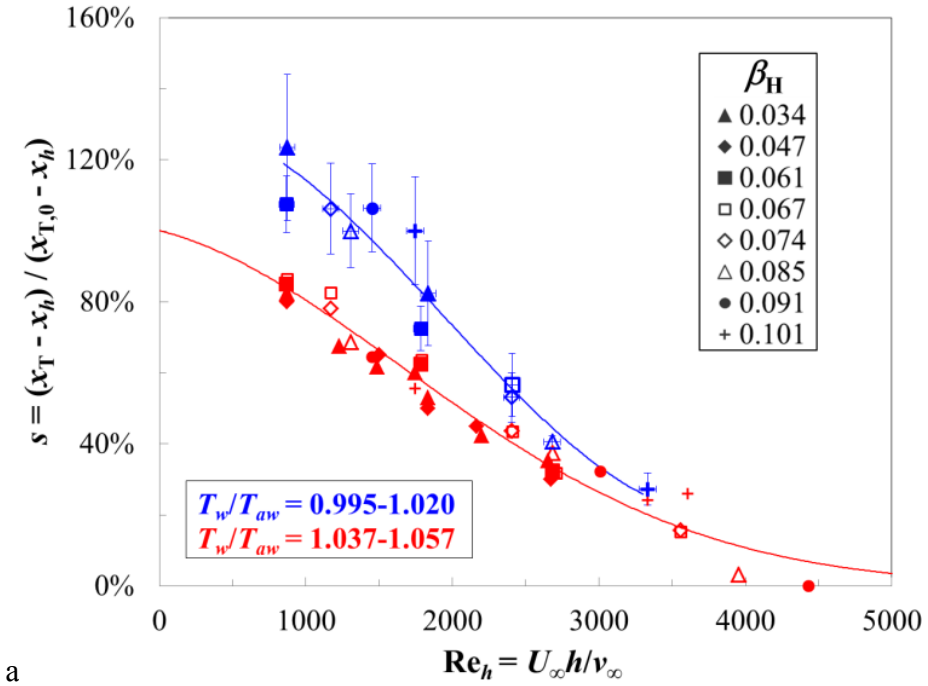

a

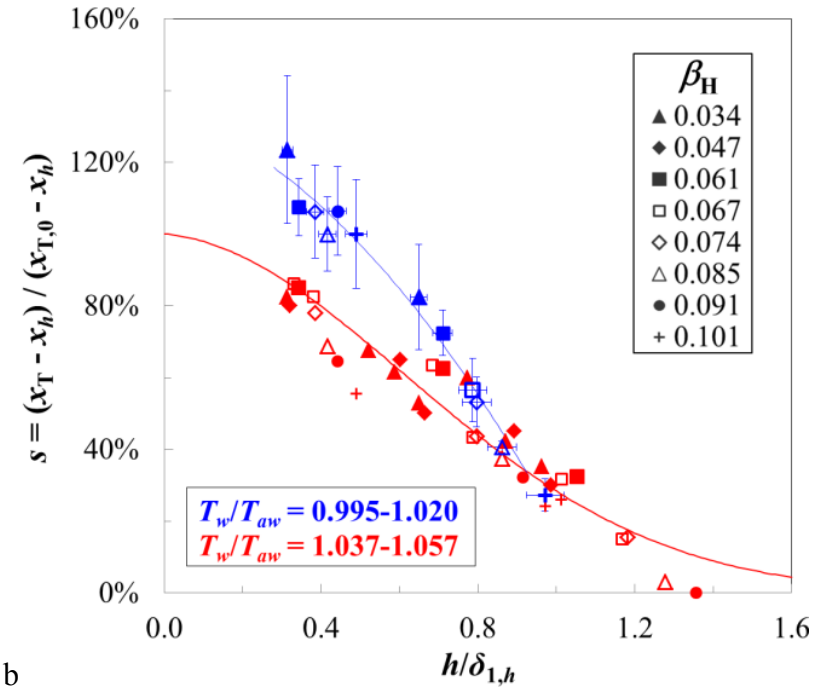

b

Fig. E.5.7. Relative change in transition location at M = 0.65 as a function of the step Reynolds number (a) and of the relative step height (b).

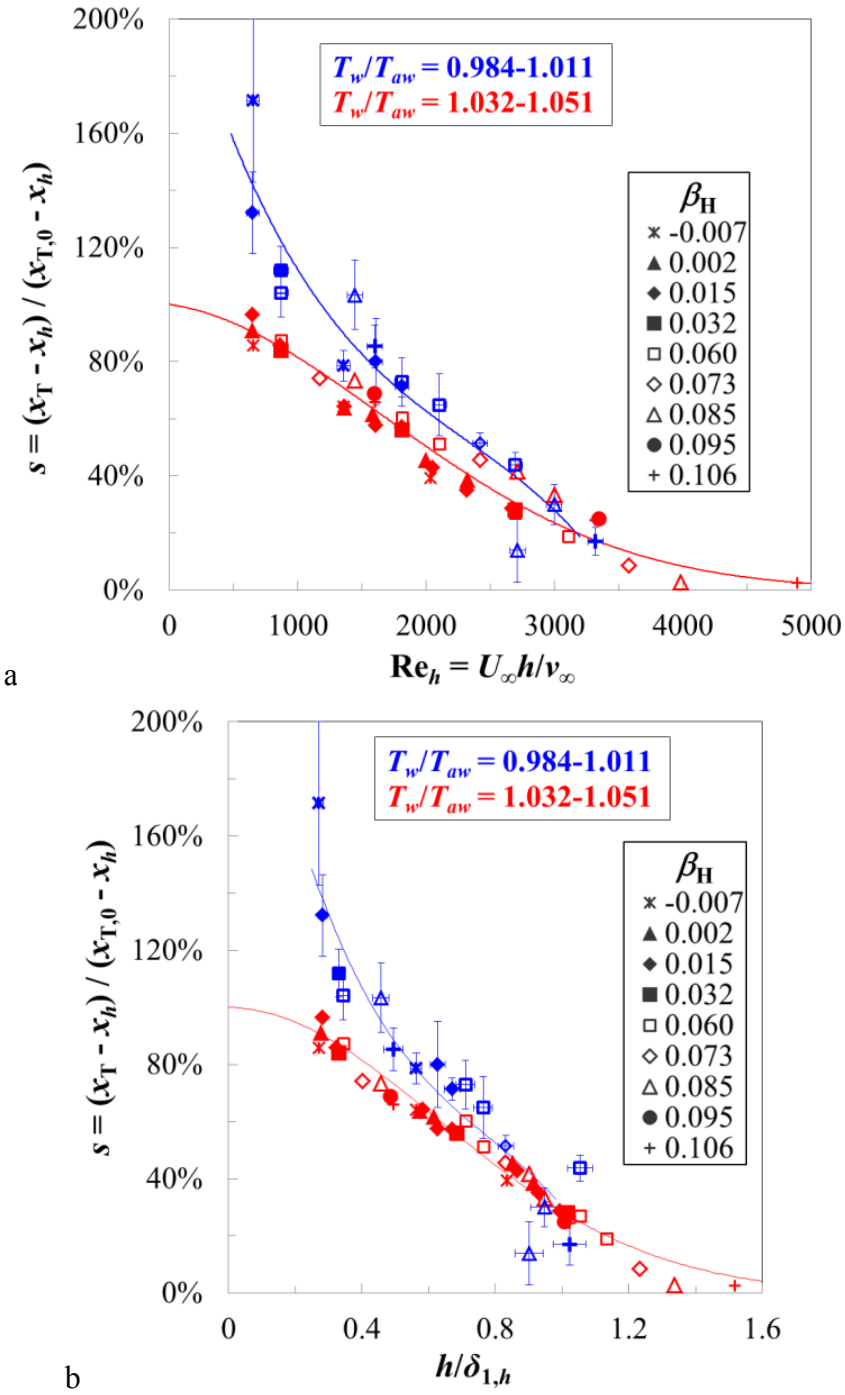

Fig. E.5.8. Relative change in transition location at M = 0.5 as a function of the step Reynolds number (a) and of the relative step height (b).

E.6 Example for the change in sensitivity of boundary-layer transition to variations in T_w/T_{aw}

The results obtained at M = 0.77 and $\beta_H = 0.096$ for different chord Reynolds numbers and wall temperature ratios are considered in this section. The TSP results at Re = $10 \cdot 10^6$ have already been shown in Fig. 5.2.4.4; just the results at Re = 8 and $9 \cdot 10^6$ are now presented in Fig. E.6.1 and Fig. E.6.2, respectively. As can be seen in Fig. E.6.1, a decrease in wall temperature ratio from

$T_w/T_{aw} = 1.052$ to 1.009 at $\mathrm{Re} = 8 \cdot 10^6$ led to a movement of the transition location from $x_T/c = 58 \pm 1$ % to 63 ±3 %. In contrast, at $\mathrm{Re} = 9 \cdot 10^6$, the change in the transition location due to a variation in T_w/T_{aw}, if any, is very small. As T_w/T_{aw} was decreased from $T_w/T_{aw} = 1.060$ to 1.013, an increase of 1 % in x_T/c had been determined using the transition detection algorithm (see Section 4.2): this is within the measurement uncertainty for the latter case, which is $\Delta(x_T/c) = \pm 2.2$ %. An important difference between the three cases is the step Reynolds number, which increased from approximately $\mathrm{Re}_h = 2400$ to 3000 as the chord Reynolds number was increased from $\mathrm{Re} = 8$ to $10 \cdot 10^6$. Similarly, the relative step height increased from $h/\delta_{1,h} = 0.78$ to 0.88.

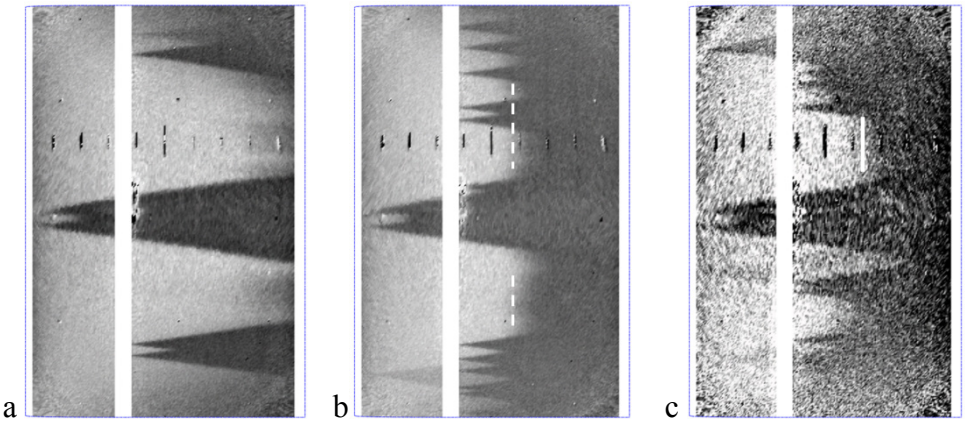

Fig. E.6.1. TSP results at M = 0.77, Re = $8 \cdot 10^6$, and $\beta_H = 0.096$. a: $h/\delta_{1,h} \sim 0$, $T_w/T_{aw} = 1.055$, no transition; b: $h/\delta_{1,h} = 0.78$, $T_w/T_{aw} = 1.052$, $x_T/c = 58 \pm 1.1$ %; c: $T_w/T_{aw} = 1.009$, $h/\delta_{1,h} = 0.81$, $x_T/c = 63 \pm 3$ %.

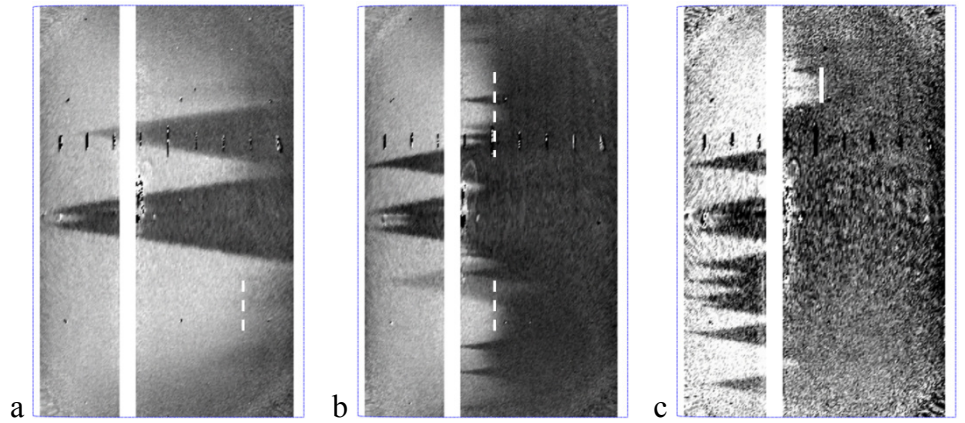

Fig. E.6.2. TSP results at M = 0.77, Re = $9 \cdot 10^6$, and $\beta_H = 0.096$. a: $h/\delta_{1,h} \sim 0$, $T_w/T_{aw} = 1.055$, $x_T/c = 78 \pm 2.2$ %; b: $h/\delta_{1,h} = 0.81$, $T_w/T_{aw} = 1.060$, $x_T/c = 51 \pm 0.6$ %; c: $T_w/T_{aw} = 1.013$, $h/\delta_{1,h} = 0.84$, $x_T/c = 52 \pm 2.2$ %.

E.7 Conditions under which boundary-layer transition was sensitive to changes in the wall temperature ratio at M = 0.35 and 0.77

The transition location x_T/c measured in the presence of forward-facing steps for all the cases at M = 0.35 is plotted as a function of $h/\delta_{1,h}$ in Fig. E.7.1. The symbols are assigned to the experimental data in the same manner as in Fig. 6.5.3.4b.

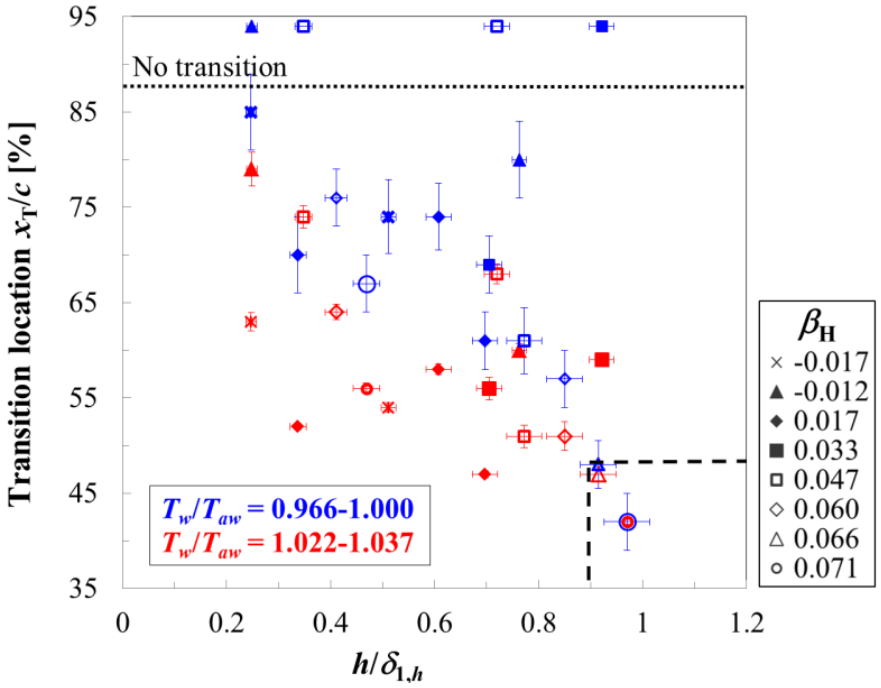

Fig. E.7.1. Variation of the transition location at M = 0.35 as a function of the relative step height.

Since the experimental results are represented in absolute values in Fig. E.7.1, the change in transition location clearly depends also on chord Reynolds number, streamwise pressure gradient, variation in T_w/T_{aw}, and transition location at standard T_w/T_{aw}. Nevertheless, this representation of the results is useful to show the conditions at which boundary-layer transition becomes insensitive to changes in the wall temperature ratio. The limiting region where a variation in wall temperature ratio has no appreciable effect on transition is shown in Fig. E.7.1 by the dashed lines. This should not be taken as indicating an abrupt change in the behavior of the boundary layer, but rather as a guide for the conditions under which the influence of the surface heat flux on boundary-layer transition in the presence of forward-facing steps has to be accounted for. The different behavior of boundary-layer transition for conditions inside and outside this "box" is related to the effects discussed in Section 6.5.3. In particular, the step-induced amplification of streamwise instabilities is large at approximately $h/\delta_{1,h} > 0.9$, and transition is likely to start in the region of adverse pressure gradient

downstream of the step location. In this case, boundary-layer transition is essentially insensitive to changes in the wall temperature ratio. However, transition can still be influenced by the wall temperature ratio if the the laminar boundary layer lasts over the recovery zone. (For example, when the chord Reynolds number is low, as in the case at $h/\delta_{1,h} = 0.92$ and $\beta_H = 0.033$ in Fig. E.7.1: the Reynolds number here is $Re = 4.75 \cdot 10^6$.)

The results at M = 0.77 are shown in Fig. E.7.2 in the same way as in Fig. E.7.1. The region in which boundary-layer transition was found to be insensitive to changes in T_w/T_{aw} is (ideally) delimited by the values $h/\delta_{1,h} = 0.8$ and $x_T/c = 52$ %. The effect of surface heat flux on boundary-layer transition at $h/\delta_{1,h} > 0.8$ and $x_T/c > 52$ % could not be investigated at M = 0.77 because of the constraints in the achievable variation of the parameters (discussed in Appendix D.3): $x_T/c > 52$ % was achieved at $h/\delta_{1,h} > 0.8$ with the step-3 configuration at $Re < 6 \cdot 10^6$, but the wall temperature ratio could not be varied. The limiting value for temperature effects on boundary-layer transition at M = 0.77 ($h/\delta_{1,h} \sim 0.8$) is lower than the corresponding value at M = 0.35 ($h/\delta_{1,h} \sim 0.9$). This may be due to a larger size of the step-induced separated flow regions and to the increase of the streamwise extent of the recovery zone at larger Mach numbers and fixed $h/\delta_{1,h}$. The limiting transition location at M = 0.77 ($x_T/c > 52$ %) is also larger than that at M = 0.35, probably for the same reasons. However, these values have to be considered as guidelines only.

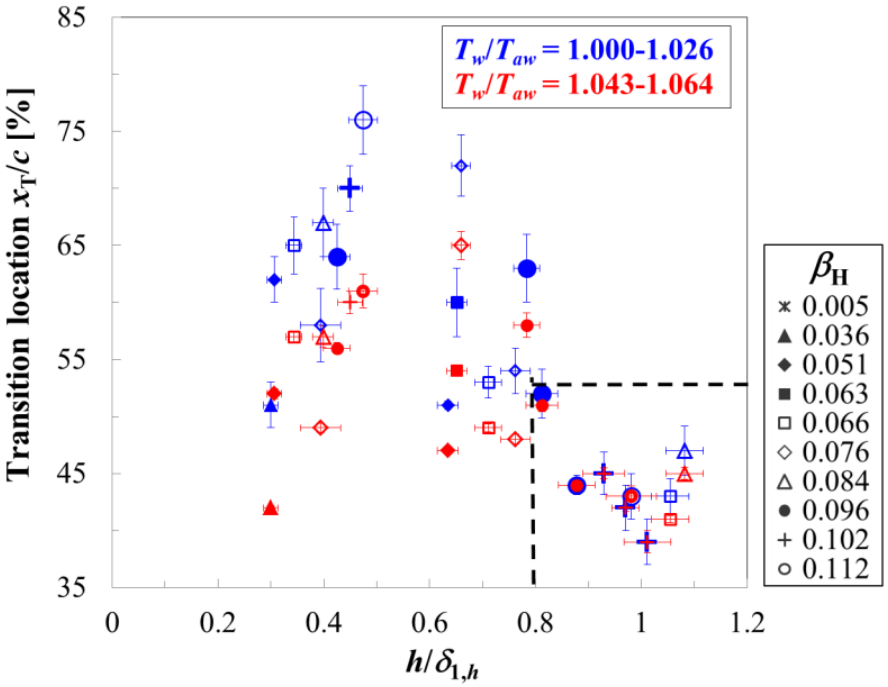

Fig. E.7.2. Variation of the transition location at M = 0.77 as a function of the relative step height.

E.8 Combined effect of forward-facing steps and wall temperature ratio with the roughness Reynolds number as non-dimensional step parameter

The change in transition location $s = (x_T\text{-}x_h)/(x_{T,0}\text{-}x_h)$ is plotted as a function of the roughness Reynolds number Re_k in Fig. E.8.1 to Fig. E.8.4 for the Mach numbers M = 0.77 to 0.35. These plots are analogous to those shown in Section 6.5.3 and in Appendix E.5, where Re_h and $h/\delta_{1,h}$ were used as non-dimensional step parameters. The results obtained at standard wall temperature ratio are shown by red symbols, with the corresponding fitted functions being shown by red lines (see Fig. 6.2.2.3, Fig. E.3.12, Fig. E.3.14, and Fig. 6.3.4). The results obtained at reduced wall temperature ratio are shown by blue symbols; they are fitted by 3rd order polynomial functions, which are shown by blue lines. At all four Mach numbers, a reduced wall temperature ratio had a favorable influence on boundary-layer transition up to $\mathrm{Re}_k \sim 1200$.

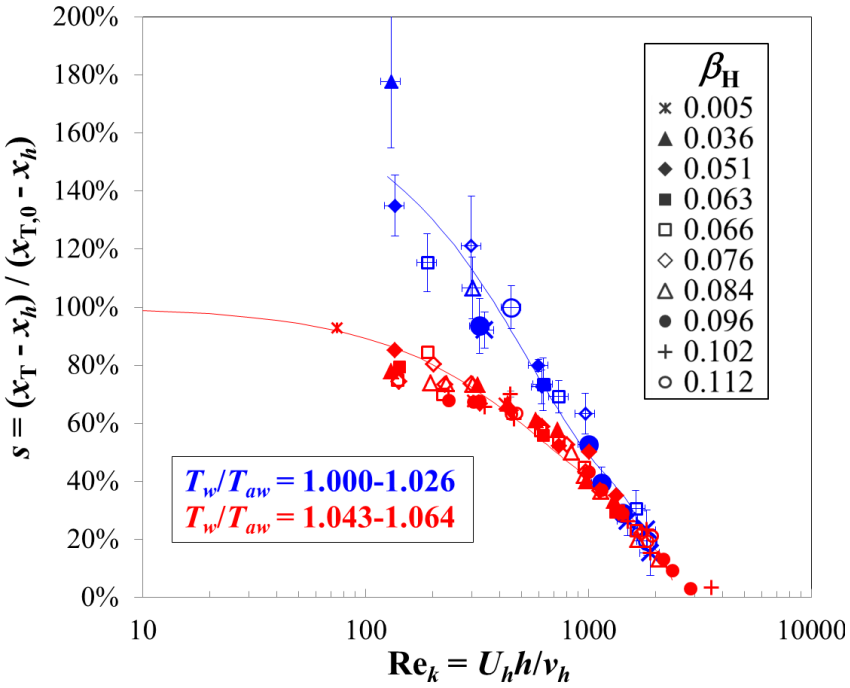

Fig. E.8.1. Relative change in transition location at M = 0.77 as a function of the roughness Reynolds number.

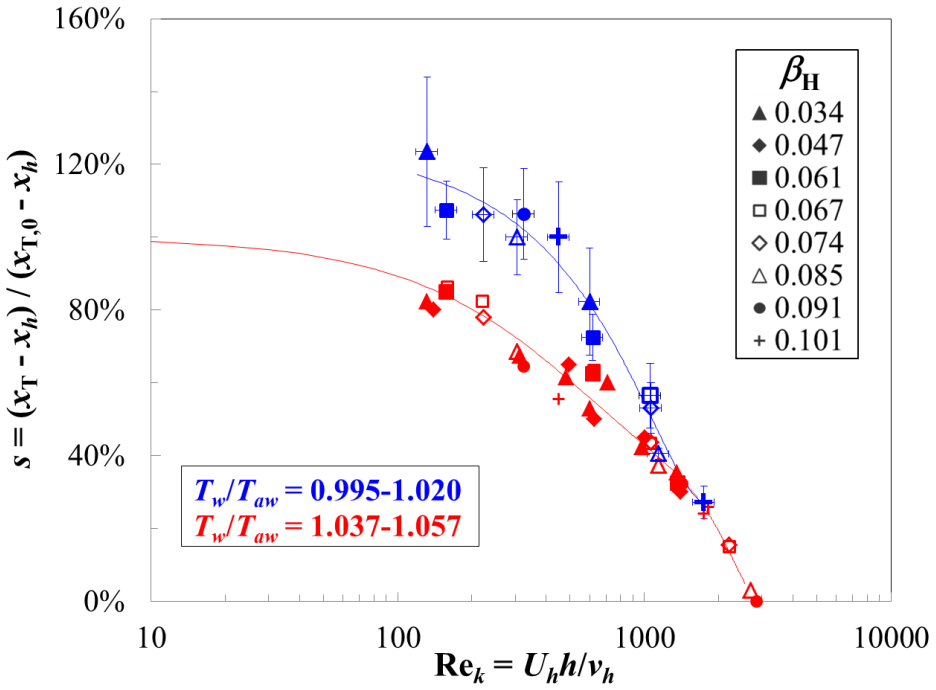

Fig. E.8.2. Relative change in transition location at M = 0.65 as a function of the roughness Reynolds number.

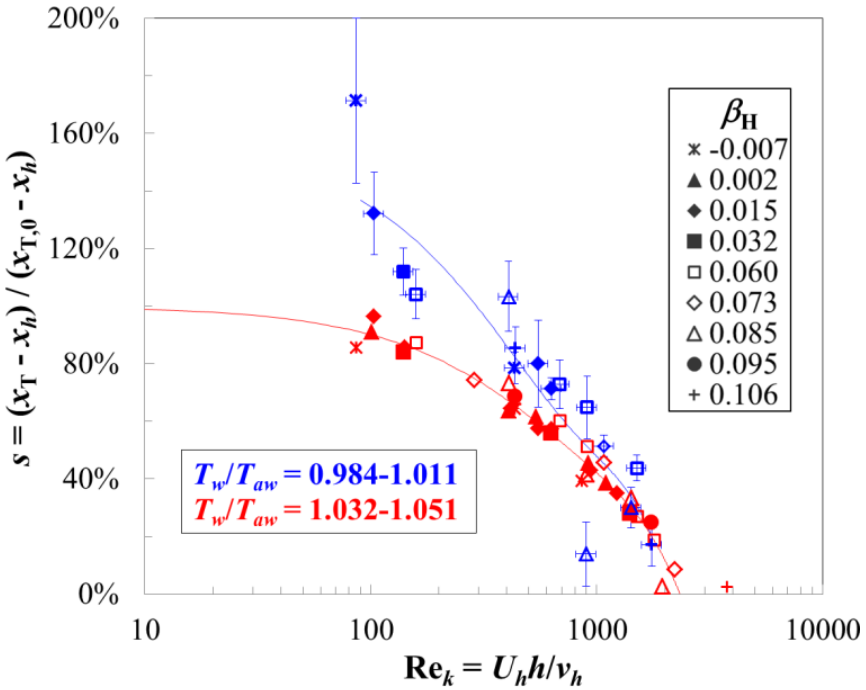

Fig. E.8.3. Relative change in transition location at M = 0.5 as a function of the roughness Reynolds number.

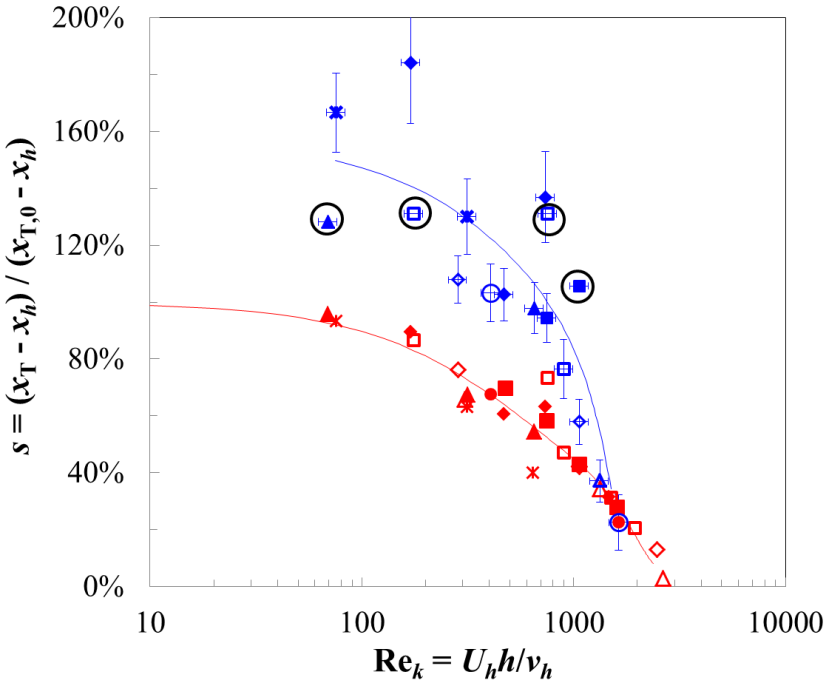

Fig. E.8.4. Relative change in transition location at M = 0.35 as a function of the roughness Reynolds number. The data points enclosed by black circles indicate lower limits for *s*, since the boundary layer remained laminar over the whole model upper surface.

E.9 Effect of forward-facing steps on boundary-layer transition at the same, reduced wall temperature ratio for M = 0.35, 0.5, and 0.65

The results obtained at M = 0.35, 0.5, and 0.65 are plotted as s vs. $h/\delta_{1,h}$ in Fig. E.9.1a, Fig. E.9.2a, and Fig. E.9.3a, where the values of $x_{T,0}$ and $h/\delta_{1,h}$ are those obtained at reduced T_w/T_{aw}. The number of experimental data present in these plots is markedly reduced as compared to that in Fig. 6.3.2 to Fig. 6.3.4, since the number of completed runs at reduced T_w/T_{aw} had been strongly limited by surface contamination (see Appendix C.2.1). Moreover, in some cases at reduced T_w/T_{aw} the boundary layer remained laminar on the whole upper surface of the model, so that these data were not used in this analysis. The functions fitted to the experimental data at standard T_w/T_{aw} (see Eq. (6.4.2)) are shown by solid lines in the figures.

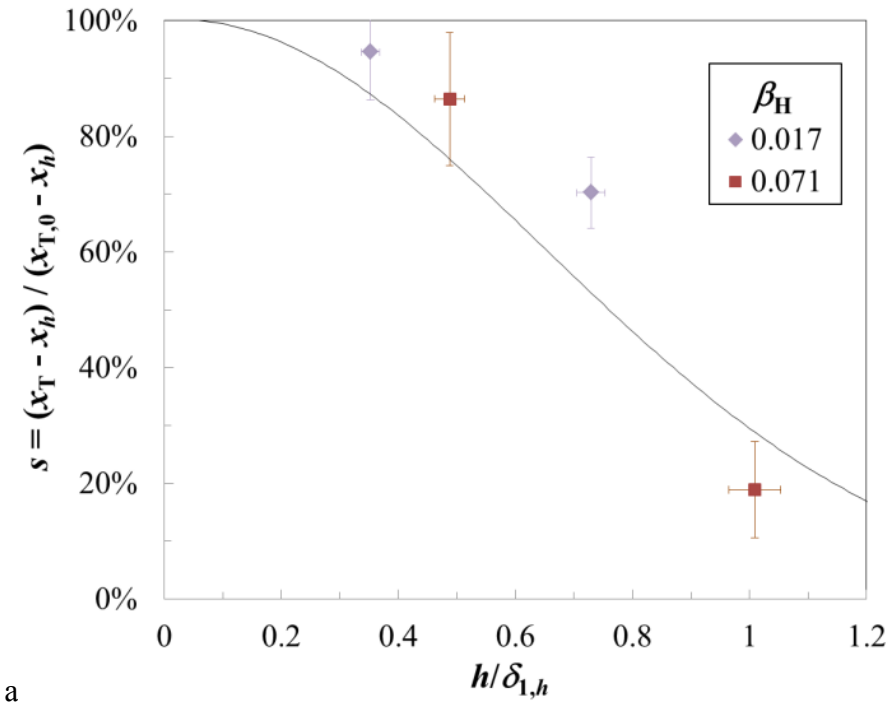

a

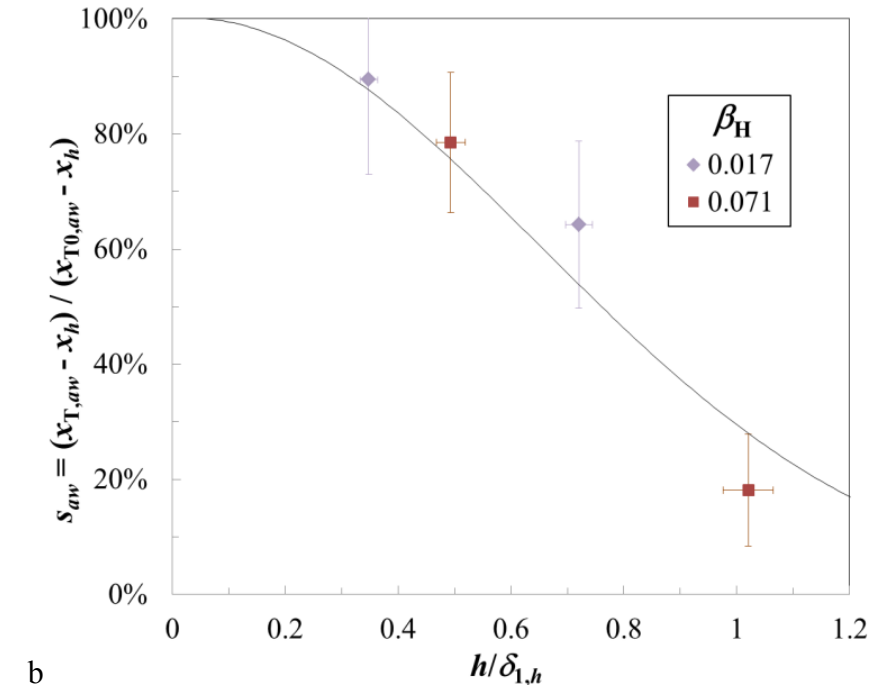

b

Fig. E.9.1. a: relative change in transition location as a function of the relative step height at M = 0.35 and T_w/T_{aw} = 0.983-1.007; the transition location $x_{T,0}$, obtained on the smooth configuration, was also measured at reduced T_w/T_{aw}. b: relative change of the adiabatic wall transition location as a function of the relative step height.

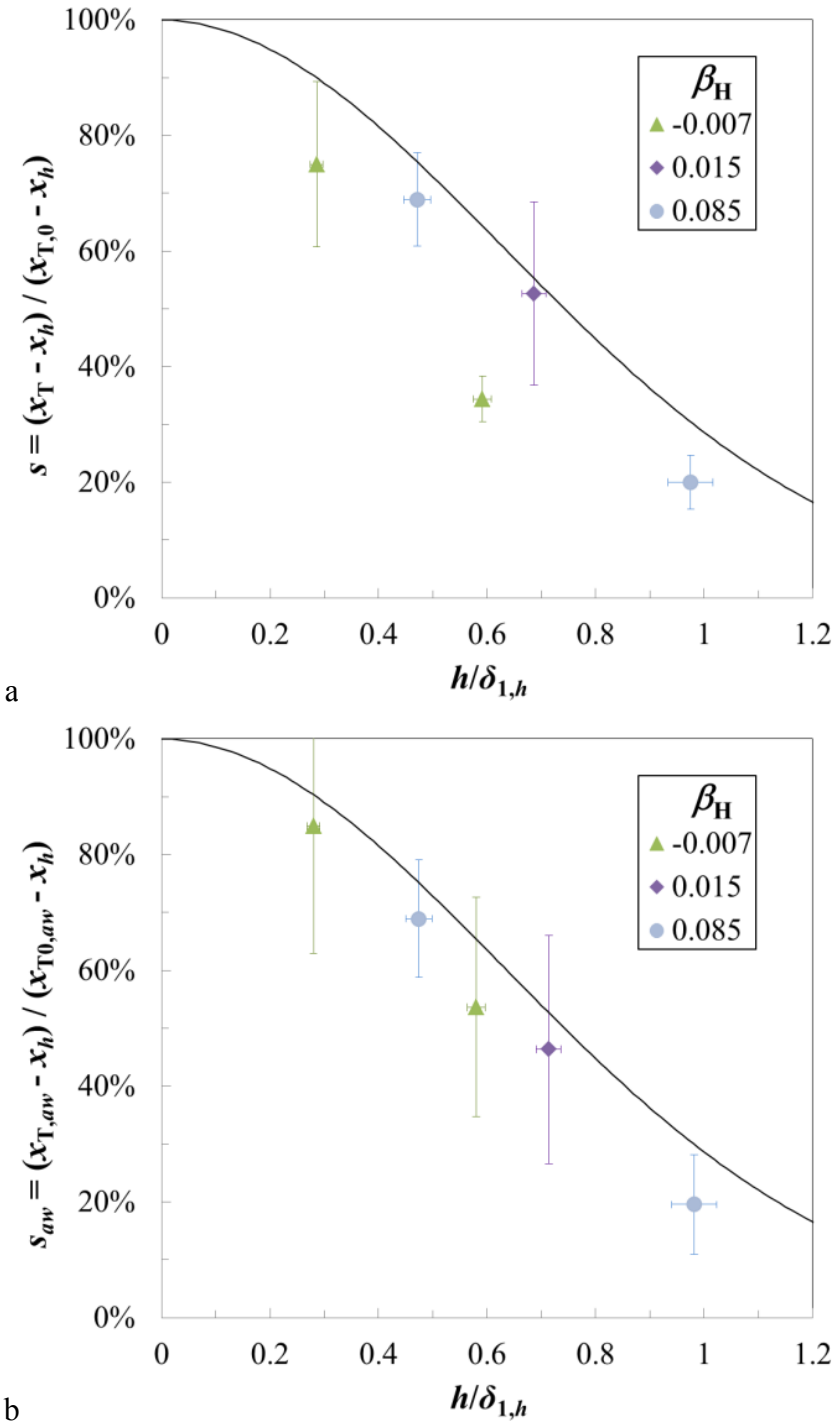

Fig. E.9.2. a: relative change in transition location as a function of the relative step height at M = 0.5 and T_w/T_{aw} = 0.977-1.010; the transition location $x_{T,0}$, obtained on the smooth configuration, was also measured at reduced T_w/T_{aw}. b: relative change of the adiabatic wall transition location as a function of the relative step height.

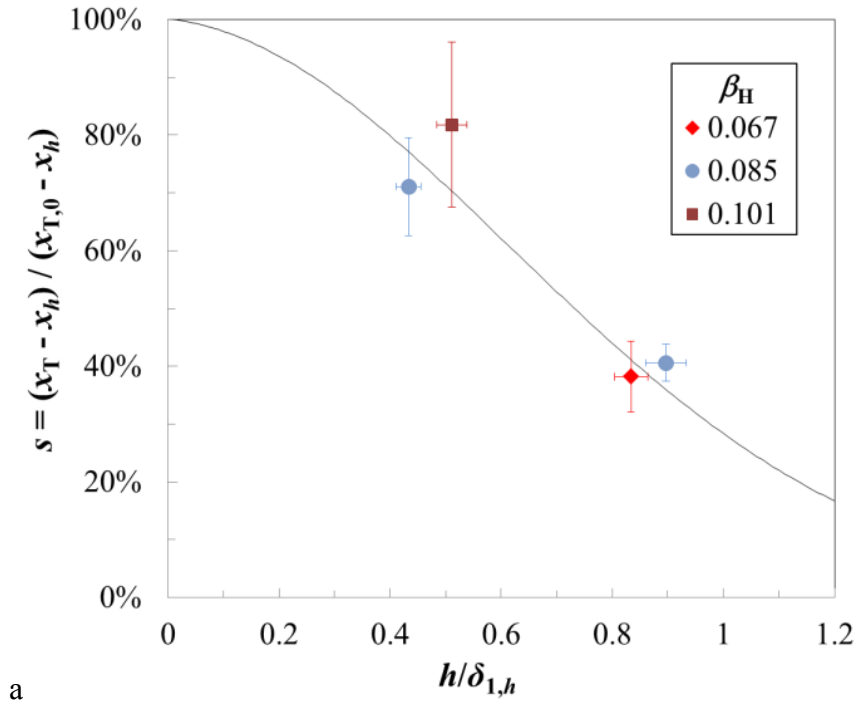

a

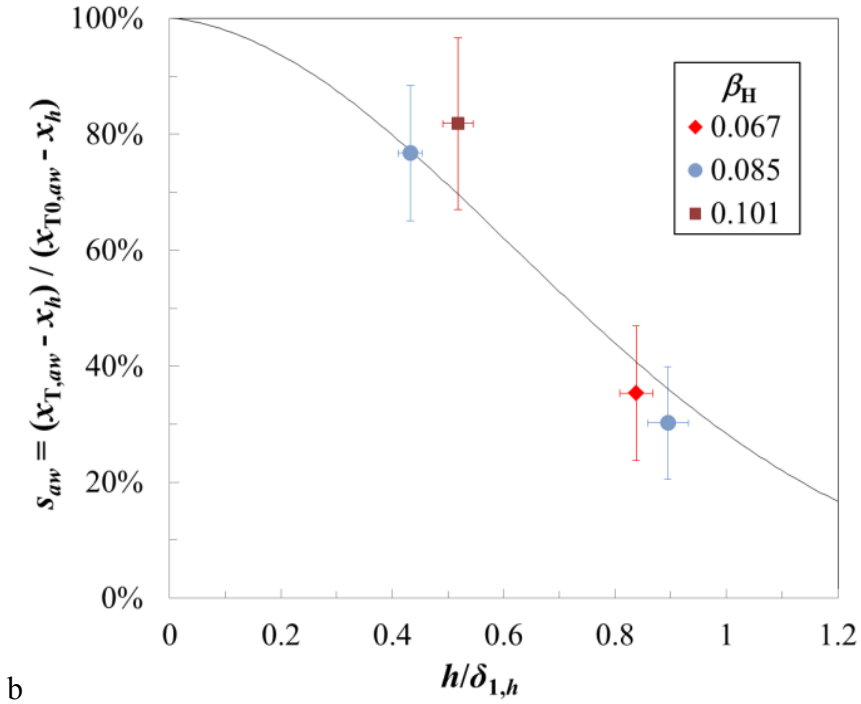

b

Fig. E.9.3. a: relative change in transition location as a function of the relative step height at M = 0.65 and T_w/T_{aw} = 0.998-1.011; the transition location $x_{T,0}$, obtained on the smooth configuration, was also measured at reduced T_w/T_{aw}. b: relative change of the adiabatic wall transition location as a function of the relative step height.

Some of the (few) experimental results show a behavior different from that observed at standard T_w/T_{aw}. Another parameter, however, has to be accounted for in these plots: the value of the wall temperature ratio at which the transition locations x_T and $x_{T,0}$ were measured. The larger deviations of the experimental data from the fitted functions are mainly due to different values of T_w/T_{aw} for x_T and $x_{T,0}$. A means to compensate for these differences is the use of $s_{aw} = (x_{T,aw}$-

$x_h)/(x_{T0,aw}\text{-}x_h)$ as characteristic parameter for the change in transition location, where $x_{T,aw}$ and $x_{T0,aw}$ are the adiabatic wall transition locations for step and smooth configurations, respectively. The relative change in transition location s_{aw} at M = 0.35, 0.5, and 0.65 is plotted as a function of $h/\delta_{1,h}$ in Fig. E.9.1b, Fig. E.9.2b, and Fig. E.9.3b, respectively. The value of $\delta_{1,h}$ used in these figures is obtained from laminar boundary-layer computations, performed using COCO with the smooth configuration and adiabatic wall (see Section 4.3). The agreement of the data points with the approximation functions for standard T_w/T_{aw} is better than that obtained in Fig. E.9.1a, Fig. E.9.2a, and Fig. E.9.3a. At $h/\delta_{1,h} > 0.8\text{-}0.9$, however, the change in sensitivity of boundary-layer transition to variations in T_w/T_{aw} has to be taken into account. When a reduction in T_w/T_{aw} leads to larger values of $x_{T,0}$ but to a negligible change in x_T, lower values of s_{aw} are obtained, as compared to the corresponding values of s at standard T_w/T_{aw}. This can be seen for the data points at $h/\delta_{1,h} \sim 1$ in Fig. E.9.1b and Fig. E.9.2b. Note that, if the laminar boundary layer lasts over the recovery zone at $h/\delta_{1,h} > 0.8\text{-}0.9$ without undergoing transition, and transition sensitivity remains approximately the same as that of the smooth configuration, the influence of T_w/T_{aw} on boundary-layer transition is already accounted for in the relation $s = (x_T\text{-}x_h)/(x_{T,0}\text{-}x_h)$ vs. $h/\delta_{1,h}$. This relation remains essentially unaffected by the thermal condition at the model surface, provided that both x_T and $x_{T,0}$ were measured at the same wall temperature ratio.

References

[1] International Air Transport Association. Annual Review 2015. http://www.iata.org/about/Documents/iata-annual-review-2015.pdf. [Retrieved 04 12 15]

[2] European Commission. European Aeronautics: A Vision for 2020. Report of the Group of Personalities. http://ec.europa.eu/research/growth/aeronautics2020/pdf/aeronautics2020_en.pdf. [Retrieved 29 09 14]

[3] J. Szodruch. Die Zukunft der Luftfahrt. Die europäische Vision 2020. Presentation at Haus der Luft- und Raumfahrt, Bonn, Germany, 30th May 2006. http://www.dglr.de/literatur/publikationen/DGLR_Szodruch_Vision2020.pdf. [Retrieved 29 09 14].

[4] European Commission. Flightpath 2050. Europe's Vision for Aviation. Report of the High Level Group on Aviation Research, 2011. http://ec.europa.eu/transport/modes/air/doc/flightpath2050.pdf. [Retrieved 29 09 14]

[5] Airbus S.A.S. Delivering the Future. Global Market Forecast 2011-2030. http://www.airbusgroup.com/dam/assets/airbusgroup/int/en/investor-relations/documents/2011/Presentations/2011-2030_Airbus_full_book_delivering_the_future.pdf. [Retrieved 29 09 14]

[6] U.S. Energy Information Administration. U.S. Gulf Coast Kerosene-Type Jet Fuel Spot Price FOB. http://tonto.eia.gov/dnav/pet/hist/LeafHandler.ashx?n=PET&s=EER_EPJK_PF4_RGC_DPG&f=D. [Retrieved 04 12 15]

[7] A. L. Braslow. A History of Suction-Type Laminar-Flow Control with Emphasis on Flight Research. Monographs in Aerospace History, No. 13, 1999.

[8] Deutsche Lufthansa AG. Lufthansa – First choice. Annual Report 2014. http://investor-relations.lufthansagroup.com/fileadmin/downloads/en/financial-reports/annual-reports/LH-AR-2014-e.pdf. [Retrieved 04 12 15]

[9] D. M. Bushnell, M. H. Tuttle. Survey and Bibliography on Attainment of Laminar Flow Control in Air Using Pressure Gradient and Suction, Volume I. NASA RP 1035, 1979.

[10] R. D. Joslin. Aircraft Laminar Flow Control. Annual Review of Fluid Mechanics, Vol. 30, 1998, pp. 1-29.

[11] W. S. Saric, H. L. Reed. Toward Practical Laminar Flow Control – Remaining Challenges. AIAA Paper No. 2004-2311, 2004.

[12] A. Drake, A. M. Bender, A. J. Korntheuer, R. V. Westphal, B. J. McKeon, S. Gerashchenko, W. Rohe, G. Dale. Step Excrescence Effects for Manufacturing Tolerances on Laminar Flow Wings. AIAA Paper No. 2010-375, 2010.

[13] P. M. H. W. Vijgen, S. S. Dodbele, B. J. Holmes, C. P. van Dam. Effects of Compressibility on Design of Subsonic Fuselages for Natural Laminar Flow. Journal of Aircraft, Vol. 25, No. 9, 1988, pp. 776-782.

[14] E. Coustols, A. M. Savill. Turbulent Skin-Friction Drag Reduction by Active and Passive Means. AGARD R-786, 1992, pp. 8-1 to 8-80.

[15] J. Reneaux. Overview on Drag Reduction Technologies for Civil Transport Aircraft. Proc. ECCOMAS 2004, edited by P. Neittaanmäki, T. Rossi, S. Korotov, E. Oñate, J. Périaux, D. Knörzer, University of Jyväskylä, Finland, 2004.

[16] S. Klumpp, M. Meinke, W. Schröder. Drag reduction by spanwise transversal surface waves. Journal of Turbulence, Vol. 11, No. 22, 2010, pp. 1-13.

[17] D. Roggenkamp, W. Jessen, W. Li, M. Klaas, W. Schröder. Experimental investigation of turbulent boundary layers over transversal moving surfaces. CEAS Aeronautical Journal, Vol. 6, No. 3, 2015, pp. 471-484.

[18] W. Li, W. Jessen, D. Roggenkamp, M. Klaas, W. Silex, M. Schiek, W. Schröder. Turbulent drag reduction by spanwise traveling ribbed surface waves. European Journal of Mechanics B/Fluids, Vol. 53, 2015, pp. 101-112.

[19] H. Schlichting, K. Gersten. Boundary-Layer Theory. 8th ed., Springer-Verlag, Berlin Heidelberg, 2000. Chap. 6: Boundary-Layer Equations in Plane Flow: Plate Boundary Layer.

[20] W. Schröder. Fluidmechanik. 3th ed., Aachener Beiträge zur Strömungsmechanik, Vol. 7, Wissenschaftsverlag Mainz, Aachen, Germany, 2010. Chap. 16: Turbulente Grenzschichten.

[21] D. Arnal, J. P. Archambaud. Laminar-Turbulent Transition Control: NLF, LFC, HLFC. AGARD RTO-EN-AVT-151, 2009, pp. 15-1 to 15-21.

[22] G. Schrauf. Status and Perspectives of Laminar Flow. The Aeronautical Journal, Vol. 109, No. 1102, 2005, pp. 639-644.

[23] F. George. Piaggio Aero P180 Avanti II. Business & Commercial Aviation, September 2007, pp. 116-125.

[24] F. S. Collier, Jr. An Overview of Recent Subsonic Laminar Flow Control Flight Experiments. AIAA Paper No. 1993-2987, 1993.

[25] B. J. Holmes, C. J. Obara. Observations and Implications of Natural Laminar Flow on Practical Airplane Surfaces. Journal of Aircraft, Vol. 20, No. 12, 1983, pp. 993-1006.

[26] B. J. Holmes, C. J. Obara, L. P. Yip. Natural Laminar Flow Experiments on Modern Airplane Surfaces. NASA TP-2256, 1984.

[27] H. Hansen. Laminar Flow Technology – The Airbus View. Proc. 27th Congress of the International Council of the Aeronautical Sciences, ICAS, 2010, pp. 453-461.

[28] J. Wallace. The Dream Continues… Frontiers, October 2013, pp. 22-31.

[29] S. Fancher, J. Ozimek. 737 MAX Development. Presentation at Paris Air Show, 19th June 2013.

[30] B. J. Holmes, C. J. Obara, G. L. Martin, C. S. Domack. Manufacturing Tolerances for Natural Laminar Flow Airframe Surfaces. SAE Paper No. 850863, 1985.

[31] A. H. Nayfeh. Influence of Two-Dimensional Imperfections on Laminar Flow. SAE Paper No. 921990, 1992.

[32] D. Arnal. Boundary Layer Transition: Prediction, Application to Drag Reduction. AGARD R-786, 1992, pp. 5-1 to 5-59.

[33] R. D. Wagner, D. W. Bartlett, F. S. Collier, Jr. Laminar Flow – The Past, Present, and Prospects. AIAA Paper No. 1989-0989, 1989.

[34] J. P. Nenni, G. L. Gluyas. Aerodynamic Design and Analysis of an LFC Surface. Aeronautics and Astronautics, Vol. 14, No. 7, 1966, pp. 52-57.

[35] D. P. Rizzetta, M. R. Visbal. The Effect of Two-Dimensional Geometric Disturbances on Boundary-Layer Stability. AIAA Paper No. 2013-3108, 2013.

[36] D. P. Rizzetta, M. R. Visbal. Numerical Simulation of Excrescence Generated Transition. AIAA Journal, Vol. 52, No. 2, 2014, pp. 385-397.

[37] A. V. Dovgal, V. V. Kozlov. Hydrodynamic instability and receptivity of small scale separation regions. Laminar-Turbulent Transition, edited by D. Arnal, R. Michel, Springer-Verlag, Berlin Heidelberg, 1990, pp. 523-531.

[38] J. Perraud, A. Séraudie. Effects of Steps and Gaps on 2D and 3D Transition. Proc. ECCOMAS 2000, edited by E. Oñate, G. Bugeda, B. Suárez, Technical University of Catalonia, Barcelona, Spain, 2000.

[39] A. Drake, A. M. Bender, W. D. Solomon, Jr., A. J. Vavra. Air Vehicle Technology Integration Program (AVTIP) Delivery Order 0020: Prediction of Manufacturing Tolerances For Laminar Flow. Report AFRL-VA-WP-TR-2005-3060, Northrop Grumman Corp., 2005.

[40] Y. X. Wang, M. Gaster. Effect of surface steps on boundary layer transition. Experiments in Fluids, Vol. 39, No. 4, 2005, pp. 679-686.

[41] J. D. Crouch, V. S. Kosorygin, L. L. Ng. Modeling the effects of steps on boundary layer transition. Proc. Sixth IUTAM Symposium on Laminar-Turbulent Transition, edited by R. Govindarajan, Springer Netherlands, 2006, pp. 37-44.

[42] D. M. Driver, A. Drake. Skin Friction Measurements Using Oil-Film Interferometry in NASA's 11-Foot Transonic Wind Tunnel. AIAA Journal, Vol. 46, No. 10, 2008, pp. 2401-2407.

[43] A. M. Bender, J. R. Elliott, Y. Shinagawa, A. J. Korntheuer, A. Drake, R. V. Westphal, S. Gerashchenko, B. J. McKeon, S. Yoshioka. An Approach to Measuring Step Excrescence Effects in the Presence of a Pressure Gradient. AIAA Paper No. 2010-0373, 2010.

[44] S. Gerashchenko, B. J. McKeon, R. V. Westphal, A. M. Bender, A. Drake. Hot-Wire Measurements of the Influence of Surface Steps on Transition in Favorable Pressure Gradient Boundary Layers. AIAA Paper No. 2010-374, 2010.

[45] C. A. Edelmann, U. Rist. Impact of Forward-Facing Steps on Laminar-Turbulent Transition in Subsonic Flows. New Results in Numerical and Experimental Fluid Mechanics IX, edited by A. Dillmann, G. Heller, E. Krämer, H.-P. Kreplin, W. Nitsche, U. Rist, Notes on Numerical Fluid Mechanics and Multidisciplinary Design, Vol. 124, Springer International Publishing, 2014, pp. 155-162.

[46] C. A. Edelmann, U. Rist. Impact of Forward-Facing Steps on Laminar-Turbulent Transition in Transonic Flows. AIAA Journal, Vol. 53, No. 9, 2015, pp. 2504-2511.

[47] G. T. Duncan, Jr., B. K. Crawford, M. T. Tufts, W. S. Saric, H. L. Reed. Effects of Step Excrescences on Swept-Wing Transition. AIAA Paper No. 2013-2412, 2013.

[48] G. T. Duncan, Jr., B. K. Crawford, M. T. Tufts, W. S. Saric, H. L. Reed. Effects of Step Excrescences on a Swept Wing in a Low-Disturbance Wind Tunnel. AIAA Paper No. 2014-0910, 2014.

[49] R. S. Ehrmann, E. B. White. Influence of 2D Steps and Distributed Roughness on Transition on a NACA 63_3-418. AIAA Paper No. 2014-0170, 2014.

[50] J. Perraud. Laminar-turbulent transition on aerodynamic surfaces with imperfections. RTO-AVT-111, 2004, pp. 14-1 to 14-14.

[51] Airbus S.A.S. A320. Dimensions and key data. http://www.airbus.com/aircraftfamilies/passengeraircraft/a320family/a320/specifications. [Retrieved 30 01 15]

[52] Air Berlin Flight AB8706 from Berlin Tegel to Rome Fiumicino, 3rd December 2015. http://www.flightradar24.com/data/flights/ab8706/#827be58. [Retrieved 04 12 15]

[53] E. Reshotko. Boundary Layer Instability, Transition and Control. AIAA Paper No. 1994-0001, 1994.

[54] H. W. Stock. Wind tunnel–flight correlation for laminar wings in adiabatic and heating flow conditions. Aerospace Science and Technology, Vol. 6, 2002, pp. 245-257.

[55] H. Rosemann. The Cryogenic Ludwieg-Tube Tunnel at Göttingen. AGARD R-812, 1997, pp. 8-1 to 8-13.

[56] S. Koch. Zeitliche und räumliche Turbulenzentwicklung in einem Rohrwindkanal und deren Einfluss auf die Transition an Profilmodellen. DLR Report FB 2004-19, 2004.

[57] C. Tropea, A. L. Yarin, J. F. Foss. Springer Handbook of Experimental Fluid Mechanics, Springer-Verlag, Berlin Heidelberg, 2007. Chap. 7.4: Transition-Detection by Temperature-Sensitive Paint.

[58] O. Reynolds. An experimental investigation of the circumstances which determine whether the motion of water shall be direct or sinuous, and of the law of resistance in parallel channels. Philosophical Transactions of the Royal Society of London, Vol. 174, 1883, pp. 935-982.

[59] L. Prandtl. Über Flüssigkeitsbewegung bei sehr kleiner Reibung. Verhandlungen des III. Internationalen Mathematiker-Kongresses, Heidelberg, Germany, 1904, pp. 484-491.

[60] H. Schlichting, K. Gersten. Boundary-Layer Theory. 8th ed., Springer-Verlag, Berlin Heidelberg, 2000. Chap. 1: Some Features of Viscous Flow, and Chap. 2: Fundamentals of Boundary-Layer Theory.

[61] P. A. Davidson. Turbulence: An Introduction for Scientists and Engineers. Oxford University Press, USA, 2004. Chap. 1: The ubiquitous nature of turbulence.

[62] D. Arnal, G. Casalis. Laminar-turbulent transition prediction in three-dimensional flows. Progress in Aerospace Sciences, Vol. 36, 2000, pp. 173-191.

[63] E. Reshotko. Paths to Transition in Wall Layers. AGARD RTO-EN-AVT-151, 2009, pp. 1-1 to 1-8.

[64] W. S. Saric. Laminar-Turbulent Transition: Fundamentals. AGARD R-786, 1992, pp. 4-1 to 4-32.

[65] E. Reshotko. Boundary-Layer Stability and Transition. Annual Review of Fluid Mechanics, Vol. 8, 1976, pp. 311-349.

[66] Y. S. Kachanov. Physical Mechanisms of Laminar-Boundary-Layer Transition. Annual Review of Fluid Mechanics, Vol. 26, 1994, pp. 411-482.

[67] I. Tani. Boundary-Layer Transition. Annual Review of Fluid Mechanics, Vol. 1, 1969, pp. 169-196.

[68] D. Arnal. Description and prediction of transition in two-dimensional incompressible flow. AGARD R-709, 1984, pp. 2-1 to 2-71.

[69] L. M. Mack. Boundary-layer linear stability theory. AGARD R-709, 1984, pp. 3-1 to 3-81.

[70] D. I. A. Poll. Transition description and prediction in three-dimensional flows. AGARD R-709, 1984, pp. 5-1 to 5-23.

[71] T. Herbert. Secondary instability of boundary layers. Annual Review of Fluid Mechanics, Vol. 20, 1988, pp. 487-526.

[72] H. L. Reed, W. S. Saric. Stability of three-dimensional boundary layers. Annual Review of Fluid Mechanics, Vol. 21, 1989, pp. 235-284.

[73] H. Bippes. Basic experiments on transition in three-dimensional boundary layers dominated by crossflow instability. Progress in Aerospace Sciences, Vol. 35, 1999, pp. 363-412.

[74] W. S. Saric, H. L. Reed, E. B. White. Stability and Transition of Three-Dimensional Boundary Layers. Annual Review of Fluid Mechanics, Vol. 35, 2003, pp. 413-440.

[75] H. Blasius. Grenzschichten in Flüssigkeiten mit kleiner Reibung. Zeitschrift für angewandte Mathematik und Physik, Vol. 56, 1908, pp. 1-37.

[76] W. Schröder. Fluidmechanik. 3th ed., Aachener Beiträge zur Strömungsmechanik, Vol. 7, Wissenschaftsverlag Mainz, Aachen, Germany, 2010. Chap. 15: Laminare Grenzschichten.

[77] W. S. Saric, H. L. Reed, E. B. White. Boundary-layer receptivity to freestream disturbances and its role in transition. AIAA Paper No. 1999-3788, 1999.

[78] M. V. Morkovin. Panoramic view of changes in vorticity distribution in transition instabilities and turbulence. Boundary Layer Stability and Transition to Turbulence, edited by D. C. Reda, H. L. Reed, R. Kobayashi, FED-114, ASME, New York, 1991, pp. 1-12.

[79] M. V. Morkovin, E. Reshotko, T. Herbert. Transition in open flow systems – a reassessment. Bulletin of the American Physical Society, Vol. 39, No. 9, 1994, p. 1882.

[80] W. S. Saric, H. L. Reed. Paths to Transition in Wall Layers and Introduction to Stability Problems. VKI Lecture Series 2014-07: Progress in Flow Instability Analysis and Laminar-Turbulent Transition Modeling, Von Karman Institute for Fluid Dynamics, Sint-Genesius-Rode, Belgium, 2014.

[81] W. S. Saric, H. L. Reed, E. J. Kerschen. Boundary-Layer Receptivity to Freestream Disturbances. Annual Review of Fluid Mechanics, Vol. 34, 2002, pp. 291-319.

[82] Y. S. Kachanov. Routes of Boundary-Layer Transition. Proc. IUTAM Symposium on One Hundred Years of Boundary Layer Research, edited by G. E. A. Meier, K. R. Sreenivasan, H.-J. Heinemann, Springer, Dordrecht, the Netherlands, 2006, pp. 95-104.

[83] S. Hein. Nonlinear Nonlocal Transition Analysis. DLR Report FB 2005-10, 2005.

[84] S. Schaber. Auswirkungen von Schall und Absaugverteilungen auf die Einsatzfähigkeit der Hybridlaminartechnik. Mensch & Buch Verlag, Berlin, 2001.

[85] H. Schlichting, K. Gersten. Boundary-Layer Theory. 8th ed., Springer-Verlag, Berlin Heidelberg, 2000. Chap. 15: Onset of Turbulence (Stability Theory).

[86] W. S. Saric. Introduction to Linear Stability. AGARD RTO-EN-AVT-151, 2009, pp. 2-1 to 2-56.

[87] F. P. Bertolotti, T. Herbert. Analysis of the Linear Stability of Compressible Boundary Layers Using the PSE. Theoretical and Computational Fluid Dynamics, Vol. 3, 1991, pp. 117-124.

[88] C.-L. Chang, M. R. Malik, G. Erlebacher, M. Y. Hussaini Compressible Stability of Growing Boundary Layers Using Parabolized Stability Equations. AIAA Paper No. 1991-1636, 1991.

[89] F. P. Bertolotti, T. Herbert, P. R. Spalart. Linear and nonlinear stability of the Blasius boundary layer. Journal of Fluid Mechanics, Vol. 242, 1992, pp. 441-474.

[90] M. Simen, F. P. Bertolotti, S. Hein, A. Hanifi, D. Henningson, U. Dallmann. Nonlocal and nonlinear instability theory. Proc. ECCOMAS Conference on Computational Fluid Dynamics, edited by S. Wagner, J. Périaux, E. H. Hirschel, John Wiley & Sons, Chichester, UK, 1994, pp. 169-179.

[91] T. Herbert. Parabolized stability equations. Annual Review of Fluid Mechanics, Vol. 29, 1997, 245-283.

[92] J. Pretsch. Die Stabilität einer ebenen Laminarströmung bei Druckgefälle und Druckanstieg. Jahrbuch der deutschen Luftfahrtforschung, 1941, pp. I 58-75.

[93] A. Stolte, F. P. Bertolotti, M. Simen. Nonlocal Instability Analysis of Transonic Flow Past the ATTAS Laminar Glove. DLR Report IB 223-95 A07, 1995.

[94] G. Schrauf, T. Herbert, G. Stuckert. Evaluation of Transition in Flight Tests Using Nonlinear Parabolized Stability Equation Analysis. Journal of Aircraft, Vol. 33, No. 3, 1996, pp. 554-560.

[95] G. B. Schubauer, H. K. Skramstad. Laminar boundary-layer oscillations and transition on a flat plate. NACA Report No. 909, 1948.

[96] A. V. Dovgal, V. V. Kozlov, A. Michalke. Laminar Boundary Layer Separation: Instability and Associated Phenomena. Progress in Aerospace Sciences, Vol. 30, No. 1, 1994, pp. 61-94.

[97] M. E. Goldstein, L. S. Hultgren. Boundary layer receptivity to long-wave disturbances. Annual Review of Fluid Mechanics, Vol. 21, 1989, pp. 137-166.

[98] E. J. Kerschen. Boundary layer receptivity theory. Applied Mechanics Reviews, Vol. 43, No. 5, Part 2, 1990, pp. S152-S157.

[99] M. Choudhari, C. L. Streett. Theoretical predictions of boundary-layer receptivity. AIAA Paper No. 1994-2223, 1994.

[100] J. D. Crouch, Theoretical studies on the receptivity of boundary layers. AIAA Paper No. 1994-2224, 1994.

[101] C. S. Wells, Jr. Effects of free stream turbulence on boundary layer transition, AIAA Journal, Vol. 5, No. 1, 1967, pp. 172-174.

[102] N. S. Dougherty, Jr., D. F. Fisher. Boundary-Layer Transition on a 10-Degree Cone: Wind Tunnel / Flight Data Correlation. AIAA Paper No. 1980-0154, 1980.

[103] U. Michel, E. Froebel. Lower limit for the velocity fluctuation level in wind tunnels. Experiments in Fluids, Vol. 6, No. 1, 1988, pp. 49-54.

[104] F. K. Owen, A. K. Owen. Effects of Freestream Flow Quality on Boundary Layer Transition in the National Transonic Facility. AIAA Paper No. 2013-1135, 2013.

[105] M. E. Goldstein. Scattering of acoustic waves into Tollmien-Schlichting waves by small streamwise variations in surface geometry. Journal of Fluid Mechanics, Vol. 154, 1985, pp. 509-529.

[106] A. J. Dietz. Local boundary-layer receptivity to a convected free-stream disturbance. Journal of Fluid Mechanics, Vol. 378, 1999, pp. 291-317.

[107] R. A. King, K. S. Breuer. Acoustic receptivity and evolution of two-dimensional and oblique disturbances in a Blasius boundary layer. Journal of Fluid Mechanics, Vol. 432, 2001, pp. 69-90.

[108] W. Würz, D. Sartorius, M. J. Kloker, V.I. Borodulin, Y.S. Kachanov, B.V. Smorodsky. Nonlinear instabilities of a non-self-similar boundary layer on an airfoil: Experiments, DNS, and theory. European Journal of Mechanics B/Fluids, Vol. 31, 2012, pp. 102-128.

[109] P. S. Klebanoff, K. D. Tidstrom and L. M. Sargent. The three-dimensional nature of boundary-layer instability. Journal of Fluid Mechanics, Vol. 12, 1962, pp. 1-34.

[110] H. L. Reed, W. S. Saric, D. Arnal. Linear Stability Theory Applied to Boundary Layers. Annual Review of Fluid Mechanics, Vol. 28, 1996, pp. 389-428.

[111] S. Hein, A. Hanifi, G. Casalis. Nonlinear Transition Prediction. Proc. ECCOMAS 2000, edited by E. Oñate, G. Bugeda, B. Suárez, Technical University of Catalonia, Barcelona, Spain, 2000.

[112] H. J. Obremski, M. V. Morkovin, M. Landahl. A portfolio of stability characteristics of incompressible boundary layer. AGARD AGARDograph No. 134, 1969.

[113] H. W. Emmons. The laminar-turbulent transition in a boundary layer - Part I. Journal of the Aeronautical Sciences, Vol. 18, No. 7, 1951, pp. 490-498.

[114] G. B. Schubauer, P. S. Klebanoff. Contributions on the mechanics of boundary-layer transition. NACA TN 3489, 1955.

[115] H.-P. Kreplin, G. Höhler. Application of the Surface Hot Film Technique for Laminar Flow Investigations. Proc. 1st European Forum on Laminar Flow Technology, Deutsche Gesellschaft für Luft- und Raumfahrt - Lilienthal-Oberth e.V., Bonn, Germany, Paper No. 92-01-017, 1992, pp. 123-131.

[116] D. Arnal, G. Casalis, R. Houdeville. Practical Transition Prediction Methods: Subsonic and Transonic Flows. AGARD RTO-EN-AVT-151, 2009, pp. 7-1 to 7-34.

[117] B. J. Abu-Ghannam, R. Shaw. Natural transition of boundary layers - The effects of turbulence, pressure gradient, and flow history. Journal of Mechanical Engineering Science, Vol. 22, 1980, pp. 213-228.

[118] Y. X. Wang. Instability and transition of boundary layer flows disturbed by steps and bumps. PhD thesis, Queen Mary, University of London, 2004.

[119] A. Meijering, W. Schröder. Experimental Analysis of Separated Transitional Transonic Airfoil Flow. AIAA Paper No. 2001-2987, 2001.

[120] N. S. Dougherty, Jr., F. W. Steinle, Jr. Transition Reynolds Number Comparisons in Several Major Transonic Tunnels. AIAA Paper No. 1974-0627, 1974.

[121] D. F. Fisher, N. S. Dougherty, Jr. In-Flight Transition Measurement on a 10° Cone at Mach Numbers From 0.5 to 2.0. NASA TP 1971, 1982.

[122] P. R. Ashill, C. J. Betts, I. M. Gaudet. A Wind Tunnel Study of Transitional Flows on a Swept Panel Wing at High Subsonic Speeds. Proc. CEAS 2nd European Forum on Laminar Flow Technology, AAAF, Paris, Paper No. 10.1, 1996, pp. 10.3-10.17.

[123] F. J. Keller, T. Wang. Flow and Heat Transfer Behavior in Transitional Boundary Layers With Streamwise Acceleration. Journal of Turbomachinery, Vol. 118, No. 2, 1996, pp. 314-326.

[124] F. Hausmann, W. Schröder. Coated Hot-Film Sensors for Transition Detection in Cruise Flight. Journal of Aircraft, Vol. 43, No. 2, 2006, pp. 456-465.

[125] M. F. Blair, M. J. Werle. Combined Influence of Free-Stream Turbulence and Favorable Pressure Gradients on Boundary Layer Transition and Heat Transfer. UTRC Report No. R81-914388-17, 1981.

[126] S. Zhong, T. P. Chong, H. P. Hodson. A Comparison of Spreading Angles of Turbulent Wedges in Velocity and Thermal Boundary Layers. Journal of Fluids Engineering, Vol. 125, 2003, pp. 267-274.

[127] M. V. Morkovin. Critical Evaluation of Transition from Laminar to Turbulent Shear Layers with Emphasis on Hypersonically Traveling Bodies. AFFDL TR-68-149, 1969.

[128] E. Reshotko. Stability and transition - How much do we know? Proc. U.S. National Congress of Applied Mechanics, ASME, New York, 1987, pp. 421-434.

[129] E. Reshotko. Drag Reduction by Cooling in Hydrogen-Fueled Aircraft. Journal of Aircraft, Vol. 16, No. 9, 1979, pp. 584-590.

[130] H. Schlichting, K. Gersten. Boundary-Layer Theory. 8th ed., Springer-Verlag, Berlin Heidelberg, 2000. Chap. 7: General Properties and Exact Solutions of the Boundary-Layer Equations for Plane Flows.

[131] D. R. Hartree. On an equation occurring in Falkner and Skan's approximate treatment of the equations of the boundary layer. Proc. Cambridge Philosophical Society, Vol. 33, part 2, 1937, pp. 223-239.

[132] P. S. Granville. The calculation of viscous drag of bodies of revolution. U.S. Navy Department Report No. 849, 1953.

[133] K. Bussmann, H. Münz. Die Stabilität der laminaren Reibungsschicht mit Absaugung. Jahrbuch der deutschen Luftfahrtforschung I, 1942, pp. 36-39.

[134] W. Linke. Über den Strömungswiderstand einer beheizten ebenen Platte. Luftfahrtforschung, Vol. 19, 1942, pp. 157-160.

[135] C. W. Frick, G. B. McCullogh. Tests of a Heated Low Drag Airfoil. NACA ACR-244, 1942.

[136] H. W. Liepmann, G. H. Fila. Investigations of Effects of Surface Temperature and Single Roughness Elements on Boundary-Layer Transition. NACA Report 890, 1947.

[137] L. Lees, C. C. Lin. Investigation of the Stability of the Laminar Boundary Layer in a Compressible Fluid. NACA TN 1115, 1946.

[138] E. G. Hauptmann. The Influence of Temperature Dependent Viscosity on Laminar Boundary-Layer Stability. International Journal of Heat and Mass Transfer, Vol. 11, 1967, pp. 1049-1052.

[139] L. I. Boehman, M. G. Mariscalco. The Stability of Highly Cooled Compressible Laminar Boundary Layers. AFFDL TR-76-148, 1976.

[140] P. Schäfer, J. Severin, H. Herwig. The Effect of Heat Transfer on the Stability of Laminar Boundary-Layers. International Journal of Heat and Mass Transfer, Vol. 38, No. 10, 1995, pp. 1855-1863.

[141] S. Özgen. Effect of Heat Transfer on Stability and Transition Characteristics of Boundary-Layers, International Journal of Heat and Mass Transfer, Vol. 47, No. 22, 2004, pp. 4697-4712.

[142] A. R. Wazzan, C. Gazley. The Combined Effects of Pressure Gradient and Heating on the Stability and Transition of Water Boundary Layer. Proc. 2nd International Conference on Drag Reduction, BHRA Fluid Engineering, Cambridge, MA, Paper No. E3, 1977.

[143] Y. S. Kachanov, V. V. Kozlov, V. Y. Levchenko. Experimental Study of the Influence of Cooling on the Stability of Laminar Boundary Layers. Izvestia Sibirskogo Otdielenia Akademii Nauk SSSR, Seria Technicheskikh Nauk, No. 8-2, 1974, pp. 75-79.

[144] S. B. Harrison, D. J. Mee, T. V. Jones. Experiments on the Influence of Heating on Boundary-Layer Transition in Favourable Pressure Gradients. Proc. Eurotherm Seminar No. 25, University of Pau and Pays de l'Adour, Pau, France, 1991, pp. 26-31.

[145] M. Costantini, U. Fey, U. Henne, C. Klein. Nonadiabatic Surface Effects on Transition Measurements Using Temperature-Sensitive Paints. AIAA Journal, Vol. 53, No. 5, 2015, pp. 1172-1187.

[146] F. T. Lynch, M. F. Fancher, D. R. Patel, G. R. Inger. Nonadiabatic Model Wall Effects on Transonic Airfoil Performance in a Cryogenic Wind Tunnel. AGARD CP-348, 1984, pp. 14-1 to 14-11.

[147] E. Reshotko. Control of Transition – Heating and Cooling, AGARD RTO-EN-AVT-151, 2009, pp. 14-1 to 14-18.

[148] M. Costantini, S. Hein, U. Henne, C. Klein, S. Koch, L. Schojda, V. Ondrus, W. Schröder. Pressure Gradient and Non-adiabatic Surface Effects on Boundary-Layer Transition. AIAA Journal, Vol. 54, No. 11, 2016, pp. 3465-3480.

[149] M. Gaster. A note on a relation between temporally increasing and spatially increasing disturbances in hydrodynamic stability. Journal of Fluid Mechanics, Vol. 14, 1962, pp. 222-224.

[150] J. L. van Ingen. The e^N Method for Transition Prediction. Historical Review of Work at TU Delft. AIAA Paper No. 2008-3830, 2008.

[151] A. M. O. Smith, N. Gamberoni. Transition, Pressure Gradient and Stability Theory. Technical Report ES-26388, Douglas Aircraft Company, 1956.

[152] J. L. van Ingen. A suggested semi-empirical method for the calculation of the boundary layer transition region. Report V.T.H.-74, TU Delft, 1956.

[153] G. Schrauf, J. Perraud, D. Vitiello, F. Lam. Comparison of Boundary-Layer Transition Predictions Using Flight Test Data. Journal of Aircraft, Vol. 35, No. 6, 1998, pp. 891-897.

[154] G. Schrauf. Large-Scale Laminar-Flow Tests Evaluated with Linear Stability Theory. Journal of Aircraft, Vol. 41, No. 2, 2004, pp. 224-230.

[155] T. Streit, K. H. Horstmann, G. Schrauf, S. Hein, U. Fey, Y. Egami, J. Perraud, I. S. El Din, U. Cella, J. Quest. Complementary Numerical and Experimental Data Analysis of the ETW Telfona Pathfinder Wing Transition Tests. AIAA Paper No. 2011-0881, 2011.

[156] N. Voogt. Flight Testing of a Fokker 100 Aircraft with Laminar Flow Glove. Proc. CEAS 2nd European Forum on Laminar Flow Technology, AAAF, Paris, Paper No. 2.1, 1996, pp. 2-3 to 2-14.

[157] B. J. Holmes. Progress in Natural Laminar Flow Research. AIAA Paper No. 1984-2222, 1984.

[158] M. D. Maddalon, A. L. Braslow. Simulated airline-service-flight tests of laminar-flow control with perforated-surface suction system. NASA TP 2966, 1990.

[159] D. Arnal, C. Bulgubure. Drag reduction by boundary layer laminarization. La Recherche Aerospatiale, No. 3, 1996, pp. 157-165.

[160] M. J. Hood. The Effects of Surface Waviness and of Rib Stitching on Wing Drag. NACA TN 724, 1939.

[161] A. Fage. The Smallest Size of a Spanwise Surface Corrugation which Affects Boundary-Layer Transition on an Aerofoil. ARC Reports and Memoranda No. 2120, 1943.

[162] B. H. Carmichael. Surface waviness criteria for swept and unswept laminar suction wings. Report No. NOR-59-438 (BLC-123), Northrop Aircraft, Inc., 1959.

[163] A. H. Nayfeh, S. A. Ragab, A. A. Al-Maaitah. Effect of bulges on the stability of boundary layers, Physics of Fluids, Vol. 31, No. 4, 1988, pp. 796-806.

[164] A. A. Al-Maaitah, A. H. Nayfeh, S. A. Ragab. Effect of wall cooling on the stability of compressible subsonic flow over smooth humps and backward-facing humps. Physics of Fluids A, Vol. 2, No. 3, 1990, pp. 381-389.

[165] J. A. Masad, A. H. Nayfeh. Effect of a bulge on the subharmonic instability of subsonic boundary layers, AIAA Journal, Vol. 30, No. 7, 1992, pp. 1731-1737.

[166] J. A. Masad, V. Iyer. Transition Prediction and Control in Subsonic Flow Over a Hump, NASA CR 4543, 1993.

[167] Y. Wie, M. R. Malik. Effect of surface hardness on boundary layer transition in two-dimensional flow. Computers and Fluids, Vol. 27, No. 2, 1998, pp. 157-181.

[168] A. Wörner, U. Rist, S. Wagner. Influence of humps and steps on the stability characteristics of a 2D laminar boundary layer, AIAA Paper No. 2002-0139, 2002.

[169] Northrop Corp. Final Report on LFC Aircraft Design Data Laminar Flow Control Demonstration Program. Report No. NOR 67-136, 1967.

[170] F. A. Zuniga, A. Drake, R. A. Kennelly, Jr., D. J. Koga, R. V. Westphal. Transonic Flight Test of a Laminar Flow Leading Edge With Surface Excrescences. AIAA Paper No. 1994-2142, 1994.

[171] A. Drake, R. V. Westphal, F. A. Zuniga, R. A. Kennelly, Jr., D. J. Koga. Wing Leading Edge Joint Laminar Flow Tests. NASA TM 4762, 1996.

[172] D. Arnal, J. Perraud, A. Séraudie. Attachment Line and Surface Imperfection Problems. AGARD RTO-EN-AVT-151, 2009, pp. 9-1 to 9-20.

[173] M. Forte, J. Perraud, A. Séraudie, S. Beguet, L. Gentili, G. Casalis. Experimental and Numerical Study of the Effect of Gaps on Laminar Turbulent Transition of Incompressible Boundary Layers. Procedia IUTAM, Vol. 14 C, Elsevier, Amsterdam, 2015, pp. 448-458.

[174] J. Zahn, U. Rist. Impact of Deep Gaps on Laminar–Turbulent Transition in Compressible Boundary-Layer Flow. AIAA Journal, Vol. 54, No. 1, 2016, pp. 66-76.

[175] W. S. Saric, J. A. Hoos, R. H. Radeztsky, Jr. Boundary-layer receptivity of sound with roughness. Boundary Layer Stability and Transition to Turbulence, edited by D. C. Reda, H. L. Reed, R. Kobayashi, FED-114, ASME, New York, 1991, pp. 69-76.

[176] S. Hein. Linear and nonlinear nonlocal instability analysis for two-dimensional laminar separation bubbles. Laminar-Turbulent Transition, edited by H. F. Fasel, W. S. Saric, Springer-Verlag, Berlin Heidelberg, 2000, pp. 681-686.

[177] V. Theofilis, S. Hein, U. Dallmann. On the origins of unsteadiness and three-dimensionality in a laminar separation bubble. Philosophical Transactions of the Royal Society London A, Vol. 358, 2000, pp. 3229-3246.

[178] U. Rist. Instability and Transition Mechanisms in Laminar Separation Bubbles. RTO-EN-AVT-104, 2005, pp. 5-1 to 5-29.

[179] S. Burgmann, W. Schröder. Investigation of the vortex induced unsteadiness of a separation bubble via time-resolved and scanning PIV measurements. Experiments in Fluids, Vol. 45, No. 4, 2008, pp. 675-691.

[180] E. Reshotko, A. Tumin. Role of Transient Growth in Roughness-Induced Transition. AIAA Journal, Vol. 42, No. 4, 2004, pp. 766-770.

[181] R. S. Downs III, E. B. White, N. A. Denissen. Transient Growth and Transition Induced by Random Distributed Roughness. AIAA Journal, Vol. 46, No. 2, 2008, pp. 451-462.

[182] P. S. Klebanoff, K. R. Tidstrom. Mechanism by which a two-dimensional roughness element induces boundary-layer transition. Physics of Fluids, Vol. 15, No. 7, 1972, pp. 1173-1188.

[183] M. Hahn, W. Pfenninger. Prevention of Transition over a Backward Step by Suction. Journal of Aircraft, Vol. 10, No. 10, 1973, pp. 618-622.

[184] A. A. Al-Maaitah, A. H. Nayfeh, S. A. Ragab. Effect of Suction on the Stability of Subsonic Flows over Smooth Backward-Facing Steps. AIAA Journal, Vol. 28, No. 11, 1990, pp. 1916-1924.

[185] Private communication with V. S. Kosorygin, Khristianovich Institute of Theoretical and Applied Mechanics, Siberian Branch of Russian Academy of Sciences, Novosibirsk, Russia, 2014. kosor@itam.nsc.ru.

[186] A. M. Bender, A. Drake. Air Vehicle Technology Integration Program (AVTIP) Delivery Order 0020: Prediction of Manufacturing Tolerances for Laminar Flow, Task 6. Report AFRL-VA-WP-TR-2007-3086, Northrop Grumman Corp., 2007.

[187] H. Ludwieg. Der Rohrwindkanal. Zeitschrift für Flugwissenschaften, Vol. 3, No. 7, 1955, pp. 206-216.

[188] Airbus S.A.S. A310. Dimensions and key data. http://www.airbus.com/aircraftfamilies/out-of-production/a310/specifications. [Retrieved 30 01 15]

[189] Airbus S.A.S. A340. Dimensions and key data. http://www.airbus.com/aircraftfamilies/passengeraircraft/a340family/a340-300/specifications. [Retrieved 30 01 15]

[190] J. Amecke. Direkte Berechnung von Wandinterferenzen und Wandadaption bei zweidimensionaler Strömung in Windkanälen mit geschlossenen Wänden. DFVLR Report FB 85-62, 1985.

[191] R.-D. Cécora, H. Rosemann. Experimental and Numerical Investigations of the Laminar Airfoil NLF9. New Results in Numerical and Experimental Fluid Mechanics IX, edited by A. Dillmann, G. Heller, E. Krämer, H.-P. Kreplin, W. Nitsche, U. Rist, Notes on Numerical Fluid Mechanics and Multidisciplinary Design, Vol. 124, Springer International Publishing, 2014, pp. 193-201.

[192] U. Fey, Y. Egami, C. Klein. Temperature-Sensitive Paint Application in Cryogenic Wind Tunnels: Transition Detection at High Reynolds Numbers and Influence of the Technique on Measured Aerodynamic Coefficients. 22nd International Congress on Instrumentation in Aerospace Simulation Facilities Record, IEEE, Piscataway, NJ, 2007, pp. 1-17.

[193] H. Ludwieg, W. Lorenz-Meyer, H. Grauer-Cartensen. The Ludwieg Tube. AVA Report 251 74 A 28, 1974.

[194] M. B. Giles, M. Drela. Two-Dimensional Transonic Aerodynamic Design Method. AIAA Journal, Vol. 25, No. 9, 1987, pp. 1199-1206.

[195] M. Drela, M. B. Giles. Viscous-Inviscid Analysis of Transonic and Low Reynolds Number Airfoils. AIAA Journal, Vol. 25, No. 10, 1987, pp. 1347-1355.

[196] G. Schrauf. COCO – A Program to Compute Velocity and Temperature Profiles for Local and Nonlocal Stability Analysis of Compressible, Conical Boundary Layers with Suction. Report, Zarm Technik, Bremen, Germany, 1998.

[197] S. Melber-Wilkending, G. Schrauf, M. Rakowitz. Aerodynamic Analysis of Flows with Low Mach- and Reynolds-Number Under Consideration and Forecast of Transition on the Example of a Glider. New Results in Numerical and Experimental Fluid Mechanics V, edited by H.-J. Rath, C. Holze, H.-J. Heinemann, R. Henke, H. Hönlinger, Notes on Numerical Fluid Mechanics and Multidisciplinary Design, Vol. 92, Springer-Verlag, Berlin Heidelberg, 2006, pp. 9-16.

[198] Private communicatiom with S. Hein, Institute of Aerodynamics and Flow Technology, Deutsches Zentrum für Luft- und Raumfahrt e.V. (DLR), Göttingen, 2013. Stefan.Hein@dlr.de.

[199] G. Schrauf. LILO 2.1 – User's Guide and Tutorial. Technical Report 6, GSSC, Bremen, Germany, 2006.

[200] M. W. Tufts, H. L. Reed, W. S. Saric. Design of an Infinite-Swept-Wing Glove for an In-Flight DRE Experiment. AIAA Paper No. 2013-2411, 2013.

[201] C. Tropea, A. L. Yarin, J. F. Foss. Springer Handbook of Experimental Fluid Mechanics, Springer-Verlag, Berlin Heidelberg, 2007. Chap. 12.3: Boundary-Layer Stability and Transition.

[202] N. Lin, H. L. Reed, W. S. Saric. Effect of leading edge geometry on boundary-layer receptivity to freestream sound. Instability, Transition and Turbulence, edited by M. Y. Hussaini, A. Kumar, C. L. Streett, Springer-Verlag, New York, 1992, pp. 421-440.

[203] R. W. Wlezien. Measurement of acoustic receptivity. AIAA Paper No. 1994-2221, 1994.

[204] T. A. Buter, H. L. Reed. Boundary-layer receptivity to freestream vorticity. Physics of Fluids, Vol. 6, No. 10, 1994, pp. 3368-3379.

[205] L.-U. Schrader, L. Brandt, C. Mavriplis, D. S. Henningson. Receptivity to free-stream vorticity of flow past a flat plate with elliptic leading edge. Journal of Fluid Mechanics, Vol. 653, 2010, pp. 245-271.

[206] W. S. Saric, E. B. White, Influence of high-amplitude noise on boundary-layer transition to turbulence. AIAA Paper No. 1998-2645, 1998.

[207] G. Redeker, R. Mueller, A. Blanchard, J. Reneaux. Evaluation of Transonic Laminar Airfoil Tests Under Cryogenic Conditions Including Stability Analysis and Computational Results. Proc. 1st European Forum on Laminar Flow Technology,

Deutsche Gesellschaft für Luft- und Raumfahrt - Lilienthal-Oberth e.V., Bonn, Germany, Paper No. 92-01-019, 1992, pp. 141-151.

[208] M. Kruse, T. F. Wunderlich, L. A. Heinrich. A Conceptual Study of a Transonic NLF Transport Aircraft with Forward Swept Wings. AIAA Paper No. 2012-3208, 2012.

[209] U. Fey, Y. Egami, R. H. Engler. High Reynolds Number Transition Detection by Means of Temperature-Sensitive Paint. AIAA Paper No. 2006-0514, 2006.

[210] Mahr GmbH. Betriebsanleitung Perthometer S2. Göttingen, Germany, 2001.

[211] K. Asai, H. Kanda, T. Kunimasu, T. Liu, J. P. Sullivan. Boundary-Layer Transition Detection in a Cryogenic Wind Tunnel Using Luminescent Paint. Journal of Aircraft, Vol. 34, No. 1, 1997, pp. 34-42.

[212] T. Liu, J. P. Sullivan. Pressure- and Temperature-Sensitive Paints. Springer-Verlag, Berlin Heidelberg, 2005. Chap. 1: Introduction, and Chap. 2: Basic Photophysics.

[213] Y. Egami, C. Klein, U. Henne, M. Bruse, V. Ondrus, U. Beifuss. Development of a Highly Sensitive Temperature-Sensitive Paint for Measurements under Ambient (0 – 60 °C) Conditions. AIAA Paper No. 2009-1075, 2009.

[214] V. Ondrus, R. Meier, C. Klein, U. Henne, M. Schäferling, U. Beifuss. Europium 1,3-di(thienyl)propane-1,3-diones with outstanding properties for temperature sensing. Sensors and Actuators A: Physical, Vol. 233, 2015, pp. 434-441.

[215] T. Liu, J. P. Sullivan. Pressure- and Temperature-Sensitive Paints, Springer-Verlag, Berlin Heidelberg, 2005. Chap. 8: Time Response.

[216] S. Ohmi, H. Nagai, K. Asai, K. Nakakita. Effect of TSP Layer Thickness on Global Heat Transfer Measurement in Hypersonic Flow. AIAA Paper 2006-1048, 2006.

[217] U. Fey, R. H. Engler, Y. Egami, Y. Iijima, K. Asai, U. Jansen, J. Quest. Transition Detection by Temperature Sensitive Paint at Cryogenic Temperatures in the European Transonic Wind Tunnel (ETW). 20th International Congress on Instrumentation in Aerospace Simulation Facilities Record, IEEE, Piscataway, NJ, 2003, pp. 77-88.

[218] W. H. Beck, C. Klein, U. Henne, J. Martinez Schramm, A. Wagner, K. Hannemann, T. Gawehn, A. Gülhan. Application of Temperature and Pressure Sensitive Paints to DLR Hypersonic Facilities: “lessons learned”. AIAA Paper 2015-0023, 2015.

[219] R. E. Rayle. An investigation of the influence of orifice geometry on static pressure measurements. MSc thesis, Massachusetts Institute of Technology, Cambridge, MA, 1949

[220] R. Shaw. The influence of hole dimensions on static pressure measurements. Journal of Fluid Mechanics, Vol. 7, 1960, pp. 550-564.

[221] C. Klein, U. Henne, W. E. Sachs, U. Beifuss, V. Ondrus, M. Bruse, R. Lesjak, M. Löhr, A. Becher, J. Zhai. Combination of Temperature-Sensitive Paint (TSP) and Carbon Nanotubes (CNT) for Transition Detection. AIAA Paper No. 2015-1558, 2015.

[222] Keyence Corporation. Digital Microscope. VHX-2000 series. http://www.keyence.com/products/microscope/digital-microscope/vhx-2000/index.jsp. [Retrieved 16 02 15].

[223] W. E. Sachs. ToPas Source Code, Part 1 of 3: Design Principles and Basic Source Code. DLR Report IB-2007-C-22, 2007.

[224] W. E. Sachs. ToPas Source Code, Part 2 of 3: 2D Source Code. DLR Report IB-2007-C-23, 2007.

[225] W. E. Sachs. ToPas Source Code, Part 3 of 3: 3D Source Code. DLR Report IB-2007-C-24, 2007.

[226] F. Meyer, L. Kleiser. Numerical Investigation of Transition in 3D Boundary Layers. AGARD CP-438, 1989, pp. 16-1 to 16-17.

[227] J. H. M. Fransson, L. Brandt, A. Talamelli, C. Cossu. Experimental study of the stabilization of Tollmien-Schlichting waves by finite amplitude streaks. Physics of Fluids, Vol. 17, No. 5, 2005, pp. 054110-1 to 054110-15.

[228] H. Akima. A New Method of Interpolation and Smooth Curve Fitting Based on Local Procedures. Journal of the Association for Computing Machinery, Vol. 17, No. 4, 1970, pp. 589-602.

[229] J. B. Adcock, C. B. Johnson. A Theoretical Analysis of Simulated Transonic Boundary Layers in Cryogenic-Nitrogen Wind Tunnels. NASA TP 1631, 1980.

[230] B. Wagner. Boundary Layer Calculations for Cryogenic Wind Tunnel Flows. Recent Contributions to Fluid Mechanics, edited by W. Haase, Springer-Verlag, Berlin Heidelberg, 1982, pp. 283-293.

[231] G. Vogelpohl. Viscosität (Zähigkeit). Landolt-Börnstein: Zahlenwerte und Funktionen aus Physik, Chemie, Astronomie, Geophysik und Technik. 6th ed., Vol. 4: Technik, Part 1: Stoffwerte und mechanisches Verhalten von Nichtmetallen, edited by J. Bartels, P. ten Bruggencate, K.-H. Hellwege, K. Schäfer, E. Schmidt, Springer-Verlag, Berlin Göttingen Heidelberg, Chap. 42 2, 1955.

[232] H. L. Reed, P. Balakumar. Compressible boundary-layer stability theory. Phisics of Fluids A 2, Vol. 8, 1990, pp. 1341-1349.

[233] Private communication with S. Hucke, German-Dutch Wind Tunnels, 2010. Stefan.Hucke@dnw-germany.aero.

[234] J. A. Masad, M. R. Malik. Transition Correlation in Subsonic Flow over a Flat Plate. AIAA Journal, Vol. 31, No. 10, 1993, pp. 1953-1955.

[235] R. Narasimha. The laminar-turbulent transition zone in the boundary layer. Progress in Aerospace Sciences, Vol. 22, No. 1, 1985, pp. 29-80.

[236] S. Igarashi, H. Sasaki, M. Honda. Influence of Pressure Gradient upon Boundary Layer Stability and Transition. Acta Mechanica, Vol. 73, 1988, pp. 187-198.

[237] G. J. Walker, J. P. Gostelow. Effects of Adverse Pressure Gradients on the Nature and Length of Boundary Layer Transition. Journal of Turbomachinery, Vol. 112, No. 2, 1990, pp. 196-205.

[238] A. L. Braslow. Review of the Effect of Distributed Surface Roughness on Boundary-Layer Transition. NASA TM-79879, 1960.

[239] A. L. Braslow. A Review of Factors Affecting Boundary-Layer Transition. NASA TN-D-3384, 1966.

[240] J. A. Masad, M. R. Malik. Link Between Flow Separation and Transition Onset. AIAA Journal, Vol. 33, No. 5, 1995, pp. 882-887.

[241] S. A. Ragab, A. H. Nayfeh, R. C. Krishna. Stability of compressible boundary layers over a smooth backward-facing step. AIAA Paper No. 1990-1449, 1990.

[242] H. L. Dryden. Review of published data on the effect of roughness on transition from laminar to turbulent flow. Journal of the Aeronautical Sciences, Vol. 20, No. 7, 1953, pp. 477-482.

[243] A. M. O. Smith, D. W. Clutter. The Smallest Height of Roughness Capable of Affecting Boundary-Layer Transition. Journal of the Aerospace Sciences, Vol. 26, No. 4, 1959, pp. 229-245.

[244] A. M. O. Smith. A Discourse on Roughness, Turbulence and Noise and What Is Known About Their Effects on Transition. Part 1. Allowable Values of Discrete Roughness, Continuous Roughness and Waviness. Report DTN-7802-7A, Dynamics Technology, Inc., 1979.

[245] M. Costantini, S. Risius, C. Klein. Experimental Investigation of the Effect of Forward-Facing Steps on Boundary-Layer Transition. Procedia IUTAM, Vol. 14 C, Elsevier, Amsterdam, 2015, pp. 152-162.

[246] I. Tani. Effect of Two-Dimensional and Isolated Roughness on Laminar Flow. Boundary Layer and Flow Control, Vol. 2, edited by G. V. Lachmann, Pergamon Press, Oxford, UK, 1961, pp. 637-656.

[247] I. Tani, R. Hama, S. Mituisi. On the permissible roughness in the laminar boundary layer. Report No. 199, Aeronautical Research Institute, University of Tokyo, 1940.

[248] J. Stüper. The Influence of Surface Irregularities on Transition with Various Pressure Gradients. Report A 59, Division of Aeronautics, CSIR, Australia, 1949.

[249] E. G. Feindt. Untersuchungen über die Abhängigkeit des Umschlages laminar-turbulent von der Oberflächenrauhigkeit und der Druckverteilung. Jahrbuch der Schiffbautechnischen Gesellschaft, Vol. 50, 1956, pp. 180-203.

[250] M. Costantini, S. Risius, C. Klein, W. Kühn. Effect of forward-facing steps on boundary layer transition at a subsonic Mach number. New Results in Numerical and Experimental Fluid Mechanics X, edited by A. Dillmann, G. Heller, E. Krämer, C. Wagner, C. Breitsamter, Notes on Numerical Fluid Mechanics and Multidisciplinary Design, Vol. 132, Springer International Publishing, 2016, pp. 203-213.

[251] P. S. Klebanoff, W. G. Cleveland, K. D. Tidstrom. On the evolution of a turbulent boundary layer induced by a three-dimensional roughness element. Journal of Fluid Mechanics, Vol. 237, 1992, pp. 101-187.

[252] S. Goldstein. A note on roughness. ARC Reports and Memoranda No. 1763, 1936.

[253] A. Fage, J. H. Preston. On transition from laminar to turbulent flow in the boundary layer. Proceedings of the Royal Society of London A, Vol. 178, 1941, pp. 201-227.

[254] P. S. Klebanoff, G. B. Schubauer, K. D. Tidstrom. Measurements of the Effect of Two-Dimensional and Three-Dimensional Roughness Elements on Boundary-Layer Transition. Journal of the Aeronautical Sciences, Vol. 22, 1955, pp. 803-804.

[255] D. G. Mabey. A Summary of Effects of Heat Transfer in Aerodynamics and Possible Implications for Wind Tunnel Tests. AIAA Paper No. 1991-0401, 1991.

[256] J. W. Wetmore, J. A. Zalovcik, R. C. Platt. A Flight Investigation of the Boundary-Layer Characteristics and Profile Drag of the NACA 35-215 Laminar-Flow Airfoil at High Reynolds Numbers. NACA WR L-532, 1941.

[257] J. A. Zalovcik. A Profile-Drag Investigation in Flight on an Experimental Fighter-Type Airplane - The North American XP-51 (Air Corps Serial NO. 41-38). NACA ACR 245, 1942.

[258] J. A. Zalovcik. Profile-Drag Coefficients of Conventional and Low-Drag Airfoils as Obtained in Flight. NACA ACR L4E31, 1944.

[259] J. A. Zalovcik. Flight Investigation of Boundary-Layer and Profile Drag Characteristics of Smooth Wing Sections of a P-47D Airplane. NACA ACR L5H11a, 1945.

[260] R. H. Plascott. Profile Drag Measurements on Hurricane II Z.3687 Fitted with Low-Drag Section Wings. RAE Report No. Aero 2153, 1946.

[261] F. Smith, D. J. Higton. Flight Tests on King Cobra FZ.440 to Investigate the Practical Requirements for the Achievement of Low Profile Drag Coefficients on a "Low Drag" Aerofoil. ARC Reports and Memoranda No. 2375, 1950.

[262] B. M. Jones. Flight Experiments on the Boundary Layer. Journal of the Aeronautical Sciences, Vol. 5, No. 3, 1938, pp. 81-101.

[263] I. H. Abbott, A. E. Von Doenhoff, L. S. Stivers, Jr. Summary of Airfoil Data. NACA Report 824, 1945.

[264] A. D. Young, J. E. Serby, D. E. Morris. Flight Tests on the Effect of Surface Finish on Wing Drag. ARC Reports and Memoranda No. 2258, 1939.

[265] A. L. Braslow, F. Visconti. Investigation of Boundary-Layer Reynolds Number for Transition on an NACA $65_{(215)}$-114 Airfoil in the Langley Two-Dimensional Low-Turbulence Pressure Tunnel. NACA TN 1704, 1948.

[266] E. J. Richards. A Review of Aerodynamic Cleanness. Journal of the Royal Aeronautical Society, Vol. 54, 1950, pp. 137-186.

[267] A. L. Braslow, D. L. Burrows, N. Tetervin, F. Visconti. Experimental and Theoretical Studies of Area Suction for the Control of the Laminar Boundary Layer on an NACA 64A010 Airfoil. NACA Report 1025, 1951.

[268] M. R. Head, D. Johnson, M. Coxon. Flight Experiments on Boundary-Layer Control for Low Drag. ARC Reports and Memoranda No. 3025, 1955.

[269] L. K. Loftin, Jr., E. A. Horton. Experimental Investigation of Boundary-Layer Suction Through Slots To Obtain Extensive Laminar Boundary Layers on a 15-Percent-Thick Airfoil Section at High Reynolds Numbers. NACA RM L52D02, 1952.

[270] G. V. Lachmann. Laminarisation Through Boundary Layer Control. Proc. 4^{th} AGARD General Assembly. AGARD AG14/P5, 1954, pp. 108-127.

[271] B. Edwards. Laminar Flow Control - Concepts, Experiences, Speculations. AGARD R-654, 1977, pp. 4-1 to 4-41.

[272] W. Pfenninger, E. E. Groth, R. C. Whites, B. H. Carmichael, J. M. Atkinson. Note About Low Drag Boundary Layer Suction Experiments in Flight on a Wing Glove of a F94-A Airplane. Report No. NAI-54-849 (BLC-69), Northrop Aircraft, Inc., 1954.

[273] M. C. Fischer, A. S. Wright, Jr., R. D. Wagner. A flight test of laminar flow control leading-edge systems. AIAA Paper No. 1983-2508, 1983.

[274] M. Gaster. A simple device for preventing turbulent contamination on swept leading edges. Journal of the Royal Aeronautical Society, Vol. 69, 1965, pp. 788-789.

[275] J. Quest. ETW – High Quality Test Performance In Cryogenic Environment. AIAA Paper No. 2000-2206, 2000.

[276] H. Rosemann, E. Stanewsky, G. Hefer. The Cryogenic Ludwieg-Tube of DLR and its new adaptive wall test section. AIAA Paper No. 1995-2198, 1995.

[277] G. Schrauf. Transition Prediction Using Different Linear Stability Analysis Strategies. AIAA Paper No. 1994-1848, 1994.

[278] G. Schrauf. Evaluation of the A320 Hybrid Laminar Fin Experiment. Proc. ECCOMAS 2000, edited by E. Oñate, G. Bugeda, B. Suárez, Technical University of Catalonia, Barcelona, Spain, 2000.

[279] T. I. Aamodt, Characterization of ZnS:Cr films for Intermediate Band Solar Cells. MSc thesis, Norwegian University of Science and Technology, Trondheim, Norway, 2011.

[280] W. Nitsche, A. Brunn. Strömungsmesstechnik. 2nd ed., Springer-Verlag, Berlin Heidelberg, 2006. Chap. 4.4.1: Preston-Rohr-Verfahren.

[281] A. D. Reeh. Natural Laminar Flow Airfoil Behavior in Cruise Flight through Atmospheric Turbulence. PhD thesis, Technical University of Darmstadt, Germany, 2014.

[282] K. Richter, S. Koch A. D. Gardner, H. Mai, A. Klein, C. H. Rohardt. Experimental Investigation of Unsteady Transition on a Pitching Rotor Blade Airfoil. Journal of the American Helicopter Society, Vol. 59, No. 3, 2014, pp. 1-12.

[283] O. Burkhardt. Erprobung und Anwendung von Oberflächensensoren und Sensorarrays zur Erfassung instationärer Wandschubspannungen an Schaufelprofilen. PhD thesis, Technical University of Berlin, 2004.

[284] B. K. Crawford, G. T. Duncan, Jr., D. E. West, W. S. Saric. Laminar-Turbulent Boundary Layer Transition Imaging Using IR Thermography. Optics and Photonics Journal, Vol. 3, 2013, pp. 233-239.

[285] E. Schülein. Optical Skin Friction Measurements in Short-duration Facilities. AIAA Paper No. 2004-2115, 2004.

[286] C. J. Kähler, U. Scholz, J. Ortmanns. Wall-shear-stress and near-wall turbulence measurements up to single pixel resolution by means of long-distance micro-PIV. Experiments in Fluids, Vol. 41, No. 2, 2006, pp. 327-341.

[287] S. Scharnowski, R. Hain, C. J. Kähler. Reynolds stress estimation up to single-pixel resolution using PIV-measurements. Experiments in Fluids, Vol. 52, No. 4, 2012, pp. 985-1002.

[288] C. J. Kähler, S. Scharnowski, C. Cierpka. On the uncertainty of digital PIV and PTV near walls. Experiments in Fluids, Vol. 52, No. 6, 2012, pp. 1641-1656.

[289] C. Tropea, A. L. Yarin, J. F. Foss. Springer Handbook of Experimental Fluid Mechanics, Springer-Verlag, Berlin Heidelberg, 2007. Chap. 12.4: Measurements Considerations in Non-Canonical Flows.

[290] J. Czarske. Laser Doppler velocity profile sensor using a chromatic coding. Measurement Science and Technology, Vol. 12, 2001, pp. 52-57.

[291] Y. Egami, U. Fey, J. Quest. Development of New Two-Component TSP for Cryogenic Testing. AIAA Paper No. 2007-1062, 2007.

[292] C. Tropea, A. L. Yarin, J. F. Foss. Springer Handbook of Experimental Fluid Mechanics, Springer-Verlag, Berlin Heidelberg, 2007. Chap. 4.4: Pressure-Sensitive Paint (PSP).

[293] Sun Microsystems, Inc. mediaLib User's Manual. Part Number: 802-7799-06, Palo Alto, CA, 1989. Chap. 3.5: Advanced Processing Operations.

[294] Private communication with U. Henne, Institute of Aerodynamics and Flow Technology, Deutsches Zentrum für Luft- und Raumfahrt e.V. (DLR), Göttingen, 2010. Ulrich.Henne@dlr.de.

[295] H. Späht. Spline-Algorithmen zur Konstruktion glatter Kurven und Flächen. 3rd ed., R. Oldenbourg Verlag, Munich Wien, 1983. Chap. 6: Ausgleich mit kubischen Spline-Funktionen.

[296] M. C. Fischer. Spreading of a Turbulent Disturbance. AIAA Journal, Vol. 10, No. 7, 1972, pp. 957-959.

[297] J. P. Clark, P. J. Magari, T. V. Jones. On the Distribution of the Heat Transfer Coefficient in Turbulent and "Transitional" Wedges. International Journal of Heat and Fluid Flow, Vol. 14, No. 3, 1993, pp. 217-222.

[298] B. J. Holmes, C. J. Obara. Flight Research on Natural Laminar Flow Applications. Natural Laminar Flow and Laminar Flow Control, edited by R. W. Barnwell, M. Y. Hussaini, ICASE/NASA LaRC Series, Springer-Verlag, New York, 1992, pp. 73-142.

[299] U. Fey, Y. Egami, C. Klein. Using CryoTSP as a Tool for Transition Detection and Instability Examination at High Reynolds Numbers. New Results in Numerical and Experimental Fluid Mechanics VI, edited by C. Tropea, S. Jakirlic, H.-J. Heinemann, R. Henke, H. Hönlinger, Notes on Numerical Fluid Mechanics and Multidisciplinary Design, Vol. 96, Spinger-Verlag, Berlin Heidelberg, 2008, pp. 227-234.

[300] J. H. M. Fransson, A. Talamelli. On the generation of steady streamwise streaks in flat-plate boundary layers. Journal of Fluid Mechanics, No. 698, 2012, pp. 211-234.

[301] U. Walter. ETW User Guide. Revision A. ETW Report D/95001/A, 2004. https://www.etw.de/cms/uploads/pdfs/ETW_UserGuide.pdf. [Retrieved 03 02 15].

[302] A. E. Von Doenhoff, E. A. Horton. A Low-speed Experimental Investigation of the Effect of a Sandpaper Type of Roughness on Boundary-layer Transition. NACA Report 1349, 1958.

[303] Private communication with S. Hucke, German-Dutch Wind Tunnels, 2012. Stefan.Hucke@dnw-germany.aero.

[304] The MathWorks, Inc. Welch's power spectral density estimate. http://de.mathworks.com/help/signal/ref/pwelch.html. [Retrieved 18 06 15]

[305] E. Hering, R. Martin, M. Stohrer. Physik für Ingenieure. 4th ed., VDI Verlag, Düsseldorf, 1992. Chap. 7: Akustik.

[306] R. Parker, S. A. T. Stoneman. The Excitation and Consequences of Acoustic Resonances in Enclosed Fluid Flow Around Solid Bodies. Proceedings of the Institution of Mechanical Engineers, Part C: Journal of Mechanical Engineering Science, Vol. 203, 1989, pp. 9-19.

[307] M. C. Welsh, A. N. Stokes, R. Parker. Flow-resonant sound interaction in a duct containing a plate: Part I, semi-circular leading edge. Journal of Sound and Vibration, Vol. 95, No. 3, 1984, pp. 305-323.

[308] N. A. Cumpsty, D. S. Whitehead. The excitation of acoustic resonance by vortex shedding. Journal of Sound and Vibration, Vol. 18, No. 3, 1971, pp. 353-369.

[309] C. J. Wood. The effect of lateral vibration on vortex shedding from blunt based aerofoils. Journal of Sound and Vibration, Vol. 14, No. 1, 1971, pp. 91-102.

[310] T. F. Brooks, D. S. Pope, M. A. Marcolini. Airfoil Self-Noise and Prediction. NASA RP 1218, 1989.

[311] M. V. Lowson, S. P. Fiddes, E. C. Nash. Laminar Boundary Layer Aeroacoustic Instabilities. AIAA Paper No. 1994-0358, 1994.

[312] R. Parker, M. C. Welsh. Effect of sound on flow separation from blunt flat plates. International Journal of Heat and Fluid Flow, Vol. 4, No. 2, 1983, pp. 113-127.

[313] B. Plogmann, A. Herrig, W. Würz. Experimental investigations of a trailing edge noise feedback mechanism on a NACA 0012 airfoil. Experiments in Fluids, Vol. 54, No. 5, 2013, pp. 1480-1493.

[314] S. Deng, L. Jiang, C. Liu. DNS for flow separation control around an airfoil by pulsed jets. Computers and Fluids, Vol. 36, No. 6, 2007, pp. 1040-1060.

[315] L. E. Jones, R. D. Sandberg, N. D. Sandham. Stability and receptivity characteristics of a laminar separation bubble on an aerofoil. Journal of Fluid Mechanics, Vol. 648, 2010, pp. 257-296.

[316] R. A. Heinrich, M. Choudhari, E. J. Kerschen. A comparison of boundary layer receptivity mechanisms. AIAA Paper No. 1988-3758, 1988.

[317] M. Choudhari. Acoustic receptivity of compressible boundary layers: Receptivity via surface-temperature variations. NASA CR-4599, 1994.

[318] P. W. Hammerton, E. J. Kerschen. Boundary-layer receptivity for a parabolic leading edge. Journal of Fluid Mechanics, Vol. 310, 1996, pp. 243-267.

[319] D. Arnal, G. Casalis, J. Cousteix, J. Reneaux. Laminar-turbulent transition in subsonic boundary layers - Research and applications in France. AIAA Paper No. 1997-1905, 1997.

Nomenclature

Latin letters

a: one-quarter of waviness wavelength, major semi-axis of modified super-ellipse [m]

a, b, c: parameters used in Eq. (6.4.1)

A: disturbance amplitude [m/s]

AoA: angle-of-attack [°]

b: wing span, minor semi-axis of modified super-ellipse, gap width [m]

c: chord length [m], phase velocity [m/s]

c_f: skin-friction coefficient

c_p: pressure coefficient

d: model thickness, gap depth [m]

f: frequency [Hz]

g: TSP calibration function

h: step height, half amplitude of wave [m]

i: imaginary unit

I: luminescent intensity

k: roughness height [m], constant for wedge flow velocity distribution, TSP characteristic constant

k: exponent of power function $(T_w/T_{aw})^{-k}$

K: acceleration parameter $(\nu/U_e^2)(\mathrm{d}U_e/\mathrm{d}x)$

M: Mach number, based on freestream velocity and freestream speed of sound

M_e: Mach number at the boundary-layer edge, based on the local velocity and speed of sound

m: shape parameter of wedge flow, exponent for modified super-ellipse

N: amplification factor, i.e., natural logarithm of amplification ratio

p: pressure [Pa]

p, q, r: parameters used in Eq. (6.4.2)

Pr: Prandtl number, based on freestream dynamic viscosity, heat capacity, and heat conductivity

q: freestream dynamic pressure [Pa], generic flow quantity

Q: generic mean-flow quantity

r: recovery factor

R^*: specific gas constant [J/(kg·K)]

R_a: average roughness [m]

Re: Reynolds number, based on chord length, freestream velocity, and freestream kinematic viscosity

Re/c: unit Reynolds number, based on freestream velocity and freestream kinematic viscosity

Re_b: gap Reynolds number, based on gap width, freestream velocity, and freestream kinematic viscosity

Re_h: step Reynolds number, based on step height, freestream velocity, and freestream kinematic viscosity

Re_{ind}: Reynolds number, below which all modal boundary-layer disturbances are asymptotically stable

Re_k: Reynolds number, based on roughness height, flow velocity and fluid kinematic viscosity on top of the roughness element in absence of the roughness

Re_x: Reynolds number, based on streamwise location, freestream velocity, and freestream kinematic viscosity

Re_δ: Reynolds number, based on boundary-layer thickness, flow velocity and fluid kinematic viscosity at the boundary-layer edge

Re_θ: momentum thickness Reynolds number, based on boundary-layer momentum thickness, flow velocity and fluid kinematic viscosity at the boundary-layer edge

RS: TSP relative sensitivity [K^{-1}]

R_z: mean roughness depth [m]

S: constant temperature for Sutherland's law [K]

s: relative change in transition location $(x_T-x_h)/(x_{T,0}-x_h)$

s_N: relative change in transition N-factor $(N_T-N_h)/(N_{T,0}-N_h)$

St: Strouhal number, based on fluctuation frequency, maximal model thickness, and freestream velocity

t: time [s]

T: temperature [K]

Tu: turbulence level

u, v, w: velocity components in x-, y-, and z- direction [m/s]

u_τ: friction velocity [m/s]

U, V, W: mean-velocity components in *x*-, *y*-, and *z*- direction [m/s]

x: chordwise coordinate, positive starting from the model leading edge to the model trailing edge [m]

y: spanwise coordinate, positive starting from the model port side to the model starboard side [m]

z: wall-normal coordinate, positive upward [m]

z^+: non-dimensional wall-normal distance based on friction velocity and kinematic viscosity

Greek letters

α: streamwise wavenumber [m^{-1}]

β_H: Hartree parameter

γ: heat capacity ratio, intermittency factor

δ: boundary-layer thickness [m]

δ_1: boundary-layer displacement thickness [m]

δ_{99}: boundary-layer thickness at the distance from the wall corresponding to $U(\delta) = 99\ \%\ U_e$ [m]

Δ: difference, uncertainty

θ: boundary-layer momentum thickness [m]

λ: wavelength [m]

Λ: Pohlhausen parameter $(\delta_{99}^2/\nu)(\mathrm{d}U_e/\mathrm{d}x)$

μ: dynamic viscosity [Pa·s]

ν: kinematic viscosity [m^2/s]

ρ: density [kg/m^3]

τ: shear stress [Pa], shim thickness [m]

φ: sweep angle [°], amplitude function of primary mode

ψ: stream function [m^2/s]

ω: angular frequency [rad/s]

Subscripts

∞: freestream

I: Branch I location

II: Branch II location
0: total, smooth, initial
aw: adiabatic wall
b: gap location
c: charge
cr: critical
e: boundary-layer edge
em: emission
end: end of the transition region
ex: excitation
h: step location
HR: Helmholtz resonance
i: integer index, imaginary part of complex quantity
ind: indifferent stability
j, k: integer indices
max: maximum value
r: real part of complex quantity
ref: reference
start: start of the transition region
s: inflection point
T: transition
x: streamwise location
w: wall

Superscripts

’: fluctuating

Symbols

^: non-dimensional

Abbreviations

ALI: Attachment-Line Instabilities

CCD: Charge-Coupled Device

CFI: CrossFlow Instabilities

DLR: Deutsches Zentrum für Luft- und Raumfahrt e.V. (German Aerospace Center)

DNS: Direct Numerical Simulation

DNW: Deutsch Niederländische Windkanäle (German-Dutch Wind Tunnels)

ETW: European Transonic Windtunnel GmbH

GMF: Global Market Forecast

HLFC: Hybrid Laminar Flow Control

ICAO: International Civil Aviation Organization

IR: InfraRed

KRG: Kryo-Rohrwindkanal Göttingen (Cryogenic Ludwieg-Tube Göttingen)

LDA: Laser Doppler Anemometry

LED: Light-Emitting Diode

LES: Large Eddy Simulation

LF: Laminar Flow

LFC: Laminar Flow Control

LST: Linear Stability Theory

MSE: Modified Super-Ellipse

NACA: National Advisory Committee for Aeronautics

NLF: Natural Laminar Flow

ONERA: Office National d'Études et de Recherches Aérospatiales (French Aerospace Lab)

OSE: Orr-Sommerfeld Equation

PaLASTra: flat Plate for the Analysis of the effect on LAminar-turbulent transition of Surface imperfections, wall Temperature ratio and pressure gRAdient

PIV: Particle Image Velocimetry

PSE: Parabolized Stability Equations

PTV: Particle Tracking Velocimetry

RANS: Reynolds Averaged Navier-Stokes

rms: root mean square

RPK: Revenue Passenger-Kilometer

ToPas: Three-dimensional Optical Pressure Analysis System

TS: Tollmien-Schlichting

TSP: Temperature-Sensitive Paint